AD-A172 341 REPORT OF THE WORKING GROUP ON AERODYNAMICS OF AIRCRAFT AFTERBODY(U) ADVISORY GROUP FOR AEROSPACE RESEARCH AND DEVELOPMENT NEUILLY-SUR-SEINE (FRANCE) JUN 86 1/4

UNCLASSIFIED AGARD-AR-226 F/G 20/4 NL

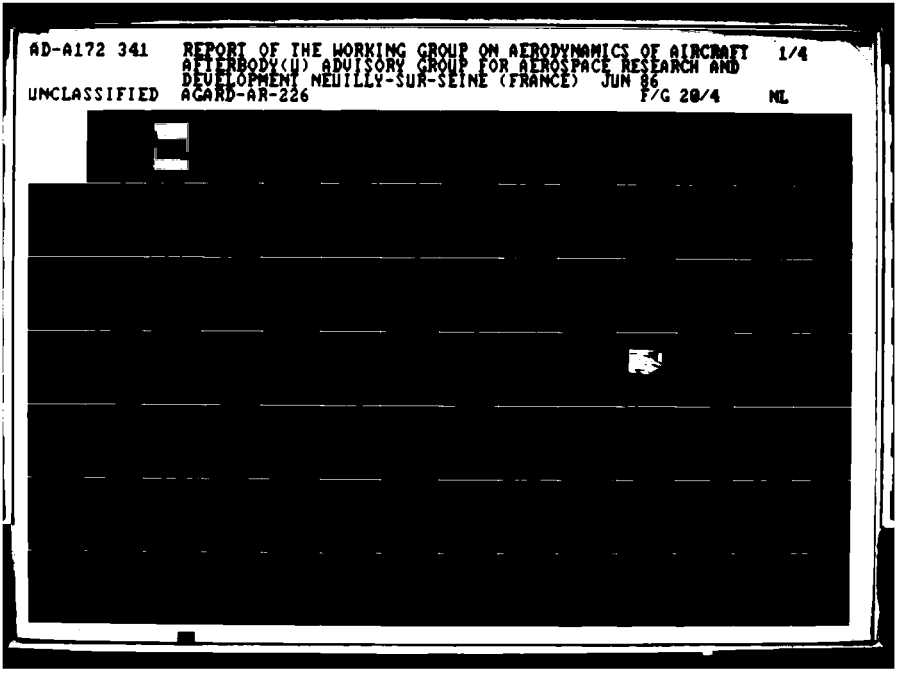

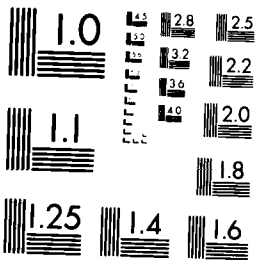

(2)

AGARD-AR-226

AGARD-AR-226

AGARD

ADVISORY GROUP FOR AEROSPACE RESEARCH & DEVELOPMENT

7 RUE ANCELLE 92200 NEUILLY SUR SEINE FRANCE

AGARD Advisory Report No.226

Report of the Working Group on Aerodynamics of Aircraft Afterbody

NORTH ATLANTIC TREATY ORGANIZATION

DISTRIBUTION AND AVAILABILITY
ON BACK COVER

NORTH ATLANTIC TREATY ORGANIZATION

ADVISORY GROUP FOR AEROSPACE RESEARCH AND DEVELOPMENT

(ORGANISATION DU TRAITE DE L'ATLANTIQUE NORD)

AGARD Advisory Report No.226

AERODYNAMICS OF AIRCRAFT AFTERBODY

Report of the Working Group on Aerodynamics of Aircraft Afterbody

This Advisory Report was prepared at the request of the Fluid Dynamics Panel of AGARD.

THE MISSION OF AGARD

The mission of AGARD is to bring together the leading personalities of the NATO nations in the fields of science and technology relating to aerospace for the following purposes:

- Exchanging of scientific and technical information;
- Continuously stimulating advances in the aerospace sciences relevant to strengthening the common defence posture;
- Improving the co-operation among member nations in aerospace research and development;
- Providing scientific and technical advice and assistance to the Military Committee in the field of aerospace research and development (with particular regard to its military application);
- Rendering scientific and technical assistance, as requested, to other NATO bodies and to member nations in connection with research and development problems in the aerospace field;
- Providing assistance to member nations for the purpose of increasing their scientific and technical potential;
- Recommending effective ways for the member nations to use their research and development capabilities for the common benefit of the NATO community.

The highest authority within AGARD is the National Delegates Board consisting of officially appointed senior representatives from each member nation. The mission of AGARD is carried out through the Panels which are composed of experts appointed by the National Delegates, the Consultant and Exchange Programme and the Aerospace Applications Studies Programme. The results of AGARD work are reported to the member nations and the NATO Authorities through the AGARD series of publications of which this is one.

Participation in AGARD activities is by invitation only and is normally limited to citizens of the NATO nations.

Published June 1986

ISBN 92-835-1533-1

Printed by Specialised Printing Services Limited
40 Chigwell Lane, Loughton, Essex IG10 3TZ

PREFACE

Aircraft afterbody design is still one of the most critical problems for industry, especially in fighter aircraft development. The flow around the rear part of the fuselage is characterized by the simultaneous occurrence of interfering physical phenomena such as thick turbulent boundary layers, viscous flow separation, hot jet interference at the base and the boat tail, and jet plume explanation in three-dimensional transonic and supersonic flow. Even experimental techniques hardly fulfill, at the present time, requirements for correct wind tunnel simulation of all effects.

During engineering work, drag prediction and drag minimization procedures for complex configurations are strongly dependent on the reliability of numerical and experimental flowfield simulation.

In recognition of this, the AGARD Fluid Dynamics Panel established the Working Group WG08 to evaluate the state-of-the-art in "Experimental and Computational Techniques for Aircraft Afterbodies".

The work followed by ten years the publication of AGARDograph 208 on "Improved Nozzle Testing Techniques in Transonic Flow", which was the first attempt within AGARD to handle the complicated subject and was organized by an Ad Hoc Group of the Propulsion and Energetics Panel.

The Working Group WG08 reports now on progress which has been made, both in experimental and numerical techniques since that time.

P.Sacher
Chairman, WG08

P.Carrière
Co-chairman, WG08

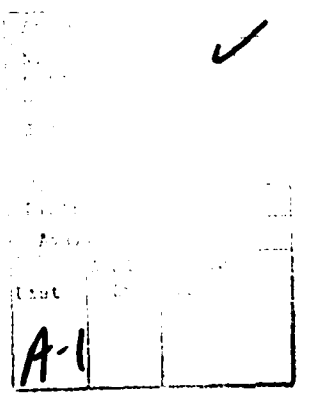

CONTENTS

*) The data relating to the Appendix have been prepared in the form of microfiche which accompany this publication.

NOMENCLATURE

Unless otherwise noted the following nomenclature has been used throughout this report

A	*cross-sectional area*
A_{MAX}	maximum cross-sectional area of body
A_{WING}	wing area
AIAA	American Institute of Aeronautics and Astronautics
AEDC	Arnold Engineering Development Center, Arnold Air Force Station, Tenn.
AFFDL	Air Force Flight Dynamics Laboratory, Wright-Patterson A.F.Base, Ohio now: AFWAL Air Force Wright Aeronautical Laboratories, Wright-Patterson AFB, Ohio
ASME	American Society of Mechanical Engeneers
AVA	Aerodynamische Versuchsanstalt, Göttingen
BMVg	Bundesminister der Verteidigung, West-Germany
C_A	afterbody axial force coefficient, $C_A = \frac{\text{axial force}}{q_\infty \cdot A_{MAX}}$
C_A^+	afterbody axial force coefficient, $C_A^+ = \frac{\text{axial force}}{q_\infty \cdot A_{WING}}$
C_D	drag coefficient, $C_D = \frac{\text{drag}}{q_\infty \cdot A_{MAX}}$
C_D^+	drag coefficient, $C_D^+ = \frac{\text{drag}}{q_\infty \cdot A_{WING}}$
C_{DF}	friction drag coefficient, $C_{DF} = \frac{\text{friction drag}}{q_\infty \cdot A_{MAX}}$
C_{DP}	pressure drag coefficient, $C_{DP} = \frac{\text{pressure drag}}{q_\infty \cdot A_{MAX}}$
C_{DT}	total drag coefficient, $C_{DT} = \frac{\text{pressure drag + friction drag}}{q_\infty \cdot A_{MAX}}$
C_p	pressure coefficient, $C_p = \frac{P-P_\infty}{q_\infty} = \frac{P-P_\infty}{\frac{\gamma}{2} P_\infty M_\infty^2}$
D	drag; maximum diameter of afterbody
DEA	Data Exchange Agreement AF 71 G 7425
DFVLR	Deutsche Forschungs- u. Versuchsanstalt für Luft- und Raumfahrt
DLR	Deutsche Luft- und Raumfahrt
drag build-up	$-\frac{1}{A_{max}} \int_{x_{BT}}^{x} C_p \left(\frac{dz}{dx}\right)_{BT} dx$ Shoulder
F	gross thrust
F_i	isentropic fully expanded gross thrust
F_N	net thrust (F or F_i minus free stream inlet momentum)
FFA	Flugtekniska Försökanstalten, The Aeronautical Research Institute of Sweden, Stockholm
ICAS	International Council of the Aeronautical Sciences (papers available from AIAA)

k	turbulent kinetic energy, $k = \frac{1}{2}(\overline{u'^2} + \overline{v'^2} + \overline{w'^2})$
	approximation $\overline{v'^2} = \frac{\overline{u'^2} + \overline{w'^2}}{2}$
L	length, reference length, afterbody length
M	local Mach-number
M_j	jet exit Mach-number
M_∞	free-stream Mach-number
MBB	Messerschmitt-Bölkow-Blohm GmbH, Postfach 801160, 8 München 80
NACA	National Advisory Committee for Aeronautics
NASA	National Aeronautics and Space Administration
NPR	nozzle pressure ratio, $NPR = P_{tj}/P_\infty$
ONERA	Office National d'Etudes et de Recherches Aerospatiales, BP 72, 92322 Chatillon Cédex, France
p	local static pressure
P_∞	free-stream static pressure
P_t	local total pressure, $P_t = P(1+\frac{\gamma-1}{2}M^2)^{\frac{\gamma}{\gamma-1}}$
P_{t_∞}	free stream total pressure
P_j	jet static pressure
P_{tj}	jet total pressure
P_{t_p}	pitot pressure
q	dynamic pressure, for perfect gas $q = \frac{\gamma}{2}pM^2$
q_∞	free stream dynamic pressure, for perfect gas $q_\infty = \frac{\gamma}{2}p_\infty M_\infty$
RAE	Royal Aircraft Establishment, UK
Re	Reynolds-Number, $Re = \frac{\rho_\infty U_\infty L}{\mu}$ L = body length, unless otherwise stated
T	local temperature (absolute)
T_∞	free-stream static temperature (absolute)
T_t	local total temperature (absolute), $T_t = T(1+\frac{\gamma-1}{2}M^2)$
T_{t_∞}	free stream total temperature (absolute)
T_{tj}	jet total temperature (absolute)
TU	Technische Universität
U, V, W	velocity components in x-, y-, z-direction
U_∞	free stream velocity
$-\overline{u'w'}$	Reynolds shear stress correlation ($\tau = -\rho\overline{u'w'}$)

VKI — von Karman Institute for Fluid Dynamics, Belgium

x, y, z — Cartesian coordinates

(for chapter 2:
- o free stream flow direction in positive x-direction from left to right
- o x-origin at jet exit
- o results plotted in x-z-plane)

x_{sep}, z_{sep} — separation location on boattail surface

ZAMM — Zeitschrift für Angewandte Mathematik und Mechanik

β — boattail angle

γ — specific heat ratio = 1.4

μ — dynamic viscosity

ρ — density

ρ_∞ — free stream density

τ_w — wall skin friction

for chapter 2: flow angle in x-z-plane, positive counter clockwise, zero for flow in positive x-direction

$\sigma(u)$ — rms of fluctuating velocity component u

$\sigma(w)$ — rms of fluctuating velocity component w

δ — boundary layer thickness

δ^* — boundary layer displacement thickness

θ — boundary layer momentum thickness

Additional indices for axial force and drag coefficients:

AB — afterbody = base + boattail = B+BT

B — base

BT — boattail

CB — complete body = forebody + afterbody = FB+AB

FB — forebody (may include wing)

Examples:

c_{DFBT} — boattail friction drag coefficient

c_{DPB} — base pressure drag coefficient

c_{DTAB} — afterbody total drag coefficient (boattail + base, pressure + friction)

Units of variables are m, kg, sec, kPa, °K, unless otherwise stated.

1. INTRODUCTION

1.1 Objectives and Scope of Work

In 1974 the AGARD Working group No. 4 presented the first results and findings of a multinational experimental programme on Improved Nozzle Testing Techniques in Transonic Flow. These efforts were organized by an Ad Hoc Group of the AGARD Propulsion and Energetics Panel (PEP) with support and cooperation of the Fluid Dynamics Panel (FDP).

Test results of the experimental programme on 3 types of axisymmetric afterbodies and analyses were reported in Agardograph 208 "Improved Nozzle Testing Techniques in Transonic Flow" in October 1975 (Ref. 1.5.1.) and in AGARD Advisory report No. 94 (Ref. 1.5.2.).

The above mentioned programme generated a large amount of experimental results, which provided an improved understanding of the phenomena concerning the afterbody/nozzle flow and moreover an insight into the shortcomings of afterbody testing techniques as applied in wind tunnels.

After WGO4 terminated its activities, many additional research programmes were performed in order to clarify the phenomena found in the multinational programme. Considerable effort has been devoted to improve wind tunnel testing techniques in order to establish better estimates of nozzle afterbody drag for the design of new military type aircraft. In addition, in recent years numerical methods for drag evaluation and prediction have considerably improved and, more specifically, many analytical models for predicting pressure distribution and drag of nozzle afterbodies in the transonic speed regime have been presented. These analytic methods make it possible to perform parametric studies and flow field analyses of the free-stream, jet flow and their interactions, difficult to obtain from wind tunnel experiments. The major advantage of applying these theoretical methods is that wind tunnel programmes can be better aimed to the specified goals.

Both activities on afterbody/nozzle aerodynamics are of utmost importance for performance and handling qualities of future military aircraft projects. In order to contribute to these efforts, a new working group on afterbody/nozzle aerodynamics was organized by the Fluid Dynamic Panel of AGARD in June 1982 with the support of the Propulsion and Energetics Panel.

The main goal of the working group was to critically review recent activities on afterbody/nozzle aerodynamics, nozzle integration and jet/airframe interference effects, addressing both the computational and experimental techniques.

Terms of reference (TOR) for the study were:

Computational methods

- o Assess status of inviscid flow methods including jet effects.
- o Assess status of solutions for afterbody flow computations including viscous effects (both jet/free stream mixing and boundary layer)
- o Assess status of solutions of the full or thin-layer parabolized Navier-Stokes equations.
- o Evaluate the critical range and accuracy of available methods with respect to afterbody drag prediction.

Experimental methods

- o Review afterbody testing and test results since 1975, with special attention to drag/thrust evaluation.
- o Evaluate progress in afterbody testing.
  - with conventional jet simulation
  - with TPS techniques
- o Analyse wind tunnel test techniques.
- o Summarize methods to detect flow instabilities and unsteady boundary-layer separation effects including afterbody buffeting.
- o Report on wind tunnel correction methods for afterbody tests.
- o Propose recommendations for future experimental investigations.

The work of the study group was performed by two subcommittees which dealt with the computational methods and the experimental testing technique respectively. The outcome of the studies is accordingly organized and discussed in the present report.

1.2 Group Members and Meetings

To carry out the ambitious work defined in the terms of reference a number of qualified aeronautical engineers were nominated by the national delegates of the Fluid Dynamics and Propulsion and Energetics Panel. These people involved came from universities, research institutes and from aircraft industry. For the first time experimental and theoretical specialists were brought together in an AGARD WG to work on the same subject.

The WG thus formed had the following members:

G. Besigk	MBB - Munich	Germany
N.C. Bissinger	MBB - Munich	Germany
D.L. Bowers	AFWAL - Wright Patterson	US
E.C. Carter	ARA - Bedford	UK
P. Carriere	ONERA - PARIS	France (FDP)
J. Delery	ONERA - Paris	France
J. Dunham	RAE - Pyestock	UK (PEP)
J.M. Hardy	SNECMA	France
J.A. Laughrey	AFWAL - Wright Patterson	US
B. Munniksma	NLR - Amsterdam	Netherlands
M. Onorato	Polytecnico di Torino	Italy (FDP)
F. Porrato	AIT - TURIN	Italy
B. Wagner	Dornier - Friedrichshafen	Germany
A. Zacharias	MBB - Munich	Greece(FDP)

The Group was chaired by

P. Sacher	MBB - Munich	Germany (FDP)

with the assistance of

L.E. Putnam	NASA - Langley	US

(Subcommittee A for Theoretical Methods)

F. Aulehla	MBB - Munich	Germany

(Subcommittee B for Experimental Methods)

In addition several invited specalists have contributed at different meetings:

M. Onofri	(IT/3rd meeting)
M. Pandolfi	(IT/3rd meeting)
L. Zannetti	(IT/3rd meeting)
J. Hodges	(UK/4th meeting)
T.W.F. Moore	(UK/4th meeting)
H.R. Radespiel	(US/5th meeting)

Five meetings were arranged to accomplish the tasks within the TOR:

21st/22nd June 1982 — first meeting in Paris

- discussion of TOR
- review of state of the art in different countries
- definition of test cases for theory.

23rd/24th Nov. 1982 — second meeting in Ottobrunn/Munich, Germany

- assignment for members in two subcommittees
- assignment of tasks
- setup of time-schedule

7th/8th June 1983 — third meeting in Turin, Italy

- preliminary results on test cases
- collection of experimental contributions
- setup of draft report format.

22nd/24th Nov. 1983 — fourth meeting in Bedford, U.K.

- Subcommittee A/presentation of results of test cases
- Subcommittee B/presentation of draft for final report
- discussion of proposals for final recommendations (subcommittees A and B).

19th/20th/21th June 1984 — fifth meeting at NASA - Langley, US

- agreement of draft manuscript
- Report organization and formalities

1.3 REPORT ORGANIZATION

1.3.1 Computational Methods

Chapter 2 of this report is concerned with the assessment of the capabilities of theoretical methods for predicting afterbody/nozzle aerodynamic flow characteristics. To accomplish this objective, a literature search was first conducted to determine methods which are being used or are being developed to predict such flows. (The result of this literature search is presented in Chapter 2.1.) From this review of the literature, it was apparent that in order to accomplish an assessment of the state-of-the-art in a reasonable time, the working group would have to limit the range of geometric and flow variables considered. Therefore, the assessment was limited to defining the capability of theoretical methods for predicting flow over axisymmetric nozzle/afterbody configurations at zero angle-of-attack. It is recognized by the working group that much work is underway, developing and using methods to predict propulsion system installation aerodynamics for complete aircraft and missiles. However, methods for predicting the flow over axisymmetric configurations have reached a high level of development. The working group, therefore, selected 13 test cases to be used for the assessment of computational results. (These test cases are described in Chapter 2.2.) The prime criteria for the selection of these test cases were the availability of extensive measurements of surface pressure, boundary layer, and flow field characteristics. All test cases selected had jet exhaust flow simulated by high-pressure air. Cases were selected to show the effects of nozzle geometry, nozzle pressure ratio, freestream Mach number, jet exhaust temperature, and tunnel blockage. Nozzles with both sharp lip and blunt bases at the nozzle exit were included.

Contributions were solicited from those theory developers previously identified during the literature search. Calculations of at least two or more of the test cases were received from 18 different contributors. The computation techniques varied in complexity from relatively simple multi component methods for blunt-base nozzles with supersonic jets in supersonic external flow, to solutions of the Navier-Stokes equations for both the sharp-lip and blunt-base test cases. Many contributors provided solutions from inviscid-viscous interaction methods for the sharp-lip transonic flow cases. Also, several contributors provided solutions based on the inviscid Euler equations for some of the test cases. Comparisons of the theoretical predictions with the experimental data are presented in Chapter 2.3. (Note that the experimental data for the test cases have been included on microfiche as part of this report). A detailed description of the theoretical methods used by the contributors and an evaluation of the prediction methods is given in Chapters 2.4 and 2.5. Conclusions and recommendations resulting from the analysis of theoretical results are provided in Chapter 2.6.

The different chapters in the theoretical part were written by the group members listed below. Consensus about the contents of these contributions was reached within the subcommittee.

Chapter 2.1	Survey on Afterbody Calculation Methods by Dr. N.C. Bissinger
Chapter 2.2	Description of Test Cases by Dr. J. Dunham and Dr.-Ing. A. Zacharias
Chapter 2.3	Compilation of Results by Dr. N.C. Bissinger
Chapter 2.4	Evaluation of Inviscid and Patched Calculation Methods by J. Delery
Chapter 2.5	Evaluation of Navier-Stokes Contributions by Dr. B. Wagner
Chapter 2.6	Conclusion and Recommendations by L.E. Putnam

1.3.2 Experimental Methods

Experimental testing techniques as applied in wind tunnel investigations on afterbody configurations is discussed in Chapter 3. This section includes information about the extent of aerodynamic losses attributed to the aircraft afterbody, the advanced jet simulation techniques, the state of the art of testing techniques in wind tunnels, afterbody flow instabilities and a consideration of errors and correction methods in wind tunnels.

In Chapter 3.1, the general considerations concerning the extent of afterbody drag changes, drag magnitudes and sensitivity to pressure integration are given, followed by a discussion of effects of engine spacing, nozzle interfairing and base area.

Chapter 3.2 deals mainly with experimental jet simulation techniques used in more recent investigations. Jet temperature effects, turbine powered simulators, ejectors and annular jet techniques are considered in detail.

Section 3.3 gives a state-of-the-art assessment of testing techniques for aircraft afterbody drag evaluation with special attention to force balance, surface pressure integration and model support interference.

Afterbody flow instabilities (Chapter 3.4) and a detailed analysis of errors and correction methods in wind tunnel and flight test (Chapter 3.5) are included and as a consequence, conclusions and recommendations for future work are given by the Subcommittee (Chapter 3.6).

In group B all members made contributions to all chapters. These contributions were edited by the group members listed below.

Chapter 3.1 General Considerations
by F. Aulehla

Chapter 3.2 Jet Simulation
by E.C. Carter

Chapter 3.3 State-of-the-Art Assessment of Testing Techniques for Aircraft Afterbodies
by D.L. Bowers

Chapter 3.4 Afterbody Flow Instabilities (Buffeting)
by G. Besigk and F. Porrato

Chapter 3.5 Error Analysis and Correction Methods for Afterbody Tests
by J.A. Laughrey

Chapter 3.6 Conclusions and Recommendations
by F. Aulehla

1.4 FUNDAMENTALS AND WG04 BACKGROUND (1974)

1.4.1 Fundamental and physical aspects of afterbody flow and jet plume interaction

Airframe/engine interference losses in terms of thrust minus drag result from the interaction between the inlet streamtube, the aircraft forebody and afterbody, nozzle and jet plume. To demonstrate the fundamental aspects governing these interactions, a simplified airframe/engine configuration is shown in the following figure.

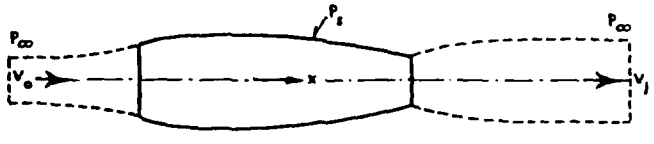

Fig. 1.4.1 Fundamental flow field single stream nacelle

The configuration is assumed to be axisymmetric with the axis parallel to the free stream.

In potential flow the sum of the pressure forces in flow direction acting on a control volume as shaped by the inlet stream tube, body and jet plume is zero. In addition, if there is no potential flow interaction between forebody and afterbody, sums of the pressure forces on the separate upstream and downstream part of the control volume are zero.

This conclusion provides a basis for identification of the interaction between the external flow field around the afterbody and the exhaust plume. Whereas the sum of the pressure forces is zero, the afterbody force must vary as a function of the degree of jet plume expansion outside the exhaust nozzle. Hence, the afterbody force includes the buoyancy term due to the jet plume. In order to derive the afterbody drag or incremental drag, afterbody forces have to be corrected for this buoyancy which is equal to the net external force exerted by the internal flow on the jet boundary.

In practice, however neither the internal nozzle flow model nor the complex jet exhaust flow model can be specified uniquely. As recommended in Ref. 1.5.3, where a comprehensive study on the fundamental aspects of engine/airframe interactions is given, an explicit bookkeeping system accounting for all airframe forces and engine thrust should be adopted.

The transonic afterbody/nozzle flow field is influenced by strong viscous/inviscid interactions as demonstrated in the following figure.

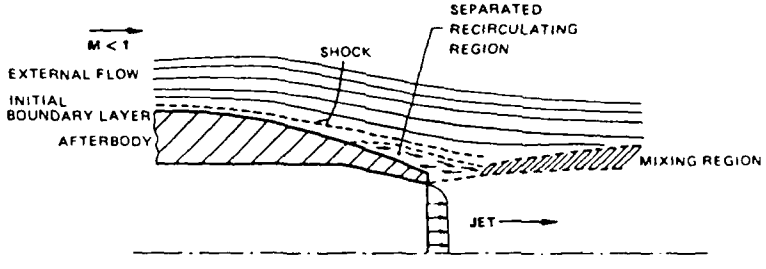

Fig. 1.4.2 Afterbody flow field

The complex flow field around the afterbody is characterized by shock waves, shock wave boundary layer interaction, and boundary layer/jet exhaust interactions coupled with boundary layer separations induced by steep boattails or underexpanded jet plume shapes. Furthermore, heat from the afterbody and nozzle is transferred to the surrounding flow, which destabilizes the boundary layer of the decelerating flow around the boattail.

Moreover, for highly integrated fighter aircraft the flow field is highly three dimensional. Mutual interactions are present between empennage, control surface, wing and afterbody. For close coupled intake/exhaust configurations, even the inlet flow has to be taken into account.

Hence, the flow at the back end of a fighter aircraft is very complex and the understanding of the flow physics involved is a must to investigate this afterbody flow utilizing both computational and experimental methods.

1.4.2 Impact of Afterbody Performance on Total Aircraft Drag

Optimum airframe/nozzle integration has become more important with fighter aircraft requiring variable geometry nozzles for operation with or without reheat over a broad range of Mach numbers. An indication of the magnitude of twin-jet afterbody drag related to the aircraft total drag is given in Fig. 1.4.3 (Ref. 1.5.4).

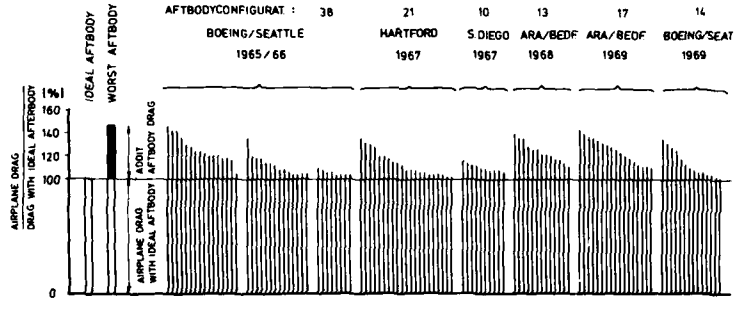

Fig. 1.4.3 Magnitude of Afterbody Drag

The reference configuration is an ideal slender afterbody with the same maximum cross section and equivalent nozzle size. Some configurations were tested in different facilities as indicated.

The drag of the worst configuration tested can amount to about 45 % above the value of the ideal configuration. This series of sequential tests show that aerodynamic improvement to a drag level close to the ideal afterbody configuration is possible.

Important parameters which have a significant influence on twin-jet afterbody drag include nozzle type, boattail angle, base area, nozzle spacing and type of interfairing. This subject will be discussed in Chapter 3.1. Here, only representative drag increments for different nozzle types are indicated in Fig. 1.4.4 (Ref. 1.5.4).

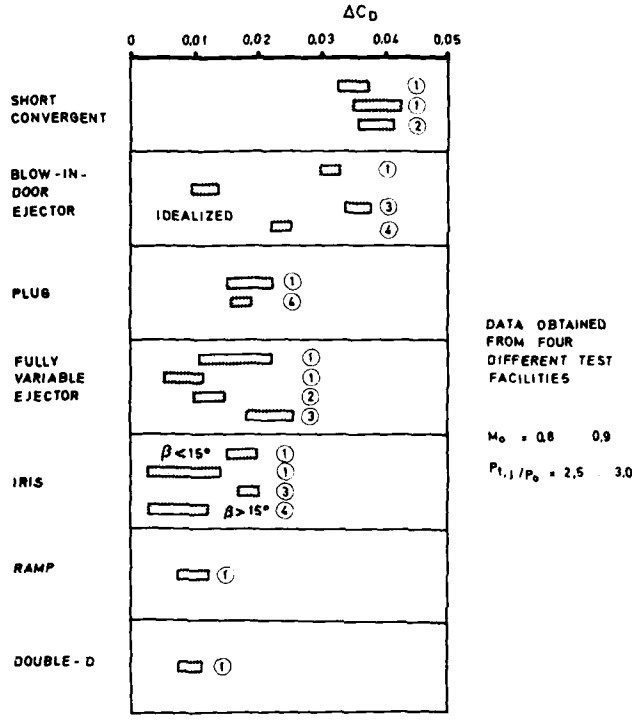

Fig. 1.4.4 Drag of Various Nozzle Concepts Obtained from Different Test Rigs

The model with the short convergent nozzles gives the highest drag increment $\Delta C_{Dmax} \approx 0.042$ (reduced according to fuselage frontal area) whereas a model with iris nozzle and boattail angles β=15° has the lowest drag increment of 0.020. The total variation in afterbody drag for nozzle types shown corresponds to approximately 20 % of the total drag of a typical twin-jet fighter at zero lift in the transonic flight regime.

From the described considerations it can be concluded that insight into the afterbody performance is of vital importance in an early stage of the development of a fighter aircraft.

Country	Establishment	Test section	$Re/_m$ at M = .9	Model arrangement	afterbody (A B) Nozzles	prime objectives	Parameters	Report Reference	Overall Analysis	Report Ref.
France	ONERA-SNECMA	400 x 400 mm perforated top and bottom walls 24% porosity	13×10^6	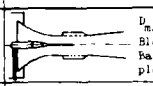 D_{max} 80,100,120 mm Blockage .7,1.1,1.6% Balance + pressure plotting	15° AGARD A B, AGARD nozzle for D_m = 80mm & self defined nozzles for D_{max} = 100 and 120 mm	- Boundary layer blowing - Tunnel blockage - Nozzle coefficients - A B drag	$0.6 \leq M_\infty \leq 0.95$ $1 \leq NPR \leq 5$ δ^*/D_{max}, two values	5	N P R effects on A B drag	13
Germany	DFVLR (Braunschweig)	500 mm diam. closed circular test section	13×10^6	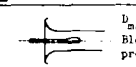 D_{max} 100 mm Blockage 4 % pressure plotting	self defined HFB AB and nozzle	- cold vs. hot jets - boundary layer control - A B drag	$0.2 \leq M_\infty \leq 0.6$ T_{tjet} = 290°K, 790°K $1 \leq NPR \leq 3$ δ^*/D_{max}, two values	6	Jet effects on A B drag	14
	DFVLR (Porz-Wahn)	640 mm diam. free jet	20×10^6	 D_{max} 67 mm Blockage 3.9 % pressure plotting	10°, 15°, 25° AGARD AB AGARD nozzle	- A B drag - jet spreading	$0.5 \leq M_\infty \leq 0.96$ $1 \leq NPR \leq 6.7$	7		
	MBB-DFVLR (Göttingen)	1000 x 1000 mm perforated walls 6 % porosity	$7\text{-}19 \times 10^6$	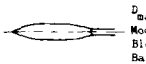 D_{max} 120 mm Modellength 800 mm Blockage 1.1 % Balance+pressure plotting	3 self defined A B No nozzle	- Re effects - A B drag related to forebody drag	$0.5 \leq M_\infty \leq 0.9$ $5 \leq ReLx10^6 \leq 15$	8		
Netherlands	N.L.R.	270 x 270 mm slotted top and bottom walls 11 % porosity	20×10^6	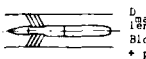 D_{max} 80mm Modellength 850,1200mm Blockage 7% Balance + pressure plotting	15° AGARD A B AGARD nozzle + self defined wide nozzle	- Boundary layer thickness, - cold vs. hot jet, - jet distortions, - nozzle coefficients, A B drag	$0.8 \leq M \leq 0.96$ $1 \leq NPR \leq 4.6$, δ^*/D_{max}, two values T_{tj} = 290°, 630°K 2 jet dist. levels	9	Effects on nozzle coefficients	15
United Kingdom	Rolls Royce	534 mm (across flats octagonal slotted walls) 11 % porosity	13×10^6	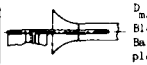 D_{max} = 101.6 mm Blockage 1.4 % Balance + pressure plotting	10°, 15°, 25° AGARD AB AGARD nozzle	- Boundary layer blowing - A B drag	$0.75 \leq M_\infty \leq 0.95$ $1.7 \leq NPR \leq 4.8$ δ^*/D_{max}, two values	10	Effects of A B geometry	16
U.S.A.	AEDC-PDL	4877 x 4877 mm perforated walls 6 % porosity	$3.3\text{-}17 \times 10^6$	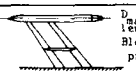 D_{max} 250.4 mm model length 3740 mm Blockage .7% pressure plotting	10°, 15°, 25° AGARD AB AGARD nozzle	- Re effects - A B drag - Tunnel blockage - model support - Hot - cold jets - theoretical analysis - wall porosity	$0.6 \leq M_\infty \leq 1.5$ $0.8 \leq Re_{D_{max}} \times 10^{-6} \leq 4$ $1 \leq NPR \leq 12$	11	Re effects on A B drag	17
				 D_{max} 39.1 mm model length 565 mm Blockage .02 % pressure plotting	15° AGARD AB AGARD nozzle		$0.8 \leq M_\infty \leq 0.95$ $.13 \leq Re_{D_{max}} x10^{-6} \leq .67$ NPR = 3		Tunnel environment effects on A B drag	18
	ARL-CFF	508 x 711 mm perforated walls 0 - 10 % porosity	$20\text{-}170 \times 10^6$	 D_{max} 39.1 mm model length 565 mm Blockage .32 % pressure plotting	15° AGARD AB AGARD nozzle		M_∞ = .8 $.78 \leq Re_{D_{max}} x10^{-6} \leq 6.6$			
				 D_{max} 76.2 mm model length 762 mm Blockage 1.1 % pressure plotting	10°, 15°, 25° AGARD AB no nozzle		M_∞ = .8 $1.5 \leq Re_{D_{max}} x10^{-6} \leq 13$ porosity 4%, 6%, 8%	12		
	NASA (Langley)	4877 mm (across flats octagonal slotted walls) 4 % porosity		 D_{max} 152.4 mm model length 1410 mm Blockage 0.1% Balance + pressure plotting	10°, 15°, 25° AGARD AB AGARD nozzle		$0.4 \leq M_\infty \leq 1.2$ $1 \leq NPR \leq 10$	11		

Fig. 1.4.5 Test set-up and test conditions, joint programme of AGARD Working Group No. 4 (Ref. 1.5.1).

1.4.3 Review on the PEP Working Group No.4, Improved Nozzle Testing Technique in Transonic Flow.

AGARD Working Group No. 4 initiated in 1972 a multinational programme on improved nozzle testing in which nine organisations from five nations participated. The joint programme of research was concentrated on the afterbody/nozzle testing technique in transonic wind tunnels. Objectives were:

- o to obtain a better understanding of the phenomena connected with the rather complex afterbody/nozzle flow
- o to study the merits of wind tunnel testing for prediction of afterbody nozzle performance

The defined programme was aimed at an experimental investigation of the external and internal aerodynamics of afterbody/nozzle configurations in the transonic speed regime. For a comparative study, three axisymmetric afterbody nozzle configurations were defined with boattail angles of 10°, 15° and 25° respectively, with the same closure and one internal convergent nozzle contour.

The tests covered the Mach number range of 0.6 to 0.95 and nozzle pressure ratios (NPR) of 1 to 7. Some participants of the programme extended the test range to Mach numbers up to 1.5 and a NPR of 15. A survey of the test set-ups and test conditions is given in Fig. 1.4.5.

The test results and analyses utilizing all available data from the programme were published in Ref. 1.5.1. The analyses included the following subjects:

- o The model and jet effects as influenced by geometry, Mach number, NPR, initial boundary layer, jet and model surface temperature and jet distortion.
- o The wind tunnel and support effects attributed to Reynolds number, wind tunnel wall interference, and buoyancy.

Furthermore, test results from models not directly representative of the defined configurations were discussed in order to add some critical information about the applied afterbody/nozzle test techniques.

The following sections will discuss briefly the conclusions and recommendations as presented by the various authors. Reference is made to the appropriate sections of the report (Ref. 1.5.1).

1.4.4 Analysis of effects of parameters

The results as obtained from test on the configurations by variation of NPR shows, in terms of boattail pressure force coefficient, C_{DP}, the following trends (see Fig. 1.4.6) for subsonic free stream Mach numbers.

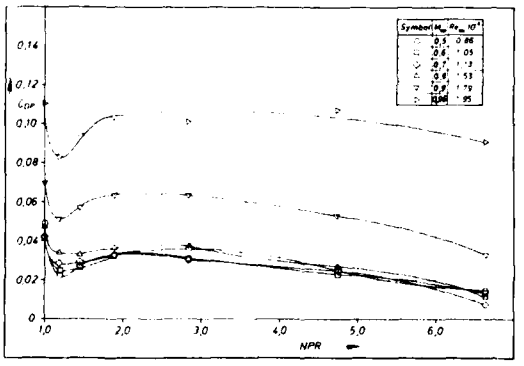

Fig. 1.4.6 Pressure Force coefficient as function of NPR

- o If NPR is increased from jet-off (NPR = 1), C_{Dp} drops initially and starts to rise between NPR = 1.25 → 2 up to a constant level comparable to the level of the jet-off condition.

- o For NPR larger than 3, where plume size increases due to the underexpanded jet, C_{Dp} decreases monotonously.

In Part II (sec. D) authors concluded, that for NPR > 3 the displacement effect of the plume dominates whereas at NPR 1.5 - 3 the effects from entrainment and displacement seems to be balanced.

From all collected data and other data from a wide range of geometries tested elsewhere, in Part II (sec. A), it was concluded that C_{Dp} and drag rise Mach number correlated quite well with the mean boattail chord angle. The boattail pressure force coefficient C_{Dp} increases and the drag rise Mach number decreases if the boattail angle is increased.

The observed jet temperature effects on C_{Dp} Part I (sec. C, E, G) and Part II (sec. D) appeared to be dependent on whether only the jet temperature was raised above the value of free stream or both the jet and model surface temperature were increased. The latter was the consequence of uncontrolled heat transfer from the hot jet gases to the model wall. The isolated jet temperature effect was explained from the larger initial jet plume angle of the hot jet relative to the cold jet, resulting in a more pronounced displacement effect and hence a higher pressure on the boattail. (Fig. 1.4.7)

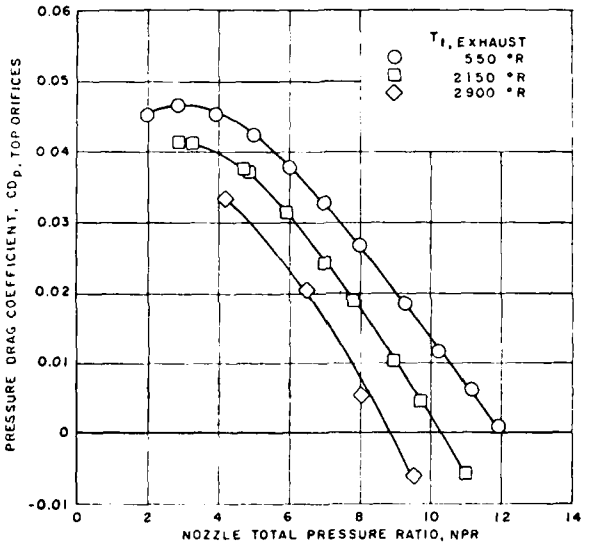

Fig. 1.4.7 Nozzle exhaust temperature effects on 15° boattail, Mach = 0.9

For models with both hot jet and hot model surface, only little effect on the boattail pressure distribution with respect to a cold jet was found. From these findings it was speculated, that heat transfer to the boundary layer surrounding the boattail might cause a marked decrease of the boattail pressure. (i.e. less pressure recovery on the boattail).

For the standard AGARD configuration, no distinct effect of jet distortion was found on the boattail pressure distribution, Part I (sec. E).

In Part I (sec. F) effects of varying Reynolds number and initial boundary layer displacement thickness on the boattail for the Mach range 0.8 - 0.95 were discussed. Variation of displacement thickness was obtained either from boundary layer blowing or changing the length of the model. From the results it was shown that:

- o For gentle boattail angles, the general trend was towards a slight decrease in C_{Dp} when the initial boundary layer thickness was increased. This effect was explained from the less effective curvature of the boattail as felt by the inviscid flow.

- o Results from steep boattails showed conflicting trends. Increase as well as decrease of C_{Dp} was noted dependent on Reynolds number.

1.4.5 Data scatter due to different testing techniques

Models were tested in seven wind tunnels with differences in support arrangement, blockage, buoyancy, wall type and the methods for the determination of reference free stream conditions (see Fig. 1.4-5).

From pressure distributions it was concluded, Part II (sec. E), that up to M = 0.95 there was very little difference in the flow over the shoulder (expansion region) for the various facilities. However, significant data variance appeared in the recompression region of the boattail. Obtained data showed variance in boattail pressure force coefficients, C_{DP}, from 0.010 to 0.026 at M = 0.8 and 0.017 to 0.065 at M = 0.9. Part I (sec. F), and Part II (sec. A, E and F) deal with the effects of the different wind tunnel testing techniques on the afterbody flow behaviour. In Part II (sec. E) blockage and buoyancy effects were considered using model and wind tunnel wall pressure distributions from analytical techniques. For high blockage it was found that wall interference increases the local flow Mach number in the region of the boattail close to the nozzle lip. With respect to the effect of buoyancy, originating from the downstream tunnel diffuser only a qualitive feeling was obtained. It was postulated, that diffuser back pressure creates a more adverse pressure gradient for the boattail flow to negotiate in the recompression region, thereby causing earlier flow separation.

A detailed analysis, Part II (sec. F) of the influence of Reynolds number (as achieved by altering the density in the wind tunnel) on complete body and part body indicated that part of the dependency of C_{DP} on Reynolds number was in fact due to small deviations in the free stream static pressure in the wind tunnel test section. A similar finding was noted in Part I (sec. G). As a result of this assessment, an additional calibration of the wind tunnel was performed in which Reynolds number was the primary variable.

To provide additional insight into the effects of support interference, Reynolds number and model fineness ratio, the experimental results were compared with those of analytical models. Some of the most important findings are listed below.

- o Inviscid flow calculations confirmed the observed pressure gradients on the model were caused by sting-strut support interference. The conclusion was drawn, that support interference must be a subject of major concern of wind tunnel test techniques, Part II (sec. F).

- o Variation in pressure distribution with Reynolds number was obtained with a viscous/inviscid strong interaction theory similar to that observed from experimental data, Part I (sec. F).

- o From inviscid flow calculations for bodies with different fineness ratio L/D_{max} it was indicated that the local Mach number ahead of the boattail is higher when L/D_{max} is decreased, Part II (sec. E).

- o In Part II (sec. F) results from calculations showed that geometric changes of the afterbody affect the flow over the forebody. Both findings lead to the conclusion that in studying the afterbody, the forebody has to be presented correctly and the metric/non-metric splitline has to be chosen very carefully.

1.4.6 Conclusions and recommendations (WG04 in 1976, see ref. 1.5.2)

It was generally concluded that the result of the efforts of the multinational programme was another step towards a more complete understanding of afterbody aerodynamics and that further experimental and computational efforts are required.

It was recommended to:

- o investigate the influence of exhaust temperature

- o refine and extend analytical procedures to cases with shock wave boundary layer interaction

- o develop the use of computational procedures to assess wind tunnel wall-interference

- o perform a refinement in wind tunnel calibrations.

1.5 References

1.5.1 Ferri, A.	Improved Nozzle Testing Techniques in Transonic Flow. AGARDograph No. 208 October 1975.
1.5.2 Jaarsma, F.	Improved Nozzle Testing Techniques in Transonic Flow. AGARD AR-94 (TER on PEP WG04), 1976.
1.5.3 MIDAP Study Group	Guide to in-flight Measurement of turbojets and fan engines. AGARDograph no. 237 January 1979.
1.5.4 Aulehla, F. and Lotter, K.	Nozzle/Airframe Interference and Integration AGARD-LS-53(4) 1974.
1.5.5 Brazier, M.E. and Ball, W.H.	Accounting of Aerodynamic Forces on Airframe/ Propulsion Systems. AGARD-CP-150(22) 1974.

1.6 ACKNOWLEDGEMENT

The chairman of this Working Group is pleased to acknowledge the support of the government agencies involved and of the managements of different institutions which have invited the members to the meeting in their country.

With that respect we have to thank specially M.Onorato from Politecnico di Torino and F.Porrato from AIT, A.B.Haines and E.C.Carter from ARA Bedford, L.E.Putnam from NASA-Langley and the management of MBB Military Fighter and Helicopters Division for the local arrangements and for providing the meeting rooms and perfect organization.

Finally we have benefited to a great extent from the effort of our Panel executive Bob Rollins, who gave us his advice and significant help during the lifetime of the Working Group.

2. COMPUTATIONAL METHODS

2.1 SURVEY ON AFTERBODY CALCULATION METHODS

2.1.1 INTRODUCTION

Many mathematical models for the calculation of afterbody flows have been presented in past years. A literature search of these models has been conducted. In the following sections, short descriptions of these calculations methods are presented, ordered according to the equations or models used to calculate jet-freestream-afterbody interactions. It is interesting to note that all methods calculate the flow around afterbodies at free flight conditions. Only one report on calculations addressing the very important problem of wall interference effects in windtunnels has been found. However, many of the methods could in principle be applied to afterbodies in closed wind tunnels.

2.1.2 NAVIER-STOKES EQUATIONS

Wherever Navier-Stokes equations are mentioned here, the Reynolds averaged Navier-Stokes equations are meant. This set of equations represents the conservation of mass, momentum and energy supplemented by two equations of state for a perfect gas. Turbulence modelling is needed to obtain the same number of equations as there are unknowns. Of the numerous turbulence models available the following have been applied in the references:

. Two-layer algebraic turbulence models
. Relaxation eddy viscosity model
. Constant eddy viscosity
. Patching of different models for different flow regimes.

Most of the references (Refs. 2.1.1 to 2.1.16) have not calculated the flow around afterbodies with a base. In some cases the actual afterbody geometry has to be modified, e.g. base corners have to be rounded, or the base has to be replaced by a thin, sharp trailing edge. Refs. 2.1.11 and 2.1.16 calculate the flow around afterbodies with jets without using any geometrical modifications.

2.1.3 THIN LAYER AND PARABOLIZED NAVIER-STOKES EQUATIONS

The Navier-Stokes equations can be approximated by the thin layer method. This method is based on assumptions similar to the boundary layer equations, i.e. streamwise diffusion terms are small compared with the normal diffusion terms. All viscous terms with gradients parallel to the body contour are neglected. In contrast to boundary layer theory, the normal momentum equation is not replaced by the assumption of zero pressure gradient.

For supersonic flows it is possible, by neglecting all time derivatives and the streamwise viscous diffusion terms and by modifying the streamwise convective flux vector, to make the equations parabolic in the streamwise coordinate. The modification of the streamwise convective flux vector is necessary because otherwise, in the subsonic flow close to body surface, the equations would not be parabolic in the streamwise direction. This modification has been done by several researchers by manipulating the pressure in the subsonic flow region. For example Schiff and Steger (Ref. 2.1.32) use the "Subsonic Layer Model" where the pressure gradient normal to the surface within a subsonic layer is zero, whereas Roberts and Forester (Ref. 2.1.33) decouple the streamwise and lateral plane pressure gradients and assume the streamwise pressure gradient to be constant in planes normal to the main stream. Both methods use a "boundary layer type" coordinate system and are valid for large Reynolds numbers only.

In Refs. 2.1.17 to 2.1.31 laminar and turbulent flows at subsonic and supersonic Mach numbers around two-dimensional or axisymmetric models are calculated. The models include isolated jets and afterbodies with or without jet or jet simulator. Small to moderate angles of attack are considered for axisymmetric bodies.

The relations for ideal gases with constant Prandtl-number are used in steady and unsteady flow calculations. For laminar flows the Sutherland formula is used. For turbulent flows two different turbulence models are applied:

. Two transport equations
. Two-layer eddy viscosity models.

To save computer time and storage, some authors use simpler methods for parts of the flow, e.g. around the forebody. The results of these calculations are used as input for the calculation of the afterbody flow. In Ref. 2.1.25 the flow downstream of the jet exit is divided into two overlapping zones: the inviscid freestream and the viscous jet regions. The flow in the inviscid region is calculated by a panel method, the flow in the

viscous region by the thin-layer Navier-Stokes equations. The overall solution is found by iteration where the solution of one zone is used as the boundary value for the calculation of the other zone.

2.1.4 PATCHED MODELS

2.1.4.1 INVISCID FLOW METHODS

In this approach the jet is considered as part of the afterbody and solutions are sought of the potential flow equation for the combined body (afterbody plus jet). Most often linearized "panel methods" are used (Refs. 2.1.34 to 2.1.40). In Refs. 2.1.42 and 2.1.43 a finite element method is applied to solve the incompressible potential equation. In Refs. 2.1.44 and 2.1.45 the flow is calculated from the full potential equation. Transonic small perturbation methods have also been used (Refs. 2.1.46 and 2.1.47).

The jet can be represented by a solid body or a wake (Ref. 2.1.41). Engine power effects are simulated by different jet shapes or by constant jet shapes with transpiration. Both the jet shape/or the amount of transpiration must be derived from either experimental data (Ref. 2.1 43) or from other calculation techniques, e.g. Navier-Stokes calculations (Ref. 2.1.45).

Which inviscid calculation method or exhaust jet model is being used depends on the complexity of the body geometry and the purpose of the calculations. For highly complex geometries, such as engine-pylon-wing-fuselage configurations (Ref. 2.1.41) or afterbody models in a windtunnel (Ref. 2.1.34), usually panel methods are applied. Engine nacelle-pylon-wing combinations have been treated by the solution of the full potential equation (Ref. 2.1.45)."Solid body" jets suffice for calculations for which the influence of the engine nacelle with jet onto other components, say the wing of a transport aircraft, is of interest. The "wake exhaust" model gives more information on the influence of fuselage or wing onto the afterbody/jet flow.

2.1.4.2 INVISCID/VISCOUS INTERACTION METHODS AND MULTI-COMPONENT MODELS

These methods simulate the flow around afterbodies by splitting the flow up into regions which can be calculated by existing methods or known solutions. The most common approach is to split the flow into an inviscid part and viscous regions, and to "patch" together the solutions by using various methods. Very often, empirical results for separation point and reattachment point location, geometry of separation region, and pressure and velocity destribution within the separation regions are needed to include their effects on afterbody flow. Strong interaction regions in the flow, e.g. shock/boundary layer interactions, are very difficult to model with these methods.

The two earliest methods were derived for supersonic flow about two-dimensional downstream facing steps. One of them, the theory of Crocco and Lees (Ref. 2.1.48), has never been extended to axisymmetric cases with jets. The second theory, closely connected with the names Chapman and Korst (for example Ref. 2.1.59), has been extended by Korst and several co-workers to axisymmetric afterbodies with a base and jet. Sirieix and Carrière at ONERA (e.g. Ref. 2.1.91 to 2.1.104) improved the empirical part of the theory by conducting relevant wind tunnel tests from which they derived a "recompression deflection angle criterion". Wind tunnel tests have been conducted for the same reason by White and Agrell at FFA (Ref. 2.1.81).

Addy (Ref. 2.1.69 and 2.1.70) wrote and published a computer program for the calculation of afterbody flows using this theory. At ONERA a modified method was derived based on the Chapman-Korst model (Refs. 2.1.91 and 2.1.104). This method takes into account mass and momentum injection into the base region as well as the effect of the approaching boundary layer by an "equivalent base bleed" concept. Based on this concept Wagner at Dornier (Refs. 2.1.83 and 2.1.85) investigated the effects of detail changes in the flow model of Addy. Both Wagner and White/Agrell (Ref. 2.1.84) extended their program version to flows around afterbodies at small angles of attack.

In Fig. 2.1.7.1 the flow phenomena that the flow model of Korst et al. attempts to describe as close as possible are depicted. Both the jet and the freestream flow are at supersonic Mach numbers. The assumptions, calculation methods, and empirical input that the Addy program uses are shown in Fig. 2.1.7.2. This program calculates the inviscid flow up to the confluence point with the help of irrotational characteristics. The two recompression shocks at the confluence point are determined by the requirement of common pressure and flow direction behind them. The mixing layers on each side of the separated base flow region are approximated by self-similar two-dimensional mixing layer velocity distributions. Mass and momentum conservation considerations, assumptions, or empirical data on the recompression of the flow through the confluence point make it possible to determine base pressure iteratively. Because energy conservation considerations are included, it is also possible to consider jets with total temperatures different from the freestream. Extensions, variations, and improvements of the flow model (Fig.2.1.7.3), have been tried by several authors (see Refs. 2.1.49 to 2.1.104).

Presz (Refs. 2.1.105 to 2.1.109) developed a patched method especially for axisymmetric afterbodies with jets or jet simulators which exhibit flow separation at subsonic freestream Mach numbers. He derived a control volume criterion for the separation point location. The shape of the discriminating streamline which separates the reverse flow region from the main flow is found by a momentum mass conservation approach.

Moulden/Wu (Refs. 2.1.110 to 2.1.113) developed a computer program for the calculation of the flow around various missile configurations (including jets) at transonic flight Mach numbers. The iso-energetic calculation of the afterbody/base/jet interference is very similar to the one of Korst, i.e. it is also restricted to purely supersonic flows. Several techniques are applied to calculate the inviscid flow around missile bodies from the transonic flow small perturbation equation. Thwaites' method (Ref. 2.114) is adopted for laminar boundary layers and Nash's technique (Ref. 2.1.115) is used for turbulent ones.

Tanner (Refs. 2.1.117 to 2.1.123) not only extended the two-dimensional Chapman-Korst model but developed methods of his own for the calculation of axisymmetric afterbody (without jet) base pressures at subsonic and supersonic Mach numbers. His ideas are based on the connection between the drag of a body and the increase in entropy of the flow across it derived by Oswatitsch. Using empirical data he is able to calculate drag for angles of attack up to 20 degrees at supersonic Mach numbers.

Grossman and Melnik (Ref. 2.1.124) apply a method for the calculation of the inviscid flow which is similar to the one used by South and Jameson. For the inviscid jet flow they solve the Euler equations, fitting imbedded shock waves and Mach disks. The inviscid plume shape is found by iteration, i.e. by calculating the pressure distribution on a guessed plume shape from the solution of the full potential equation for body and plume, and then by calculating a new plume shape from the pressure distribution until the plume shape or its surface pressures converge. The turbulent boundary layer on the body as well as the mixing layers on the jet plume are obtained by Green's Lag-Entrainment Method (Ref. 2.1.125). The plume surface is treated as a wake centerline with zero skin friction and, compared with the body boundary layer, a doubled turbulent length scale. In strong interaction regions on the body, e.g. near shock waves or corners, the boundary layer displacement thickness is replaced by a conic section to get a smooth effective body. Yaeger (Ref. 2.1.126) extended this flow model by adding a somewhat modified Presz's method (Ref. 2.1.108) for boundary layer separation on the afterbody.

Chow, Bober and Anderson (Ref. 2.1.127) couple a finite-difference analysis of the full transonic potential equation with the integral boundary-layer method of Sasman and Cresci (Ref. 2.1.128). Their model is an afterbody with a sting as a jet simulator. With the results of the inviscid flow as input, the displacement thickness of the boundary layer is calculated and an "effective body shape" constructed by adding this displacement thickness to the actual body geometry. By repeating these calculations the final pressure distribution can be found iteratively. Damping is required at higher free-stream Mach numbers. A modified version of this method has been applied to a blunt based projectile in Ref. 2.1.129.

The method of Cosner and Bower (Ref. 2.1.130) differs from that of Grossman, Melnik and Yaeger mainly by the method the turbulent boundary layer on the body and the mixing layer on the jet plume are calculated. Their integral procedure is an extension of the work of Bower (Ref. 2.1.131). The shape factor is bridged empirically around separation and reattachment point regions. The inviscid boundary of the plume is treated as a non-adiabatic moving wall and the boundary layer calculation is continued from the afterbody onto this wall. The iteration procedure needs "a significant amount of damping" to be stable.

By using conservation of mass considerations Yaros (Ref. 2.1.132) sought a correction to the inviscid plume shape due to entrainment effects. On the body the full potential equation (South-Jameson Transonic Program) is solved for the inviscid flow and a "fast" boundary layer program (Bartz program) is used to calculate the displacement thickness to be added to the body geometry. The shape of a jet within quiescent external flow calculated by the method of characteristics is the starting geometry for the plume shape . The final pressure distribution on the afterbody is found by calculating the inviscid flow about the effective body, i.e. actual body and inviscid jet plume geometry plus displacement thickness.

Ref. 2.1.142 presents what can be considered the final stage of a patched calculation method developed by several researchers, mainly Wilmoth, Dash, and Pergament (Refs. 2.1.133 to 2.1.143). The schematic flow field it describes is shown in Fig. 2.1.7.4 and is subdivided into the regions of Fig. 2.1.7.5. As in other patched methods, the inviscid external flow is calculated from the full potential equation by the South and Jameson method. (Ref. 2.1.144). The boundary layer on the afterbody is computed by the use of a modified Reshotko-Tucker integral solution (Ref. 2.1.145). The method of Presz as described above is used to simulate possible separation regions on the afterbody. The flow in the inviscid jet exhaust plume is found from Dash's (Ref. 2.1.146)

shock-capturing/shock- fitting solution of the Euler equations. For the calculation of the jet mixing layer the "overlaid" procedure of Dash and Pergament (Ref. 2.1.135) is applied. The iteration steps are similar to all other methods presented so far and include the inviscid flow calculations, determination of the displacement thickness of the boundary layer and mixing layer, and modification of body/jet geometry to form an effective body using an under-relaxation technique.

Kuhn (Refs. 2.1.147 and 2.1.148) employs the method of South and Jameson (Ref. 2.1.144) for the calculation of the inviscid flow over body and plume and a modified Henson-Robertson shock-expansion one-dimensional method (Ref. 2.1.149) or the method of characteristics for the inviscid jet flow. By applying an inverse integral boundary layer method at separation points he is able to iteratively determine separation location and separation bubble displacement thickness distribution. Also included in the flow model is the simulation of boundary layer separation due to shock interaction.

The approach by Dutouquet and Hardy (Refs. 2.1.150 and 2.1.151) determines the inviscid part of both the external and the nozzle flow through the solution of the stream function equation by a relaxation technique. The external boundary layer is computed by the finite difference method of Spalding-Patankar (Ref. 2.1.152). The nozzle boundary layer is neglected. Coupling of the inviscid flow with the boundary layer flow is performed through the correction of the body geometry by the boundary layer displacement thickness. For cases with boattail separation the pressure downstream of the separation point is assumed to be constant.

The "velocity splitting" method was used by Cosner in Refs. 2.1.153 to 2.1.155 to solve the steady state Navier-Stokes equations for the transonic external flow of afterbody and jet plume. In this approach the velocity vector is split into a potential part and a residual component, and the static pressure is defined as a function of the potential velocity part only. This approach reduces computation times considerably. Boundary layers, separation, and strong interaction regions on the body can be calculated directly. For axisymmetric afterbodies (Ref. 2.1.153) inviscid jet flow was calculated by the method of characteristics. The jet/freestream interaction was found iteratively by using the pressure distribution on the plume from the Navier-Stokes solution to derive a corrected plume shape and vice versa. In Ref. 2.1.154 examples with solid jet simulators only are presented.

In Ref. 2.1.156 Chima and Gerhart report on a patched method for the calculation of axisymmetric afterbodies with solid jet simulators at subsonic flight Mach numbers. With a finite element code they solve the coupled irrotationality and compressible continuity equations for the inviscid flow, the results of which they couple iteratively with a Sasman-Cresci type integral boundary layer code. Neither flow separation nor jet flows are considered.

In Ref. 2.1.157 Hodges presents a method for predicting the subsonic flow over axisymmetric afterbodies that patches together three sections of the flow. The method of characteristics for the calculation of the jet, a surface singularity method (Panel method) for the inviscid external flow and a lag-entrainment integral method for the boundary layer and mixing region are used. Simple models for separated flow regions and the entrainment of air are applied. An assessment of this method and the one of Ref.2.1.142 has been conducted in Ref. 2.1.159. Since then the method has been modified to handle jet temperature effects and blunt afterbody bases (Ref. 2.1.158).

Radespiel (Ref. 2.1.160) constructed a calculation method by coupling the solution of the Euler equations from the Streamtube Curvature algorithm (STC) (Ref. 2.1.161) with the solution for the boundary layer and free shear layer from the implicit marching procedure GENMIX (Ref. 2.1.162). For the free shear layer a k-ε-γ turbulence model has been found to be superior to a k-ϵ turbulence model (Ref. 2.1.163). The method is restricted to afterbodies without base and without flow separation. The nozzle pressure ratio should be less tnan three.

Most of the methods presented so far perform quite well for afterbody flows with weak viscous/inviscid interactions. In Ref. 2.1.164 Dash and Wolf extended the (weak interaction) SKIPPY code (Refs. 2.1.146 and 2.1.165) to flows with strong interactions by implementing a parabolized Navier-Stokes procedure for the jet. They also investigated the effects of three different turbulence models.

Ref. 2.1.166 (Kern, Hopcraft) reports on afterbody flow results obtained by coupling a two-dimensional Navier-Stokes solution for the jet with a potential flow analysis of the external flow. Steps towards a code that couples complex potential flow and/or Navier-Stokes codes to PANAIR (Ref. 2.1.167) are defined. The aim of this investigation is the calculation of the flow around closely coupled engine-nacelle/strut/wing configurations.

The method of Swanson, Rubin and Khosla (Ref. 2.1.168) is similar to that of Cosner (Ref. 2.1.153) in the use of the steady state Navier-Stokes equations. However, instead of the velocity splitting a multiplicative composite velocity is used. The original approach has been extended to transonic and turbulent flows and has been applied to axisymmetric afterbody configurations with solid jet simulators. The results in reverse flow regions differ from the measurements. Improvements in the turbulence model are supposed to reduce these differences.

In Ref. 2.1.169 (Boppe) a patched flow model that differs from others only in details is described. For subsonic/transonic external inviscid flow the Full-Potential equation is solved. A shock-fitting method for the solution of the Euler equations is applied to supersonic external inviscid flow. The displacement thickness of the afterbody boundary layer calculated from Green's lag-entrainment integral boundary layer method (Ref. 2.1.125) is added to the solid body. Local control volume analysis is used in determining separation point and reattachment point locations of recirculating flow regions. The Euler equations are solved for supersonic exhaust jet flow. Entrainment of external flow into the supersonic jet is accounted for by adding a displacement thickness to the jet boundary that corresponds to a fully developed turbulent mixing profile between two incompressible streams of different velocities. The merging of the upstream boundary layer and the jet mixing displacement surfaces is described as "smoothing".

Tinoco and Chen (Ref. 2.1.170) present a calculation method for transonic flow around isolated engine nacelles and an extension of the method in Ref. 2.1.44 for wing-body-strut-nacelle configurations. The flow around the isolated nacelle and in the jet is calculated by an Euler code (Ref. 2.1.201). A boundary layer calculation for the internal inlet and the external fan cowl is coupled to this code and the inviscid flow geometry is updated by the boundary layer displacement thickness during iteration cycles. The solid plume shape and the transpiration necessary to simulate engine power effects introduced in Ref. 2.1.44 for installed nacelles are calculated here from an axisymmetric Navier-Stokes code (Ref. 2.1.5).A boundary layer analysis is conducted on the wing only.

Reviews of many of the methods described above can also be found in Refs. 2.1.171 to 2.1.174.

2.1.5 EULER EQUATIONS

Solutions of the Euler equations can be used in multi-component models for flows with varying total pressure and temperature and for which rotational effects cannot be neglected. They can also be considered as "stepping stones" towards the solution of the full Navier-Stokes equations.

In all references both the freestream flow and the jet flow have been calculated by the Euler equations. Whereas Refs. 2.1.175 to 2.1.178 split the flow into domains, Refs. 2.1.179 to 2.1.182 consider the entire flow as one domain. The solutions are found by time-dependent computations using either a predictor-corrector scheme of MacCormack (Refs. 2.1.175 to 2.1.181) or a fourth order Runge-Kutta scheme (Ref. 2.1.182) for the time integration.

Although the results shown look quite realistic, there are still numerical problems to be solved. Artificial inviscid separation and questionable entropy production at stagnation points and in shock regions are two examples. In Ref. 2.1.182 these are assumed to depend on the boundary conditions and the numerical filtering used in that specific code.

2.1.6 REFERENCES

The following list of references naturally cannot be complete. An attempt was made, however, to collect the most fundamental papers on the topic. It should be noted that for some of the references quoted government permission may be needed for publication.References published up to the first quarter of 1984 have been surveyed.

References 2.1.183 to 2.1.203 primarily contain test data on afterbodies only. They are not quoted in the chapters above.

2.1.1	Holst T.L.	Numerical Solution of Axisymmetric Boattail Fields with Plume Simulators. AIAA-77-224
2.1.2	Forester C.K.	Numerical Simulation of the Interaction of Jet and Freestream Flows in Engine Exhaust Systems. AIAA-78-144
2.1.3	Mikhail A.G. Hankey W.L. Shang J.S.	Computation of a Supersonic Flow Past an Axisymmetric Nozzle Boattail with Jet Exhaust. AIAA Journal, Vol. 18, No. 8, Article No. 78-993R, pp. 869-875

2.1.4	Waskiewicz J.D. Shang J.S. Hankey W.L.	Numerical Simulation of Near Wakes Utilizing a Relaxation Turbulence Model. AIAA Journal, Vol. 18, No. 12, Article No. 79-0148R, pp. 1440-1445
2.1.5	Peery K.M. Forester C.K.	Numerical Simulation of Multistream Nozzle Flows. AIAA Journal, Vol. 18, No. 9, Article No. 79-1549R
2.1.6	Swanson R.C.	Numerical Solutions of the Navier-Stokes Equations for Transonic Afterbody Flows. NASA TP 1784, 1980
2.1.7	Cline M.C. Wilmoth R.G.	Computation of High Reynolds number Internal/External Flows. AIAA-81-1194
2.1.8	Jacocks J.L. Peters W.L. Guyton F.C.	Comparison of Computational and Experimental Jet Effects. AIAA-81-1492
2.1.9	Peery K.M. Russell D.L.	A Numerical Investigation of Exhaust Plume Temperature Effects on Nonaxisymmetric Nozzle/Aftbody Performance. AGARD CP-301, May 1981
2.1.10	Yoshikawa K.K. Wray A.A.	Steady and Nonsteady Supersonic Turbulent Afterbody Flow. NASA TP 1769, 1981
2.1.11	Hasen G.A.	Navier-Stokes solutions for an axisymmetric nozzle. AIAA-81-1474
2.1.12	Hasen G.A.	Navier-Stokes Solutions for Supersonic Coflowing Axisymmetric Nozzle with a Thick Base Annulus. Ph.D. Thesis, Air Force Institute of Technology AFIT/DS/AA/81-2
2.1.13	Deiwert G.S.	Numerical Simulation of High Reynolds Number Transonic Flows. AIAA-74-603
2.1.14	Jacocks J.L.	Computation of Axisymmetric Separated Nozzle-Afterbody Flow. AEDC-TR-79-71
2.1.15	Shrewsbury G.D Tassa Y.	Numerical Simulation of Transonic Flow About Isolated Afterbodies. AIAA-83-0498
2.1.16	Wagner B.	Estimation of Angle of Attack Effect by Component Analysis and Axisymmetric Navier-Stokes Solutions for Missile Afterbodies with Jet. A Symposium on Rocket/Plume Fluid Dynamic Interactions. 5-7 April, 1983, Huntsville. Ala., USA
2.1.17	Barton J.M. Birch S.F. Paynter G.C. Crouch R.W.	An experimental and numerical study of three-dimensional turbulent jets. AIAA-78-994
2.1.18	Hung C.M.	Numerical Solution of Supersonic Laminar Flow over an Inclined Body of Revolution. AIAA Journal, Vol. 18, No. 8, 1980, Article No. 79-1547R
2.1.19	Saheli F.P.	Experimental and Analytical Evaluation of Three-Dimensional Exhaust Plumes. AIAA-80-1399

2.1.20	Deiwert G.S.	Numerical Simulation of Three-Dimensional Boattail Afterbody Flowfields. AIAA Journal, Vol. 19, No. 5, 1981, Article No.80-1347R
2.1.21	Deiwert G.S.	A Computational Investigation of Supersonic Axisymmetric Flow Over Boattails Containing a Centered Propulsive Jet. AIAA-83-0462
2.1.22	Deiwert G.S. Rothmund H.	Three-Dimensional Flow Over a Concical Afterbody Containing a Centered Propulsive Jet: A Numerical Simulation. AIAA-83-1709
2.1.23	Fox. J.H.	Predicting Plume-Induced Separation on Bluff-Base Bodies. AIAA-84-0315
2.1.24	Sturek Mylin Heavy	Computational Study of the Flow Over Boattailed Shell at Supersonic Speeds. 6. DEA Meeting, April 1981,Göttingen
2.1.25	Roberts D.W.	Prediction of Subsonic Aircraft Flows with Jet Exhaust Interactions. AGARD CP-301, Toulouse, May 81
2.1.26	Swanson R.C.	Navier-Stokes Solutions for Nonaxisymmetric Nozzle Flows. AIAA-81-1217
2.1.27	Nietubicz C.J. Pulliam T.H. Steger J.L.	Numerical Solution of the Azimuthal-Invariant Thin-Layer Navier-Stokes Equations.AIAA-79-0010
2.1.28	Thomas P.D.	Numerical Method for Predicting Flow Characteristics and Performance of Nonaxisymmetric Nozzles - Theory. NASA CR-3147, 1979
2.1.29	Thomas P.D.	Numerical Method for Predicting Flow Characteristics and Performance of Nonaxisymmetric Nozzles Part 2 - Applications. NASA CR 3264, 1980
2.1.30	Vatsa V.N. Werle M.J. Anderson O.L. Hankins G.B.	Solutions for Three-Dimensional Over- or Underexpanded Exhaust Plumes. AIAA Journal Vol. 20, No. 9, 1982
2.1.31	Sahu J. Nietubitz C.J.	Numerical Computation of Base Flow for a Missile in the Presence of a Centered Jet. AIAA-84-0527
2.1.32	Schiff L.B. Steger J.L.	Numerical Simulation of Steady Supersonic Viscous Flow. AIAA Journal, Vol. 18, No. 12, 1980
2.1.33	Roberts D.W. Forester C.K.	Parabolic Procedure for Flows in Ducts with Arbitrary Cross Sections. AIAA Journal, Vol. 17, No. 1, 1979
2.1.34	Grün N.	Theoretische Untersuchungen zum Heckumströmungsproblem von Kampfflugzeugen und Vergleich mit experimentellen Ergebnissen. MBB/FE124/S/STY/39, 1982
2.1.35	Struck H. Klevenhusen K.D.	The Calculation of Flow Fields by Means of Panel Methods. Euromech Colloquium 1975, Braunschweig/Rhode, 1976
2.1.36	Haberland C. Göde E. Sauer G.	Calculation of the Flow Field around Engine-Wing-Configurations. ICAS-80-4.1

2.1.37	Klevenhusen K.D. Jakob H. Struck H.	Calculation of Wing-Body-Nacelle Interference in Subsonic and Transonic Potential Flow. AGARD-CP-301, 1981
2.1.38	Le Gall G. Bousquet J. Yermia M.	Une Methode Numerique Pour L'Etude De L'Intercation Nacell-Jet-Voilure En Ecoulement Tridimensionnel Non Visqueux. AGARD-CP-301, 1981
2.1.39	Voogt N. van Hentst J. v.d. Kolk J. Th.	Aerodynamic Aspects of High Bypass Ratio Engine Installation on a Fuselage Afterbody. AGARD-CP-301, 1981
2.1.40	Gillette W.B.	Nacelle Installation Analysis for Subsonic Transport Aircraft. AIAA-77-102
2.1.41	Chen A.W. Tinoco E.N.	PAN AIR Applications to Aero-Propulsion Integration. AIAA-83-1368
2.1.42	Zacharias A.	Experimentelle und theoretische Untersuchungen über die Wechselwirkung zwischen Triebwerksstrahl und dem umgebenden Strömungsfeld. Dissertation TU Braunschweig, 1981
2.1.43	Zacharias A.	An Experimental and Theoretical Investigation of the Interaction Between the Engine Jet and the Surrounding Flow Field with Regard to the Pressure Drag on Afterbodies. AGARD-CP 308, 1981
2.1.44	Yu N.J.	Transonic Flow Simulations for Complex Configurations with Surface Fitted Grids. AIAA-81-1258
2.1.45	Tinoco E.N. Chen A.W.	Transonic CFD Applications to Engine/Airframe Intergration. AIAA-84-0381
2.1.46	Golden D.P. Barber T.J. Chin W.C.	An Axisymmetric Nacelle and Turboprop Inlet Analysis with Flow-Through and Power Simulation Capabilities. AIAA-82-0256
2.1.47	Wai J.C. Yoshihara H. Abeyonnis W.K.	Transonic Perturbation Analysis of Wing-Fuselage-Nacelle-Pylon Configurations with Powered Jet Exhausts. AIAA-82-0255
2.1.48	Crocco L. Lees L.	A Mixing Theory for the Interaction Between Dissipative Flows and Nearly Isentropic Streams. J.Aero. Sci., Vol. 19, No. 10, Oct. 1952
2.1.49	Kirk F.N.	An Approximate Theory of Base Pressure in Two-Dimensional Flow at Supersonic Speeds. RAE Tech. Note Aero. 2377, 1954 (published 1959)
2.1.50	Nash J.F.	A Review of Research on Two-Dimensional Base Flow. Aero. Research Council R. & M. No. 3323, London, 1963
2.1.51	Nash J.F.	The Effect of an Initial Boundary Layer on the Development of a Turbulent Free Shear Layer. Aero. Research Council C.P. No. 682, London, 1963
2.1.52	Nash J.F.	An Analysis of Two-Dimensional Turbulent Base Flow, Including the Effect of the Approaching Boundary Layer. Aero. Research Council R. & M. No. 3344, London, 1963
2.1.53	Page R.H.	A Review of Component Analysis of Base Pressure for Supersonic Turbulent Flow. Proceedings 10th Int. Symp. Space Technology/Science, Tokyo 1973

2.1.54	Kessler T.J.	A Theory for Two-Dimensional Supersonic Turbulent Base Flows. AIAA-69-68
2.1.55	Roberts J.B.	On the Prediction of Base Pressure in Two-Dimensional Supersonic Turbulent Flow. Aero. Research Council R. & M. No. 3434, 1966
2.1.56	Chapman D.R.	An Analysis of Base Pressure at Supersonic Velocities and Comparison with Experiment. NACA Report 1051, 1950
2.1.57	Kurzweg H.H.	Interrelationship Between Boundary Layer and Base Pressure. J. Aero. Sci., 1951
2.1.58	Korst H.H. Page R.H. Childs M.E.	Compressible Two-Dimensional Jet Mixing at Constant Pressure. Univ. Illinois M.E.-TN-392-1, 1954
2.1.59	Korst H.H.	A Theory for Base Pressures in Transonic and Supersonic Flow. J. Applied Mechanics, 1956
2.1.60	Korst H.H Tripp W.	The Pressure on a Blunt Trailing Edge Separating Two Supersonic Two-Dimensional Air Streams of Different Mach Number and Stagnation Pressure but Identical Stagnation Temperature. Proc. 5th Midwestern Conf. of Fluid Mech., Univ. Michigan (1957)
2.1.61	Charwat A.F. Yakura J.K.	An Investigation of Two-Dimensional Supersonic Base Pressures. J. Aero Sci, Febr. 1958
2.1.62	Chapman D.R. Kuehn D.M. Larson H.K.	Investigation of Separated Flows in Supersonic and Subonic Streams with Emphasis on the Effect of Transition. NACA Report 1356, 1958
2.1.63	Chow W.L.	On the Base Pressure Resulting From the Interaction of a Supersonic External Stream With a Sonic or Subsonic Jet. J. Aero/Space Sci., March 1959
2.1.64	Korst H.H. Chow W.L.	Non-Isoenergetic Turbulent (Pr_t = 1) Jet Mixing Between Two Compressible Streams at Constant Pressure. NASA CR-419, 1966
2.1.65	White R.A.	Effect of Sudden Expansions or Compressions on the Turbulent Boundary Layer. AIAA Journal, Vol. 4, No. 12, 1966
2.1.66	Bauer R.C.	An Analysis of Two-Dimensional Laminar and Turbulent Compressible Mixing. AIAA Journal, Vol. 4, No. 3, 1966
2.1.67	Korst H.H.	Turbulent Separated Flows. VKI CN 66b, 1967
2.1.68	Page R.H. Hill W.G. Kessler T.J.	Reattachment of Two-Dimensional Supersonic Turbulent Flows. ASME 67-FE-20
2.1.69	Addy A.L.	Analysis of the Axisymmetric Base-Pressure and Base-Temperature Problem with Supersonic Interacting Freestream-Nozzle Flows Based on the Flow Model of Korst, et. al.-Part II. US Army RD-TR-69-13
2.1.70	Addy A.L.	Analysis of the Axisymmetric Base-Pressure and Base-Temperature Problem with Supersonic Interacting Freestream-Nozzle Flows Based on the Flow Model of Korst, et. al.-Part III. US Army RD-TR-69-14

2.1.71	Addy A.L.	Experimental-Theoretical Correlation of Supersonic Jet-on Base Pressure for Cylindrical Afterbodies. J. Aircraft, Vol. 7, No. 5, 1970
2.1.72	Dixon R.J. Richardson J.M. Page R.H.	Turbulent Base Flow on an Axisymmetric Body with a Single Exhaust Jet. J. Spacecraft, Vol. 7, No. 7, 1970
2.1.73	Korst H.H. Chow W.L.	On the Correlation of Analytical and Experimental Free Shear Layer Similarity Profiles by Spread Rate Parameters. Basic Engineering, Sept. 1971
2.1.74	White R.A.	Optimum Afterbody Considerations For Supersonic Flow With A Centered Propulsive Nozzle Including The Effects of Flow Separation. FFA Report AU-863, 1971
2.1.75	Addy A.L. White R.A.	Optimization of Drag Minimums Including Effects of Flow Separation. ASME Paper No. 72-WA/Aero-1, 1972
2.1.76	Addy A.L. Korst H.H. White R.A. Walker B.J.	A Study of Flow Separation in the Base Region and its Effects during Powered Flight. AGARD CP-124 (1973)
2.1.77	Schmidt W.R. Herpfer E.	Zusammenstellung experimenteller Unterlagen zum Heckwiderstand von Flugkörpern im Transschall- und im Überschallbereich und Vergleich mit theoretischen Berechnungsmethoden. BMVg-FBWT 73-27 (1973); Dornier System
2.1.78	White R.A. Addy A.L. Agrell J.	An Improved Experimental-Theoretical Base Pressure Correlation for Conical and Cylindrical Afterbodies with Centered Propulsive Nozzle. Proceedings 10th Int. Symp. Space Techn./Sci., Tokyo 1973
2.1.79	Gerhart P.M. Korst H.H.	On the Free Shear Layer Downstream of a Backstep in Supersonic Flow. ASME Paper No. 73-FE-3, 1973
2.1.80	White R.A.	The Calculation of Supersonic Axisymmetric Afterbody Flow with Jet-Interference and Possible Flow Separation. FFA TN-AU-912, 1974
2.1.81	Agrell J. White R.A.	An Experimental Investigation of Supersonic Axisymmetric Flow over Boattails Containing a Centered Propulsive Jet. FFA TN-AU-913, 1974
2.1.82	Chow W.L. Spring D.J.	Viscous Interaction of Flow Redevelopment after Flow Reattachment with Supersonic External Streams. AIAA Journal, Vol. 13, No. 12, 1975
2.1.83	Wagner B.	Untersuchungen zum Heckwiderstandsproblem an eingezogenen Hecks mit Treibstrahl. Dornier Bericht 76/56B; BMVg-Vertrag Nr. T/RF42/RF420/51120, 1976
2.1.84	White R. Agrell J.	Boattail and Base Pressure Prediction Including Flow Separation for Afterbodies with a Centered Propulsive Jet and Supersonic External Flow at Small Angles of Attack. AIAA-77-958
2.1.85	Wagner B.	Untersuchung des Treibstrahleinflusses auf die Strömungsverhältnisse am Flugkörperheck. Dornier Bericht 78/21B; BMVg-Vertrag Nr. T/RF42/70016/71415, 1978
2.1.86	Weng C.H.	Axisymmetric Supersonic Turbulent Base Pressures. AIAA Journal, Vol. 16, No. 6, 1978

2.1.87	Wagner B.	Flow Predictions for the Supersonic Jet-Afterbody Interference Problem. DEA Meeting, Meersburg, 1979
2.1.88	Schetz J.A. Billig F.S. Favin S.	Approximate Analysis of Axisymmetric Supersonic Base Flows with Injection. AIAA Journal, Vol. 18, No. 8, 1980
2.1.89	Wagner B. White R.A.	Supersonic Base Flow Problem in Presence of an Exhaust Jet. AIAA Journal, Vol. 18, No. 8, 1980
2.1.90	Wagner B.	Jet-Afterbody Interference on Missiles in Supersonic Flow. AGARD CP 307, London 1981
2.1.91	Sirieix M. Mirande J. Délery J.	Experiences Fondamentales Sur Le Recollement Turbulent D'Un Jet Supersonic. AGARD-CP4, 1966
2.1.92	Carrière P.	Effet d'une Injection de Fluide dans l'Eau-Morte sur les Conditions de Recollement d'un Ecoulement Plan Supersonique. Comptes Rendus de l'Académie des Sciences de Paris, t. 251, pp. 2877-2879 (1960)
2.1.93	Carrière P. Sirieix M.	Facteurs d'Influence du Recollement d'un Ecoulement Supersonique. 10th International Congress of Applied Mechanics, Stresa, Italy (1960)
2.1.94	Sirieix M. Solignac J.L.	Contribution à l'Etude Experimentale de la Couche de Mélange Isobare d'Un Ecoulement Supersonique. AGARD-CP-4 (1966)
2.1.95	Sirieix M. Délery J. Mirande J.	Recherches Expérimentales Fondamentales Sur Les Écoulements Séparés Et Applications. ONERA TP No. 520 (1967)
2.1.96	Carrière P.	Effets de L'Écoulement Interne Sur Le Comportement Aérodynamique D'Un Avion a Réaction. ICAS Paper No. 68-03
2.1.97	Carrière P.	Analyse Théorique du Décollement et du Recollement Turbulent au Bord de Fuite d'un Aubage aux Vitesses Supersoniques. Symposium on "Flow Research on Blading", Brown-Bovery Company, Baden, Switzerland (1969)
2.1.98	Carrière P.	Apercu De Quelques Résultats Nouveaux Obtenus A L'O.N.E.R.A. Sur Les Phénomènes De Décollement Et De Recollement. ONERA TP No. 1072 (1972)
2.1.99	Solignac J.L. Délery J.	Contribution à l'Etude Aérodynamique des Systèmes Propulsifs à Double Flux. Israel Journal of Technology, Vol. 10, No. 1-2, pp. 97-111 (1972) and ONERA TP 1050, 1972
2.1.100	Carrière P.	Aperçu de quelques résultats nouveaux obtenus à l'ONERA sur les phénomènes de décollement et de recollement. ZAMM 53, T3-T14 (1973)
2.1.101	Carrière P. Sirieix M. Délery J.	Methods De Calcul Des Ecoulements Turbulents Decolles En Supersonique. Prog. Aerospace Sci., Vol. 16, No. 4, 1975
2.1.102	Délery J. Sirieix M.	Ecoulements de Culot. AGARD LS98, 1979

2.1.103	Sirieix M.	Pression De Culot Et Processus De Mélange Turbulent En Ecoulement Supersonique Plan. La Recherche Aeronautique No. 78/1980
2.1.104	Délery J.	ONERA Research on Afterbody Viscous/Inviscid Interactions with Special Emphasis on Base Flow Problems. Symposium on "Rocket/Plume Fluid Dynamics Interactions", Huntsville, Alabama, 5-7 April, 1983 and ONERA TP 1983-26
2.1.105	Presz W. Konarski M. Grund E.	Prediction of Installed Nozzle Flowfields. J. Aircraft, Vol. 8, No. 12, 1971
2.1.106	Presz W.M.	Turbulent Boundary Layer Separation on Axisymmentric Afterbodies. Ph.D. Thesis, Univ. of Connecticut, 1974
2.1.107	Presz W.M. Pitkin E.T.	Flow Separation over Axisymmetric Afterbody Models. J. Aircraft, Vol. 11, No. 11, 1974
2.1.108	Presz W.M. Pitkin E.T.	Analytical Model of Axisymmetric Afterbody Flow Separation. J. Aircraft, Vol. 13, No. 7, 1976
2.1.109	Presz W.M. King R.W. Buteau J.D.	An Improved Analytical Model of the Separation Region on Boattail Nozzles at Subsonic Speeds. NASA CR 3028, 1978
2.1.110	Wu J-M. Aoyama K. Moulden T.H.	Transonic Flow Fields Around Various Bodies of Revolution Including Preliminary Studies on Viscous Effects with and without Plume. US Army Missile Command Report RD-TR-71-12, 1971
2.1.111	Wu J-M. Moulden T.H. Uchiyama N.	Aerodynamic Performance of Missile Configurations at Transonic Speeds Including the Effects of a Jet Plume. US Army Missile Command Report RD-76-23, 1976
2.1.112	Moulden T.H.	U.S. MICOM-UTSI Computer Program for Plume-Induced Separation at Transonic Speeds, Version 2: June 1979. University of Tennessee Space Institute, 1979
2.1.113	Moulden T.H.	Guide to the Operation of the MICOM/UTSI Computer Program for Plume Induced Separation at Transonic Speeds: Version 2, June 1979. U.S. Army Missile Command, Redstone Aresenal, Alabama TR-RD-CR-81-2, July 1980
2.1.114	Thwaites B.	Approximate Calculation of the Laminar Boundary Layer. Aero Quarterly, Volume 1, 1949, p. 245.
2.1.115	Nash J.F.	A Practical Calculation Method for Compressible Turbulent Boundary-Layers in Two-Dimensional Flows. Lockheed Georgia Research Memo, ER 9428, 1976.
2.1.116	Tanner M.	Ein Beitrag zur Theorie der kompressiblen abgelösten Strömung um Keile. DLR-FB 72-57 (1972)
2.1.117	Tanner M.	Theoretical Prediction of Base Pressure for Steady Base Flow. Progress in Aerospace Sciences, Vol. 14 (1973) Pergamon Press
2.1.118	Tanner M.	Theoretische Bestimmung des Basisdruckes bei zweidimensionaler Überschallströmung. DFVLR-AVA Bericht TB 251-75 A05 (1975)

2.1.119	Tanner M.	Eine Theorie zur Bestimmung des Basisdruckes bei rotationssymmetrischer Überschallanströmung. DFVLR-AVA-Bericht IB 251-75 A20 (1975)
2.1.120	Tanner M.	Einfluß der Grenzschichtdicke auf den Basisdruck bei zweidimensionaler und rotationssymmetrischer Überschallströmung. DRL-FB 76-43 (1976)
2.1.121	Tanner M.	Zur theoretischen Bestimmung des Basisdruckes von angestellten rotationssymmetrischen Rümpfen. DFVLR-AVA-Bericht IB 251-76 A21 (1976)
2.1.122	Tanner M.	Theoretische Bestimmung des Basisdruckes von Flugkörperrümpfen mit turbulentem Totwasser bei Überschallgeschwindigkeiten. DFVLR-FB80-29, 1980
2.1.123	Tanner M.	Bestimmung des Basisdrucks von Flugkörpern bei Unterschallgeschwindigkeiten mittels einer empirischen Formel. Z. Flugwiss. Weltraumforsch. 5 (1981), Heft 4
2.1.124	Grossman B. Melnik R.E.	The Numerical Computation of the Transonic Flow over Afterbodies Including the Effect of Jet-Plume and Viscous Interactions. AIAA-75-62
2.1.125	Green J.E. Weeks D.J. Brooman J.W.F.	Prediction of Turbulent Boundary Layers and Wakes in Compressible Flow by a Lag-Entrainment Method. R.A.E. Technical Report 7223[illegible], January 1973.
2.1.126	Yaeger L.S.	Transonic Flow over Afterbodies Including the Effects of Jet-Plume and Viscous Interactions with Separation. AIAA-77-228
2.1.127	Chow W.L. Bober L.J. Anderson B.H.	Numerical Calculation of Transonic Boattail Flow. NASA TN D-7984, 1975
2.1.128	Sasman P.K. Cresci R.J	Compressible Turbulent Boundary Layer with Pressure Gradient and Heat Transfer. AIAA Journal, Vol. 4, No. 1, Jan. 1966
2.1.129	Chow W.L.	Base Pressure of a Projectile Within the Transonic Flight Regime. AIAA-84-0230
2.1.130	Cosner R.R. Bower W.W.	A Patched Solution of the Transonic Flowfields About an Axisymmetric Boattail. AIAA-77-227
2.1.131	Bower W.W.	Analytical Procedure for the Calculation of Attached and Separated Subsonic Diffusor Flow. Journal of Aircraft, Vol. 13, No. 1, Jan. 1976
2.1.132	Yaros S.F.	Prediction of Pressure Distributions on Axisymmetric Bodies in Transonic Flow. AIAA-77-226
2.1.133	Wilmoth R.G.	Analytical Study of Viscous Effects on Transonic Flow over Boattail Nozzles. AIAA-77-223
2.1.134	Wilmoth R.G.	Computation of Transonic Boattail Flow with Separation. NASA TP 1070, 1977
2.1.135	Dash S.M. Pergament H.S.	A Computational Model for the Prediction of Jet Entrainment in the Vicinity of Nozzle Boattails (The BOAT code). NASA CR 3075, 1978

2.1.136	Dash S.M. Wilmoth R.G. Pergament H.S.	Overlaid Viscous/Inviscid Model for the Prediction of Near-Field Jet Entrainment. AIAA Journal, Vol. 17, No. 9, 1979
2.1.137	Wilmoth R.G. Dash S.M. Pergament H.S.	A Numerical study of Jet Entrainment Effects on the Subsonic Flow over Nozzle Afterbodies. AIAA-79-0135
2.1.138	Pergament H.S. Dash S.M. Varma A.K.	Evaluation of Turbulence Models for Rocket and Aircraft Plume Flowfield Predictions. ARAP Report No. 370-I, 1979, Prepared for: Naval Weapons Center, China Lake, California.
2.1.139	Wilmoth R.G. Dash S.M.	A Viscous-Inviscid Interaction Model of Jet Entrainment. AGARD CP 291, 1980
2.1.140	Wilmoth R.G.	Viscous-Inviscid Calculations of Jet Entrainment Effects on the Subsonic Flow over Nozzle Afterbodies. NASA TP 1626, 1980.
2.1.141	Dash S.M. Pergament H.S. Thorpe R.D.	Computational Models for the Viscous/Inviscid Analysis of Jet Aircraft Exhaust Plumes. NASA CR 3289, 1980
2.1.142	Wilmoth R.G.	RAXJET: A Computer Program for Predicting Transonic Axisymmetric Flow over Nozzle Afterbodies with Supersonic Jet Exhausts. NASA TM 83235, 1982
2.1.143	Wilmoth R.G.	Aerodynamic Interactions with Turbulent Jet Exhaust Plumes. Presented at JANNAF 13th Plume Technology Meeting, Houston, Texas, April 27-29, 1982
2.1.144	South J.C. Jameson A.	Relaxation Solutions for Inviscid Axisymmetric Transonic Flow over Blunt or Pointed Bodies. Proc. of the AIAA Computational Fluid Dynamics Conference, Palm Springs, CA, July 1973.
2.1.145	Reshotko E. Tucker M.	Approximate Calculation of the Compressible Turbulent Boundary Layer With Heat Transfer and Arbitrary Pressure Gradient. NACA TN 4154, 1957.
2.1.146	Dash S.M. Thorpe R.D.	A New Shock-Capturing/Shock-Fitting Computational Model for Analyzing Supersonic Inviscid Flows (The SCIPPY Code). Rep.No. 366, Aeronaut. Res. Assoc. Princeton, Inc., Nov. 1978
2.1.147	Kuhn G.D.	Calculation of Separated Turbulent Flows on Axisymmetric Afterbodies Exhaust Plume Effects. AIAA-79-0303
2.1.148	Kuhn G.D.	An Improved Interaction Method for Exhaust Nozzle Boattail Flows. AIAA-80-0197
2.1.149	Henson J.R. Robertson J.E.	Methods of Approximating Jet Boundaries for Highly Underexpanded Supersonic Nozzles. AEDC TDR-TR 62-7, May 1962.
2.1.150	Dutouquet L. Hardy J.M.	Engine Aerodynamic Installation by Numerical Simulation. AIAA-80-0108
2.1.151	Hardy J.M. Dutouquet L.	Etudes d'écoulements multiflux par juxtaposition de processus numériques différents. L'Aéronautique et l'Astronautique. No. 90, pp. 47-62 (1981)

2.1.152	Patankar S.V. Spalding D.B.	A finite - difference procedure for solving the equation of two-dimensional boundary-layer. Int. J. Heat and Mass Transfer Vol. 10, 1967, p. 1389-1411
2.1.153	Cosner R.R.	Fast Navier-Stokes Solutions of Transonic Flowfield About Axisymmetric Afterbodies. AIAA-80-0193
2.1.154	Cosner R.R.	Relaxation Solution of Viscous Transonic Flow about Fighter-Type Forebodies and Afterbodies. AIAA-82-0252
2.1.155	Mace J.L. Cosner R.R.	Analysis of Viscous Transonic Flow Over Aircraft Forebodies and Afterbodies. AIAA-83-1366
2.1.156	Chima R.V. Gerhart P.M.	Finite Element Analysis of Inviscid Subsonic Boattail Flow. AIAA Journal, Vol. 20 No. 2, 1982.
2.1.157	Hodges J.	A Method for Calculating Subsonic Flows over Axisymmetric Afterbodies, Including Viscous and Jet Effects. RAE TR 82097, October 1982
2.1.158	Hodges J.	Private Communications. RAE, Bedford, England, 1983
2.1.159	Putnam L.E. Hodges J.	Assessment of NASA and RAE Viscous-Inviscid Interaction Methods for Predicting Transonic Flow over Nozzle Afterbodies. AIAA-83-1789
2.1.160	Radespiel R.	Private Communication.DFVLR, Braunschweig, 1983
2.1.161	Ferguson D.R. Keith J.S.	Modifications to the Streamtube Curvature Program. NASA CR-132705, 1975
2.1.162	Spalding D.B.	GENMIX - A General Computer Program for Two-Dimensional Parabolic Phenomena HMT-Series, Vol. I, Pergamon Press, 1977.
2.1.163	Radespiel R.	Turbulenzmodell für die Berechnung von Triebwerksstrahlen. DFVLR IB 129-21/82, 1982
2.1.164	Dash S.M. Wolf D.E.	Interactive Phenomena in Supersonic Jet Mixing Problems. AIAA-83-0288
2.1.165	Dash S.M. Thorpe R.D.	Shock - Capturing Model for One- and Two-Phase Supersonic Exhaust Flow. AIAA Journal Vol. 19, No. 7, July 1981, p. 842
2.1.166	Kern P.R.A. Hopcroft R.G.	Progress Toward the Analysis of Complex Propulsion Installation Flow Phenomena. AIAA-83-1367
2.1.167	Magnus A.E. Epton M.A.	PAN-AIR - A Computer Program for Predicting Subsonic or Supersonic Linear Potential Flows About Arbitrary Configurations Using a Higher Order Panel Method. Volume I - Theory Document (Version 1.0). NASA CR 3251, 1980
2.1.168	Swanson R.C. Rubin S.G. Khosla P.K.	Calculation of Afterbody Flows with a Composite Velocity Formulation. AIAA-83-1736
2.1.169	Boppe C.W.	Elements of Computational Engine - Airframe Integration. AIAA-84-0117

2.1.170 Tinoco E.N.
Chen A.W.
Transonic CFD Applications to Engine/Airframe Integration. AIAA-84-0381

2.1.171 Carpenter P.W.
Tabakoff W.
Survey and Evaluation of Supersonic Base Flow Theories. NASA CR-97129, 1968

2.1.172 Calarese W.
Review of Methods of Solution of Afterbody/Exhaust Nozzle Flow Fields. AFFDL-TR-74-108, Jan. 1974

2.1.173 Putnam L.
Mace J.
A Survey of Aft Body Flow Prediction Methods. AIAA-81-1694

2.1.174 Klopfer G.H.
Nielsen J.N.
Computational Fuid Dynamic Applications to Missile Aerodynamics. AGARD-CP-336, 1982

2.1.175 Zannetti L.
Onofri M.
Aerodynamics of Aircraft Afterbody; Numerical Simulation. AIAA-84-0284

2.1.176 Zannetti L.
Transonic Flow Field in Two-Dimensional or Axisymmetric Convergent Nozzle. Proceeding of Second GAMM-Conference on Numerical Methods in Fluid Mechanics, DFVLR, Cologne, Oct. 11 to 13, 1977

2.1.177 Cambier L.
Ghazzi W.
Veuillot J.P.
Viviand H.
A Multi-Domain Approach for the Computation of Viscous Transonic Flows by Unsteady Type Methods. To appear in: Recent Advances in Numerical Methods in Fluids, Volume 3: Viscous Flow Computational Methods. Ed.: Dr. W.G. Habashi, Pineridge Press, Swansea, U.K.

2.1.178 Cambier L.
Ghazzi W.
Veuillot J.P.
Viviand H.
Une Approche Par Domaines Pour Le Calcul D'Ecoulements Compressibles. ONERA TP 1981-143 and 5e Colloque International sur les methods de calcul scientifique et technique de l'INRIA, Versailles, 14-18 decembre 1981.

2.1.179 Eberle A.
Erste Ergebnisse zur numerischen Behandlung der Triebwerksstrahl-Heck-Interferenz. MBB-UFE122-AERO-MT-580, 1982

2.1.180 Bissinger N.
Eberle A.
Heckumströmung und Heckwiderstand von Kampfflugzeugen. Theoretische Untersuchungen der Umströmung von stumpfen Heckformen mit Triebwerksstrahl. MBB/FE122/S/STY/50, 1982

2.1.181 Eberle A.
Similarity Transformations of the Euler Equations and their Numerical Evaluation. MBB-UFE122-AERO-MT-669(1983)

2.1.182 Chen H.C.
Yu N.J.
Rubbert P.E.
Jameson A.
Flow Simulations for General Nacelle Configurations Using Euler Equations. AIAA-83-0539

2.1.183 Bromm A.F.
O'Donnell R.M.
Investigation at Supersonic Speeds of the Effect of Jet Mach Number and Divergence Angle of the Nozzle upon the Pressure of the Base Annulus of a Body of Revolution. NACA RM L54I16, 1954

2.1.184 Cortright E.M.
Schroeder A.H.
Investigation at Mach Number 1.91 of Side and Base Pressure Distributions over Conical Boattails without and with Jet Flow Issuing from Base. NACA RM E51F26, 1958.

2.1.185 Baughman E.L.
Kochendorfer F.D.
Jet Effects on Base Pressures of Conical Afterbodies at Mach 1.91 and 3.12. NACA RM E57E06, 1957

2.1.186	Love E.S.	Base Pressure at Supersonic Speeds on Two-Dimensional Airfoils and on Bodies of Revolution with and without Fins having Turbulent Boundary Layers. NACA TN 3819, 1957
2.1.187	Harries M.H.	Pressure on Axisymmetric Base in a Transonic or Supersonic Free Stream in the Presence of a Jet. FFA Report 111, 1967
2.1.188	Craven A.H. Chester D.H. Graham B.H.	Base Pressure at Supersonic Speeds in the Presence of a Supersonic Jet. College of Aeronautics, Report No. 144, Cranfield, UK, 1960
2.1.189	Reid J.	The Effect of a Central Jet on the Base Pressure of a Cylindrical Afterbody in a Supersonic Stream. Aer. Research Council R. & M. No. 3224, London, 1961
2.1.190	Reid J.	The Effect of Jet Temperature on Base Pressure. RAE TR 68176, 1968
2.1.191	Reubush D.E. Putnam L.E.	An Experimental and Analytical Investigation of the Effect on Isolated Boattail Drag of Varying Reynolds Number up to 130 x 10^6. NASA TN D-8210, 1976
2.1.192	Putnam L.E. Abeyounis W.K.	Experimental and Theoretical Study of Flow Fields Surrounding Boattail Nozzles at Subsonic Speeds. AIAA-76-675
2.1.193	Mason M.L. Putnam L.E.	Pitot Pressure Measurements in Flow Fields Behind Circular-Arc Nozzles with Exhaust Jets at Supersonic Free-Stream Mach Numbers. NASA TM-80169, 1979
2.1.194	Price Jr. E.A.	An Investigation of F-16 Nozzle-Afterbody Forces at Transonic Mach Numbers with Emphasis on Model Scale Effects. AEDC-TR-80-57, Sept. 1981
2.1.195	Porteiro J.L.F. Page R.H. Przemberel C.E.G.	Modificaiton of Subsonic, Axisymmetric Near-Wakes Using Boundary Layer and Base Mass Transfer. AIAA-81-1267
2.1.196	Solignac J.L.	Experimental Study of the Separation at the Trailing Edge of an Axisymmetrical Contoured After-Body. La Recherche Aérospatiale, O.N.E.R.A, No. 1980-3
2.1.197	Lacau R.G. Desnoyer D. Delery J.	Analyse au Velocimetre Laser de l'Ecoulement en Aval d'Arrière-Corps de Missiles. AGARD-CP-336, 1982
2.1.198	Reubush D.E.	Experimental Study of the Effectiveness of Cylindrical Plume Simulators for Predicting Jet-on Boattail Drag at Mach Numbers up to 1.30. NASA TN-D-7795, 1974
2.1.199	Reubush D.E. Runckel J.F.	Effect of Fineness Ratio on Boattail Drag of Circular-Arc Afterbodies having Closure Ratios of 0.50 with Jet Exhaust at Mach Numbers up to 1.30. NASA TN D-7192, 1973
2.1.200	Abeyounis W.K. Putnam L.E.	Investigation of the Flow Field Surrounding Circular-Arc Boattail Nozzles at Subsonic Speeds. NASA TP-1633, 1980
2.1.201	Abeyounis W.K.	Boundary-Layer Separation on Isolated Boattail Nozzles. NASA TP-1226, 1978

2.1.202	Koppenwallner G. Rammenzweig D.	Untersuchungen zum Einfluß des Flugkörper-Treibstrahls auf die Druckverteilung am Heckbereich. DFVLR-IB 251-80 A 31, Göttingen 1980.
2.1.203	Koppenwallner G. Rammenzweig D. Strunck V.	Rocket exhaust jet flow and upstream flow field interference - Experiments and flow field analysis. AGARD-CP-336, 1982

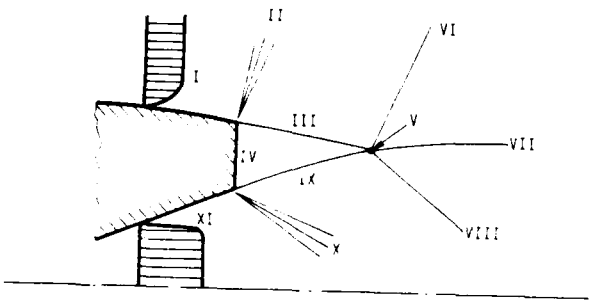

I Afterbody boundary layer = f (body geometry, Mach number, Re number)
II Separation and expansion / compression at base
III Mixing layer at free stream boundary of base flow region
IV Base flow region, p_B = ?
V Confluence point
VI Recompression shock in free stream
VII Slip stream
VIII Recompression shock in jet
IX Mixing layer at jet boundary of base flow region
X Separation and expansion / compression of nozzle boundary layer
XI Nozzle boundary layer

Fig. 2.1.7.1 Supersonic Afterbody Flow With Supersonic Jet

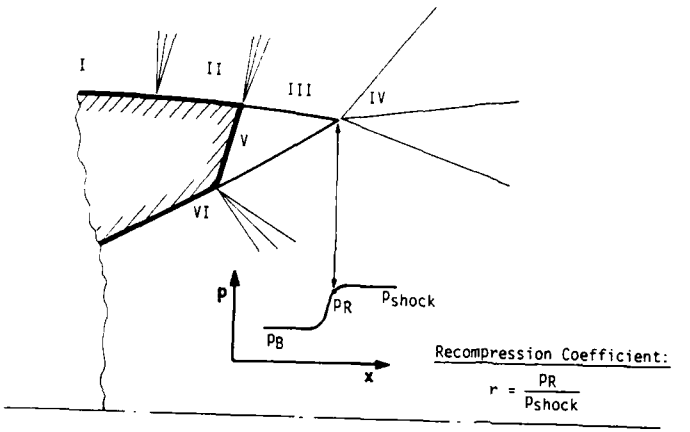

I Uniform supersonic flow, no boundary layers

II PRANDTL/MEYER exp./compr. and method of irrotational characteristics for cylindrical, conical, parabolic, tangent-ogive and conical flares afterbodies (no strong shocks)

III Constant pressure boundary (trial value) in characteristics calculations;
Iso- or non iso-energetic two-dimensional turbulent mixing (restricted theory, CHAPMAN/KORST model)

IV Empirical recompression coefficient r for cylindrical afterbodies (r = 1 for other geometries, as KORST) accounts for incomplete recompression at reattachment point

V Upper bound of trial value for base pressure determined from boundary layer separation criterion of ZUKOSKI (at afterbody and nozzle);
Zero back flow velocity;
Base bleed possible

Fig. 2.1.7.2 Assumptions, Calculation Methods and Empirical Input for Addy Program

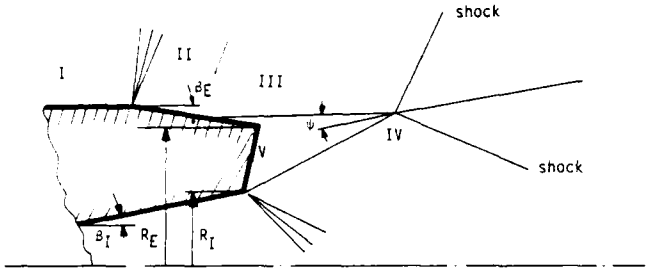

I Body boundary layer included by "equivalent base bleed" (Ref.2.1.92)

II Change of momentum thickness during expansion calculated by e.g. formula of NASH (Ref.2.1.52);
Axisymmetric rotational method of characteristics (Ref.2.1.72);
Boattail flow separation approximated by terminating body at separation point (from ZUKOSKY's criterion) (Ref.2.1.74);
Modified separation criteria (Refs.2.1.62, 2.1.90, 2.1.97)

III MANGLER transformation from two-dim. to axisymmetric coordinates for KORST's restricted theory (Ref.2.1.72);
Virtual-origin shift to account for boundary layer (Refs.2.1.49, 2.1.54, 2.1.76, 2.1.104);
Effective mixing length between separation point and merge point using simplified back flow velocity in V (Ref.2.1.76);
Linear base flow boundary, i.e. axial pressure gradient (Ref.2.1.72)

IV Empirical improvement of recompression coefficient $r = r(\frac{R_I}{R_E})$ for cylindrical and conical boattails (Ref.2.1.74);
New recompression coefficient $r = r(R_I; R_E; \beta_I; \beta_F)$ (Ref.2.1.80);
ONERA angular reattachment law (Ref.2.1.93);
Modified ONERA criterion (Ref.2.1.90)

V Simplified back flow velocity (see III) (Ref.2.1.76)

Fig. 2.1.7.3: Extension, Variations and Improvements to Flow Model for Blunt Base Configurations with Jets, Derived from Korst Model

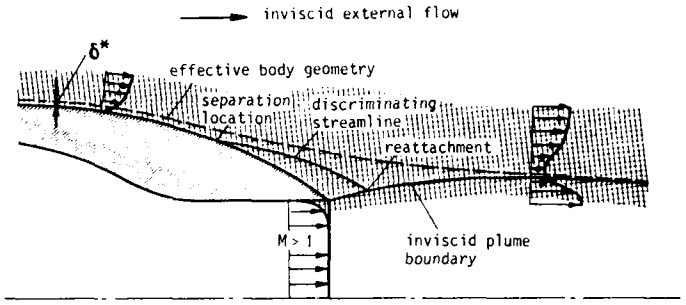

Fig. 2.1.7.4: Schematic of Nozzle Afterbody Flow Field (from Ref. 2.1.142)

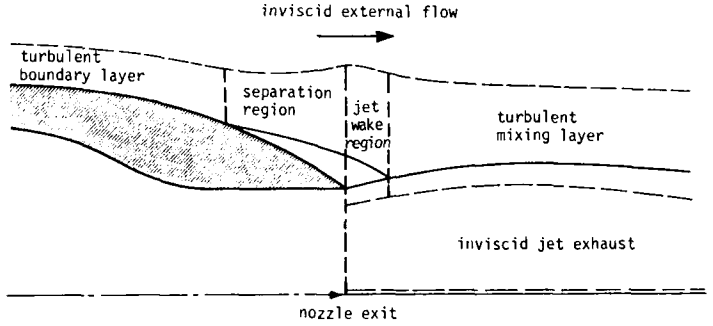

Fig. 2.1.7.5: Patched Viscous-Inviscid Interaction Model (from Ref. 2.1.142)

2.2 DESCRIPTION OF TEST CASES

2.2.1 INTRODUCTION

A critical review of the computer programs available to the Working Group was undertaken, by applying them to selected experimental test cases. Experience in other branches of computational fluid mechanics has shown that this "test case" approach is a generally revealing and constructive activity. It clarifies the scope of the various programs and gives some indication of their current relative standing. It must be emphasized at the outset, however, that a limited review of the type undertaken here can never provide a full assessment either of the present accuracy of predictions or of the relative merit of the different modelling or computational procedures for further development.

Several features of a flow field program ideally need to be assessed:-

(1) the accuracy with which the geometry is represented by the computational grid

(2) the quality of fluid behaviour modelling within the field and at its boundaries

(3) the accuracy, stability, and convergence of the solution algorithms

(4) the effect of grid density

(5) the size of computer needed and the speed of execution.

All these 5 points are best checked by test cases with a known exact solution; no such cases are known in the present context. A massive effort, using many test cases, would be needed to check all these five points for any of the programs, and that effort was not available to the Working Group. Therefore, the more limited objective was selected of illustrating the scope of the programs made available to the WG, and giving some indication of their predictive quality.

2.2.2 TEST CASE SELECTION

So the selection of test cases was made using the following criteria:-

(i) the number of cases should be small

(ii) they should be confined to an axisymmetric single stream nozzle and afterbody and cover the major variables involved:

flight speed
jet pressure ratio and temperature
afterbody shape
presence or absence of base regions
possible presence of wind tunnel walls

They should encompass cases in which boundary layer separation did and did not occur on the afterbody.

(iii) the experimental information should be as accurate and as comprehensive as possible, with measurements of flow field details as well as afterbody pressure distribution.

(iv) there could be no restrictions on the publication of the data, so that the cases would be available for research workers to test their own programs in the future.

A fairly wide range of possible cases was offered, including one of the "AGARD" afterbodies selected for testing by the previous Working Group.
Table 1 shows the final selection; it will be seen that each of the variables mentioned in (ii) is covered at least once. In each experiment, only one or two test points from the range of test conditions potentially available could be chosen.

Unfortunately, technical difficulties prevented the test results being obtained for test case 4 (hot jet), the calculations having already been done.

	Origin Reference	Flight Mach No.	nozzle pressure ratios	approx jet temperature °K	afterbody shape, angle	base region?	wind tunnel blockage variation?	boattail separation?	MEASUREMENTS on the afterbody	MEASUREMENTS in the jet
1			2.9		8°			no		
2	NASA	0.8	2.9	300	circular 17°	no	no	yes	P	P,V
2A			5.0		arc 17°			yes		
3				300			no			
4	DFVLR/MBB	0.7	3.0	900	(AGARD A1)	no		no	P, bl	P,V,T
5				300	circular arc					
6				300	10°		yes			
7	NASA	2.2	11.13	300	conical, 5°	no	no	no	P	P,V
8	ONERA/AERO SPATIALE	0.85	37.03	300	conical, 6°	yes	no	no	P	V,Tu
9			17.08*		0°			no		
10	FFA	2.0	102.5*	300	conical 0°	yes	no	no	P	none
11			17.08*		6°			no		
12			102.5*		6°			yes		

P = pressure, V = velocity, T = temperature, Tu = turbulence, bl = boundary layer
* plus base pressure prediction for jet static pressure ratios in the range 1 to 15

Table 2.2.1: Test cases

Brief details of the test cases follow. Their full experimental results are tabulated in an Appendix, included in the form of a microfiche.

2.2.3 ACCURACY OF TEST RESULTS

No estimates have been made (or provided by the experimenters) of the accuracy of the quoted results. In each of the experiments, there will have been quantifiable random inaccuracies resulting from normal instrumentation inaccuracies, but such errors in this type of test would not be significantly large in the context of the present comparisons with theory. However, the possibility of important systematic errors in this type of test - especially affecting the net drag coefficient - is recognised. Such errors could arise from non-uniform entry flow, from model support interference, from poor downstream conditions, or from minor model defects. They are fully discussed in later chapters. They cannot by their nature be quantified by the experimenter. The Working Group therefore selected tests undertaken by teams with great experience fully aware of the pitfalls exposed, for example, by the earlier AGARD PEP Working Group 4 ten years ago. Furthermore, tests were chosen (as far as possible) to allow comparisons to be made of the effect of changing one parameter within a single test series, so as to minimise the importance of any systematic errors. It will be noted also that no attempt has been made to apply "wind tunnel blockage corrections" to the quoted results since blockage is one of the parameters investigated.

2.2.4 CONTRIBUTORS OF THE TEST CASES

Test Case	Contributor	Country	Address/Company
1, 2, 2A, 7	Lawrence E. Putnam	USA	Mail Stop 80 Nasa Langley Research Center Hampton, VA 23665
8	Jean Delery	F	O.N.E.R.A 29, Ave. de la Division Leclerc F-92320 Chatillon
9, 10, 11, 12	Dr. B. Wagner	D	Theoretische Aerodynamik (BF 30) Dornier GmbH Postfach 1420 D-7990 Friedrichshafen 1
	J. Agrell	S	FFA-Aeronautical Institut of Sweden P.O. Box 11021 S-16111 Bromma Sweden
3, 4, 5, 6	Dr. A Zacharias	D	Messerschmitt-Bölkow-Blohm GmbH Military Aircraft Division,LKE123 P.O. Box 80 11 60 8000 München 80

2.2.5 DATA AVAILABLE

Test Cases	Measurement Location x/D	Incompressible Values δ_i^*/D	ϑ_i/D	H_i	Compressible Values δ_c^*/D	ϑ_c/D	H_c	Remarks
1	-2,935	0,0168	0,0074	2,28	0,0184	0,0071	2,60	} from M/M_∞
2	-1,967	0,0168	0,0074	2,28	0,0184	0,0071	2,60	} measured
3,4,(5,6)*	-2,658	0,0153	0,0097	1,57	0,0169	0,0095	1,78	from U/U_∞ meas.
7	-0,598	0,0201	0,0100	2,01	0,0258	0,0084	3,07	from Pt/Pt_∞ meas.
8	-0,200			1,40	0,0374	0,0227	1,65	by experimentalist
9,10,11,12	-1,30			1,37	0,0279	0,0088	3,18	by exp.(exept H_i)

* For Test Cases 5 and 6 not related to actual body diameter but to body diameter of Test Cases 3 and 4.

Table 2.2.2: Initial Boundary Layer Data

	Test Case	1	2	2A	3	4	5	6	7	8	9	10	11	12
Model	Surface Pressure Distribution													
	- External	X	X	X	X		X	X	X	X	X	X	X	X
	- Internal								X					
	- Base Pressure									x	x	x	x	x
	Surface Temperature Distribut.													
	- External													
	- Internal													
	Boundary Layer Profiles													
	- Upstream of Jet Exhaust	X	X	X	X		X	X	X	X				
	- At Jet Exit				X		X	X						
	- B.L. Separation Location		x	x										x
Jet- and Flow-Field	Pitot Pressure Profiles in													
	- Surrounding Flow	X	X	X	X		X	X						
	- Jet	X	X	X	X		X	X						
	- Shear Layer Jet	X	X	X	X		X	X						
	Temperature Profiles in													
	- Surrounding Flow													
	- Jet													
	- Shear Layer Jet/Surround.Flow													
	Velocity Profiles in													
	- Surrounding Flow				X		X	X		X				
	- Jet				X		X	X						
	- Shear Layer Jet/Surround.Flow				X		X	X		X				
	Turbulent Shear Stress									x				
	Local Mach-Number													
	- Surrounding Flow	X	X	X					X					
	- Jet													
	- Shear Layer Jet/Surround.Flow													
	Flow Angle in													
	- Surrounding Flow	X	X	X					X	x				
	- Jet													
	- Shear Layer									X				
Tunnel Wall	Pressure Distribution on the Tunnel Wall				X		X	X						
	Schlieren pictures										x	x	x	x

Table 2.2.3: Summary of available data

2.2.5.1 TEST CASES 1, 2 and 2A - NASA LANGLEY CIRCULAR ARC BOATTAIL AT M_{∞} = 0.80

I - Model Configuration (see Figures 2.2.1, 2.2.2, 2.2.3, 2.2.4)

A. Forebody - 14° Cone/Circular Arc/Cylinder (see Figure 2.2.2)
B. Nozzle for Test Case 1 (see Figure 2.2.3)
Length to Maximum Diameter Ratio l/D = 1.768
Base Diameter to Maximum Diameter Ratio d_B/D, l/D = 0.51
Chord Boattail Angle β = 8°
C. Nozzle for Test Case 2 and 2A (see Figure 2.2.4)
l/D = 0.80, d_B/D = 0.51, β = 17°

II. Model Installation in Tunnel (See Fig. 2.2.5) 0.098 % blockage

III. Free Stream and Jet Conditions

M_{∞} = 0.80 NPR = 2.9 for Test Case 1 and 2

$P_{t_{\infty}}$ = 101.0 kPa NPR = 5.0 for Test Case 2A

$T_{t_{\infty}}$ = 310K T_{tj} = 300K

IV. Data Available

A. External Surface Pressures
B. Local Mach Number and Flow Angle in Flow Field Outside Jet Exhaust
C. Pitot Pressure in Jet Exhaust and in Shear Layer Between Jet and External Stream
D. Boundary Layer Separation Location
E. Boundary Layer Profiles Upstream of boattail

V. References

2.2.1, 2.2.2, 2.2.3, 2.2.4, 2.2.5, 2.2.6

NASA AIR-POWERED CONE-CYLINDER MODEL

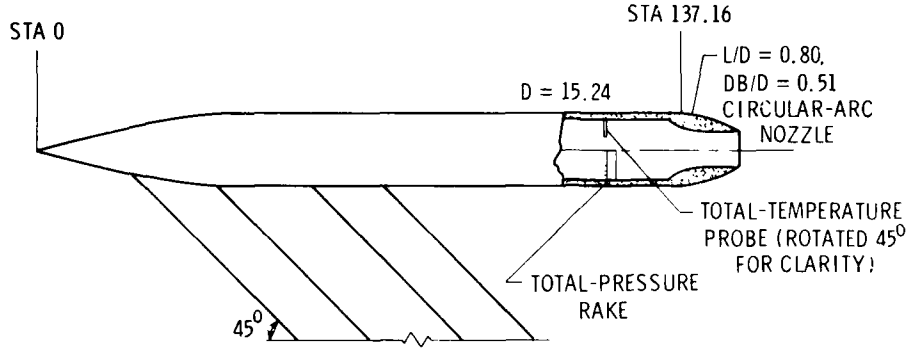

Figure 2.2.1: Drawing of exhaust-nozzle simulator. (All dimensions are in centimeters unless otherwise noted.)

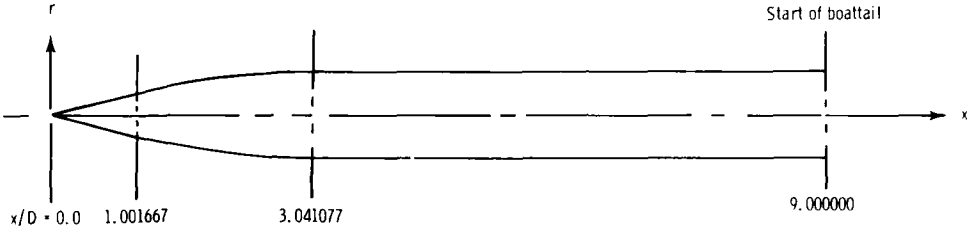

x/D	r/D	x/D	r/D
0.0	0.0	1.8	0.408170
.1	.024925	1.9	.422439
.2	.049850	2.0	.435487
.3	.074775	2.1	.447323
.4	.099700	2.2	.457950
.5	.124626	2.3	.467373
.6	.149551	2.4	.475596
..7	.174476	2.5	.482623
.8	.199401	2.6	.488456
.9	.224326	2.7	.493099
1.0	.249251	2.8	.496553
1.1	.273551	2.9	.498820
1.2	.296564	3.0	.499900
1.3	.318300	3.1	.500000
1.4	.338771		
1.5	.357985		
1.6	.375951		
1.7	.392677	9.0	.500000

- From $x/D = 0.0$ to $x/D = 1.001667$

  $r/D = 0.249251(x/D)$

- From $x/D = 1.001667$ to $x/D = 3.041077$

  $r/D = -7.932489 + \sqrt{-(x/D)^2 + 6.082154(x/D) + 61.858721}$

- From $x/D = 3.041077$ to $x/D = 9.000000$

  $r/D = 0.500000$

Figure 2.2.2: Details of 14°-cone/circular-arc/cylinder forebody.

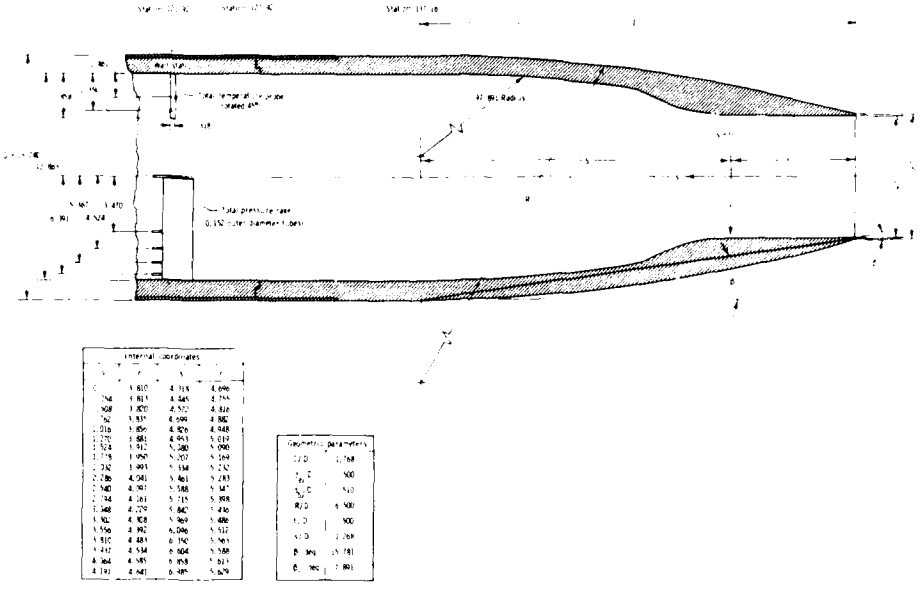

Figure 2.2.3: Details of nozzle configuration for AGARD WG-08 Test Case 1. All dimensions are in centimeters unless otherwise noted.

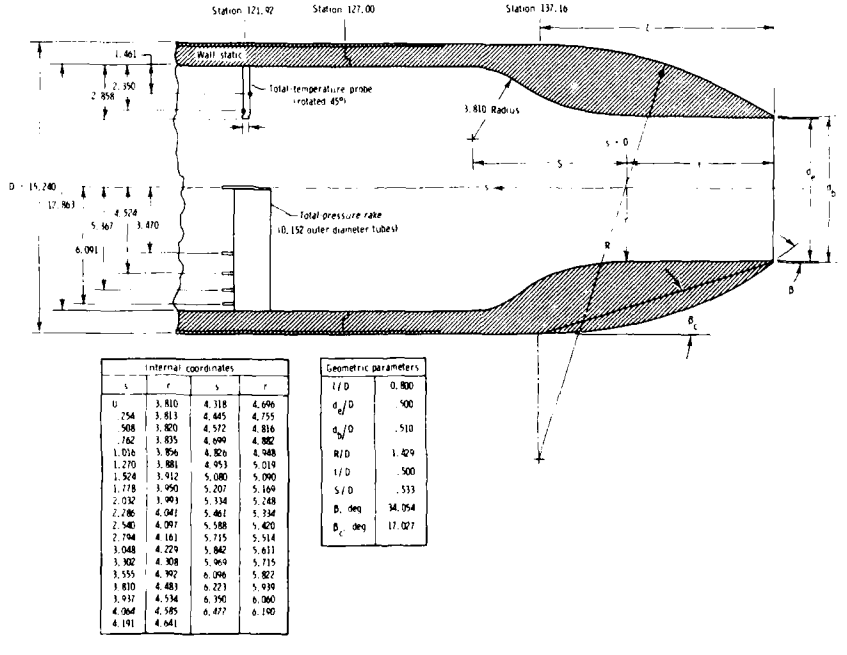

Internal coordinates			
s	r	s	r
0	3.810	4.318	4.696
.254	3.813	4.445	4.755
.508	3.820	4.572	4.816
.762	3.835	4.699	4.882
1.016	3.856	4.826	4.948
1.270	3.881	4.953	5.019
1.524	3.912	5.080	5.090
1.778	3.950	5.207	5.169
2.032	3.993	5.334	5.248
2.286	4.041	5.461	5.334
2.540	4.097	5.588	5.420
2.794	4.161	5.715	5.514
3.048	4.229	5.842	5.611
3.302	4.308	5.969	5.715
3.555	4.392	6.096	5.822
3.810	4.483	6.223	5.939
3.937	4.534	6.350	6.060
4.064	4.585	6.477	6.190
4.191	4.641		

Geometric parameters	
ℓ/D	0.800
d_e/D	.900
d_b/D	.510
R/D	3.429
t/D	.500
S/D	.533
β, deg	34.054
β_c, deg	17.027

Figure 2.2.4: Details of nozzle configuration for AGARD-WG-08 Test Case 2 and 2A All dimensions are in centimeters unless otherwise noted.

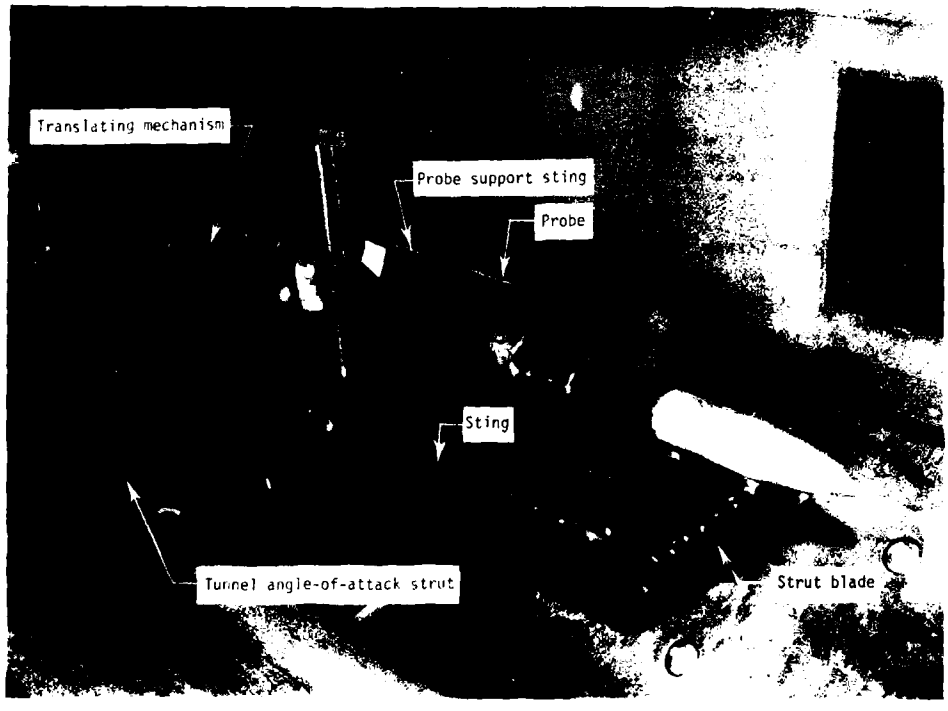

Figure 2.2.5: Photograph of model and flow survey device in the NASA Langley 16-Foot Transonic Tunnel.

2.2.5.2 TEST CASES 3, 4, 5 AND 6 - AGARD MODEL A-1 with $\beta = 10°$ AND $M_{\infty} = 0.70$

I. Model Configuration (See Figures 2.2.6 and 2.2.7)

A. Forebody - Cylinder (See Figure 2.2.8)
B. Nozzle - AGARD A1

$l/D = 1.6578$

$D_B/D = .4154$

$\beta = 10°$

II. Model Installation in Tunnel (See Figure 2.2.8)

A. For size of model relative to tunnel see Figure 2.2.7 and 2.2.8
B. For test cases 3 and 4 calculations are to be made by assuming model is in free air. That is tunnel walls are *not* present.

III. Free-Stream and Jet Conditions

$M_{\infty} = 0.70$ NPR = 3.0

$T_{t\infty} = 300K$

$P_{t\infty} = 101.0$ kPa

$T_{tj} = 300K$ for all cases except case 4

$T_{tj} = 900K$ for case 4

IV. Data Available

A. External Surface Pressures
B. Velocity and Temperature Profiles in External and Jet Exhaust Flows
C. Boundary Layer Profiles
D. Model Surface Temperatures
E. Tunnel Wall Static Pressures.

V. References

2.2.7, 2.2.8, 2.2.9, 2.2.10

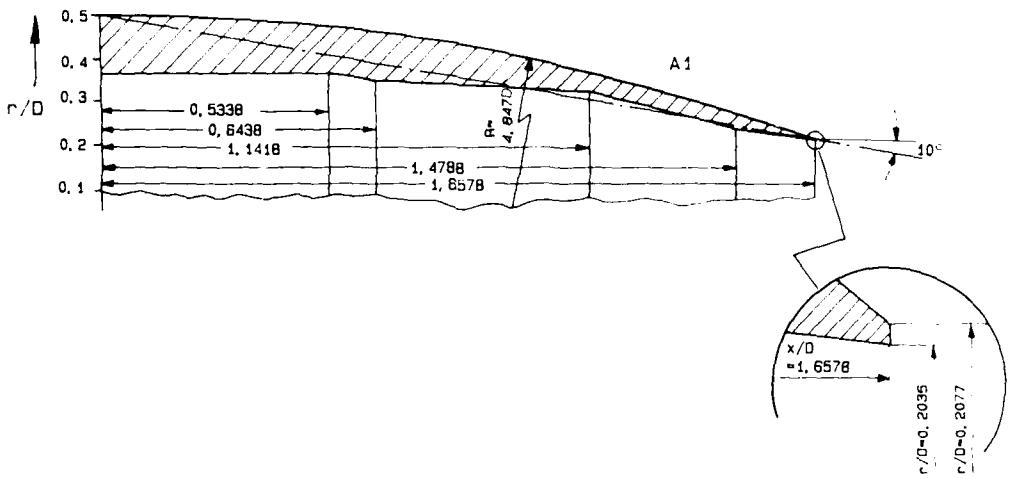

Figure 2.2.6: Details of the AGARD A-1 model. All dimensions are non-dimensionalized by the body maximum diameter.

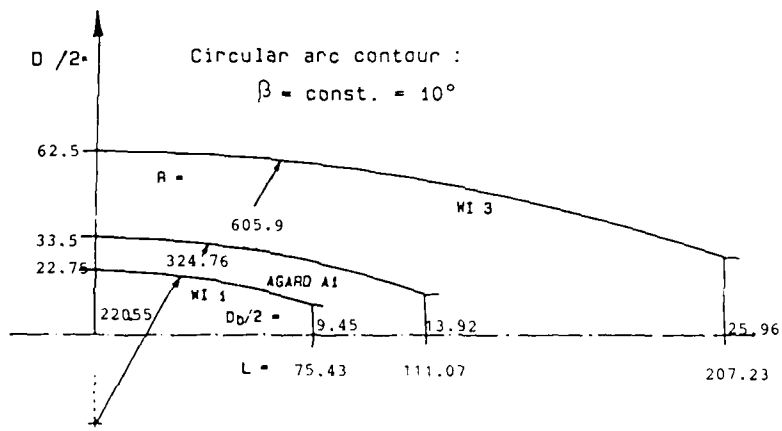

AGARD WG-08 Test Case	Model / Geom. Par.		D [mm]	L [mm]	D_b [mm]	R [mm]	β [°]	$\lambda_1 = \frac{L}{D}$	$\lambda_2 = \frac{D_b}{D}$	$\lambda_3 = \frac{R}{D}$	Tunnel Blockage
5		WI 1	45.5	75.43	18.90	220.55	10	1.6578	0.4153	4.8472	1.07%
3 + 4		AGARD A1	67.0	111.07	27.83	324.76	10	1.6578	0.4154	4.8472	2.32%
6		WI 3	125.0	207.23	51.92	605.9	10	1.6578	0.4154	4.8472	8.07%

Note: Test cases 3 and 4 are to be computed for 0.0% blockage. That is, calculations are to be made assuming tunnel walls are not present.

Figure 2.2.7: Details of the blockage models. All dimensions are in millimeters unless otherwise noted.

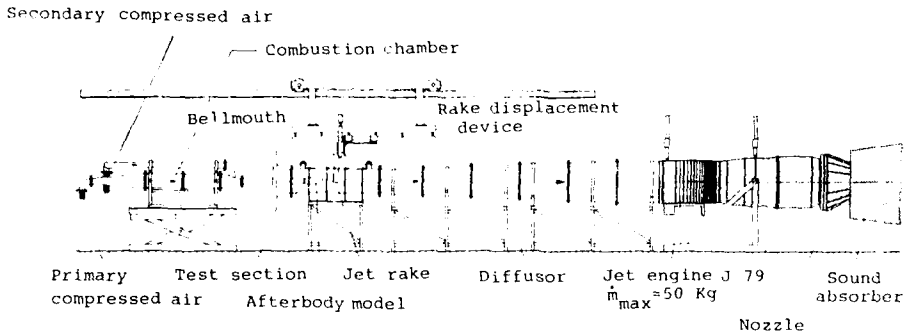

Jet Induction wind tunnel (SIB) of DFVLR

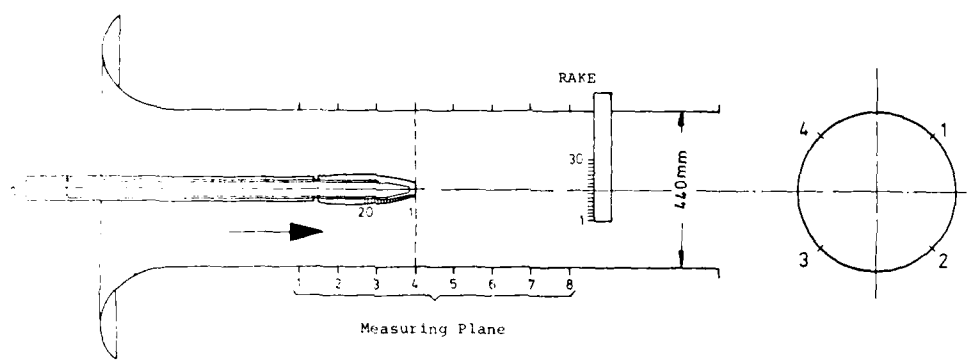

Figure 2.2.8: Model arrangement in the jet induction wind tunnel (SIB) of DFVLR.

2.2.5.3 TEST CASE 7 - NASA LANGLEY β= 5° CONICAL BOATTAIL AT M_{∞}= 2.20

I. Model Configuration (see Figures 2.2.9 and 2.2.10)

A. Forebody - 14° Cone Cylinder
B. Boattail (configuration 6 of Figure 2.2.10) l/D = 0.60
Boattail Angle β= 5°

II. Model Installation in Tunnel (see Figures 2.2.9 and 2.2.11)

III. Free Stream and Jet Conditions

M_{∞} = 2.20 NPR = 11.13

$P_{t\infty}$ = 124.1 kPa $T_{t\ j}$ = 300K

$T_{t\infty}$ = 316.67K

IV. Data Available

A. External Surface Pressures
B. Internal Surface Pressures
C. Local Flow Angle, Mach Number, and Static Pressure in Flow Field Outside Exhaust
D. Boundary Layer Profiles Upstream of boattail

V. References

2.2.11, 2.2.12

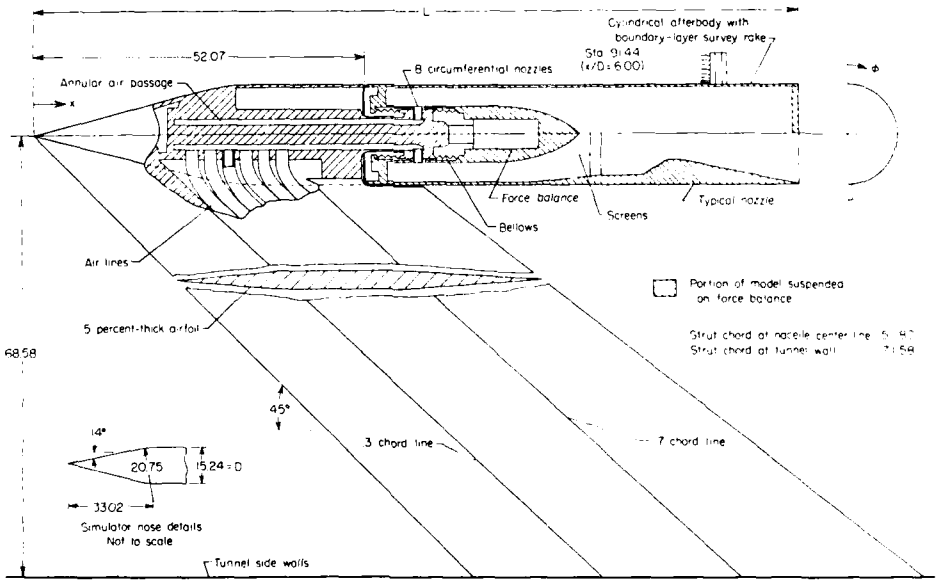

Figure 2.2.9: Sketch of jet-engine exhaust-nozzle simulator. All dimensions in centimeters unless otherwise noted.

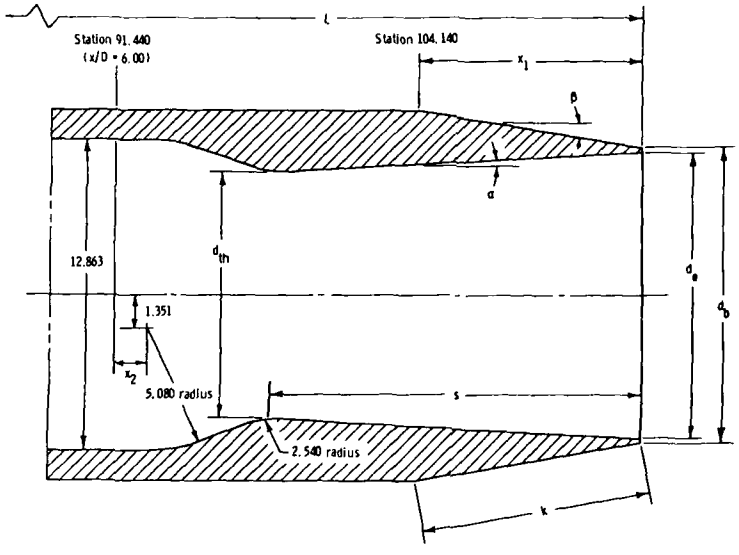

$M_{j,des}$	α, deg	β, deg	x_1	L	k	s	d_{th}	d_e	d_b	A_{th}	A_e	A_e/A_{th}	x_2
2.024	6.04	5	9.109	113.249	9.144	15.105	10.223	13.417	13.646	82.08	141.39	1.722	1.778

Figure 2.2.10: Details of nozzle. All dimensions are in centimeters except as noted. Areas listed are in square centimeters.

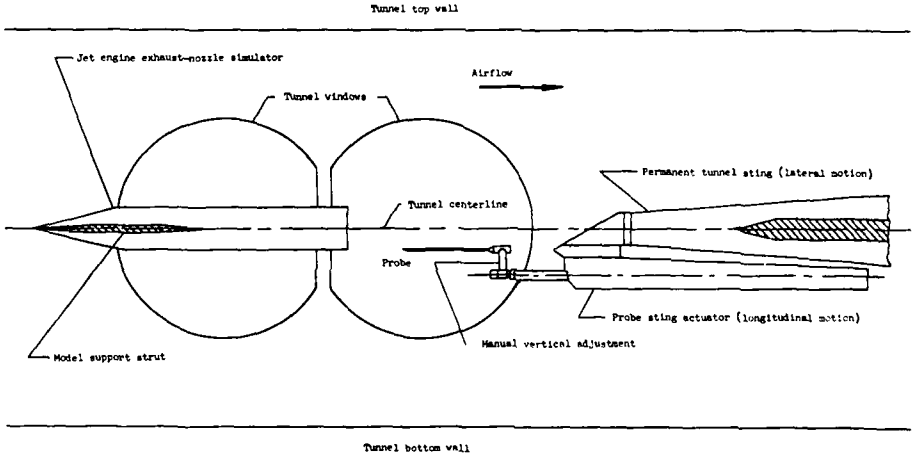

Figure 2.2.11: Wind-tunnel flow-field survey apparatus.

2.2.5.4 TEST CASE 8 - ONERA/AEROSPATIALE CONICAL BOATTAIL WITH $\beta = 6°$ AND BASE

I. Model Configuration (see Figures 2.2.12 and 2.2.13)

A Axisymmetric afterbody with conical boattail ($\beta = 6°$) and nozzle.

B Geometrical definition of the external contour of the afterbody shown in Figure 2.2.12

C Geometrical definition of the nozzle given Figure 2.2.13

II. Model Installation in Tunnel (see Figure 2.2.14)

Nose sting mounted model. Tested in the ONERA S3Ch transonic wind-tunnel (continuous return wind tunnel). Model installation is shown in Figure 2.2.14. The model is mounted with zero yaw and zero angle of attack in the center of the WT.

The S3Ch WT has a quasi-octagonal test section (Cross sectional area equal to 0.66 m^2) inscribed in a circle of diameter D = 1 m.

The upper and lower walls are perforated (porosity to 0.20) and slightly diverging (30').

Geometry of test section is shown in figure 2.2.15.

III. Free Stream and Jet Conditions

1. External Flow

$M_{\infty} = 0.85$

$P_{t\infty} = 100$ kPa

$T_{t\infty} = 325$ K (mean test value)

In fact the tabulated (and plotted) quantities (i.e. mean velocity components and Reynolds tensor components) are relative to a conventional stagnation temperature:

$$T_{t\infty} = 288 \text{ K}$$

Boundary-layer characteristics:

The external layer has been probed for 4 angular positions ($\varphi = 0, 90°, 180°$ and $270°$) at a station located 20mm upstream of the base (X = -20 mm). Its averaged integral properties are:

- displacement thickness: $\delta^* = 0.00374$ m;
- momentum thickness: $\vartheta = 0.00227$ m;

} compressible values

- incompressible shape parameter $H_i = 1.40$;
- estimated physical thickness: $\delta = 0.024$ m.

2. Nozzle flow

$M_j = 2.9$.

This is a mean value, the flow being not strictly uniform in the nozzle exit plane.

$$\frac{P_j}{P_{\infty}} = 1,17 \text{ (for } M_j = 2.9).$$

$T_{tj} = 300$ K.

IV. Data available

Pressures on the afterbody;

Mean-velocity components and Reynolds tensor components in the near wake flow region (by use of a two-color LDV system).

V. References

2.2.13

ONERA/AEROSPATIALE TEST CASE

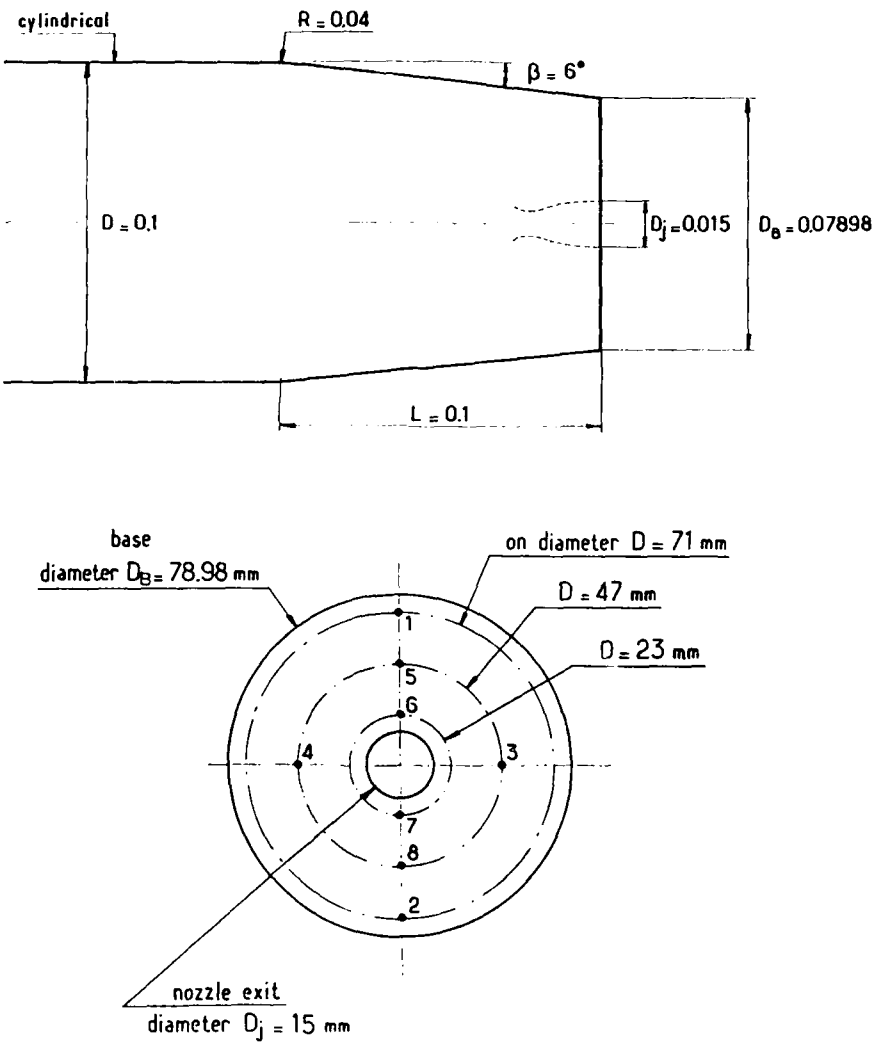

Figure 2.2.12: Geometrical Definition of the Afterbody (conical boattail, L = D, β = 6°) All dimensions in m

ONERA AEROSPATIALE Test Case

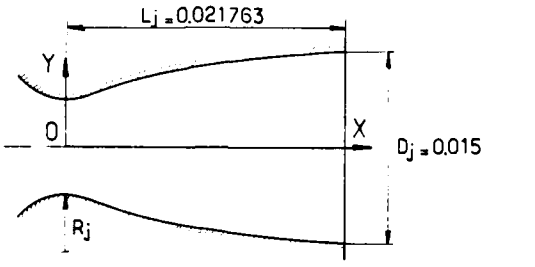

Radius of curvature at the throat Rj = 0.00445

	X 10^3	Y 10^3
1	0	3.750
2	0.596	3.751
3	1.192	3.755
4	1.788	4.031
5	2.344	4.230
6	2.930	4.441
7	3.515	4.641
8	4.102	4.828
9	4.688	5.016
10	5.273	5.191
11	5.859	5.355
12	6.445	5.508
13	7.031	5.648
14	7.617	5.777
15	8.203	5.906
16	8.789	6.023
17	9.375	6.129
18	9.961	6.234
19	10.547	6.328
20	11.133	6.422

	X 10^3	Y 10^3
21	11.719	6.504
22	12.305	6.586
23	12.891	6.656
24	13.477	6.727
25	14.063	6.797
26	14.648	6.855
27	15.234	6.926
28	15.820	6.984
29	16.406	7.031
30	16.992	7.070
31	17.578	7.109
32	18.164	7.145
33	18.750	7.254
34	19.336	7.313
35	19.922	7.359
36	20.508	7.418
37	21.094	7.465
38	21.753	7.500

Figure 2.2.13: Geometrical Definition of the Nozzle
All dimensions in m

ONERA AEROSPATIALE Test Case

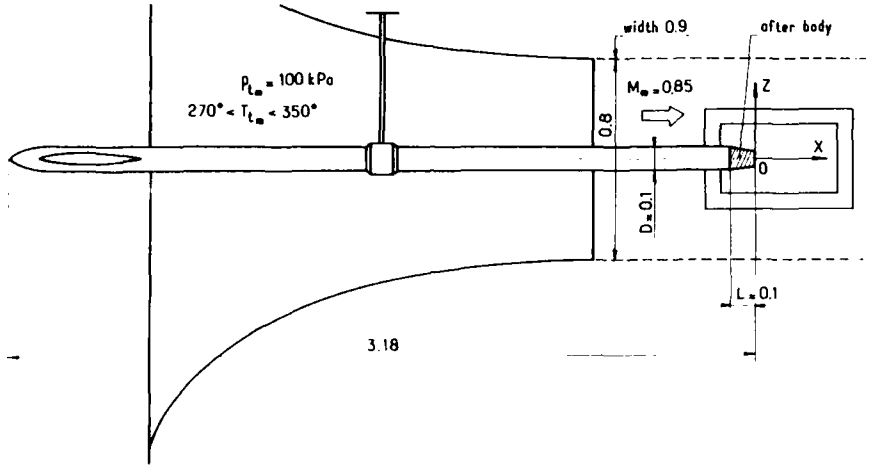

Figure 2.2.14: Model Installation in the Onera S3 Ch WT (All dimensions in m)

ONERA AEROSPATIALE Test Case

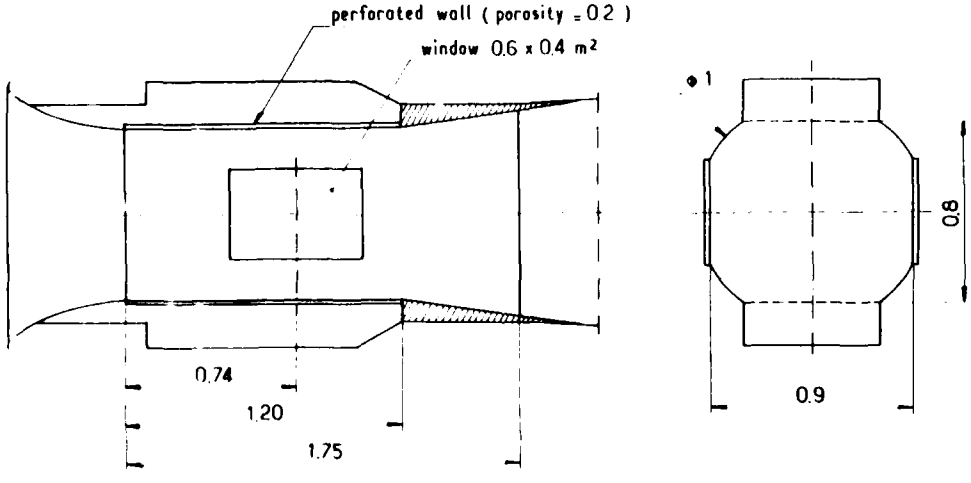

Figure 2.2.15: ONERA S3 Ch Transonic Wind Tunnel - Test Section Geometry (All dimensions in m)

2.2.5.5 TEST CASES 9,10, 11 AND 12 - FFA CONICAL BOATTAIL WITH BASE AT $M_\infty = 2.01$

I. Model Configuration (see Figure 2.2.17)

Two boattail angles: $\beta_I = 0°; 6°$; (6° conical boattail chosen since this is an optimum angle 2.2.15, 2.2.16

Afterbody length: $L/D = 1$

Nozzle: nearly uniform conical flow $\beta = 20°$; $M_j = 2.5$ (nozzle exit)
nozzle calibration: see Figure 2

Radius ratio: $R_{1I}/R_{2E} = 0.6$

II. Model Installation in Tunnel (see Figure 2.2.16)

Suck down windtunnel with stagnation conditions corresponding to ambient atmospheric conditions (tunnel cross section 0,46 x 0,57 m^2 corresponding to 3 percent blockage)

Reynolds number per meter: $Re = 13 \times 10^6 \frac{1}{m}$ (boundary layer transition strip 85 mm from nose)

III. Free Stream and Jet Conditions

External Mach number: $M_\infty = 2.01$

Static pressure ratios: $P_j/P_\infty = 1.0; 6.0$

Cold jet: $T_{tj} = T_{t\infty} = 286$ K

IV. Data available

Tabulated pressure recordings from FFA Technical AU-913. The numbers of the pressure orifices correspond to the positions given in the test case decription. P_2 is a reference pressure taken on the model surface 2.2 diameters ahead of the base and representing $P_\infty \approx P_E$.

Plots of base pressure and separation point position are presented for the whole pressure ratio range and for all boattail angles tested in order to give a complete impression of the experiments.

Schlieren pictures for cases 9, 10, 11 and 12.

Since oilflow pictures are only available for pressure ratio $P_j/P_\infty = 9.0$ at boattail angle $\beta_E = 6°$, such a photograph and the corresponding Schlieren picture are also included in order to reveal the excellent agreement in separation prediction between oilflow visualization and extrapolation of the corresponding shock wave onto the the body surface.

External Boundary Layer

V. References

2.2.14, 2.2.15, 2.2.16

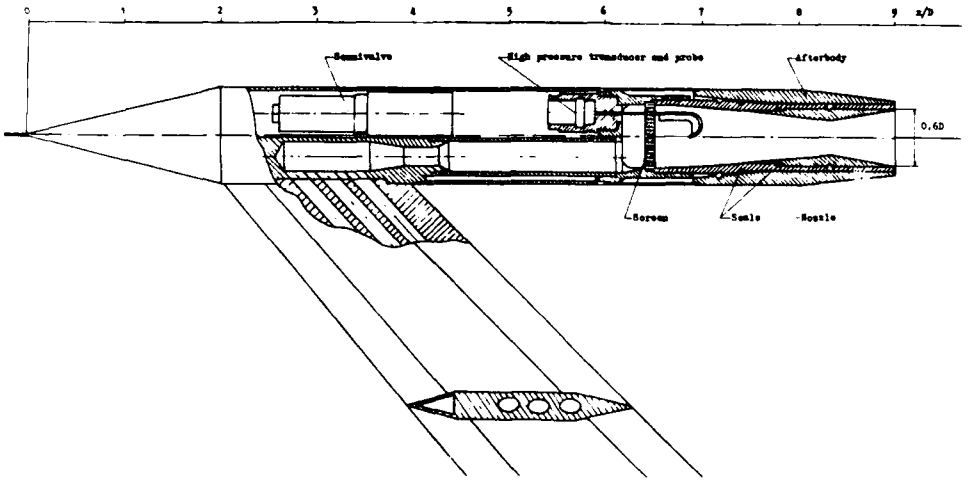

Figure 2.2.16: Details of wind tunnel model

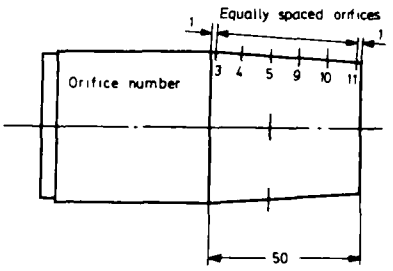

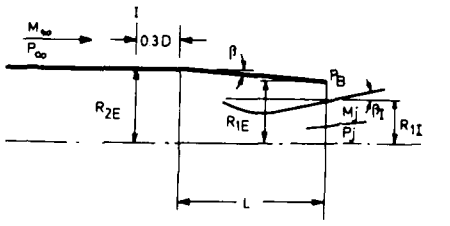

General Configuration and Nomenclature

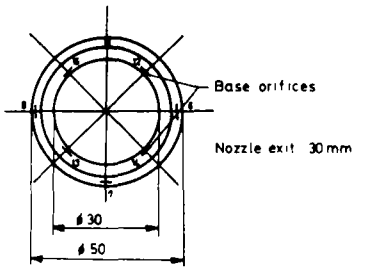

Location of base pressure taps:
Test case 9,10: $D_T/D = 0.82$
Test case 11,12: $D_T/D = 0.75$

Afterbody orifice locations

$M_j = 2.5 \quad \beta_1 = 20$

x mm	y mm	Mach-number
0	0	2.24
0	7.5	2.50
3	0	2.48

Nozzle calibration

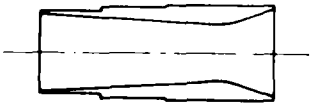

x mm	0.00	-6.00	-12.00	-14.00	-16.00	-17.00
y mm	15.00	12.82	10.63	9.92	9.45	9.32
x mm	-18.00	-19.00	-20.00	-21.00	-45.00	-77.00
y mm	9.26	9.25	9.26	9.??	11.13	13.53

Nozzle coordinates

Figure 2.2.17: Details of nozzle. All dimensions are in millimeters unless otherwise noted.

2.2.6 REFERENCES

2.2.1 Reubush, David E.: Experimental Study of the Effectiveness of Cylindrical Plume Simulators for Predicting Jet-On Boattail Drag at Mach Numbers Up to 1.30. NASA TN D-7795, 1974

2.2.2 Reubush, David E.; Runckel Jack F.: Effect of Fineness Ration on Boattail Drag of Circular-Arc Afterbodies Having Closure Ratios of 0.50 with Jet Exhaust at Mach Numbers Up to 1.30. NASA TN D-7192, 1973

2.2.3 Abeyounis, William K.; Putnam, Lawrence E.: Investigation of the Flow Field Surrounding Circular-Arc Boattail Nozzle at Subsonic Speeds. NASA TP-1633, 1980

2.2.4 Mason, Mary L.; Putnam, Lawrence E.: Pitot Pressure Measurements in Flow Fields Behind Circular-Arc Nozzles with Exhaust Jets at Subsonic Free- Stream Mach Numbers. NASA TM-80169, 1979

2.2.5 Abeyounis, William K.: Boundary-Layer Separation on Isolated Boattail Nozzles. NASA TP-1226, 1978

2.2.6 Reubush, David E.; Putnam, Lawrence E.: An Experimental and Analytical Investigation of the Effect on Isolated Boattail Drag of Varying Reynolds Number Up to 130 x 10^6. NASA TN-D-8210, 1976

2.2.7 Ferri, A. Editor; Improved Nozzle Testing Techniques in Transonic Flow. AGARD AG-208, 1975.

2.2.8 Zacharias, A.: Experimental and Theoretical Investigations of the Interaction between the Engine Jet and the Surrounding Flow Field with regard to the Pressure Drag on Afterbodies. AGARD-CP-308 on "Fluid Dynamics of Jets with Application to V/STOL", November 1981.

2.2.9 Zacharias, A.: Windtunnel Measurements on Afterbody Models and Jet Simulation for Test Case of the AGARD WG08 "Aerodynamics of Aircraft Afterbody". MBB-UFE123-AERO-MT-652, 1983

2.2.10 Zacharias, A.: Jet Velocity Profiles for Test Cases of the AGARD WG08 "Aerodynamics of Aircraft Afterbody", *MBB-UFE123-Aerotest-MT-2/83*, 1983

2.2.11 Putnam, Lawrence E.; Capone, Francis J.: Experimental Determination of Equivalent Solid Bodies to Represent Jets Exhausting into a Mach 2.20 External Stream. NASA TN-D-5553, 1969

2.2.12 Compton, William B., III; Runckel, Jack F.: Jet Effects on the Boattail Axial Force of Conical Afterbodies at Subsonic and Transonic Speeds. NASA TM-X-1960, 1972

2.2.13 R.G. Lacau, D. Desnoyer and J. Delery "Analyse au vélocimetre laser de l'*écoulement en aval* d'arriere-corps de missile", AGARD CPP 336 on "Missile Aerodynamics", September 1982.

2.2.14 Agrell, J. and White, R.A.: An experimental investigation of supersonic axisymmetric flow over boattails containing a centered propulsive jet. FFa Technical Note AU-913, 1974 (The Aeronautical Research Institute of Sweden)

2.2.15 Addy, A.L. and White, R.A.: Optimization of drag minimum including effects of flow separation. ASME Trans., J. of Engineering for Industry, Feb. 1973 (Also ASME Paper No. 72-Wa/Aero-1)

2.2.16 Addy, A.L.: Thrust-minus-drag optimization by base bleed and/or boattailing. *Journal of Spacecraft and Rockets*, Vol. 7, 1970, pp. 1360 - 1362

2.3 COMPILATION OF RESULTS

The figures should be self-explanatory if one notes that the jet exit is at X/D = 0.0 for all test cases. For the same test case some plots (e.g. c_p along boattail or drag build-up) are included several times, each containing results of different contributors. In that case, the first plot shows the results of all contributors without identification including the experimental data. This figure is followed by figures in which either Navier-Stokes, IVI, or Euler results have been plotted as specified in each figure. The curves in these plots are marked by the identification number of each contributor. These identification numbers are specified in the table of Fig. 2.3.1.

The boattail pressure drag coefficient CDPBT has been calculated by most of the contributors by using the trapezoidal rule. The test data have been integrated before and after extrapolating the measured boattail pressure coefficient linearly from the last measuring station to the end of the boattail. Both values are presented. The result of the extrapolation has been marked by a dashed line in the bar graph for CDPBT.

Thirteen figures have been devised to present the data of each test case:

Fig. 1: Boattail wall pressure coefficient
Fig. 2: Drag buildup along boattail
Fig. 3: Axial velocity on jet centerline
Fig. 4: Mach number on jet centerline
Fig. 5: Static temperature along jet centerline
Fig. 6: Pitot pressure along jet centerline
Fig. 7: Bar graph of base drag coefficient
Fig. 8: Bar graph of boattail pressure drag coefficient
Fig. 9: Bar graph of boattail friction drag coefficient
Fig. 10: Bar graph of total boattail drag coefficient
Fig. 11: Skin friction coefficient
Fig. 12: Pressure coefficient along base grid line
Fig. 13: Tunnel wall pressure coefficient

In cases where there was no data available for specific figures these figures have been skipped without renumbering of the other figures.

ID No.	Participant	Organization	Method	Test Case											
				1	2	2A	3	4	5	6	7	8	9	10	11	12
1	ZANNETTI/ONOFRI	Turin Politecnico	EULER	x							x					
2	VUILLOT/VEUILLOT	ONERA	EULER	x	x	x	x									
3	BISSINGER/EBERLE	MBB-LKE	EULER	x	x	x	x		x	x			x		x	
4	PUTNAM/WILMOTH	NASA-Langley	I.V.I.	x	x	x	x	x								
5	KUHN	NIELSEN ENG.	I.V.I.	x	x		x	x								
6	HODGES	RAE	I.V.I.	x	x	x	x	x								
7	HARDY/DUTOUQUET	SNECMA	I.V.I.	x	x	x	x									
8	RADESPIEL	DFVLR	I.V.I.	x			x	x	x	x						
9	ZACHARIAS	MBB-LKE	B.E.M.	x	x	x	x	x	x	x						
10	DELERY	ONERA	M.C.M.										x	x	x	x
11	LACAU/BERRUE	AEROSPATIALE	ADDY										x	x	x	x
12	ADDY	U. of Illinois	ADDY										x	x	x	x
13	MOORE	BAe	ADDY								x		x	x	x	x
14	WAGNER	DORNIER	M.C.M.										x	x	x	x
15	MOORE	BAe	MOULDEN								x		x	x	x	x
16	WAGNER	DORNIER	N.S.	x	x	x	x				x	x	x		x	
17	DEIWERT	NASA-Ames	N.S.	x	x		x	x			x	x	x	x	x	x
18	FORESTER/KERN	BOEING	N.S.		x											x

EULER Solution of Euler Equations
I.V.I. Inviscid/Viscous Interaction Method
B.E.M. Boundary Element Method
M.C.M. Multi Component Method
ADDY Addy Program
MOULDEN Moulden Program
N.S. Solution of Navier-Stokes Equations

FIG. 2.3.1: Participants and Methods used in AGARD Working Group 08

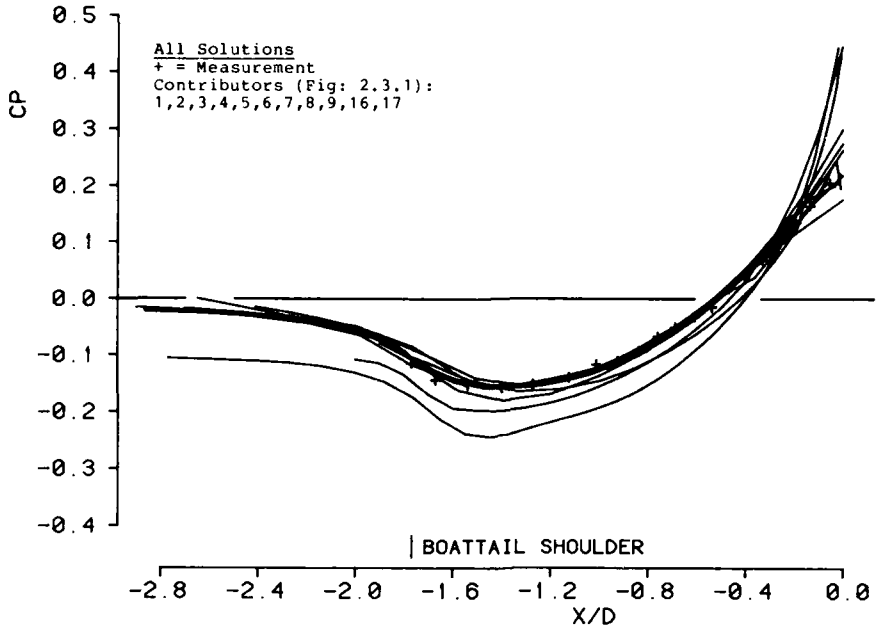

FIG.NO.: 2.3.1.1a
BOATTAIL WALL PRESSURE COEFFICIENT

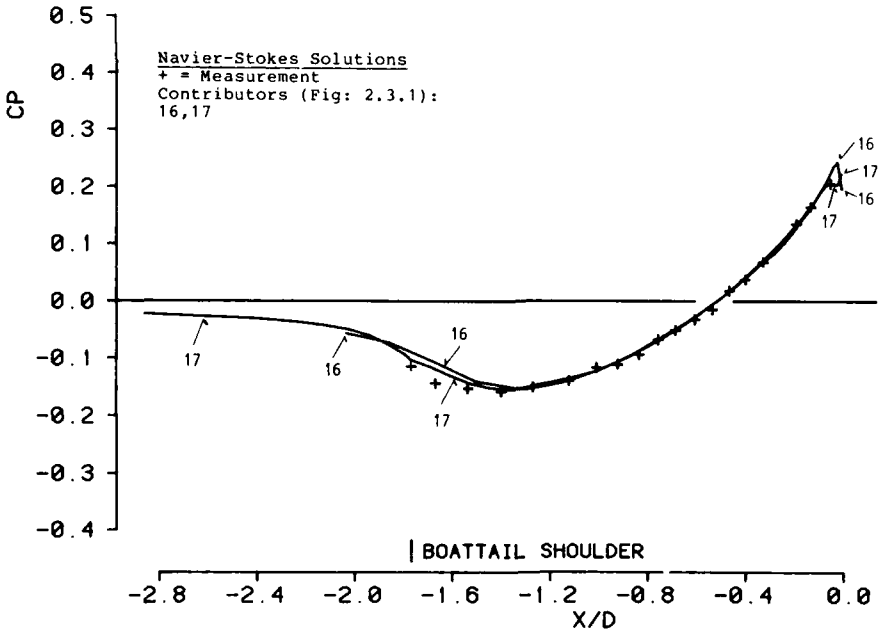

FIG.NO.: 2.3.1.1b
BOATTAIL WALL PRESSURE COEFFICIENT

WG08 : TEST CASE 1

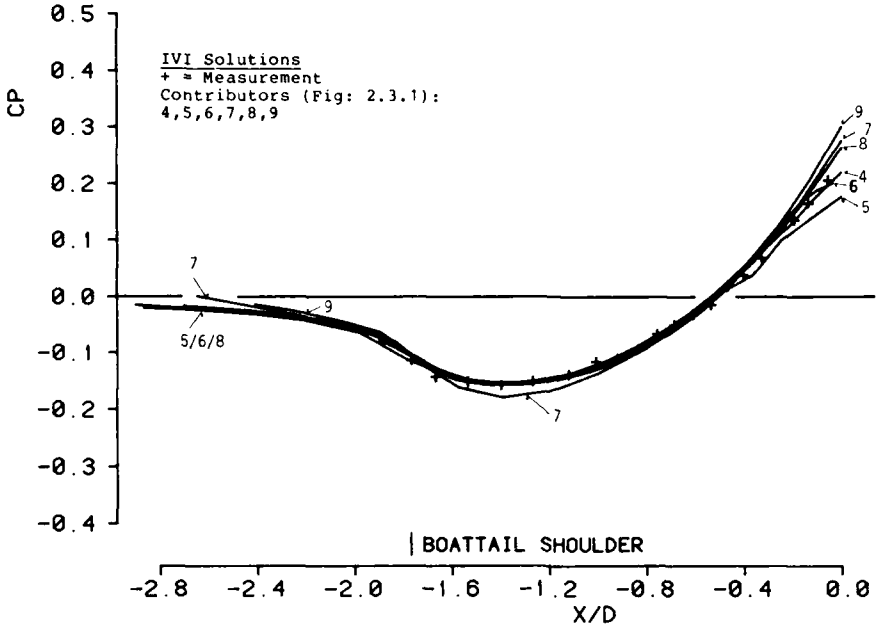

FIG.NO.: 2.3.1.1c
BOATTAIL WALL PRESSURE COEFFICIENT

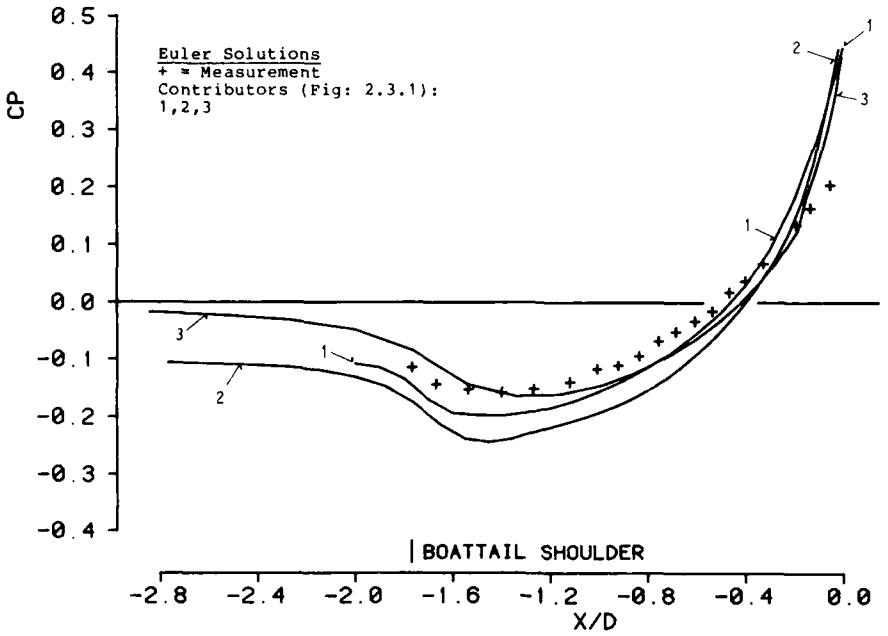

FIG.NO.: 2.3.1.1d
BOATTAIL WALL PRESSURE COEFFICIENT

WG08 : TEST CASE 1

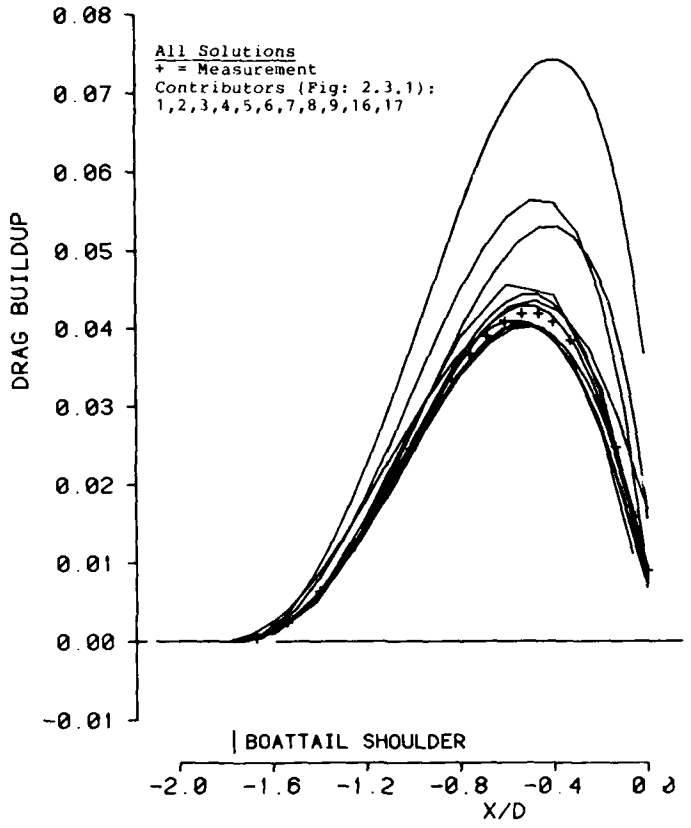

FIG.NO.: 2.3.1.2a
DRAG BUILDUP ALONG BOATTAIL

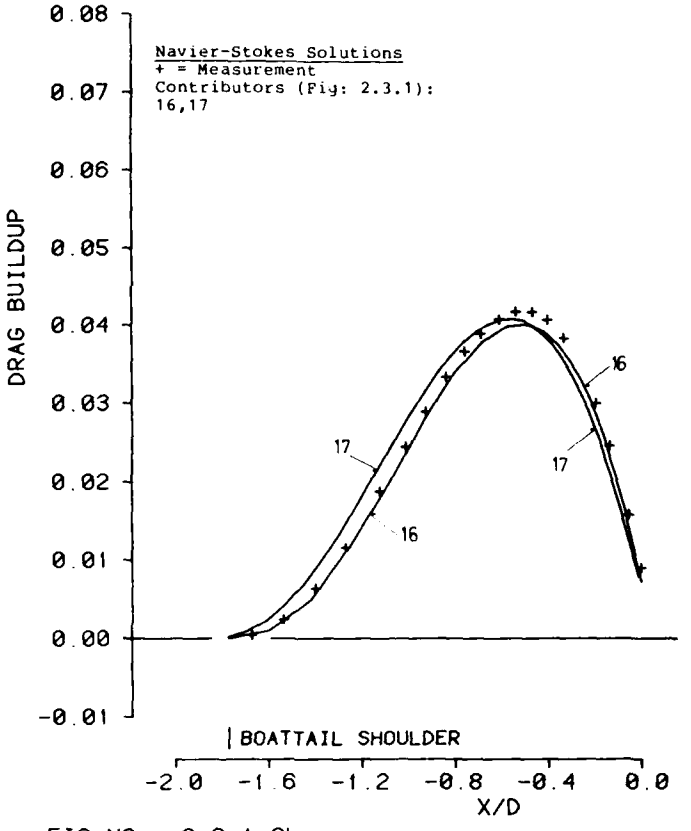

FIG.NO.: 2.3.1.2b
DRAG BUILDUP ALONG BOATTAIL

WG08 : TEST CASE 1

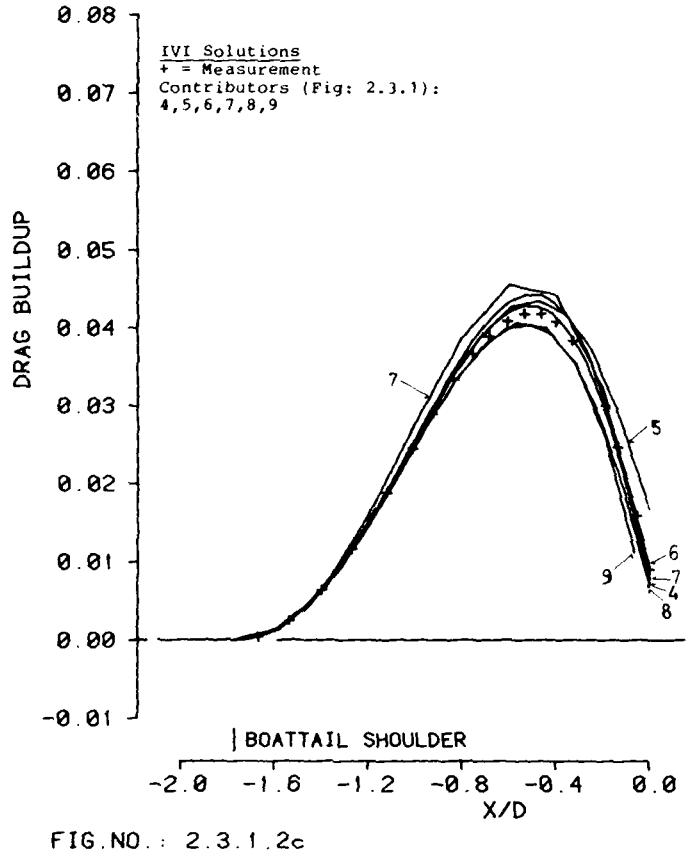

FIG.NO.: 2.3.1.2c
DRAG BUILDUP ALONG BOATTAIL

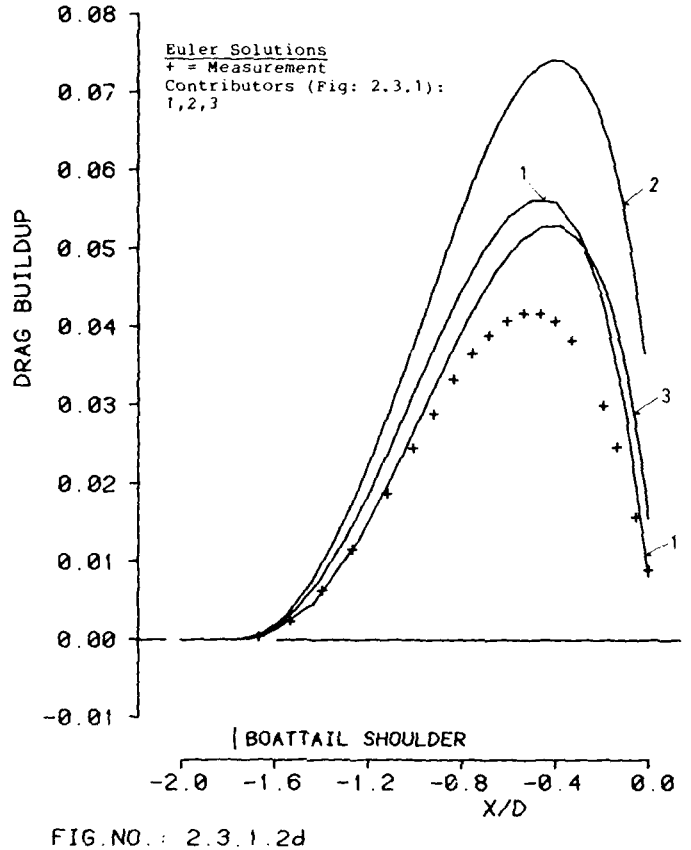

FIG.NO.: 2.3.1.2d
DRAG BUILDUP ALONG BOATTAIL

WG08 : TEST CASE 1

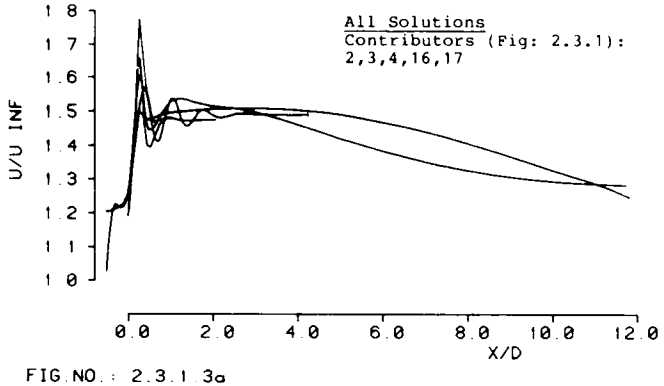

FIG.NO.: 2.3.1.3a
AXIAL VELOCITY ON JET CENTERLINE

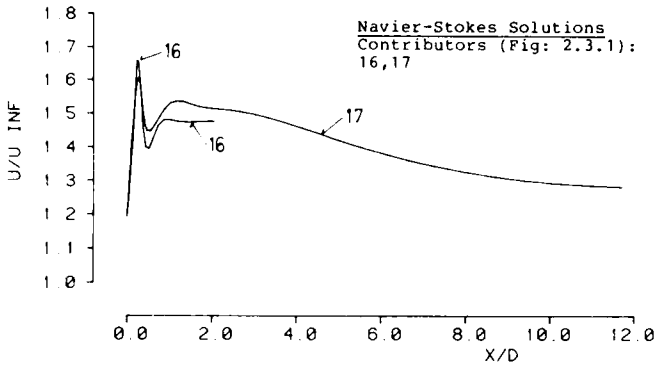

FIG.NO.: 2.3.1.3b
AXIAL VELOCITY ON JET CENTERLINE

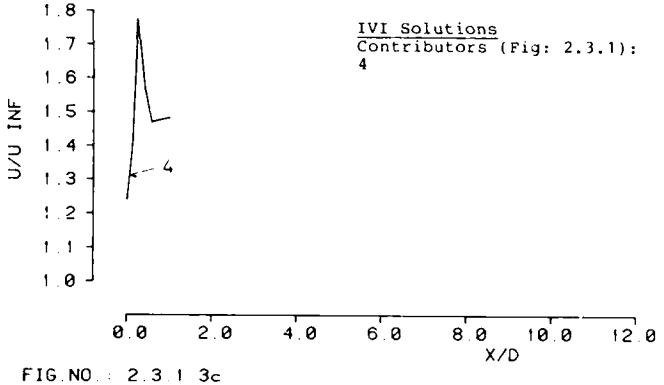

FIG.NO.: 2.3.1.3c
AXIAL VELOCITY ON JET CENTERLINE

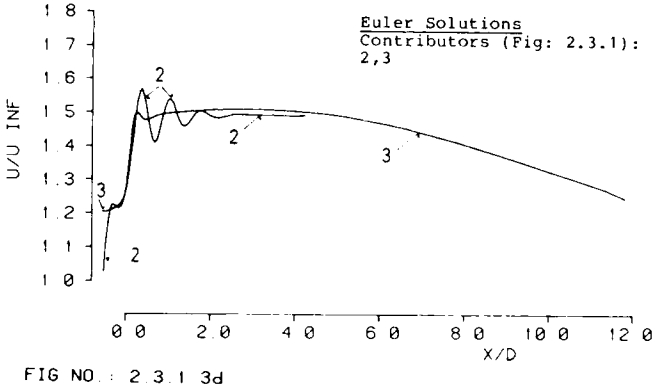

FIG NO.: 2.3.1.3d
AXIAL VELOCITY ON JET CENTERLINE

WG08 : TEST CASE 1

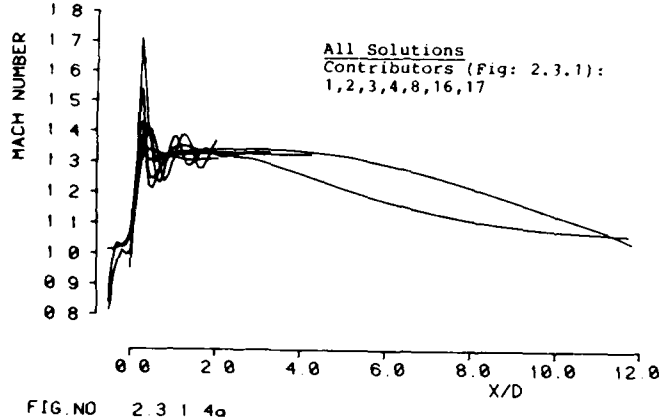

FIG.NO 2.3.1.4a
MACH NUMBER ON JET CENTERLINE

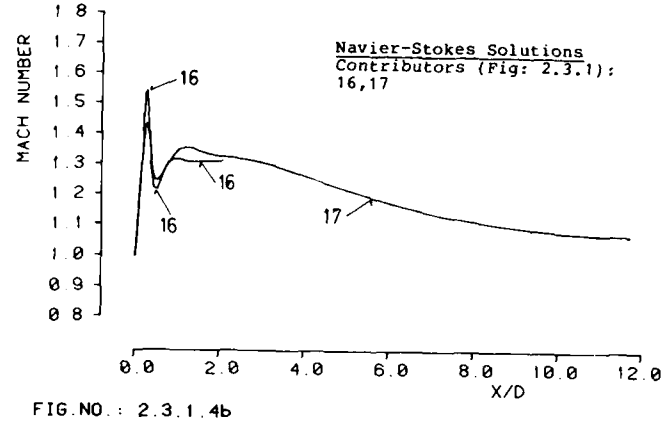

FIG.NO.: 2.3.1.4b
MACH NUMBER ON JET CENTERLINE

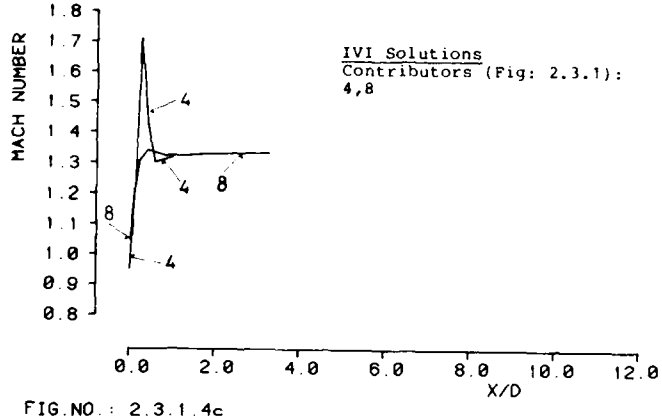

FIG.NO.: 2.3.1.4c
MACH NUMBER ON JET CENTERLINE

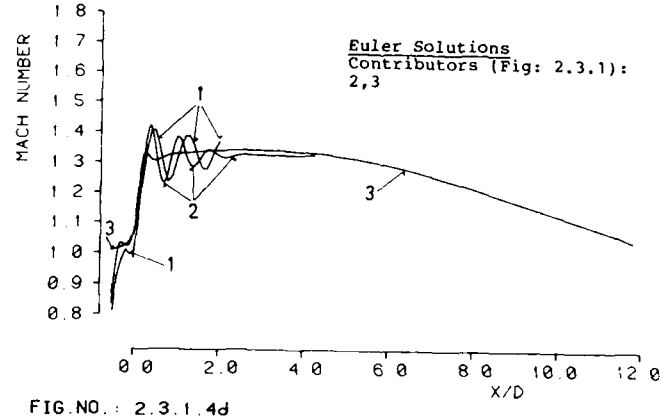

FIG.NO.: 2.3.1.4d
MACH NUMBER ON JET CENTERLINE

WG08 : TEST CASE 1

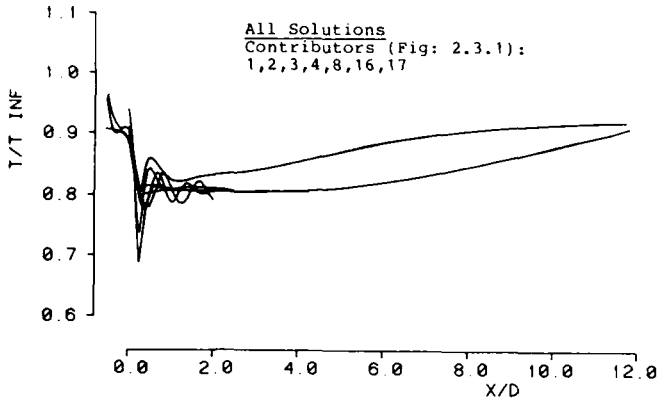

FIG.NO.: 2.3.1.5a
STATIC TEMPERATURE ALONG JET CENTERLINE

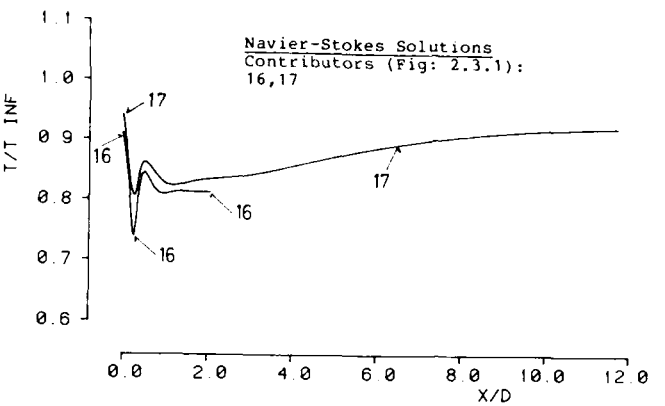

FIG.NO.: 2.3.1.5b
STATIC TEMPERATURE ALONG JET CENTERLINE

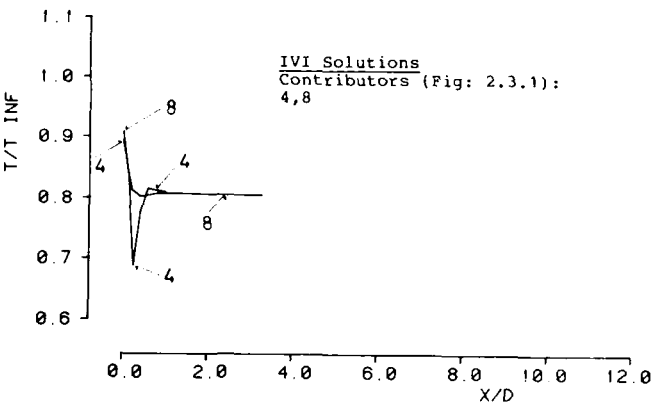

FIG.NO.: 2.3.1.5c
STATIC TEMPERATURE ALONG JET CENTERLINE

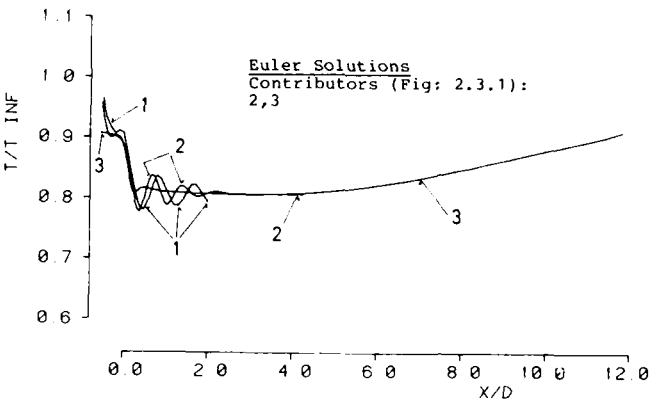

FIG.NO.: 2.3.1.5d
STATIC TEMPERATURE ALONG JET CENTERLINE

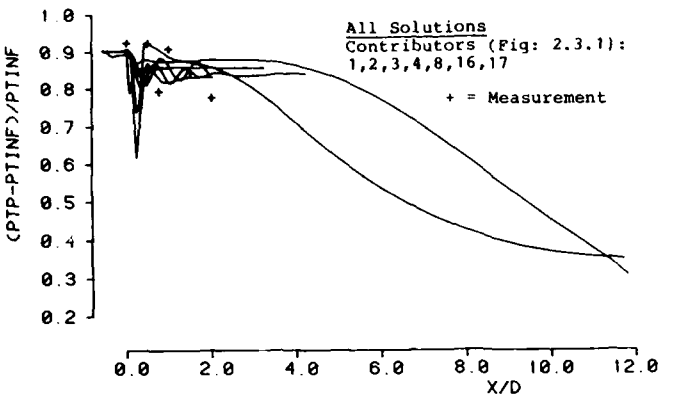

FIG.NO.: 2.3.1.6a
PITOT PRESSURE ALONG JET CENTERLINE

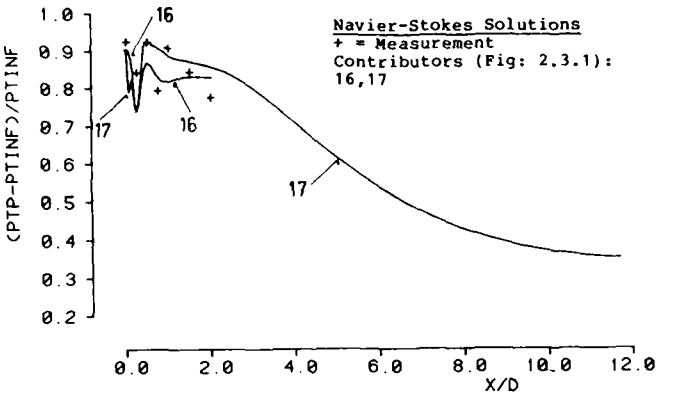

FIG.NO.: 2.3.1.6b
PITOT PRESSURE ALONG JET CENTERLINE

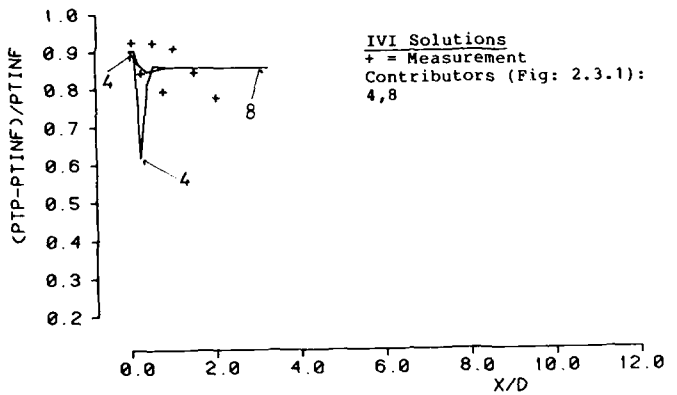

FIG.NO.: 2.3.1.6c
PITOT PRESSURE ALONG JET CENTERLINE

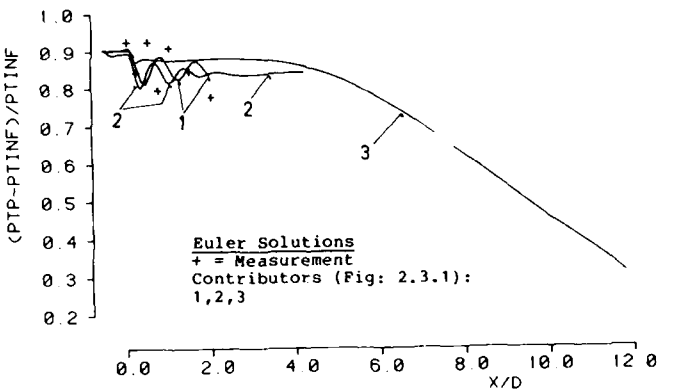

FIG.NO.: 2.3.1.6d
PITOT PRESSURE ALONG JET CENTERLINE

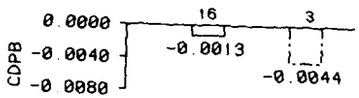

FIG.NO.: 2.3.1.7
BAR GRAPH OF BASE DRAG COEFFICIENT

FOR CONTRIBUTOR IDENTIFICATION
SEE FIG.NO.: 2.3.1

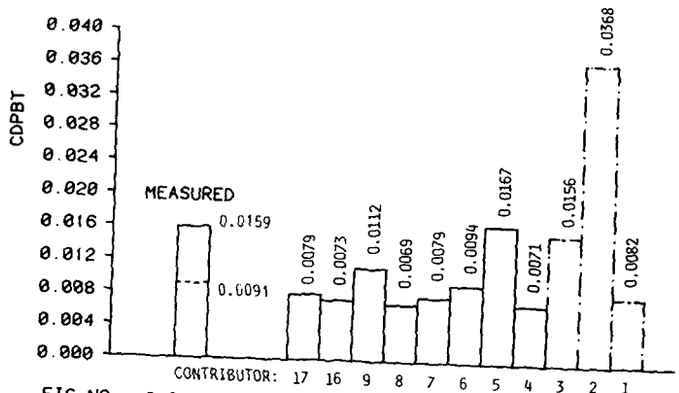

FIG.NO.: 2.3.1.8
BAR GRAPH OF BOATTAIL PRESSURE DRAG COEFFICIENT

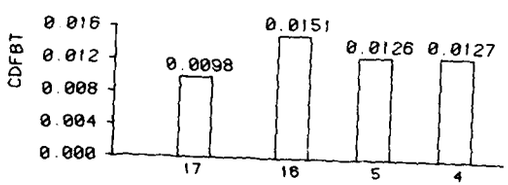

FIG.NO.: 2.3.1.9
BAR GRAPH OF BOATTAIL FRICTION DRAG COEFFICIENT

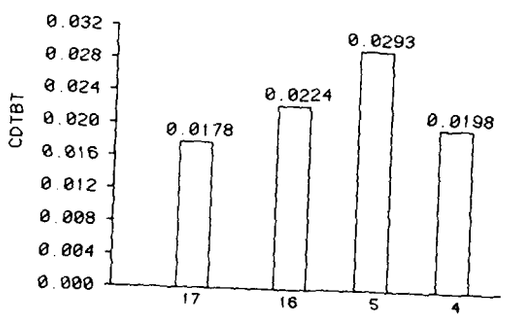

FIG.NO.: 2.3.1.10
BAR GRAPH OF TOTAL BOATTAIL DRAG COEFFICIENT

WG08 TEST CASE 1

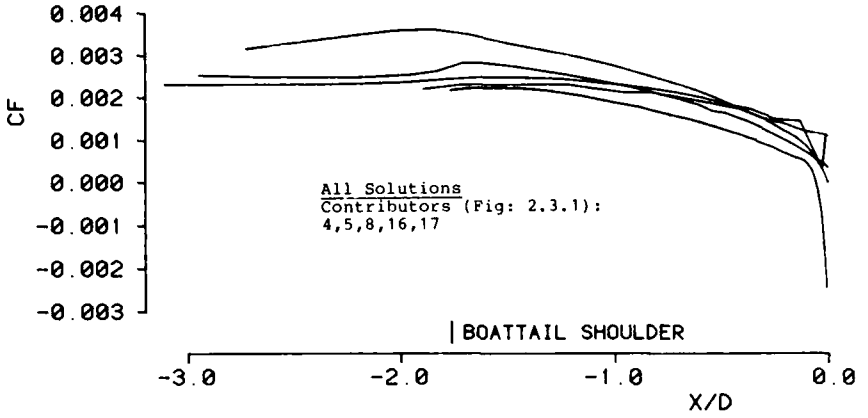

FIG.NO.: 2.3.1.11a SKIN FRICTION COEFFICIENT

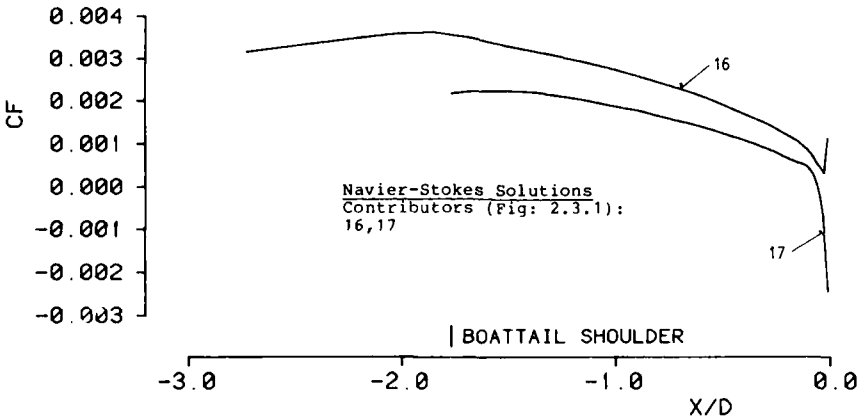

FIG.NO.: 2.3.1.11b SKIN FRICTION COEFFICIENT

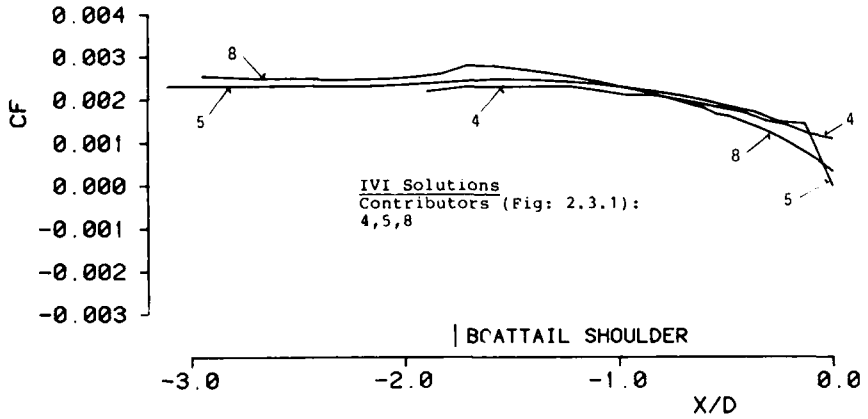

FIG.NO.: 2.3.1.11c SKIN FRICTION COEFFICIENT

WG08 : TEST CASE 1

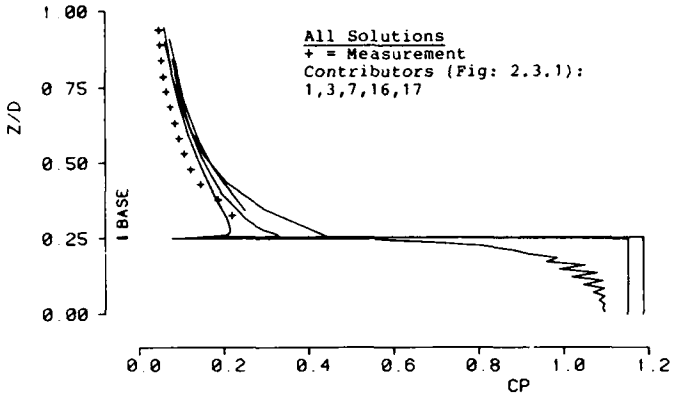

FIG.NO.: 2.3.1.12a
PRESSURE COEFFICIENT ALONG BASE GRID LINE

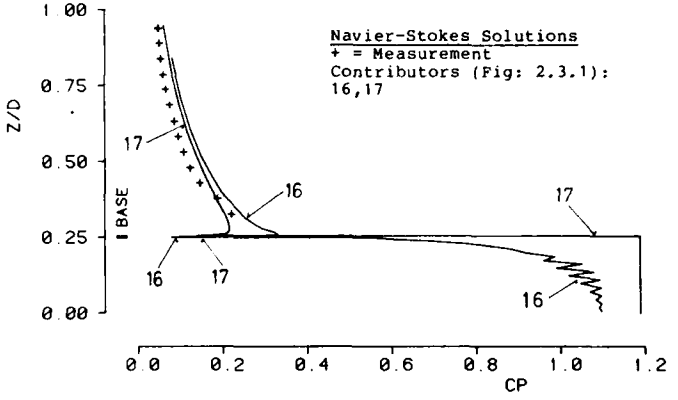

FIG.NO.: 2.3.1.12b
PRESSURE COEFFICIENT ALONG BASE GRID LINE

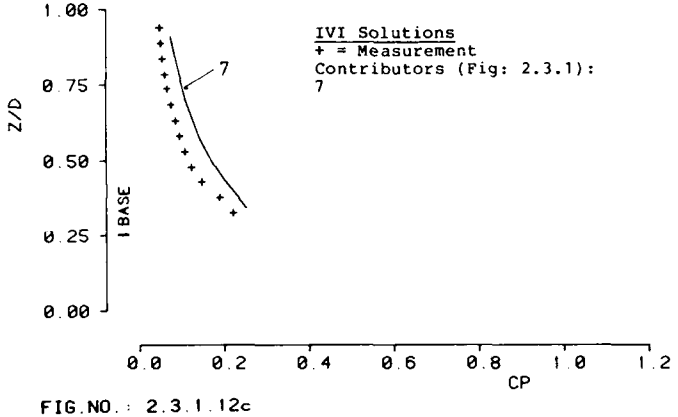

FIG.NO.: 2.3.1.12c
PRESSURE COEFFICIENT ALONG BASE GRID LINE

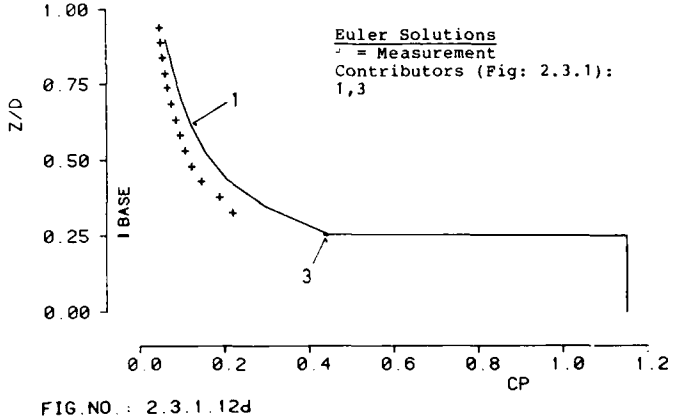

FIG.NO.: 2.3.1.12d
PRESSURE COEFFICIENT ALONG BASE GRID LINE

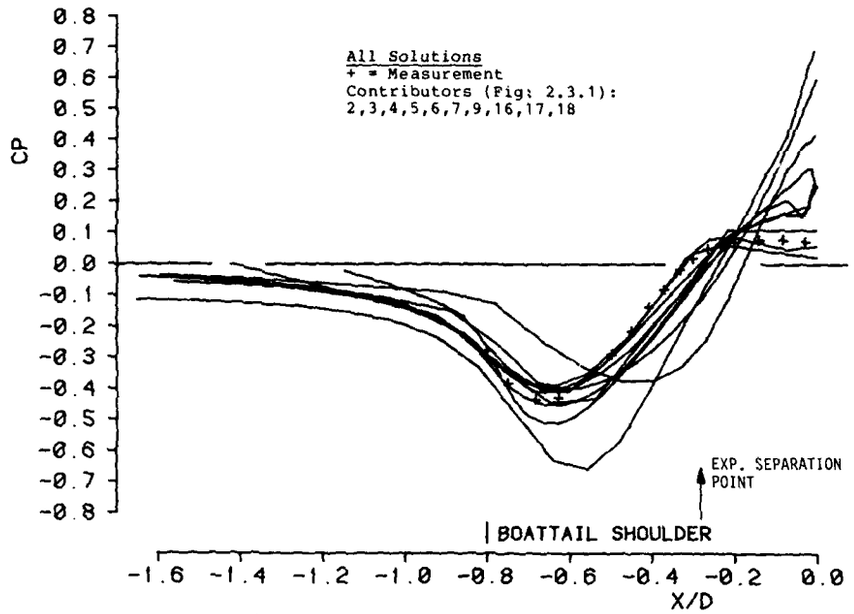

FIG.NO.: 2.3.2.1a
BOATTAIL WALL PRESSURE COEFFICIENT

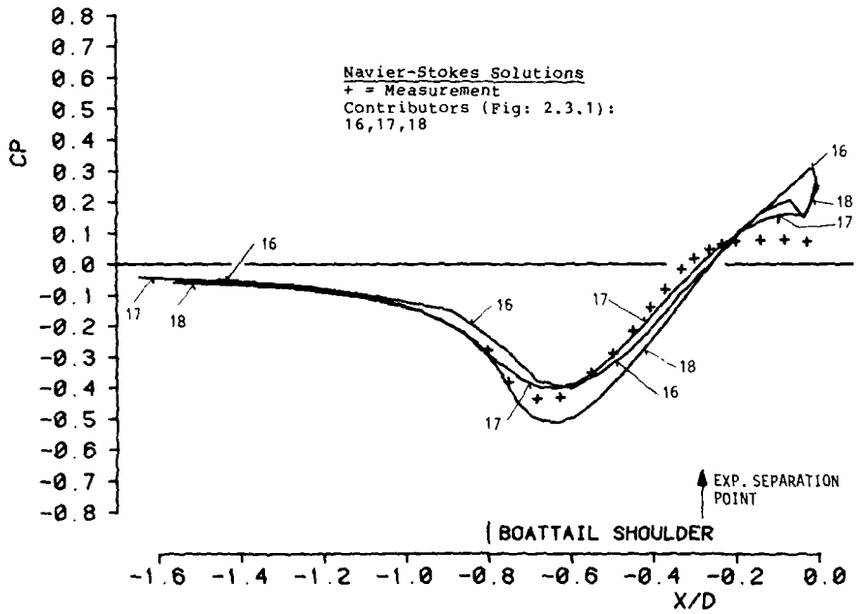

FIG.NO.: 2.3.2.1b
BOATTAIL WALL PRESSURE COEFFICIENT

WG08 : TEST CASE 2

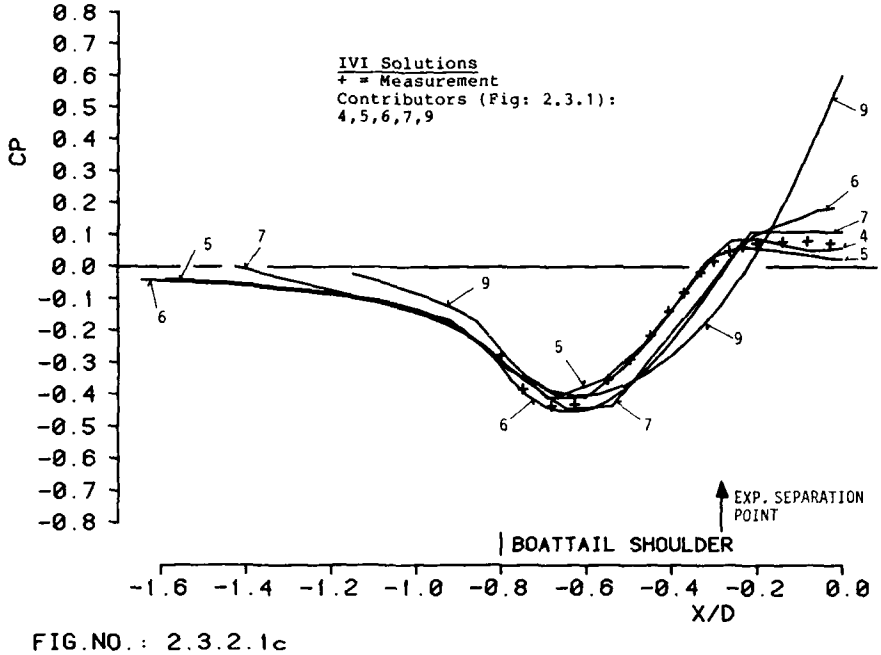

FIG.NO.: 2.3.2.1c
BOATTAIL WALL PRESSURE COEFFICIENT

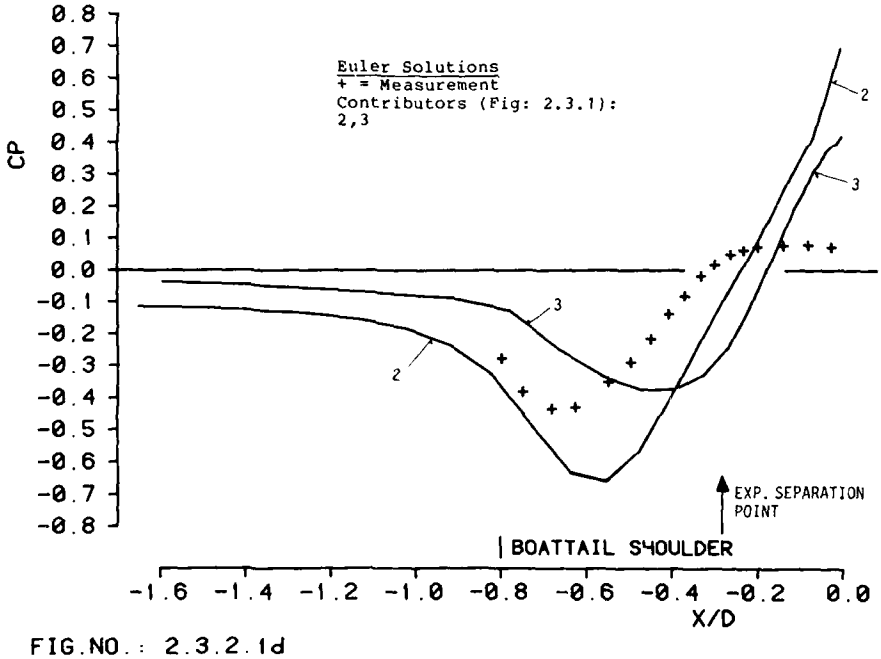

FIG.NO.: 2.3.2.1d
BOATTAIL WALL PRESSURE COEFFICIENT

WG08 : TEST CASE 2

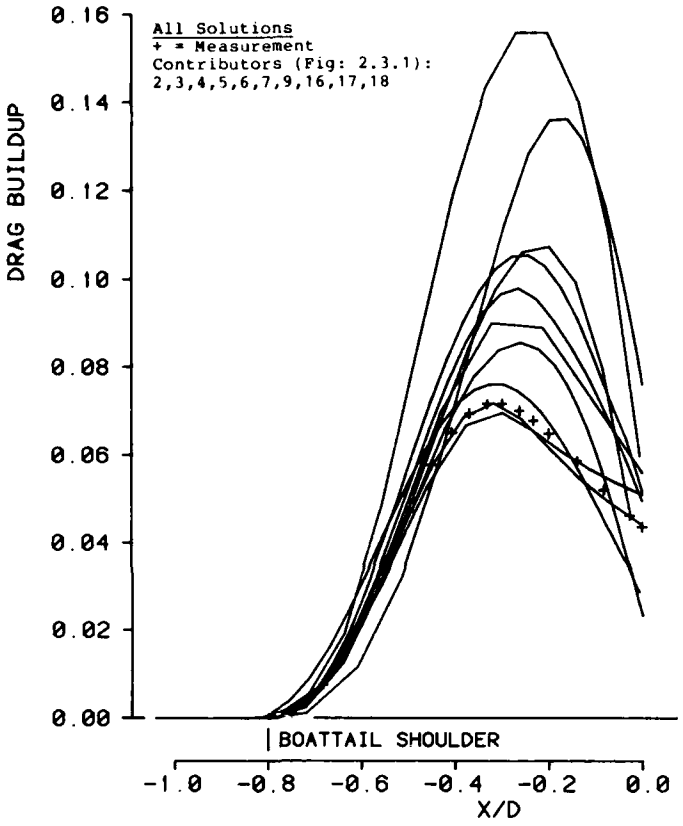

FIG.NO.: 2.3.2.2a
DRAG BUILDUP ALONG BOATTAIL

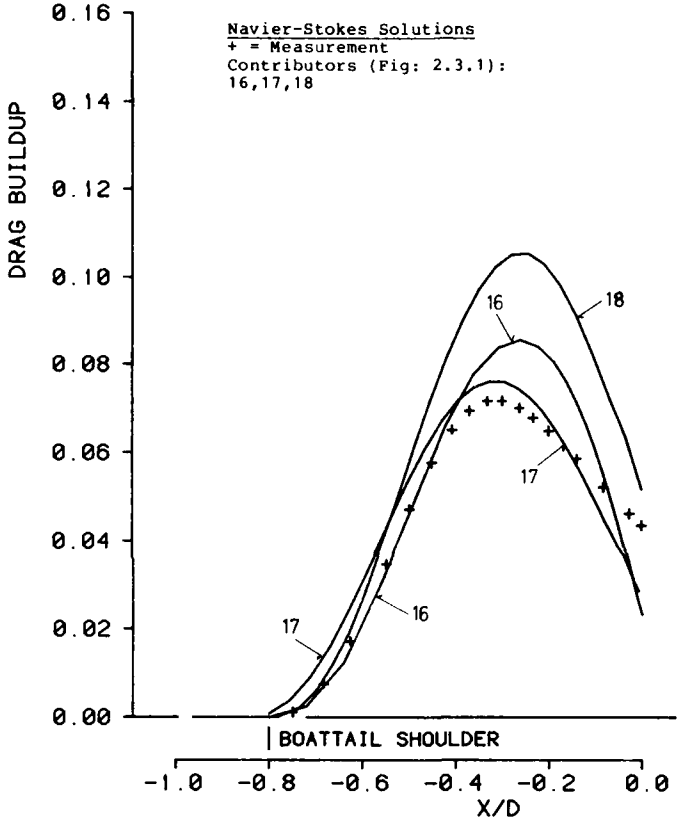

FIG.NO.: 2.3.2.2b
DRAG BUILDUP ALONG BOATTAIL

WG08 : TEST CASE 2

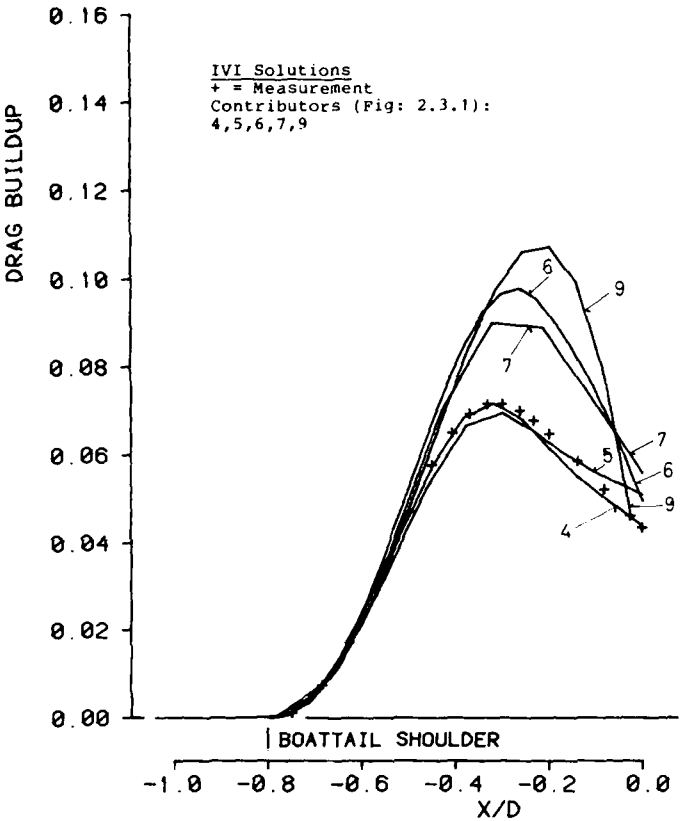

FIG.NO.: 2.3.2.2c
DRAG BUILDUP ALONG BOATTAIL

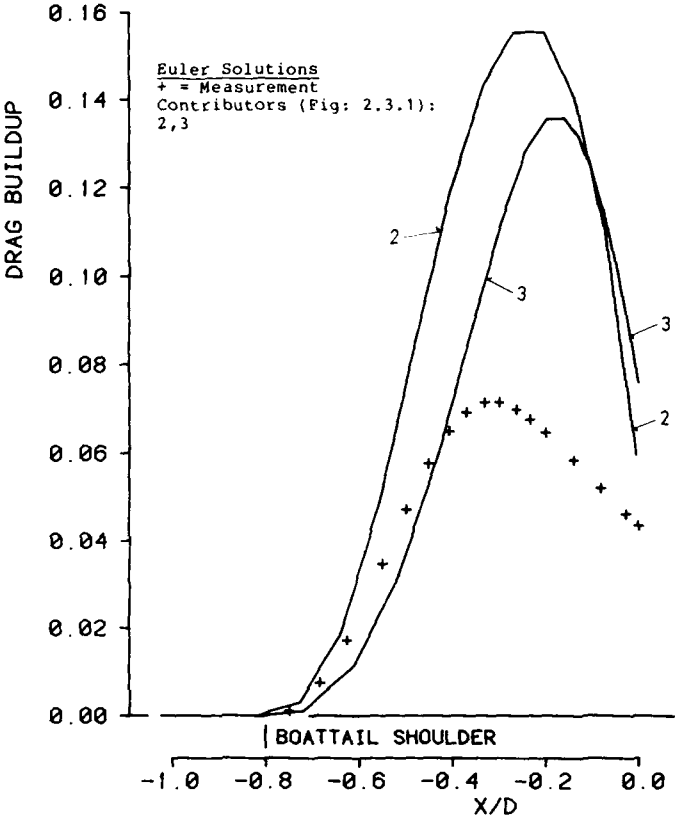

FIG.NO.: 2.3.2.2d
DRAG BUILDUP ALONG BOATTAIL

WG08 : TEST CASE 2

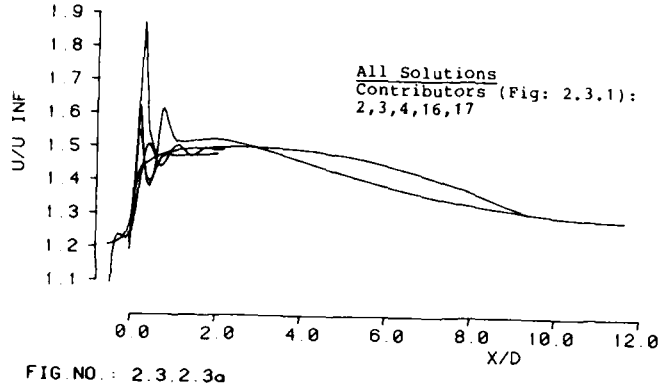

FIG.NO.: 2.3.2.3a
AXIAL VELOCITY ON JET CENTERLINE

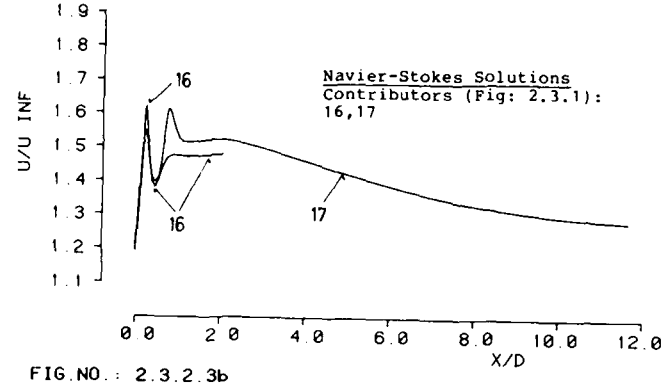

FIG.NO.: 2.3.2.3b
AXIAL VELOCITY ON JET CENTERLINE

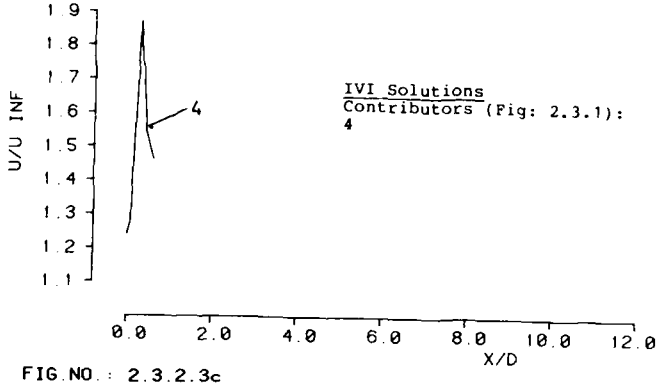

FIG.NO.: 2.3.2.3c
AXIAL VELOCITY ON JET CENTERLINE

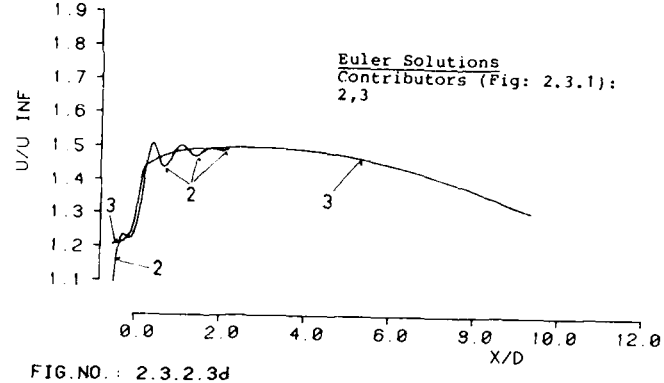

FIG.NO.: 2.3.2.3d
AXIAL VELOCITY ON JET CENTERLINE

WG08 : TEST CASE 2

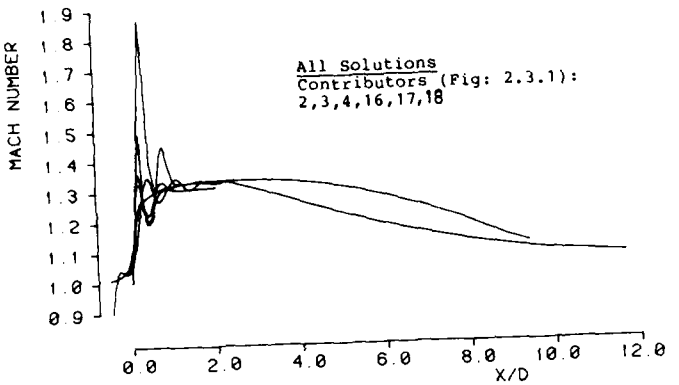

FIG.NO.: 2.3.2.4a
MACH NUMBER ON JET CENTERLINE

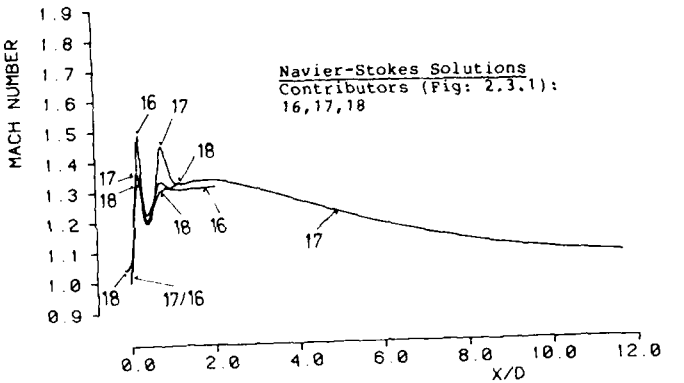

FIG.NO.: 2.3.2.4b
MACH NUMBER ON JET CENTERLINE

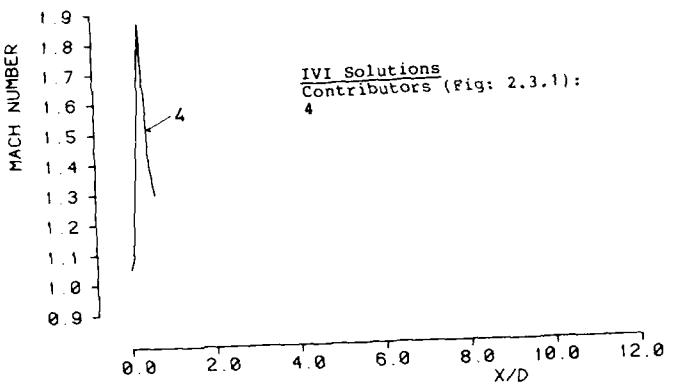

FIG.NO.: 2.3.2.4c
MACH NUMBER ON JET CENTERLINE

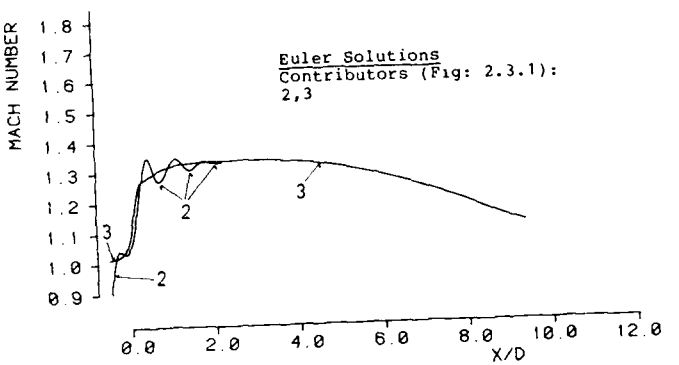

FIG.NO.: 2.3.2.4d
MACH NUMBER ON JET CENTERLINE

WG08 : TEST CASE 2

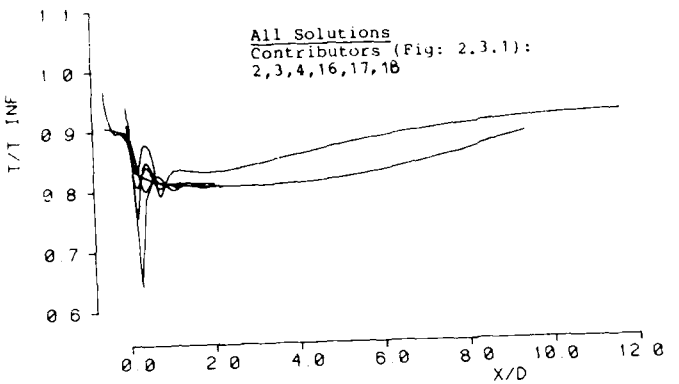

FIG NO.: 2.3.2.5a
STATIC TEMPERATURE ALONG JET CENTERLINE

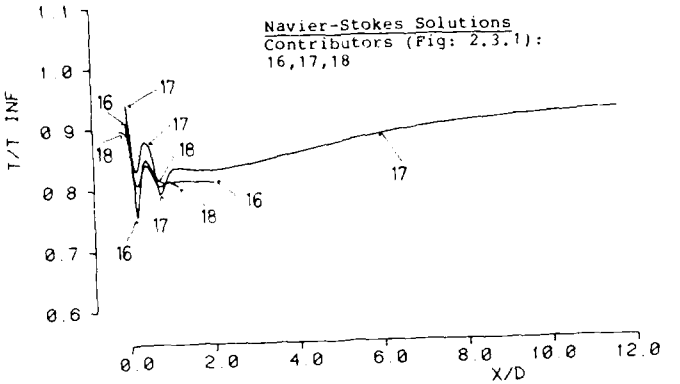

FIG.NO.: 2.3.2.5b
STATIC TEMPERATURE ALONG JET CENTERLINE

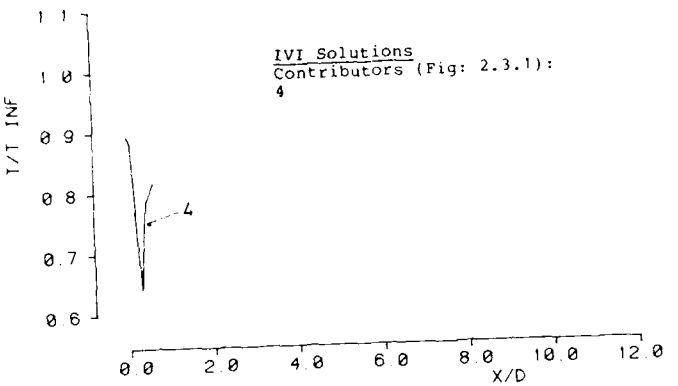

FIG.NO.: 2.3.2.5c
STATIC TEMPERATURE ALONG JET CENTERLINE

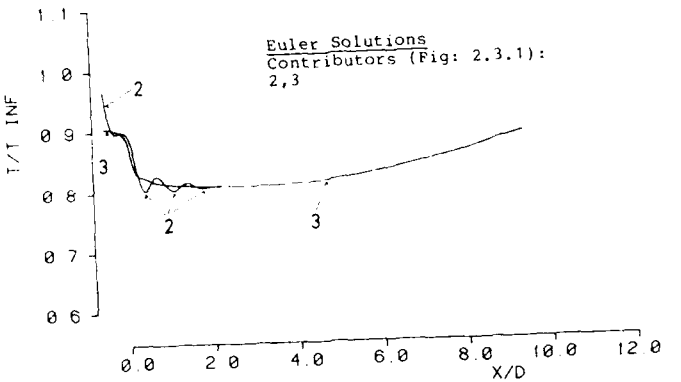

FIG.NO.: 2.3.2.5d
STATIC TEMPERATURE ALONG JET CENTERLINE

WG08 TEST CASE 2

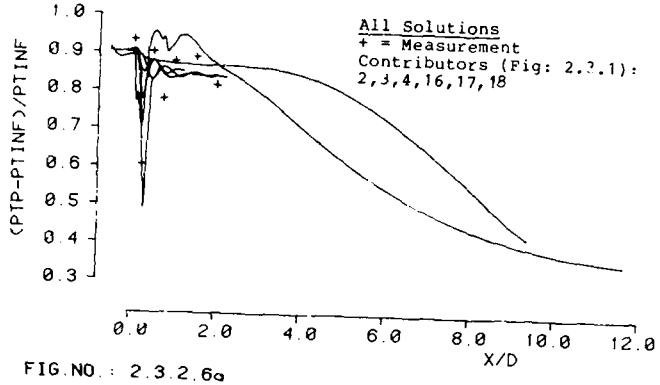

FIG.NO.: 2.3.2.6a
PITOT PRESSURE ALONG JET CENTERLINE

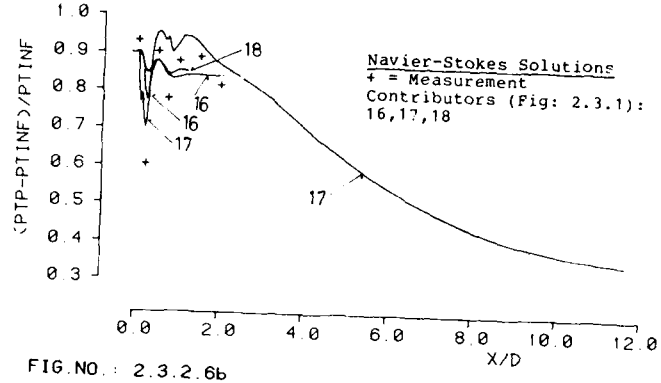

FIG.NO.: 2.3.2.6b
PITOT PRESSURE ALONG JET CENTERLINE

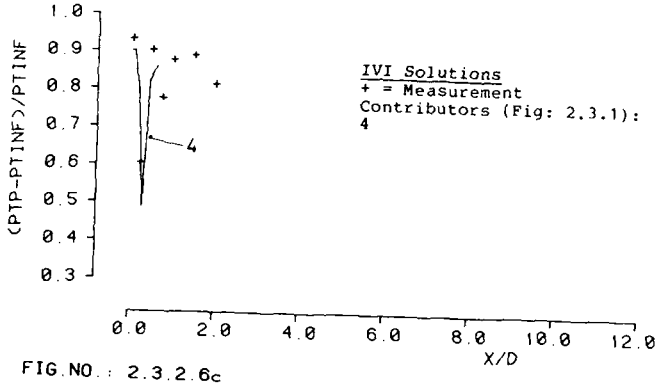

FIG.NO.: 2.3.2.6c
PITOT PRESSURE ALONG JET CENTERLINE

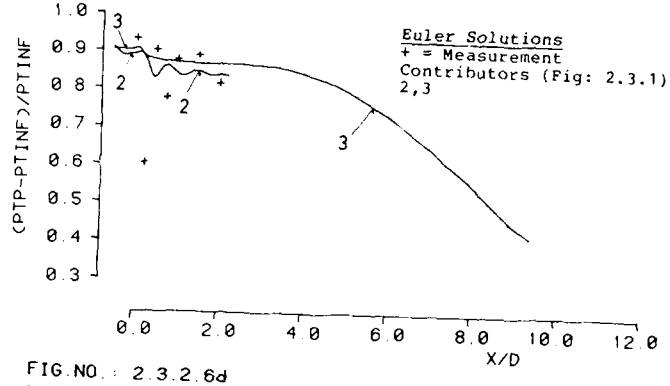

FIG.NO.: 2.3.2.6d
PITOT PRESSURE ALONG JET CENTERLINE

WG08 : TEST CASE 2

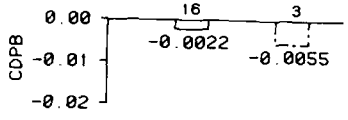

FIG.NO.: 2.3.2.7
BAR GRAPH OF BASE DRAG COEFFICIENT

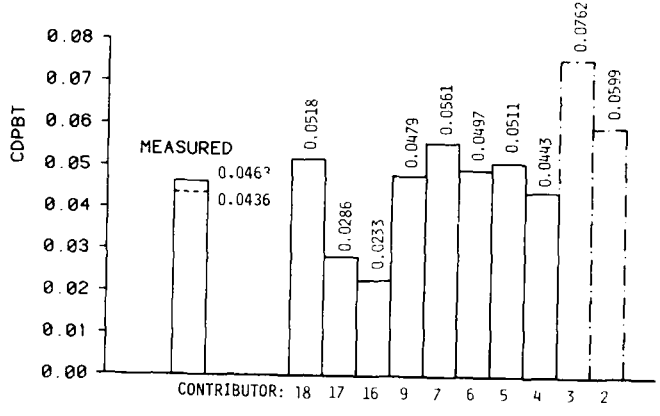

FIG.NO.: 2.3.2.8
BAR GRAPH OF BOATTAIL PRESSURE DRAG COEFFICIENT

FOR CONTRIBUTOR IDENTIFICATION
SEE FIG.NO.: 2.3.1

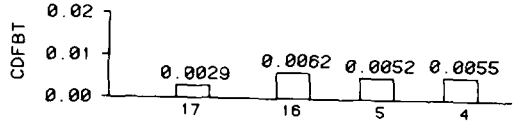

FIG.NO.: 2.3.2.9
BAR GRAPH OF BOATTAIL FRICTION DRAG COEFFICIENT

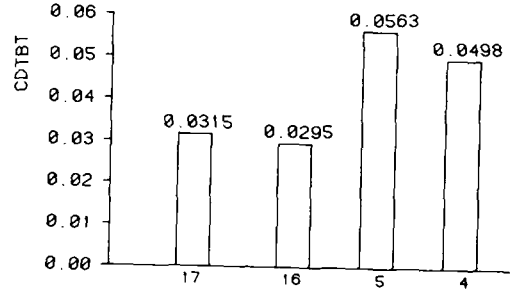

FIG.NO.: 2.3.2.10
BAR GRAPH OF TOTAL BOATTAIL DRAG COEFFICIENT

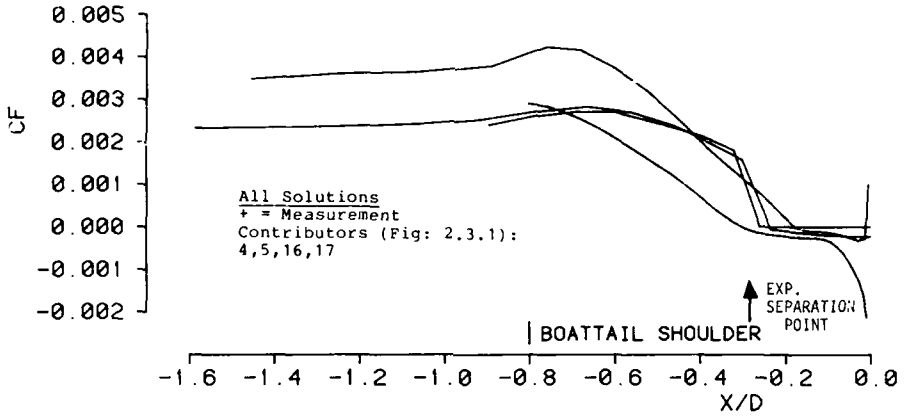

FIG.NO.: 2.3.2.11a

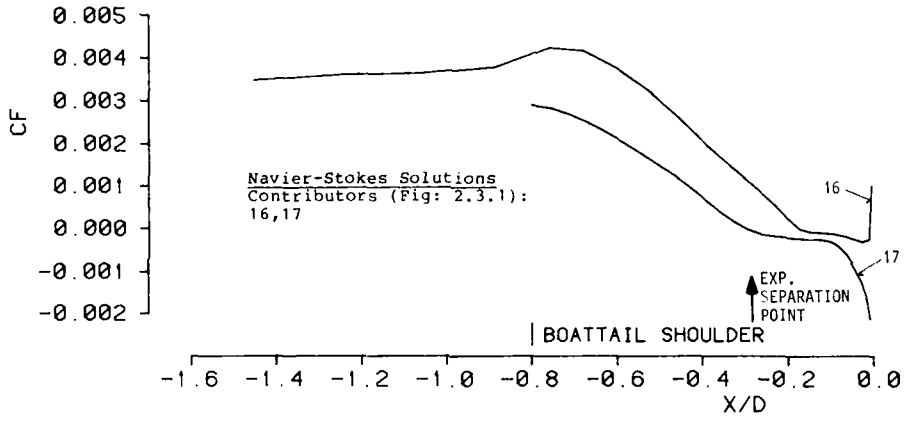

FIG.NO.: 2.3.2.11b

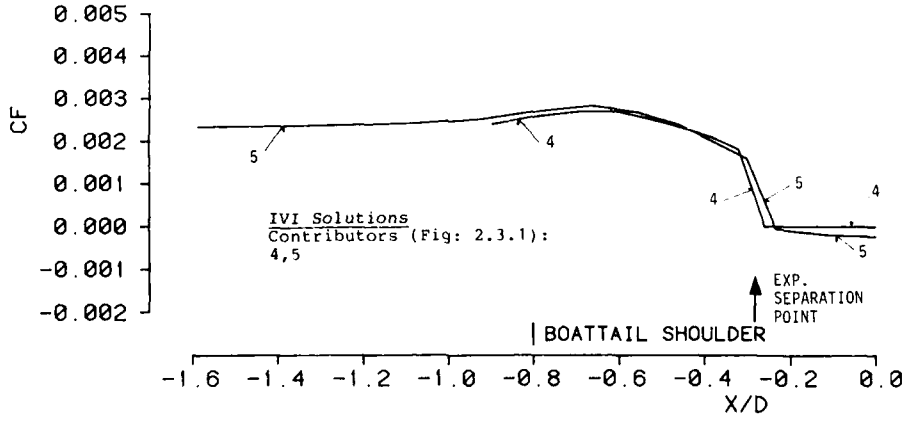

FIG.NO.: 2.3.2.11c

SKIN FRICTION COEFFICIENT

WG08 : TEST CASE 2

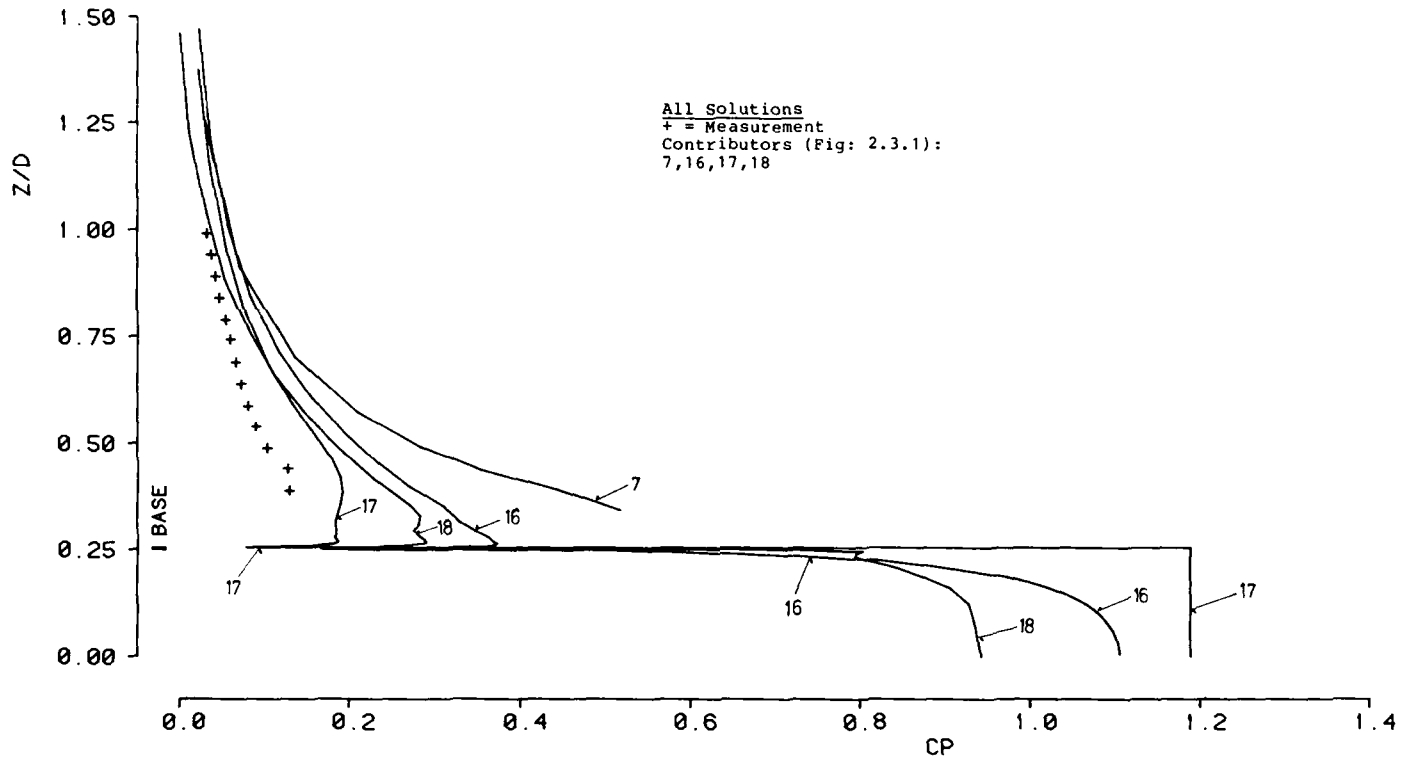

FIG.NO.: 2.3.2.12
PRESSURE COEFFICIENT ALONG BASE GRID LINE

WG08 : TEST CASE 2

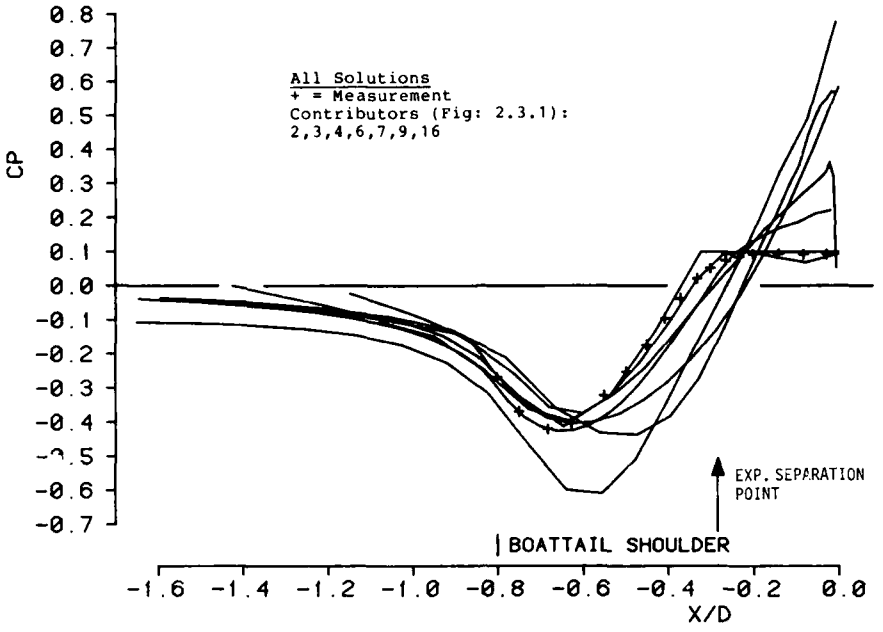

FIG.NO.: 2.3.2A.1a
BOATTAIL WALL PRESSURE COEFFICIENT

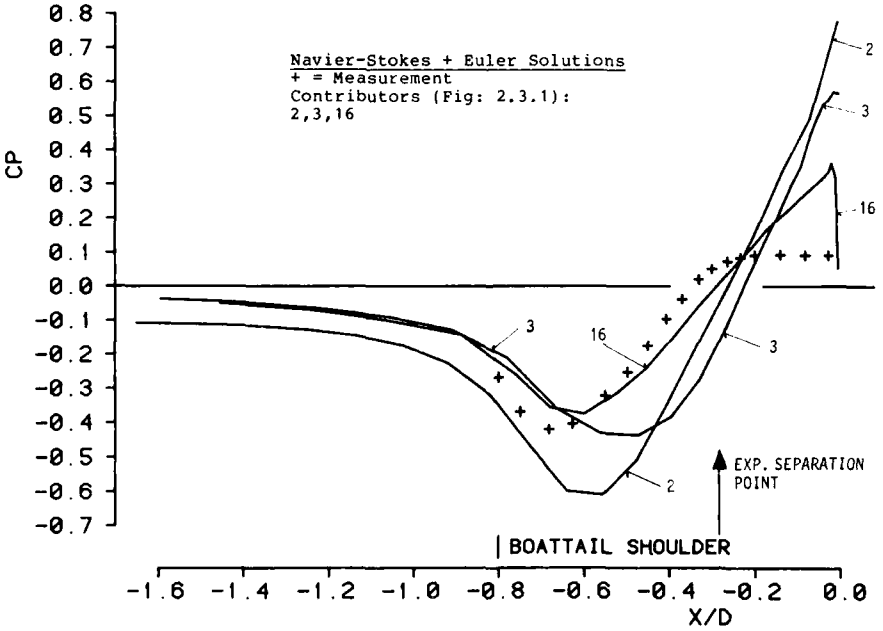

FIG.NO.: 2.3.2A.1b
BOATTAIL WALL PRESSURE COEFFICIENT

WG08 : TEST CASE 2A

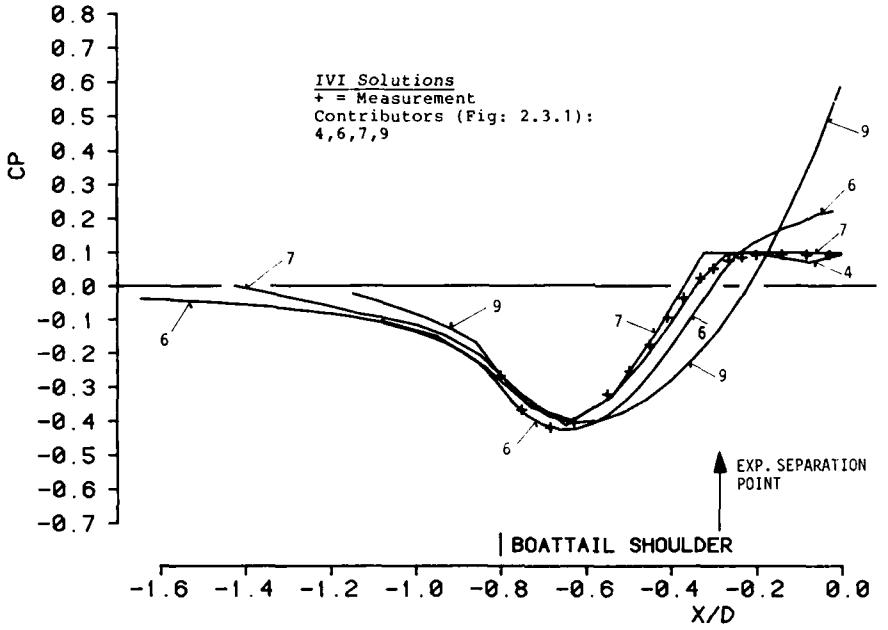

FIG.NO.: 2.3.2A.1c
BOATTAIL WALL PRESSURE COEFFICIENT

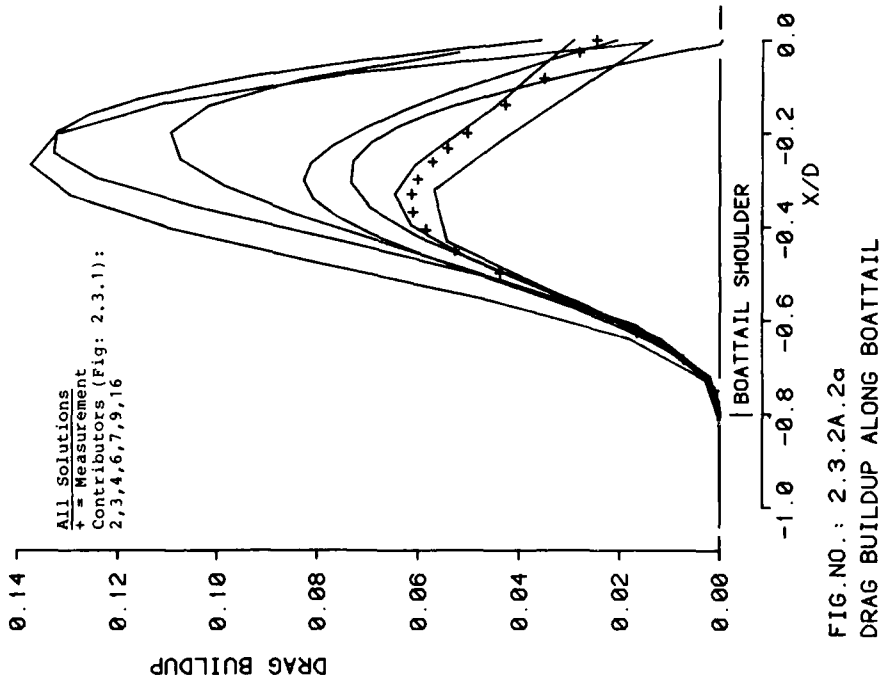

FIG.NO.: 2.3.2A.2a
DRAG BUILDUP ALONG BOATTAIL

WG08 : TEST CASE 2A

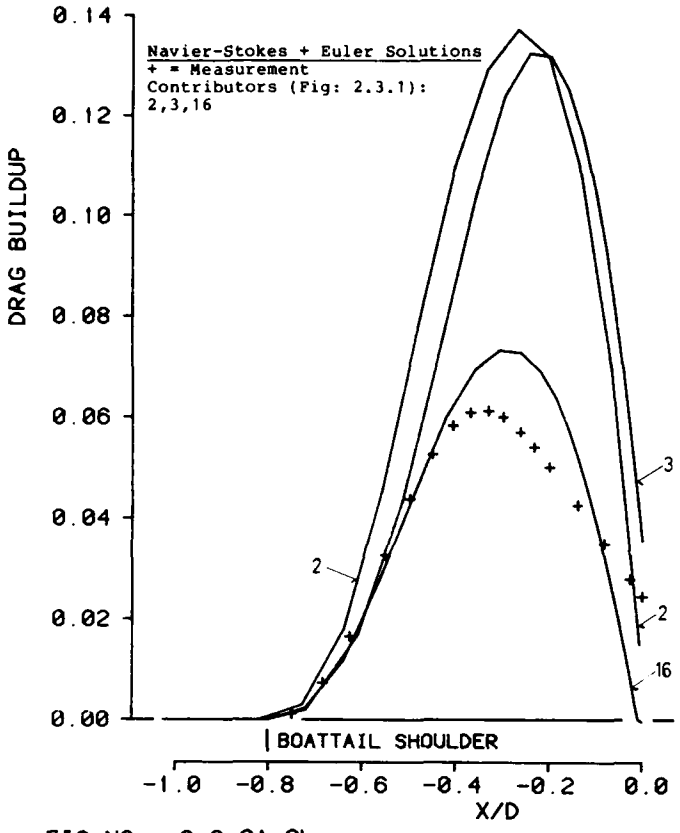

FIG.NO.: 2.3.2A.2b
DRAG BUILDUP ALONG BOATTAIL

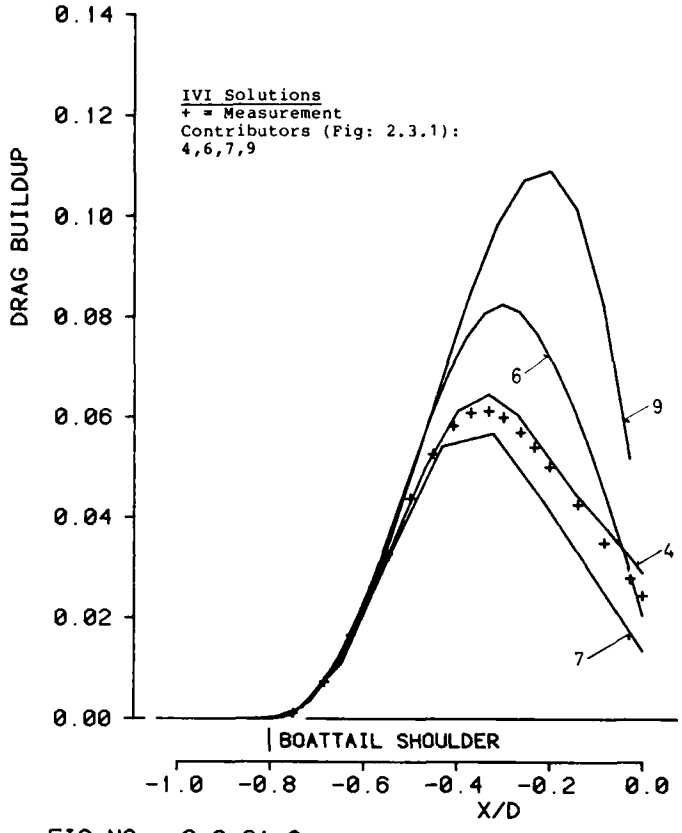

FIG.NO.: 2.3.2A.2c
DRAG BUILDUP ALONG BOATTAIL

WG08 : TEST CASE 2A

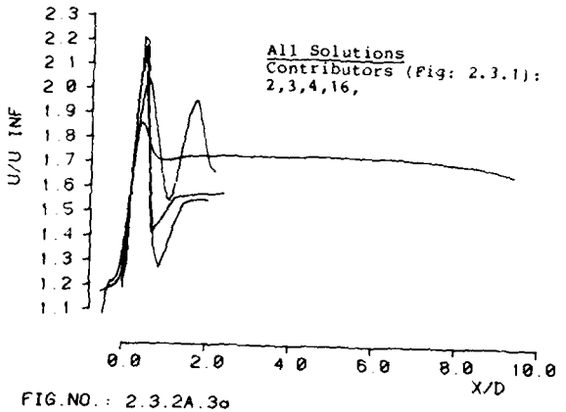

FIG.NO.: 2.3.2A.3a
AXIAL VELOCITY ON JET CENTERLINE

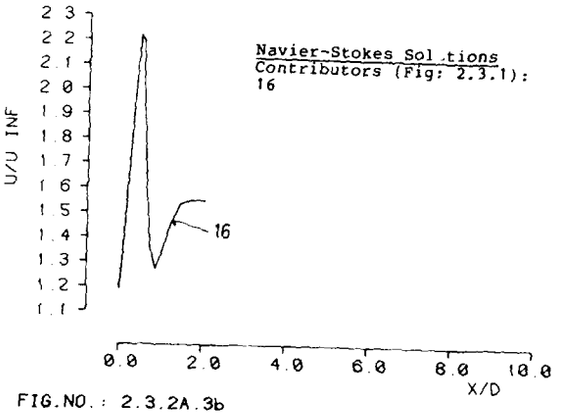

FIG.NO.: 2.3.2A.3b
AXIAL VELOCITY ON JET CENTERLINE

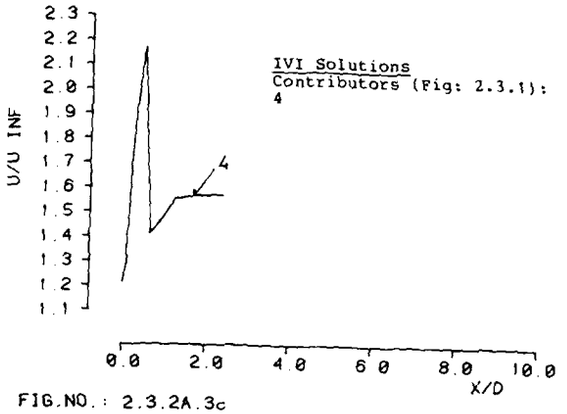

FIG.NO.: 2.3.2A.3c
AXIAL VELOCITY ON JET CENTERLINE

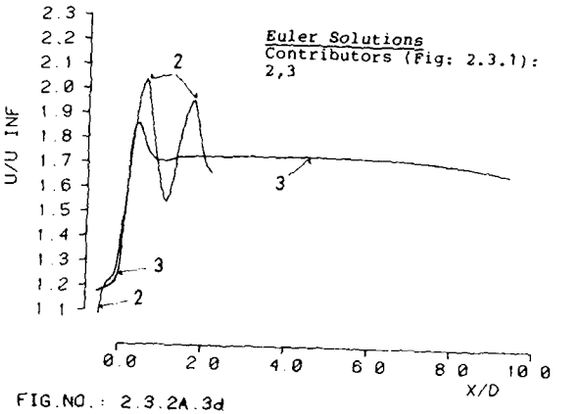

FIG.NO.: 2.3.2A.3d
AXIAL VELOCITY ON JET CENTERLINE

WG08 : TEST CASE 2A

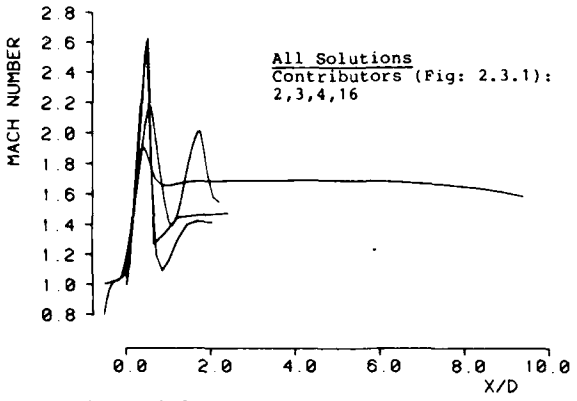

FIG.NO.: 2.3.2A.4a
MACH NUMBER ON JET CENTERLINE

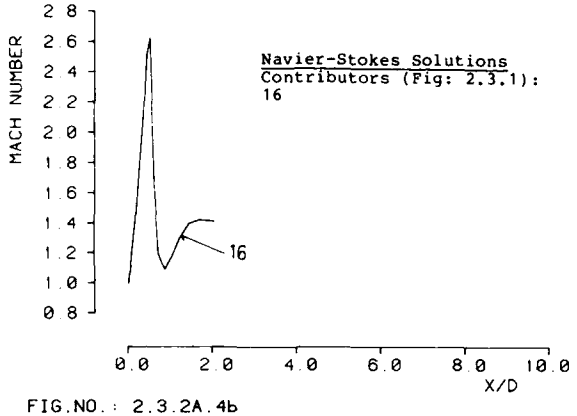

FIG.NO.: 2.3.2A.4b
MACH NUMBER ON JET CENTERLINE

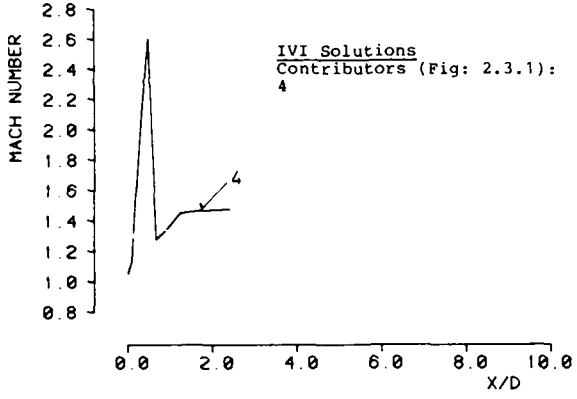

FIG.NO.: 2.3.2A.4c
MACH NUMBER ON JET CENTERLINE

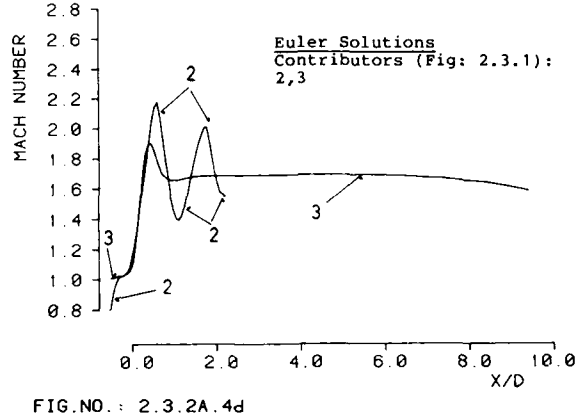

FIG.NO.: 2.3.2A.4d
MACH NUMBER ON JET CENTERLINE

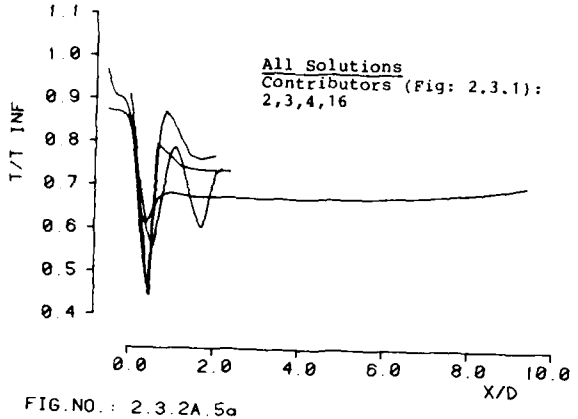

FIG.NO.: 2.3.2A.5a
STATIC TEMPERATURE ALONG JET CENTERLINE

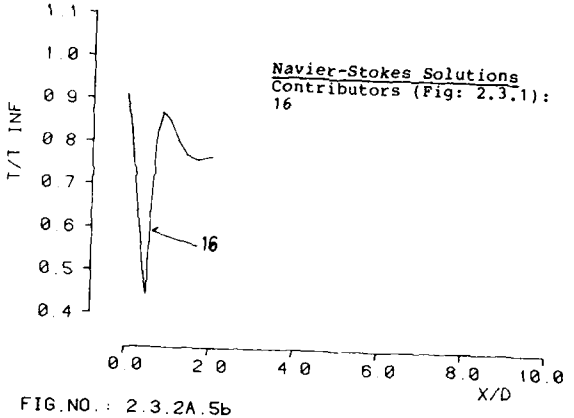

FIG.NO.: 2.3.2A.5b
STATIC TEMPERATURE ALONG JET CENTERLINE

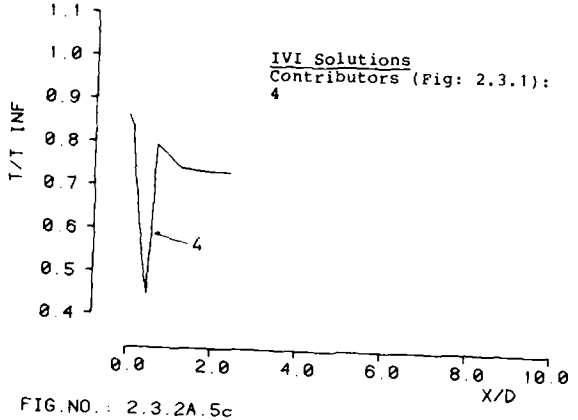

FIG.NO.: 2.3.2A.5c
STATIC TEMPERATURE ALONG JET CENTERLINE

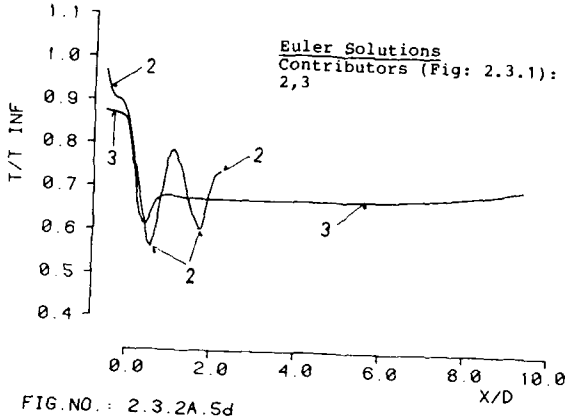

FIG.NO.: 2.3.2A.5d
STATIC TEMPERATURE ALONG JET CENTERLINE

WG08 : TEST CASE 2A

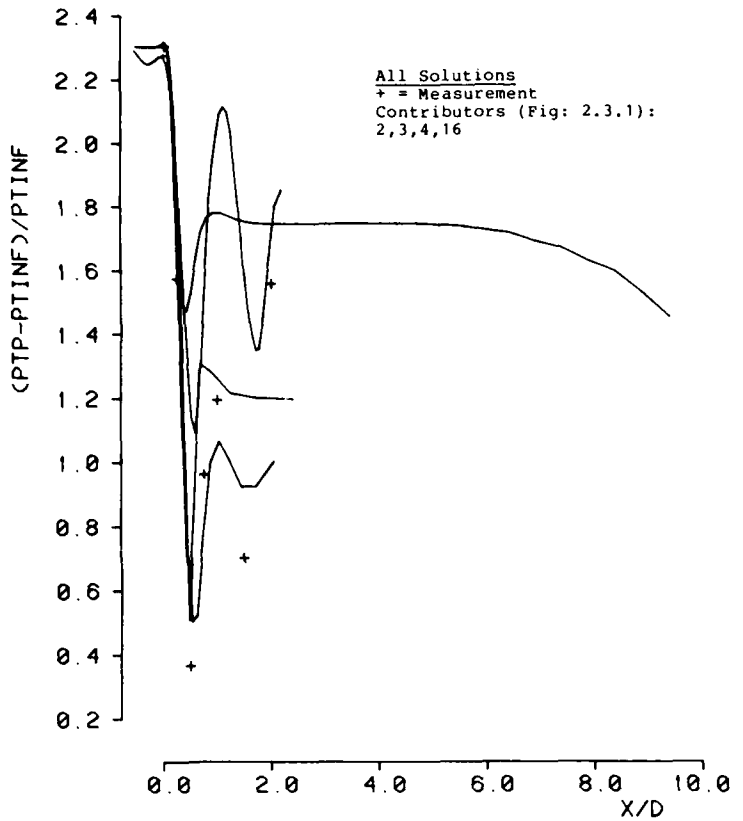

FIG.NO.: 2.3.2A.6a
PITOT PRESSURE ALONG JET CENTERLINE

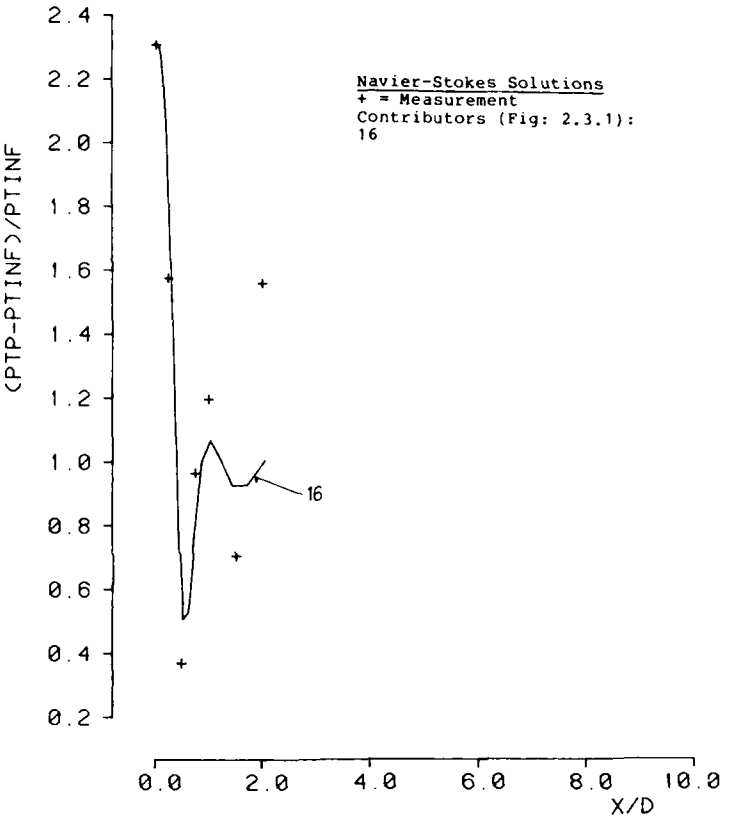

FIG.NO.: 2.3.2A.6b
PITOT PRESSURE ALONG JET CENTERLINE

WG08 : TEST CASE 2A

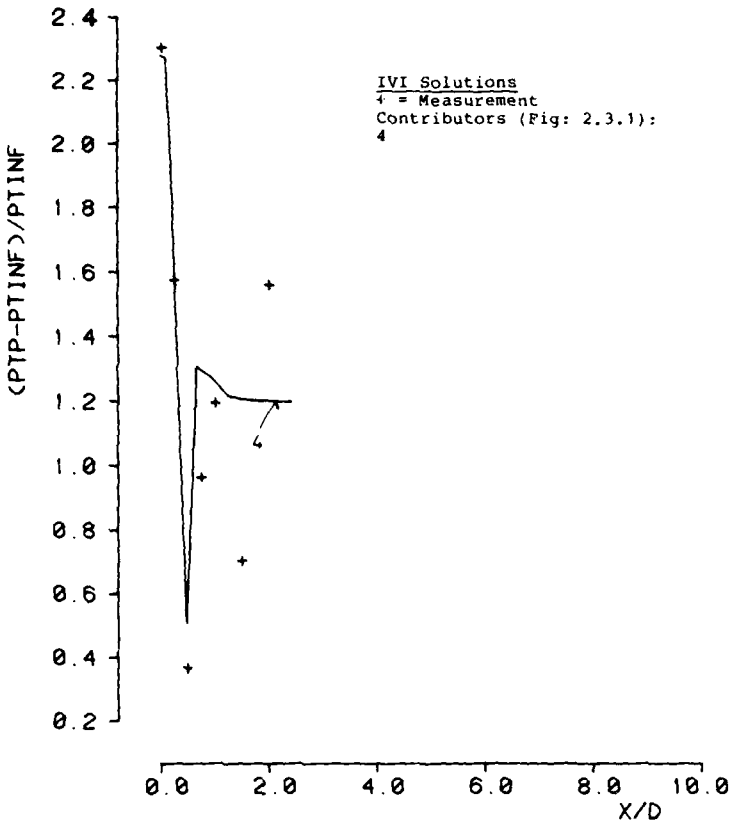

FIG.NO.: 2.3.2A.6c
PITOT PRESSURE ALONG JET CENTERLINE

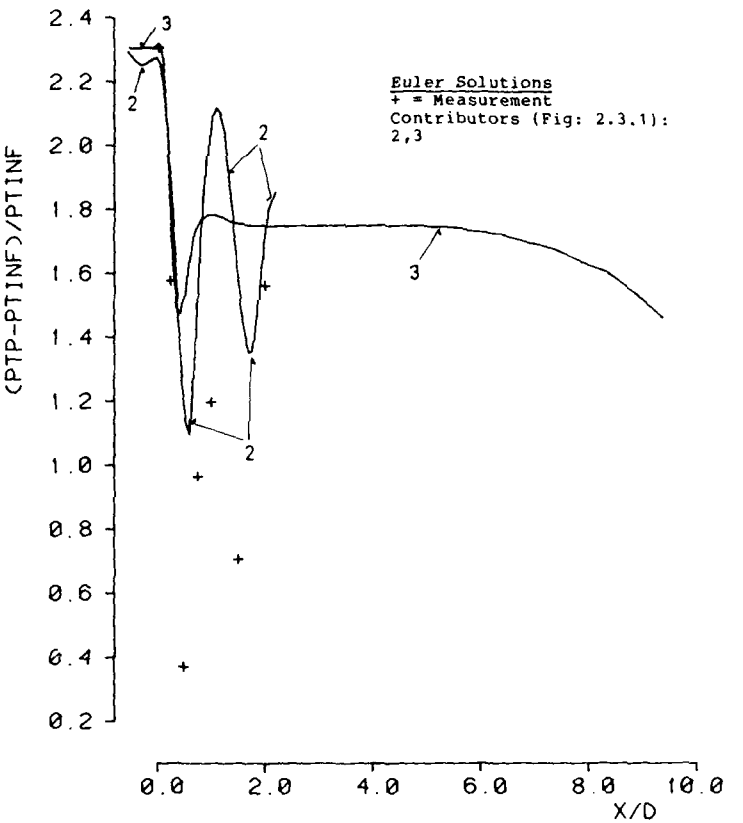

FIG.NO.: 2.3.2A.6d
PITOT PRESSURE ALONG JET CENTERLINE

WG08 : TEST CASE 2A

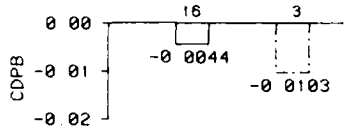

FIG.NO.: 2.3.2A.7
BAR GRAPH OF BASE DRAG COEFFICIENT

FOR CONTRIBUTOR IDENTIFICATION
SEE FIG.NO.: 2.3.1

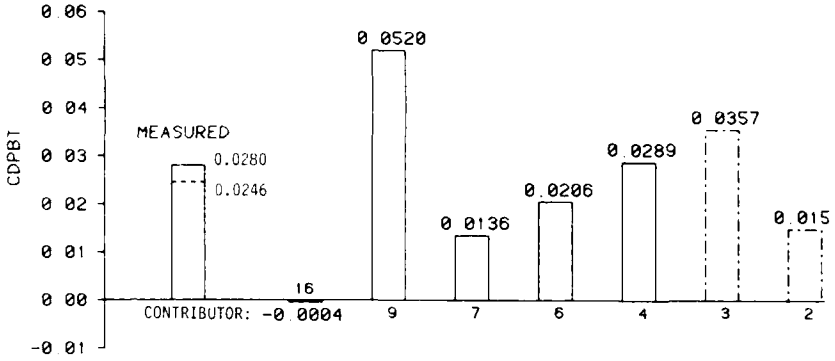

FIG.NO.: 2.3.2A.8
BAR GRAPH OF BOATTAIL PRESSURE DRAG COEFFICIENT

FIG.NO.: 2.3.2A.9
BAR GRAPH OF BOATTAIL FRICTION DRAG COEFFICIENT

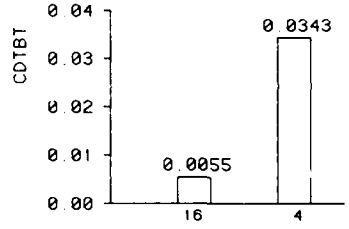

FIG.NO.: 2.3.2A.10
BAR GRAPH OF TOTAL BOATTAIL DRAG COEFFICIENT

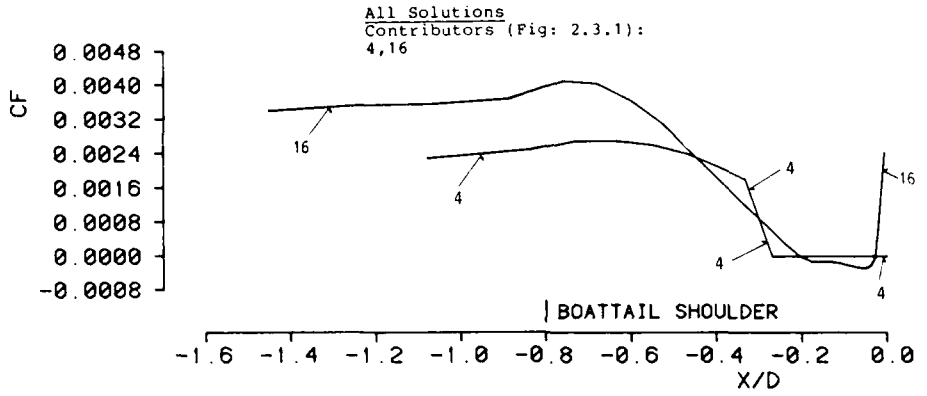

FIG.NO.: 2.3.2A.11
SKIN FRICTION COEFFICIENT

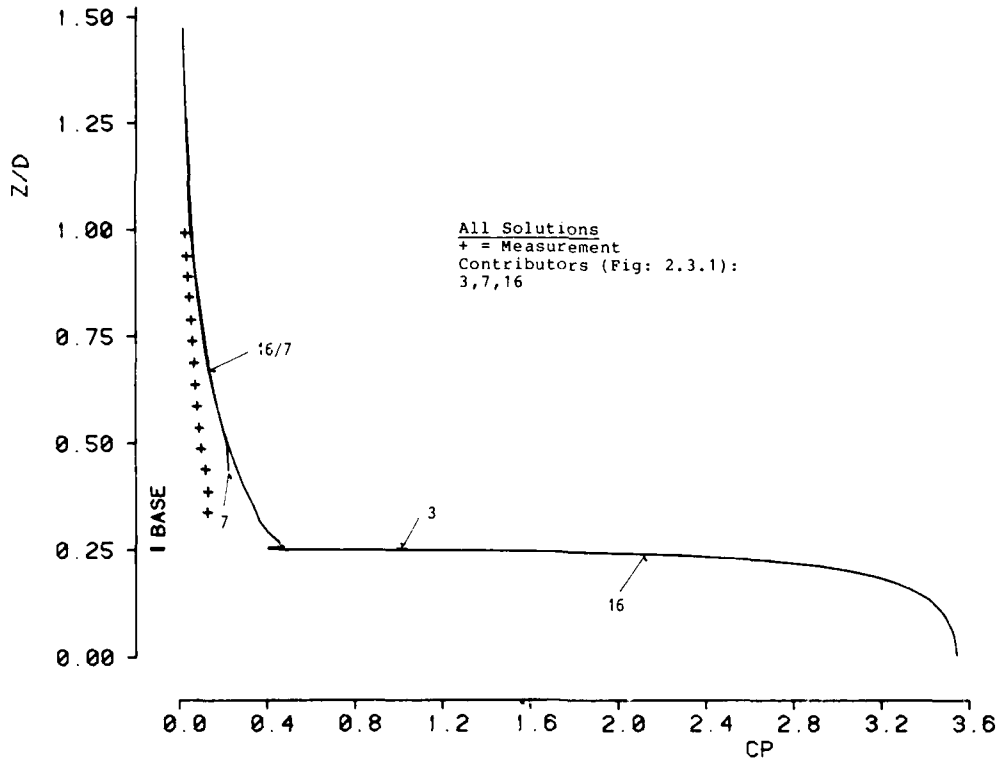

FIG.NO.: 2.3.2A.12
PRESSURE COEFFICIENT ALONG BASE GRID LINE

WG08 : TEST CASE 2A

AD-A172 341 REPORT OF THE WORKING GROUP ON AERODYNAMICS OF AIRCRAFT AFTERBODY(U) ADVISORY GROUP FOR AEROSPACE RESEARCH AND DEVELOPMENT NEUILLY-SUR-SEINE (FRANCE) JUN 86 2/4

UNCLASSIFIED AGARD-AR-226 F/G 20/4 NL

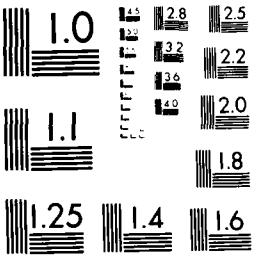

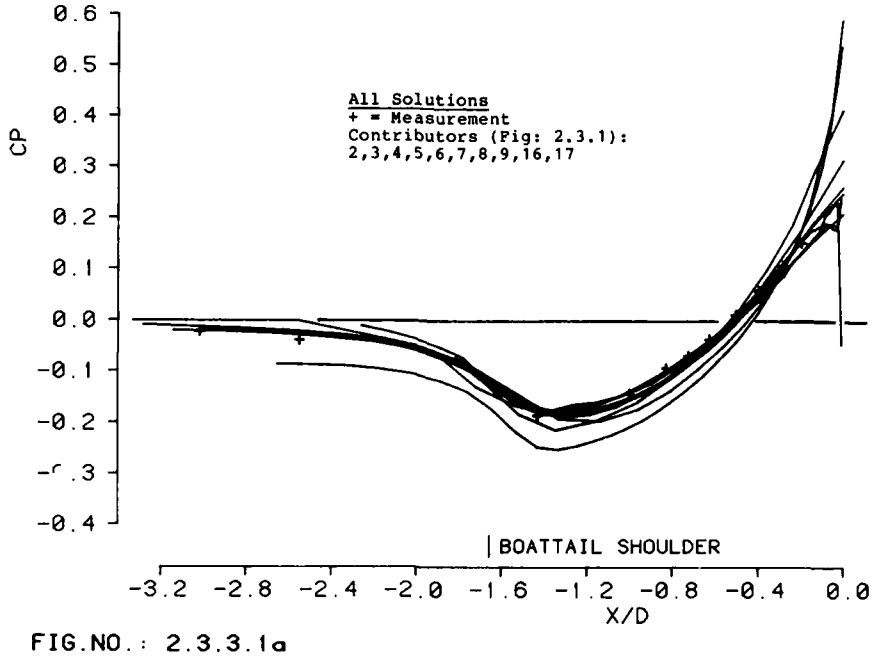

FIG.NO.: 2.3.3.1a
BOATTAIL WALL PRESSURE COEFFICIENT

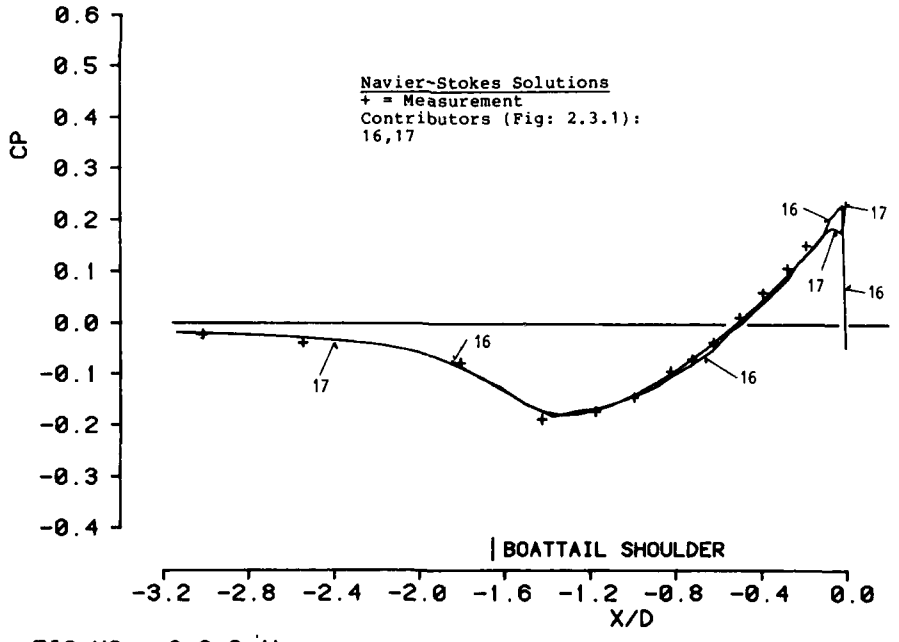

FIG.NO.: 2.3.3.1b
BOATTAIL WALL PRESSURE COEFFICIENT

WG08 : TEST CASE 3

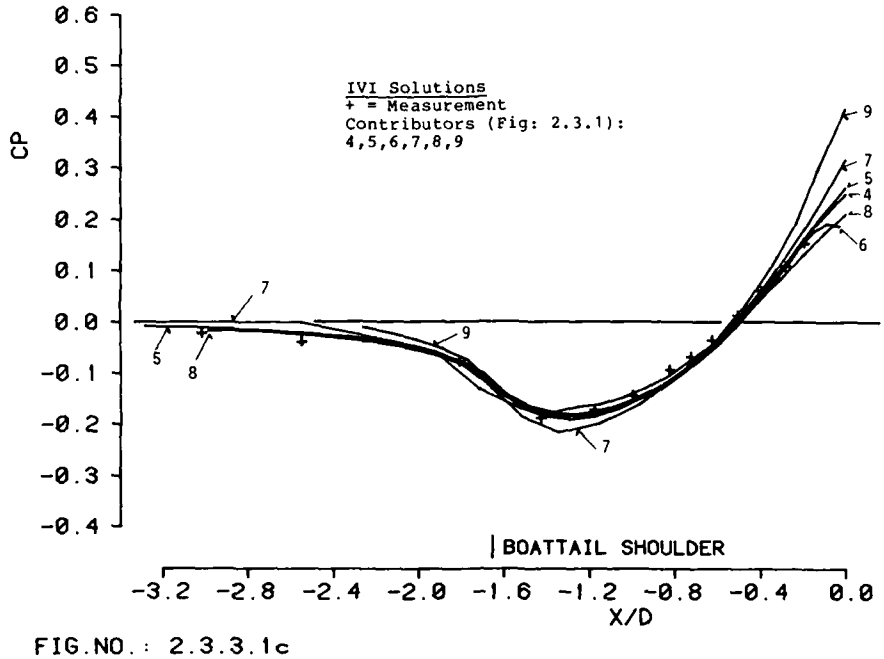

FIG.NO.: 2.3.3.1c
BOATTAIL WALL PRESSURE COEFFICIENT

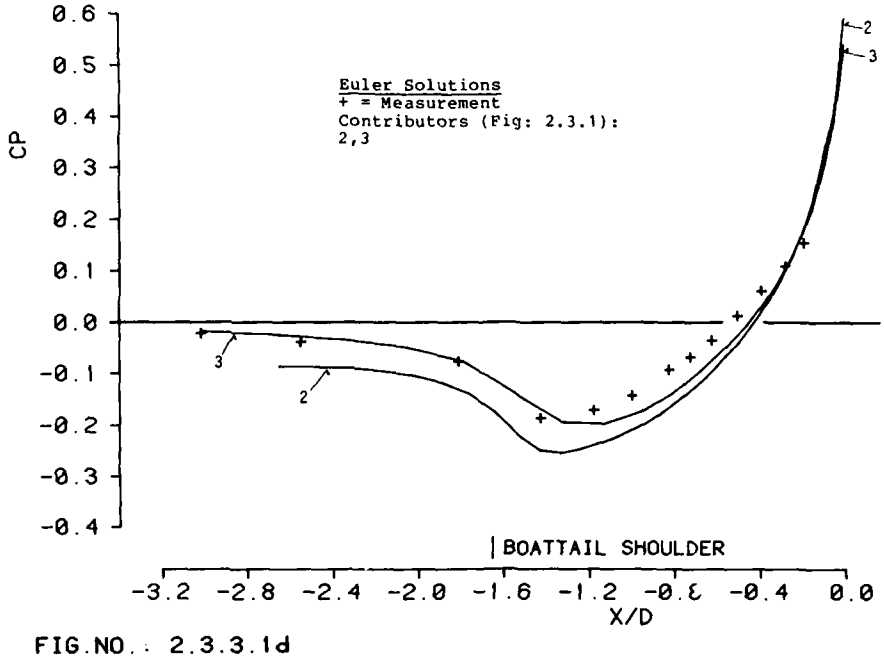

FIG.NO.: 2.3.3.1d
BOATTAIL WALL PRESSURE COEFFICIENT

WG08 : TEST CASE 3

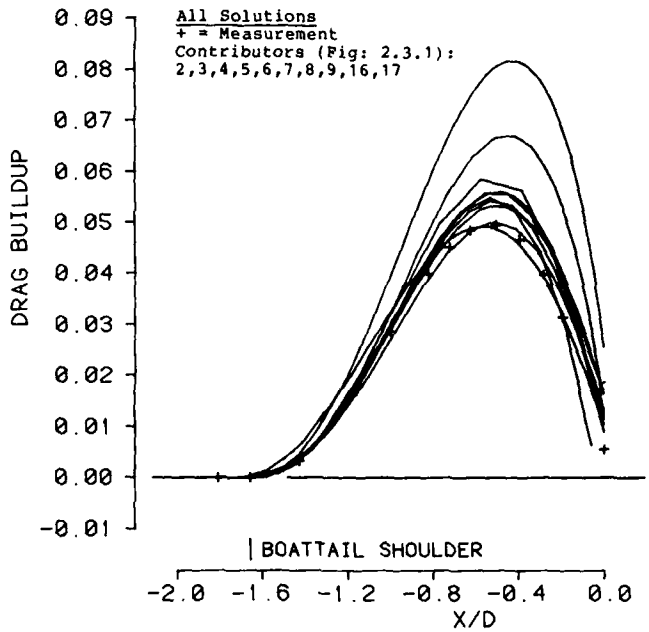

FIG.NO.: 2.3.3.2a
DRAG BUILDUP ALONG BOATTAIL

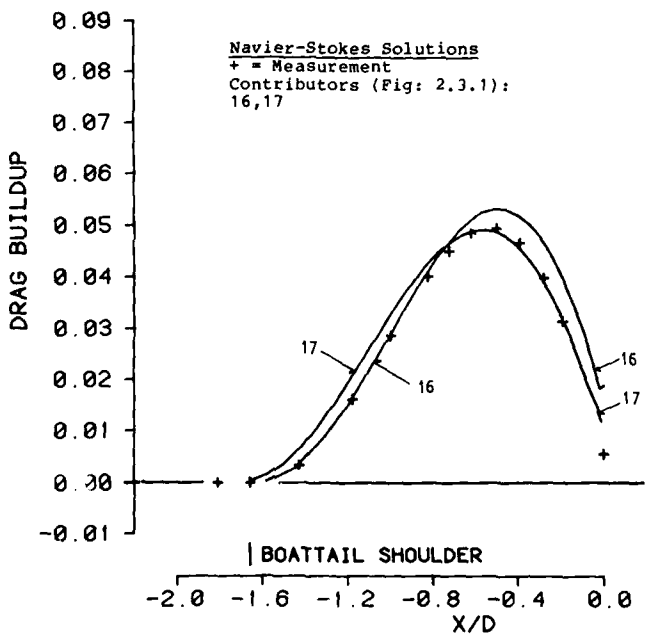

FIG.NO.: 2.3.3.2b
DRAG BUILDUP ALONG BOATTAIL

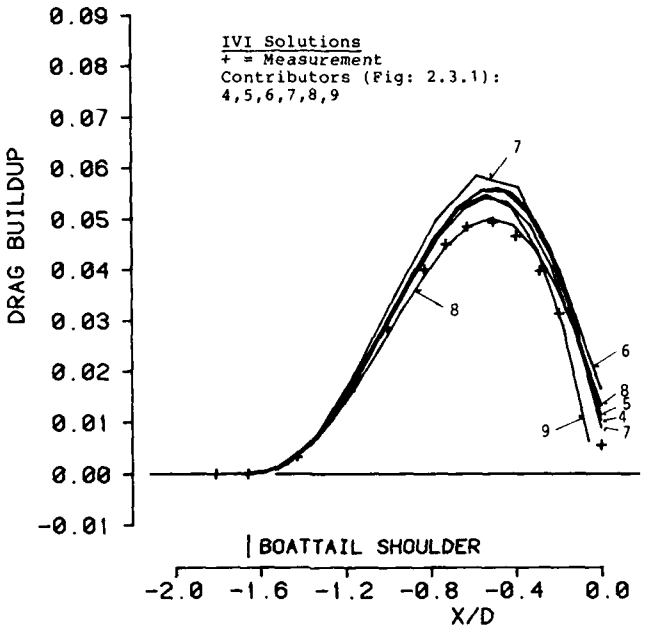

FIG.NO.: 2.3.3.2c
DRAG BUILDUP ALONG BOATTAIL

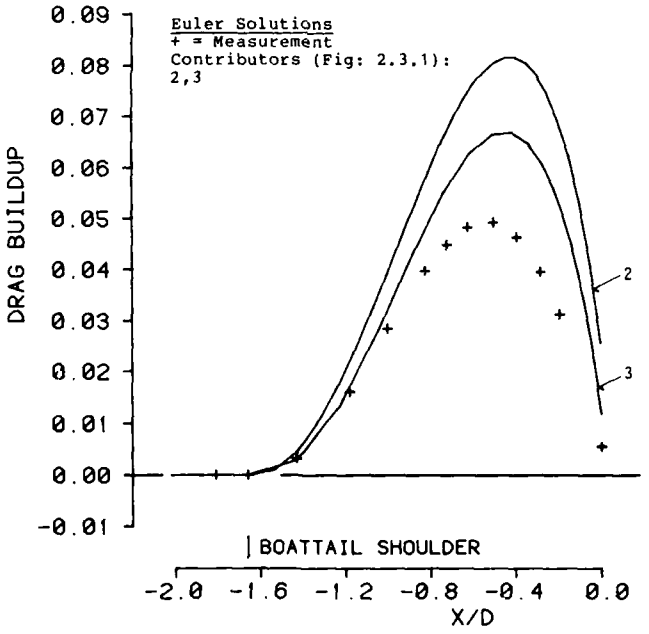

FIG.NO.: 2.3.3.2d
DRAG BUILDUP ALONG BOATTAIL

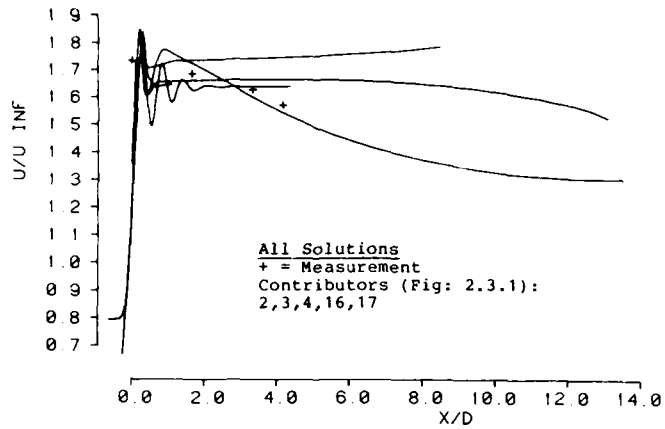

FIG.NO.: 2.3.3.3a
AXIAL VELOCITY ON JET CENTERLINE

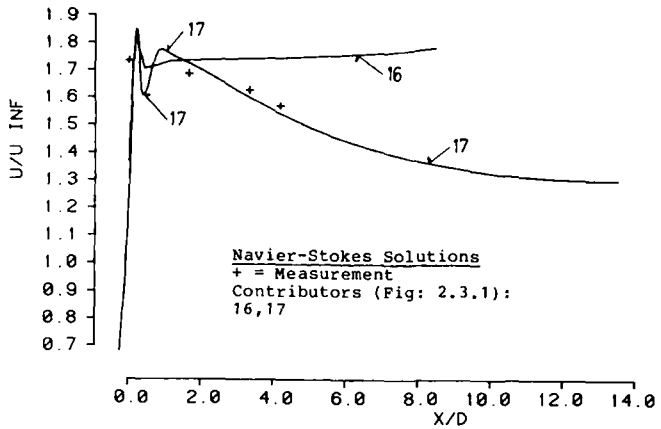

FIG.NO.: 2.3.3.3b
AXIAL VELOCITY ON JET CENTERLINE

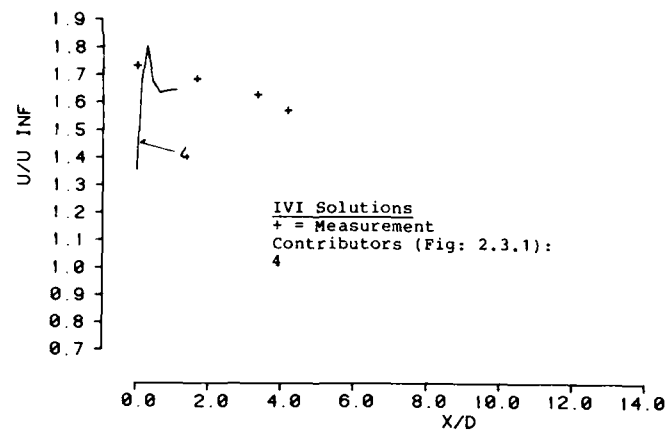

FIG.NO.: 2.3.3.3c
AXIAL VELOCITY ON JET CENTERLINE

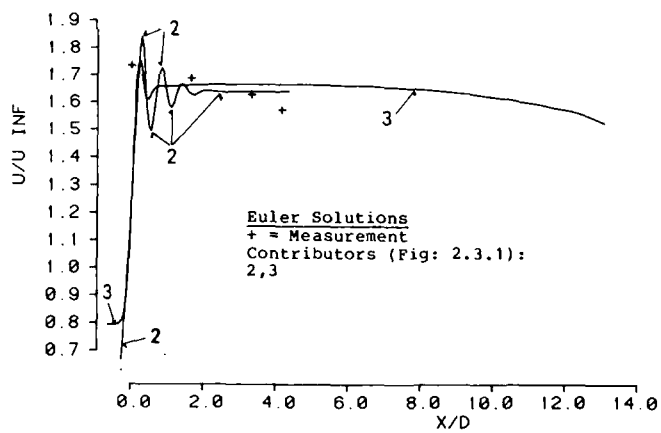

FIG.NO.: 2.3.3.3d
AXIAL VELOCITY ON JET CENTERLINE

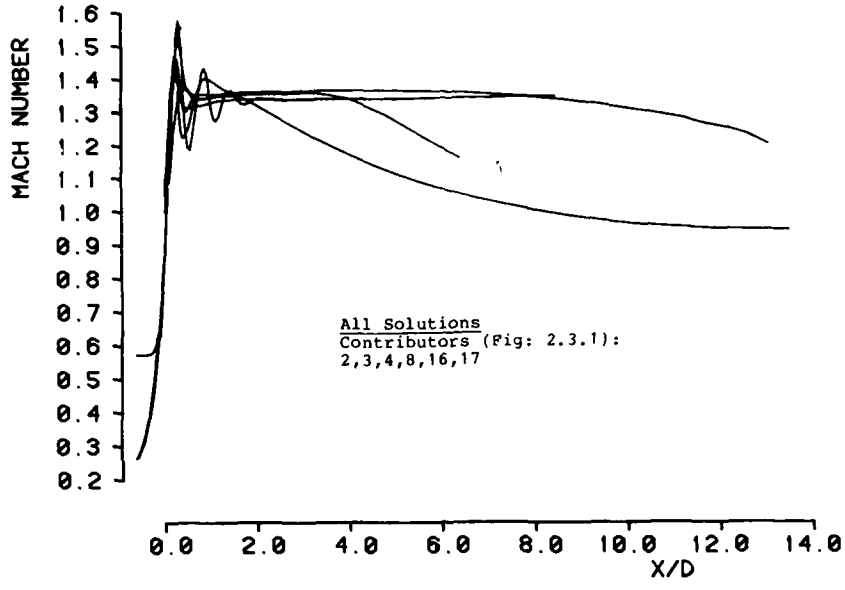

FIG.NO.: 2.3.3.4a
MACH NUMBER ON JET CENTERLINE

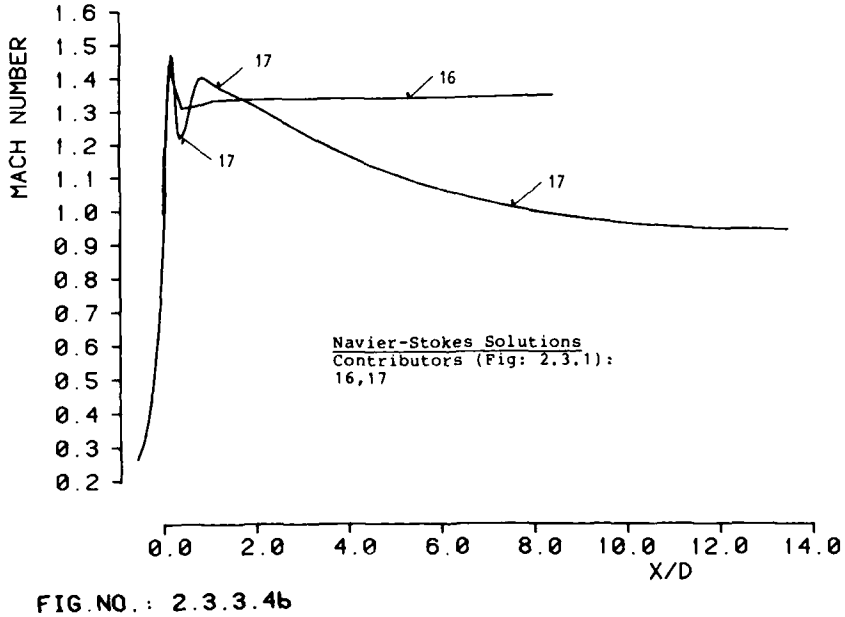

FIG.NO.: 2.3.3.4b
MACH N''MBER ON JET CENTERLINE

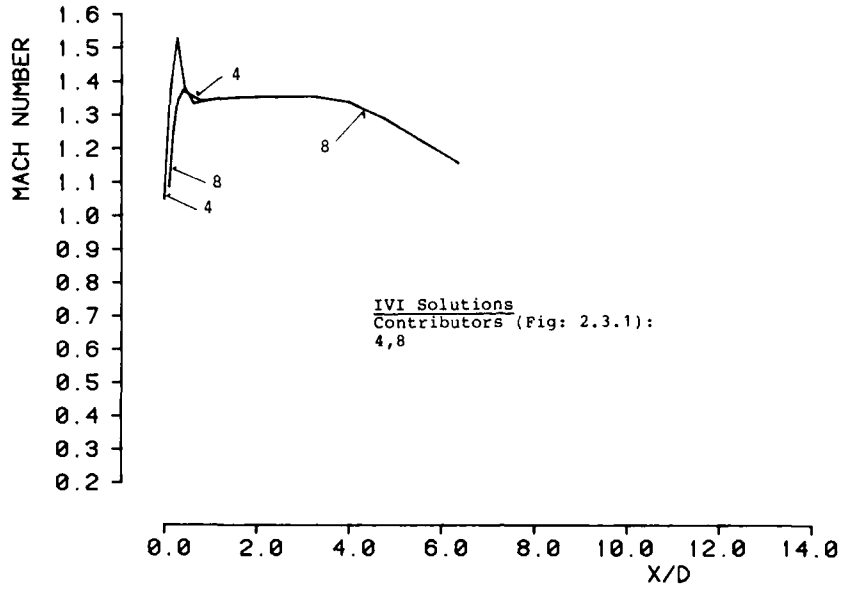

FIG.NO.: 2.3.3.4c
MACH NUMBER ON JET CENTERLINE

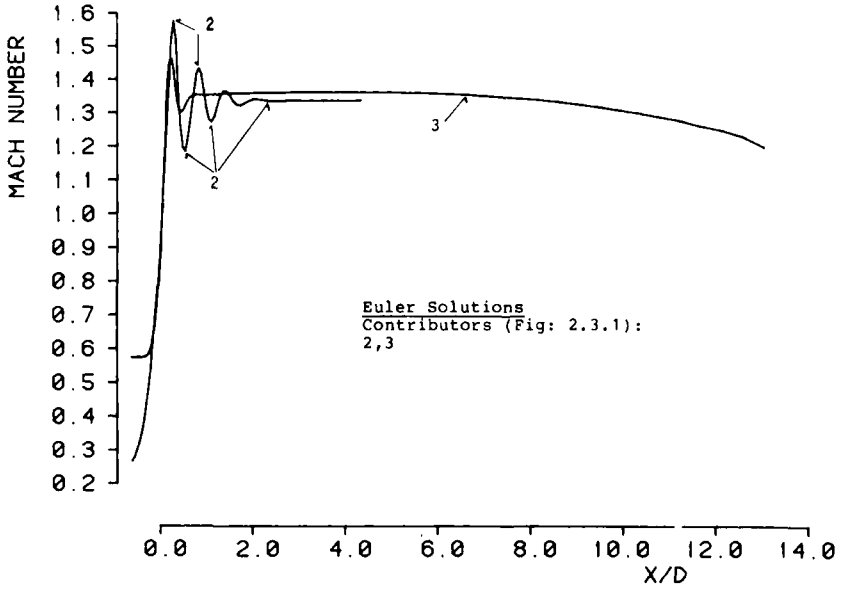

FIG.NO.: 2.3.3.4d
MACH NUMBER ON JET CENTERLINE

WG08 : TEST CASE 3

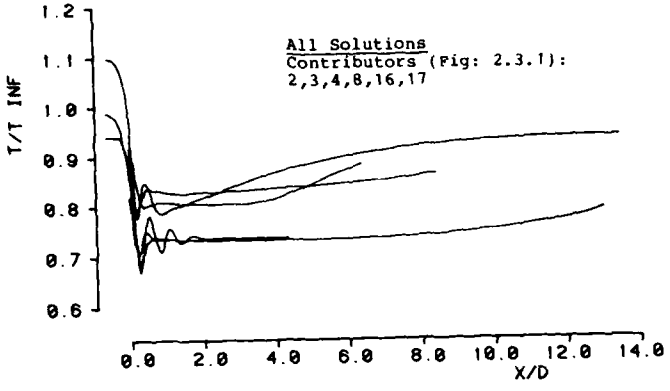

FIG.NO.: 2.3.3.5a
STATIC TEMPERATURE ALONG JET CENTERLINE

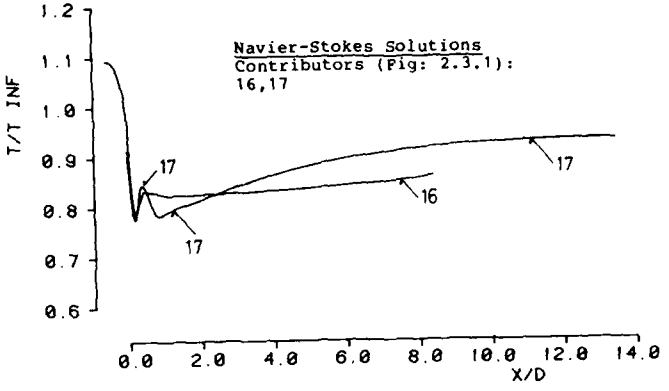

FIG.NO.: 2.3.3.5b
STATIC TEMPERATURE ALONG JET CENTERLINE

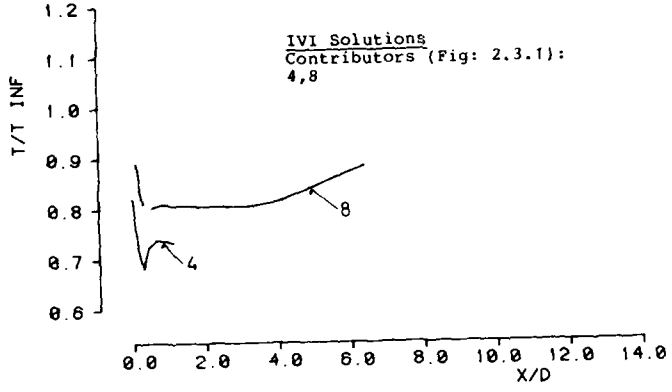

FIG.NO.: 2.3.3.5c
STATIC TEMPERATURE ALONG JET CENTERLINE

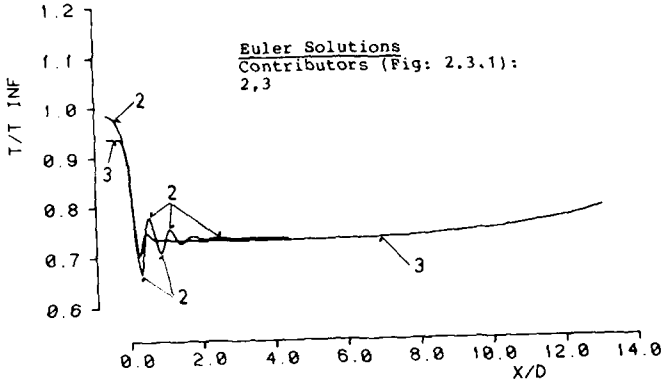

FIG.NO.: 2.3.3.5d
STATIC TEMPERATURE ALONG JET CENTERLINE

WG08 : TEST CASE 3

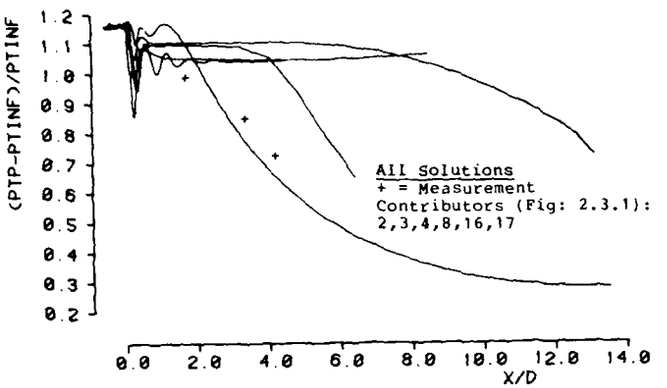

FIG.NO.: 2.3.3.6a
PITOT PRESSURE ALONG JET CENTERLINE

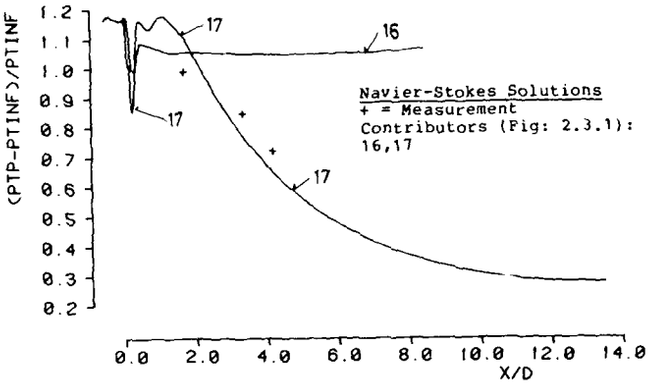

FIG.NO.: 2.3.3.6b
PITOT PRESSURE ALONG JET CENTERLINE

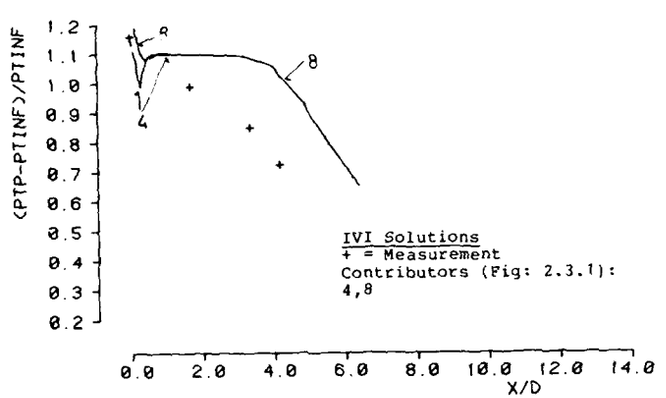

FIG.NO.: 2.3.3.6c
PITOT PRESSURE ALONG JET CENTERLINE

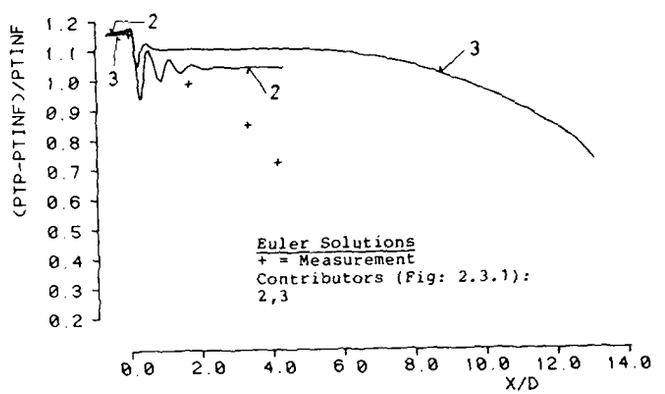

FIG.NO.: 2.3.3.6d
PITOT PRESSURE ALONG JET CENTERLINE

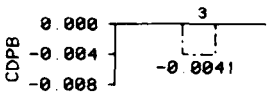

FIG.NO.: 2.3.3.7
BAR GRAPH OF BASE DRAG COEFFICIENT

FOR CONTRIBUTOR IDENTIFICATION
SEE FIG.NO.: 2.3.1

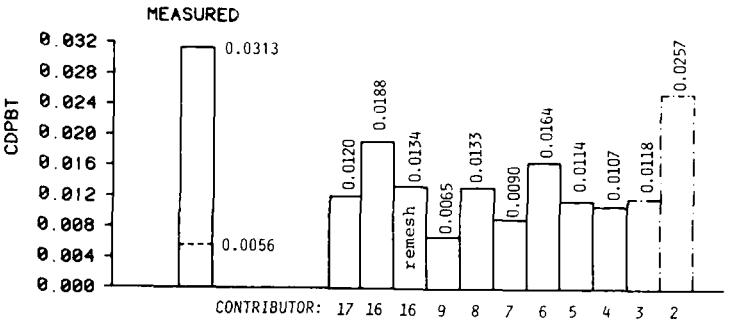

FIG.NO.: 2.3.3.8
BAR GRAPH OF BOATTAIL PRESSURE DRAG COEFFICIENT

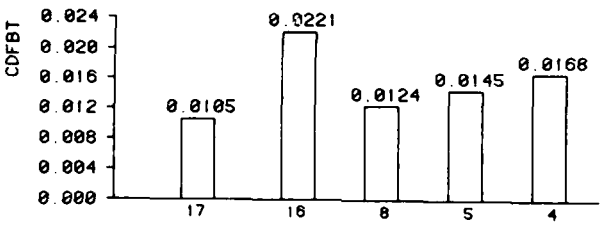

FIG.NO.: 2.3.3.9
BAR GRAPH OF BOATTAIL FRICTION DRAG COEFFICIENT

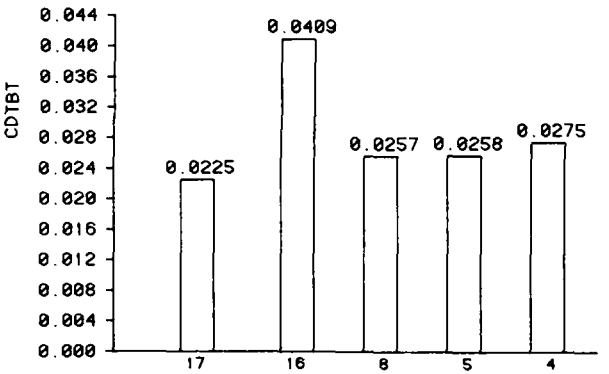

FIG.NO.: 2.3.3.10
BAR GRAPH OF TOTAL BOATTAIL DRAG COEFFICIENT

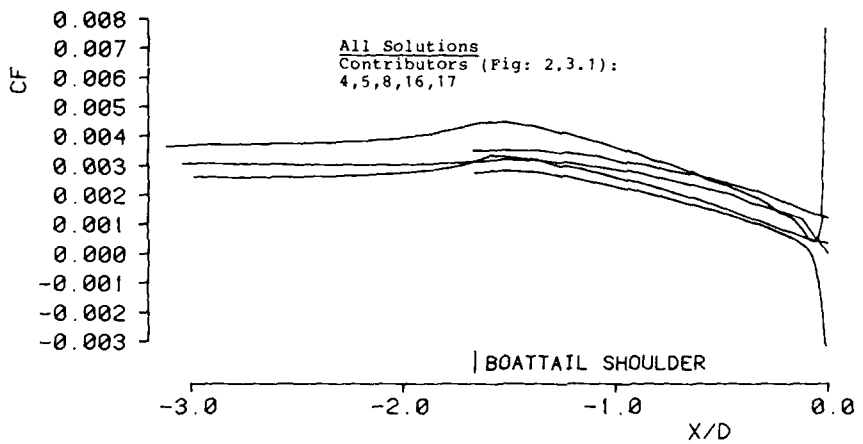

FIG.NO.: 2.3.3.11a

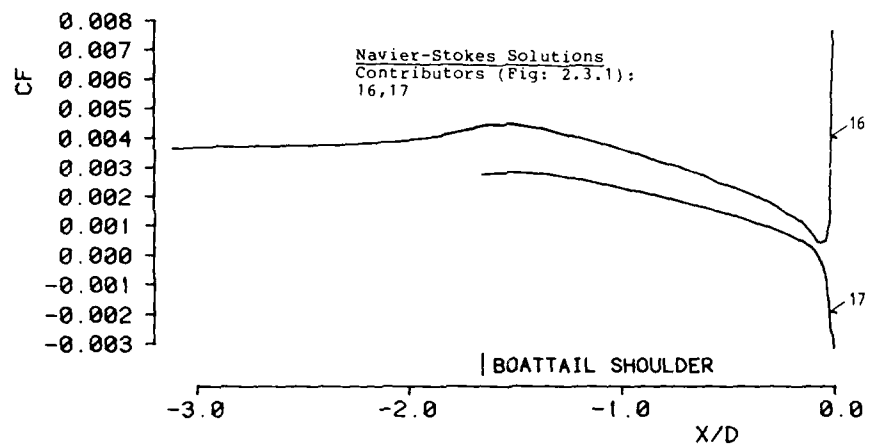

FIG.NO.: 2.3.3.11b

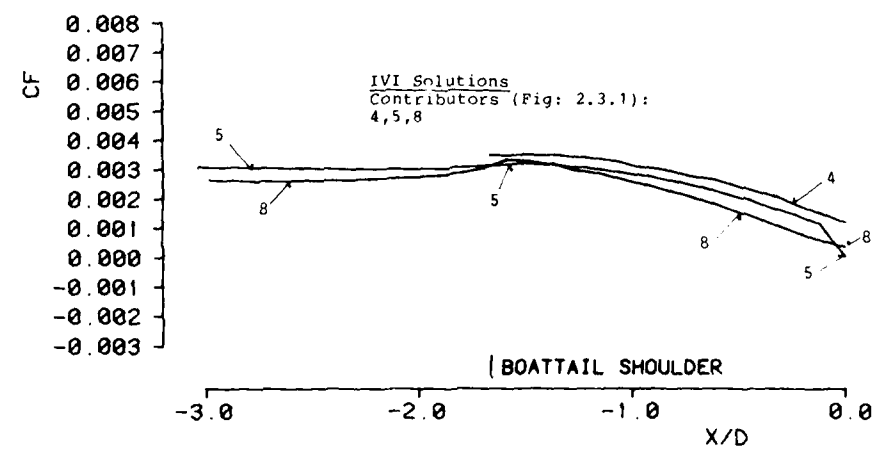

FIG.NO.: 2.3.3.11c

SKIN FRICTION COEFFICIENT

WG08 : TEST CASE 3

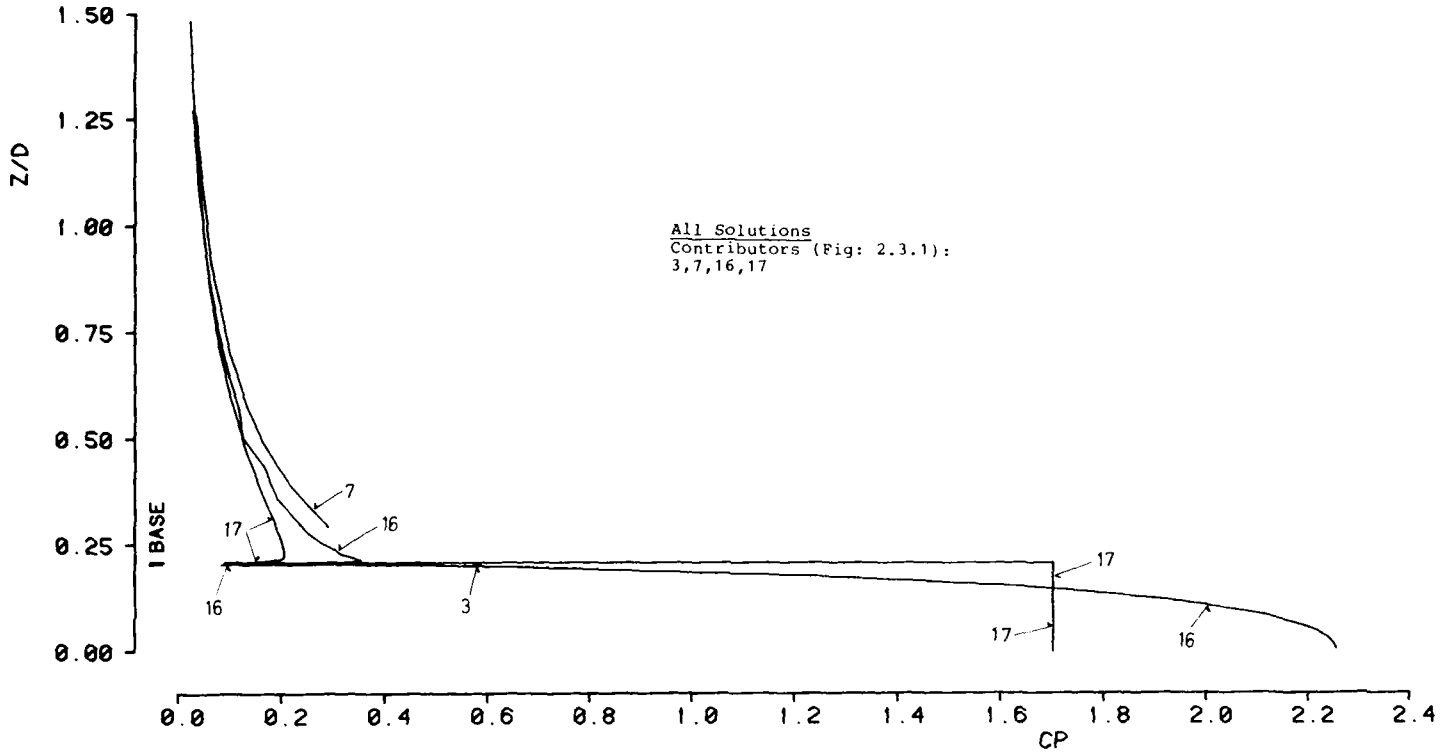

FIG.NO.: 2.3.3.12
PRESSURE COEFFICIENT ALONG BASE GRID LINE

WG08 : TEST CASE 3

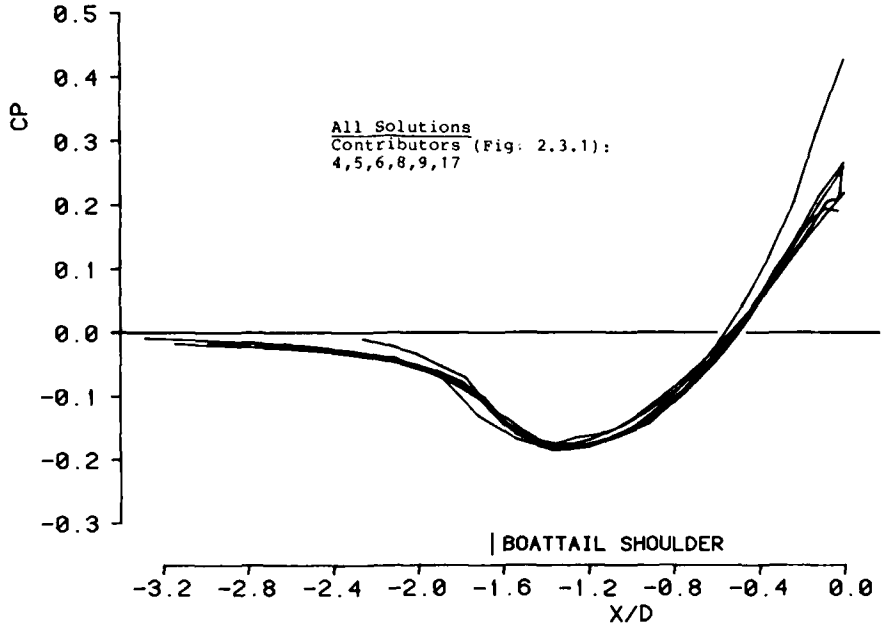

FIG.NO.: 2.3.4.1a
BOATTAIL WALL PRESSURE COEFFICIENT

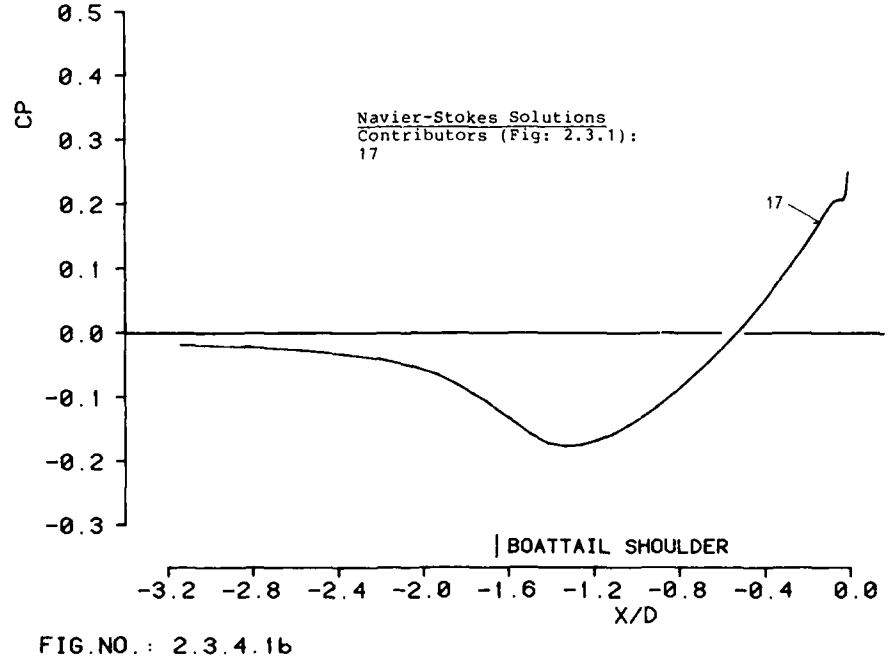

FIG.NO.: 2.3.4.1b
BOATTAIL WALL PRESSURE COEFFICIENT

WG08 : TEST CASE 4

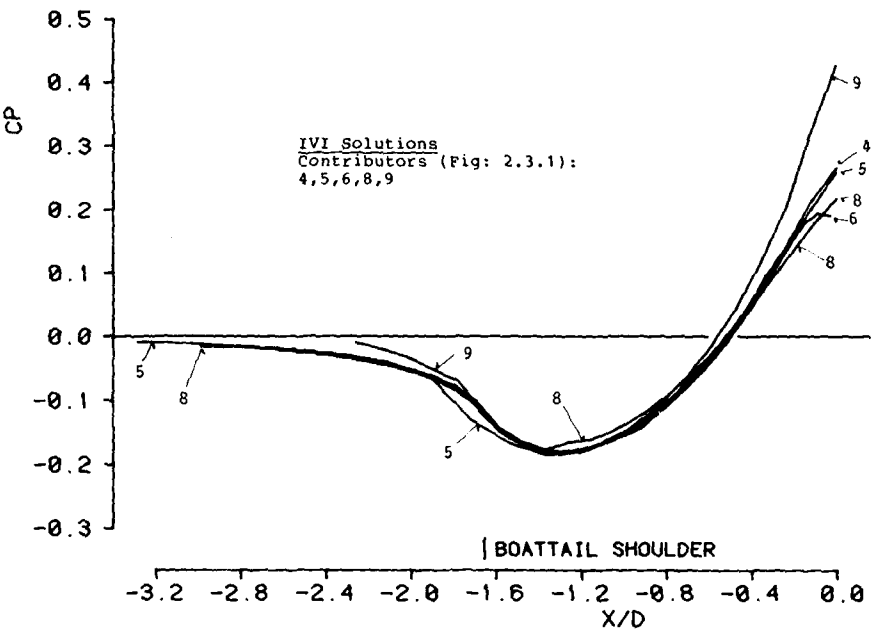

FIG.NO.: 2.3.4.1c
BOATTAIL WALL PRESSURE COEFFICIENT

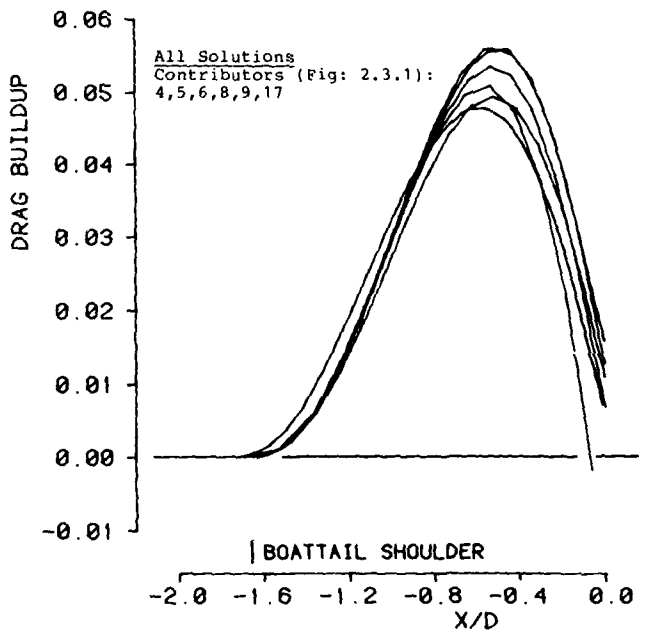

FIG.NO.: 2.3.4.2a
DRAG BUILDUP ALONG BOATTAIL

WG08 : TEST CASE 4

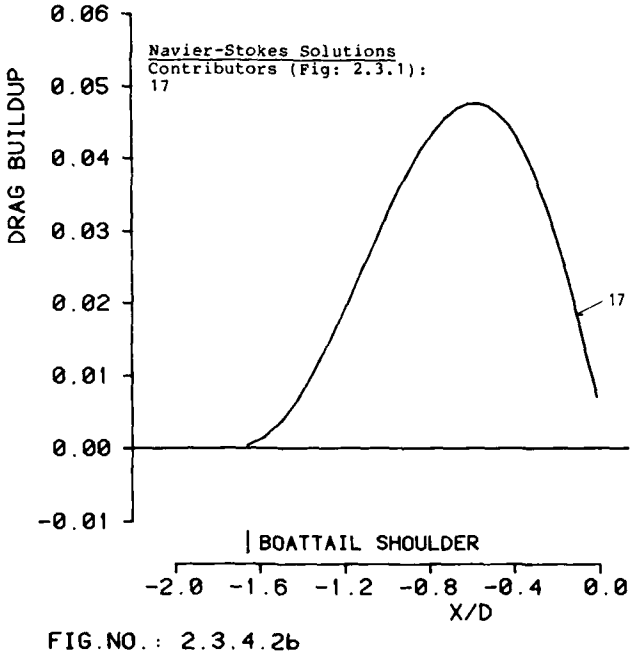

FIG.NO.: 2.3.4.2b
DRAG BUILDUP ALONG BOATTAIL

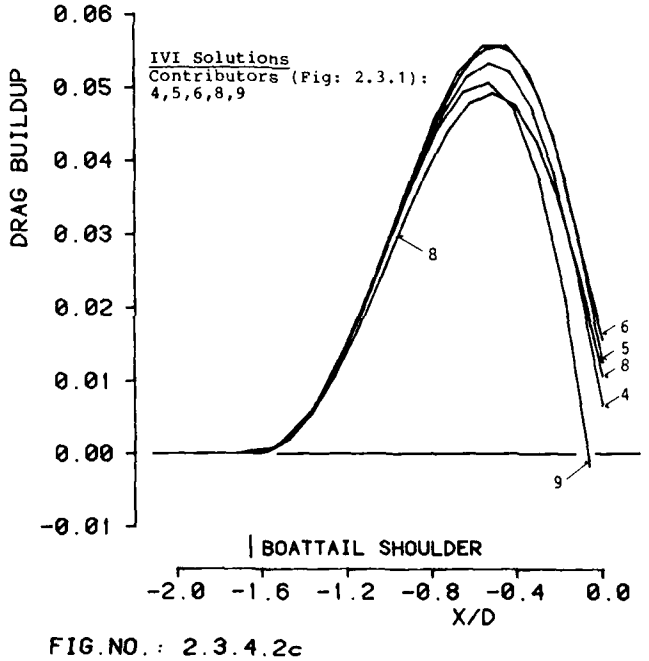

FIG.NO.: 2.3.4.2c
DRAG BUILDUP ALONG BOATTAIL

WG08 : TEST CASE 4

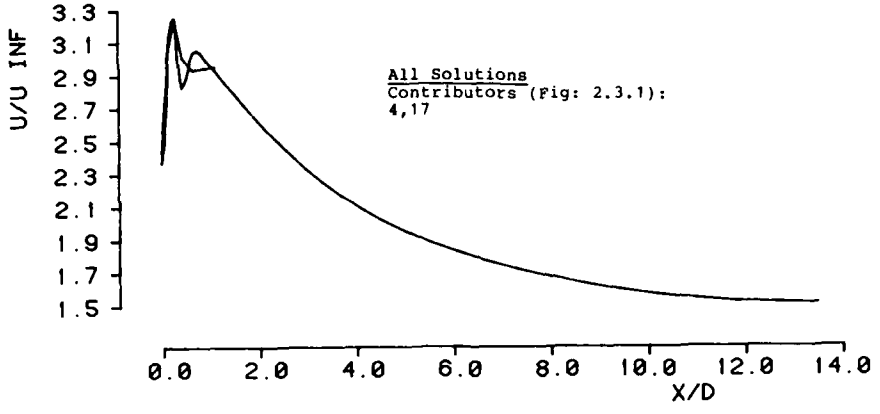

FIG.NO.: 2.3.4.3a
AXIAL VELOCITY ON JET CENTERLINE

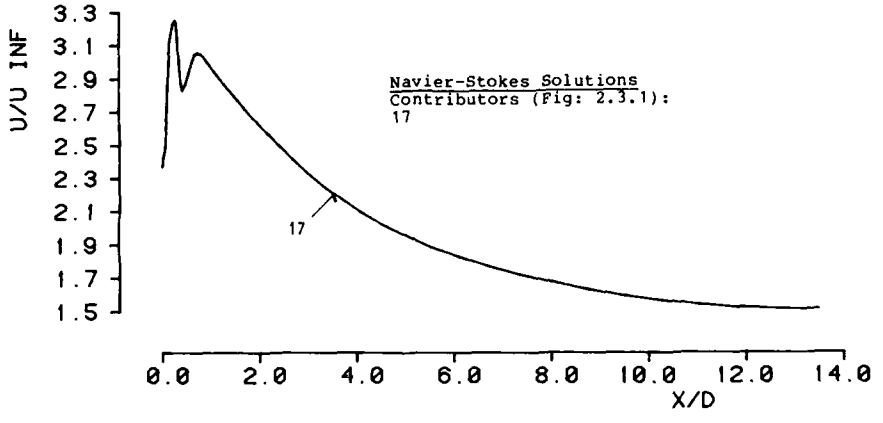

FIG.NO.: 2.3.4.3b
AXIAL VELOCITY ON JET CENTERLINE

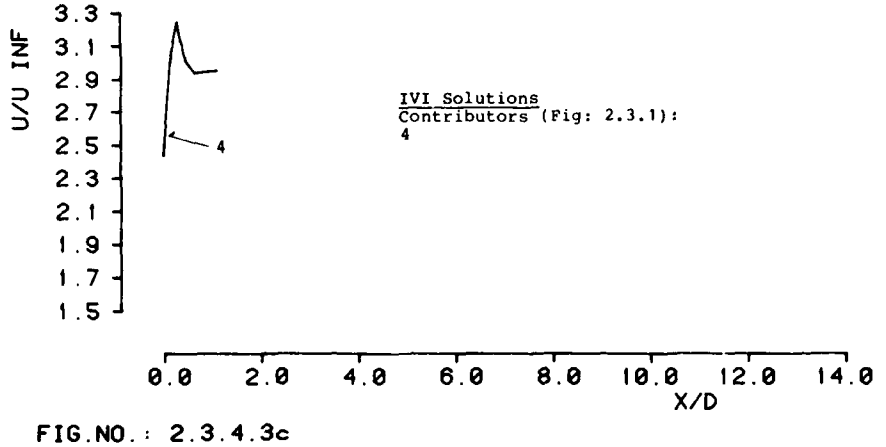

FIG.NO.: 2.3.4.3c
AXIAL VELOCITY ON JET CENTERLINE

WG08 : TEST CASE 4

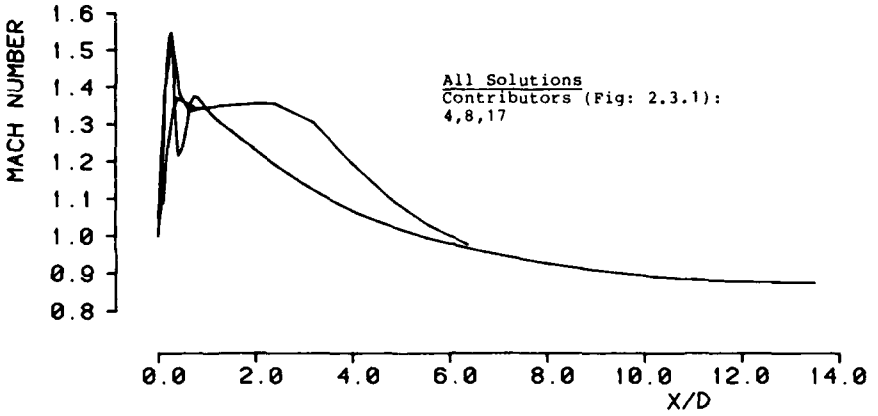

FIG.NO.: 2.3.4.4a
MACH NUMBER ON JET CENTERLINE

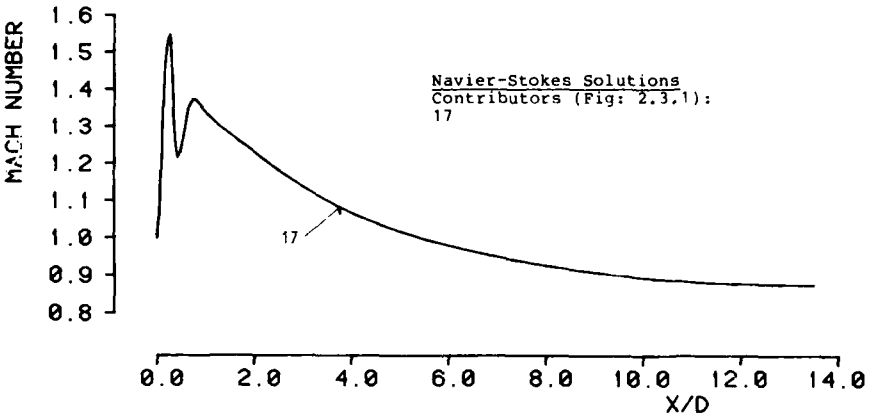

FIG.NO.: 2.3.4.4b
MACH NUMBER ON JET CENTERLINE

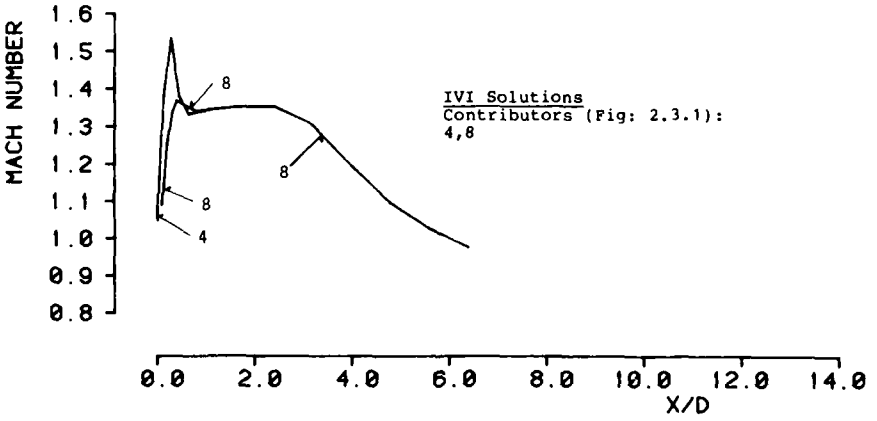

FIG.NO.: 2.3.4.4c
MACH NUMBER ON JET CENTERLINE

WG08 : TEST CASE 4

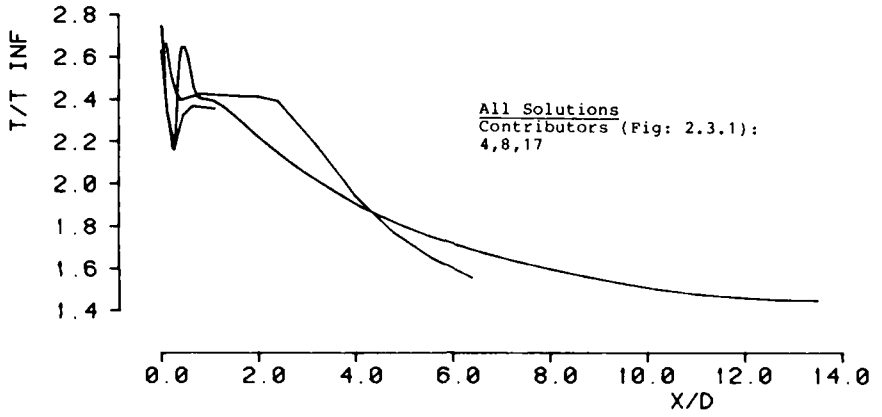

FIG.NO.: 2.3.4.5a
STATIC TEMPERATURE ALONG JET CENTERLINE

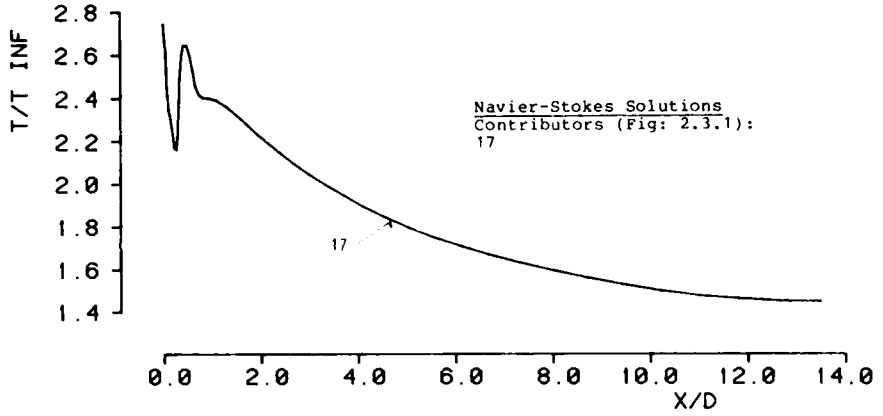

FIG.NO.: 2.3.4.5b
STATIC TEMPERATURE ALONG JET CENTERLINE

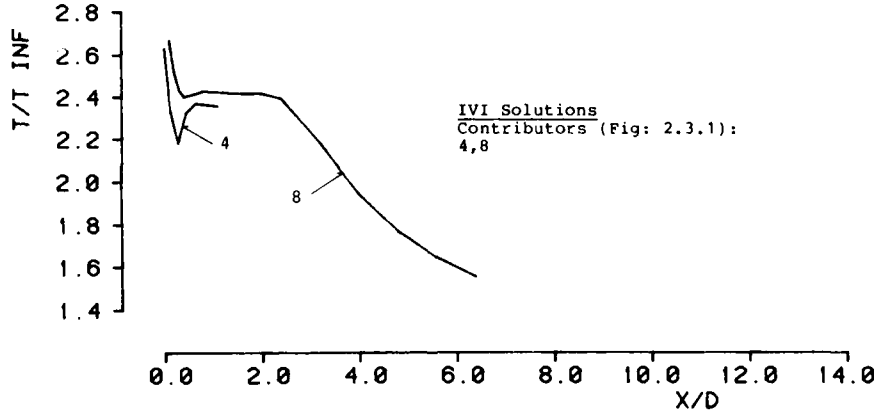

FIG.NO.: 2.3.4.5c
STATIC TEMPERATURE ALONG JET CENTERLINE

WG08 : TEST CASE 4

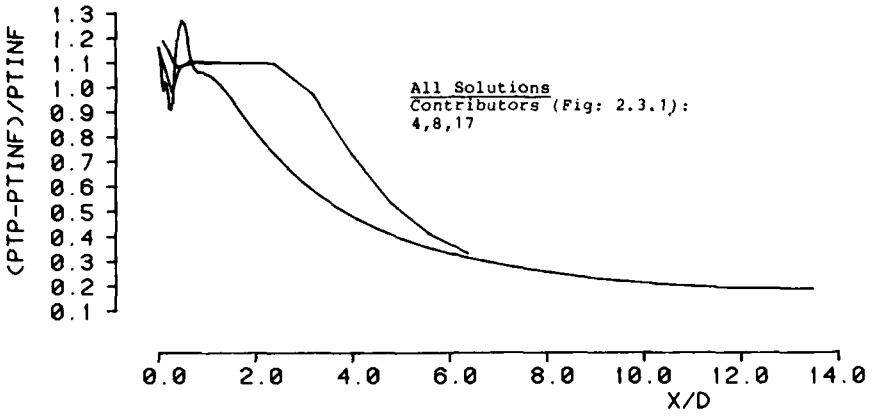

FIG.NO.: 2.3.4.6a
PITOT PRESSURE ALONG JET CENTERLINE

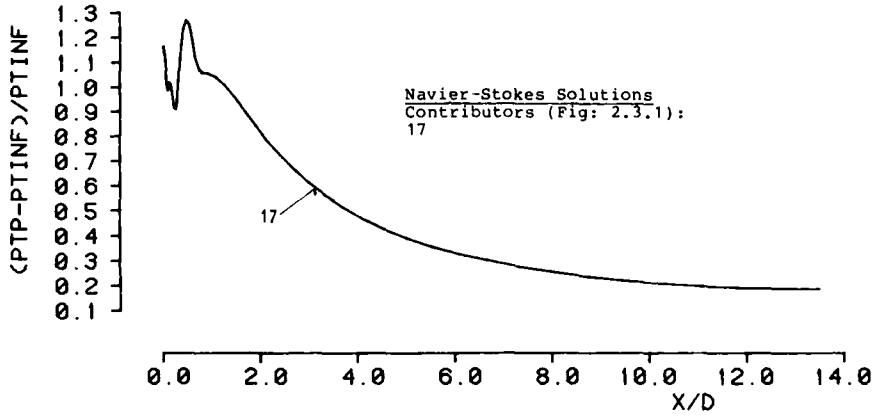

FIG.NO.: 2.3.4.6b
PITOT PRESSURE ALONG JET CENTERLINE

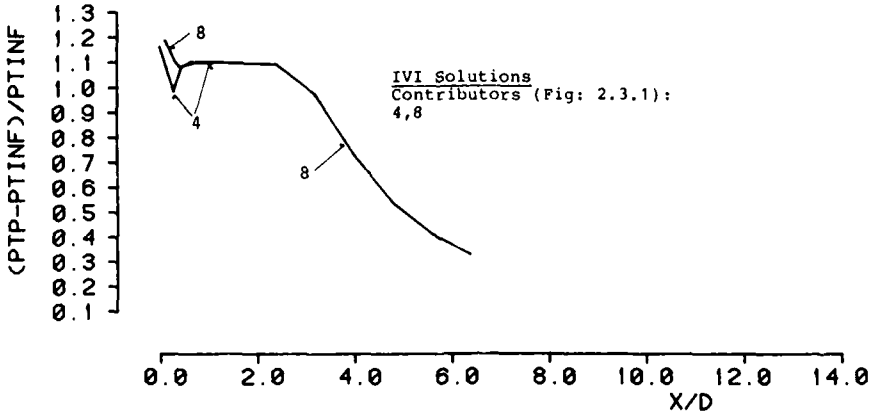

FIG.NO.: 2.3.4.6c
PITOT PRESSURE ALONG JET CENTERLINE

WG08 : TEST CASE 4

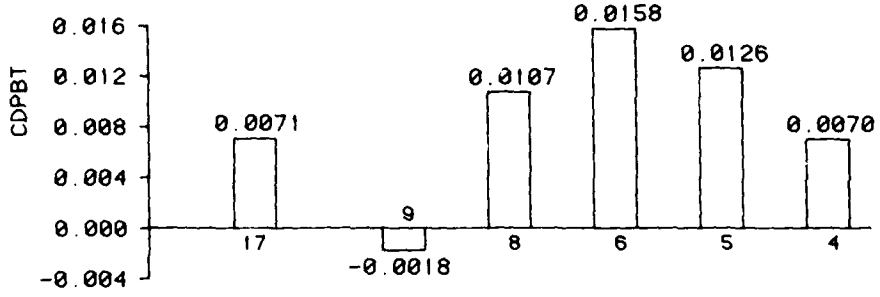

FIG.NO.: 2.3.4.8
BAR GRAPH OF BOATTAIL PRESSURE DRAG COEFFICIENT

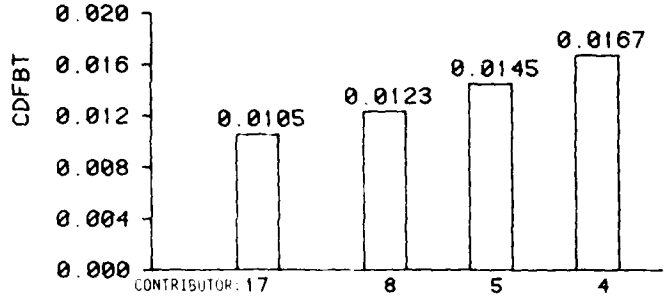

FIG.NO.: 2.3.4.9
BAR GRAPH OF BOATTAIL FRICTION DRAG COEFFICIENT

FOR CONTRIBUTOR IDENTIFICATION
SEE FIG.NO.: 2.3.1

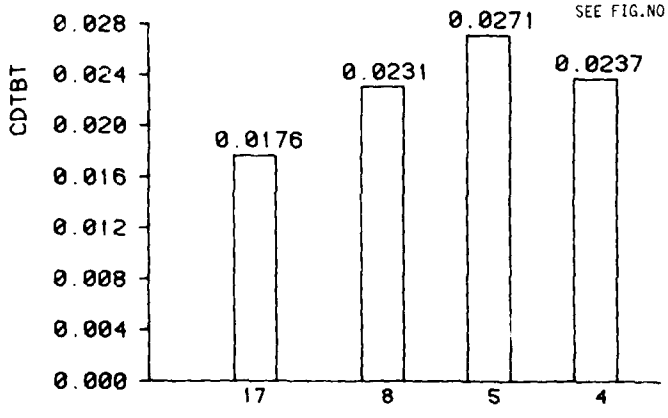

FIG.NO.: 2.3.4.10
BAR GRAPH OF TOTAL BOATTAIL DRAG COEFFICIENT

WG08 : TEST CASE 4

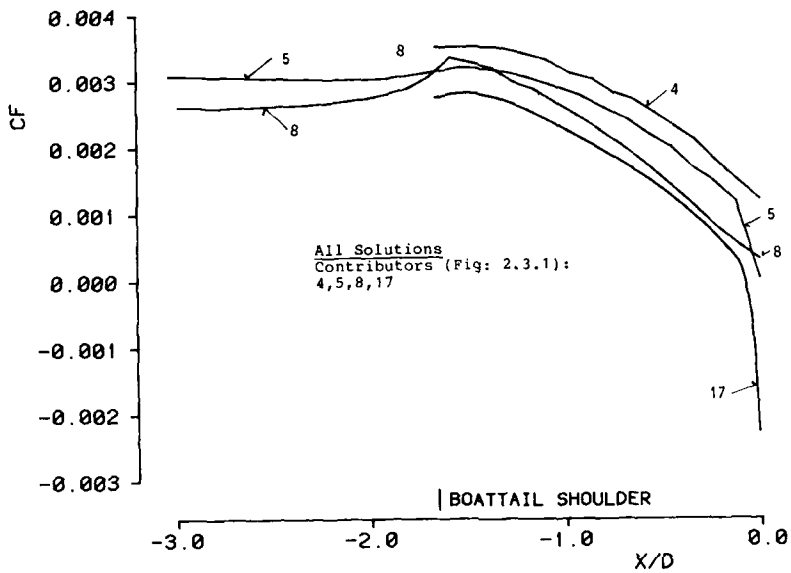

FIG.NO.: 2.3.4.11
SKIN FRICTION COEFFICIENT

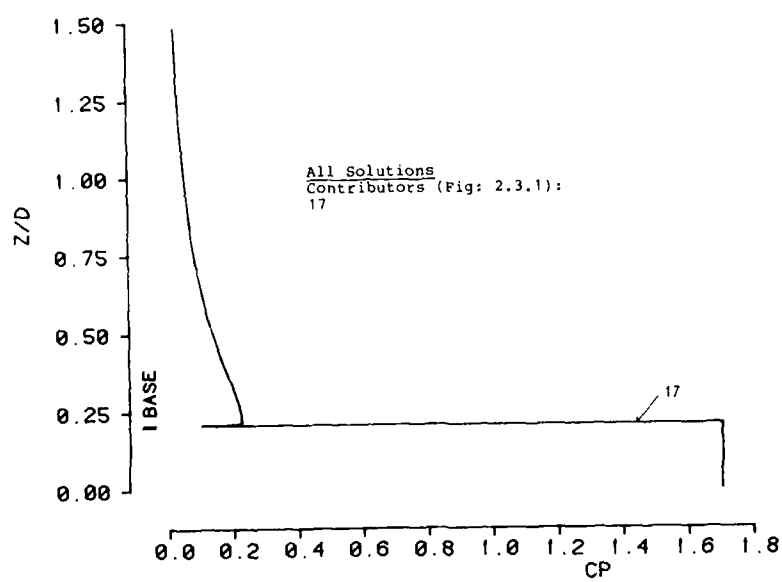

FIG.NO.: 2.3.4.12
PRESSURE COEFFICIENT ALONG BASE GRID LINE

WG08 : TEST CASE 4

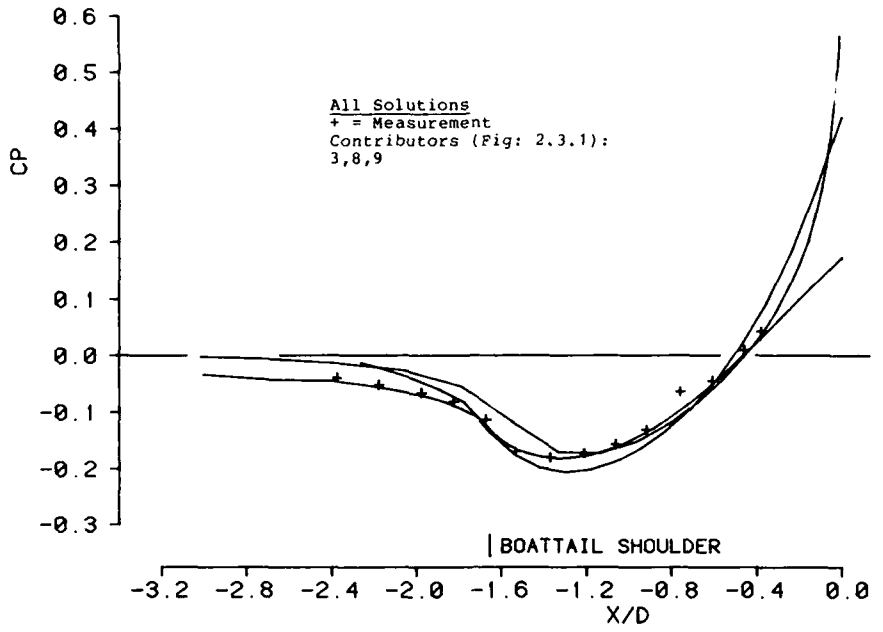

FIG.NO.: 2.3.5.1a
BOATTAIL WALL PRESSURE COEFFICIENT

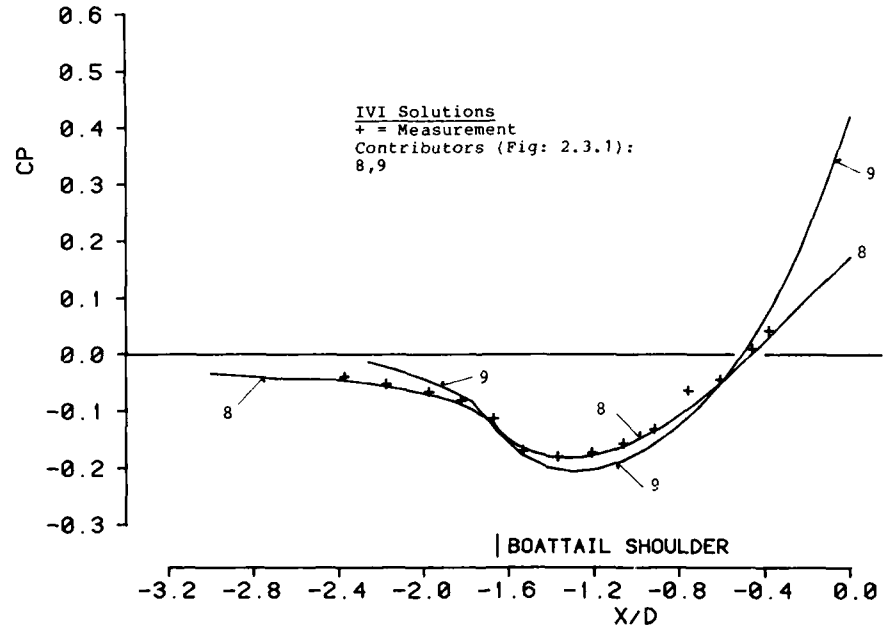

FIG.NO.: 2.3.5.1b
BOATTAIL WALL PRESSURE COEFFICIENT

WG08 : TEST CASE 5

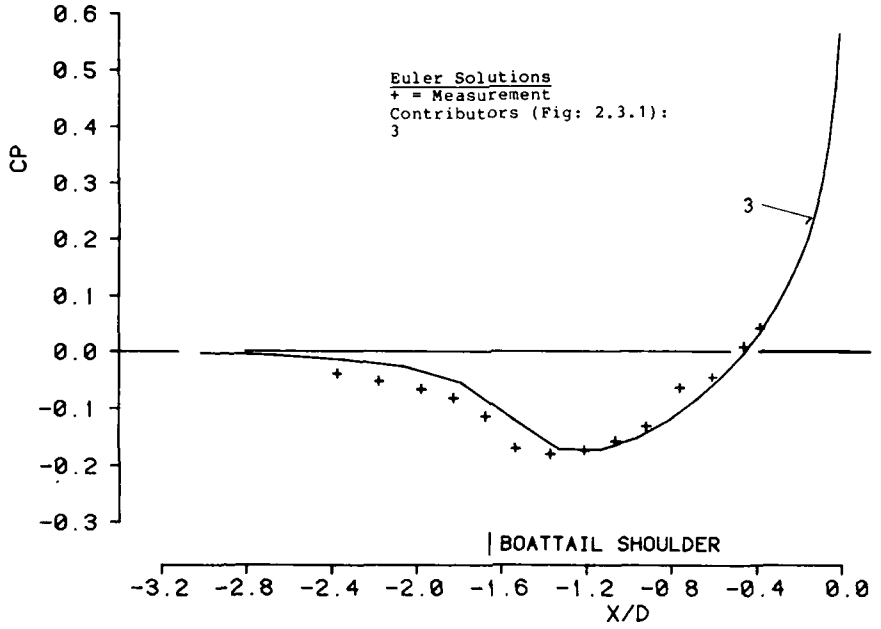

FIG.NO.: 2.3.5.1c
BOATTAIL WALL PRESSURE COEFFICIENT

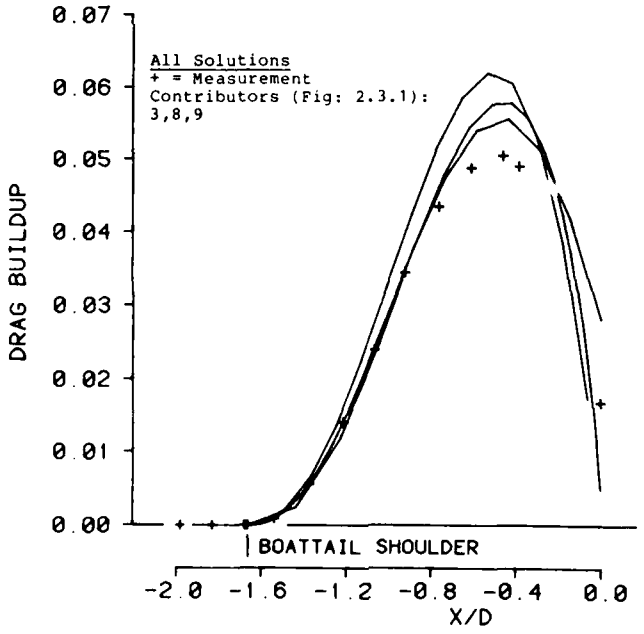

FIG.NO.: 2.3.5.2a
DRAG BUILDUP ALONG BOATTAIL

WG08 : TEST CASE 5

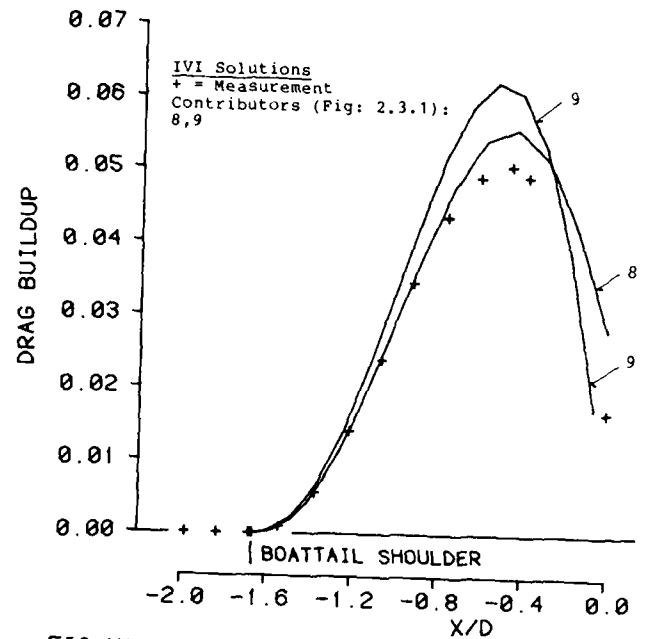

FIG.NO.: 2.3.5.2b
DRAG BUILDUP ALONG BOATTAIL

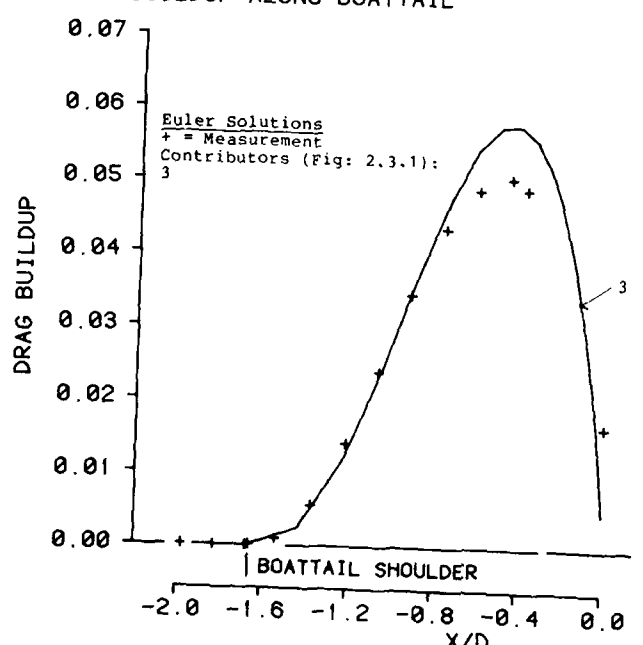

FIG.NO.: 2.3.5.2c
DRAG BUILDUP ALONG BOATTAIL

WG08 : TEST CASE 5

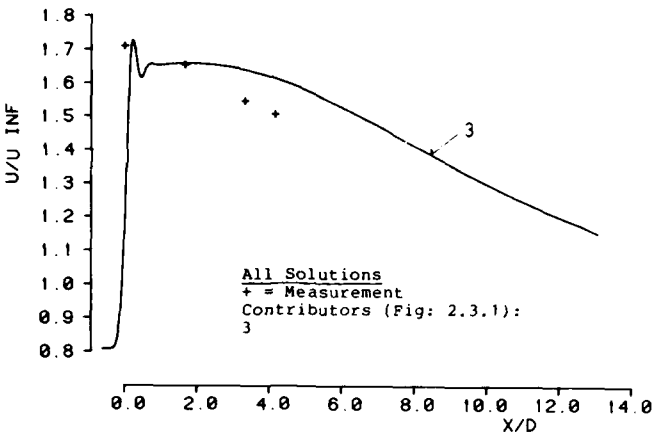

FIG.NO.: 2.3.5.3
AXIAL VELOCITY ON JET CENTERLINE

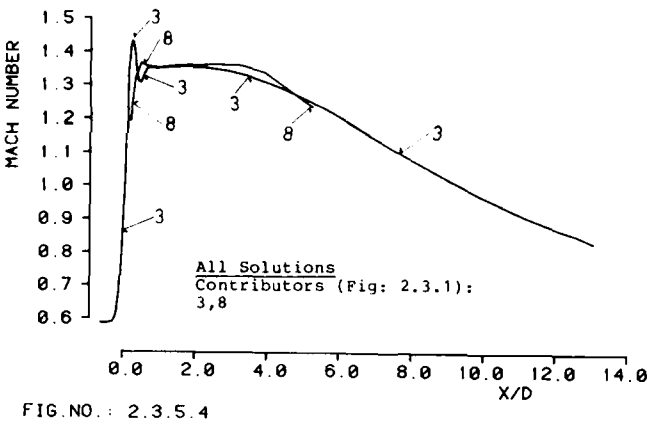

FIG.NO.: 2.3.5.4
MACH NUMBER ON JET CENTERLINE

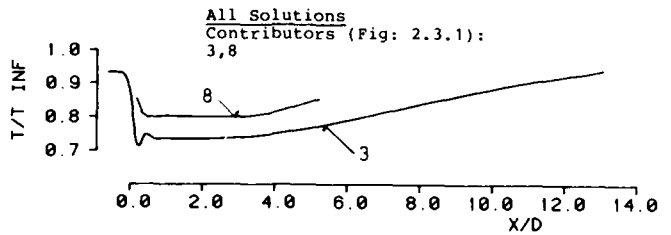

FIG.NO.: 2.3.5.5
STATIC TEMPERATURE ALONG JET CENTERLINE

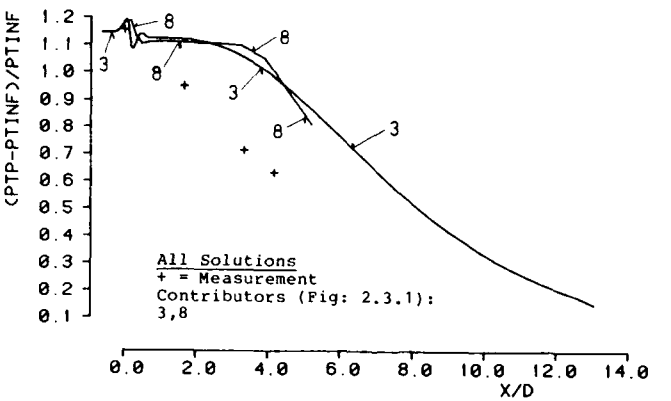

FIG.NO.: 2.3.5.6
PITOT PRESSURE ALONG JET CENTERLINE

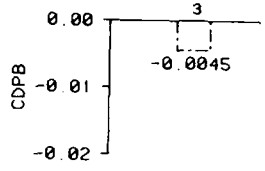

FIG.NO.: 2.3.5.7
BAR GRAPH OF BASE DRAG COEFFICIENT

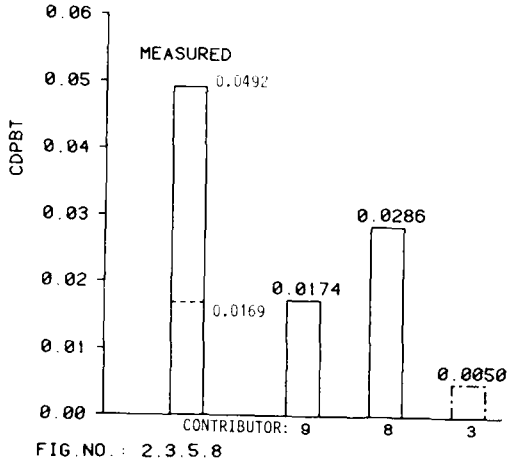

FIG.NO.: 2.3.5.8
BAR GRAPH OF BOATTAIL PRESSURE DRAG COEFFICIENT

FOR CONTRIBUTOR IDENTIFICATION
SEE FIG.NO.: 2.3.1

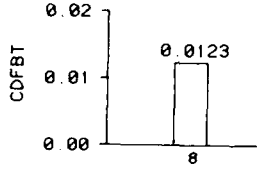

FIG NO 2.3.5.9
BAR GRAPH OF BOATTAIL FRICTION DRAG COEFFICIENT

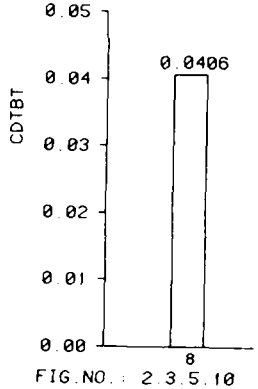

FIG.NO.: 2.3.5.10
BAR GRAPH OF TOTAL BOATTAIL DRAG COEFFICIENT

WG08 : TEST CASE 5

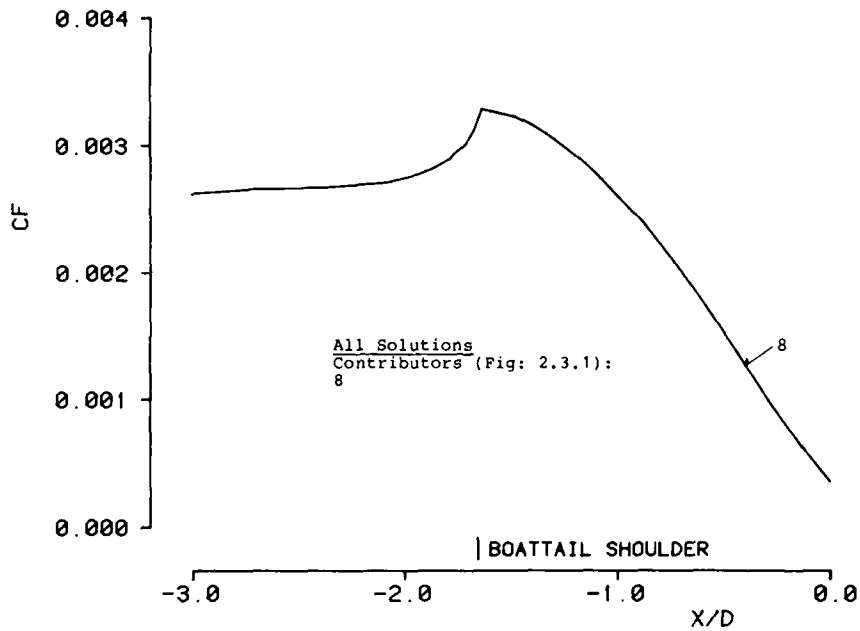

FIG.NO.: 2.3.5.11
SKIN FRICTION COEFFICIENT

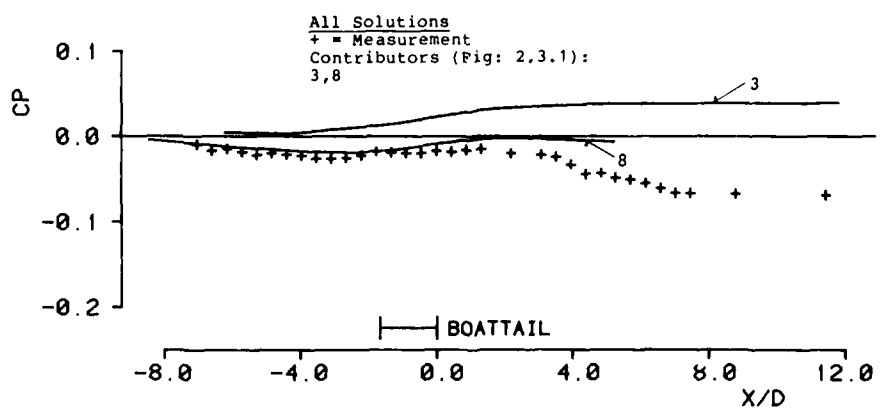

FIG.NO.: 2.3.5.13
TUNNEL WALL PRESSURE COEFFICIENT

WG08 : TEST CASE 5

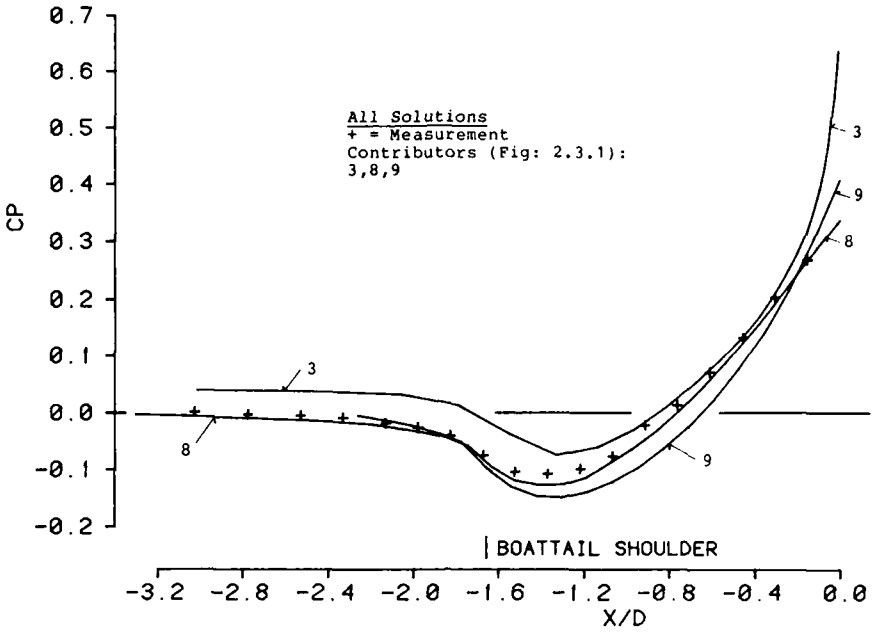

FIG.NO.: 2.3.6.1a
BOATTAIL WALL PRESSURE COEFFICIENT

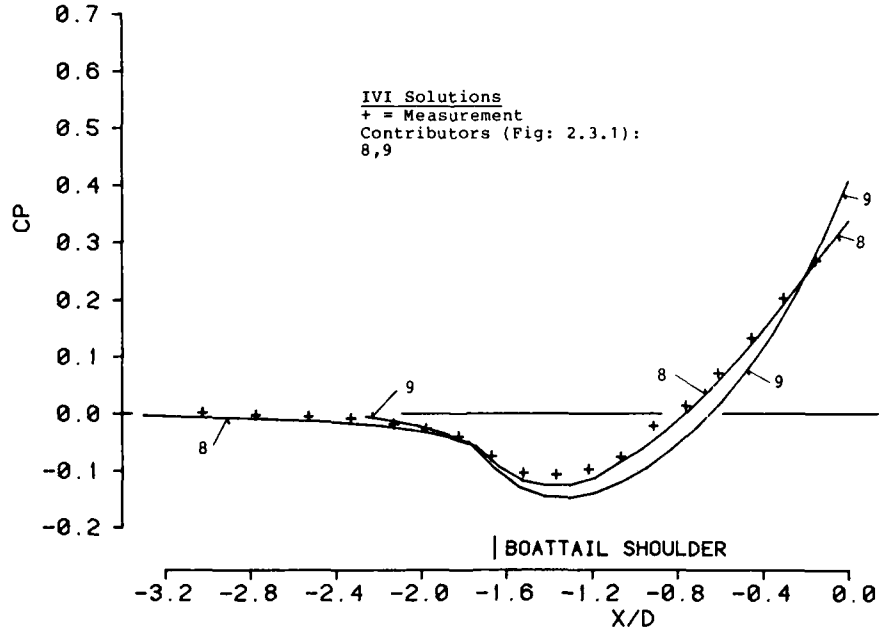

FIG.NO.: 2.3.6.1b
BOATTAIL WALL PRESSURE COEFFICIENT

WG08 : TEST CASE 6

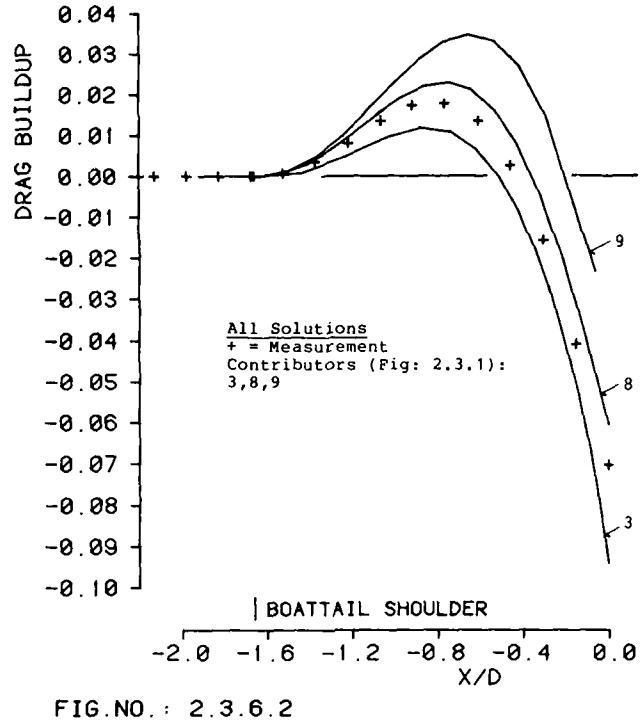

FIG.NO.: 2.3.6.2
DRAG BUILDUP ALONG BOATTAIL

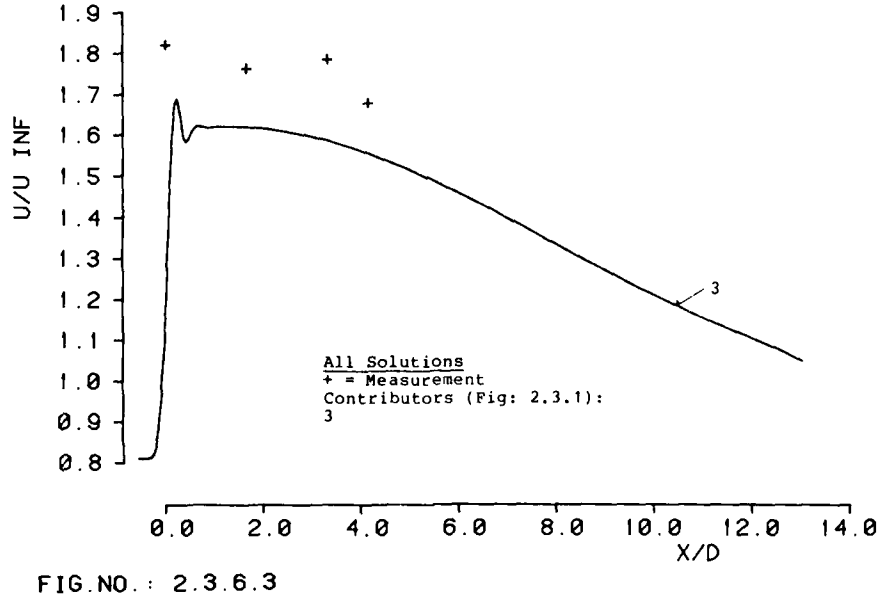

FIG.NO.: 2.3.6.3
AXIAL VELOCITY ON JET CENTERLINE

WG08 : TEST CASE 6

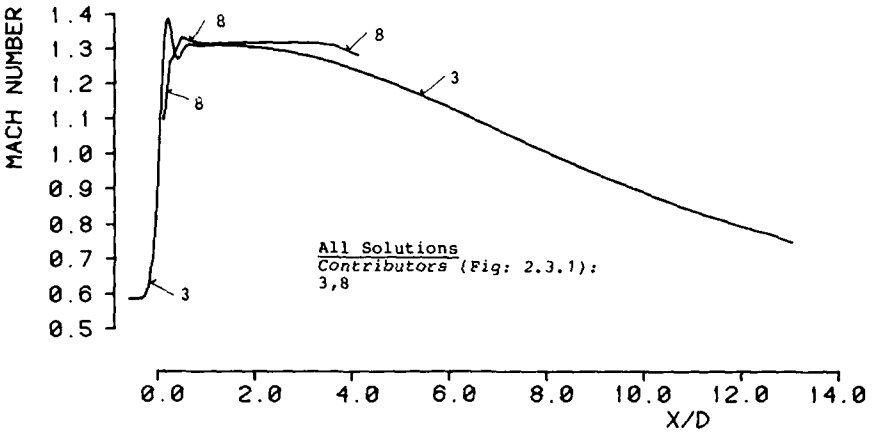

FIG.NO.: 2.3.6.4
MACH NUMBER ON JET CENTERLINE

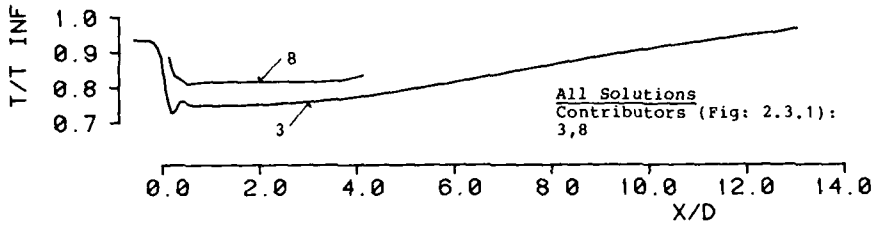

FIG.NO.: 2.3.6.5
STATIC TEMPERATURE ALONG JET CENTERLINE

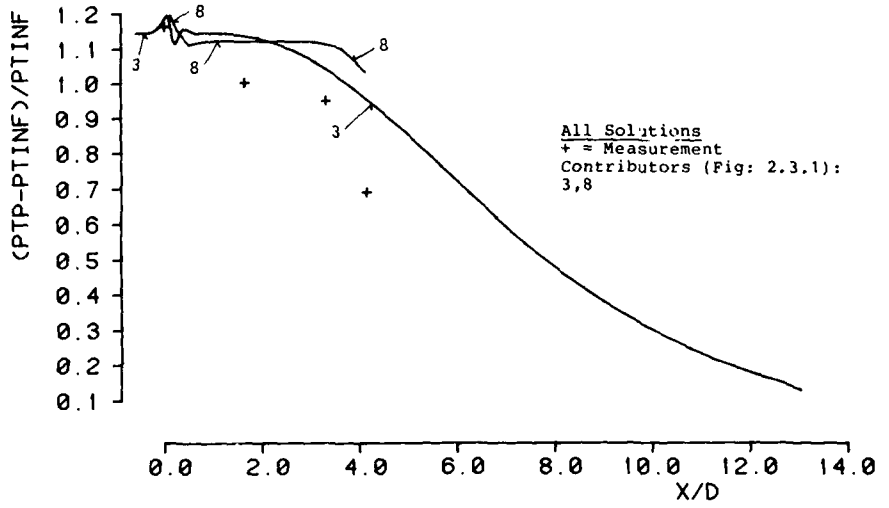

FIG.NO.: 2.3.6.6
PITOT PRESSURE ALONG JET CENTERLINE

WG08 : TEST CASE 6

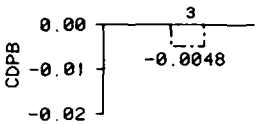

FIG.NO.: 2.3.6.7
BAR GRAPH OF BASE DRAG COEFFICIENT

FOR CONTRIBUTOR IDENTIFICATION
SEE FIG.NO.: 2.3.1

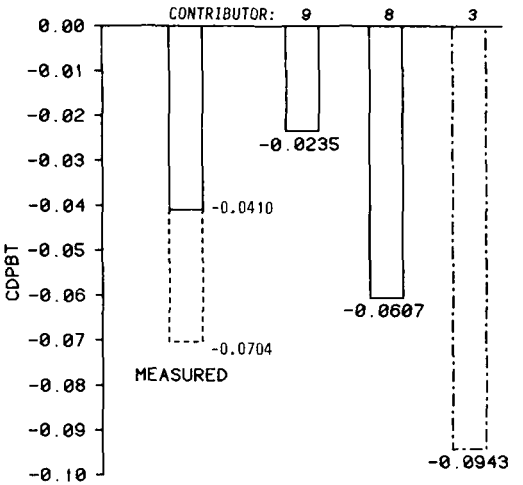

FIG.NO.: 2.3.6.8
BAR GRAPH OF BOATTAIL PRESSURE DRAG COEFFICIENT

FIG.NO.: 2.3.6.9
BAR GRAPH OF BOATTAIL FRICTION DRAG COEFFICIENT

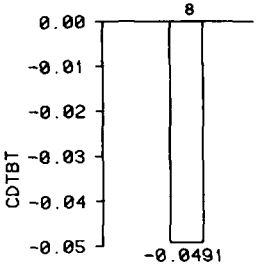

FIG.NO.: 2.3.6.10
BAR GRAPH OF TOTAL BOATTAIL DRAG COEFFICIENT

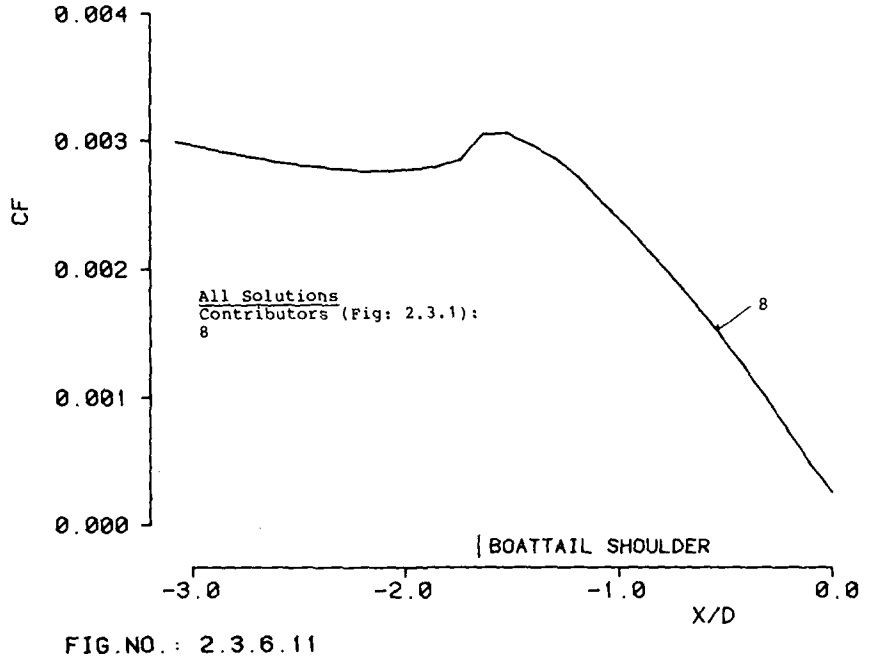

FIG.NO.: 2.3.6.11
SKIN FRICTION COEFFICIENT

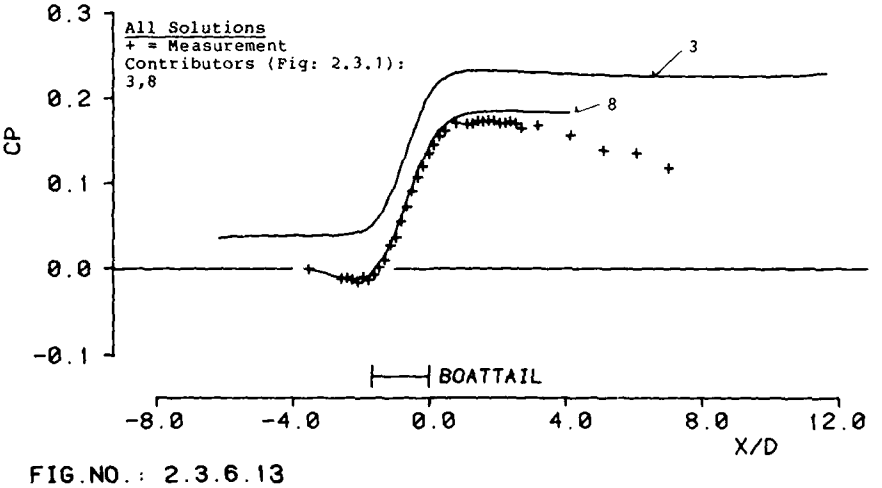

FIG.NO.: 2.3.6.13
TUNNEL WALL PRESSURE COEFFICIENT

WG08 : TEST CASE 6

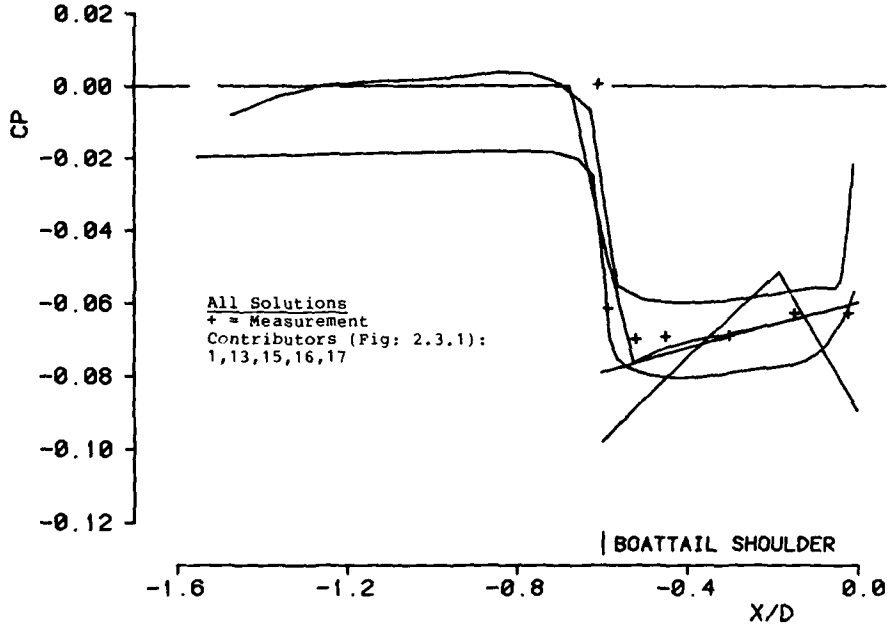

FIG.NO.: 2.3.7.1a
BOATTAIL WALL PRESSURE COEFFICIENT

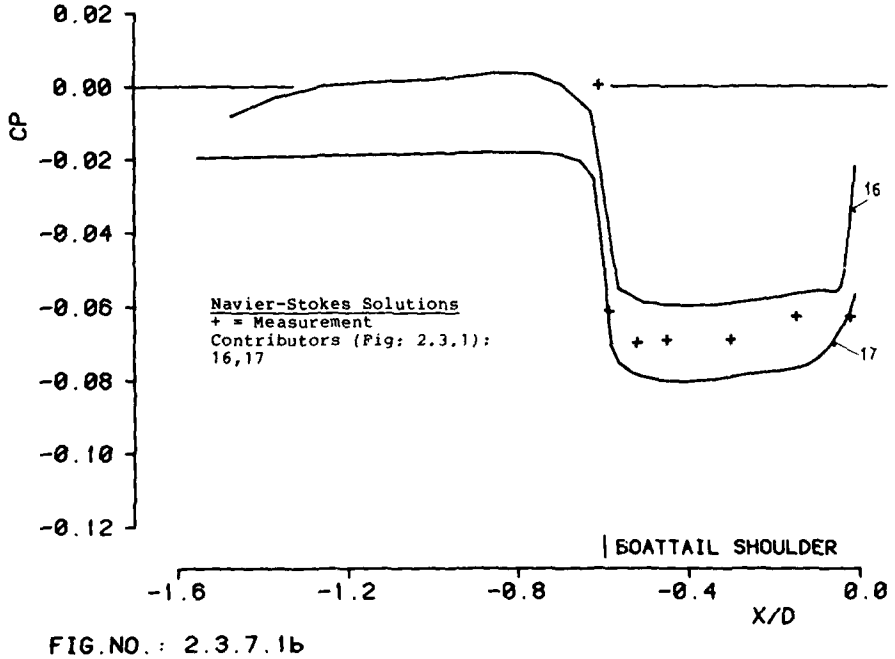

FIG.NO.: 2.3.7.1b
BOATTAIL WALL PRESSURE COEFFICIENT

WG08 : TEST CASE 7

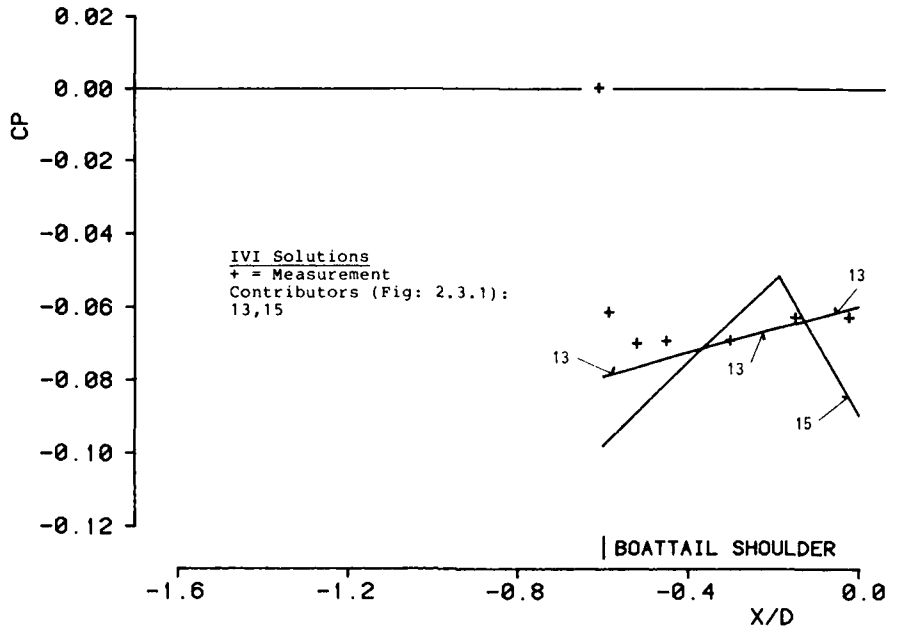

FIG.NO.: 2.3.7.1c
BOATTAIL WALL PRESSURE COEFFICIENT

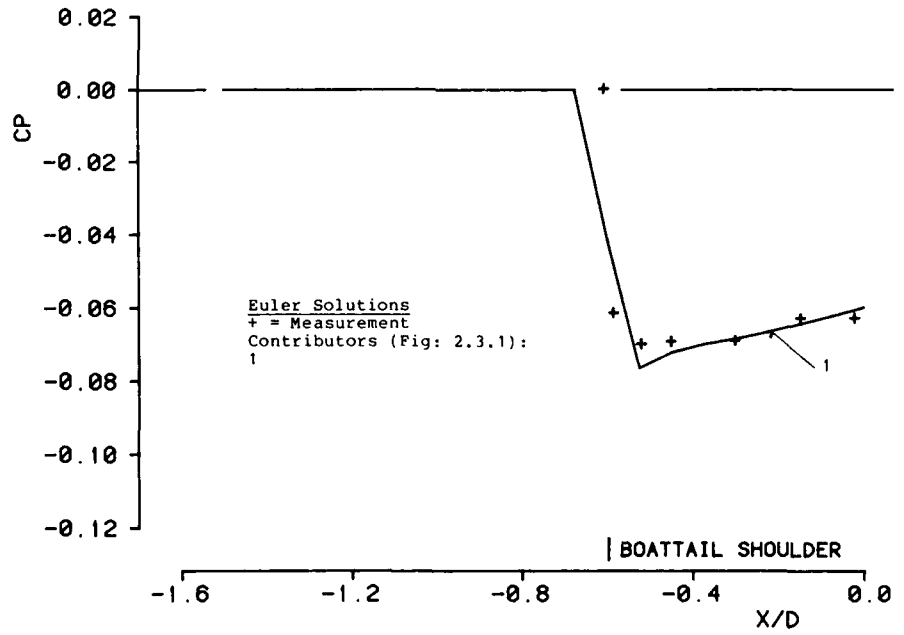

FIG.NO.: 2.3.7.1d
BOATTAIL WALL PRESSURE COEFFICIENT

WG08 : TEST CASE 7

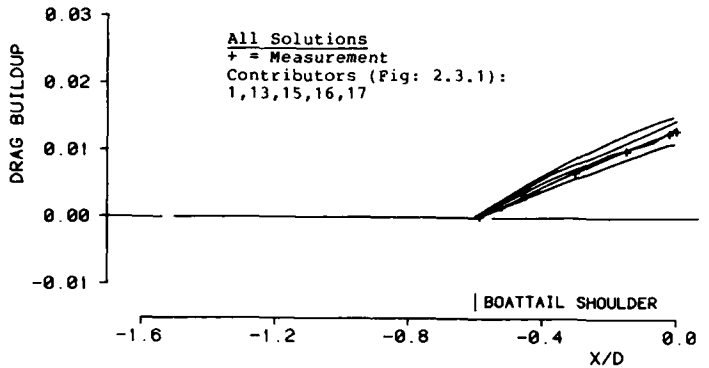

FIG.NO.: 2.3.7.2a
DRAG BUILDUP ALONG BOATTAIL

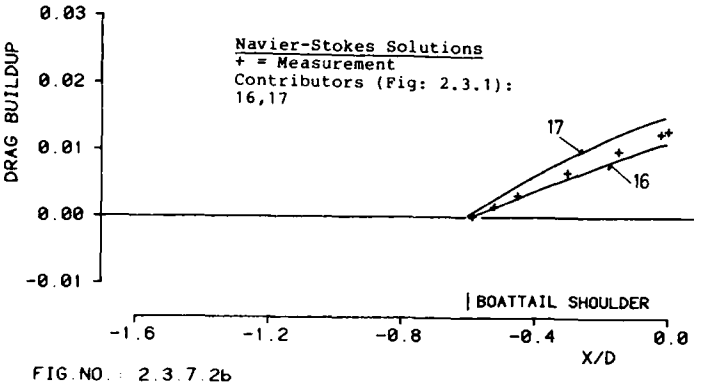

FIG.NO.: 2.3.7.2b
DRAG BUILDUP ALONG BOATTAIL

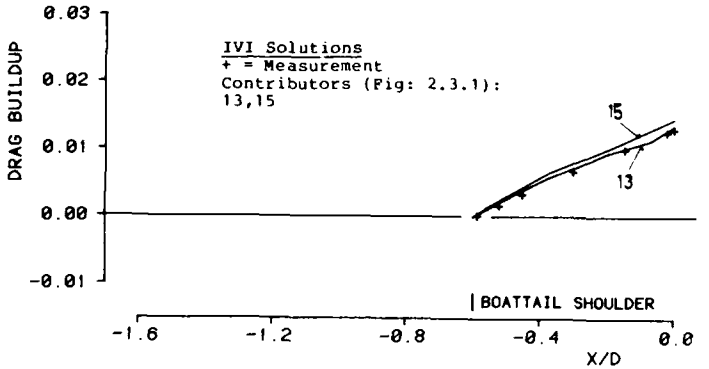

FIG.NO.: 2.3.7.2c
DRAG BUILDUP ALONG BOATTAIL

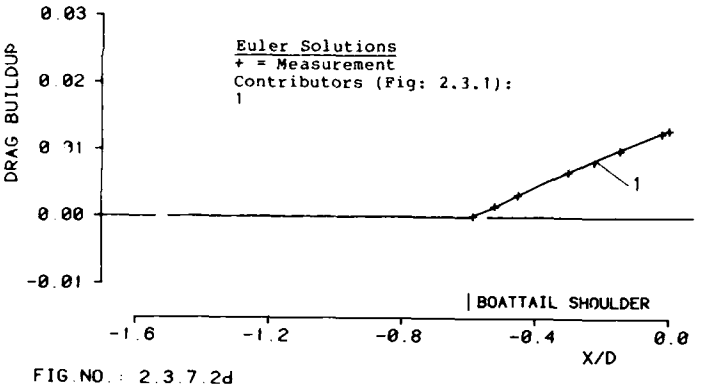

FIG.NO.: 2.3.7.2d
DRAG BUILDUP ALONG BOATTAIL

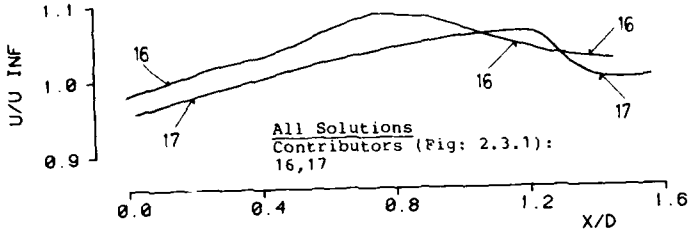

FIG.NO.: 2.3.7.3
AXIAL VELOCITY ON JET CENTERLINE

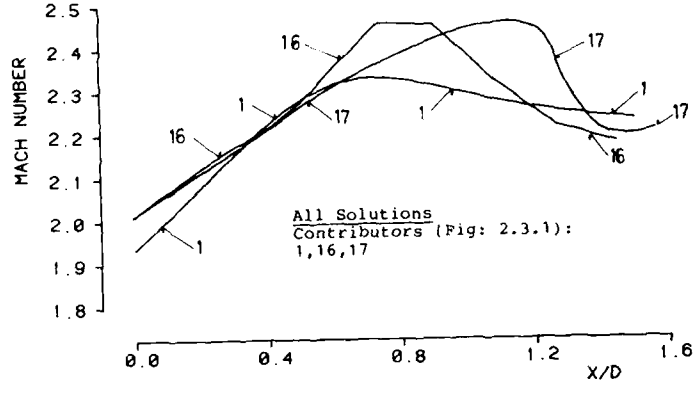

FIG.NO.: 2.3.7.4
MACH NUMBER ON JET CENTERLINE

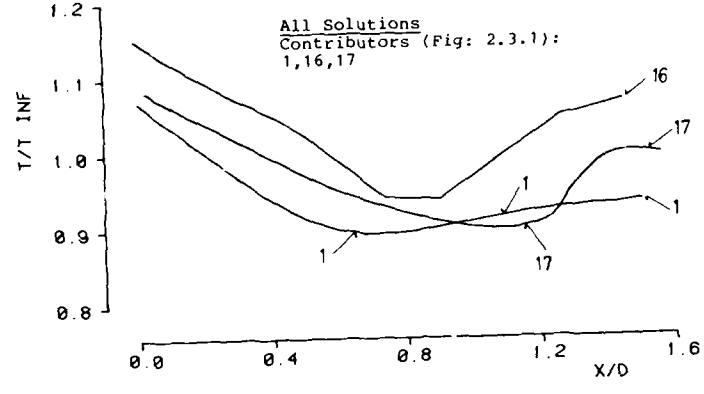

FIG.NO.: 2.3.7.5
STATIC TEMPERATURE ALONG JET CENTERLINE

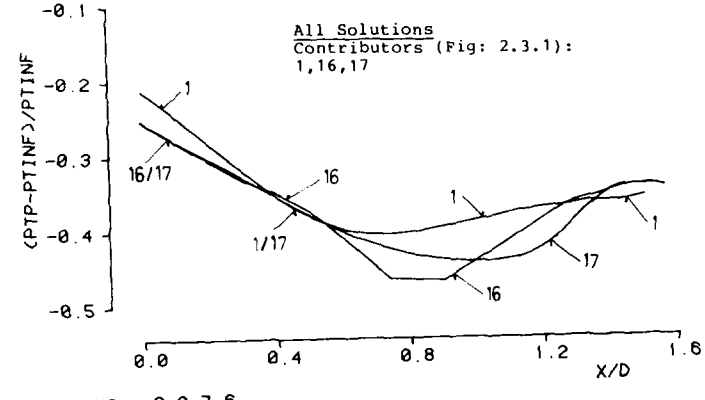

FIG.NO.: 2.3.7.6
PITOT PRESSURE ALONG JET CENTERLINE

WG08 : TEST CASE 7

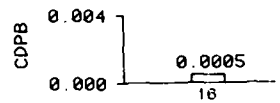

FIG.NO.: 2.3.7.7
BAR GRAPH OF BASE DRAG COEFFICIENT

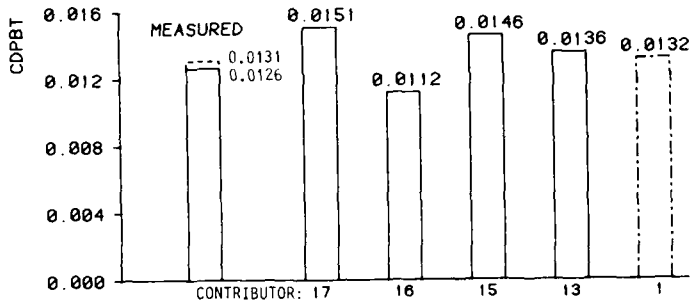

FIG.NO.: 2.3.7.8
BAR GRAPH OF BOATTAIL PRESSURE DRAG COEFFICIENT

FOR CONTRIBUTOR IDENTIFICATION
SEE FIG.NO.: 2.3.1

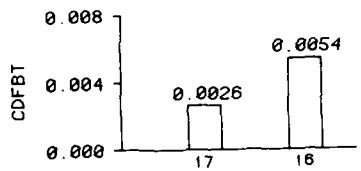

FIG.NO.: 2.3.7.9
BAR GRAPH OF BOATTAIL FRICTION DRAG COEFFICIENT

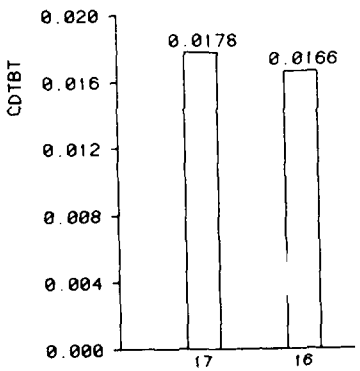

FIG.NO.: 2.3.7.10
BAR GRAPH OF TOTAL BOATTAIL DRAG COEFFICIENT

WG08 : TEST CASE 7

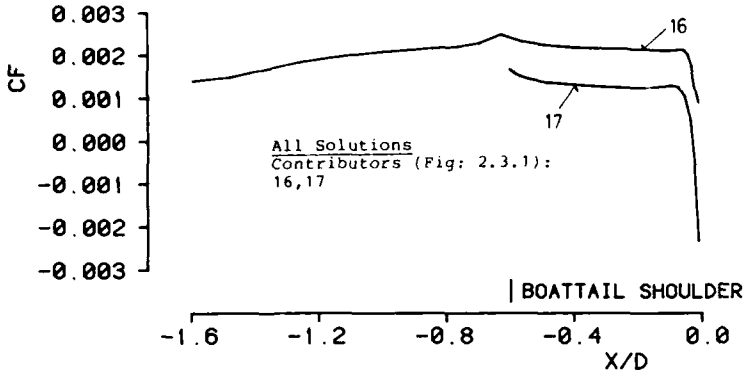

FIG.NO.: 2.3.7.11
SKIN FRICTION COEFFICIENT

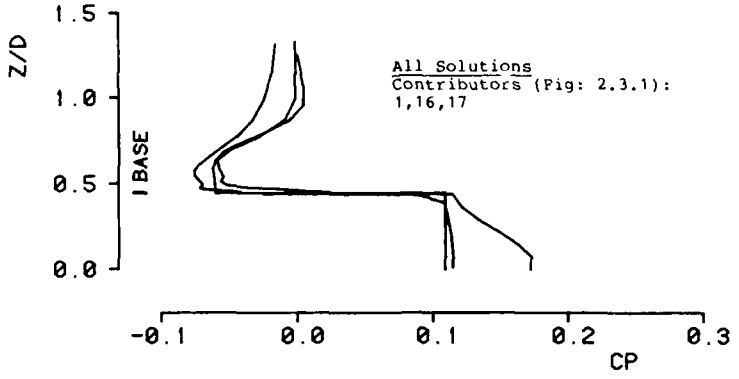

FIG.NO.: 2.3.7.12a
PRESSURE COEFFICIENT ALONG BASE GRID LINE

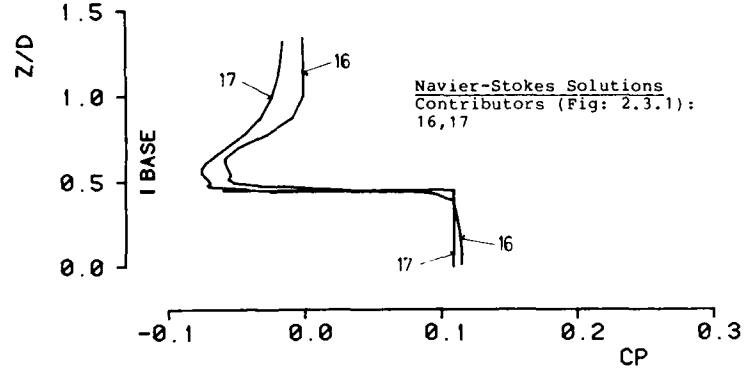

FIG.NO.: 2.3.7.12b
PRESSURE COEFFICIENT ALONG BASE GRID LINE

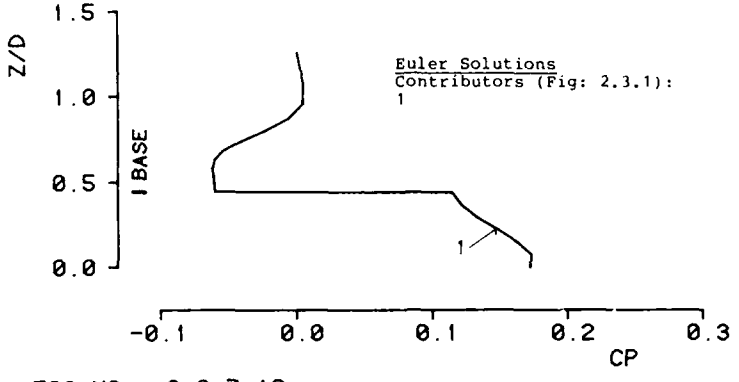

FIG.NO.: 2.3.7.12c
PRESSURE COEFFICIENT ALONG BASE GRID LINE

WG08 : TEST CASE 7

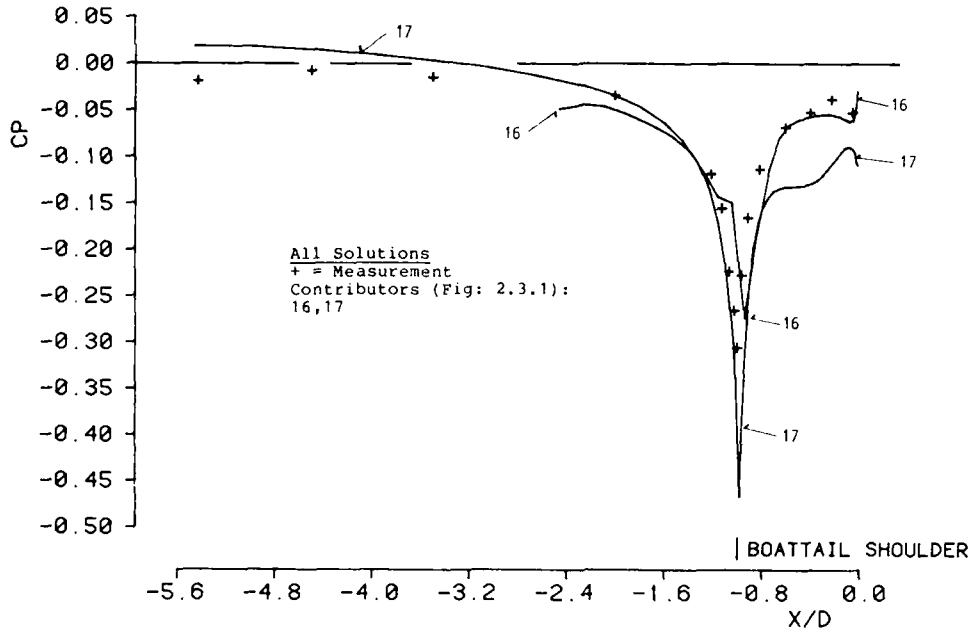

FIG.NO.: 2.3.8.1
BOATTAIL WALL PRESSURE COEFFICIENT

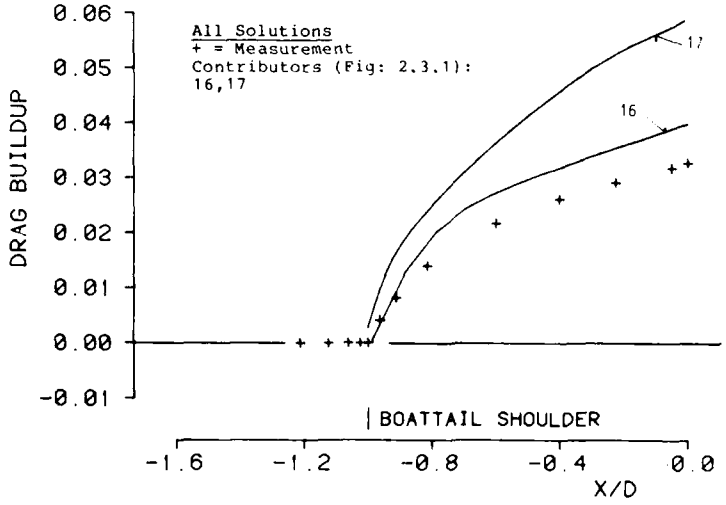

FIG.NO.: 2.3.8.2
DRAG BUILDUP ALONG BOATTAIL

WG08 : TEST CASE 8

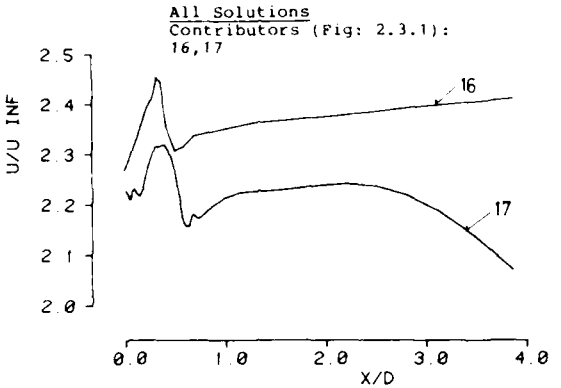

FIG NO : 2.3.8.3
AXIAL VELOCITY ON JET CENTERLINE

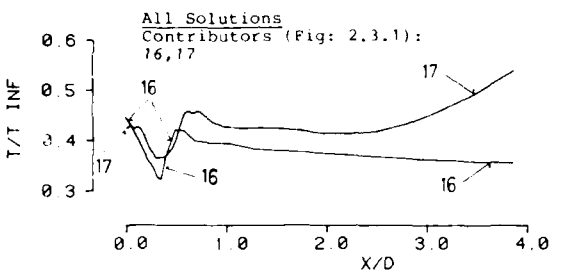

FIG.NO.: 2.3.8.5
STATIC TEMPERATURE ALONG JET CENTERLINE

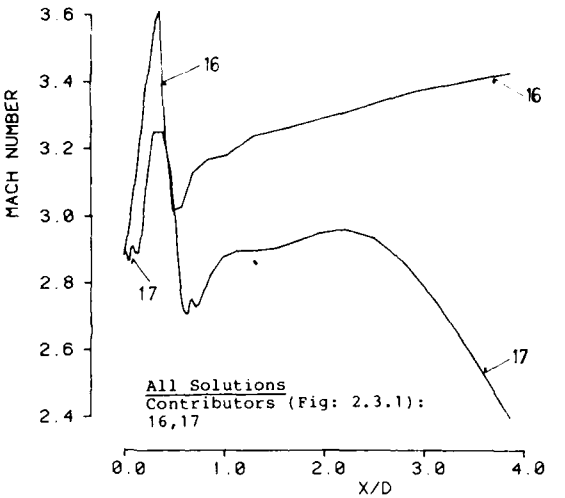

FIG.NO.: 2.3.8.4
MACH NUMBER ON JET CENTERLINE

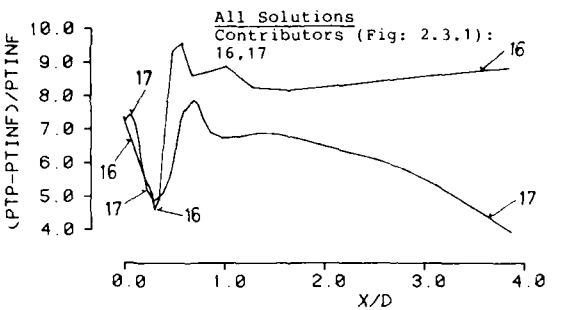

FIG.NO.: 2.3.8.6
PITOT PRESSURE ALONG JET CENTERLINE

WG08 : TEST CASE 8

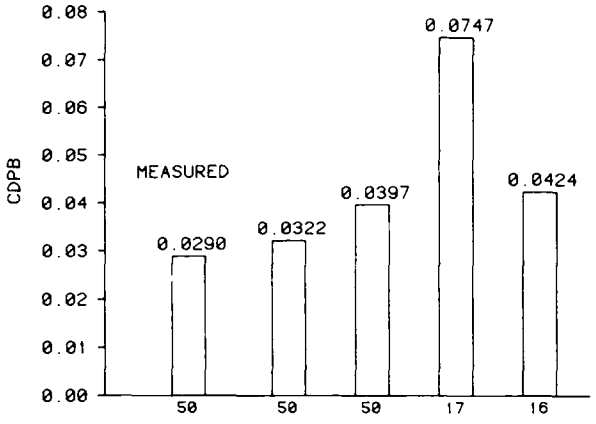

FIG.NO.: 2.3.8.7
BAR GRAPH OF BASE DRAG COEFFICIENT

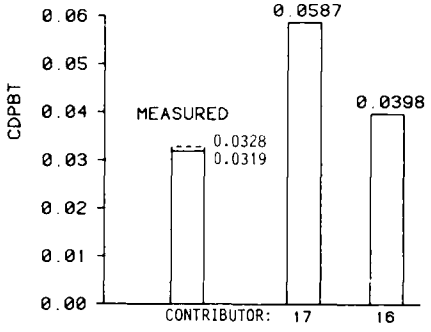

FIG.NO.: 2.3.8.8
BAR GRAPH OF BOATTAIL PRESSURE DRAG COEFFICIENT

FOR CONTRIBUTOR IDENTIFICATION
SEE FIG.NO.: 2.3.1

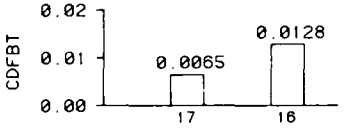

FIG.NO.: 2.3.8.9
BAR GRAPH OF BOATTAIL FRICTION DRAG COEFFICIENT

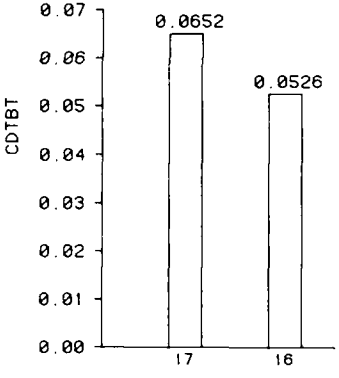

FIG.NO.: 2.3.8.10
BAR GRAPH OF TOTAL BOATTAIL DRAG COEFFICIENT

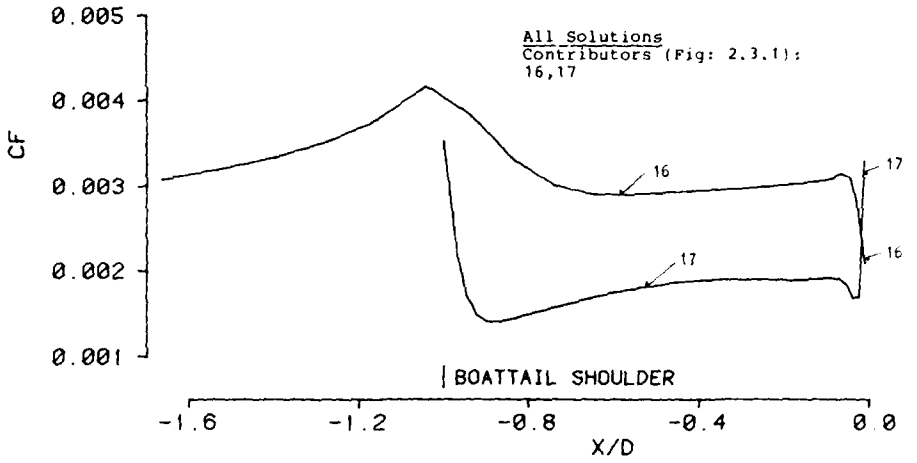

FIG.NO.: 2.3.8.11
SKIN FRICTION COEFFICIENT

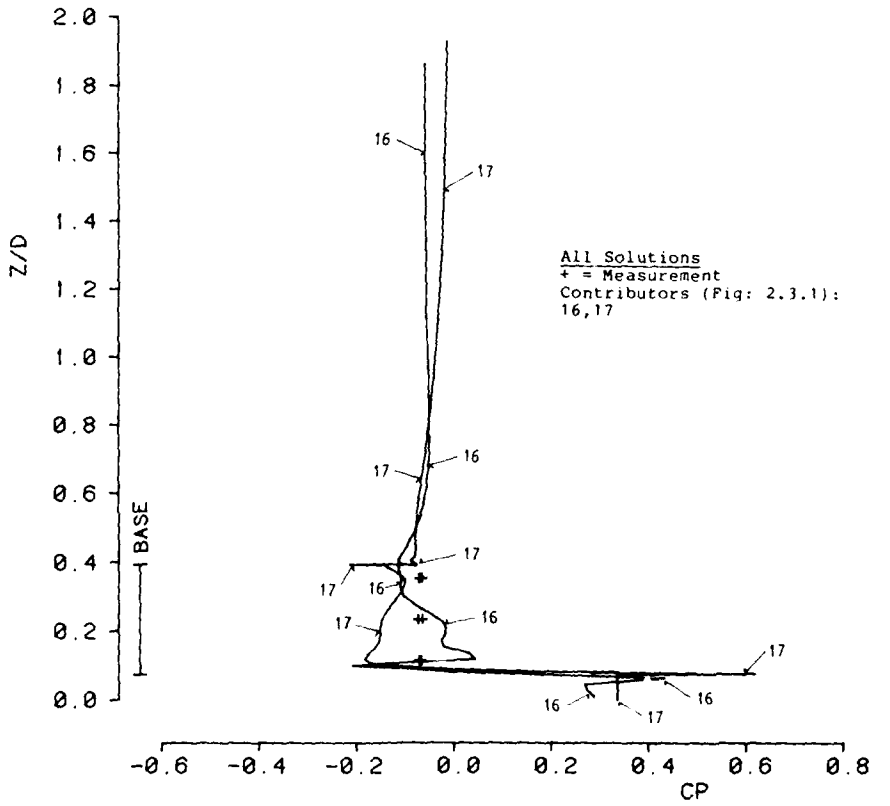

FIG.NO.: 2.3.8.12
PRESSURE COEFFICIENT ALONG BASE GRID LINE

WG08 : TEST CASE 8

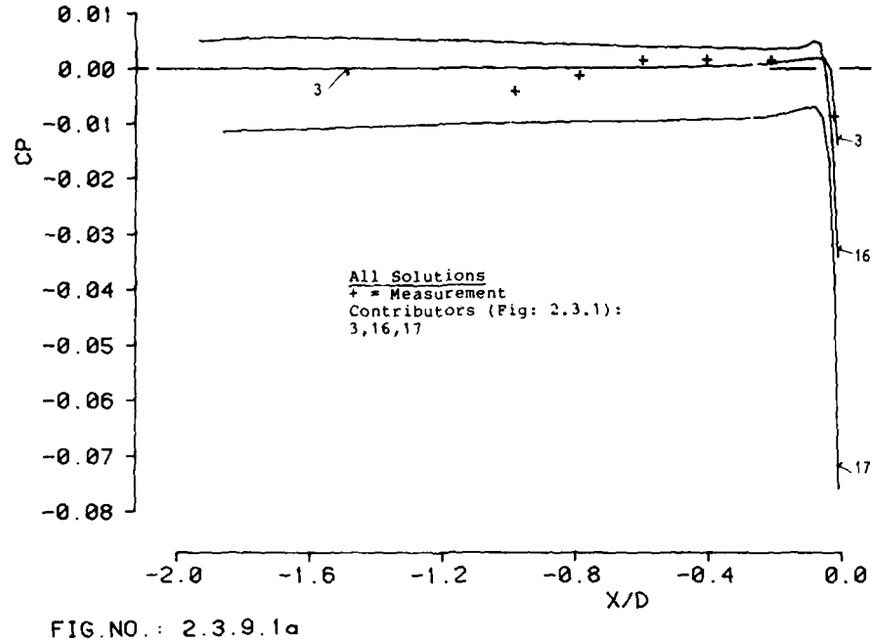

FIG.NO.: 2.3.9.1a
BOATTAIL WALL PRESSURE COEFFICIENT

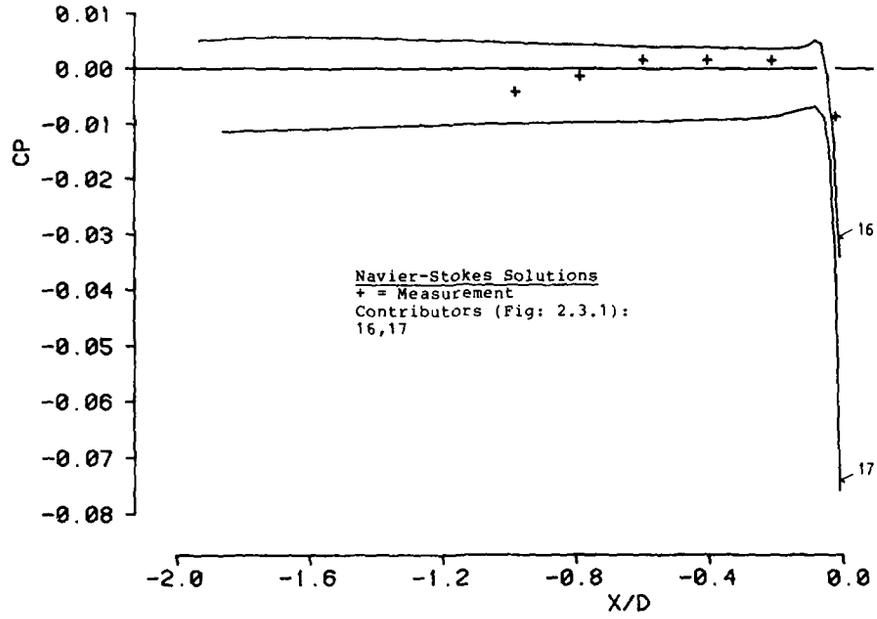

FIG.NO.: 2.3.9.1b
BOATTAIL WALL PRESSURE COEFFICIENT

WG08 : TEST CASE 9

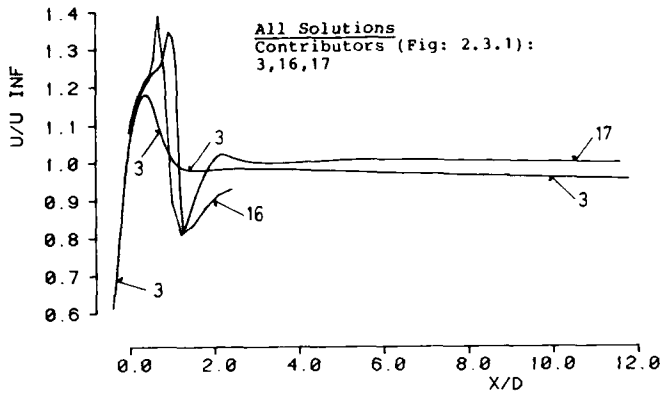

FIG.NO.: 2.3.9.3a
AXIAL VELOCITY ON JET CENTERLINE

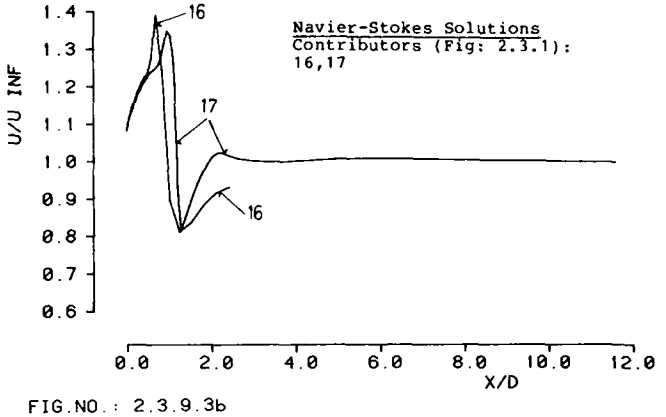

FIG.NO.: 2.3.9.3b
AXIAL VELOCITY ON JET CENTERLINE

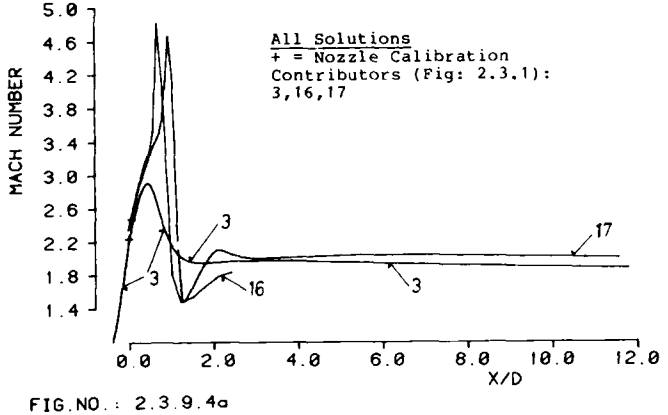

FIG.NO.: 2.3.9.4a
MACH NUMBER ON JET CENTERLINE

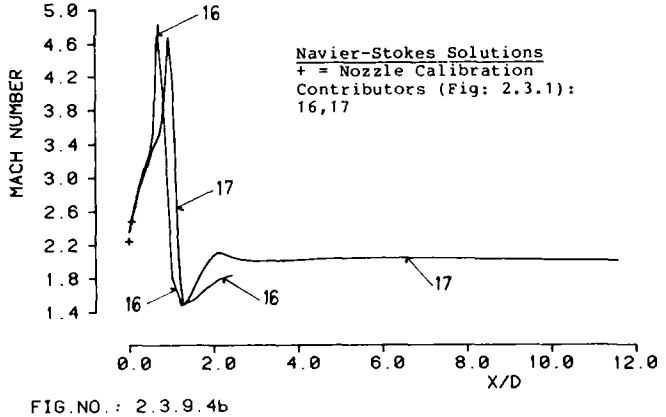

FIG.NO.: 2.3.9.4b
MACH NUMBER ON JET CENTERLINE

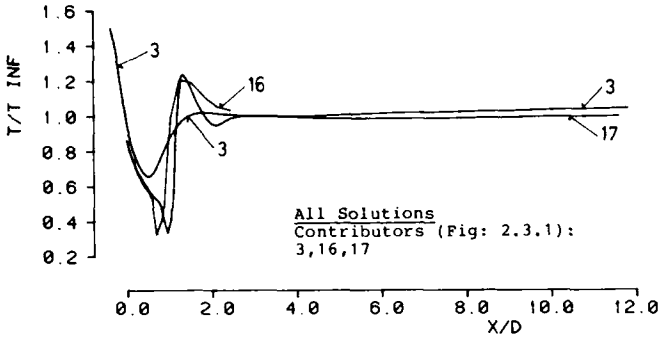

FIG.NO.: 2.3.9.5a
STATIC TEMPERATURE ALONG JET CENTERLINE

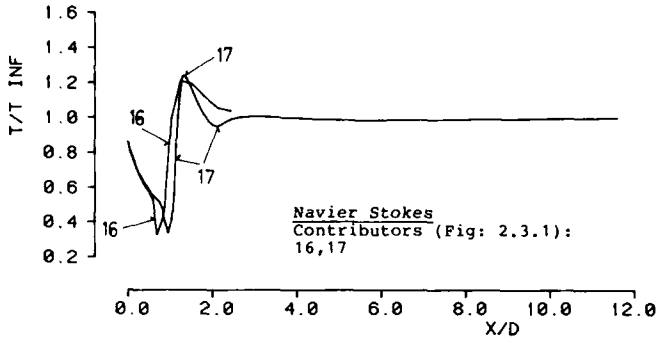

FIG.NO.: 2.3.9.5b
STATIC TEMPERATURE ALONG JET CENTERLINE

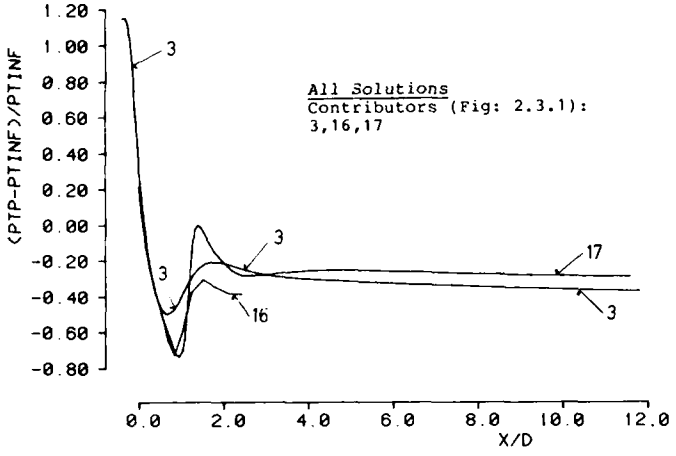

FIG.NO.: 2.3.9.6a
PITOT PRESSURE ALONG JET CENTERLINE

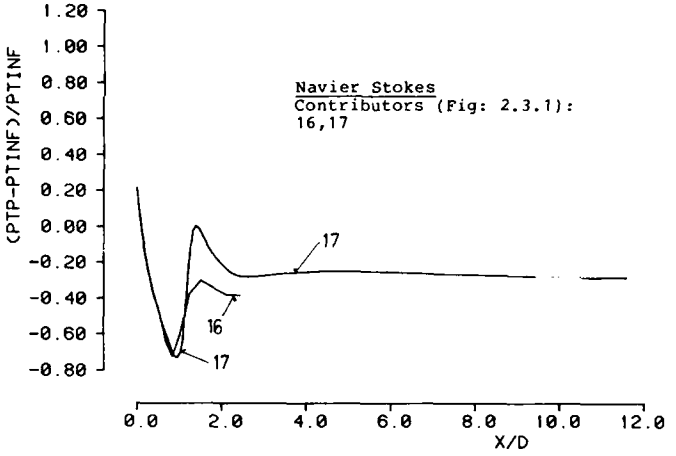

FIG.NO.: 2.3.9.6b
PITOT PRESSURE ALONG JET CENTERLINE

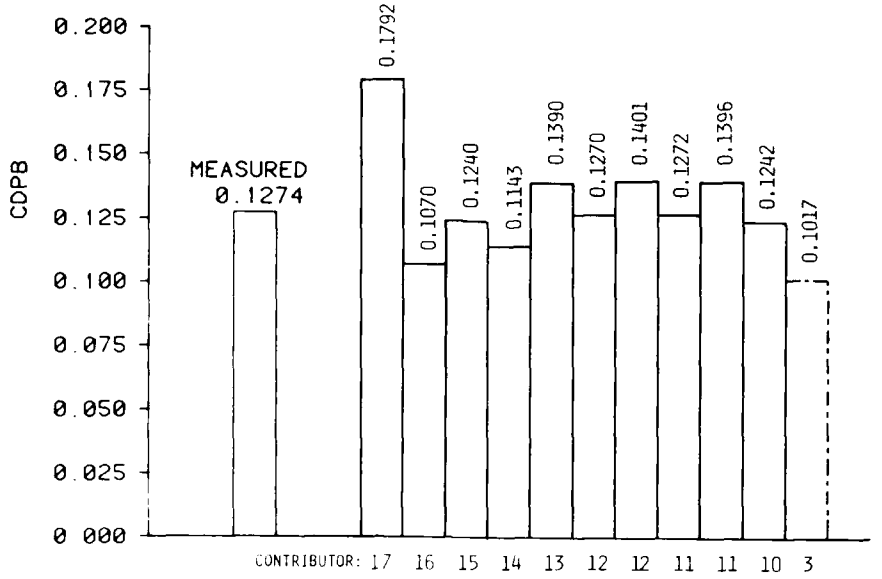

FIG.NO.: 2.3.9.7
BAR GRAPH OF BASE DRAG COEFFICIENT

FOR CONTRIBUTOR IDENTIFICATION
SEE FIG.NO.: 2.3.1

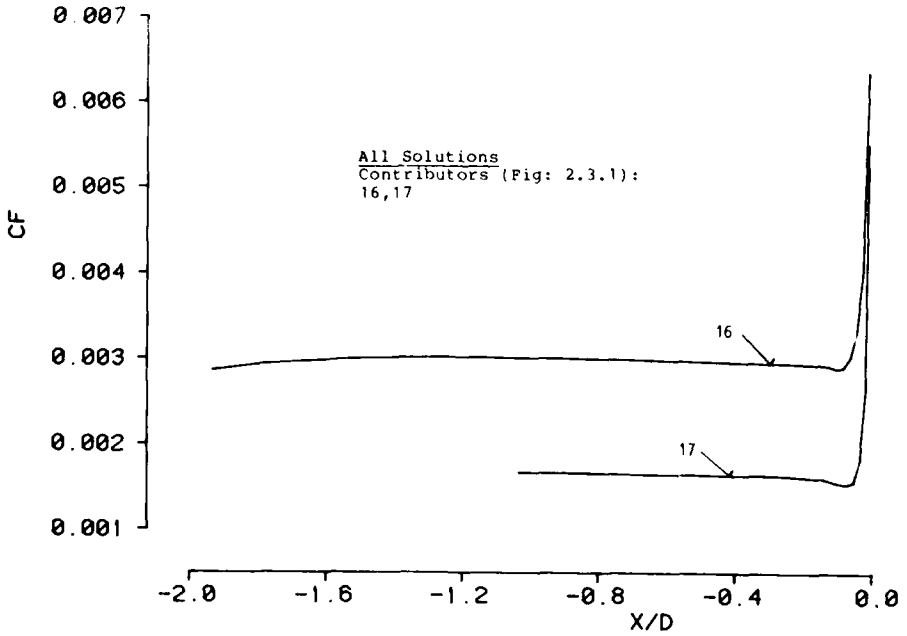

FIG.NO.: 2.3.9.11
SKIN FRICTION COEFFICIENT

WG08 : TEST CASE 9

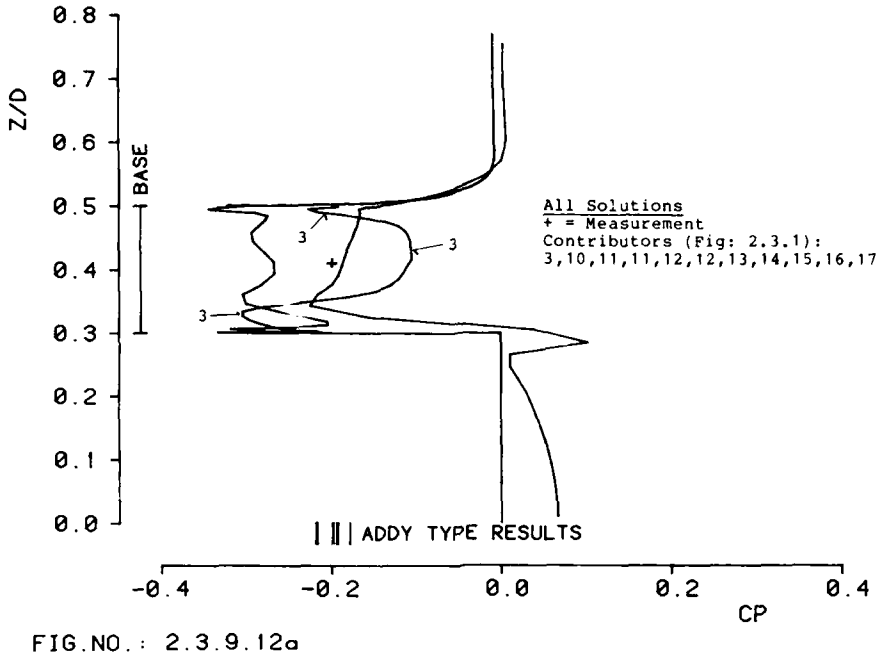

FIG.NO.: 2.3.9.12a
PRESSURE COEFFICIENT ALONG BASE GRID LINE

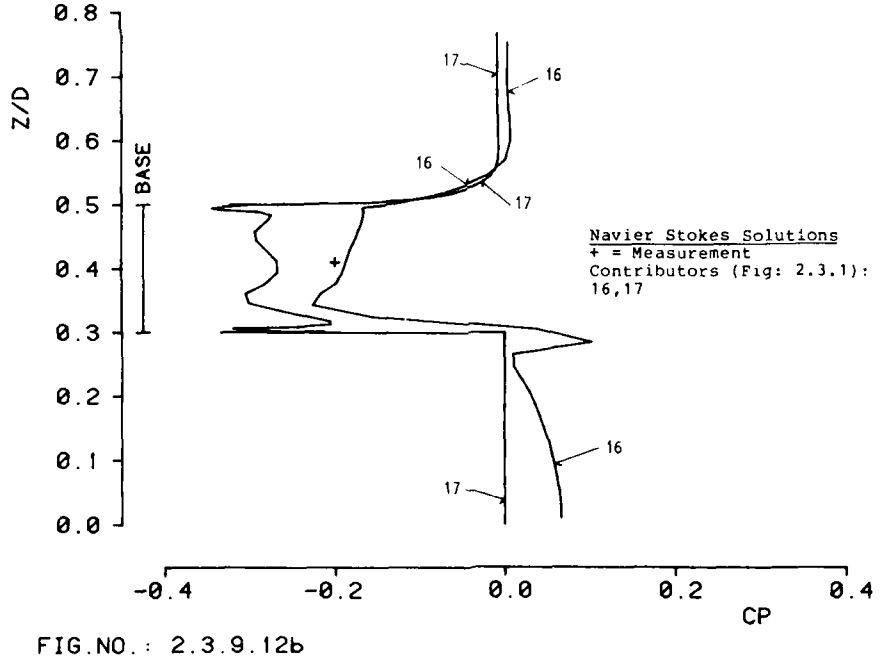

FIG.NO.: 2.3.9.12b
PRESSURE COEFFICIENT ALONG BASE GRID LINE

WG08 : TEST CASE 9

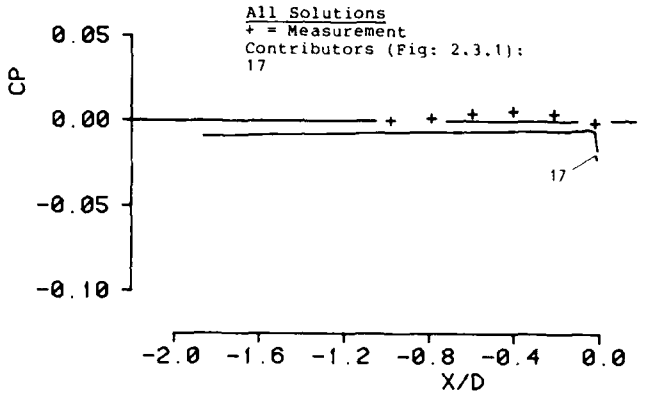

FIG.NO.: 2.3.10.1
BOATTAIL WALL PRESSURE COEFFICIENT

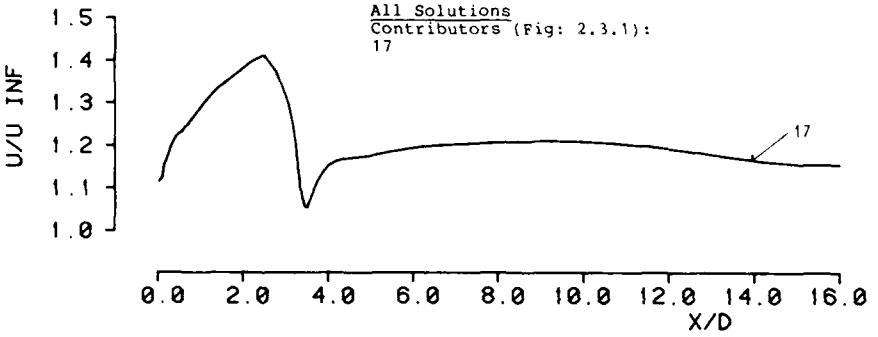

FIG.NO.: 2.3.10.3
AXIAL VELOCITY ON JET CENTERLINE

WG08 : TEST CASE 10

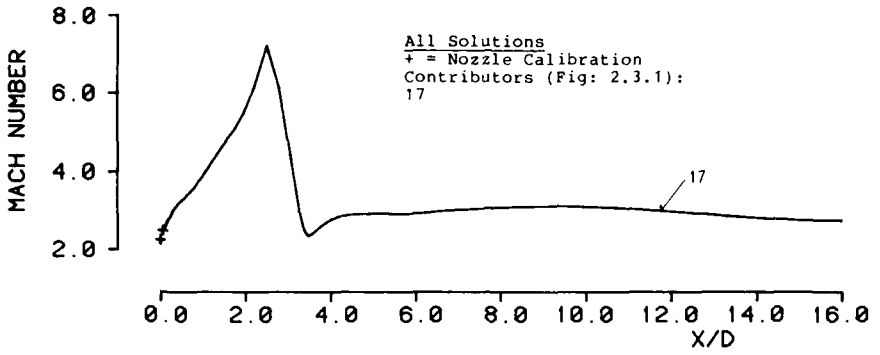

FIG.NO.: 2.3.10.4
MACH NUMBER ON JET CENTERLINE

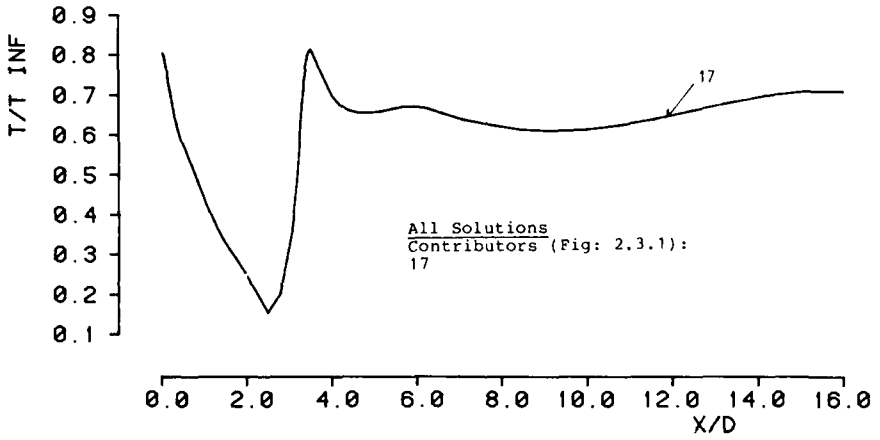

FIG.NO.: 2.3.10.5
STATIC TEMPERATURE ALONG JET CENTERLINE

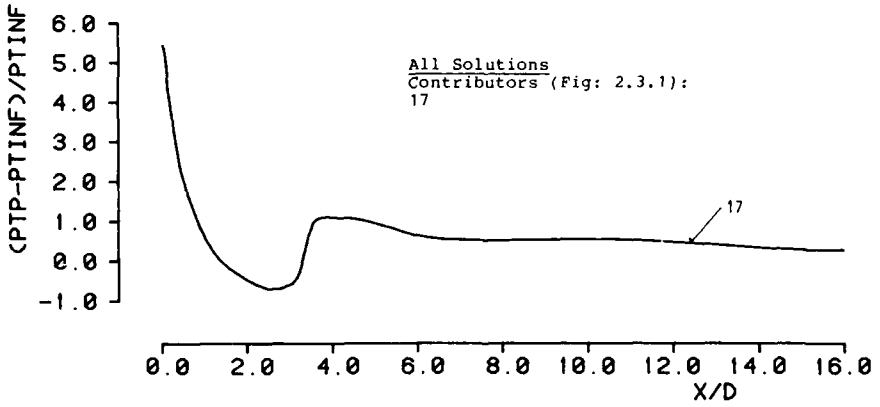

FIG.NO.: 2.3.10.6
PITOT PRESSURE ALONG JET CENTERLINE

WG08 : TEST CASE 10

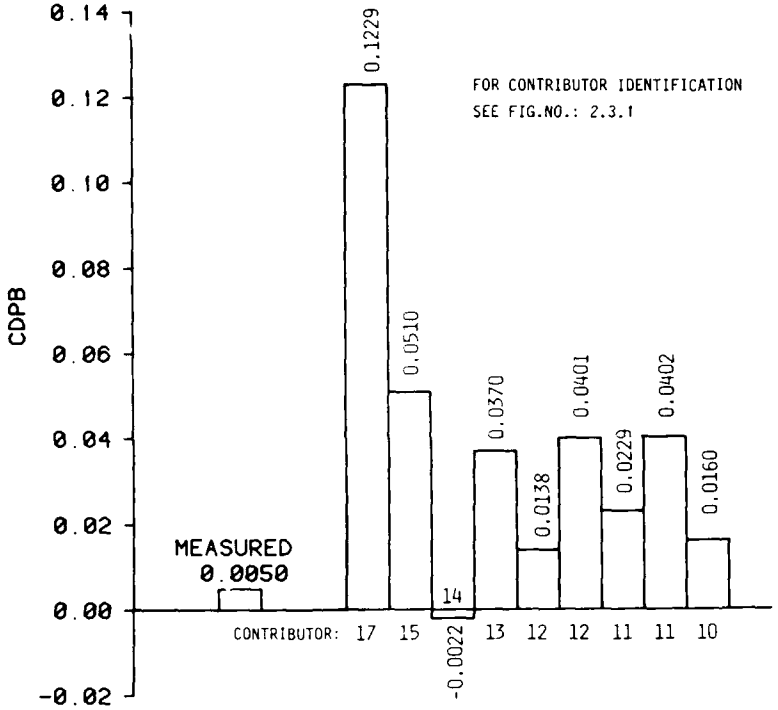

FIG.NO.: 2.3.10.7
BAR GRAPH OF BASE DRAG COEFFICIENT

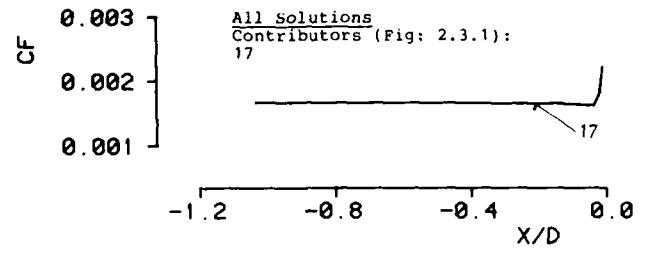

FIG.NO.: 2.3.10.11
SKIN FRICTION COEFFICIENT

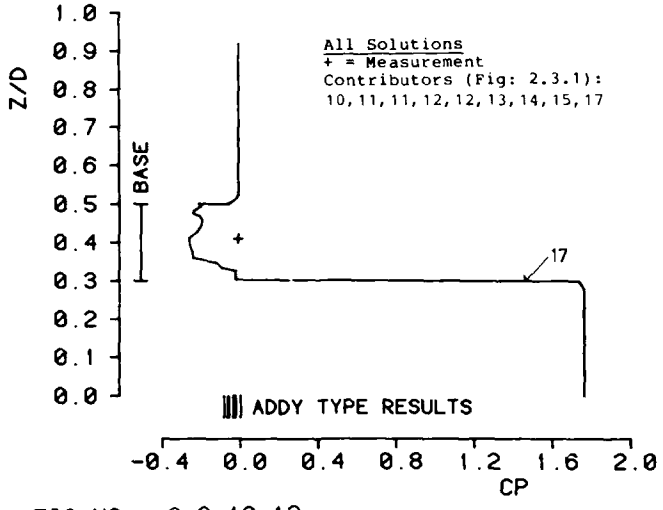

FIG.NO.: 2.3.10.12
PRESSURE COEFFICIENT ALONG BASE GRID LINE

WG08 : TEST CASE 10

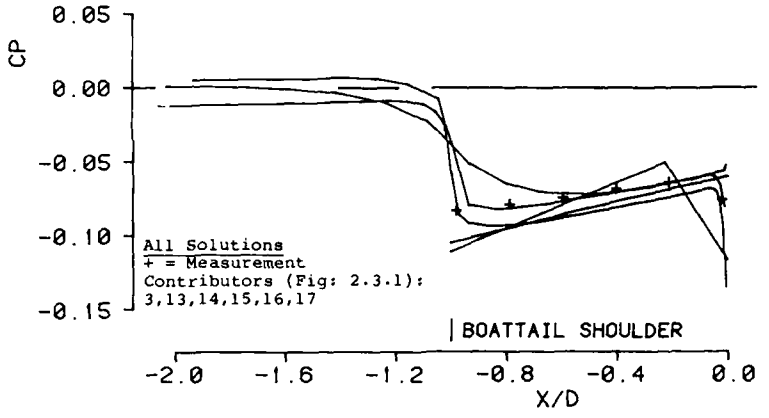

FIG.NO.: 2.3.11.1a
BOATTAIL WALL PRESSURE COEFFICIENT

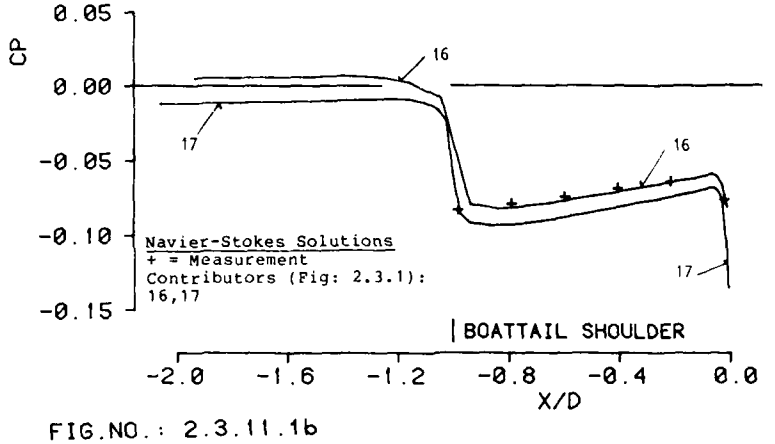

FIG.NO.: 2.3.11.1b
BOATTAIL WALL PRESSURE COEFFICIENT

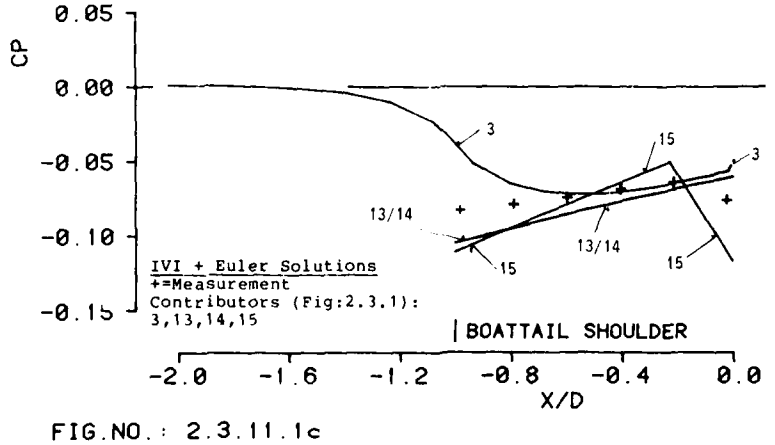

FIG.NO.: 2.3.11.1c
BOATTAIL WALL PRESSURE COEFFICIENT

WG08 : TEST CASE 11

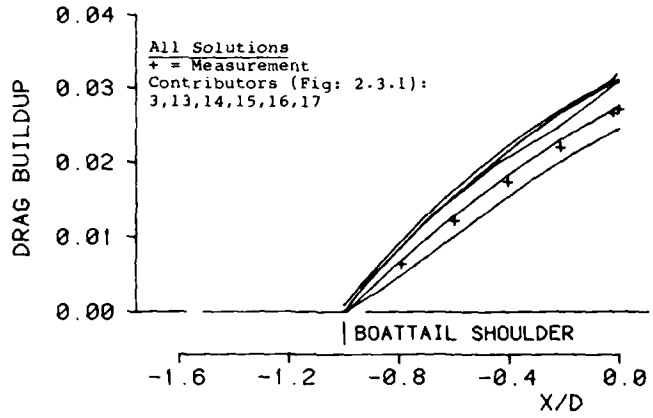

FIG.NO.: 2.3.11.2a
DRAG BUILDUP ALONG BOATTAIL

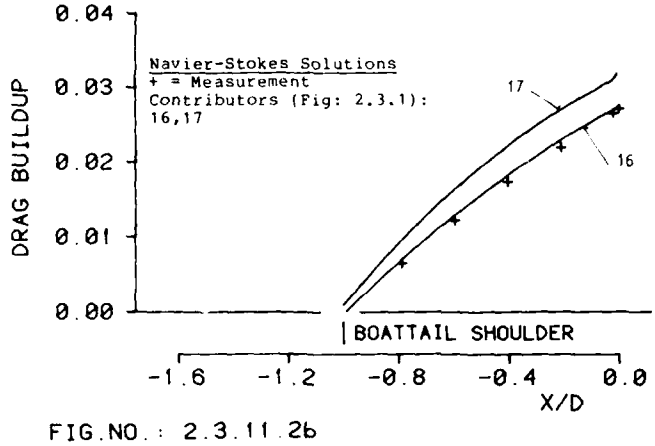

FIG.NO.: 2.3.11.2b
DRAG BUILDUP ALONG BOATTAIL

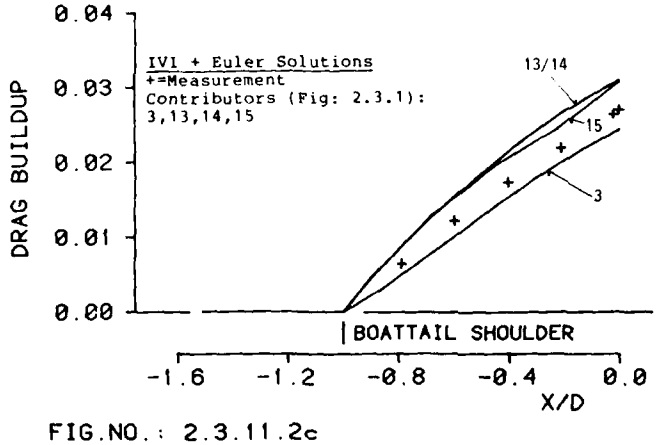

FIG.NO.: 2.3.11.2c
DRAG BUILDUP ALONG BOATTAIL

WG08 : TEST CASE 11

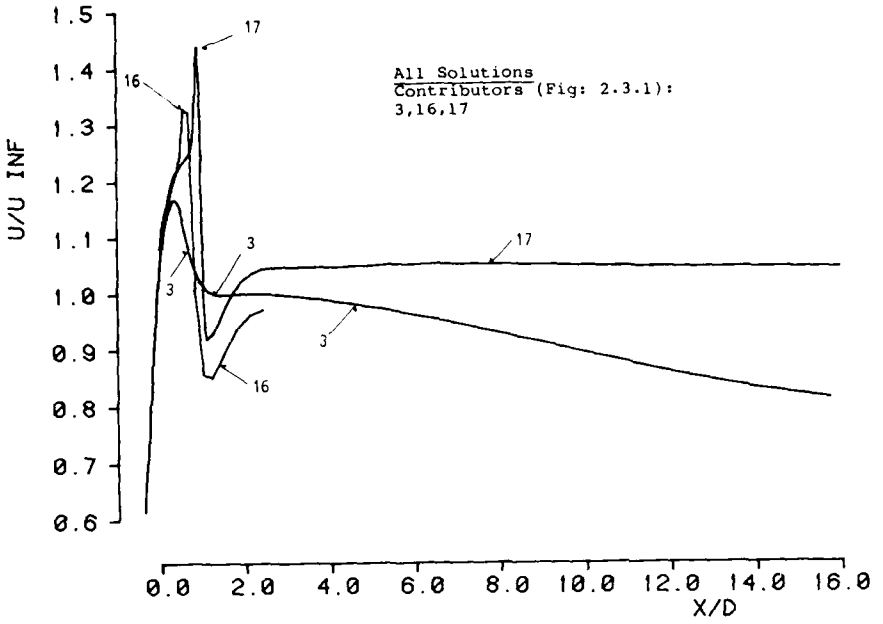

FIG.NO.: 2.3.11.3
AXIAL VELOCITY ON JET CENTERLINE

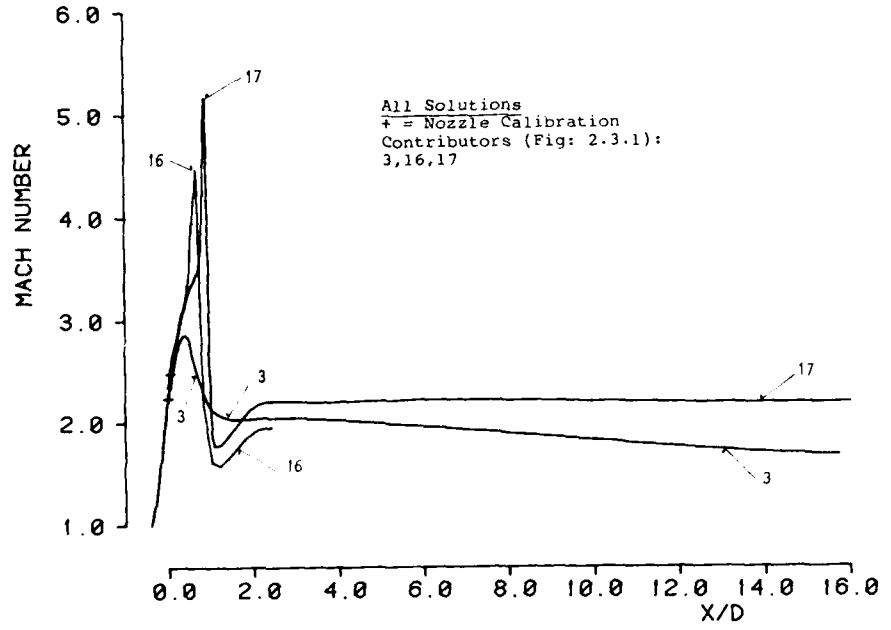

FIG.NO.: 2.3.11.4
MACH NUMBER ON JET CENTERLINE

WG08 : TEST CASE 11

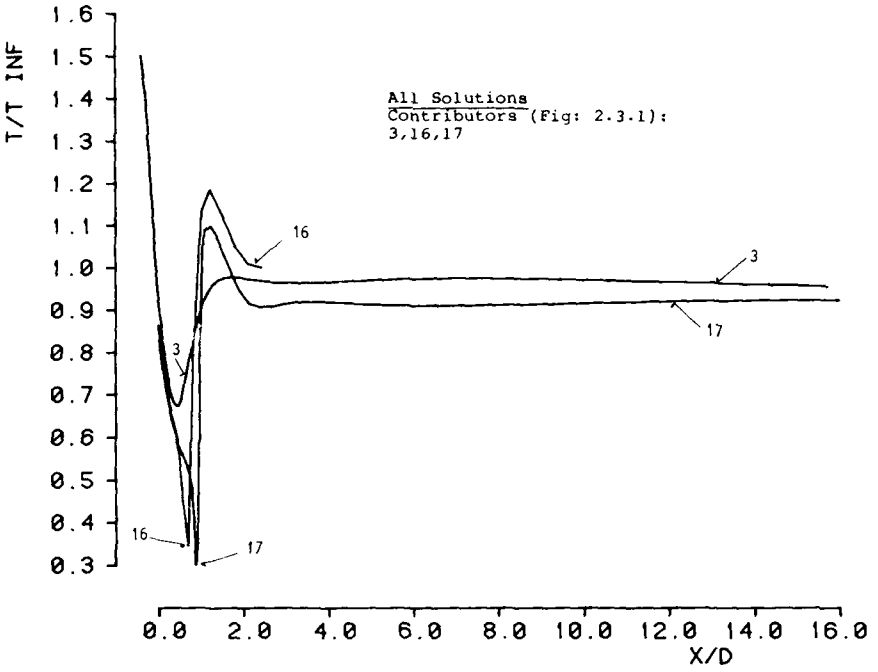

FIG.NO.: 2.3.11.5
STATIC TEMPERATURE ALONG JET CENTERLINE

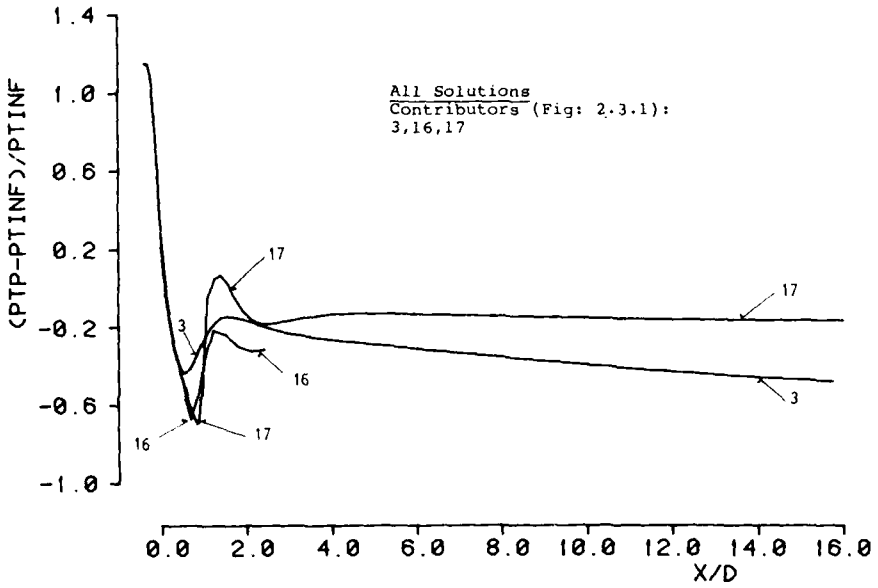

FIG.NO.: 2.3.11.6
PITOT PRESSURE ALONG JET CENTERLINE

WG08 : TEST CASE 11

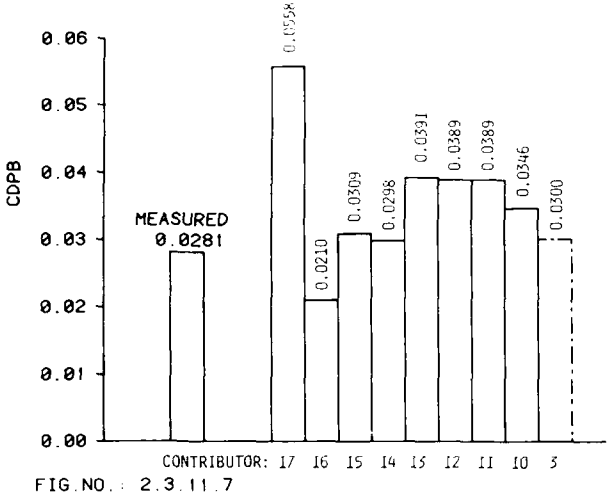

FIG.NO.: 2.3.11.7
BAR GRAPH OF BASE DRAG COEFFICIENT

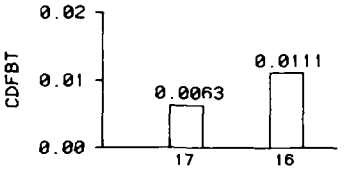

FIG.NO.: 2.3.11.9
BAR GRAPH OF BOATTAIL FRICTION DRAG COEFFICIENT

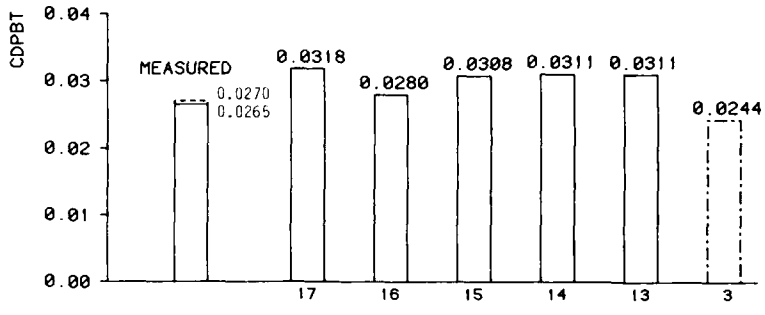

FIG.NO.: 2.3.11.8
BAR GRAPH OF BOATTAIL PRESSURE DRAG COEFFICIENT

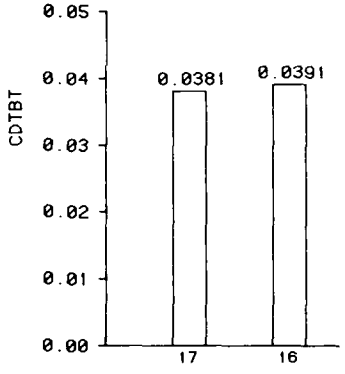

FIG.NO.: 2.3.11.10
BAR GRAPH OF TOTAL BOATTAIL DRAG COEFFICIENT

FOR CONTRIBUTOR IDENTIFICATION
SEE FIG.NO.: 2.3.1

WG08 : TEST CASE 11

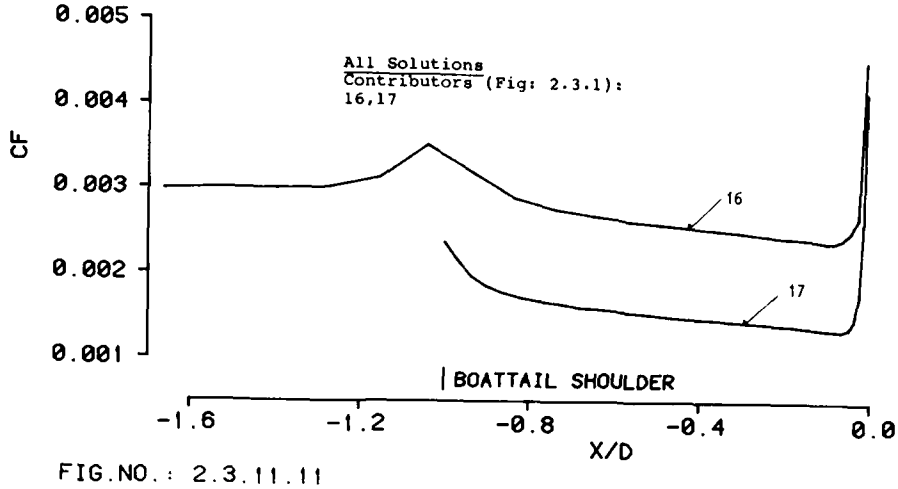

FIG.NO.: 2.3.11.11
SKIN FRICTION COEFFICIENT

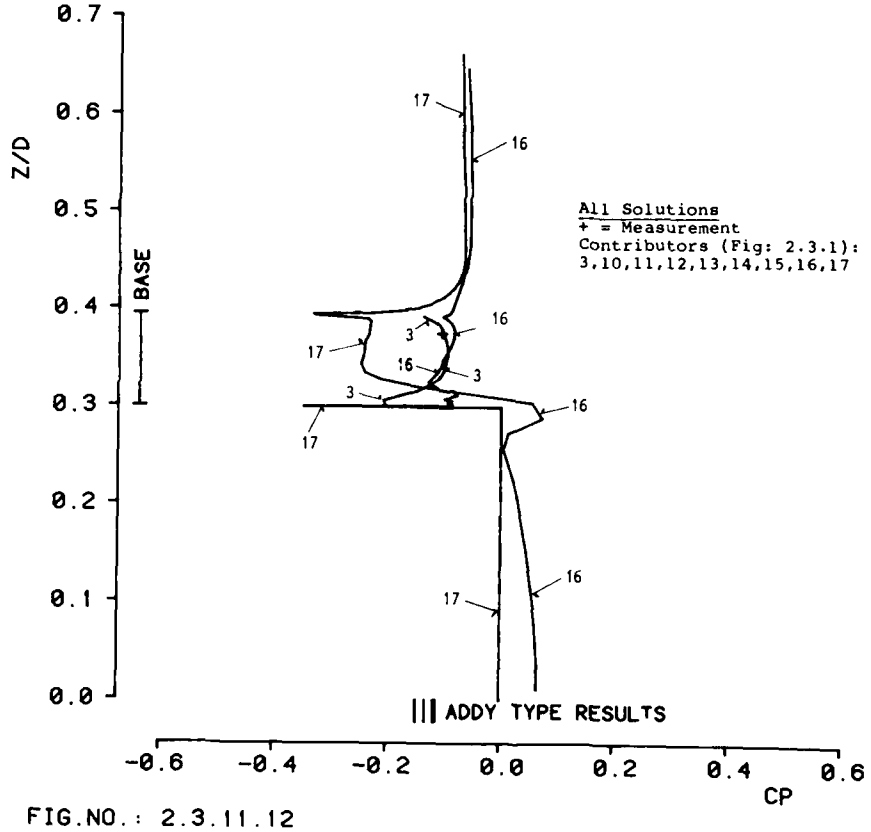

FIG.NO.: 2.3.11.12
PRESSURE COEFFICIENT ALONG BASE GRID LINE

WG08 : TEST CASE 11

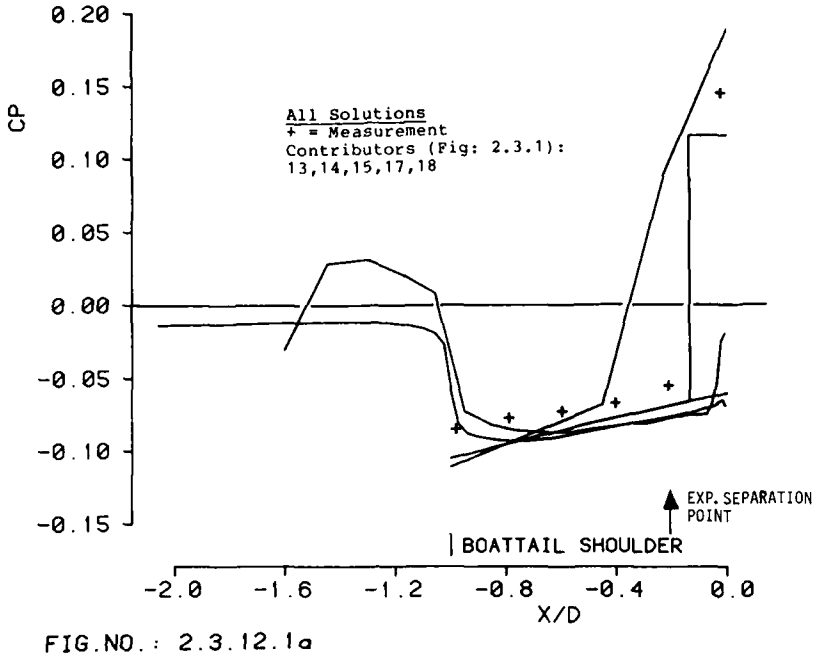

FIG.NO.: 2.3.12.1a
BOATTAIL WALL PRESSURE COEFFICIENT

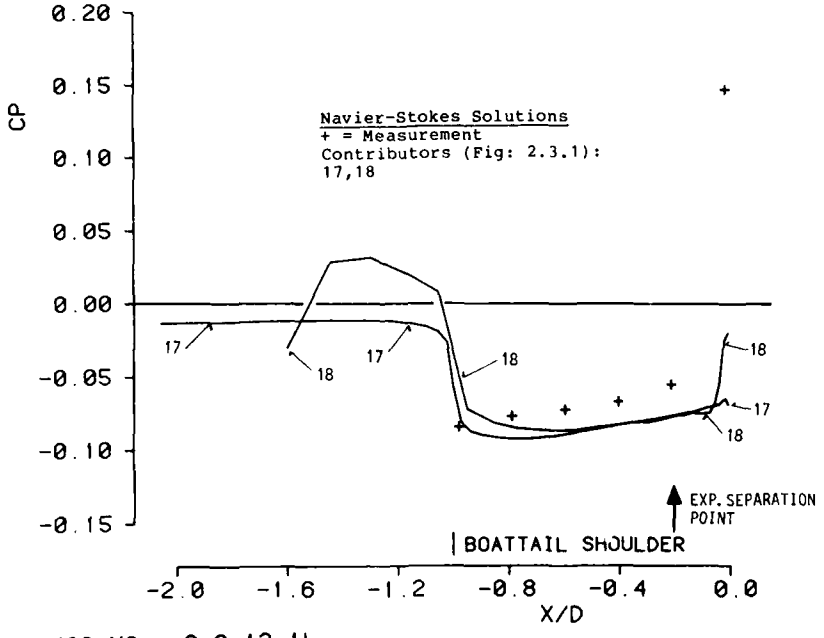

FIG.NO.: 2.3.12.1b
BOATTAIL WALL PRESSURE COEFFICIENT

WG08 : TEST CASE 12

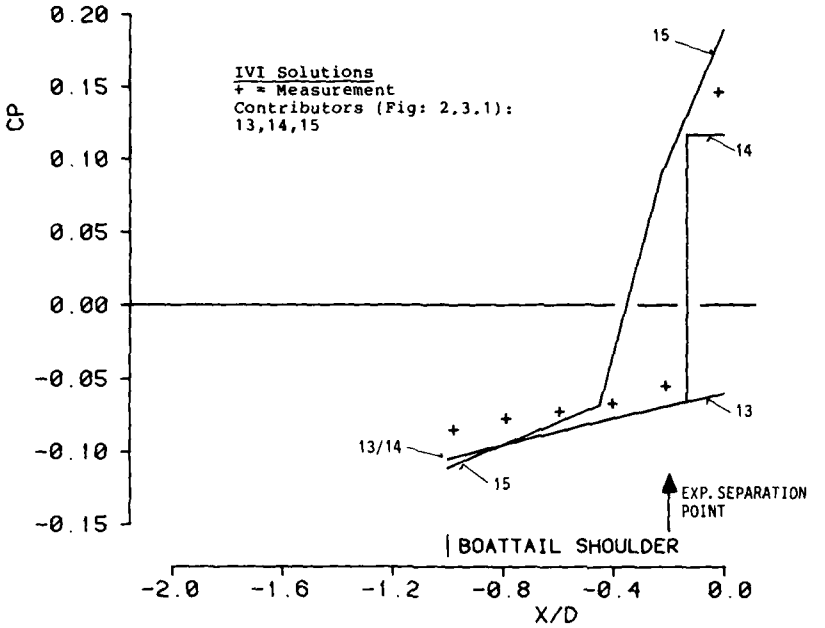

FIG.NO.: 2.3.12.1c
BOATTAIL WALL PRESSURE COEFFICIENT

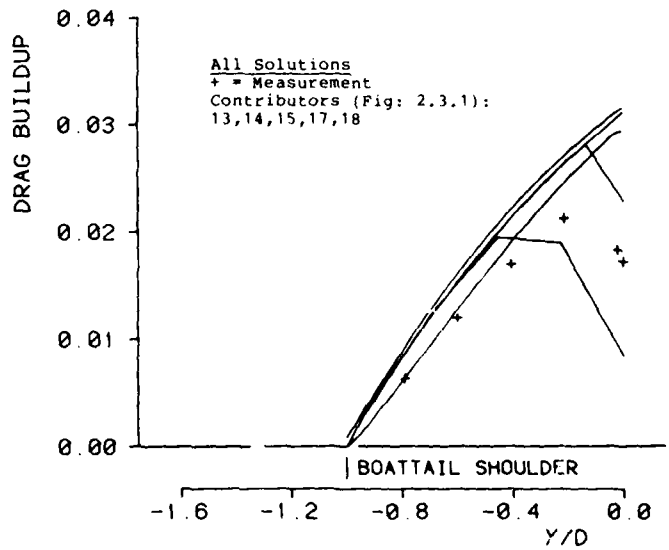

FIG.NO.: 2.3.12.2a
DRAG BUILDUP ALONG BOATTAIL

WG08 : TEST CASE 12

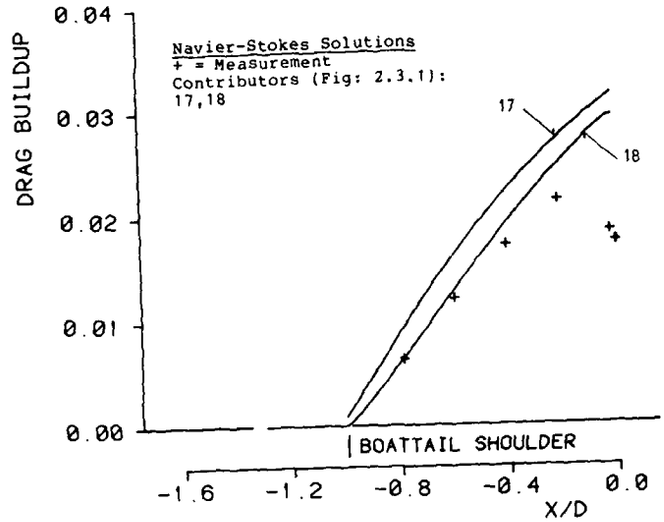

FIG.NO.: 2.3.12.2b
DRAG BUILDUP ALONG BOATTAIL

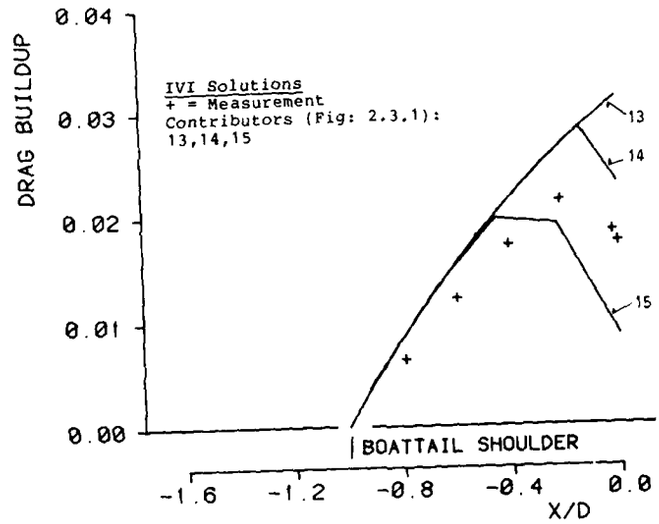

FIG.NO.: 2.3.12.2c
DRAG BUILDUP ALONG BOATTAIL

WG08 : TEST CASE 12

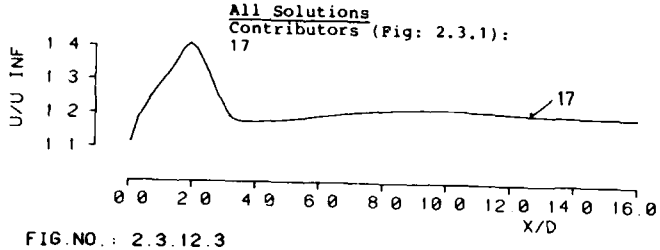

FIG.NO.: 2.3.12.3
AXIAL VELOCITY ON JET CENTERLINE

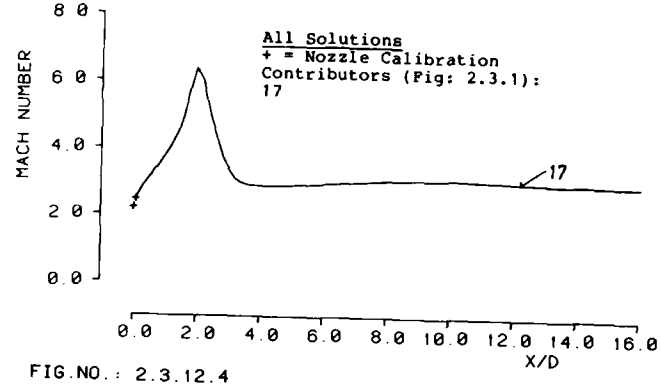

FIG.NO.: 2.3.12.4
MACH NUMBER ON JET CENTERLINE

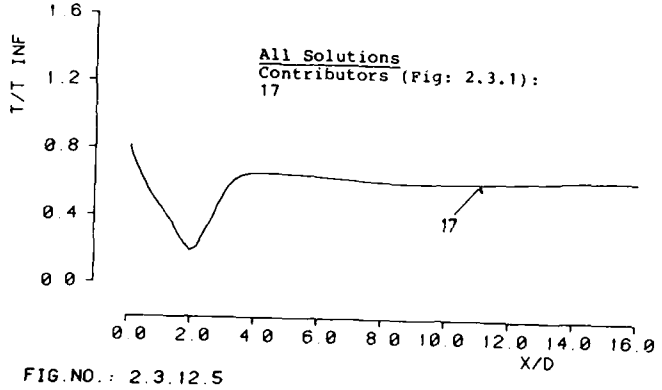

FIG.NO.: 2.3.12.5
STATIC TEMPERATURE ALONG JET CENTERLINE

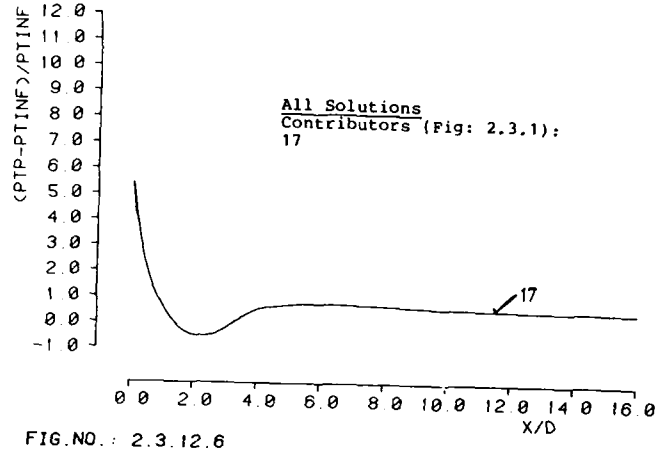

FIG.NO.: 2.3.12.6
PITOT PRESSURE ALONG JET CENTERLINE

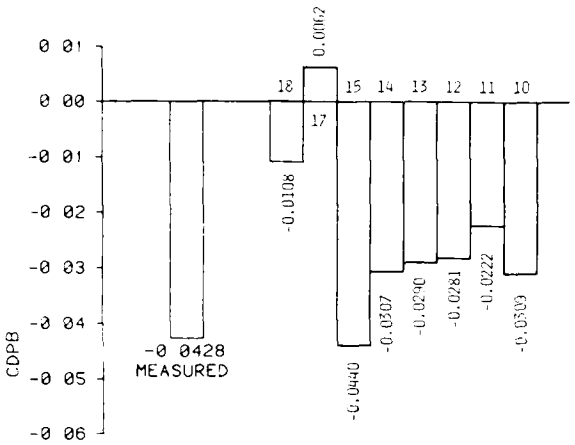

FIG.NO.: 2.3.12.7
BAR GRAPH OF BASE DRAG COEFFICIENT

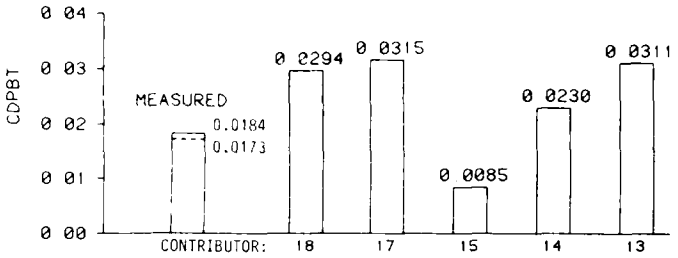

FIG.NO.: 2.3.12.8
BAR GRAPH OF BOATTAIL PRESSURE DRAG COEFFICIENT

FOR CONTRIBUTOR IDENTIFICATION
SEE FIG.NO.: 2.3.1

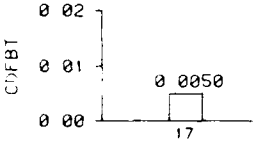

FIG.NO.: 2.3.12.9
BAR GRAPH OF BOATTAIL FRICTION DRAG COEFFICIENT

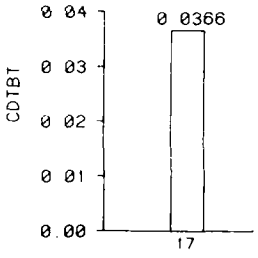

FIG.NO.: 2.3.12.10
BAR GRAPH OF TOTAL BOATTAIL DRAG COEFFICIENT

WG08 TEST CASE 12

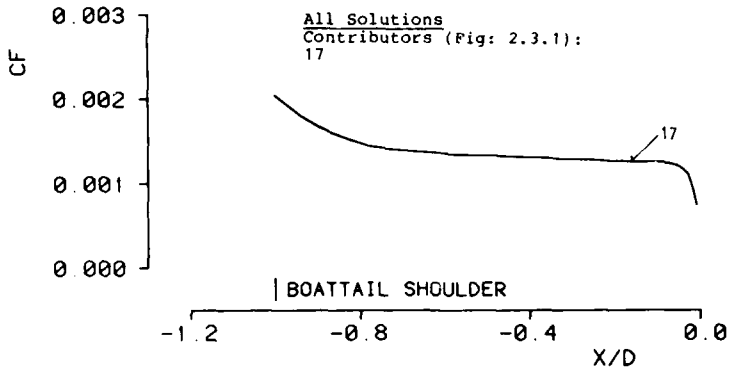

FIG.NO.: 2.3.12.11
SKIN FRICTION COEFFICIENT

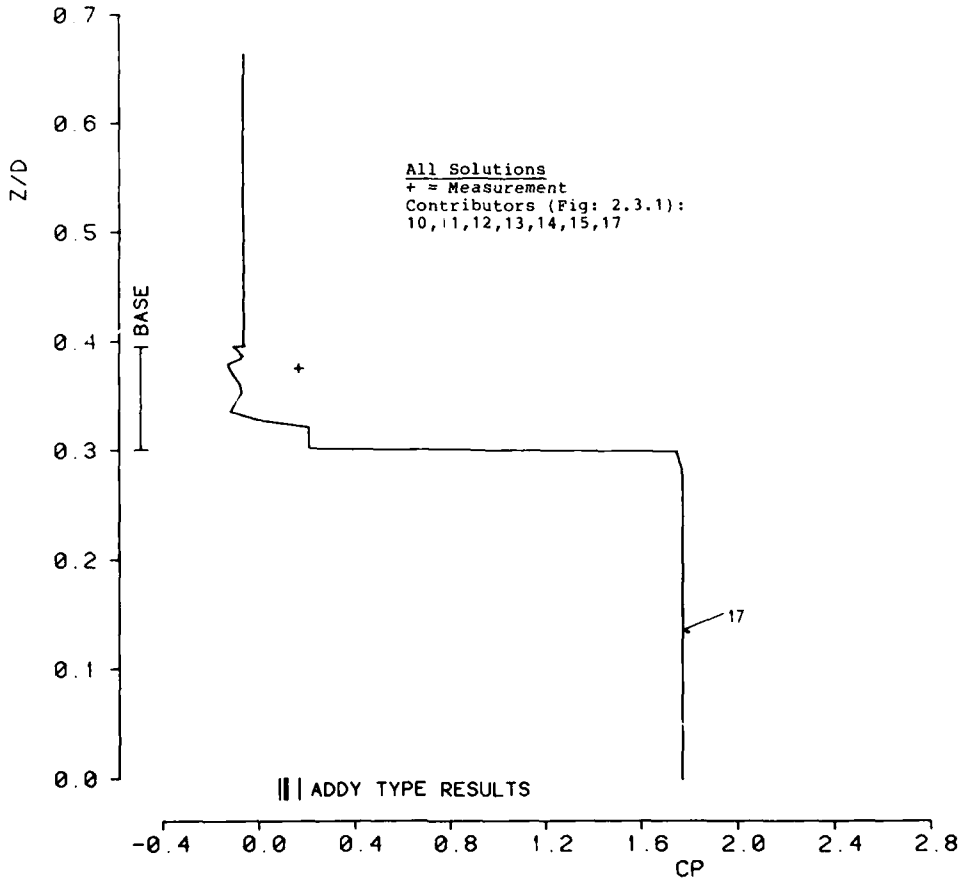

FIG.NO.: 2.3.12.12
PRESSURE COEFFICIENT ALONG BASE GRID LINE

WG08 : TEST CASE 12

2.4. - *EVALUATION OF INVISCID AND PATCHED CALCULATION METHODS*

2.4.1 - *Brief description of calculation methods* -

2.4.1.1. - *Perfect fluid calculations* -

Introductory remarks -

Four contributions comprise perfect fluid calculations. Three of them are solutions of the Euler equations. According to this approach viscous effects are neglected and consequently the entire flow is assumed to be inviscid, a classical slip condition being prescribed on solid boundaries, and frontiers between different streams being considered as slip lines. The fourth method (contributor n° 9, see table I at the end of this section) is in fact an original method solving the potential equation for the external flow.

It should be said that comparison of such calculations with experiment has no significance in situations where separation is likely to occur -or occurs effectively- on the afterbody. Indeed in this case strong viscous effects are present in the flow so that an entirely inviscid flow model can be totally unrealistic. The main interest of the Euler contributions lies in fact in a comparison of the accuracy and of the reliability of different codes aiming at the solution of the same equations applied to identical configurations. Such a comparison is of course extremely useful since any introduction of a viscous correction -as in Inviscid/Viscous Interactive methods- obviously requires a sufficiently accurate basic inviscid flow calculation.

Furthermore, purely inviscid calculations are interesting for at least two other reasons :

i - they are needed for flow diagnostic and they can be extremely useful to evaluate wind tunnel blockage effects (see Section 2.4.2.2. below) ;

ii - Euler codes are a stepping stone toward Navier-Stokes codes. Navier-Stokes codes which do not give the correct inviscid flow part will never be able to calculate the correct viscous flow.

The contribution of Zannetti and Onofri - [2.4.1-7.] *(number 1)*

In this numerical method the Euler equations are solved for a compressible rotational flow which can be fully subsonic, transonic or fully supersonic. The steady state solution is sought by the use of a time marching technique. However, the method of solution adopted here utilizes an original procedure based upon the theory of characteristics [2.4.8].

In order to have a numerical scheme always consistent with the wave propagation phenomena implicitly described by the time-dependent Euler equations, the governing equations are recast as compatibility relations on characteristic surfaces. The form of the equations finally adopted is in fact the result of three characteristic surfaces. Each of the retained equations contains derivatives computed along two lines on a characteristic surface, namely the bicharacteristics along which the signals propagate and another line. The above linear combination eliminates all terms not related to bicharacteristics or particle paths.

The numerical scheme adopted belongs to the so-called lambda family. The spatial partial derivatives are approximated by a one-sided finite difference in order to take into account the proper direction of propagation of signals along bicharacteristics.

For the present application the computational domain is divided into two subdomains $\mathcal{D}_1$ and $\mathcal{D}_2$ (see Fig. 2.4.1) by means of a cut line issuing from the afterbody trailing edge TE :

- subdomain $\mathcal{D}_1$ is the internal flow - or exhaust plume. It is confined by the centre line Σ_{41}, the nozzle wall , the cut line Σ_{51} and the permeable boundaries Σ_{11} and Σ_{31} .

- subdomain $\mathcal{D}_2$ is the external flow. It is confined by the upper wall Σ_{32} and the cut line Σ_{52} . It can extend to infinity in the y direction or it can be confined by the wall of a tunnel. It is limited by two permeable boundaries Σ_{12} at its entrance, Σ_{32} at its exit.

The cut line separating $\mathcal{D}_1$ and $\mathcal{D}_2$ is in fact a streamline which is also a contact discontinuity if the stagnation conditions and the thermodynamic properties of the fluids in $\mathcal{D}_1$ and $\mathcal{D}_2$ are different. This contact discontinuity Σ_{51} is computed as an explicit discontinuity. It is considered as an impermeable and perfectly deformable wall. On the two sides of Σ_{51} the tangential component of the flow velocity and the total pressure can be discontinuous, while the static pressure and the normal component of the flow velocity are continuous. At the start of the calculation an initial flow configuration and shape of the jet is assumed. Since it is not compatible with a steady state solution a transient phase is generated.

During the transient phase of the calculation, this contact discontinuity changes its shape in order to satisfy the conditions of impenetrability and continuity of the static pressure across it. At the end of the transient phase a final shape which satisfies the steady state flow condition is obtained.

The applied boundary conditions are as follows :

i - on the upstream permeable boundaries Σ_{11} and Σ_{12} (see Fig. 2.4.1) the total pressure P_t , total temperature T_t and flow angle θ are prescribed if the incoming flow is subsonic. If it is supersonic all the four flow properties (namely P_t , T_t , θ plus the static pressure P) must be prescribed on Σ_{11} and Σ_{12} .

ii - at the outlet permeable boundaries two cases must also be considered :

. if the flow is subsonic the pressure is prescribed,
. while if the flow is supersonic no boundary conditions are needed.

iii - on the upper boundary Σ_{ii} and on the solid walls a slip condition is applied, i.e. the slope of the velocity vector is prescribed.

iv - on the axis Σ_{iv} symmetry is stated.

Thus the problem has in fact four kinds of boundary :

a - solid wall and center line,
b - inlet permeable surfaces,
c - outlet permeable surfaces,
d - interface (the contact discontinuity)

All these boundaries are treated so as to be consistent with the physical phenomena which take place in the actual transient phase. The use of the bicharacteristics compatibility relations allows a rational implementation of these boundary conditions.

Two different grids are used in the two subdomains $\mathcal{D}_1$ and $\mathcal{D}_2$. In the inner flow the mesh lines are defined by the X = const. and Y = const. lines where :

$$X = x$$

$$Y = (y - y_L) / (y_U - y_L)$$

with x and y cartesian coordinates, y_U and y_L being the ordinates of the upper and lower boundaries respectively.

The external flow region is mapped in a similar way in the case of a nozzle in a tunnel ; while if the region extends to infinity, the Y co-ordinates are stretched according to the formula :

$$Y = \frac{\tanh[k(2y/D-1)] - \tanh(kA)}{1 - \tanh(A)}$$

where k is a stretching parameter, D is the maximum diameter of the afterbody, $A = k(2y_L/D-1)$ in which y_L is the ordinate of the lower boundary (wall of the afterbody and interface). The line $Y = 1$ corresponds to infinity in the y direction. The location of the last computed Y = const. line is at about one and a half or two diameters D depending on the test case.

In all the test cases 40 x 6 intervals in the inner region and 40 x 13 in the outer region have been used (see example of mesh in Fig. 2.4.2).

The contribution of Vuillot and Veuillot -[2.4.9-10] (number 2)

In this method the Euler equations are solved numerically by a pseudo-unsteady type method in which the stagnation enthalpy is assumed always constant. An advantage of this assumption is to avoid the solution of the energy equation. As a result the unsteady phase of the calculation has no physical meaning since the constancy of enthalpy is only satisfied when a steady state is reached.

The continuity and momentum equations are integrated step-by-step in time by using an explicit predictor-corrector scheme with a local time step technique. The spatial derivatives are discretized directly in the physical plane (x , y) by means of finite difference formulae.

As shown in Fig. 2.4.1 the computational domain is divided into two subdomains $\mathcal{D}_1$ and $\mathcal{D}_2$ by means of a cut line issuing from the afterbody trailing edge. In fact, as in the previous method, domain $\mathcal{D}_1$ identifies with the exhaust jet and domain $\mathcal{D}_2$ with the external flow. The enthalpy which is constant in each subdomain may be different from one to the other.

As in the previous method the cut line separating $\mathcal{D}_1$ and $\mathcal{D}_2$ is a streamline on which compatibility conditions between the two adjacent flows are enforced, namely equality of pressure and flow direction. This streamline is fitted as a mesh line whether or not it is a real slip line. In the course of the unsteady phase of the calculation this streamline is moving until it reaches an equilibrium position when convergence is reached. Thus the mesh has to be readjusted at every time step.

The applied boundary conditions are the following :

i - on the inlet boundaries Σ_{i1} and Σ_{i2} (see Fig. 2.4.1) the direction of the velocity vector θ (here $\theta = 0$) and the stagnation pressures P_{t_1} and P_{t_∞} are prescribed if the flows are subsonic. All the flow properties would be given at these boundaries if the incoming streams were supersonic.

ii - on the outlet boundaries Σ_{s1} and Σ_{s2} the two cases are distinguished :

. if the Mach number is subsonic a non reflection condition is applied,
. if the Mach number is supersonic no conditions have to be prescribed.

iii - on the upper boundary Σ_{ii} a slip condition is applied

iv - on the axis Σ_{iv} symmetry is stated.

The treatment of the above boundary conditions is achieved by means of a technique based on compatibility relations derived from the theory of characteristics.

Artificial viscosity terms are added to the equations in order to ensure the stability of the scheme and to capture shocks (if any) correctly.

The mesh is defined by two families of lines. The I-lines are vertical and the J-lines are interpolated between a J1-line and a J2-line, which are the given boundaries of each domain. The initial exhaust plume boundary is horizontal. The mesh is refined inside the nozzle in the I-direction and near the cut line for subdomain $\mathcal{D}_2$ in the J-direction.

The following table gives the number of mesh points for each computed test case. An example of a mesh is shown in Fig. 2.4.3.

Test case	R	L	Number of mesh points				
			on the body	in x direction		in y direction	
				in	in	in	in
1	3	6	67	81	86	15	19
2	3	3	37	48	51	15	19
2A	3	3	37	48	51	15	19
3	3	6	63	81	86	15	19

L and R are defined in Fig. 2.4.1.

The initial conditions are uniform flow except upstream of the nozzle exit plane in subdomain $\mathcal{D}_1$. There the initial flow is a one-dimensional flow calculated by means of an isentropic law.

The calculations were executed on a CRAY-1 computer. For each calculation the number of iterations was equal to 8 000 but in fact convergence was achieved well before for most test cases (for instance 2 500 time steps were sufficient for test case 2 as shown in Fig. 2.4.4).

The contribution of Bissinger and Eberle [2.4.11] (number 3)

This code solves the time dependent Euler equations supplemented by the energy equation. It uses a fully conservative predictor-corrector method (quasi-conservative for test cases 9 and 11).

A finite volume discretization technique is employed with flux difference splitting. Natural damping is provided by eigenvalue decomposition. Local time stepping is used.

The flow region for which the calculations are done usually extends from 11 times the maximum body diameter D upstream to 25 D downstream of the nozzle exit plane. The lateral extent is between 9 D and 12 D.

The boundaries of the computational domain are treated in a way that differs somewhat from the methods described above. At the entrance and exit all flow variables known are specified and kept constant. By characteristic flux considerations information about the flow variables needed are fed into the flow calculations. At solid body surfaces a slip condition is applied. Free stream conditions are set at the outer boundary. In cases with wind tunnel wall (test cases 5 and 6) the outer boundary is treated like a solid wall. Symmetry is enforced along the symmetry axis. The following tables gives the number of grid points for each computed test case :

Test case	Number of grid points
1	100 x 74
2	75 x 74
2A	75 x 74
3	100 x 100
5	100 x 72
6	100 x 37
9	100 x 98
11	100 x 92

Convergence criterion is a residual defined as the maximum of the sum of th absolute values of the difference between iterations of each variable at each grid point. In addition, changes in static pressure along the whole length of the grid line forming the nozzle contour and the change of the boattail pressure drag coefficient CDPBT with iterations are considered.

The number of iterations ranges from 6 000 to 15 000. Improvements in grid shape are possible which should reduce number of iterations and computer time.

For the calculation of the flow of test cases 5 to 6 (axisymmetric afterbody in a cylindrical wind tunnel) the pressure at the exit of the computational domain has to be specified. Because this pressure is not known at the start of the calculation, the final answer can be found only by an iteration procedure during which this exit pressure is varied. In the first step the calculation was started with an exit pressure equivalent to the measured wall pressure at *about the same streamwise station*. The result of the calculation gave a value of the pressure coefficient at the body wall which did not go to zero far upstream of the nozzle exit plane. For the second calculation step the original exit pressure was corrected by roughly the deviation of the body wall pressure from zero of the first step. The results contributed to this Working Group are the results of the second step.

The contribution of Zacharias [2.4.12-14] *(number 9)*

In this method the external flow is assumed incompressible and irrotational. In these conditions the stream function ψ defined by :

$$U = \frac{\partial \psi}{\partial y} \qquad\qquad V = -\frac{\partial \psi}{\partial x}$$

satisfies the Laplace equation : $\Delta \psi = 0$. Use of the stream function is particularly recommended since in the present problem the tangential velocity V_t along the afterbody contour and/or the tunnel wall is required. In effect it can be readily shown that :

$$V_t = -\frac{\partial \psi}{\partial n}$$

where n is the direction normal to the surface.

An empirical flow model is used to simulate the propulsive jet. In it the displacement effect is represented by means of a solid conical body whose semi-angle corresponds to the jet spreading angle α . Furthermore the entrainment effect of the jet is represented by a sink effect. For this purpose a velocity distribution normal to the jet boundary is prescribed as shown in Fig. 2.4.5. The jet spreading angle α and the velocity distribution of jet entrainment W^* have been established from extensive experiments and compiled mathematically in the form of polynomials :

$$\alpha = f\ (M_\infty\ ,\ P_{tj}/P_\infty\ ,\ T_{tj}/T_\infty\ ,\ \beta\ ) \qquad (\beta = \text{boattail angle})$$

$$W^* = g\ (M_\infty\ ,\ P_{tj}/P_\infty\ ,\ T_{tj}/T_\infty\ ,\ \beta\ ,\ x\ )$$

The Laplace equation along with the appropriate boundary conditions in the inlet and outlet sections, on the afterbody, the tunnel wall contour and the jet is solved by using the Boundary Element Method. The basic principles of this method are as follows.

By means of weighting with the fundamental solution and the application of Green's function it is possible to carry over the Laplace equation $\Delta \phi = 0$ which is used for potential problems into Green's second equation :

$$\int_\Omega \left[\phi^* \Delta^2 \phi - \phi \Delta^2 \phi^*\right] d\Omega = \int_\Gamma \left[\phi^* \partial\phi/\partial n - \phi\ \partial\phi^*/\partial n\ \right] d\sigma$$

The fundamental solution thus represents the solution of the Laplace equation in an infinitely extended space for a source singularity of intensity 1. The fundamental solution for the two-dimensional case is :

$$\phi^* = \frac{1}{2\pi} \ln r$$

where r is the distance from the singularity.

If the properties of this fundamental solution are taken into consideration in Green's second equation then it reads as follows for any point i in an enclosed domain :

(1) $$C\phi_i = \int_\Gamma \left[\phi^*\ \partial\phi/\partial n - \phi\ \partial\phi^*/\partial n\ \right] d\sigma$$

where C is a constant dependent on the location of the point. Inside the domain $C = 1$ and for smooth boundaries $C = 0.5$ (in the above equation n is the unit normal to the surface).

By sub-dividing the boundary into elements and predetermining the functional behavior of the potential ϕ and of the gradient $\partial\phi/\partial n$ along the boundary elements, the equation 1 can be represented in the form of matrices :

(2) $$C\underline{\phi_i} = \underline{H}\ \frac{\partial \phi}{\partial n} - \underline{Q}\ \underline{\phi}$$

$\partial\phi/\partial n$ and ϕ are the columns of the nodal values of the gradient and the potential, whereas $\underline{H}$ and $\underline{\Phi}$ are the corresponding influence matrices.

If point i is moved to the boundary, Eq. 2 can be formulated for all the boundary elements as follows :

$$\underline{Q}\ \underline{\phi} = \underline{H}\ \underline{q}$$

$$q = \frac{\partial \phi}{\partial n} \qquad\qquad \phi_{ii} = -\Sigma \phi_{ij} \qquad\qquad j \neq i$$

In the case of a mixed boundary value problem the equation system is rearranged so that the unknown boundary values can be combined to form a one column vector. This rearrangement results in a system of equations in which the unknown boundary value of the potential and the gradient are combined in column $\underline{X}$ and the known boundary values of these quantities in column $\underline{Y}$. This new system of equations $\underline{A}\,\underline{X} = \underline{Y}$ is used to calculate the unknown boundary values, where matrix $\underline{A}$ is created by rearranging matrices $\underline{G}$ and $\underline{H}$.

An example of mesh for the Boundary Element Method is represented in Fig. 2.4.6.

Once the equation for the stream function has been solved by means of this method, the Prandtl-Glauert rule is applied to represent the compressibility effect on pressure distributions.

2.4.1.2 - Inviscid-Viscous Interactive methods of calculation -

Basic principles -

The basic idea of Inviscid-Viscous Interactive (IVI) methods also called coupling methods - consists in splitting the flow field into :

i - an external or outer region where viscous effects (laminar as well as turbulent stresses) are assumed to play a negligible role,

ii - one or several inner region(s) in which dissipative effects are essential. These regions are boundary-layers, wakes, mixing zones, ...

The usual IVI is a substitute for solving the full time-averaged Navier-Stokes equations for flows in which dissipative effects are confined within regions the size of which is small when compared to a characteristic length scale of the problem (chord-length of a profile, blade-to-blade distance of a cascade, afterbody diameter,...).

Thus in the IVI approach the external flow has to satisfy the simpler Euler equations, which are frequently replaced by the potential equation if the inviscid flow is - or is assumed to be-irrotational. It should be noted that what is called the "external flow" can in fact comprise several streams ; for instance the external and the exhaust jet in the case of a propulsive afterbody.

On the other hand, the dissipative regions can be calculated using various flow models differing in their level of sophistication :

i - the full Navier-Stokes equations can be used [2.4.15] ,

ii - analytical methods based on asymptotic expansion or perturbation techniques are sometimes employed [2.4.16],

iii - the most popular -and most economical- model however makes use of the Prandtl thin shear layer equations which are solved either by finite difference techniques or more frequently by integral methods.

Mixed procedures can in fact be envisaged : for instance boundary-layer equations are applied in the major part of the viscous flow except in small regions where their validity in questionable (shock foot region, trailing edge flow, largely separated zone, etc...). These sub-domains are represented by more refined analyses using either analytical methods or numerical solving of the full Navier-Stokes equations.

However since all the methods tested by the contributors to this Working Group use the classical Prandtl equations to represent the viscous layers, we will not comment on other possible approaches.

Briefly speaking, development of an IVI method requires the following ingredients which will be described in the presentation of the various tested IVI methods :

i - an accurate and fast solver of the inviscid flow equations,

ii - an accurate (i.e. physically realistic) method to compute dissipative flow regions,

iii - representative and if possible convenient compatibility relations between the outer and inner flow regions. These compatibility relations result in a coupling equation , the form of which may lead to delicate problems in transonic or supersonic flow.

iv - an efficient iterative procedure to ensure a fast convergence of the interactive calculation between the two flow regions.

The flow schematization employed in the case of the afterbody problem is represented in Fig. 2.4.7. It consists of two inviscid flow regions ; namely the external stream which is frequently transonic and the exhaust jet which frequently expands to supersonic conditions. The dissipative part of the flow field comprises the following "sub-regions" which are frequently calculated by using different models :

i - the turbulent-boundary-layer developing on the upstream part of the afterbody outer part,

ii - a separated flow region developing from the separation point of the incoming boundary-layer. This region only exists if the jet pluming or/and the shape of the afterbody downstream part induce a sufficiently strong adverse pressure gradient.

III - a jet-wake region forming downstream of the afterbody trailing edge. It is constituted by the merging of the afterbody boundary-layer (eventually separated) and of the nozzle boundary-layer which is usually very thin due to the smaller development distance and the strong favorable pressure gradient inside the nozzle.

IV - the turbulent mixing-layer developing along the frontier separating the external flow and the exhaust jet.

It should be said that in many methods of calculation the nozzle boundary-layer is neglected because of its extreme thinness.

The contribution of Putnam and Wilmoth - [2.4.17] (number 4)

This method is in fact known as the RAJET analytical method. In it the inviscid external flow solution is obtained with the relaxation procedure of South and Jameson [2.4.18] for solving the exact nonlinear potential flow equation. This procedure is valid for subsonic, transonic and supersonic irrotational flow over blunt or pointed bodies of revolution. Slighly supersonic Mach numbers are permissible as long as the entropy production by shock-waves is negligible.

The inviscid jet plume flow field is solved by a specialized aircraft version of the shock-capturing/shock-fitting inviscid plume procedure of Dash et al. [2.4.19]. The solution is obtained by explicit spatial marching of the Euler equations for a uniform composition gas mixture. Mach disks are located by shock-fitting at the triple point and incorporating the iterative procedure of Abbett [2.4.20] to treat the Mach disk streamtube. For small Mach disks and regular shock reflection from the axis, the Abbett procedure is not used and the Mach disk streamtube is approximated by a constant area "sting". Also, for low Mach number jets, the flow field dowstream of the Mach disk is approximated by an isentropic decay procedure described by Dash et al. [2.4.19]. In this method, the nozzle exit Mach number must be greater than 1.05.

The viscous part of the flow is divided into the four distinct regions represented in Fig. 2.4.7 and already described in the previous paragraph.

The attached boundary-layer region is solved with a modified version of the Reshotko and Tucker integral method for turbulent flows [2.4.21]. This method employs the momentum and moment-of-momentum integral boundary-layer equations written in an incompressible plane deduced from the physical plane by a compressible-incompressible transformation. The velocity distribution is represented by power-law profiles and the skin-friction coefficient is computed with the well known Ludwieg-Tillman relation extended to compressible flow through application of the reference enthalpy concept. Another empirical law is used to express the viscous term of the moment-of-momentum equation. This boundary-layer calculation yields the displacement thickness distribution over the body and the boundary-layer profile at the nozzle exit needed to initialize the mixing layer calculation. In fact, the nozzle internal boundary-layer, being most often quite thin compared to the external flow boundary-layer, its thickness is estimated from flat-plate theory.

For separated flow, the reverse flow is divided from the flow by a discriminating streamline springing from the body at the separation point and that intersects the plume boundary at the reattachment point (see Fig. 2.4.8). The separation location is predicted by the method proposed by Presz [2.4.22]. In this method a control volume in the boundary-layer is considered between the point where the wall pressure goes through a minimum on the afterbody and the assumed separation point. Conservation of mass and momentum through the volume along with the use of the compressible version of the well known Coles law-of the wall-law of the wake boundary-layer profiles allows the calculation of the pressure at separation. This control volume analysis avoids the numerical difficulties met by classical direct boundary-layer methods on approaching the Goldstein type singularity at the separation point.

The shape of the discriminating streamline from the separation point to the end of the body is then calculated by the discrete control volume method of Presz et al. [2.4.22]. A conceptual model of the flow field in the vicinity of a separated afterbody is shown in Fig. 2.4.9 along with the control volume used to calculate the discriminating streamline shape. The upper surface of the control volume is inclined at an angle θ with the wall and since the upper surface is a flow streamline no mass flux passes through it. The recirculating flow streamlines are assumed to be source-like in direction with each streamline having a common origin. This assumption allows a smooth transition from the flow direction on the body to that on the discriminating streamline. The inlet and outlet sections of the calculation control volume are constructed normal to the streamlines.

Briefly speaking the method consists in applying the continuity and momentum equations to successive control volumes like those shown in Fig. 2.4.9. The velocity distributions in the reserve flow region are represented by a modification of the error-function curve giving the velocity profile in a turbulent mixing zone (see § 2.4.1.3 below). The turbulent shearing stress along the discriminating streamline is derived from tables presented by Korst and Chow [2.4.23]. However for the present AGARD test cases the discriminating streamline shape in the jet wake region is a straight line obtained by simply extrapolating the discriminating streamline slope at the end of the body to its intersection with the jet plume boundary.

Mixing layer properties are calculated by a specialized aircraft version of the overlaid mixing analysis developed by Dash and Pergament and applied in what is known as the BOAT code [2.4.24]. The overlaid concept is a direct extension of classical boundary-layer methodology to the analysis of nearfield shear layers. In boundary-layer theory, the inviscid flow pattern is first calculated followed by a boundary-layer calculation with edge conditions and pressure gradients set by the inviscid flow pattern. In the direct extension of this approach to nearfield shear-layers, the inviscid exhaust jet and external flow patterns are first determined and the nearfield shear-layer calculation is then

initiated along the inviscid plume interface (see Fig. 2.4.10). Local edge conditions and both normal and streamwise pressure gradients are specified everywhere by the inviscid external flow and the jet exhaust solutions.

The turbulence is modeled by the eddy viscosity concept along with two transport equations for the turbulence kinetic energy and the turbulence dissipation rate. The equations for the shear-layer (continuity, axial momentum, turbulence transport quantities plus species conservation in the complete BOAT version) are written with as independent variables the streamwise co-ordinate x and the streamfunction ψ. The system of parabolic equations thus obtained is solved by a finite difference marching procedure using an implicit/explicit formulation. The calculation is started at the nozzle exit for attached flow or at the reattachment location for separated flow.

In the present application, the starting velocity profiles are determined from the knowledge of the two displacement thicknesses at the origin of the shear-layer. These displacement thicknesses are provided by the calculation of the upstream part of the viscous layers. The initial velocity distributions are then deduced by a law of the wall/law of the wake type representation (see Fig. 2.4.11). Provisions are made in the program to select the initial level of the turbulent kinetic energy.

The solution of the turbulent mixing-layer yields a displacement thickness distribution arising from the jet entrainment effect as well as mixing-layer properties across the inviscid plume boundary (see Fig. 2.4.12). This displacement thickness δ^* is evaluated by integration of (see Fig. 2.4.12) :

$$d\delta^*(x)/dx = V_e(x)/U_e(x)$$

and is added to the inviscid plume interface to obtain the effective plume boundary.
The component solutions of the RAXJET method are combined into the iterative procedure shown in Fig. 2.4.13. An underrelaxation procedure is applied in adding the displacement correction to the body-plume shape and in imposing the inviscid pressure gradients on the boundary-layer solutions. Iterations are repeated until the desired convergence level is reached. For the AGARD test cases approximately 20 iterations were sufficient for convergence. Twenty viscous-inviscid iterations require 12 minutes of CPU time on a Control Data CYBER 175 computer.

The contribution of Kuhn - [2.4.25-27] (number 5)

In the method developed by Kuhn, the external inviscid flow is calculated by the method of South and Jameson [2.4.18] as implemented by Keller and South [2.4.28] with, minor modifications to accommodate the iterative interaction procedure. The inviscid exhaust jet is determined by using an approximate method in which the jet flow is assumed uniform in each cross section. The plume shape is calculated in a series of straight-line segments which approximate the curved shape of the plume. The external pressure is compared with the internal pressure at the exit plume boundary point and, depending on the comparison, an expansion or compression turn is calculated using Prandtl-Meyer theory.

To compute the boundary-layer, a compressible-incompressible transformation is first applied to the basic equations. Then the solution procedure employs an integral technique in the incompressible plane based upon the momentum and moment-of-momentum equations. The velocity profiles are represented by an improved version of the law of the wall/law of the wake formula allowing in particular a faithful representation of the profile shape in the near wall region. The viscous integrals are evaluated by a two-layer eddy viscosity model. The method applies also to laminar flow, transition from laminar to turbulent being calculated by letting the eddy viscosity change from a laminar viscosity to a fully turbulent value over a short distance. This boundary-layer method can be applied either in a direct mode -i.e. with velocity at the boundary-layer outer edge prescribed- or in an inverse mode -i.e. with the displacement thickness prescribed.

The modeling of the exhaust jet entrainment effect is based on a technique developed by Peters et al. [2.4.29] in which an integral method for the plume mixing layer is coupled with a Method of Characteristics inviscid jet calculation. The boundary of the jet is taken to be the mid-point of the mixing-layer and the displacement thickness of the mixing-layer is calculated in a manner similar to the way the displacement effect of a boundary-layer is defined. The entrainment effect of the exhaust jet is thus accounted for to a first approximation by using the displacement surface of the jet as the effective boundary upon which to calculate a boundary-layer. Then the afterbody boundary-layer is simply extended on to this approximate surface as though the jet were a solid surface. Entrainment is accounted for by the fact that the displacement surface of the mixing-layer profile is a negative quantity relative to the jet boundary.

Several techniques are available for estimating the location of separation. An iterative procedure is included in the computer program in which the separation point is adjusted to minimize the mean squared error of the viscous and inviscid solutions for the freestream velocity. A simpler technique locates separation according to an input value of the boundary-layer shape factor $H = \delta^*/\theta$. The separation location can also be provided directly as an input.

A schematic representation of the flow model is given in Fig. 2.4.14. Upstream of the separation location x_s, the boundary-layer is computed in a direct mode with the edge velocity coming from the inviscid flow calculation specified. Between x_s and a suitably chosen point x_ρ downstream of reattachment or in the plume reattachment region, the displacement thickness is prescribed. The effective displacement surface between x_s and x_ρ is assumed to be conical. In this region an inverse mode of calculation for the boundary-layer is performed. It provides a "viscous" edge velocity $U_{e\,vis}$ which may or may not agree with the "inviscid" velocity $U_{e\,inv}$ produced by the perfect fluid calculation. On the downstream part of the calculation domain the direct mode is employed anew.

The iteration cycle represented in Fig. 2.4.15 includes two loops. The inner loop is performed for given values of x_s and θ_s and consists of iteration on the boundary-layer displacement effect. When the inner loop is terminated, if separation is present, the squared deviation between the two velocity solutions $U_{e\,ns}$ and $U_{e\,mv}$ between x_s and x_p is calculated. The accuracy of the matching of the two solutions is then indicated by the value of the RMS error :

$$S = \left[\sum_{1}^{N} \frac{(U_{e\,ns} - U_{e\,mv})^2}{U_{e\,\infty}^2 \, N} \right]^{1/2}$$

If this error is not within a specified tolerance, a new outer cycle is started with new values of x_s and x_p .

The inviscid exhaust jet is calculated twice during the above iteration process. The first jet calculation is performed assuming an external flow parallel to the jet axis with constant pressure and the free stream Mach number. After four cycles of the preceding iteration a new exhaust jet is calculated using the external pressure distribution that exists at that time as calculated by the inviscid external flow calculation.

Subsequently [2.4.27] the interaction method has received several improvements :

i - relaxation of the assumption that the effective outer boundary of the separated flow is conical. In the improved iteration method, the new displacement thickness distribution is deduced from the mismatch of the "viscous" and "inviscid" outer edge velocities $U_{e\,ns}$ and $U_{e\,mv}$ following a correction procedure introduced by Carter [2.4.30]. Also it is no longer necessary to operate the boundary-layer method in a direct mode up to the separation point, but the inverse mode is used with the displacement surface prescribed over the entire afterbody flow region.

ii - use of the Method of Characteristics to compute the exhaust jet inviscid core.

iii - finally, capability to treat shock-induced separation has been added.

The present method is applicable to flows with subsonic or supersonic free streams with Mach number in the range 0.5 - 1.5 including flow with shock-wave induced separation and to bodies with either high pressure exhaust plumes or solid plume simulators.

In the calculations performed for the WG 08 the iterative procedure was used to obtain a first approximation to the separation location. Then this location was adjusted further by the author until the error between the viscous and inviscid solutions was minimized.

Initial conditions for the boundary-layer calculation are obtained from analytical solutions for boundary-layer on flat-plates. For the present calculations, the solutions for laminar flow were used, followed by a short region of transition to turbulent flow.

For the NASA Langley models the calculation was started a short distance from the tip of the nose of the model using the given flow conditions to determine the required parameters. For the AGARD models, several starting location were tried until the calculated boundary-layer displacement thickness at the beginning of the boattail matched the measured values. This resulted in the boundary-layer being started at an axial station about 5.7 diameters aft of the nose tip.

The computer run time was typically 30-45 seconds on a CDC 7600 computer for a case with the separation point specified. The number of iterations was in the range 11-16, depending on the test case considered.

For the calculation of the external inviscid flow the mesh had 81 axial points, 61 of them being on the body, and 31 radial points. The exterior boundaries were placed at infinity.

The contribution of Hodges - [2.4.31-32] (number 6)

In this method the inviscid external flow over the afterbody is computed by using the surface singularity method of Hess and Smith [2.4.33]. This method is normally used in conjunction with an approximate compressibility correction based on Gothert's rule but incorporating a refinement. The revised procedure uses the standart Gothert rule together with the surface singularity method to calculate surface Mach number M_L and pressure coefficient C'_p . An incompressible flow pressure coefficient $C_{p,i}$ is then calculated using Kuchemann's rule [2.4.34] :

$$C_{p,i} = C'_p \sqrt{\beta} \qquad \text{with :} \quad \beta = \sqrt{1 - M^2}$$

and a modified compressibility factor B defined by :

$$B^2 = 1 - M^2 \, (1 - C_{p,i} \, M_L)$$

The value of B varies along the afterbody and jet. The corrected pressure coefficient is then taken as :

$$C_p = B^{-1/2} \, C_{p,i}$$

The inviscid flow in the jet exhaust is computed by the Method of Characteristics as far as the end of the first cell. The pressures along the jet outer boundary are supplied by the inviscid external flow calculation. This method assumes that the exit velocity at the nozzle is sonic and is capable

of computing the jet exhaust flow characteristics for under-expanded jets of pressure ratios, NPR, up to 6. Since the pressure distribution on the afterbody is not sensitive to fine detail of the jet downstream of the first cell, the remainder of the jet is modeled simply by adding several more cells, identical to the first, followed by a semi-infinite cylinder.

The procedure for modeling the viscous layer is illustrated in Fig. 2.4.16. The boundary-layer displacement thickness on the afterbody and jet (regarded as a solid body) is computed with the original version of the lag-entrainment method [2.4.35]. Briefly speaking, the lag-entrainment method is an integral method based on the integral momentum equation and on Head's entrainment equation representing the rate at which mass is transferred into the boundary-layer by the turbulent mixing process. This well known method incorporates a transport-like equation to represent lag effect on the entrainment coefficient which occurs when the boundary-layer is subjected to strong adverse-or favorable- pressure gradients.

This method is also used to determine the location of separation on the afterbody. The boundary-layer is assumed to separate when the transformed shape parameter $\bar{H}$ is equal to 1.44. This criterion was developed by correlating overall pressure distributions predicted by this method rather than seeking agreement with measured separation locations.

The discriminating streamline is defined as a straight line which starts at the separation point location x_s on the afterbody and leaves the surface at an angle θ_s. The straight line intersects the boundary of the jet at what is considered as the reattachment point. The angle θ_s is defined in degrees by the empirical relation :

$$\theta_s = 1.4 + 19.0\,(1 - M_\infty)$$

which was determined by an approximate fit to experimental data. The boundary-layer flow characteristics in the shear layer between the separated region and the external flow are computed by the lag-entrainment method in which the skin friction coefficient is set equal to zero. The effective body shape in this region is determined by adding the boundary-layer displacement thickness to the discriminating streamline. The discontinuities in slope at the ends of the separated region are smoothed with quintic polynomials chosen such that radius, slope and curvature are matched at both ends (see in Fig. 2.4.17). For the intersection of the discriminating streamline with the jet boundary, the upstream end of the smoothed region is in the plane of the nozzle exit and the downstream end is a similar distance beyond the reattachment point. In the neighborhood of the separation point the boundary-layer displacement is calculated first and smoothing is applied to the displacement surface. The smoothing at separation extends over 10 percent of the afterbody length.

A rather simple approach is used to model the entrainment of external air into the mixing region developing along the exhaust jet boundary. The boundary condition on the inviscid external surface of the plume is modified to include an inflow normal to the boundary, the magnitude of which is proportional to the velocity difference across the jet boundary. Downstream of reattachment or downstream of the nozzle exit if no separation is present, a constant of proportionality (the so-called entrainment coefficient E) of 0.03 is used. In tuning the calculation procedure it was found that it was necessary to also apply an entrainment correction to the effective body shape in the separation region. Thus a value of E of -0.01 is used for the entrainment coefficient between the separation point and a point in the plane of the nozzle exit. An entrainment coefficient of 0.05 is used from the nozzle exit to reattachment. In fact, the difference in these entrainment coefficients provides a correction to the simple straight line approximation of the discriminating streamline. The results are consistent with experimental evidence which shows that the discriminating streamline is convex to the external flow for most of its length.

Since Ref.2.4.41 was published, there have been two modifications to the method. The first modification allows the calculation of flows past axisymmetric afterbodies with annular bases. The base region is treated in a similar way to a separated flow region. The boundary of the region is a straight line which has its intersection with the jet boundary smoothed with a quintic polynomial. The slope of the straight line boundary is equal to the slope of the afterbody at the jet exit plane. As for the separated region, an "entrainment" factor is applied at the boundary of the base flow region. The value of the factor, 0.02, was chosen by tuning.

The second modification is an attempt at modelling jet temperature effects. A rise in jet temperature can affect the external flow in two ways, firstly an increase in the entrainment rate caused by increased jet velocities, and secondly an increase in the mixing layer growth rate.

The first of these effects was already catered for in the entrainment model. The mixing layer is not modelled explicitly and so the second effect is treated by modelling the mixing layer growth rate as a radial velocity and adding it to the entrainment velocity. The radial velocity is calculated from :

$$V_{growth} = U_e \frac{dt}{dx} \quad \text{where } U_e = \text{velocity in external flow}$$

$$\frac{dt}{dx} = \text{rate of change of mixing layer thickness with distance downstream,}$$

having calculated dt/dx by consideration of the mass balance within the layer,

$$\frac{dt}{dx} = \frac{V_{ent}}{U_m} \frac{\rho_e}{\rho_m} \quad \text{where } V_{ent} = \text{entrainment velocity}$$

$$\rho_e = \text{external flow density}$$

U_m = mean velocity in mixing layer

ρ_m = mean density in mixing layer

Thus the net radial velocity towards the axis = $V_{ent} - V_{growth} = V_{ent} \quad \frac{1 - U_e \rho_e}{U_m \rho_m}$

As illustrated in Fig. 2.4.18 the present method uses two iteration loops. The outer iteration is between the jet calculation and the external flow calculation. The first step in this procedure is to calculate the shape of the boundary of a jet issuing in still air. The external flow is then calculated over the combined afterbody and plume. The resulting pressure distribution over the jet boundary is then used in the calculation of a new jet boundary. This procedure is continued until a converged solution is reached. Usually about eight iterations are required.

The inner iteration is between the calculation of the inviscid external flow and the boundary-layer. The pressure distribution obtained from the inviscid flow solution is supplied to the boundary-layer method along with the body and plume shape. The displacement thickness and the discriminating streamline are then added to the afterbody and plume. Because of the sensitivity of the calculation to the iteration procedure, an underrelaxation procedure is used to ensure convergence.

Boattail pressure drag coefficient is computed from the predicted pressure distribution for each iteration. Convergence of the inner loop is assumed to occur when successive values of the boattail drag coefficient differ by less than a specified value (for instance 0.00001).

The computer program written for a DEC 1099 computer takes approximately 10 minutes of CPU time to obtain a typical solution.

The contribution of Hardy and Dutouquet - [2.4.36-37] (number 7)

In the present method the inviscid external and jet exhaust flows are computed by using as dependent variable the stream function ψ . Thus the basic equation is obtained by writing the irrotationality condition, which gives :

(3) $$\frac{\partial}{\partial x}\left(\frac{1}{\rho r}\frac{\partial \psi}{\partial x}\right) + \frac{\partial}{\partial r}\left(\frac{1}{\rho r}\frac{\partial \psi}{\partial r}\right) = 0$$

The density ρ is calculated by the following equation :

$$\frac{\rho}{\rho_\infty} = \left[1 + \frac{\gamma-1}{2}\left(\frac{V^2}{a_\infty^2} - \frac{V_\infty^2}{a_\infty^2}\right)\right]^{\frac{1}{\gamma-1}}$$

For the external stream which extends to infinity the numerical resolution is in fact performed with an auxiliary stream function remaining finite when the radial distance r tends towards infinity. This function χ is defined by :

$$\chi = \psi - \psi_\infty$$

where ψ_∞ represents the behavior of the stream function ψ at infinity :

As for the external flow the physical space co-ordinates (x , r) extend to infinity, a finite computational domain is constructed -co-ordinates (X , R)- by means of the following transformation for the radial co-ordinate :

(4) $$r = \frac{R}{(B - AR)^2}$$

In this expression A and B are constants. A similar transformation is employed for the streamwise co-ordinate.

Considering the internal flow -which comprises here both the flow in the upstream part of the nozzle and the exhaust jet- a special procedure is used to solve the basic equation. As we know, the stream function equation looks like the exact potential equation in which we find the two "components" M_x and M_r of the Mach number. However this equation for the stream function contains a cross derivative whose approximation would necessitate the use of a nine-point finite difference scheme. To avoid this difficulty, a new basic equation has been written which takes the form :

(5) $$(1 - M^2)\frac{\partial^2 \psi}{\partial x^2} + \frac{\partial^2 \psi}{\partial r^2} + M^2\left(\frac{1}{\rho V}\frac{\partial \rho V}{\partial x} - \frac{\partial \theta}{\partial r}\right)\frac{\partial \psi}{\partial r} - \frac{1}{r}\frac{\partial \psi}{\partial r} = \omega$$

where $\theta = \tan^{-1}(\partial\psi/\partial x / \partial\psi/\partial y)$ and where ω is a supplementary term representing a possible variation of vorticity for the case of a non isentropic incoming flow.

The advantages of a method using the stream function as dependent variable are :

i - a faster convergence rate because of Dirichlet type boundary conditions,

ii - a mass automatically conserved,

iii - an easy extension to include vorticity effects due to non isentropic incoming flow or shock curvature,

iv - an accurate calculation of a centered supersonic expansion.

The basic equations for both flows are solved by a relaxation technique. The numerical procedure uses a five-point implicit scheme. The scheme is centered when the local Mach number is subsonic and an upwind finite difference scheme is employed in regions where the Mach number is supersonic. The method

of solution consists of performing successive resolutions of Eqs. 3 and 5 in which ρ and M are considered as given quantities provided by the preceding resolution.

The calculations are performed by prescribing the following boundary conditions :

- for the external flow : Mach number, static pressure, stagnation temperature at upstream infinity.

- for the internal flow : stagnation pressure and stagnation temperature of the flow entering the nozzle.

The mesh topologies for the external flow and the nozzle flow are represented in Figs. 2.4.19 a and b. It should be noted that the figure gives only a schematic representation of these meshes ; in reality many more grid points were used to perform the present calculations, namely :

- 40 x 20 grid points in the external stream,

- 40 x 15 grid points in the internal stream.

In the finite computational domain (X , R) the grid points are equally spaced. In the physical plane (x , r) the mesh size varies from the wall to the far field according to formula 4 given above.

The boundary-layer developing on the afterbody is computed by using the well known Patankar and Spalding [2.4.38] finite difference method along with a mixing-length type turbulence model. It is recalled that this method uses a dimensionless stream function as cross-stream variable, obtained from a Von Mises co-ordinate transformation. The boundary-layer calculation is carried on over the exhaust jet boundary, considered as a solid surface except if separation occurs on the boattail (see below).

The solution is obtained by an iteration procedure consisting basically of two steps :

1 - at first an interactive calculation is performed between the inviscid external and nozzle flows. This iteration is conducted until convergence, i.e. until the free boundary separating the two flows is frozen (the number of cycles is generally equal to 4).

2 - during the second iteration procedure the plume shape obtained when step 1 is finished is considered as invariant. Then an IVI calculation is performed between the external stream and the boundary-layer developing on the afterbody and on the plume boundary considered as a solid surface. A typical number of cycles is 20.

3 - in the case of large nozzle pressure ratio it can be necessary to start a new step 1 by making a calculation of the exhaust jet with the pressure distribution given by step 2 prescribed on its boundary.

During the IVI calculation, separation is looked for by considering that it occurs when the boundary-layer shape parameter $H = \delta^*/\theta$ reaches the value 2.6. If separation is found at a location x_s , then downstream of x_s the pressure is assumed to be constant and equal to its value at the separation point.

The AGARD WG 08 calculations have been executed on an IMB 3033U computer. For each case, the CPU time was about 4 minutes.

The contribution of Radespiel - (number 8)

In the external flow and exhaust jet the Euler equations are solved by means of the Streamtube Curvature algorithm (STC) [2.4.39] . Thus a grid of streamlines and orthogonal trajectories is set up as shown in the example presented in Fig. 2.4.20. The positions of streamlines are calculated by means of successive approximations of continuity and normal momentum equations. The STC algorithm is suitable for regions of different stagnation temperature and different stagnation pressure. It allows a rapid calculation of the inviscid part of the flow field for configurations comprising several external-internal streams provided that the jet pressure ratio NPR is in the range below 3. At the outer edge of the computational domain both wall boundary and far field options are available. For the latter case a small perturbation linear potential theory is assumed in the far field region.

The boundary-layer type equations are solved by the GENMIX implicit marching procedure which is applied both for wall boundary-layers and free shear layers [2.4.40] . The GENMIX code solves the mass-weighted averaged mean momentum and stagnation enthalpy equations and three transport equations for turbulent quantities : the turbulence kinetic energy k , the dissipation rate ε and an intermittency factor γ . Concerning the calculation of free shear layers, the (k-ε-γ) turbulence model proved superior to the standard (k-ε) model [2.4 41] . Viscous sublayers near walls are bridged by adequate wall functions.

On the one hand the viscous algorithm GENMIX is linked to the STC solution with the help of the local pressure gradient which is approximated by integration of :

$$\frac{\rho U^2}{R} = - \frac{\partial p}{\partial n}$$

orthogonal to the mean flow direction (U and ρ denote viscous quantities while $1/R$ denotes the inviscid curvature). This concept leads to a realistic representation of viscous pressure gradients at the wall and a smooth fit of viscous flow quantities to the inviscid flow at the edge of the turbulent region. The matched viscous solution for the jet region is established from the jet axis to the edge of the turbulent mixing region.

On the other hand, the viscous flow quantities are used in the STC algorithm for the approximation of continuity in every streamtube. Thus turbulent viscous deceleration and acceleration are accounted for in the inviscid part of the solution.

The IVI calculation procedure is as follows.

The program first computes purely inviscid streamlines and orthogonal trajectories. Having reached the prescribed grid refinement and streamline position tolerance, viscous and inviscid calculations are done in turn. Upstream wall boundary-layers are adjusted to fit the experimentally measured thickness. At the jet exit plane a thin ($0.001\ D$) turbulent equilibrium mixing layer is assumed between the inviscid nozzle flow and the wall boundary-layer. Thus initial profiles of flow quantities are prescribed from the jet axis to the outer edge of the boundary-layer.

During the IVI process underrelaxation must be applied. The relaxation factor gets half the value after the first couple of iterations.

No smoothing of viscous results is necessary.

The program constructs a mesh of streamlines and orthogonal trajectories. During the IVI process, the streamlines encounter deceleration or acceleration due to viscous effects. Both inviscid and viscous equations are integrated towards the wall so that no displacement thicknesses are added. Convergence is controlled by computing the value of afterbody pressure drag during the iteration process. Convergence history of the calculated test cases is shown in Fig. 2.4.21. The following table gives detailed information on conditions of calculation, mesh sizes, iteration number and computer time.

		Case 1	Case 3	Case 4	Case 5	Case 6
No. of viscous-inviscid iterations		14	14	12	12	12
No. inviscid meshpoints		561	614	614	555	509
No. inviscid meshpoints on the body		32	30	30	33	30
No. inviscid streamlines		17	18	18	18	15
No. inviscid orthog.		55	65	65	62	61
Ext. boundary condition streamwise		Farfield	Farfield	Farfield	wall, added	wall, added
Ext. boundary at r/D		2.82	3.27	3.27	4.84	1.76
Upstream bound. at x/D		-4.0	-6.9	-6.9	-9.6	-3.5
Downstream bound. at x/D		3.3	6.4	6.4	5.2	4.14
Relaxation of Coupling procedure		0.4 -0.2	0.4 -0.2	0.4 -0.2	0.4 -0.2	0.4 -0.2
Cross stream mesh points viscous Alg.	wall	21-23	21-22	21-22	21-23	21-22
	jet	43	48	48	51	44
Streamwise steps of viscous Alg.	wall	711	734	734	775	650
	jet	506	672	651	536	608
CPU		750	780	650	600	690
Computer		Siemens 7870				

For test cases 5 to 6, turbulent boundary-layer thickness was added to the tunnel wall. According to the experiments, the computed pressure distributions matched the reference pressure at the tunnel wall at the location x = -0.44 m.

2.4.1.3 - *Multi-Component Methods for base flows* -

Underlying physical description of base-flow -

The very complex flow that establishes behind the base of a missile equipped with a propulsive nozzle is schematically represented in Fig. 2.4.22. The figure shows the *streamline pattern* of a mean steady flow. In most practical situations the flows which separate at the base are turbulent so that in reality such streamlines are fictitious since they are relevant to a mean flow in the sense of statistical turbulence (i.e. Reynolds averaging). In reality the flow is highly fluctuating and its instantaneous structure far more complex than the mean organization shown in Fig. 2.4.22. However the streamlines thus constructed are those which would result *from a modeling* of the flow within the framework of the classical time-averaged Navier-Stokes equations concept.

The *base-flow region* is at a quasi-uniform pressure P_B and constitutes what is frequently called the dead-air region. Two turbulent mixing layers develop between the outer high velocity inviscid streams and the dead-air region. To summarise briefly, the internal organization of the dead-air region is almost always marked by the presence of a fluid circulation promoting exchanges between external and internal flows as shown in Fig. 2.4.22. The slower flow (here the external flow) gives up some mass flow entrained by the faster flow (here the nozzle flow).

A necessary condition for the above steady flow solution to be possible is that *the mass-flow* q_e fed into the dead-air region by the external flow be equal to the mass-flow q_j extracted by the entrainment effect of the propulsive jet.

The above flow pattern must be notified in the following circumstances :

i - when the outer flow is faster than the internal flow,

ii - when separation occurs either on the afterbody surface upstream of the base shoulder or inside the nozzle (see below).

iii - when mass injection or mass aspiration (base bleed) is performed through the base of the missile.

However, in every situation the main flow features represented here and the essential concept apply, the guideline to derive a realistic flow pattern being the necessity to obey the mass conservation principle.

Basic principles of the tested methods -

The different methods tested here are *all based on the same* flow schematization which is a generalization of the well known Korst's flow model for turbulent reattachment behind a rearward facing step [2.4.42]. All these theories are valid only for supersonic flows, which means that the external flow as well as the jet issuing from the nozzle must remain supersonic at least for a short distance downstream of the confluence point.

The complex real flow structure is schematized in the following way :

i - the dead-air-region - roughly limited by the triangle $S_e R_T S_j$ (see Fig. 2.4.23) is at the same pressure P_B as the two separated inviscid flows (external and internal).

ii - the viscous phenomena are superimposed on a perfect fluid structure entirely determined if the base pressure P_B is fixed.

In the case of an under-expanded nozzle flow, the external stream may separate somewhere on the afterbody upstream of the base shoulder. The same flow model is applicable, the difference being that now the external separation point S_e is located upstream of the base plane (see sketch a in Fig. 2.4.24). A similar situation can be met if the nozzle flow is highly over-expanded. In this case an internal separation may occur at a point S_j located inside the nozzle (see sketch b in Fig. 2.4.24).
The inviscid supersonic flows are presumed known down to the separation points S_e and S_j, together with the properties of the incoming boundary-layers.

For all theories the first step consists of performing an inviscid fluid calculation considering provisionally the base pressure P_B as known. The Method of Characteristics is most often used to perform this calculation. Thus it is possible to calculate the inviscid flows separating at points S_e and S_j respectively. This calculation provides in particular the constant pressure free boundaries (J_e) and (J_j) of the inviscid flows. When P_B is lower than both P_e and P_j (ostream pressures at S_e and S_j respectively), S_e and S_j are the origin of an expansion fan (a circumstance schematized in Fig. 2.4.23). But, as already pointed out, this situation is not always met : for example if the jet is under-expanded P_B can be higher than P_e and then a shock-wave emanates from S_e. Conversely if the jet is over-expanded a shock can propagate from S_j.

The two lines (J_e) and (J_j) usually meet at the inviscid confluence point R_T different from the physical reattachment point R. Downstream of R_T the two inviscid streams have a common boundary (Γ) -a slip line- on which both flows have the same pressure and the same direction. These two conditions allow the determination of the initial direction θ_{R_T} of (Γ) at R_T as also of the common downstream pressure P_{R_T} in the two flows. The determination of the downstream conditions can be done :

i - either by considering that at R_T each flow undergoes a compression shock -as sketched in Fig. 2.4.23- which is in principle the most accurate procedure to be adopted for purely inviscid flow,

ii - or by replacing the shocks by isentropic compressions ; indeed experiments show that the shock-waves form by the focusing of compression waves at a distance from R_T . The assumption of an isentropic compression should thus lead to a more accurate evaluation of θ_{R_T} .

Then the viscous effects are superimposed on this inviscid flow model. In the present situation turbulence effects manifest themselves essentially by the development of mixing-layers -or mixing-zones- along the isobaric boundaries ($\mathcal{L}_e$) and ($\mathcal{L}_j$).

To represent the properties of these mixing-layers all the theories considered utilize the approximate solution proposed by Korst for the case of a vanishingly thin boundary-layer at the separation point in terms of an error function velocity distribution :

$$(6) \qquad \frac{u}{U_e} \equiv \varphi = \frac{1}{2}\left(1 + \operatorname{erf}\eta\right) \qquad \text{where} \qquad \eta = \sigma\,\frac{y}{x}$$

σ being the spread parameter of the mixing which is given by experimental correlations.

For non-adiabatic cases in which the dead-air temperature T_B differs from the incoming flow stagnation temperature T_{t_e} (or T_{t_j}) the temperature profile is taken to be of the form :

$$\frac{T_t}{T_{t_e}} \equiv \Lambda = \frac{T_B}{T_{t_e}} + \left(1 - \frac{T_B}{T_{t_e}}\right)\varphi = \Lambda_B + (1 - \Lambda_B)\,\varphi$$

The above two-dimensional velocity profiles are located respectively to each of the isobaric boundaries ($\mathcal{L}_e$) and ($\mathcal{L}_j$) by satisfying the integral momentum balance for the respective streams on a local two dimensional basis.

The next step consists of applying a reattachment criterion for both flows which reattach at R_T on the downstream common line of confluence (Γ). At this point resides the major difference between the various methods tested here. However, this reattachment criterion whatever it is provides the exchange mass-flow rates q_e and q_j which are fed into (or extracted from) the dead-air region by the entrainment process taking place in the external and internal mixing-layers respectively. These mass-flow rates are readily calculated if the velocity and temperature distributions across the mixing-layers are known.

Also the rates of thermal energy e_e and e_j transferred (the transfer being either positive or negative) to the dead-air region can be calculated in a similar way.

Thus the mass and energy conservation principles applying in the steady state régime lead to the two following equations :

$$(7) \qquad q_e + q_j + q_B = 0$$

$$(8) \qquad e_e + e_j + e_B = 0$$

where q_B and e_B are respectively the mass-flow and the energy flow rates eventually fed into the dead-air region through the base.

The mass-flow and energy rates transferred to the dead-air region by the mixing process are written in the form :

$$q_e + q_j = 2\pi r_{R_T}\left(\bar{q}_e + \bar{q}_j\right)$$

$$e_e + e_j = 2\pi r_{R_T}\left(\bar{e}_e + \bar{e}_j\right)$$

where r_{R_T} is the distance of the confluence point R_T from the axis of revolution and $\bar{q}_e$, $\bar{q}_j$, $\bar{e}_e$ and $\bar{e}_j$ are evaluated from two-dimensional mixing theory. These quantities are proportional to the mixing spread parameter σ and to the so-called mixing length which is the distance along which the isobaric turbulent mixing takes place. Frequently this mixing length is taken as equal to the length of the isobaric boundary between the separation point and the reattachment point R_T .

Thus the two equations 7 and 8 constitute the "closure" relationships which -for prescribed values of q_B and e_B - determine uniquely the two quantities up to now undetermined ; namely the base pressure P_B and the dead-air temperature T_B . The solution procedure consists of iterating on P_B and T_B until Eqs. 7 and 8 are simultaneously satisfied.

However this solution procedure must be modified if separation occurs on the afterbody or inside the nozzle. (see Fig. 2.4.24) In this case the pressure in the separated region namely P_B is determined by a separation criterion which gives the pressure in the separated region as a function of the incoming flow properties ; separation in supersonic flow being independent of downstream conditions according to the Free-Interaction concept introduced by Chapman [2.4.43].

In the present situation, P_B being known, the base-flow theory allows the determination of the location x_S of the separation point on the afterbody or in the nozzle. The solution is now obtained by iteration on x_S (plus eventually T_B) until the balance equations 7-8 are satisfied.

The method of Délery - [2.4.44-45] *(contributor n° 10)*

Basically this method relies on the angular reattachment criterion concept introduced by Carrière and Sirieix [2.4.46]. This criterion postulates that the reattachment process is entirely governed by the state of the dissipative layer when it approaches the reattachment zone. This state can be characterized by :

i - the direction ψ of the inviscid external flow relative to the wall on which reattachment occurs (see Fig. 2.4.25),

ii - the external Mach number M_{e_B} at the outer edge of the separated dissipative layer (M_{e_B} corresponds to the base pressure P_B),

iii - the velocity and density distributions across the turbulent mixing-layer.

It is further postulated that the reattachment angle ψ must obey a relationship of the form :

$$\psi = \psi (M_{e_B} , C_q , \Lambda_B , \gamma) \tag{9}$$

where :

- Λ_B is the ratio of the dead-air temperature to the external stagnation temperature,
- γ the ratio of specific heats,
- C_q the generalized injection coefficient defined by :

$$C_q = \frac{q_B}{\rho_{e_B} U_{e_B} L} + \frac{\theta_B}{L + x_0} - \frac{i_B}{\rho_{e_B} U_{e_B}^2 L}$$

In the above expression :

- q_B is the mass-flow rate eventually injected into the dead-air region,
- i_B is the momentum carried by the fluid injected,
- θ_B is the momentum thickness of the incoming boundary-layer at the base shoulder. Thus in this formulation the boundary-layer effect is represented by means of what is now known as the "equivalent base-bleed concept".
- L is the length of the isobaric free-boundary ($L = \overline{SR_T}$ in Fig. 2.4.25) ; x_0 is the displacement of the mixing zone virtual origin introduced to take into account initial boundary-layer effects on the mixing layer development [2.4.47-48].
- U_{i_B} , ρ_{e_B} are the velocity and the density of the external inviscid stream at the pressure P_B .

Inasmuch as C_q is usually a small parameter, Eq. 9 can be written :

$$\psi = \bar{\psi} (M_{e_B} , \Lambda_B , \gamma) + C_q \frac{\partial \psi}{\partial C_q} (M_{e_B} , \Lambda_B , \gamma)$$

The unperturbated reattachment angle $\bar{\psi}$ is a known function of M_{e_B} , Λ_B and γ resulting mainly from empirical correlations. The sensitivity function $\partial \psi / \partial C_q$ is determined theoretically from solution of the isobaric turbulent mixing represented by the error function (see Eq. 6 above), the effect of the initial boundary-layer being taken into account by the origin shift concept.

The effect of axisymmetry on the unperturbated reattachment angle is represented by means of a correction function involving the geometrical shape of the isobaric free-boundaries (J_e) and (J_i) [2.4.49].

The reattachment criterion is applied to the external and to the internal flows by assuming that everything happens as if each of them reattaches on a wall achieving the common confluence direction θ_{RT} . Hence one can immediately deduce the C_q's and the corresponding mass-flow rates q_e and q_i .

In the version of the method employed for the WG 08 calculations the flows are assumed iso-energetic (no energy balance is considered) so that the solution uniqueness (in terms of base pressure P_B) is ensured by the single condition $q_e + q_i + q_B = 0$ with $q_B = 0$ for the present test cases. The mixing parameter σ is calculated from the correlation curve of Sirieix and Solignac [2.4.48] with a correction factor to take into account the axisymmetric effect. The influence on the initial boundary-layer of expansion (or compression) at the separation points is computed by the well known Reshotko and Tucker discontinuity analysis [2.4.50].

Separation on the boattail is detected by using a separation criterion derived from the Free-Interaction theory of Chapman [2.4.43]. According to this criterion the pressure P_B in the separated zone is expressed by the following relation :

$$\frac{P_B}{P_0} = 1 + k \frac{\gamma}{2} M_0^2 (2 C_{f_0})^{\frac{1}{2}} (M_0^2 - 1)^{-\frac{1}{4}}$$

in which the static pressure P_0, the Mach number M_0 and the skin-friction coefficient Cf_0 are relative to the incoming flow. The coefficient k is deduced from empirical correlations : the value k = 5.5 has been adopted here. It should be pointed out that the Free-Interaction theory is valid only at low to moderate Reynolds number as is generally the case in most wind tunnel experiments. This theory becomes questionable at high Reynolds number [2.4.51] ; then a separation criterion such as the one proposed by Zukoski [2.4.52] should be preferred.

The method of Addy - [2.4.53] *(contributors n° 11, 12 and 13)*

In Addy's method the isobaric turbulent mixing analysis is applied by neglecting completely the effect of the initial boundary-layer. The original Chapman-Korst escape criterion is used as reattachment criterion. It is recalled that this criterion states that the stagnation pressure $P_{t\ell}$ reached on the limiting streamline when the reattachment process begins must be equal to the static pressure P_S after reattachment. The downstream pressure P_S results from the oblique shock system at R_T in the inviscid flowfields (see above). However, in order to take into account the axisymmetry effect and to improve agreement with experiment Addy has modified that criterion by expressing it in the form [2.4.54] : $P_{t\ell}/P_0 = k\,(P_{R_T}/P_0)$ where k is an empirical function of the ratio of radii $\bar{r}$ at S_e and S_j : $\bar{r} = r_j/r_e$. Furthermore in the present version of the theory the quantities $\bar{q}_e$, $\bar{q}_j$, $\bar{e}_e$ and $\bar{e}_j$ of Eqs. 7-8 are evaluated by introducing effective mixing length $(L_e)_{eff}$ and $(L_j)_{eff}$ approximately determined by locating the meeting point of the two mixing-zones. This modification has been introduced to take into account the fact that in reality the isobaric mixing represents only a fraction of the lengths L_e and L_j of the inviscid isobaric free boundaries.

In the program developed by Addy the case is considered where the flows are not iso-energetic which occurs in particular when the two flows have different stagnation temperatures. In these conditions, as already explained, the temperature T_0 of the fluid imprisoned in the dead-air region is a supplementary unknown whose determination requires writing a budget equation for energy (see above). The computer code automatically determines the base pressure and the base temperature by an iterative process until Eqs. 7 and 8 are both satisfied.

The method of Wagner - [2.4.55-57] *(contributor n° 14)*

This method is originally based on the Addy's program but incorporates significant deviations from it.

Thus initial boundary-layers at the separation points are taken into account by introducing an origin shift for the isobaric turbulent mixing and the equivalent bleed concept (see above). Boundary-layer expansion (or compression) at the separation points is computed by making use of Nash formula [2.4.58] and the spread parameter is computed after the Korst and Tripp correlation [2.4.59].

But the essential difference from Addy's method lies in the use of the angular reattachment criterion *of Carrière and Sirieix including* axisymmetric correction (see above). However, in the present application of this criterion to the two shear-layer confluence problem an iterative procedure is included in order to adjust the attachment direction θ_{R_T} for achieving equal reattachment pressure P_R in both shear-layers (this condition being not fulfilled in the application of the angular criterion made by Délery). The recompression pressure rise up to the reattachment point is given by assuming an isentropic recompression on the limiting streamline from P_0 to P_R. Thus in Wagner's method the attachment direction is no more that of the confluent inviscid flows downstream of R_T. Instead the pressure at the reattachment point R is the same in the two reattaching shear-layers which seems more satisfactory from a physical point of view.

In order to calculate flow separation on boattails the separation criterion of Zukoski [2.4.52] for upstream facing steps was used including a provision for incipient separation as proposed by White and Agrell [2.4.60].

The method of Moulden -[2.4.61-62] *(contributor n° 15)*

This method is based on a flow model which predicts boundary-layer development over the body and then solves for the confluence of the resulting external shear-layer with the jet exhaust plume (internal shear-layer) behind the dead-air zone. The means by which a solution is obtained is illustrated in Fig. 2.4.26. The calculation procedure begins by making an initial estimate of the angle through which the external flow is turned at the base. The ensuing pressure change is thus known and the shape of the exhaust-plume which expands to the base pressure can be determined by a Method of Characteristics solution. The solution is classically determined by a mass-flow balance equation in which the nett mass flow returned near the confluence point and the difference evaluated.

The angle of the external shear-layer is then iteratively adjusted until this difference becomes small *(to within a specified tolerance)*, i.e. a mass balance is achieved.

An external flow separation ahead of the base is deemed to exist if the flow cannot be turned sufficiently by a shock wave to meet the convergence criterion ; the relationship between maximum turning angle and Mach number is determined on an empirical basis. In this case the flow turning angle is held constant at its maximum value and the shear-layer separation point iteratively moved forward from the base until a converged confluence solution is reached.

The calculation of boundary-layer development requires the knowledge of body pressure distribution. The program provides the option of either performing a potential flow calculation or an input of pressure coefficient values, althouth in all present applications the potential flow option has been used. For bodies with ogive noses the calculation is based either on supersonic slender body theory or an alternative transonic flow theory, the selection of which depends on the Mach number. For bodies

with cones different theoretical methods are used, according to whether the shock is attached or detached. Boattailed afterbodies are treated by alternative supersonic or transonic theories, depending upon the approach Mach number.

Moulden's method is applicable to low supersonic speeds up to a maximum of Mach 2.0. The lower limit is Mach 1.0 but experience suggests that the lowest speed for useful results is Mach 1.2. Within this speed range the program can handle bodies having ogival or conical noses, a cylindrical center section and a conical boattail afterbody having any boattail angle within the range 0 to 10 . Hot or cold exhaust plumes may be handled as well as a solid plume simulator. The program outputs body pressure coefficient, base pressure and plume shape.

2.4.2 - *Evaluation of methods by comparison with experiment* -

2.4.2.1 - *Perfect fluid calculations* -

In the present paragraph we will consider only the Euler calculations, since the Boundary Element Method of Zacharias (contribution n° 9) -which is an inviscid fluid calculation- takes into consideration the entrainment effect of the exhaust jet, this effect being of course a viscous phenomenon. Thus the contribution of Zacharias will be discussed when examining Inviscid-Viscous Interactive methods in the next section.

Test cases 1, 2, 2A and 3 have been computed both by Vuillot-Veuillot (contribution n° 2) and by Bissinger-Eberle (contribution n° 3) ; test case 1 having been also computed by Zannetti-Onofri (contribution n° 1). It is thus possible to make a comparison between the results given by different numerical methods applied to the solving of the Euler equations and considering identical flow configurations. These test cases correspond to classical aircraft afterbodies with a sharp extremity (no base) and equipped with a sonic or slightly supersonic propulsive nozzle. In all these cases the external flow is transonic.

The distributions of the boattail wall pressure coefficient for the four test cases 1, 2, 2A and 3 are plotted in Figs. 2.4.27-30. The different contributions are identified by numbers whose attribution is indicated in Table 2.4.1. The experimental results are also plotted in the figures. It is observed that relatively large differences exist between the three -or two- calculations which in principle should give identical results since they solve the same set of equations. The largest discrepancies are noticed for test case 2 and 2A which correspond to a greater value of the angle β_E at the boattail extremity. In this case the external flow expands to higher Mach numbers on the boattail rear part. The best agreement between methods is obtained for test case 3 (see Fig. 2.4.30) which is in fact the most "gentle" case.

Explanation of the differences observed between the various contributions is not an easy task since in such calculations -even if the afterbody geometry, the external upstream Mach number, and the Nozzle Pressure Ratio, are identical for all the calculations- many other parameters are chosen freely by the contributor, for instance :

- location of upstream and downstream boundaries,
- location of the upper boundary Σ_{22} (see Fig. 2.4.1) which, for the present test cases, can be taken at large but finite distance or at infinity,
- the flow variable imposed on subsonic boundaries,
- the number of grid points.

Consequently it is very delicate to reach conclusions about the accuracy of the different methods and to establish an order of merit among them. For example in the calculations performed by Vuillot and Veuillot (contribution n° 2) the upstream value of the pressure P_∞ has been prescribed on the downstream boundary. This is certainly true from a physical point of view provided that this boundary be far enough from the afterbody. However in the present situation the upper limit Σ_{22} having been located too close to the afterbody this boundary condition leads to a wall pressure which does not tend to P_∞ (or equivalently to a CP which does not tend to zero) on the upstream part of the afterbody. This behavior is obvious if one considers Fig. 2.4.3 : the outlet section Σ_{32} is evidently larger than the inlet section Σ_{12} hence, since the external flow is subsonic, the pressure in Σ_{12} must necessarily be lower than the pressure in Σ_{11} . A far better agreement with the other calculations would certainly have been obtained by adjusting the pressure in Σ_{22} in such a way that CP tended to zero in the entrance section Σ_{12} .

The Mach number distributions on the jet centerline for test cases 1, 2, 2A and 3 are plotted in Figs. 2.4.31-34. These distributions also exhibit large differences between the contributions. Thus the results obtained by contributors 1 and 2 show oscillations which probably reflect the existence of a succession of shock-waves in the supersonic exhaust jet. On the other hand contribution n° 3 gives a perfectly smooth Mach number distribution along the centerline.

Test cases 5 and 6 (see Figs. 2.4.56 and 57) of section 2.4.1.2 below have been calculated by Bissinger and Eberle only (curve number 3 on the figures) so that it is not possible to make comparisons here with other Euler calculations. In fact, test cases 5 to 6 are very close to test case 3, the afterbody geometry and the NPR being identical. The essential difference is the presence of an outer wall at a finite distance from the afterbody, the aim of these cases being the illustration of tunnel blockage effect. This question is more thoroughly disccused in section 2.4.1.2 below.

Test case 7 has been calculated by Zanneti and Onofri only (contributor n° 1). This flow situation is different from the other aircraft afterbody configurations (namely test cases 1 to 6) in that the incoming external flow is supersonic. The computed boattail wall pressure coefficient is represented in Fig. 2.4.35. In fact in the present situation the external stream undergoes a nearly simple-wave expansion at the origin of the boattail with almost negligible viscous effects so that agreement between perfect fluid theory and experiment is very good.

The two last Euler calculations performed by Bissinger and Eberle are relevant to missile afterbodies having a relatively large base, the external and nozzle flows being both supersonic. Then as we know (see above) the flow field includes a large separated zone constituting a dead-air region in contact with the base. In these circumstances the use of purely inviscid flow model is highly questionable since in the present situation viscous effects play an essential role. As can be seen from Figs. 2.4.36 and 37, the results from the Euler code do not show these separation zones. Nevertheless the base pressure drag coefficients from these calculations are not too far off the measured values (see Figs. 2.4.64 and 65). This is another hint to caution against the use of integrated variables as a measure for the quality of a code. (see remark in following sub-section).

The quantity of most practical interest for flows 9 and 11 being the base pressure, we will examine the results givent by the Euler approach in the paragraph devoted to applications of multi component methods (see § 2.4.2.3 below).

Figures 2.4.27-30 also show a comparison of Euler calculations with experiment. One notes a fairly good agreement between theory and experiment for test cases 1, 2, 5, 6 and 7. This is because in these cases viscous effects are weak. Indeed for these test cases the viscous correction is small and its order of magnitude can be comparable with the uncertainty of the perfect fluid calculation itself, either Euler equations or the potential equation bieng used. On the other hand, for test cases 2 and 2A, because of a larger boattail terminal angle (β_E = -17° instead of -8 or -10°), the adverse pressure gradient in the rear part of the afterbody is much more severe so that the boundary-layer separates. In these circumstances a purely inviscid calculation is likely to give a result very far from the reality, as is shown by Figs. 2.4.28-29. In fact, as already mentioned in § 2.4.1.1, comparing inviscid flow calculations with experiments in which the flow is manifestly separated has no real significance.

2.4.2.2 - *Inviscid-Viscous Interactive methods* -

Test cases 1, 2, 2A, 3 and 4 have been treated by the great majority of IVI methods. All these cases are relevant to aircraft-type afterbodies placed in an external stream extending in *principle* to infinity. Test cases 5 and 6 which include tunnel blockage effects have been computed by only one IVI method (contribution n° 8 of Radespiel) and also by the Boundary Element Method (contribution n° 9 of Zacharias).

Let us first consider test case 1. As already pointed out in the preceding section, due to the mild curvature of the afterbody contour the adverse pressure gradient on the rear part of the boattail is not very severe. Thus the external flow boundary-layer thickens moderately and does not separate. Furthermore, because of the modest Nozzle Pressure Ratio (NPR = 2.9) there is practically no jet pluming as shown by the tracing of iso-Mach lines in Fig. 2.4.38 (these iso-Mach lines result from the Euler calculation performed by Vuillot and Veuillot). Consequently the interaction between the external flow and the exhaust jet is small. As a consequence of these two facts viscous effects on the afterbody are weak and -as seen in the preceding section- a purely perfect fluid calculation already gives a result rather close to reality. The greatest discrepancy between experiment and perfect fluid calculations is observed very close to the boattail extremity, where the compression given by a perfect fluid model is evidently too steep. In reality there is always locally a non-negligible interaction between the external stream and the exhaust jet which involves viscous phenomena.

The distributions of boattail wall pressure coefficient given by the IVI methods (contributions n° 4 to 8) plus the BEM method (contribution n° 9) are plotted in Fig. 2.4.39. The following features are observed :

i - all the computed distributions are very close to each other. The more noticeable -but modest- deviation is that of contribution n° 7 (Hardy-Dutouquet) which slightly overpredicts the expansion on the upstream part of the afterbody.

ii - the accounting of viscous effects improves the prediction, essentially in the vicinity of the boattail extremity.

iii - the largest differences between the calculations are observed precisely in this region. These differences can have various origins : numerical accuracy of the code employed to solve the inviscid part of the flow field ; physical accuracy of the model used to predict the development of the boundary-layer on the boattail ; more or less satisfactory representation of the confluence of the external and internal boundary-layers at the origin of the jet mixing layer. Thus, contribution n° 9 overpredicts the pressure rise at the boattail extremity whereas the *method of Kuhn (contribution n° 5)* gives too small a pressure rise. Best agreement with experiment is achieved by contribution n° 4 (the RAXJET flow model) and by contribution n° 8 (calculation of Radespiel).

Also a fair agreement between calculations and experiment is noted for the drag buildup along boattail as shown in Fig. 2.4.40. It is recalled that the drag buildup is obtained by integration from the *boattail shoulder of the elementary streamwise component* of the pressure force coefficient. Thus the end value of this integral -in which quantities are appropriately scaled- is by definition the boattail pressure drag coefficient. Figure 2.4.41 gives the bar graph of boattail pressure drag coefficient. Two values are given for the experimental coefficient :

- one value (the lower) is obtained by linear extrapolation of the C_P distribution down to the boattail extremity where there is no measurement point for the pressure because of the impossibility of locating a pressure tap at the model trailing edge.

- the other value results from an integration of pressure force down to the last pressure measurement point.

The bar graph representation reveals a relatively large scatter among the calculated boattail pressure drag coefficients. Consideration of these results make it difficult to judge the quality of the theoretical models, since for this test case there is a difference of nearly 100% between the two possible experimental values. In fact interpretation of such bar graphs can be misleading and cannot be considered as a really significant criterion for the accuracy of the theoretical model :

i - the measured values of CDPBT is most often known with a large uncertainty since as already pointed out CDPBT is determined by integration of an incomplete wall pressure distribution. There results an error which can be noticeable as shown by the pressure drag buildup plotted in Fig. 2.4.40. Furthermore, the numerical scheme employed to compute the integral may have also important repercussions on the final result [2.4.63].

ii - a good agreement between the computed and measured values of CDPBT can be achieved even with a large discrepancy between the corresponding wall pressure distributions. In this case the agreement is fortuitous and results in fact from an error cancellation mechanism.

Methods employed by contributors N° 4, 5 and 8 (as also n° 7) provide also the distribution of skin friction along the boattail, so allowing calculation of the friction drag coefficient CDFBT. The bar graph of CDFBT represented in Fig. 2.4.41 shows that the three methods give comparable results. One should note that for test case 1 -as also for test cases 3 to 6- the drag due to friction is practically as high as the drag resulting from pressure forces. This fact demonstrates that for such configurations with a very progressive change in the boattail cross-section any predictive method should include a realistic calculation of the skin-friction coefficient.

For test case 2, the curvature of the boattail contour being much greater (β_E = -17° instead of -8° for test case 1), the compression at the boattail extremity is steeper. Thus in this case the external boundary-layer thickens much more than in the previous case and separates, as revealed by the plateau of the experimental wall pressure distribution (see Fig. 2.4.43). On the other hand, the NPR being equal to only 2.9, the exhaust jet remains nearly cylindrical as shown by the iso-Mach lines plot of Fig. 2.4.42 (calculation done by contributors n° 2). In the present situation viscous effects play a predominant role on the rear part of the boattail, so that -as already seen in the preceding section- a purely perfect fluid calculation gives a very poor prediction of the external flow behavior.

The distributions of boattail pressure coefficient given by contributors n° 4 to 7 are plotted in Fig. 2.4.43. For the present test case, consideration of viscous effects improves the prediction considerably. Inclusion in the theoretical model of the viscous region displacement effect -that of the external boundary-layer principally- leads to a considerable reduction in the pressure level on the rear part of the afterbody, making the distribution thus computed much closer to experiment than the distribution given by perfect fluid calculations. On the other hand, contribution n° 9 (MEB calculations) leads here to a poor prediction for the reason that the employed model is essentially inviscid, since only the entrainment and displacement effects of the exhaust jet are taken into consideration. In fact for the present case major viscous effects come from the thickening and separation of the external boundary-layer. Thus it is not surprising that the method used in contribution n° 9 is unable to predict correctly the boattail pressure distribution, since it neglects the displacement effect of the afterbody boundary-layer.

The best agreement with experiment is obtained by contribution n° 4 (the RAXJET flow model) which gives a very good prediction of both the upstream part of the wall pressure distribution and of the pressure level in the separated region. A satisfactory prediction is also achieved by contribution n° 5 (Kuhn's method) and a reasonable one by contribution n° 7 (Hardy-Dutouquet). In particular, contribution n° 7 predicts with good accuracy the pressure level of the separated flow region as well as the separation point location. Contribution n° 6 (Hodges'method) predicts an unrealistic rise in pressure near the afterbody extremity.

The plot of the drag buildup distributions along the boattail (see Fig. 2.3.2.2c of chapter 2.3) amplifies considerably the discrepancies between experiment and theory, except for contributions n° 4 and 5. The bar graphs of CDPBT and CDFBT are shown in Fig. 2.4.44. For the present configuration the boattail pressure drag coefficient is roughly 5 times greater than for test case 1. On the other hand, drag due to friction forces is nearly ten times smaller than drag due to pressure forces. This comes from the fact that the boattail is shorter than for test case 1 and that the skin friction drops rapidly to very small values because of separation.

Also the bar graph of Fig. 2.4.44 corroborates the assertion made previously that in some circumstances a poor prediction of the wall pressure distribution can nevertheless leads to a reasonable evaluation of CDPBT because of error compensation (consider for example results obtained by contributor n° 9).

In test case 2A the model is the same as that of test case 2 but now the NPR is equal to 5 instead of 2.9. In fact, as already mentioned, for this afterbody shape and these moderate values of the NPR jet pluming is of secondary importance to adverse pressure gradient effects induced by the boattail contour (Fig. 2.4.45 shows the shape of the exhaust jet resulting from an Euler calculation). Consequently the main conclusions pertaining to test case 2 remain valid for test case 2A, in particular the pressure distributions on the boattail are nearly identical in the two cases. Here the best agreement with experiment is still achieved by contribution n° 4 (see Fig. 2.4.46). In the present

case the results of contribution n° 7 are of better quality, presumably because of a more judicious adjustment of the computational mesh. Contribution n° 6 manifests the same tendency to overpredict the pressure rise on the boattail rear part. Drag buildup is given in Fig. 2.4.2A.2b and bar graphs of CDPBT and CDPBI are given in Fig. 2.4.3°.

Test case 3 is a situation in which viscous effects in the external flow have moderate repercussions because of the very progressive variation of the boattail cross section. Also there is no significant jet pluming as shown by the perfect fluid calculation of Fig. 2.4.4B. Distributions of computed boattail wall pressure coefficient are plotted in Fig. 2.4.4D. As for test case 1 all the IVI methods tested here give results in fair agreement with experiment, the most noticeable discrepancy appearing near the boattail extremity. Drag buildup along boattail is given in Fig. 2.4.3.2c and bar graphs of drag coefficients are shown in Figs. 2.4.4E.

For test case 4, the model geometry as well as the Nozzle Pressure Ratio (NPR = 3) are the same as those of test case 3, the essential difference is in the jet stagnation temperature, T_{t_j} being equal to 1000 K for test case 4 instead of 300 K for test case 3. In reality, at these relatively moderate levels, T_{t_j} has a very small influence on the flow past the afterbody. Indeed a change in the nozzle stagnation temperature is likely to have two main repercussions :

1. The shape of the inviscid exhaust plume can be modified because of real gas effects. However at this temperature level real gas effects are still small. Furthermore, as already noticed for the extremal values of the NPR, jet pluming is limited so that an exact prediction of the exhaust plume shape is not essential to accurately determine the boattail pressure distribution.

2. The properties of the mixing-layer developing along the boundary separating the jet and the external flow can be affected by a difference in the total temperatures of the two flows. However for the present test case the jet mixing layer has an almost negligible influence on the external flow upstream of the nozzle exit plane. This behavior is demonstrated by the good agreement obtained by methods (that of contributor n° 2 for instance) which neglect completely the entrainment effect of the propulsive jet.

The distributions of boattail pressure coefficient computed for test case 4 coincide practically with those corresponding to test case 3, as demonstrated by comparing the curves of Figs. 2.4.4D and 2.4.5A. One notes also the differences in the boattail pressure drag coefficient, as shown in Fig. 2.4.5B where the "cold" values have also been represented (values in rectangles) in order to facilitate comparison with "hot" values. Nonetheless, although small, practically all the observed differences are in the sense of a decrease in CDPBT at higher jet stagnation temperature. An increase in CDPBT is predicted by only one method, namely that of Kubn (contributor n° 5). In fact, a decrease in CDPBT with an increase in T_{t_j} / T_{t_∞} is predicted provided that the theoretical model takes into account the density variation caused by the temperature distribution across the jet mixing-layer (a consequence of point 2 of the above comment). The jet temperature effect has been more thoroughly examined by Radespiel [2.4.04] who carried out calculations for a ratio T_{t_j} / T_{t_∞} equal to 5 on the afterbody configuration of test cases 3 and 4. As shown by Fig. 2.4.5C for this higher value of the jet stagnation temperature, the effect on the boattail pressure distribution becomes clearly visible, the results plotted in Fig. 2.4.5A give the variation of CDPBT with T_{t_j} / T_{t_∞} as also an illustration of the effect of the turbulent Prandtl number considered in the modelling of the jet mixing-layer (calculations performed by Radespiel).

The decrease in boattail coefficient when the jet stagnation temperature increases is well confirmed by experimental results [2.4.05].

Test cases 5 and 6 illustrate the influence of wind tunnel blockage, the model geometry as well as the flow conditions being the same as for test case 3, for test case 5 the model is scaled for a 1% blockage and for test case 6 for a 8.06% blockage. For these two test cases, there is only one contribution using an IVI method of calculation (that of Radespiel contribution n° 8). There are two other contributions : one by Zobaïrs (contributor n° 9) which uses the BEM method and the other by Kinsey (Delft) (contributor n° 1) in which the Euler equations are solved. Experiment shows (see Fig. 2.4.6A) that there is a noticeable tunnel blockage effect only for test case 6, this effect being difficult to discern in test case 5. When comparing experiment with calculations it should be noted that the test case 5 calculations assume zero blocking although the test case 5 experiment was done in a wind tunnel with 1% blockage.

As shown by figs. 2.4.6B and 6C the method utilized by Radespiel gives a rather good prediction of the pressure distribution on the boattail. Also the pressure drag coefficient is fairly well predicted, credit being given to the rather large experimental and numerical uncertainty in the determination of this coefficient (see Figs. 2.4.7A and 8A). Agreement of contribution n° 9 with experiment is relatively poor. As expected, Euler calculations lead to a large overprediction of the pressure rise on the boattail extremity. It should be noted that a blockage effect of 8.06% (test case 6) is rather severe in the range of the ones met (see Fig. 2.4.7B), the change is observed both for experimental and calculated values. Thus with high tunnel blockage effect it is possible to obtain effects on the boattail.

2.4.2 Miscellaneous afterbodies

The last four test cases test cases 9 to 12 are in fact relevant to missile afterbodies. The tested models have a base whose area represents a noticeable fraction of the afterbody maximum cross-section. These models are equipped with a conical nozzle of semi-angle equal to 20° and whose nominal exit Mach number M_j is equal to 2.5. For all the tested configurations the external incoming stream is a supersonic uniform flow of Mach number M_∞ = 2.01. For test cases 9 and 10 the afterbody is cylindrical while it has a conical boattail (angle β_E = 16°) for test cases 11 and 12.

In such flows the extent of the separated region may be very large, so that this kind of flow is not easily amenable to a classical Inviscid-Viscous Interactive analysis in which it is implicitly assumed that the viscous part of the flow remains relatively thin and can be treated by a boundary-layer type analysis. For this reason no conventional IVI methods have been used to calculate test cases 9 to 12. The majority of contributions consist of applications of the Multi-Component Methods described § 2.4.1.3 above. As we know these methods are based on a rather schematic representation of the very complex real flow field. Consequently the only quantity that they claim to predict accurately is the pressure P_B acting on the base, plus for some of them the base temperature T_B in cases where the flows are not isoenergetic.

Due to the hyperbolic nature of the equations governing the two inviscid streams (namely external flow and nozzle flow) the pressure distribution on that part of the afterbody located upstream of the base does not depend on the base flow solution. Thus its determination can be done independently of the base pressure calculation itself by any convenient perfect fluid method, the Method of Characteristics for example. Eventually a boundary-layer displacement correction can be added to account for weak interaction effects. However this independence of the upstream flow on the base flow region is no longer true when there is large jet pluming since then the base pressure can become significantly higher than the pressure upstream of the base, so that separation may occur on the boattail. In this situation Multi-Component Methods generally predict also the location of the *separation point* (see § 2.4.1.3 above).

For test cases 9 to 12 the two Mach numbers M_∞ and M_j are the same and the nozzle geometry is unchanged. The varying parameters are the afterbody external shape and the Nozzle Pressure Ratio. Regarding the shape :

- test cases 9 and 10 have a cylindrical afterbody and

- test cases 11 and 12 have an afterbody with a conical boattail.

For each shape two values of the NPR are considered. However because of the very short computer time needed by Multi-Component Methods, the contributors have performed calculations for a larger number of NPR values in order to allow the tracing of curves giving continuously the variation of base pressure with the nozzle expansion ratio. Thus results are presented as curves giving the ratio P_B / P_∞ as a function of the pressure ratio P_j / P_∞, which is more commonly used than the NPR for missile afterbodies at supersonic speed.

Such curves for the cylindrical afterbody are represented in Fig. 2.4.60. The method of Addy has been employed by several contributors (n° 11, 12 and 13) who obtained of course identical results, so that these contributors have not been distinguished in the presentation of results. Also, two variants of Addy's method have been tested : one includes the empirical correction of the reattachment criterion accounting for axisymmetry effects (see § 2.4.1.3 above) ; the other uses the original Korst criterion.

At values of the expansion pressure ratio P_j / P_∞ less than 6, the best agreement with experiment is achieved by Délery's method and by the version of Addy's method which does not include the correction factor. This good agreement deteriorates at higher values of P_j / P_∞. Thus for P_j / P_∞ greater than 6 the best agreement with experiment is progressively achieved by Wagner's method. The flow model of Moulden (contributor n° 15) underpredicts the base pressure as soon as P_j / P_∞ is above 3, the discrepancy between theory and experiment increasing steadily as P_j / P_∞ increases. However, it should be said that the calculations of contributor n°15 have been done at a Mach number of 2 as this is the maximum speed for which the program of Moulden is applicable.

Results for the afterbody with boattail are represented in Fig. 2.4.61. For this case all the methods tend to underpredict the base pressure. Wagner's method provides the best prediction for values of P_j / P_∞ less than 8. For the present test case, separation is detected on the boattail. Délery's method predicts occurence of separation at the base for P_j / P_∞ close to 9 whereas according to Wagner's method separation occurs as soon as P_j / P_∞ is equal to 3. Such a large difference in the prediction of separation can be attributed in part to the definition adopted to define the appearance of separation : thus in the method employed by Délery, occurence of separation corresponds to the establishment of a well developed separated region ; on the other hand Wagner's method predicts occurence of "true" incipient separation at the boattail extremity, the situation corresponding to the first appearance of a tiny zone of reversed flow along the boattail.

Figures 2.4.62 and 63 give the same results in the form of the base pressure coefficient CPB. The bar graphs of the base pressure drag coefficient for all contributions and for conditions corresponding to test cases 9 and 12 are represented in Figs. 2.4.64 and 65. These bar graphs include Euler calculations and also Navier-Stokes calculations.

2.4.4 - *References* -

2.4.1 - Zannetti, L. "Transonic Flow Field in 2D or Axisymmetric Convergent Nozzles." Proc. 2nd GAMM Conf. on Numerical Meth. in Fluid Mech., DFVLR, pp. 2136-2138 (1977).

2.4.2 - Zannetti, L. "Time-Dependent Method to Solve the Inverse Problem for Internal Flows." AIAA Journal, Vol. 18, n° 7, pp. 754-758 (July 1980).

2.4.3 - Moretti, G. "The λ -Scheme." Computer and Fluids, Vol. 7 (1979).

2.4.4 - Zannetti, L. and Colasurdo, G. "Unsteady Compressible Flow : A Computational Method Consistent with the Physical Phenomena." AIAA Journal, Vol. 19, n° 7, pp. 852-856 (July 1981).

2.4.5 - Zannetti, L. and Moretti, G. "Numerical Experiments on the Leading Edge Flow Field." AIAA Paper n° 81-1011 (July 1981).

2.4.6 - Moretti, G. and Zannetti, L. "A New Improved Computational Technique for 2D Unsteady Compressible Flows." AIAA Paper N° 82-0168 (Jan. 1982).

2.4.7 - Zannetti, L. and Onofri, M. "Aerodynamics of Aircraft After-Body : Numerical Simulation." AIAA Paper n° 84-0284 (Jan. 1984).

2.4.8 - Carrière, P. "Calcul numérique d'un écoulement compressible stationnaire (x,y) comme limite d'un écoulement instationnaire (x,y,t)." C.R. Acad. Sc. Paris, t. 266, pp. 1015-1018 (May 1968).

2.4.9 - Viviand, H. and Veuillot, J.P. "Méthodes pseudo-instationnaires pour le calcul d'écoulements transsoniques." ONERA Pub. n° 1978-4 ; English translation ESA TT 561 (1978).

2.4.10 - Cambier, L., Ghazzi, W., Veuillot, J.P. and Viviand, H. "Une approche par domaines pour le calcul d'écoulements compressibles." Computing Methods in Applied Sciences and Engineering V, Editors : Glowinski, R. and Lions, J.L. North-Holland (1982).

2.4.11 - Eberle, A. "Similarity Transformation of the Euler Equations and their Numerical Evaluation." MBB UFE 122-AERO-MT-069 (1983).

2.4.12 - Zacharias, A. "Der Strahlinduktionskanal des Instituts fur Entwurfsaerodynamik der DFVLR Braunschweig (SIB)." DFVLR IB 129-81/13.

2.4.13 - Brebbia, C.A. "The Boundary Element Method for Engineers." Pentech Press, London (1978).

2.4.14 - Zacharias, A. "An Experimental and Theoretical Investigation of the Interaction between the Engine Jet and the Surrounding Flow Field with Regard to the Pressure Drag on Afterbodies." Monograph CP-308 on "Fluid Dynamics of Jets with Application to V/STOL." (Jan. 1982).

2.4.15 - Cambier, L., Ghazzi, W., Veuillot, J.P. and Viviand, H. "A Multi-Domain Approach for the Computation of Viscous Transonic Flows by Unsteady Type Methods." Recent Advances in Numerical Methods in Fluids, Vol. 3, W.G. Habashi editor, Pineridge Press, U.K. (1983).

2.4.16 - Stanewsky, E., Nandanan, M. and Inger, G.R. "The Coupling of a Shock/Boundary Layer Interaction Module with a Viscous-Inviscid Computation Method." AGARD CP-291 (1981).

2.4.17 - Wilmoth, R.G. "RAXJET : A Computer Program for Predicting Axisymmetric Flow over Nozzle Afterbodies with Supersonic Jet Exhaust." NASA TM-83235 (1982).

2.4.18 - South, J.C., Jr. and Jameson, A. "Relaxation Solutions for Inviscid Axisymmetric Transonic Flow Over Blunt or Pointed Bodies." AIAA Computational Fluid Dynamics Conference, pp. 54-64 (July 1973).

2.4.19 - Dash, S.M., Pergament, H.S. and Thorpe, R.D. "Computational Models for the Viscous-Inviscid Analysis of Jet Aircraft Exhaust Plumes." NASA CR-3289 (1980).

2.4.20 - Abbett, M. "Mach Disk in Underexpanded Exhaust Plumes." AIAA Journal, Vol. 9, n° 3, pp. 512-514 (March 1971).

2.4.21 - Reshotko, E. and Tucker, M. "Approximate Calculation of the Compressible Turbulent Boundary Layer With Heat Transfer and Arbitrary Pressure Gradient." NACA-TN-4154 (1957).

2.4.22 - Presz, W.M., Jr., King, R.W. and Buteau, J.D. "An Improved Analytical Model of the Separated Region on Boattail Nozzles at Subsonic Speeds." NASA CR-3028 (1978).

2.4.23 - Korst, H.H. and Chow, W.L. "Compressible Non-Isoenergetic Two-Dimensional Turbulent (Pr_t = 1) Jet Mixing at Constant Pressure -Auxiliary Integrals- Heat Transfer and Friction Coefficients for Fully Developed Mixing Profiles." University of Illinois, ME-TN-39204 (1962).

2.4.24 - Dash, S.M. and Pergament, H.S. "A Computational Model for the Prediction of Jet Entrainment in the Vicinity of Nozzle Boattails (The BOAT Code)." NASA CR-3075 (1978).

2.4.25 - Kuhn, G.D. "Computer Program for Calculation of Separated Turbulent Flows on Axisymmetric Afterbodies." AEDC TR-77-72 (1972).

2.4.26 - Kuhn, G.D. "Computer Program for Calculation of Separated Turbulent Flows on Axisymmetric Afterbodies Including Exhaust Plume Effects." AEDC TR-79-4 (1979) ; see also AIAA Journal, Vol. 18, n° 3, pp. 235-241 (March 1980).

2.4.27 - Kuhn, G.D. "An Improved Interaction Method for Calculating Exhaust Nozzle Boattail Flows." AEDC TR-80-19 (1980) ; see also AIAA Journal, Vol. 19, n° 3, pp. 358-360 (March 1981).

2.4.28 - Keller, J.D. and South, J.C., Jr. "RAXBOD : A FORTRAN Program for Inviscid Transonic Flow Over Axisymmetric Bodies." NASA TM-X-73831 (1976).

2.4.29 - Peters, C.E., Phares, W.J. and Cunningham, T.H.M. "Theoretical and Experimental Studies of Ducted Mixing and Burning of Coaxial Streams." Journal of Spacecraft and Rockets, Vol. 6, n° 12, pp. 1435-1441 (Dec. 1969).

2.4.30 - Carter, J.E. "A New Boundary-Layer Iteration Technique for Separated Flow." AIAA Paper n° 79-1450 (July 1979).

2.4.31 - Hodges, J. "A Method for Calculating Subsonic Flows Over Axisymmetric Afterbodies, Including Viscous and Jet Effects." RAE TR-82097 (1982).

2.4.32 - Putnam, L.E. and Hodges, J. "Assessment of NASA and RAE Viscous-Inviscid Interaction Methods for Predicting Transonic Flow Over Nozzle Afterbodies." AIAA Paper n° 83-1789 (July 1983).

2.4.33 - Hess, J.L. and Smith, A.M.O. "Calculation of Potential Flow About Arbitrary Bodies." Progress in Aeronautical Sciences, Vol. 8, pp. 1-138, Pergamon Press (1967).

2.4.34 - Kuchemann, D. "A Simple Rule for the Velocity Rise with Subsonic Mach Number on Ellipsoids of Revolution." J. of Aero. Sci., Vol. 18, n° 11, pp. 770 (Nov. 1951).

2.4.35 - Green, J.E., Weeks, D.J. and Brooman, J.W.F. "Prediction of Turbulent Boundary-Layers and Wakes in Incompressible Flow by a Lag-Entrainment Method." RAE TR-72231 (1973).

2.4.36 - Dutouquet, L. and Hardy, J.-M. "Engine Aerodynamic Installation by Numerical Simulation." AIAA Paper n° 80-0108 (Jan. 1980).

2.4.37 - Hardy, J.-M. and Dutouquet, L. "Etude de l'écoulement multiflux par juxtaposition de processus numériques." L'Aéronautique et l'Astronautique,n° 90 (1981).

2.4.38 - Patankar, S.V. and Spalding, D.B. "Heat and Mass Transfer in Boundary-Layers." 2nd Edition, Intertext, London (1970).

2.4.39 - Ferguson, D.R. and Keith, J.S. "Modifications to the Streamtube Curvature Program." NASA CR-132705 (1975).

2.4.40 - Spalding, D.B. "GENMIX - A General Computer Program for Two-Dimensional Parabolic Phenomena." HMT Series, Vol I, Pergamon Press (1977).

2.4.41 - Radespiel, R. "Turbulenzmodell für die Berechnung von Triebwerksstrahlen." DFVLR IB 129-21/82 (1982).

2.4.42 - Korst, H.H. "A theory for Base Pressure in Transonic and Supersonic Flow." J. Appl. Mech., 23, pp. 593-600 (1953).

2.4.43 - Chapman, D.R., Kuehn, D.M. and Larson, H.K. "Investigation of Separated Flows in Supersonic and Subsonic Streams with Emphasis on the Effect of Transition." NACA TR 1356 (1958).

2.4.44 - Délery, J. and Sirieix, M. "Base Flow Behind Missiles." AGARD LS-98 (1979).

2.4.45 - Délery, J. "ONERA Research on Afterbody Viscous/Inviscid Interactions with Special Emphasis on Base Flow Problems." Proc. of the "Symposium on Rocket/Plume Fluid Dynamic Interactions", Vol. III, Fluid Dynamics Laboratories Report 83-104, The University of Texas at Austin (April 1983) ; see also ONERA TP n° 1983-26.

2.4.46 - Carrière, P. and Sirieix, M. "Facteurs d'influence du recollement d'un écoulement supersonique." 10th International Congress of Applied Mechanics, Stresa, Italy (1960).

2.4.47 - Kirk, F.N. "An Approximate Theory for Base Pressure in Two-Dimensional Flow at Supersonic Speed." RAE TN Aero n° 3377 (1959).

2.4.48 - Sirieix, M. and Solignac J.-L. "Contribution à l'étude expérimentale de la couche de mélange turbulent isobare d'un écoulement supersonique." AGARD CP-4 (1966).

2.4.49 - Solignac, J.-L. and Délery, J. "Contribution à l'étude aérodynamique des systèmes propulsifs à double flux." Israel Journal of Technology, Vol. 10, n° 1-2, pp. 97-111 (1972).

2.4.50 - Reshotko, E. and Tucker, M. "Effect of a Discontinuity on a Turbulent Boundary-Layer Thickness Parameters with Application to Shock-Induced Separation." NACA TN-3454 (1955).

2.4.51 - Settles, G.S. "An Experimental Study of Compressible Turbulent Boundary-Layer Separation at High Reynolds Number." Ph. D. Dissertation, Aerospace and Mechanical Sciences Dept., Princeton University (Sept. 1975).

2.4.52 - Zukoski, E.E. "Turbulent Boundary-Layer Separation in Front of a Forward Facing Step." AIAA Journal, Vol. 5, n° 10, pp. 1746-1753 (Oct. 1967).

2.4.53 - Addy, A.L. "Analysis of the Axisymmetric Base Pressure and Base Temperature Problem with Supersonic Interacting Freestream-Nozzle Flows Based on the Flow Model of Korst et al." Parts I to III, Report n° RD-TR-69-12, U.S. Army Missile Command, Redstone Arsenal, Ala. (1969).

2.4.54 - Addy, A.L. "Experimental-Theoretical Correlation of Supersonic Jet-on Base Pressure for Cylindrical Afterbodies." Journal of Aircraft, Vol. 7, n° 5 (May 1970).

2.4.55 - Wagner, B. and White, R.A. "Influence of Fundamental Parameters on the Supersonic Base Flow Problem in Presence of an Exhaust Jet." AIAA Paper n° 79-0133 (Jan. 1979).

2.4.56 - Wagner, B. and White, R.A. "Supersonic Base Flow Problem in Presence of an Exhaust Jet." AIAA Journal, Vol. 18, n° 8, pp. 876-882 (Aug. 1980).

2.4.57 - Wagner, B. "Jet-Afterbody Interference on Missiles in Supersonic Flow." AGARD CP-307 (1981).

2.4.58 - Nash, J.F. "An Analysis of Two-Dimensional Turbulent Base Flow Including the Effect of the Approaching Boundary-Layer." ARC R&M n° 3344 (1962).

2.4.59 - Korst, H.H. and Tripp, W. "The Pressure on a Blunt Trailing Edge Separating Two Supersonic Two-Dimensional Air Streams of Different Mach Number and Stagnation Pressure but Identical Stagnation Temperature." Proc. of the 5th Midwestern Conference on Fluid Mechanics (1957).

2.4.60 - White, R.A. and Agrell, J. "Boattail and Base Pressure Prediction Including Flow Separation for Afterbodies with a Centered Propulsive Jet and Supersonic External Flow at Small Angle of Attack." AIAA Paper n° 77-958 (July 1977).

2.4.61 - Moulden, T.H. "Guide to the Operation of the MICOM/UTSI Computer Program for Plume Induced Separation at Transonic Speeds : Version 2." Report n° TR-RD-CR-81-2, U.S. Army Missile Command, Redstone Arsenal, Ala.

2.4.62 - Moulden, T.H. "U.S. MICOM/UTSI Computer Program for Plume Induced Separation at Transonic Speeds." (Viewgraph and additional material from the Workshop held at Redstone Arsenal on September 19-20, 1982. The University of Tennessee Space Institute).

2.4.63 - Aulehla, F. and Besigk, G. "Comment on "Afterbody Configuration Effect on Models Forebody and Afterbody Drag." AIAA Journal, Vol. 19, pp. 798-799 (Sept. 1982).

2.4.64 - Radespiel, R. Communication at the AGARD FDP WG08 meeting held at NASA-Langley (June 19-21, 1984).

2.4.65 - Robinson, C.E. and High, M.D. "Exhaust Plume Temperature Effects on Nozzle Afterbody Performance Over the Transonic Mach Number Range", AEDC-TR-74-9 (July 1974).

	Contributor	Organization	Method	1	2	2A	3	4	5	6	7	8	9	10	11	12
1	ZANNETTI-ONOFRI	Polit. Turin	EULER	X							X					
2	VUILLOT-VEUILLOT	ONERA	EULER	X	X	X	X									
3	BISSINGER-EBERLE	MBB-UF	EULER	X	X	X	X		X	X			X		X	
4	PUTNAM-WILMOTH	NASA	I.V.I.	X	X	X	X	X								
5	KUHN	NIELSEN Eng.	I.V.I.	X	X		X	X								
6	HODGES	RAE	I.V.I.	X	X	X	X	X								
7	HARDY-DUTOUQUET	SNECMA	I.V.I.	X	X	X	X									
8	RADESPIEL	DFVLR	I.V.I.	X			X	X	X	X						
9	ZACHARIAS	MBB-UF	B.E.M.	X	X	X	X	X	X	X						
10	DELERY	ONERA	M.C.M.										X	X	X	X
11	LACAU-BERRUE	AEROSPATIALE	M.C.M.										X	X	X	X
12	ADDY	U. of Ill.	M.C.M.										X	X	X	X
13	MOORE	BAe	M.C.M.								X		X	X	X	X
14	WAGNER	Dornier	M.C.M.										X	X	X	X
15	MOORE	BAe	M.C.M.								X		X	X	X	X
16	WAGNER	Dornier	N.S.	X	X	X	X				X	X	X		X	
17	DEIWERT	NASA	N.S.	X	X		X	X			X	X	X	X	X	X
18	FORESTER-KERN	Boeing	N.S.		X											X

EULER : solution of Euler equations
I.V.I. : Inviscid/Viscous Interactive method
B.E.M. : Boundary Element Method
M.C.M. : Multi Component Method
N.S. : solution of Navier-Stokes equations

Table I : COMPUTATIONAL TEST CASE PARTICIPATION

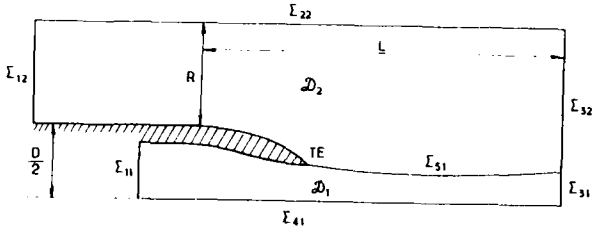

Fig. 2.4.1. – Computational domain for solution of the Euler equations.

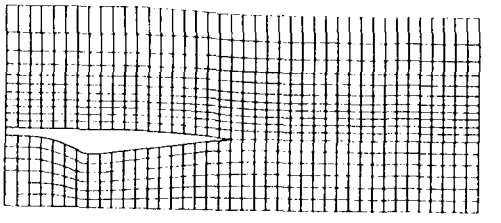

Fig. 2.4.2 – Example of mesh definition employed by Zanneti and Onofri. Test case 7.

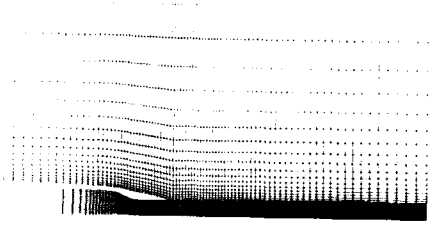

Fig. 2.4.3 – Example of mesh definition employed by Vuillot and Veuillot. Test case 1.

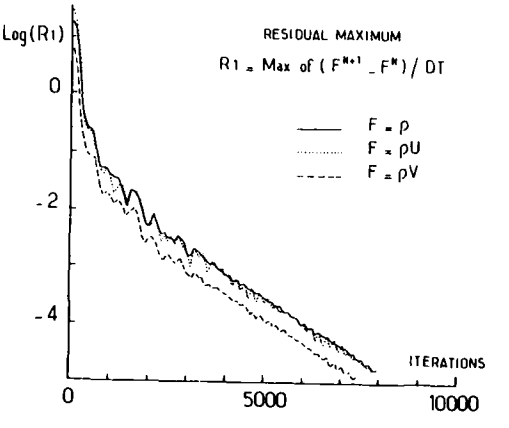

Fig. 2.4.4 – Example of convergence history Vuillot and Veuillot contribution. Test case 2.

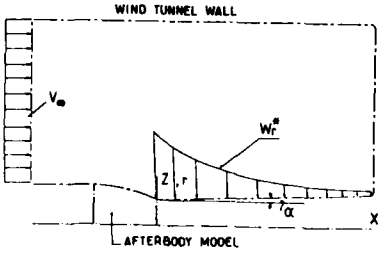

Fig. 2.4.5 – Zacharias contribution. Description of free stream and jet boundary conditions.

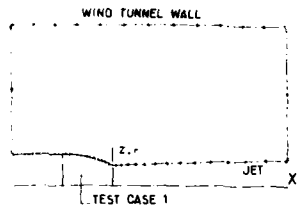

Fig. 2.4.6 – Zacharias contribution definition of boundary element mesh.

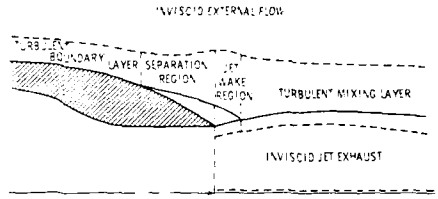

Fig. 2.4.7 – The inviscid-viscous interaction approach. The various computational regions.

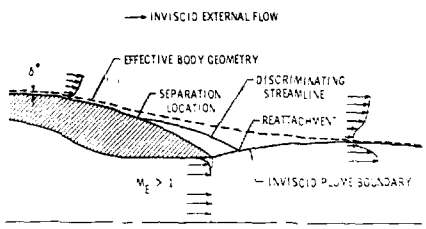

Fig. 2.4.8 – The Raxjet code. Schematization of the nozzle afterbody flowfield.

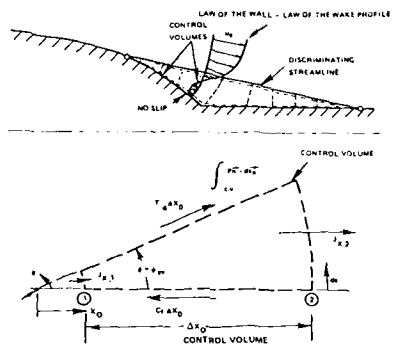

Fig. 2.4.9 – The Raxjet code. Model for calculation of the separated flow region.

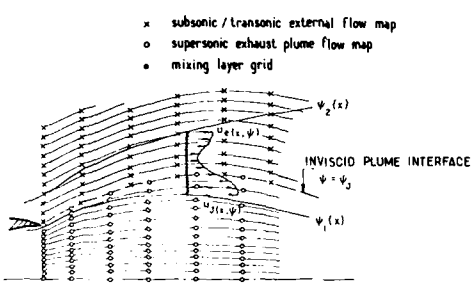

Fig. 2.4.10 – The Raxjet code. The overlaid mixing analysis for the calculation of the jet mixing layer.

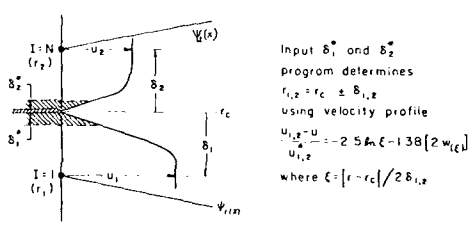

Fig. 2.4.11 – The Raxjet code. Initial velocity distributions for the mixing-layer calculation.

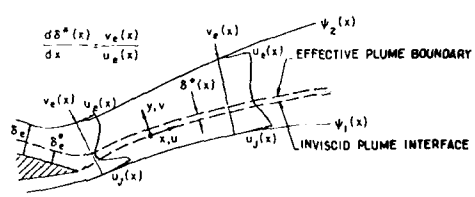

Fig. 2.4.12 – The Raxjet code. Representation of the displacement effect arising from the jet entrainment effect.

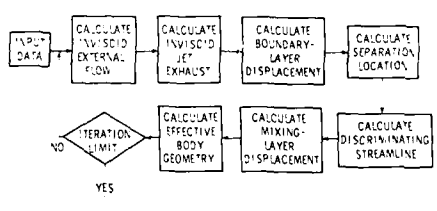

Fig. 2.4.13 – The Raxjet code. The inviscid viscous iteration scheme.

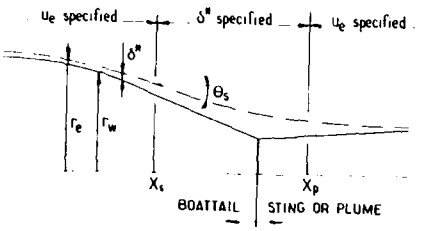

Fig. 2.4.14 – Kuhn contribution. Effective body shape for separated flow.

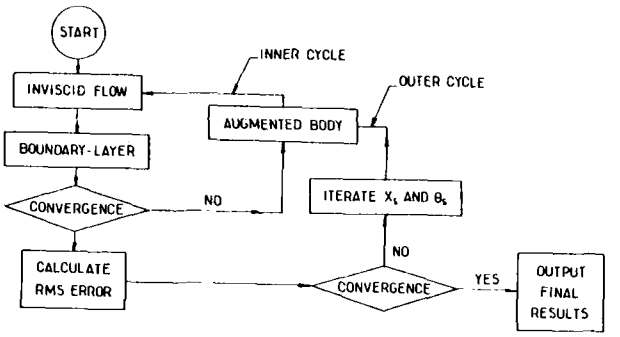

Fig. 2.4.15 – Kuhn contribution. The inviscid viscous iteration scheme.

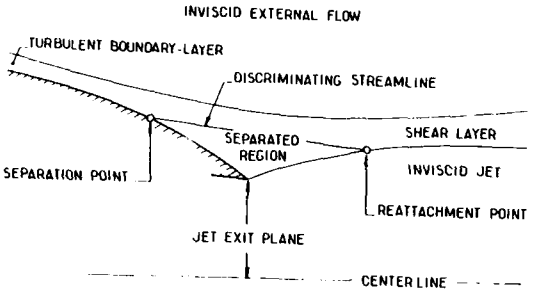

Fig. 2.4.16 – Hodges contribution. The different computational regions.

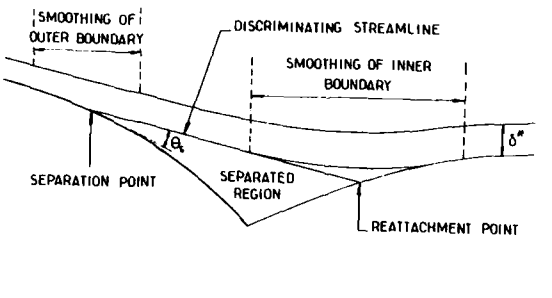

Fig. 2.4.17 – Hodges contribution. Details of the separation model.

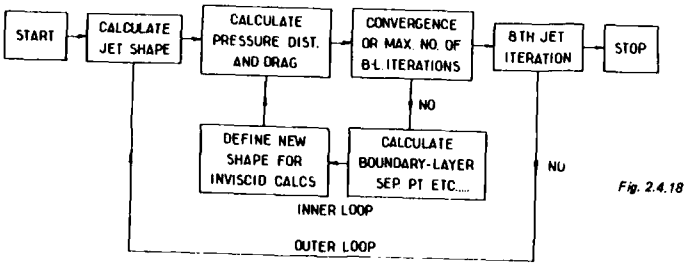

Fig. 2.4.18 – Hodges contribution. The inviscid viscous iteration scheme.

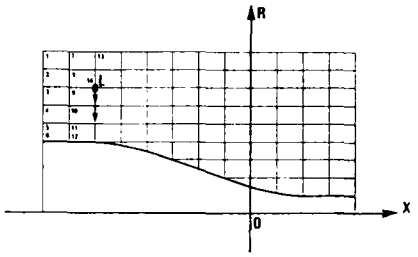

Fig. 2.4.19a –
Hardy-Dutouquet contribution. Mesh topology for external flow.

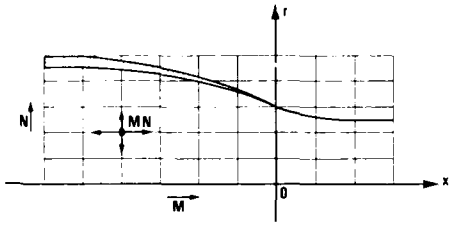

Fig. 2.4.19b –
Hardy-Dutouquet contribution. Mesh topology for nozzle flow.

Fig. 2.4.20 – Radespiel contribution. Test case 1. Example of mesh constitution.

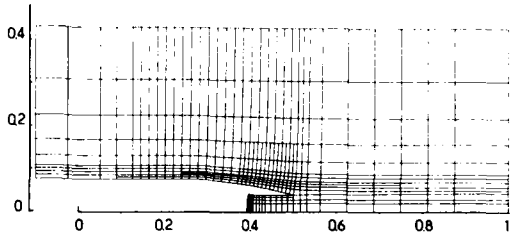

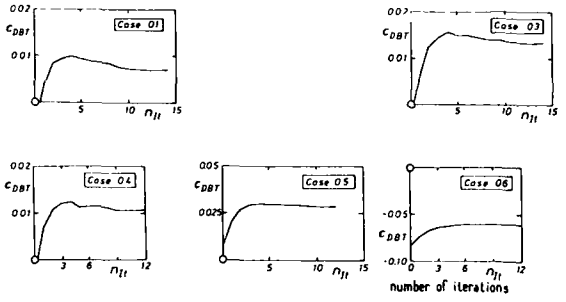

Fig. 2.4.21 – Radespiel contribution. Convergence history.

Fig. 2.4.22 – Schematic representation of base flow region.

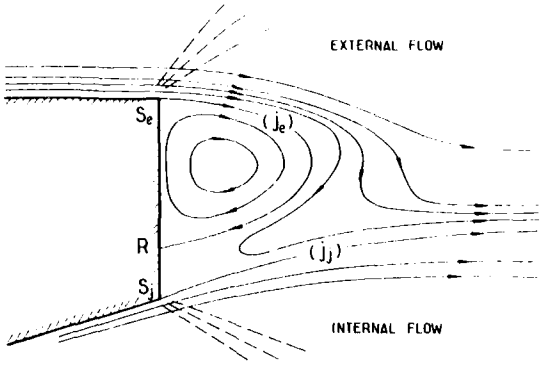

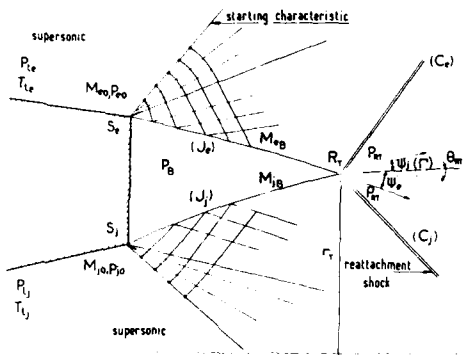

Fig. 2.4.23 – The corresponding inviscid flow model.

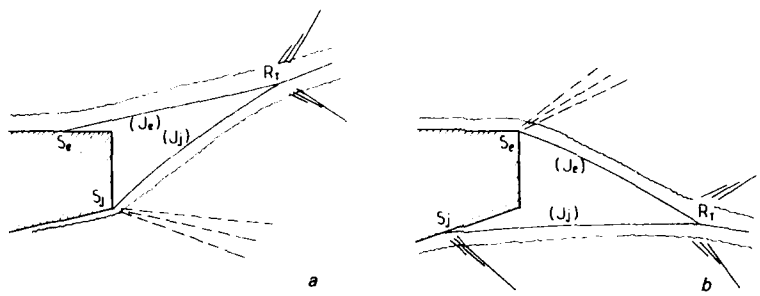

Fig. 2.4.24 – Base flow models for separation on the afterbody or inside the nozzle.
a) under expanded nozzle flow ; b) over-expanded nozzle flow.

Fig. 2.4.25 – Reattachment angle definition.
a) inviscid flow ; b) viscous flow.

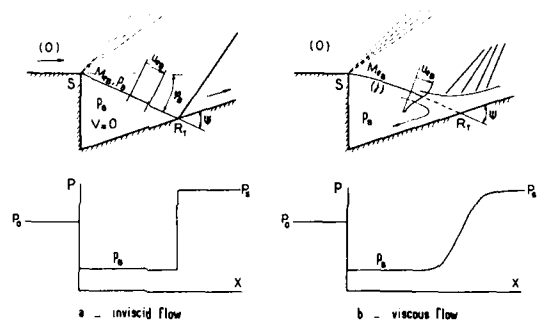

1 initial condition – expansion at base
2 intermediate step – expansion at base
3, 4 intermediate step – shock at base
5 final solution for attached flow – shock at base

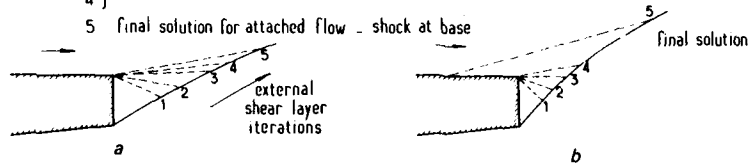

Fig. 2.4.26 – Moulden method convergence procedure.
a) attached flow (solution for all cases examined) ; b) solution for a separated flow case.

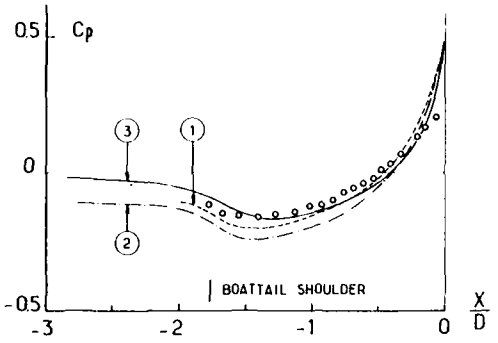

Fig. 2.4.27 – Euler calculations. Test case 1. Boattail wall pressure coefficient. (Numbers refer to contributor n° in Table I).

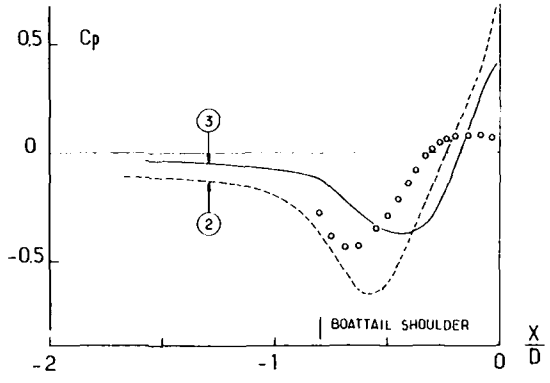

Fig. 2.4.28 – Euler calculations. Test case 2. Boattail wall pressure coefficient.

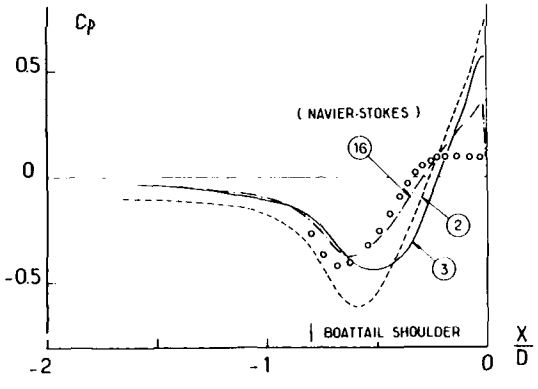

Fig. 2.4.29 – Euler calculations. Test case 2a. Boattail wall pressure coefficient.

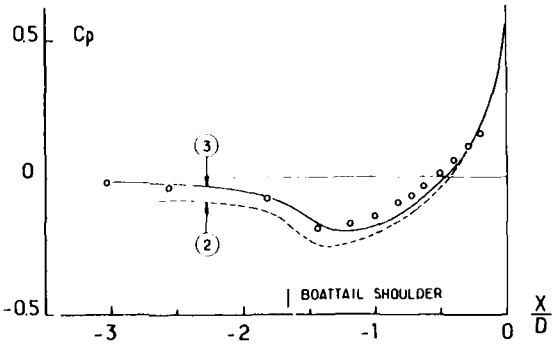

Fig. 2.4.30 – Euler calculations. Test case 3. Boattail wall pressure coefficient.

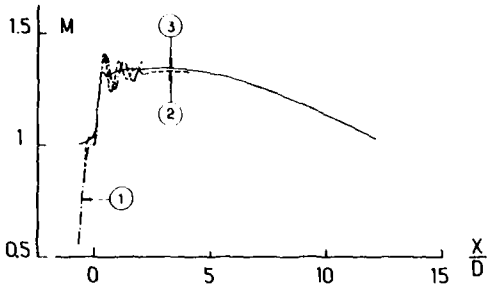

Fig. 2.4.31 – Euler calculations. Test case 1. Mach number distribution on jet centerline.

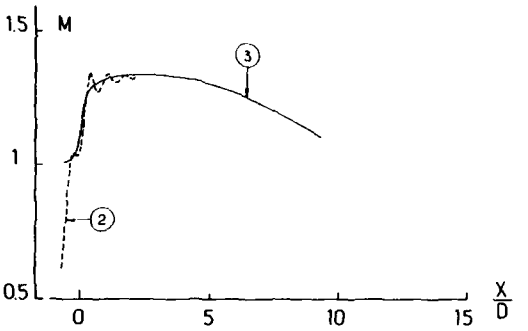

Fig. 2.4.32 – Euler calculations. Test case 2. Mach number distribution on jet centerline.

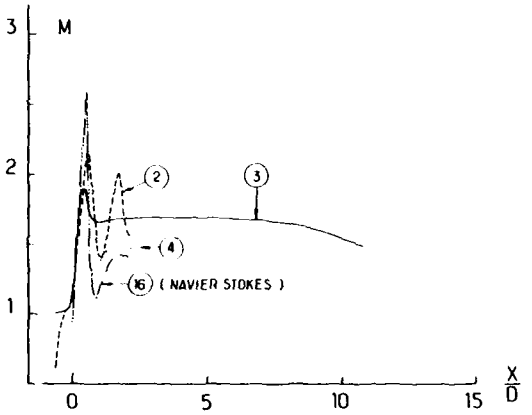

Fig. 2.4.33 – Euler calculations. Test case 2a. Mach number distribution on jet centerline.

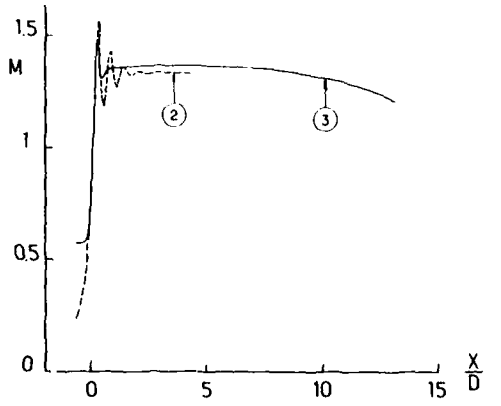

Fig. 2.4.34 – Euler calculations. Test case 3. Mach number distribution on jet centerline.

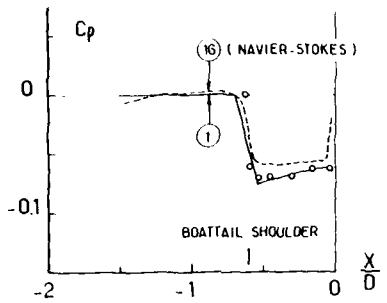

Fig. 2.4.35 – Euler calculations. Test case 7. Boattail wall pressure coefficient.

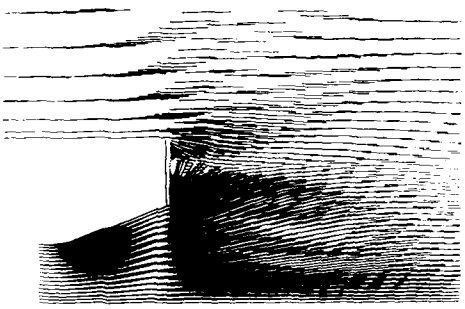

Fig. 2.4.36 – Test case 9. Velocity vectors,Bissinger/Eberle Euler solution.

Fig. 2.4.37 – Test case 11. Velocity vectors,Bissinger/Eberle Euler solution.

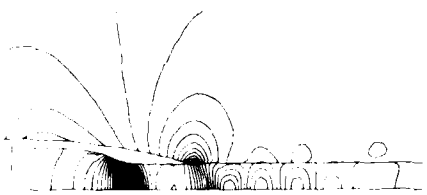

Fig. 2.4.38 – Test case 1 – Inviscid flowfield structure (contributors n° 2 calculation).

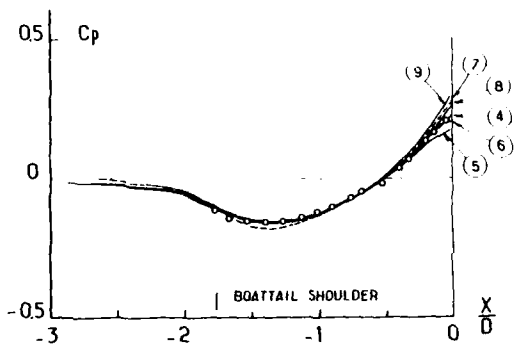

Fig. 2.4.39 – Inviscid-viscous interactive (IVI) calculations. Test case 1. Boattail wall pressure coefficient.

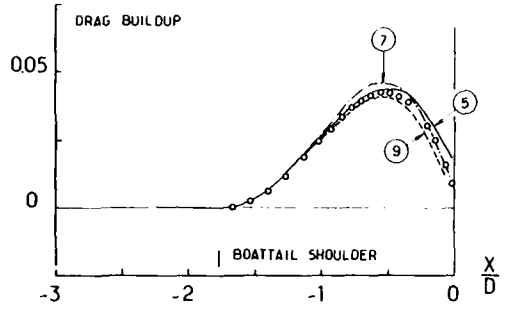

Fig. 2.4.40 – IVI calculations. Test case 1. Drag buildup along boattail.

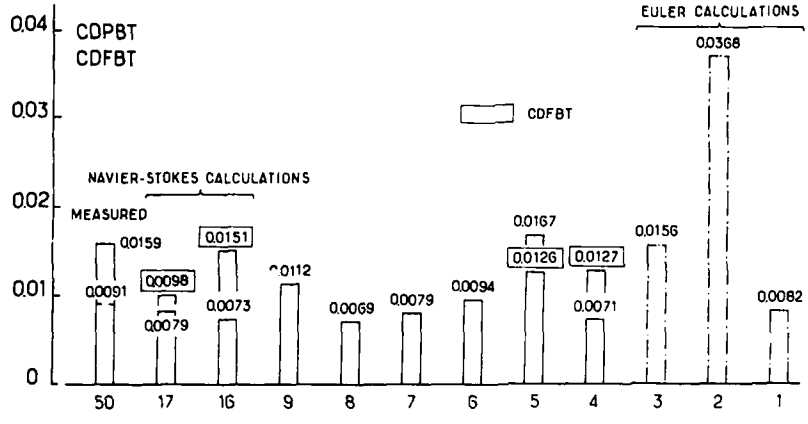

Fig. 2.4.41 – IVI calculations. Test case 1. Bar graph of boattail pressure and friction drag coefficients.

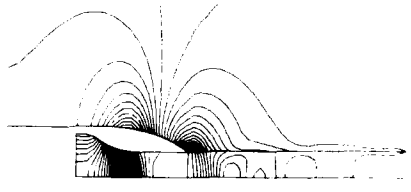

Fig. 2.4.42 – Test case 2. Inviscid flowfield structure (contributors n° 2 calculation).

Fig. 2.4.43 – IVI calculations. Test case 2. Boattail wall pressure coefficient.

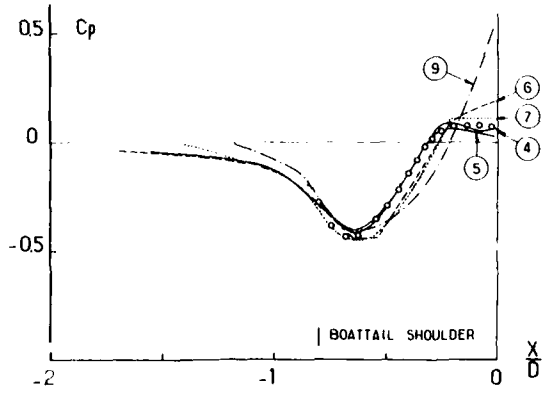

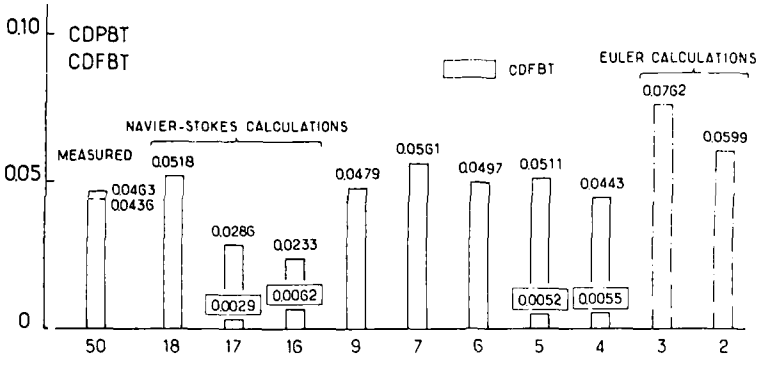

Fig. 2.4.44 – IVI calculations. Test case 2. Bar graph of boattail pressure and friction drag coefficients.

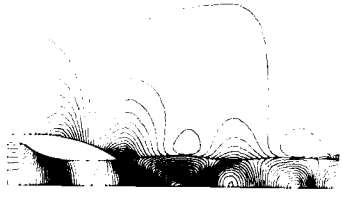

Fig. 2.4.45 – Test case 2a. Inviscid flowfield structure (contributors n° 2 calculation).

Fig. 2.4.46 – IVI calculations. Test case 2a. Boattail wall pressure coefficient.

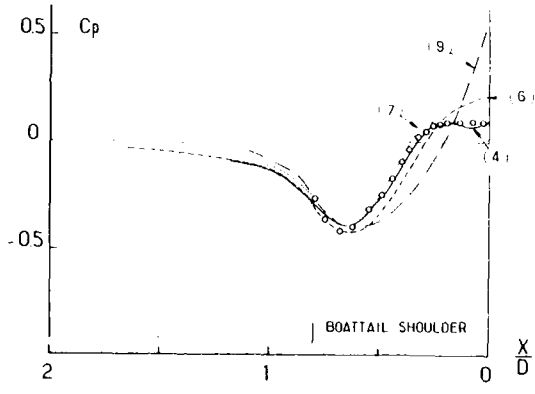

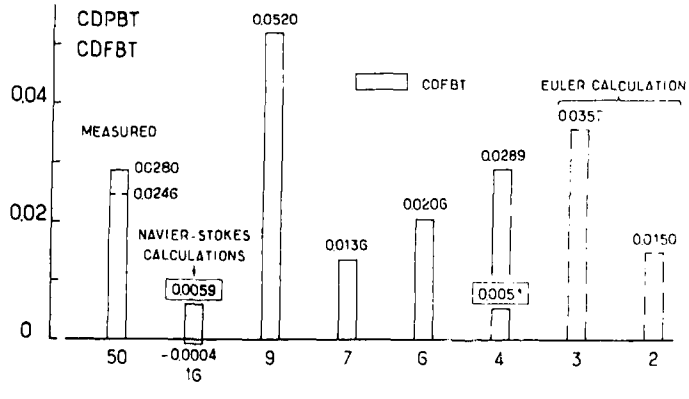

Fig. 2.4.47 – IVI calculations. Test case 2a. Bar graph of boattail pressure and friction drag coefficients.

AD-A172 341 REPORT OF THE WORKING GROUP ON AERODYNAMICS OF AIRCRAFT AFTERBODY(U) ADVISORY GROUP FOR AEROSPACE RESEARCH AND DEVELOPMENT NEUILLY-SUR-SEINE (FRANCE) JUN 86 3/4

UNCLASSIFIED AGARD-AR-226 F/G 20/4 NL

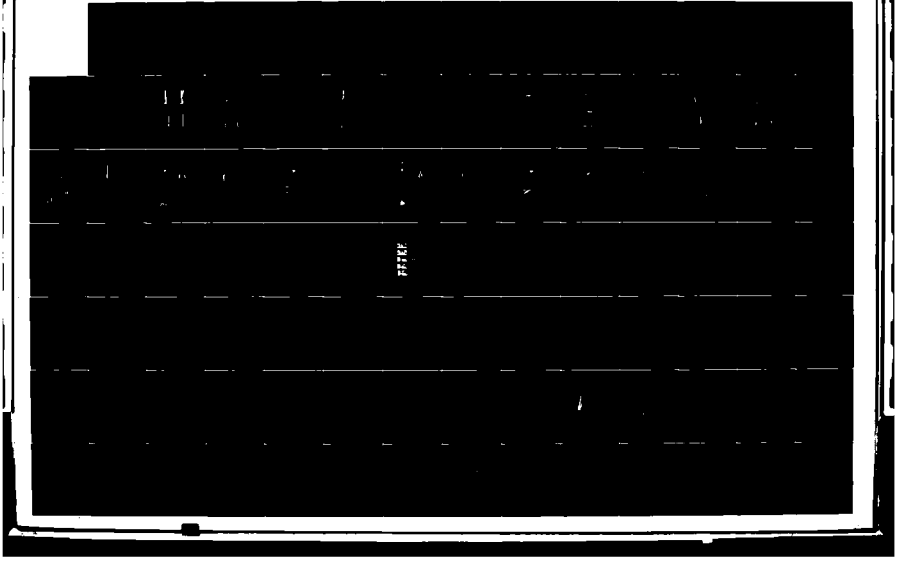

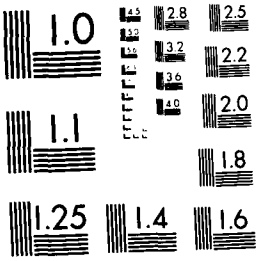

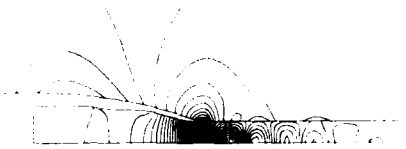

Fig. 2.4.48 – Test case 3. Inviscid flowfield structure (contributors n° 2 calculation).

Fig. 2.4.49 – IVI calculations. Test case 3. Boattail wall pressure coefficient.

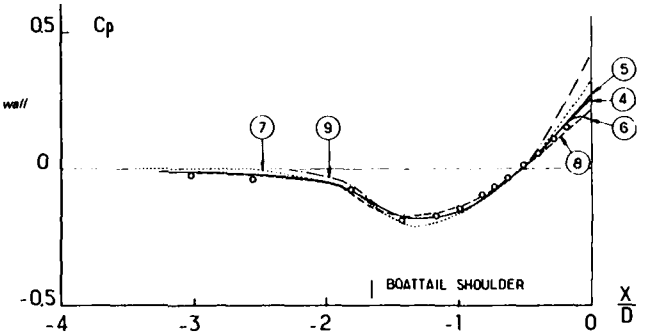

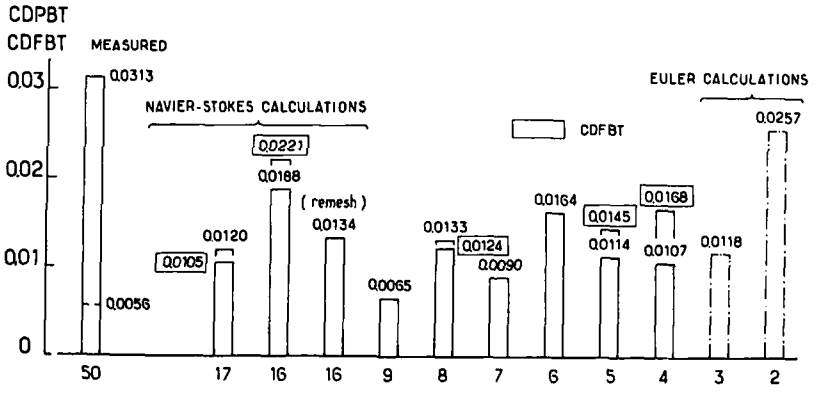

Fig. 2.4.50 – IVI calculations. Test case 3. Bar graph of boattail pressure and friction drag coefficients.

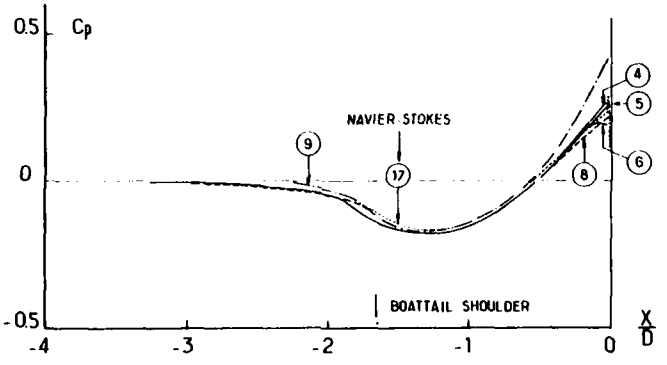

Fig. 2.4.51 – IVI calculations. Test case 4 (jet temperature effect). Boattail wall pressure coefficient.

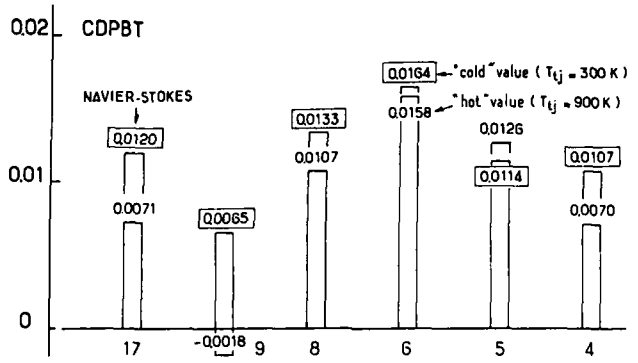

Fig. 2.4.52 – IVI calculations. Test case 4 (jet temperature effect). Bar graph of boattail pressure drag coefficient.

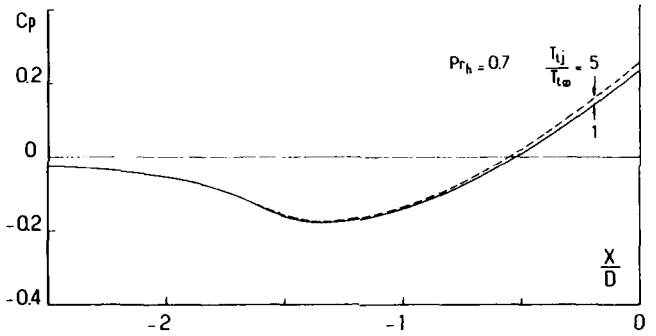

Fig. 2.4.53 – IVI calculations by Radespiel. Test case 4, geometry. Effect of jet temperature on the boattail wall pressure coefficient.

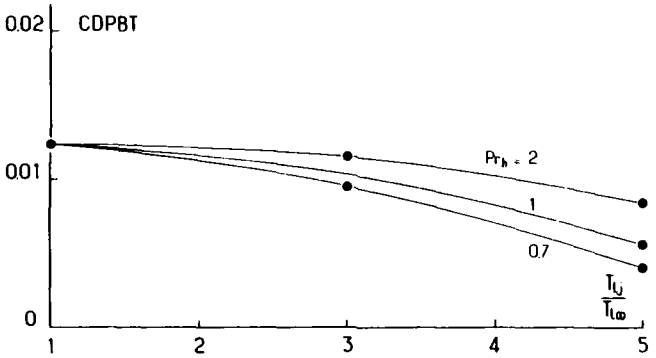

Fig. 2.4.54 – IVI calculations by Radespiel. Test case 4, geometry. Effect of jet temperature and turbulent Prandtl number on the boattail pressure drag coefficient.

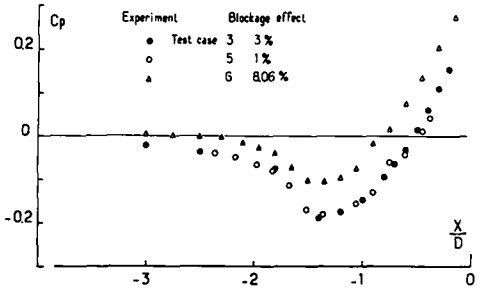

Fig. 2.4.55 – Test cases 5 and 6. Experimental distributions of boattail wall pressure coefficient. Tunnel blockage effect.

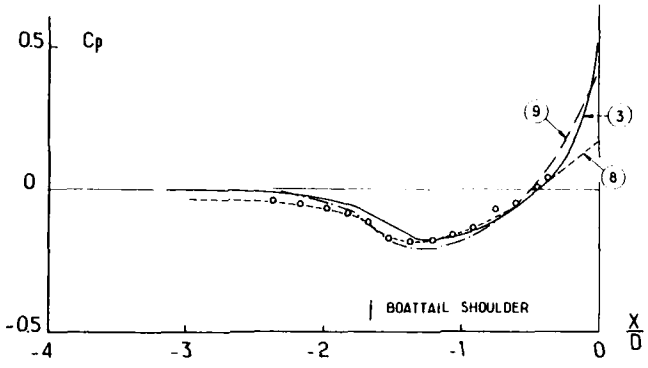

Fig. 2.4.56 – IVI calculations. Test case 5. Boattail wall pressure coefficient.

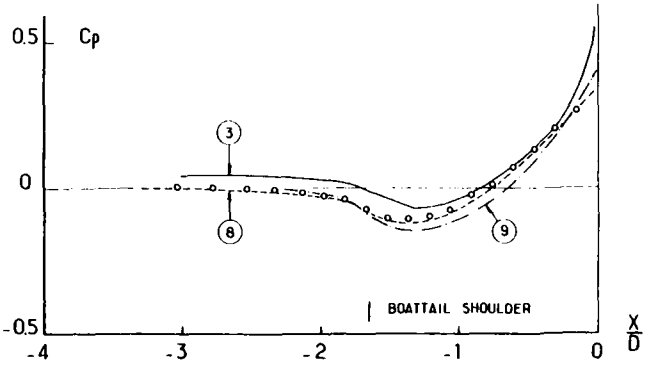

Fig. 2.4.57 – IVI calculations. Test case 6. Boattail wall pressure coefficient.

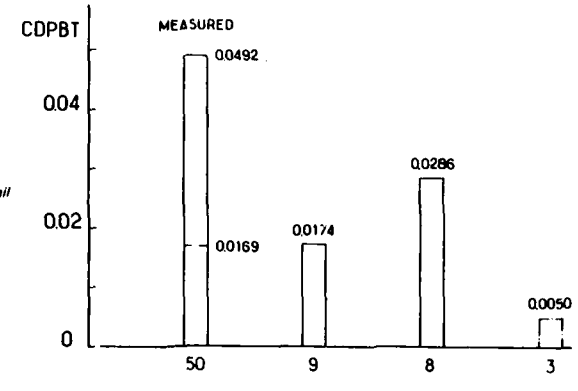

Fig. 2.4.58 – IVI calculations. Test case 5. Bar graph of boattail pressure drag coefficient.

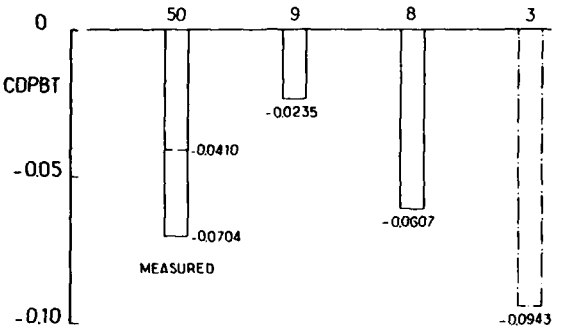

Fig. 2.4.59 – IVI calculations. Test case 6. Bar graph of boattail pressure drag coefficient.

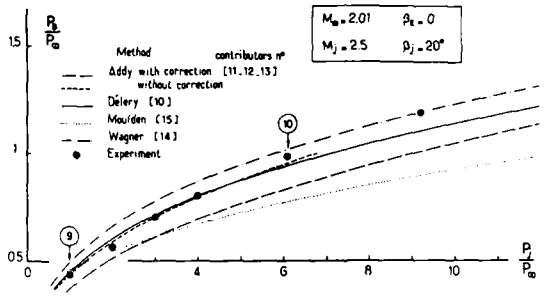

Fig. 2.4.60 – Application of MCM's to base flows. Base pressure variation with nozzle expansion ratio. Test cases 9 and 10 configuration (cylindrical afterbody).

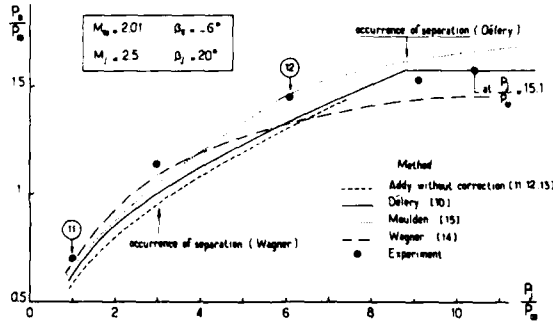

Fig. 2.4.61 – Application of MCM's to base flows. Base pressure variation with nozzle expansion ratio. Test cases 11 and 12 configuration (conical boattail).

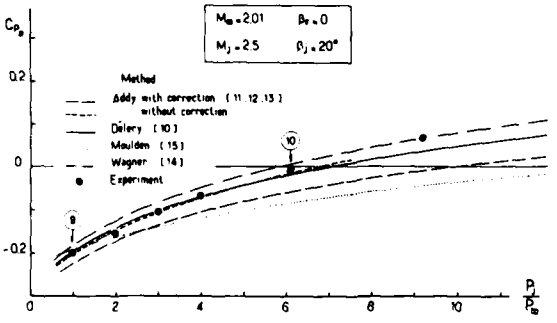

Fig. 2.4.62 – Application of MCM's to base flows. Base pressure variation with nozzle expansion ratio. Test cases 9 and 10 configuration (cylindrical afterbody).

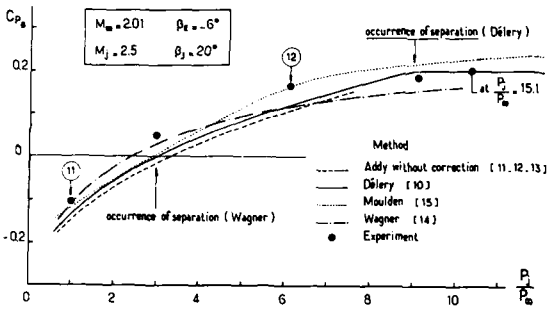

Fig. 2.4.63 – Application of MCM's to base flows. Base pressure variation with nozzle expansion ratio. Test cases 11 and 12 configuration (conical boattail).

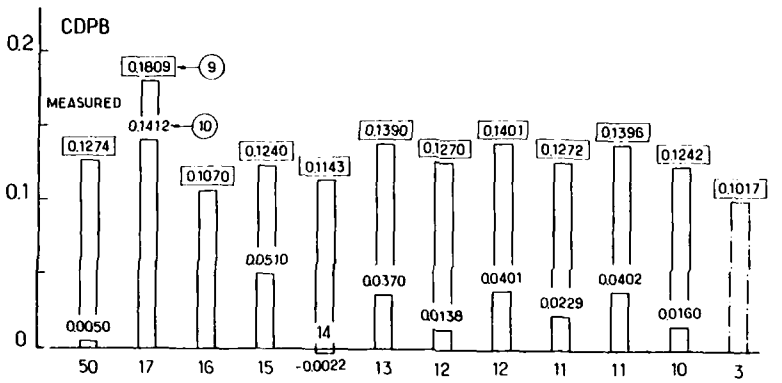

Fig. 2.4.64 – Test cases 9 and 10. (cylindrical afterbody) Bar graph of base pressure drag coefficient.

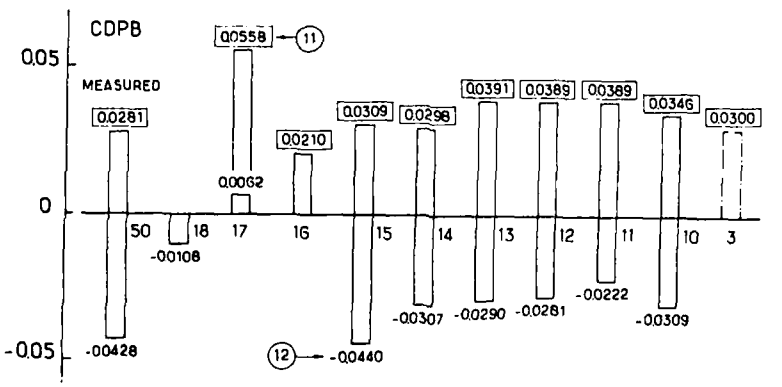

Fig. 2.4.65 – Test cases 11 and 12. (conical boattail). Bar graph of base pressure drag coefficient.

2.5 Evaluation of Navier-Stokes Contributions

2.5.1 Contributions

Navier-Stokes results have been presented by only three contributors although a considerable number of publications are already known dealing with the numerical solution of the Navier-Stokes equations for jet-afterbody interference problems. The participants 16, 17 and 18 provided solutions to the test cases as listed in Fig. 2.3.1. Hence, unfortunately only for test case 2 solutions from all three contributors are available. For test cases 1, 3, 7, 8, 9, 11 and 12 two different results were given while only one solution exists for test cases 2A, 4 and 10 and no solution for cases 5 and 6.

Some attempts have been made to validate the numerical results by variation of the numerical parameters as grid resolution, grid adaption, variation of forebody length, changing of turbulence model etc.. Contributor 16 changed the forebody length for test cases 2 and 2A and the boundary layer thickness in order to check influences coming from the upstream bondary where the initial conditions on the cylindrical part of the body have been defined by use of the experimental boundary layer data. In case 3 the fine resolution region of the wake mesh has been adapted to the calculated plume boundary in an additional run. An exercise was made for some cases by variation of the artificial smoothing terms in order to verify their influence on the solution. For cases 3 and 8 the solution has been analysed at different convergence levels. Considerable effort has been spent by contributor 17 on the construction of solution adaptive meshes using the finest meshes of all. Contributor 18 examined the effects of refined grids and different residual tolerances. Case 2 was also run by switching off the eddy viscosity in order to determine the difference between Euler and Navier-Stokes solutions.

However, despite these valuable exercises the results do not contain a systematic analysis of all effects obviously important for determining the solution. This would at least require a more detailed study of grid resolution and adaption, calculations with different codes using the same mesh and the same turbulence model, and comparisons of different turbulence models running one code in a fixed mesh and including corresponding laminar and inviscid calculations. Therefore, the following comparison of results can only represent a rough and preliminary estimate of the capabilities of Navier-Stokes methods with respect to the jet-afterbody interference problem. Nevertheless, the results indicate the potential of Navier-Stokes analysis to predict many features of the flow correctly.

2.5.2 Description of the Different Contributor's Approaches and Calculation Procedures

2.5.2.1 Participant 16 (Wagner)

The full time-dependent, Reynolds averaged Navier-Stokes equations have been solved using a finite volume method based on MacCormack's hybrid integration scheme (Ref. 2.5.1) similar to Jacock's treatment (Ref. 2.5.2). The turbulence is modelled by the two layer eddy viscosity model of Baldwin and Lomax (Ref. 2.5.3). The external flow calculations were started on the cylindrical part of the body at least two diameters upstream of the body boattail junction setting there fixed boundary conditions which use boundary layer profiles being constructed after Whitfield (Ref. 2.5.4) from the given experimental data. No corrections have been applied for the fact that the experimental values were mostly taken farther downstream. Usual no-slip, zero normal pressure gradient, and zero normal temperature gradient boundary conditions have been applied at the solid walls including the base surface. At the nozzle exit supersonic conical or sonic parallel outflow was assumed, except for case 3, by setting corresponding conditions immediately upstream of the nozzle exit. Because of the 10 degree convergent exit of test case 3 the internal flow within the nozzle and the preceeding supply tube has been modeled in order to get realistic conditions at the nozzle exit. In the latter case a vanishing base area was constructed by extrapolating slightly the external slope and extending the internal contour cylindrically while for all other cases the real base area was introduced into the calculation. The downstream boundary was located at least three diameters behind the base extending to more than six diameters for cases 3 and 8. The downstream boundary condition required zero gradient for all flow quantities. Laterally, the boundary had a distance of ten diameters from the axis, except for case 3 where it was only five diameter away. Undisturbed flow has been assumed at the lateral boundary.

The complete mesh consisted of 88 cells in streamwise direction (exception: case 3 having 108 cells streamwise) and 35 in normal direction resolving the boundary layer typically by 16 cells of increasing thickness through exponential stretching, except normal to the base where a coarse equidistant spacing is applied. Within the wake region behind the base the mesh is divided in an upper and a lower part overlapping by two cells rows and having 35 cell rows each; the wake columns are therefore counted twice in the above mentioned total of 88 cell columns. At both sides of the dividing mesh line the resolution is very fine, corresponding to the boundary layer resolution. Hence, the dividing line was intended to flow the real plume boundary as close as possible being either known from experiment or estimated by a guess of the plume expansion. Only for case 3 an additional calculation was made adjusting the dividing mesh line to follow the separation streamline during calculation. Obviously, this procedure cannot work for blunt bases because this streamline usually reattaches in the base region as can be seen, for example, by inspection of the streamlines indicated by the experimentalists (Ref. 2.5.5). As examples the original fixed mesh of case 3 (Fig. 2.5.0.1) and a part of the mesh for case 11 (Fig. 2.5.0.2) are presented. For the blunt base cases the internal shear layer at the jet boundary could not be finely resolved up to the confluence of both shear layers bounding the separation region since an excessive number of time steps must be avoided. Also the turbulence model has not been adjusted to represent this layer properly.

Convergence to steady flow has been achieved after 1200 time steps for supersonic cases and 5000 time steps for subsonic flow. Only case 3 needed 8000 steps until the internal flow field was converged. The critical transonic blunt base case 8 has been additionally run up to 10000 steps. Convergence has been judged by the behaviour of the drag coefficients and by inspecting the flow field at typical positions inside and at the boundaries. Typical flow times non-dimensionalized with body diameter and external undisturbed velocity are 7 for supersonic problems and 15 for transonic ones.

2.5.2.2 Participant 17 (Deiwert)

The Reynolds-averaged, time-dependent Navier-Stokes equations have been solved in the thin-layer approximation following Ref. 3.5.6. The timewise integration has been performed with the aid of the Beam and Warming implicit finite difference algorithm (Ref. 2.5.7). The equations are factored (spatially split) and central differences are used. The turbulence structure is also modeled by the algebraic eddy viscosity model of Baldwin and Lomax (Ref. 2.5.3). The calculations were performed with an included forebody, with the complete experimental configuration used when known. Usual Navier-Stokes boundary conditions including zero normal pressure gradient have been applied at the body surface except at base surfaces where slip conditions are admitted since neither the grid nor the present formulation of the thin layer code support the viscous effects (Ref. 2.5.8). At the nozzle exit the supersonic outflow condition is set on the base grid line which is in the nozzle range aligned to the spherical or plane surface through the nozzle lip exhibiting constant state in the conical or parallel flow, respectively. For test cases 3 and 4 the convergent outflow conditions was simplified to sonic parallel flow. In the cases 1 to 4 the very small base has been neglected by modifying slightly the external contour for vanishing base area (References 2.5.9/10). Computational boundaries are 20 body diameters apart from the body surface, and extend 25 body diameters downstream from the nozzle exit plane. Upstream boundary condition was uniform free stream. Uniform free stream has also been assumed at the far-field lateral boundary and extrapolation has been applied at the downstream boundary. A special treatment of the boundary conditions is applied at the nozzle lip also including a special relaxation procedure for turbulence description (Ref. 2.5.8). Both corners of the base exhibit double-valued boundary conditions depending on the direction of approach.

A body-oriented computational grid is constructed in a manner compatible with the thin-layer approximation. Radial grid lines on the forebody join the surface orthogonally and on the afterbody surface and jet centerline they are normal to the body axis. Typically 140 points are distributed in the streamwise direction with some 80 points on the body surface between the nose and the end of the afterbody and 60 points on the jet centerline between the end of the afterbody and the downstream outflow boundary. Clustering is used near the nose and the end of the afterbody and near the afterbody shoulder. Streamwise grid lines are distributed radially from the body surface with a high degree of clustering near the surface to resolve the turbulent boundary layer. Typically 48 points are used between the body surface and the far field boundary. An additional 20 points are distributed across the nozzle exit plane and, for configurations with blunt bases, an additional 32 points are distributed across the base for a total number of radial points of 100 for blunt based geometrics and a total number of 68 for sharp lipped nozzles.

Initially the grid lines are distributed using a simple algebraic algorithm and the grid lines are not necessarily clustered to regions of high gradients in the flowfield solution. During the course of the solution the grid is adapted to both density and pressure gradient providing clustering in regions where these gradient are large. An example of this adapted grid for a blunt - base configuration (Ref. 2.5.9) is shown in Figs. 2.5.0.3 (initial grid) and 2.5.0.4 (adapted grid) for test case 10. The application of the turbulence model includes the possibility of detecting two shear layers in a vertical grid line (Ref. 2.5.10).

Convergence typically has been achieved between 1200 and 5000 iterations corresponding to dimensionless times of 6 to 17. A solution was assumed to be converged when the flowfield over the afterbody became steady. The flow field in the far jet may not yet be converged. The meshes of contributor 17 give the best overall resolution and extend relatively far downstream.

2.5.2.3 Participant 18 (Forester/Kern)

As reported in Ref. 2.5.11 the computational algorithm is based on MacCormack's explicit method (Ref. 2.5.12) solving the complete time-dependent, Reynolds-averaged Navier-Stokes equations by use of a finite volume approach. A two layer eddy viscosity turbulence model has been used with the length scale in the outer layer by the boundary layer thickness. This turbulence model has been combined with wall functions for obtaining the wall shear stresses and convective fluxes in the mesh cells bordering solid surface boundaries. This greatly reduces the mesh required for boundary layers and avoids excessive computing times. Behind the base, the eddy viscosity is assumed to be proportional to the mixing layer thickness and the velocity difference across it. The code uses an automatic sclution adaptive grid to improve the computation of boattail pressure, base pressure and plume shape in the near field.

The calculation is started externally on the cylindrical body using initial boundary layer profiles and internally at any point inside the nozzle or at the nozzle exit as desired. The normal pressure gradient is assumed to be zero at no-slip surfaces or equal to the centrifugal force. Total pressure, total temperature and flow angle are specified at subsonic inflow boundaries with the remaining field variables obtained by assuming a zero axial gradient in each variable. At supersonic inflow boundaries all field variables are prescribed. Linear extrapolation is used for all field variables at purely supersonic outflow boundaries. Where both subsonic and supersonic flow occured at the outflow bondary, the free stream static pressure is prescribed at each cell regardless of the local Mach number. Discontinuities therefore occur in the supersonic outflow region (shocks or sudden expansions) but little upstream influence was observed because of the supersonic flow preventing upstream propagation of disturbances.

The grid consisted of between 1100 and 2400 mesh points that are carefully tailored to the gradients of the flow problems (Ref. 2.5.13). For mesh resolution studies this number was varied from 470 up to 6850 points. Convergence to residual levels of less than 10^{-5} was achieved within 3750 and 20,000 time steps depending on mesh size, flow conditions, boundary layer resolution, and prescribed convergence tolerance. The adaptive grid is used to resolve thin mixing layers and accurately compute the flow turning at the nozzle exit plane. A variation of the level of the coefficients in the artificial viscositiy is used to determine the role of smoothing upon the results. Some oscillations usually remain in the crispest solutions.

2.5.3 Discussion of Navier-Stokes Results

Separate discussions follow now for each test case. Preceeding the basic discussion of the diagrams presented in chapter 2.3 an evaluation of the flow fields is presented based on the individual plots of velocity vectors, isobars, and iso Mach lines. The iso-plots for the temperature ratio T/T_∞ also provided by contributors 17 and 18 contained not much additional useful information. Hence, these plots are omitted.

2.5.3.1 Test Case 1 (Participants 16 and 17)

The velocity vector plots (Figs. 2.5.1.1a and 2.5.1.1b) do not differ essentially. Only smooth variations can be observed going from the boattail to the wake and no flow separation is detected on the boattail. Apparently, solution 16 (Fig. 2.5.1.1a) exhibits somewhat less spread out of the free shear layer indicating less turbulent mixing than solution 17 (Fig. 2.5.1.1b). Both isobar plots (Figs. 2.5.1.2a and 2.5.1.2b) show the same flow structure revealing an initial expansion of the jet (static pressure ratio P_j/P_∞ about 1.5) and a compression following. The positions of pressure minimum and maximum on the centerline agree very well. Contribution 16 exhibits some waviness of the solution within the jet shortly behind the nozzle exit indicating probably a too coarse mesh there. Also the iso Mach curves (Figs. 2.5.1.3a and 2.5.1.3b) agree basically exhibiting only slight quantitative differences.

Both calculated pressure distributions on the boattail surface (Figs. 2.3.1.1b) are relatively close to the experimental results, especially in the rear part of the afterbody. Both show a sudden pressure drop at the very end of the boattail where no measurement was available. Contributor 17 has not modeled a base area and claims the result for the grid point at the trailing edge questionable since the boundary condition set at this grid point depends on the sweep direction followed at last in the course of the numerical procedure (Reference 2.5.8). In contrast contribution 16 included a modelling of the small base with a resolution of about ten mesh cells. The solution exhibits a base pressure level reasonably lower than the boattail pressure thus influencing probably the last cell on the boattail and causing the drop. However, by no means can it be presently judged if these details of the solution are realistic. The pressure drag build up on the boattail (Fig. 2.3.1.2b) is obviously very sensitive to the small C_p-differences between solutions 16 and 17 observed in Fig. 2.3.1.1b. these small deviations lead to the pronounced difference of Fig. 2.3.1.2b.

The velocity ratio on the centerline (Fig. 2.3.1.3b) shows the peak values exactly in the same position for solutions 16 and 17 and also the following velocity minimum is in the same position. Furthermore, the positions of the extreme values agree reasonably well with the IVI and Euler results (Fig. 2.3.3a). The extreme values are more pronounced in solution 16 than in solution 17, probably due to a coarser mesh in solution 16, but surprisingly the Navier-Stokes values range in between the Euler and IVI results. The Mach number (Fig. 2.3.1.4b) behaves very similar to the velocity. Downstream, these initial oscillations of the jet are soon damped out in the Navier-Stokes solutions, especially in solution 17 for which the mesh extends far downstream leading to a probably realistic behaviour of the jet. This damping is obviously stronger than in the Euler solutions 1 and 2 probably due to the viscous terms. The static temperature ratio on the centerline (Fig. 2.3.1.5b) confirms the previous observations except a little difference in the initial temperatures at the nozzle exit. This difference is due to a disregard of the slight difference between external and internal stagnation temperature in solution 17 and can in no way affect other solution features. Finally in Fig. 2.3.1.6b the pitot pressure on the jet centerline is compared with some experimental values. To some extent the measurements seem to support the expansions and compressions found by computation but the experimental points are too coarsely distributed to draw firm conclusions and they may be affected by some measurement errors.

The calculated base drag in Fig. 2.3.1.7 confirms the above mentioned fact of lowered base pressure level for solution 16. The calculated boattail pressure drags (Fig. 2.3.1.8) of the Navier-Stokes solutions are not far from the extrapolated value for the experiment (dashed line). But considering the possible errors using the extrapolation procedure applied to the experimental values (see chapter 2.3) the agreement with reality cannot finally be judged by this figure. A more reasonable impression may be got from Fig. 2.3.1.2b by comparison at the position of the last measurement point which is the point before the last one in this figure. Fig. 2.3.1.9 contains the friction drag calculated from four solutions. The IVI solutions 4 and 5 are between both Navier-Stokes solutions with respect to this quantity. Correspondingly, we see a comparison of total boattail drag in Fig. 2.3.1.10 where the difference in the Navier-Stokes solutions result mainly from the different friction drags shown in Fig. 2.3.1.9.

Fig. 2.3.1.11a depicts the distribution of skin friction coefficient C_f revealing that the level of solution 16 (identified by Fig. 2.3.1.11b) is considerably higher than those of the IVI results 4, 5 and 8 while solution 17 shows the smallest values of all. The behaviour of C_f at the very end of the afterbody (Fig. 2.3.1.11b) reflects the pressure behaviour of Fig. 2.3.1.1b.

Finally, the pressure coefficient in a transverse plane just at the nozzle exit is presented in Fig. 2.3.1.12b. While the values of solution 17 are exactly taken at the nozzle exit grid line, the values of solution 16 are corresponding to the first column of cell centers slightly downstream of the base but the experimental values indicated also in the figure are still farther downstream measured. Solutions 16 and 17 are closer to each other than to the experimental results in the external field and no explanation can be offered for this fact. Approaching the body, solution 17 meets the measured C_p-values while solution 16 still exceeds them. The considerable drop to the lowest base pressure value becomes by this figure quite clear for solution 16. Within the jet solution 17 exhibits exactly the theoretical values set there at the base grid line while solution 16 shows already a considerable decrease of C_p caused by the influence of the reduced pressure at the nozzle lip since the internal pressure was set to the theoretical value slightly ahead of the exit (see Chapter 2.5.2). Also the waviness of solution 16 within the jet becomes obvious in Fig. 2.3.1.12b.

2.5.3.2 Test Case 2 (Participant 16, 17 and 18)

The velocity vector plots (Figs. 2.5.2.1a to d, where Fig. 2.5.2.1d presents only the flow directions but not the actual values of the velocities) show features similar to test case 1. Although the experiment exhibited a considerably thick separated flow region, only solution 17 shows some evidence of *such a separated flow. Looking onto skin friction results, solution 17 could be seen to predict separation* very close to the position where it was experimentally observed (Ref. 2.5.10). Also solution 16 predicts separation but farther downstream in between the experimental separation point and the trailing edge. Apparently, this computed flow separation restricts the flow reversal to a very thin layer at the body surface possible coinciding with the laminar sublayer. This fact prevents the development of a reasonable bubble dimension normal to the surface, and in consequence the expected and experimentally observed pressure plateau was not achieved. Solution 18 exhibits no separation at all in terms of negative shear stress. This fact has been mainly attributed to grid sparseness normal to the wall, the use of wall functions, and too simplified and may be insufficient turbulence modelling (Ref. 2.5.13). This inaccurate prediction of separated flow zones on smooth contours appears the most severe limitation of present Navier-Stokes solutions which has to be overcome as soon as possible. Nevertheless, the accurate prediction of the separation point by solution 17 is already encouraging.

The isobar fields of Figs. 2.5.2.2a to c look very similar with the exception of the region immediately behind the trailing edge in solution 18 (Fig. 2.5.2.2c). The plume structure is essentially the same as that of case 1 (Figs. 2.5.2.1a and b) since the nozzle pressure ratio is identical. Also the iso Mach cuves are similarly structured (Figs. 2.5.2.2a to c) at least in the near field of the afterbody and at *the nozzle exit.*

The surface pressure distributions shown in Fig. 2.3.2.1b do not agree as well as in case 1 to experiment even upstream of the separation point. Especially in the region of the pressure minimum solutions 16 and 17 do not reach the experimental level while solution 18 exceeds it. All Navier-Stokes calculations do not predict the pressure plateau of the separated region although the contributions 17 and 18 do better than 16. Solution 18 appears to be wavy at the rear end presumably due to coarseness of the mesh. Again sudden pressure changes occur at the very end of the boattail as already discussed with test case 1. But now the pressure in the last boattail cell falls definitely below the pressure in the adjacent base cell for solution 16 and must therefore be attributed to numerics rather to physics. The deficiencies already discussed are reflected in the drag build up (Fig. 2.3.2.2c) where the solution 18 provides the best final value. The IVI solutions 4 and 5 are seen to get much better results (Fig. 2.3.2.2c).

The position of the velocity peak at the jet centerline (Fig. 2.3.2.3a) predicted by the Navier-Stokes calculations differ only slightly from the IVI solution 4 and the Euler solution 2, both with respect to the position of the corresponding Mach number peak and the following Mach number minimum. The *Navier-Stokes solutions are in excellent agreement to each other (Fig.* 2.3.2.4b) except the differences in peak heights. This holds similarly for the temperature (Fig. 2.3.2.5b) except the slight difference in stagnation temperature for solution 17 as already discussed with case 1. The comparison of calculated pitot pressures with experiments supports the Mach number peaks (Fig. 2.3.2.6b). The extreme behaviour of the IVI solution matches the experiment even better (Fig. 2.3.2.6c).

The base pressure drag (Fig. 2.3.2.7) is negative indicating a base pressure level exceeding P_∞. The boattail pressure drag (Fig. 2.3.2.8) is predicted best by solution 18. The underprediction of solutions 16 and 17 is to a great deal caused by the overprediction of surface pressures in the separated flow region. The friction drag computed from solution 16 and 17 differ little from the IVI results 4 and 5 (Fig. 2.3.2.9) and this part of the drag is not significant to the vaues of total drag (fig. 2.3.2.10) in contrast to test case 1.

Both skin friction distributions of the Navier-Stokes solutions 16 and 17 are different from those of the IVI results 4 and 5 which agree very well to each other. Probably, the prediction of the separation point could be improved for solution 16 if the skin friction level could be lowered. But it should be mentioned that exercises with an elongated forebody and separate ones with reduced boundary layer *thickness did not move the separation position by considerable extent. Finally, Fig.* 2.3.2.12 shows the pressure behaviour on a vertical line nearest to the base. Approaching the trailing edge from the lateral external field the deviations from the experimental values increase, being a maximum for solution 16 and a minimum for 17. Within the jet the behaviour of solutions 16 and 17 is similar to that seen in test case 1. The calculation of contribution 18 is started farther upstream inside the nozzle which may explain that the pressure distribution is even more affected by the nozzle exit state than for solution 16.

2.5.3.2A Test Case 2A (Participant 16 only)

As a result of the increased nozzle pressure ratio compared to case 2, the jet exhaust for this test case is larger in diameter (see velocity vector plot Fig. 2.5.2A.1). The higher jet pressure should have an influence on the separation point but experimentally no shift has been observed. In the calculation, the separation point moves slightly upstream but it remains still far from the measured one. Isobars (Fig. 2.5.2A.2) and iso Mach lines (Fig. 2.5.2A.3) reveal the much stronger expansion within the jet.

The surface pressure distribution is only slightly changed on the rear part of the afterbody and a considerable pressure drop is exhibited at the very end which seems not to be supported by the physics (Fig. 2.3.2A.1b). The drag build up can therefore not be accurate (Fig. 2.3.2A.2b).

The Navier-Stokes result 16 and the IVI method 4 agree excellently with respect to velocity and Mach number peak as well as temperature and pitot pressure minimum on the jet centerline (Figs. 2.3.2A.3 to 2.3.2A.6). Also the first measured minimum is reasonably approached with respect to position and height.

The base drag (Fig. 2.3.2A.7) is even more negative than for case 2 and the boattail pressure drag is far from that calculated from the experimental pressure distribution (Fig. 2.3.2A.8). The friction drag (Fig. 2.3.2A.9) is close to that given by IVI method 4 but this is obviously due to the cancellation of different errors (see skin friction distribution Fig. 2.3.2A.11). The theoretical predictions of the pressures at the base grid line (Fig. 2.3.2A.12) are in excellent agreement to each other. However, the predictions do not agree well with the experimental results.

2.5.3.3 Test Case 3 (Participants 16 and 17)

The velocity vector plots of solution 17 (Fig. 2.5.3.1b and c) differ considerably from those of contribution 16 (Fig. 2.5.3.1a) since a parallel sonic outflow was modeled in solution 17 while contribution 16 accounted for the convergent exit by computing the internal flow in order to achieve the real curved sonic line outside the nozzle. But in spite of this difference there appears no essential difference between solutions 16 and 17 with respect to isobars (Figs. 2.5.3.2a and b) and iso Mach lines (Figs. 2.5.3.3a and b). Plume and external flow field structure of solutions 16 and 17 fit well into the observations discussed previously for the other cases.

Both solutions agree well with the experimental pressures (Fig. 2.3.3.1b) in the rear part of the afterbody except the little waviness of solution 17 and an extreme pressure drop at the very end in solution 16. No physical explanation can be offered for this drop in solution 16 since a base area was not modeled and the pressure falls below the minimum value in the exit plane while it should be expected to be close to a stagnation point at the trailing edge. The drag build up (Fig. 2.3.3.2b) of solution 17 agrees now best with the experimental data.

With respect to the centerline data not many firm conclusions can be drawn since the velocity values given experimentally are too coarsely distributed (Fig. 2.3.3.3b). The downstream behaviour of solution 16 appears not to be realistic missing the deceleration by turbulent mixing. Solution 17 seems, however, to model the experimental behaviour much better as can be judged from the Mach number distributions (Fig. 2.3.3.4b). Nevertheless the agreement of solutions 16 and 17 is still satisfactory in the plume near-field. Similar findings hold for the temperature (Fig. 2.3.3.5b) and pitot pressure distributions (Fig. 2.3.3.6b) whereby solution 17 is definitely seen to model the experimentally observed downstream behaviour best. Solution 16 in the downstream region is closer to the inviscid behaviour, especially close to the Euler solution 2.

Solution 17 is closest but not very close to the experimental boattail pressure drag found with the aid of surface pressure extrapolation (Fig. 2.3.3.8). Note that for this case the linear extrapolation had to be applied over a considerable part of the boattail (see Fig. 2.3.3.1b for comparison) and may therefore be uncertain. The prediction of contribution 16 is farther from this experimental value. By a calculation with automatic adjustment of the mesh to the actual plume boundary, contribution 16 showed a considerable reduction of the pressure drag ("remesh" in Fig. 2.3.3.8). The friction drag for solution 16 is higher than for solution 17 and for the IVI results 4, 5, and 8 (Fig. 2.3.3.9) corresponding to the higher skin friction level (Fig. 2.3.3.11) ending up with a high C_f-peak which reflects the pressure behaviour discussed above while solution 17 shows a slight separation. Both pressure and friction drag contribute to the deviation of the Navier-Stokes result 16 from the IVI results with respect to total boattail drag (Fig. 2.3.3.10).

Finally, the predicted pressures at the base plane (Fig. 2.3.3.12) are in reasonable agreement to each other but large deviations between both Navier-Stokes results occur within the plume due to the difference discussed above concerning the treatment of the initial plume flow-field.

2.5.3.4 Test Case 4 (Participant 17 only)

Since for this test case only the plume stagnation temperature is different from case 3 no significant differences can be detected in the flow field patterns (Fig. 2.5.4.1 to 2.5.4.3). Also the pressure distribution (Fig. 2.3.4.1) does not differ visibly from that of case 3. However, the drag build up (Fig. 2.3.4.2b) exhibits a slight reduction.

The Mach number along the jet centerline (Fig. 2.3.4.4) shows initially a slightly more pronounced oscillation compared to case 3 (Fig. 2.3.3.4b) and drops to a somewhat lower value in the far field due to the smaller momentum of the jet. The temperature distribution (Fig. 2.3.4.5) is of course completely different from case 3 and the pitot pressures (Fig. 2.3.4.6) decrease more rapidly to a lower level in the far field again due to the smaller momentum of the jet.

The small differences just discussed result in a reduction of total pressure drag (Fig. 2.3.4.8) which in its tendency agrees with all other available results except the IVI-method 9. The friction drag, however, does not change at all (Fig. 2.5.4.9). The pressure distribution along the base grid line exhibits no visible difference to that of case 3 (Fig. 2.3.4.12).

2.5.3.5 Test Case 5

Navier-Stokes results are not available for this configuration.

2.5.3.6 Test Case 6

Navier-Stokes results are not available for this configuration.

2.5.3.7 Test Case 7 (Participants 16 and 17)

The velocity vector fields (fig. 2.5.7.1a to c) do not show dramatic effects. Isobars (Figs. 2.5.7.2a/b) and Mach number contours look similar but due to a finer resolution the isobars of solution 17 resolve the external shock wave at the boattail shoulder much better (Fig. 2.5.7.2b).

The boattail pressure distributions of the Navier-Stokes solutions 16 and 17 agree less well with the experiment than those of the Euler solution 1 (Fig. 2.3.7.1b). Comparing both Navier-Stokes solutions a correction must be considered for solution 17 which accounts for the difference to undisturbed free-stream values upstream of the boattail. Applying such a correction both Navier-Stokes solutions would agree closely. However, also the question must be raised wether a correction has to be applied to the experimental data or not since the measured pressures immediately ahead of the body-boattail junction had not reached the level of undisturbed free stream pressure p_∞. The difference between solution 16 or the corrected solution 17 and the experiment is approximately of the same amount. The large final pressure increase at the very end of the boattail in solution 16 approaches the base pressure level calculated for the small base area. Because of the coarse resolution of only two cells at the base, this result cannot be very reliable. The drag build up (Fig. 2.3.7.2b) reflects the differences in the pressures but in supersonic cases the total drag is less sensitive to those deviations since the integrated drag is steadily increasing from the body-boattail junction to the boattail end.

For the centerline data some disagreement exists between the Navier-Stokes results 16 and 17 and the Euler solution 1 (Fig. 2.3.7.3 to 2.3.7.6) which may be partially caused by use of different initial data at the nozzle exit. The Mach number at the nozzle exit (Fig. 2.3.7.4) is for example in solution 1 definitely different from the nominal value of 2.024. The different initial plume temperature (Fig. 2.3.7.5) is due to an interchange of the total temperatures of jet and external stream by mistake in solution 16 but no essential effect is expected on the rest of the calculated data from this error.

Fig. 2.3.7.7 shows the small base drag predicted by solution 16. The total pressure drag level (Fig. 2.3.7.8) is given by all solutions with similar accuracy while the friction drag is again definitely higher for solution 16 (Fig. 2.3.7.9) leading to a fortuitously good agreement for the total drag values predicted by both Navier-Stokes solutions (Fig. 2.3.7.10). With respect to the pressure distribution in the base plane the available solutions show a good agreement (Fig. 2.3.8.12a) especially solutions 1 and 16 are very close to each other in the external field.

2.5.3.8 Test Case 8 (Participants 16 and 17)

This transonic missile afterbody case exhibiting a large blunt base is a very tough test case for Navier-Stokes methods but it is also very interesting since detailed LDV measurements are available concerning mean velocities and turbulent velocity fluctuations. The calculated velocity vector plot of solution 16 (Fig. 2.5.8.1a) agrees surprisingly well with the flow field of the experiment (Ref. 2.5.5). The streamwise extent of the recirculation bubble is very similar while the calculated result shows a slightly smaller size in lateral direction resulting in an outward shift of the reattachment point at the base compared to the experiment. In contrast solution 17 shows the main vortex in the separated region rotating in the opposite sense. The isobar plots (Figs. 2.5.8.2a and b) of both Navier-Stokes solutions and the iso Mach lines (Figs. 2.5.8.3a and b) are similar but obviously more distinct than in the smooth afterbody cases 1, 3 and 7. The differences concern mainly the recirculating base region.

The experimental surface pressure distribution (Fig. 2.3.8.1) around the body-boattail junction and ahead of it is better represented by solution 17 while this prediction becomes worse near the boattail end. Solution 16 suffers from a rather coarse mesh at the body-boattail junction but it becomes very reasonable near the boattail end. Hence, none of these solutions can perfectly predict the boattail drag build up (Fig. 2.3.8.2) but result 16 is quite reasonable.

The nozzle centerline results differ considerably (Figs. 2.3.8.3 to 2.3.8.6) showing in solution 16 a larger and more extended initial expansion but finally a probably unrealistic steady increase of Mach number occurs in downstream direction (Fig. 2.3.8.4) consistent with the results for test case 3 discussed previously. Obviously, the initial disagreement between both Navier-Stokes solutions seems to be related to the different base pressure predictions (see Fig. 2.3.7.12).

The base drag (Fig. 2.3.8.7) shows the predictions 16 and 17 to give a level comparable to the experiment, solution 16 being closer to the experimental values. The boattail pressure drag (Fig. 2.3.8.8) is also better predicted by solution 16 corresponding to the better agreement of surface pressures in the rear part (Fig. 2.3.8.1). Skin friction results again appear to be much higher for solution 16 than for solution 17 (Figs. 2.5.8.9 and 2.5.8.11).

Finally, Fig. 2.3.8.12 presents the pressure behaviour in a plane at the base showing clearly the surprisingly good agreement of the mean value of the distribution predicted by 16 with the measurements while solution 17 delivers somewhat lower base pressures. But it should be mentioned that a comparison of shear stress correlations calculated from solution 16 to the experimental results looks less promising thus leaving some questions open concerning the prediction quality (Ref. 2.5.14).

2.5.3.9 Test Case 9 (Participants 16 and 17)

Solution 16 shows a main vortex in the recirculation region which rotates in opposite sense compared to case 8 (Fig. 2.5.9.1a/b). Some rough evidence is also seen for predicting the shock system indicated by the Schlieren photograph including the Mach disk at the axis. Figs. 2.5.9.1c and d reveal similar features for solution 17, but the main vortex in the separated region rotates in the opposite sense and the separated region seems to be shorter. The isobar plot of solution 17 (Fig. 2.5.9.2b) gives a very

impressive picture of the shock system because of its dense spacing of lines in contrast to the plot for contribution 16 (Fig. 2.5.9.2a). The plots of iso Mach lines (Figs. 2.5.9.3a and b) confirm the shock struc- ture but do not reveal subsonic flow behind the "Mach disk" nor the precise location of the disk.

The predicted surface pressure distributions on the cylindrical body (Fig. 2.3.9.1b) differ somewhat from the experimental values due to the treatment of the upstream regions. This fact suggests a correction of the calculated values similarly as carried out evaluating the experimental results (Ref. 2.5.15). Both solutions predict a strong pressure drop at the boattail end approximating the base pressure level due to an upstream influence through the subsonic part of the boundary layer.

The centerline distributions for solutions 16 and 17 are initially in good agreement to each other but differ somewhat from Euler solution 3 (Fig. 2.3.9.3 to 2.3.9.6). Especially the first peaks are close to each other in position and height.

The base drag prediction (Fig. 2.3.9.7) is slightly better for solution 16 since the solution 17 suffers from a too low base pressure level (Fig. 2.3.9.12). But is should be kept in mind that the "measured" value given in Fig. 2.3.9.7 is questionable because it is based on only one radial position of pressure taps. At that position solution 16 meets the experimental mean value quite well although considerable variation occurs over the rest of the base (Fig. 2.3.9.12). The degree of agreement to experiment may therefore be judged for such cases much better by comparison of pressure distributions. The difference of pressures within the jet results from the fact that the base gridline in solution 17 respresents a spherical surface with constant conical outflow conditions while solution 16 describes a vertical plane where essentially the same flow field was modeled accounting locally for the upstream position of this plane.

2.5.3.10 Test Case 10 (Participant 17 only)

This case differs from case 9 only by increasing the static pressure ratio p_j/p_∞ from 1 to 6. The velocity vector plot (Fig. 2.5.10.1) shows already the essential changes of the flow field compared to case 9. The isobars (Fig. 2.5.10.2) and the iso Mach lines (Fig. 2.5.10.3) reflect very well the experimental shock structure seen in the Schlieren photograph (see chapter 2.2).

The surface pressures are identical to solution 17 for case 9 except at the very end of the body where a smaller drop occurs due to the higher base pressure level (Fig. 2.3.10.1). The centerline distributions seem to be very reasonable (Figs. 2.5.10.3 to 6) showing now severe expansions and compressions which have to be expected within the jet. The base drag is essentially overpredicted (Fig. 2.3.10.7) due to a too low base pressure level (Fig. 2.3.10.12). But it should be considered that the unknown experimental base pressure distribution could vary across the base to a considerable extent.

2.5.3.11 Test Case 11 (Participants 16 and 17)

In contrast to case 9 solution 16 shows a main vortex rotating in clockwise sense within the separation zone (Figs. 2.5.11.1a and b). Also the internal barrel shock and the Mach disk are already indicated in Fig. 2.5.11.1a. The corresponding plots for solution 17 (Figs. 2.5.11.1c and d) look similar. Comparing Figs. 2.5.11.1b and d, again the length of the separated zone behind the base seems to differ somewhat. Because of the finer resolution Fig. 2.5.11.2b for solution 17 reveals the shock structure much better than Fig. 2.5.11.2a for solution 16. The calculated shock pattern agrees well with the Schlieren photograph (see chapter 2.2 and Ref. 2.5.9). Disregarding the coarser isobar resolution of contribution 16 both Navier-Stokes solutions agree well to each other with respect to the isobars and iso Mach lines (Figs. 2.5.11.3a and b).

The surface pressure distribution (Fig. 2.3.11.1b) exhibits excellent agreement between solution 16 and the experimental values (except the first one) on the boattail including the pressure drop at the boattail end. But it would be not fair to state less accuracy for solution 17 since the differences appear to be mainly due to the deviations already present at the cylindrical body which are caused by the different computational approaches. If we consider an adjustment of the C_p-values to zero on that portion of the body the agreement of solution 17 with the experiment would probably be even better than that of solution 16. These arguments hold also for the drag build up (Fig. 2.3.11.2b) which is in excellent agreement with the experiment for solution 16.

The centerline values of solutions 16 and 17 (Figs. 2.3.11.3 to 2.3.11.6) are similar up to the first peaks and the peak positions agree also with the Euler solution 3 but the peak heights are quite different from the Euler solution.

The base drag (Fig. 2.3.11.7) is somewhat too low for solution 16 whereby a possible variation across the base in reality should be kept in mind while it is too high for solution 17 reflecting the lower base pressure level shown in Fig. 2.3.11.12. The boattail pressure drag values (Fig. 2.3.11.8) may coincide after applying a correction as suggested above and the skin friction drag (Fig. 2.3.11.9) shows the typical difference already discussed above. The total boattail drag values (Fig. 2.3.11.10) are almost identical.

Finally, with respect to the pressure distribution in the exit region (Fig. 2.3.11.12) the Navier-Stokes solutions agree well to each other (considering the differences within the jet to be natural as discussed above) except at the base surface. It may be mentioned that the Euler solution 3 gives the best base pressure prediction at the measurement position although the pressure agreement on the boattail is only fair.

2.5.3.12 Test Case 12 (Participants 17 and 18)

The geometry of test cases 11 and 12 is identical but the static pressure ratio is increased to 6 for test case 12. the velocity vector plots (Figs. 2.5.12.1a, b and c) reveal essential flow field features. The isobars of both solutions (Fig. 2.5.12.2a and b) reflect clearly the main features of the Schlieren picture from experiment. The iso Mach line patterns within the plume (Figs. 2.5.12.3a and b) are similar to each other despite some quantitative deviations. The strong shock angle is clearly shown. Neither solution 17 or 18 show the weaker precursor shock or the associated flow separation.

The pressure distributions on the boattail are shown in Fig. 2.3.12.1b. Solution 17 differs only at the very end from that for case 11 and may be corrected as supposed there. Solution 18 reflects partially the large pressure peak measured at the boattail end which corresponds to the higher base pressure. The drag build up (Fig. 2.3.12.2b) is too high for solution 17 because of the reasons already known and solution 18 follows this trend up to the middle of the boattail where it changes to a consecutive underprediction.

On the centerline (Figs. 2.3.12.4 to 2.3.12.6) solution 17 predicts expansion peaks within the jet which occur downstream of the mesh boundary of solution 18. The predicted base drag values exhibit only fair agreement with the experimental value compared to the results of other methods (Fig. 2.3.12.7). Both ier-Stokes solutions agree well to each other with respect to the boattail drag (Fig. 2.3.12.8) and ose values are not far from the experimental result. The prediction of solution 17 can probably be urther improved by applying corrections to the pressure distribution as discussed above. The base pressure level shown only for solution 17 in Fig. 2.3.12.12 is again somewhat too low compared to the experimental value.

2.5.4 References

2.5.1	MacCormack, R.W.	An Efficient Numerical Method for Solving the Time-Dependent Compressible Navier-Stokes Equations at High Reynolds Number. NASA TMX-73129; 1976
2.5.2	Jacocks, J.L. Peters, W.L. Guyton, F.C.	Comparison of Computational and Experimental Jet Effects. AIAA-81-1492
2.5.3	Baldwin, B.S. Lomax, H.	Thin Layer Approximation and Algeraic Model for Separated Turbulent Flows. AIAA-78-257
2.5.4	Whitfield, D.L.	Analytical Description of the Complete Two-Dimensional Turbulent Boundary-Layer Velocity Profile. AIAA-78-1158
2.5.5	Lacau, R.G. Desnoyer, D. Délery, J.	Analyse au vélocimetre laser de l'ecoulement en aval d'arriere-corps de missiles. AGARD CP-336, 1982
2.5.6	Nietubicz, C.J. Pulliam, T.H. Steger, J.L.	Numerical Solultion of the Azimuthal-Invariant Thin-Layer Navier-Stokes Equations. AIAA-79-0010
2.5.7	Beam, R. Warming, R.F.	An Implicit Finite-Difference Algorithm for Hyperbolic Systems in Convervation-Law-Form. Journal of Computational Physics 22, 1976, pp. 87-110
2.5.8	Deiwert, G.S.	A Computational Investigation of Supersonic Axisymmetric Flow over Boattails Containing a Centered Propulsive Jet. AIAA-83-0462
2.5.9	Deiwert, G.S. Andrews, A.E. Nakahashi, K.	Theoretical analysis of aircraft afterbody flow AIAA-84-1524
2.5.10	Deiwert, G.S.	Private Communication, 1984
2.5.11	Peery, K.M. Forester, C.K.	Numerical Simulation of Multistream Nozzle Flows. AIAA-Journal 18, 1980, pp. 1088-1093
2.5.12	MacCormack, R.W. Paullay, A.J.	Computational Efficiency Achieved by Time Splitting of Finite Difference Operators. AIAA-72-154
2.5.13	Forester, C.K.	Comments on Navier-Stokes Calculations of AGARD WG-08 Test Cases. 1984
2.5.14	Wagner, B.	Calculation of Turbulent Flow about Missile Afterbodies Containing an Exhaust Jet. AIAA-84-1659
2.5.15	Agrell, J. White, R.A.	An Experimental Investigation of Supersonic Axisymmetric Flow over Boattails Containing a Centered Propulsive Jet. FFA Tech. Note AU-913, 1974

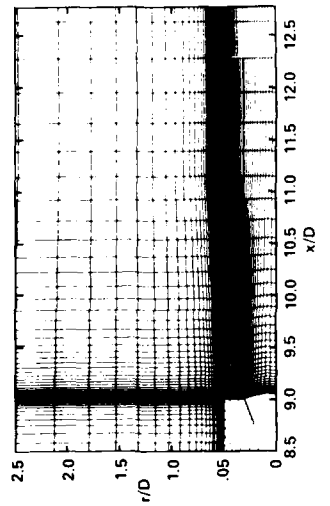

Fig. 2.5.0.3: Computational grid (initial grid point distribution), *Test Case 10, contribution 17*

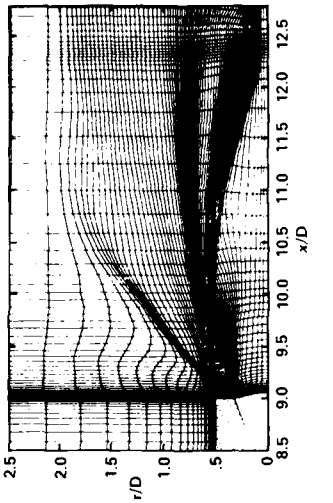

Fig. 2.5.0.4: Computational grid (solution adapted), Test Case 10, contribution 17

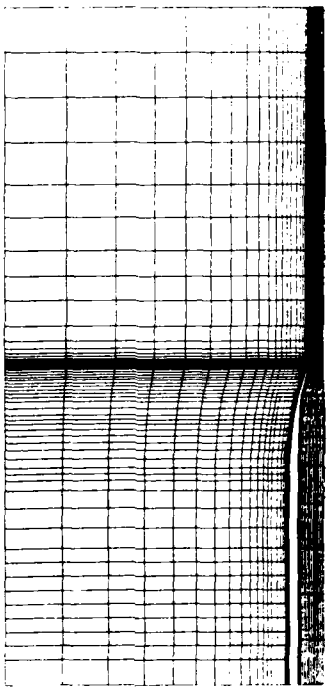

Fig. 2.5.0.1: Computational grid, Test Case 3, contribution 16

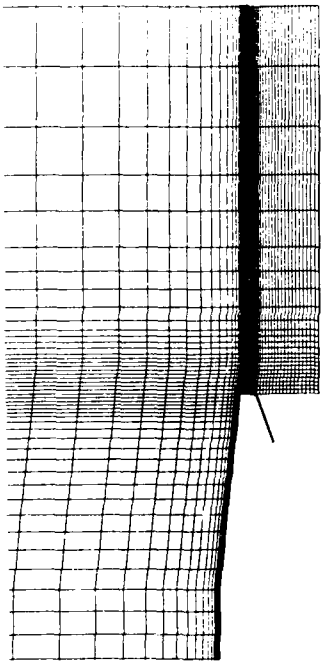

Fig. 2.5.0.2: Computational grid, Test Case *11, contribution 16*

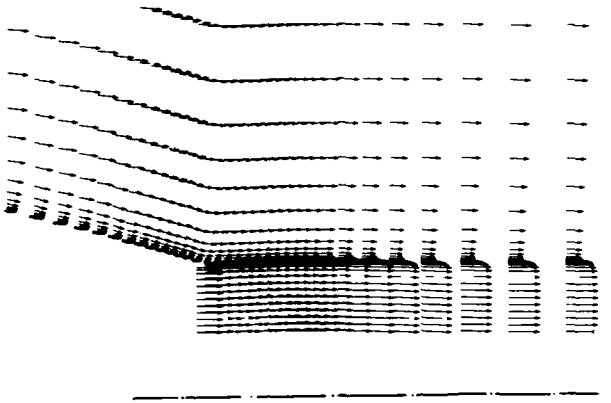

Fig. 2.5.1.1 a: Velocity vectors, Test Case 1, solution 16

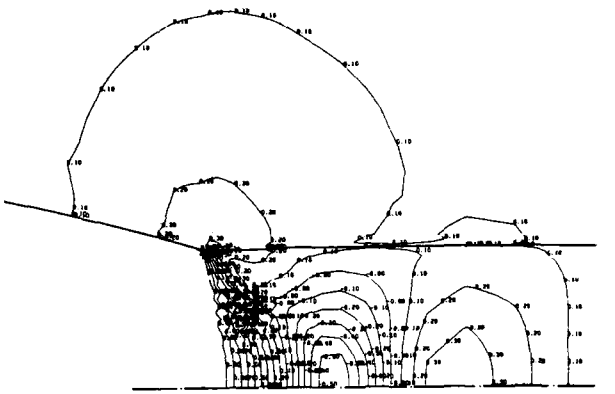

Fig. 2.5.1.2 a: Isobars, Test Case 1, solution 16

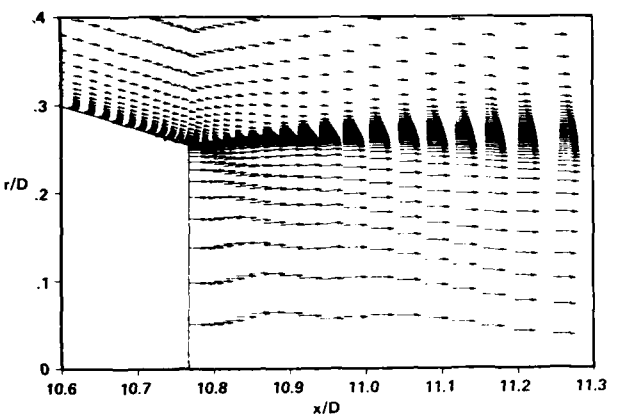

Fig. 2.5.1.1 b: Velocity vectors, Test Case 1, solution 17

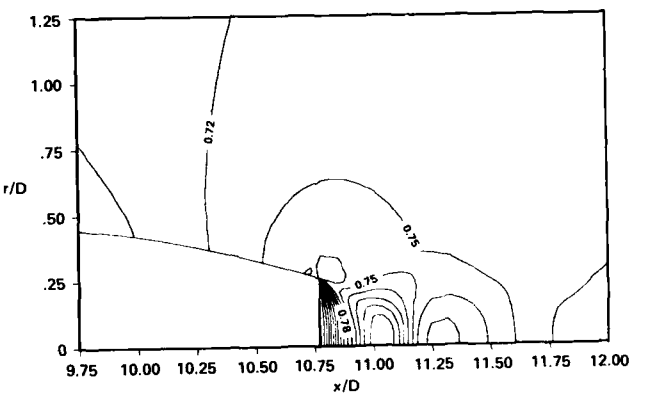

Fig. 2.5.1.2 b: Isobars, Test Case 1, solution 17

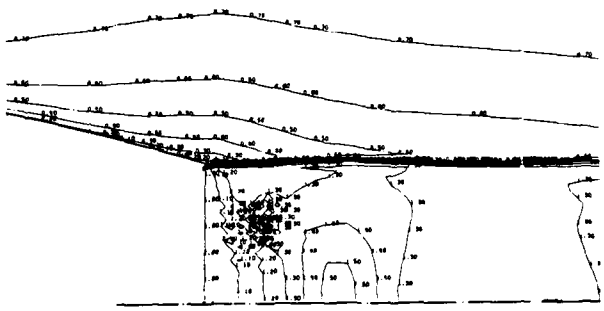

Fig. 2.5.1.3 a: Iso Mach lines, Test Case 1, solution 16

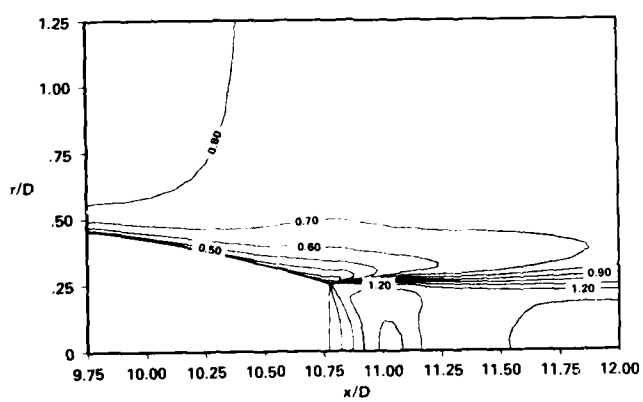

Fig. 2.5.1.3 b: Iso Mach lines, Test Case 1, solution 17

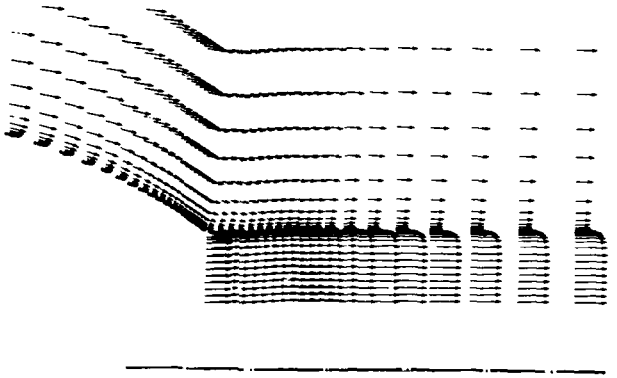

Fig. 2.5.2.1 a: Velocity vectors, Test Case 2, solution 16

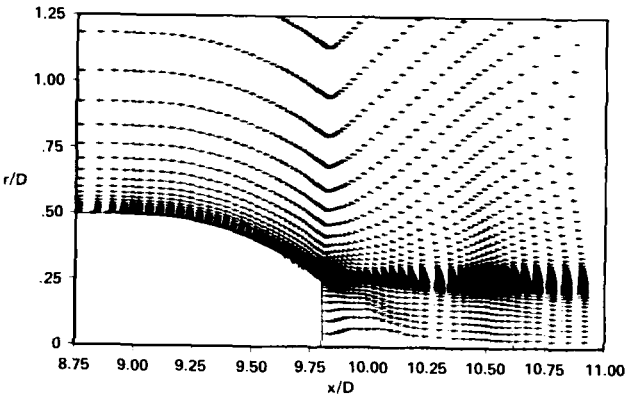

Fig. 2.5.2.1 b: Velocity vectors, Test Case 2, solution 17

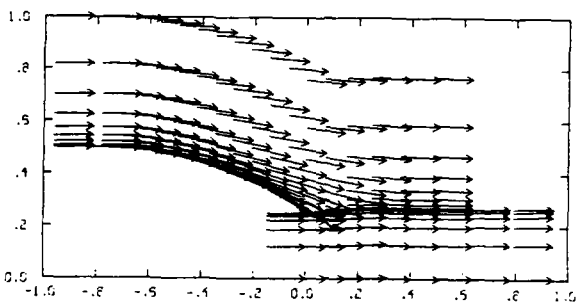

Fig. 2.5.2.1 d: Velocity vectors, Test Case 2, solution 18

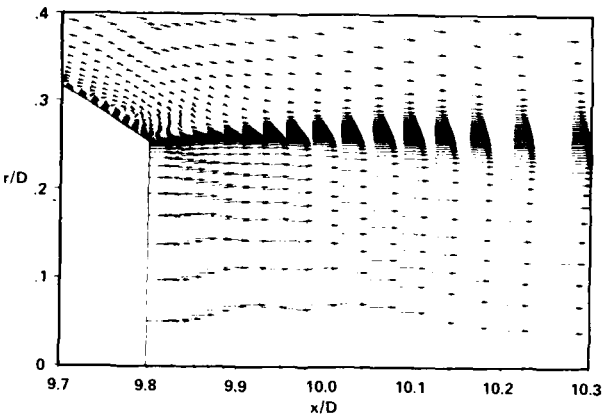

Fig. 2.5.2.1 c: Velocity vectors, Test Case 2, solution 17

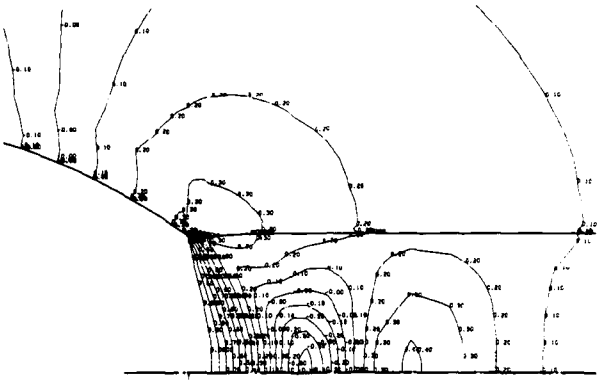

Fig. 2.5.2.2 a: Isobars, Test Case 2, solution 16

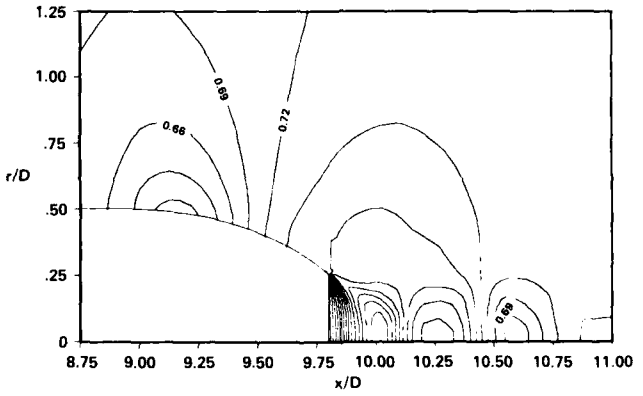

Fig. 2.5.2.2 b: Isobars, Test Case 2, solution 17

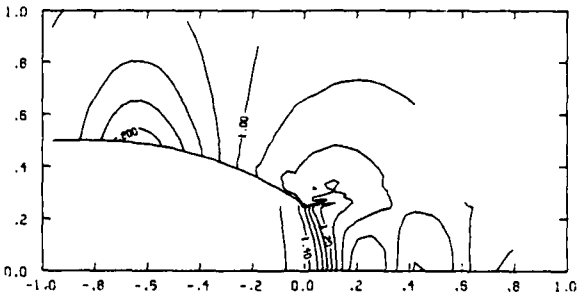

Fig. 2.5.2.2 c: Isobars, Test Case 2, solution 18

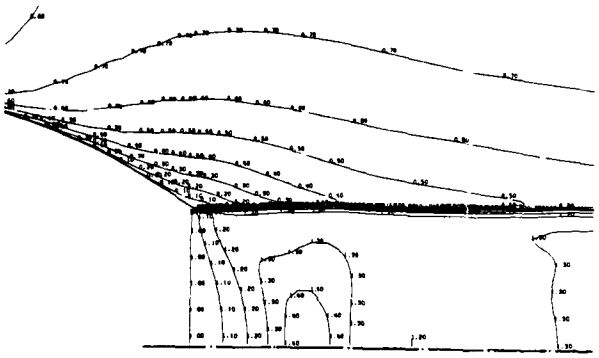

Fig. 2.5.2.3 a: Iso Mach lines, Test Case 2, solution 16

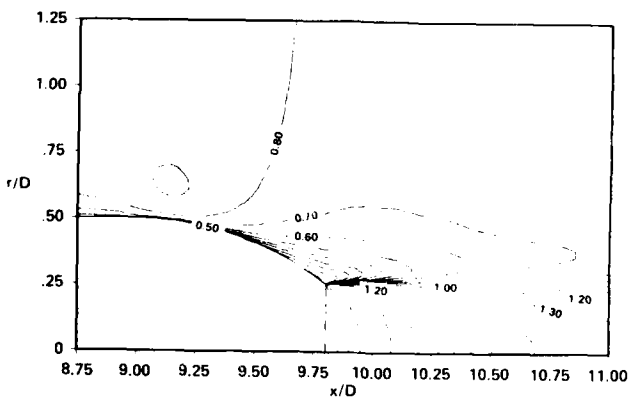

Fig. 2.5.2.3 b: Iso Mach lines, Test Case 2, solution 17

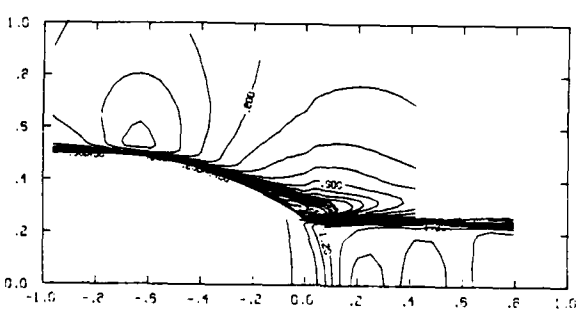

Fig. 2.5.2.3 c: Iso Mach lines, Test Case 2, solution 18

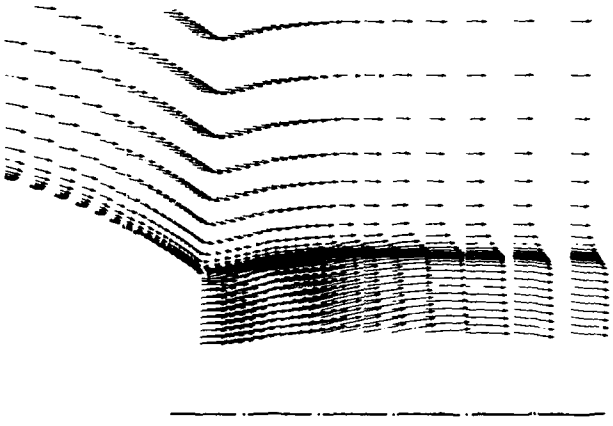

Fig. 2.5.2A.1: Velocity vectors, Test Case 2A, solution 16

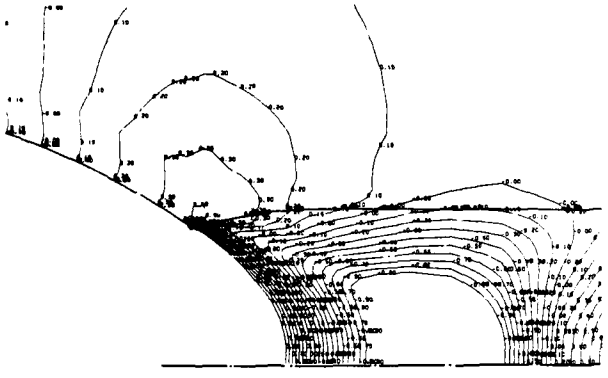

Fig. 2.5.2A.2: Isobars, Test Case 2A, solution 16

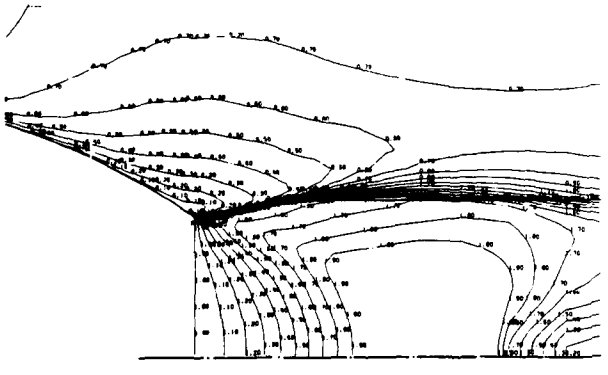

Fig. 2.5.2A.3: Iso Mach lines, Test Case 2A, solution 16

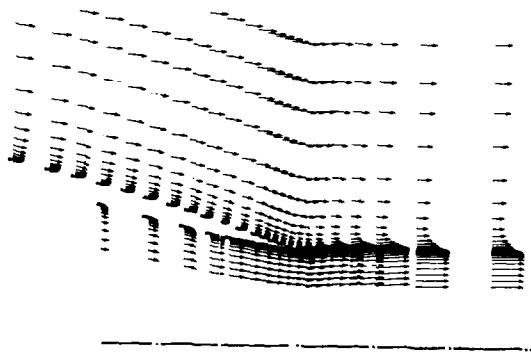

Fig. 2.5.3.1 a: Velocity vectors, Test Case 3, solution 16

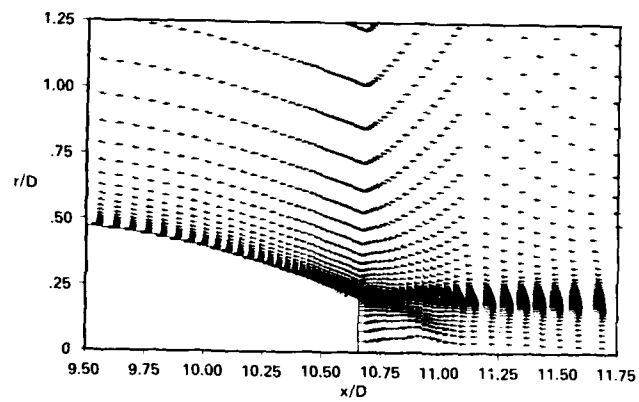

Fig. 2.5.3.1 b: Velocity vectors, Test Case 3, solution 17

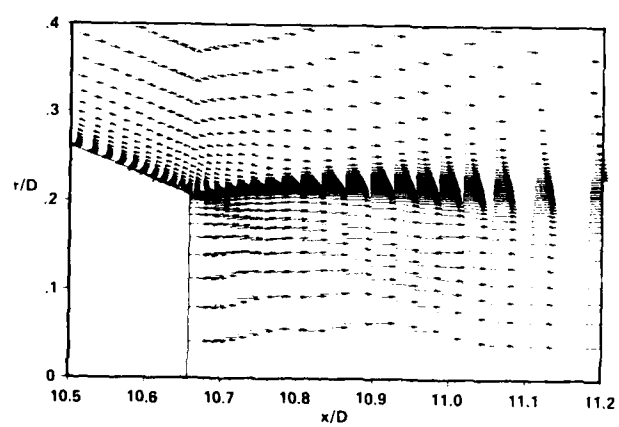

Fig. 2.5.3.1 c: Velocity vectors, Test Case 3, solution 17

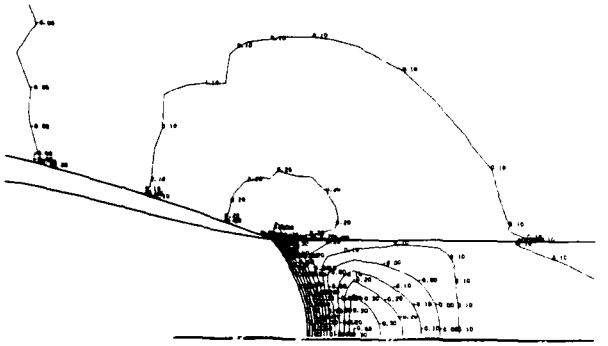

Fig. 2.5.3.2 a: Isobars, Test Case 3, solution 16

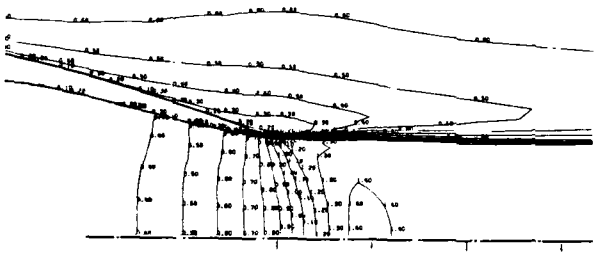

Fig. 2.5.3.3 a: Iso Mach lines, Test Case 3, solution 16

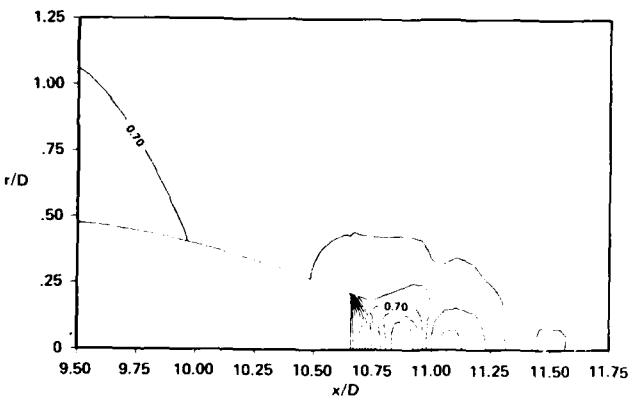

Fig. 2.5.3.2 b: Isobars, Test Case 3, solution 17

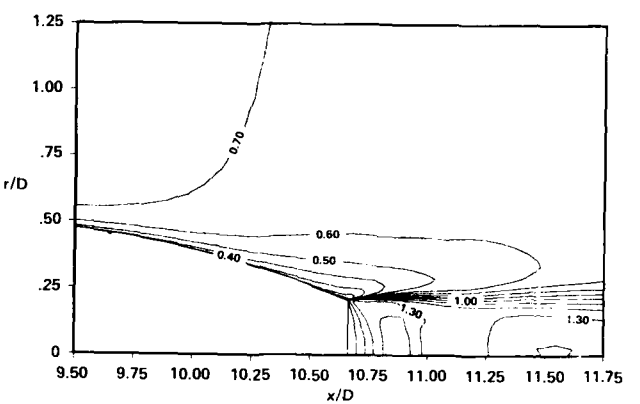

Fig. 2.5.3.3 b: Iso Mach lines, Test Case 3, solution 17

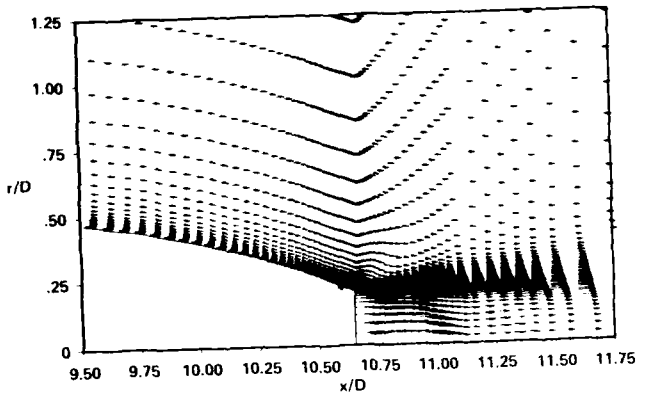

Fig. 2.5.4.1 a: Velocity vectors, Test Case 4, solution 17

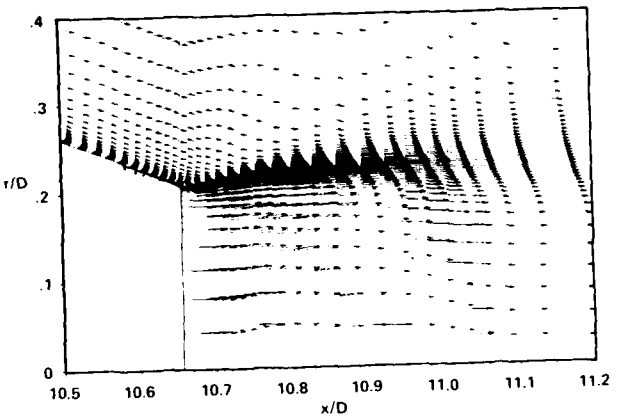

Fig. 2.5.4.1 b: Velocity vectors, Test Case 4, solution 17

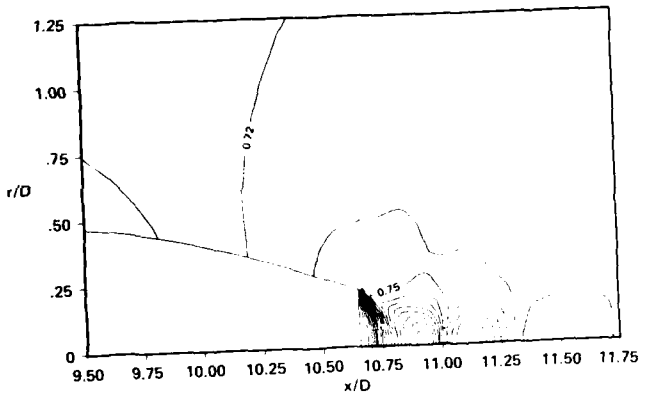

Fig. 2.5.4.2: Isobars, Test Case 4, solution 17

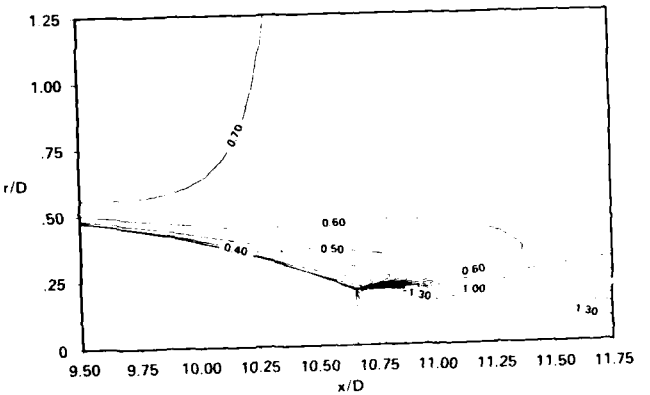

Fig. 2.5.4.3: Iso Mach lines, Test Case 4, solution 17

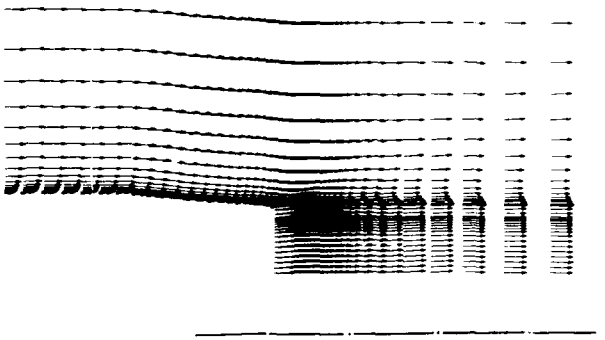

Fig. 2.5.7.1 a: Velocity vectors, Test Case 7, solution 16

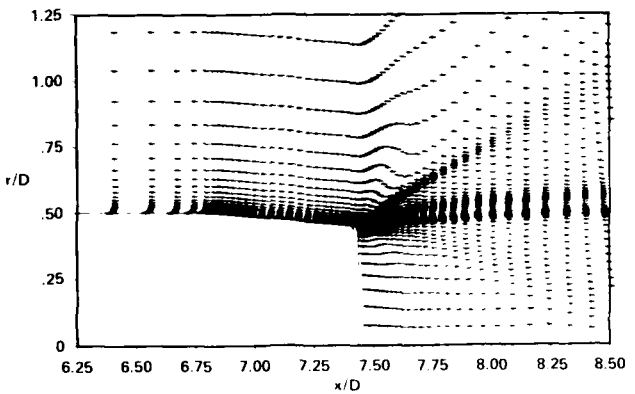

Fig. 2.5.7.1 b: Velocity vectors, Test Case 7, solution 17

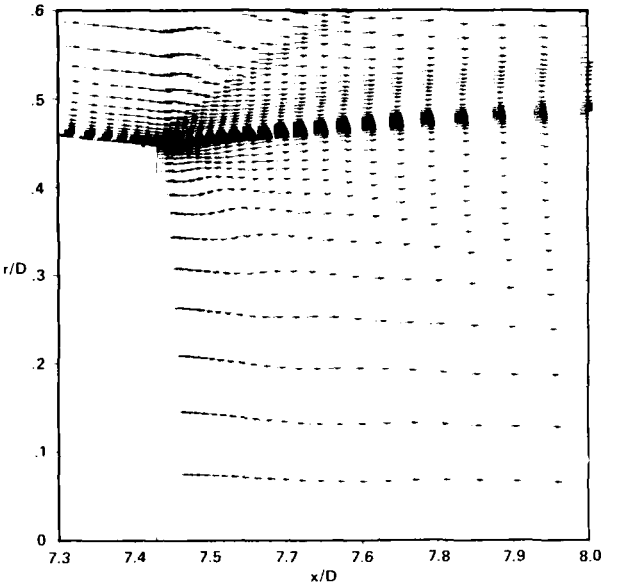

Fig. 2.5.7.1 c: Velocity vectors, Test Case 7, solution 17

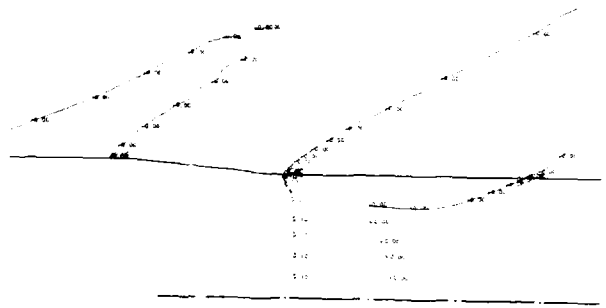

Fig. 2.5.7.2 a: Isobars, Test Case 7, solution 16

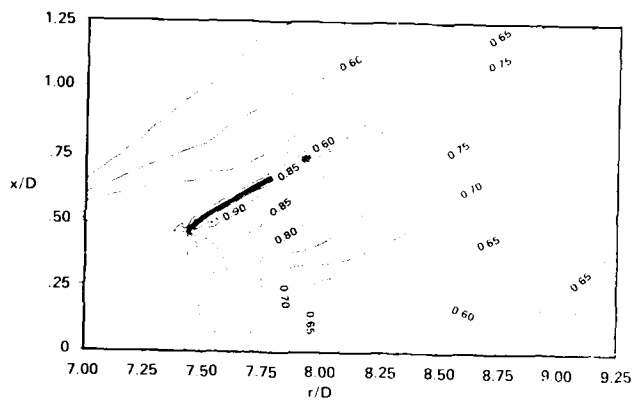

Fig. 2.5.7.2. b: Isobars, Test Case 7, solution 17

Fig. 2.5.7.3 a: Iso Mach Lines, Test Case 7, solution 16

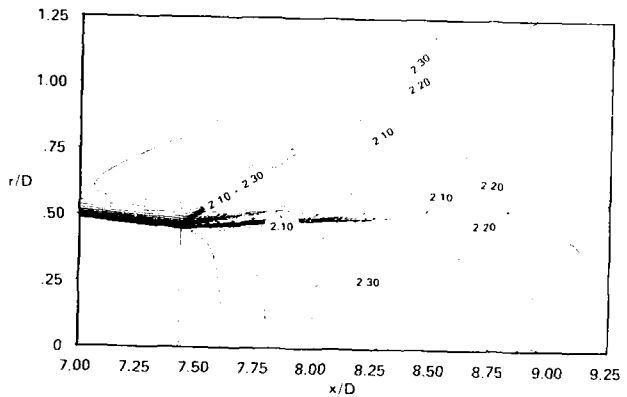

Fig. 2.5.7.3 b: Iso Mach Lines, Test Case 7, solution 17

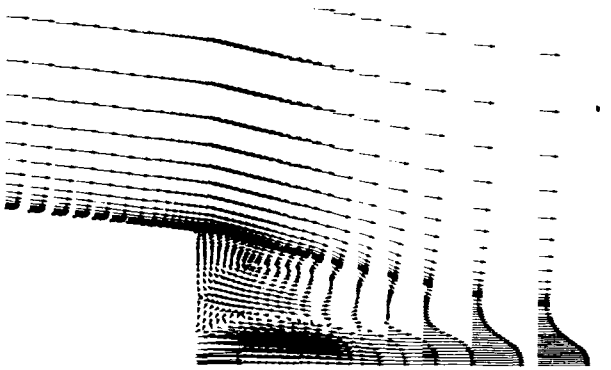

Fig. 2.5.8.1 a: Velocity vectors, Test Case 8, solution 16

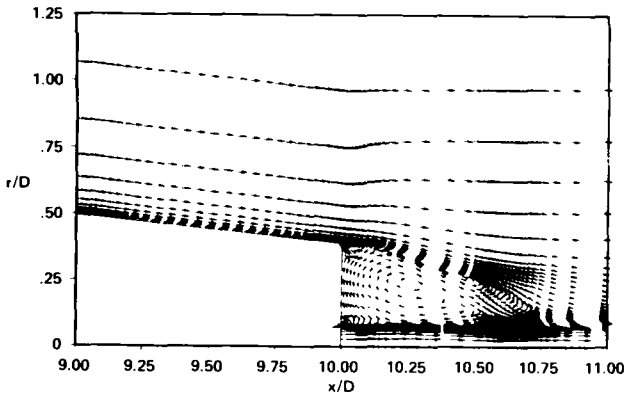

Fig. 2.5.8.1 b: Velocity vectors, Test Case 8, solution 17

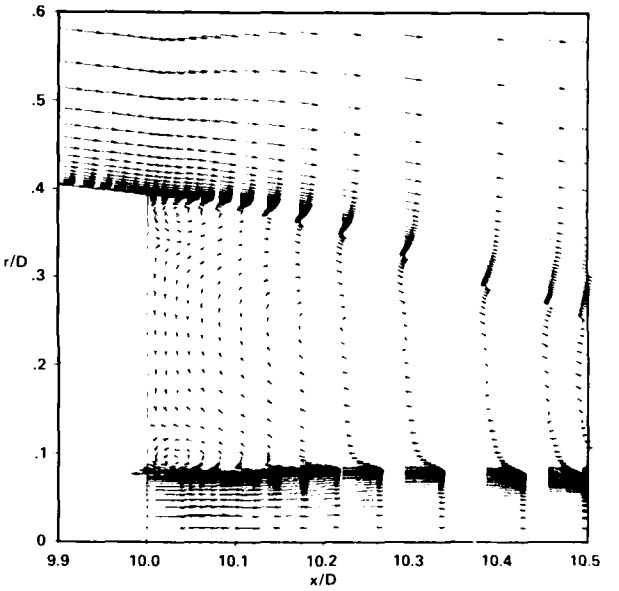

Fig. 2.5.8.1 c: Velocity vectors, Test Case 8, solution 17

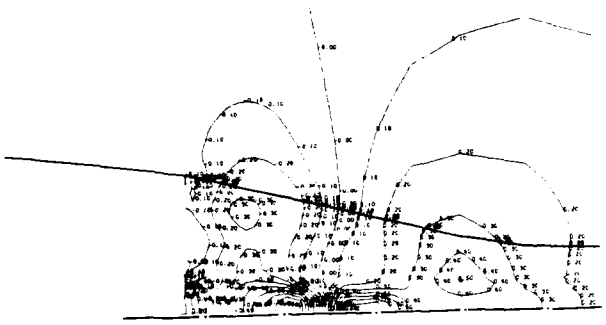

Fig. 2.5.8.2 a: Isobars, Test Case 8, solution 16

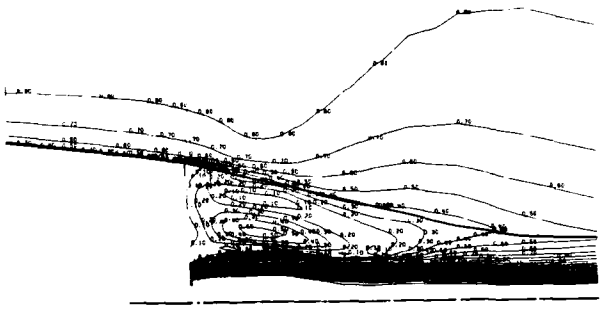

Fig. 2.5.8.3 a: Iso Mach lines, Test Case 8, solution 16

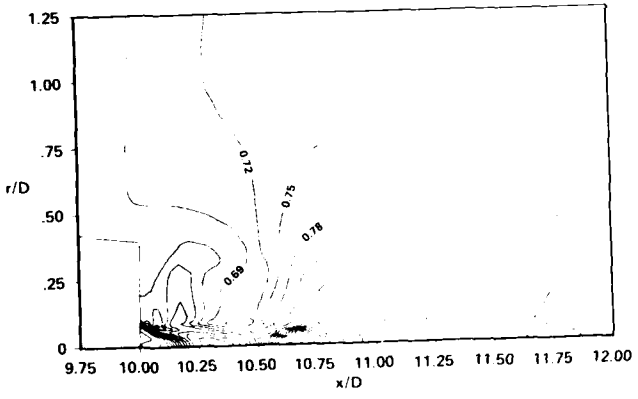

Fig. 2.5.8.2 b: Isobars, Test Case 8, solution 17

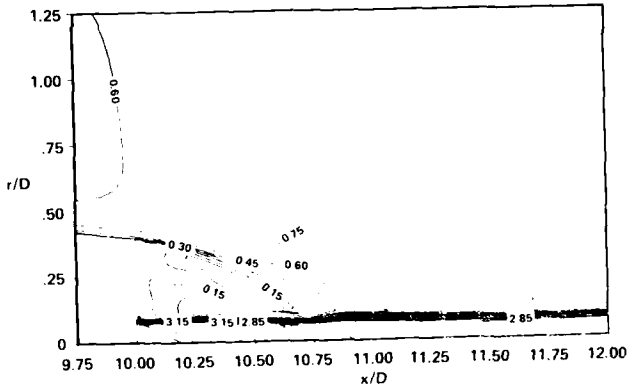

Fig. 2.5.8.3 b: Iso Mach lines, Test Case 8, solution 17

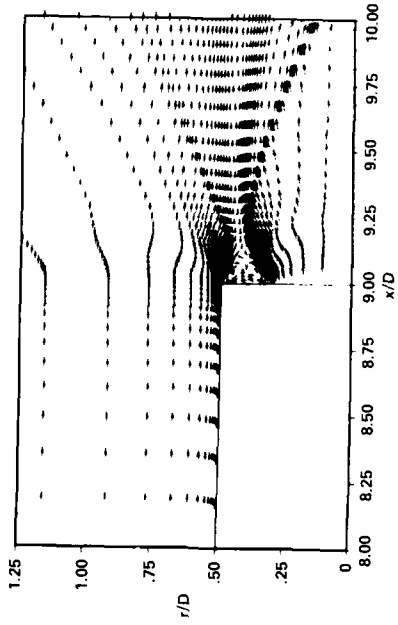

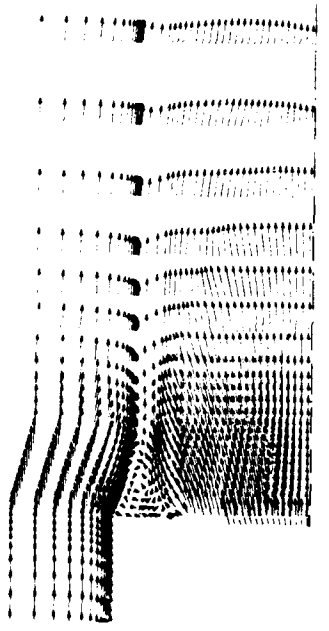

Fig. 2.5.9.1 a, b: Velocity vectors, Test Case 9, solution 16

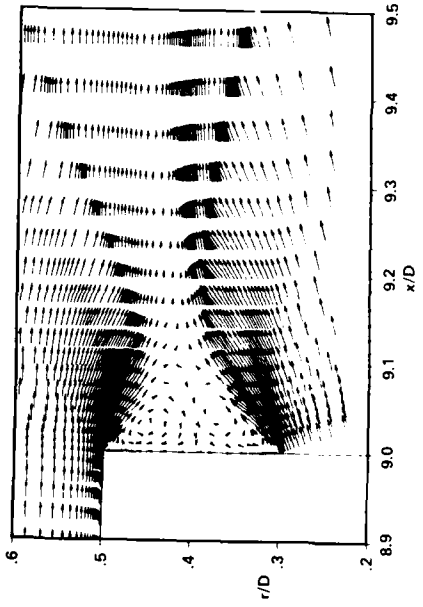

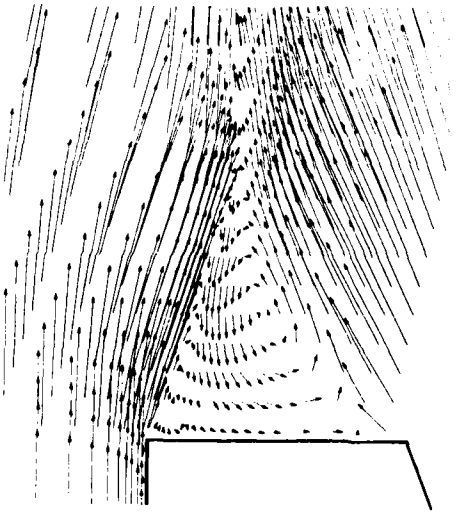

Fig. 2.5.9.1 c, d: Velocity vectors, Test Case 9, solution 17

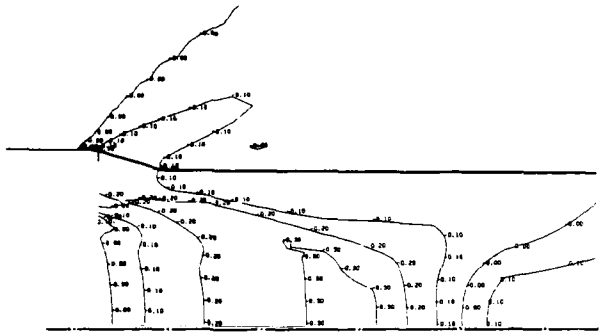

Fig. 2.5.9.2 a: Isobars, Test Case 9, solution 16

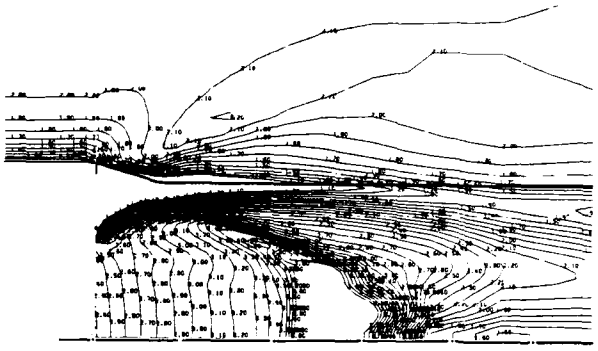

Fig. 2.5.9.3 a: Iso Mach lines, Test Case 9, solution 16

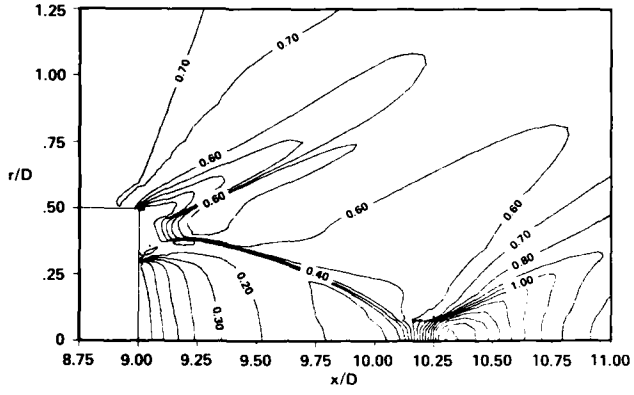

Fig. 2.5.9.2 b: Isobars, Test Case 9, solution 17

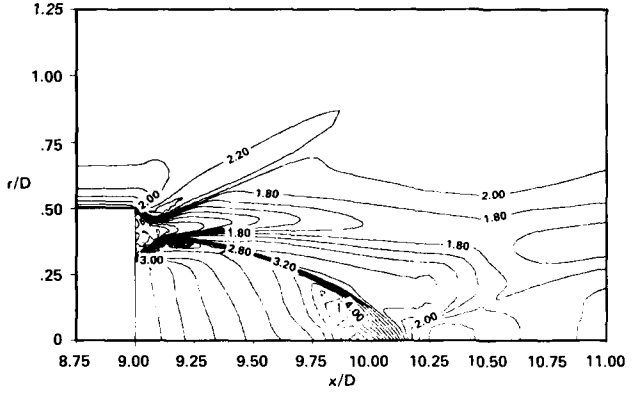

Fig. 2.5.9.3 b: Iso Mach lines, Test Case 9, solution 17

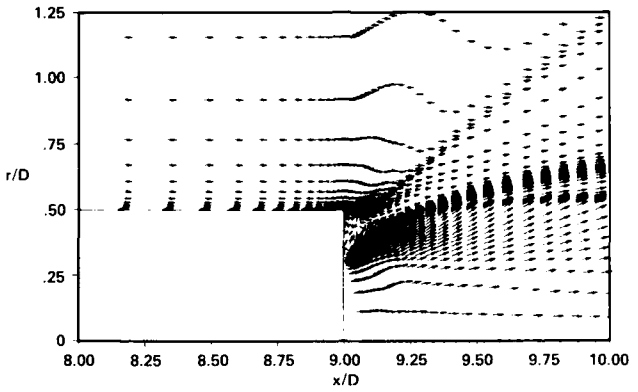

Fig. 2.5.10.1 a, b: Velocity vectors, Test Case 10, solution 17

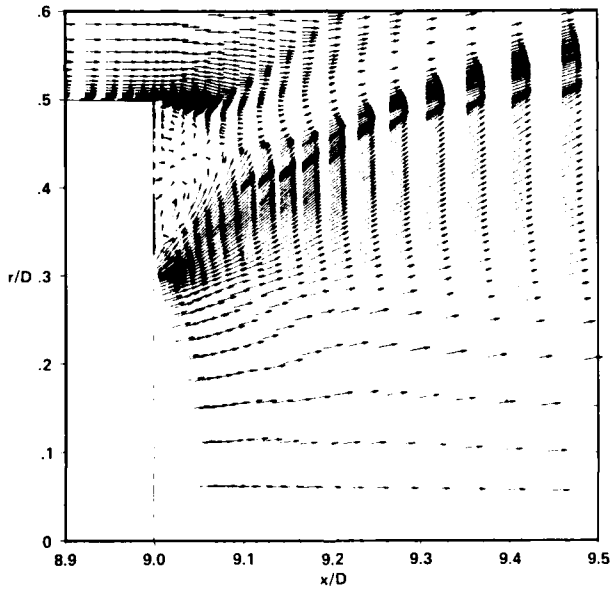

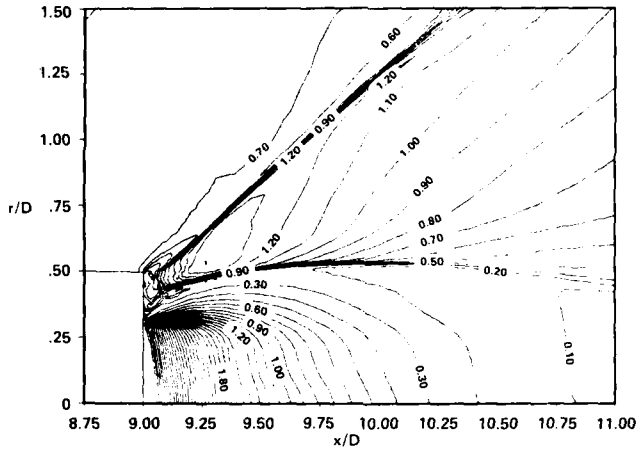

Fig. 2.5.10.2: Isobars, Test Case 10, solution 17

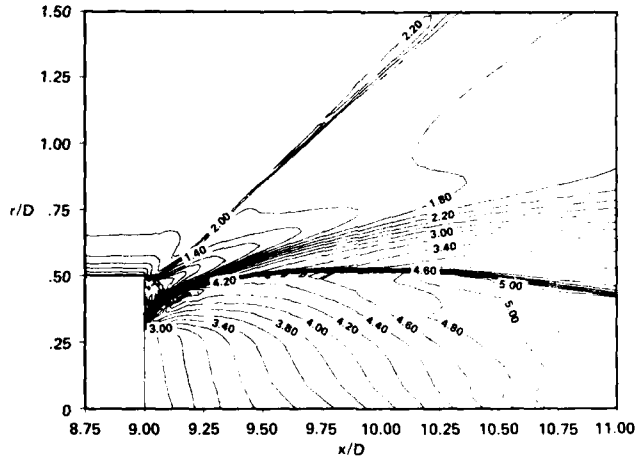

Fig. 2.5.10.3: Iso Mach lines, Test Case 10, solution 17

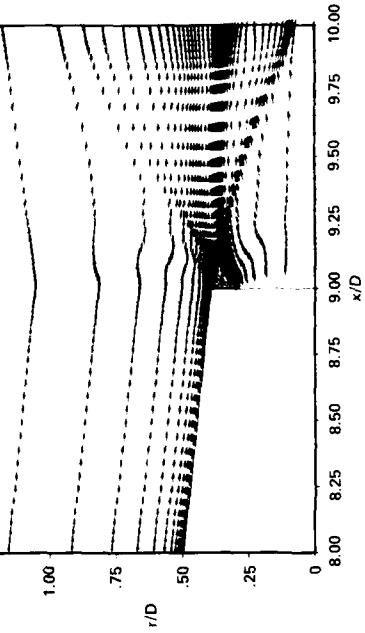

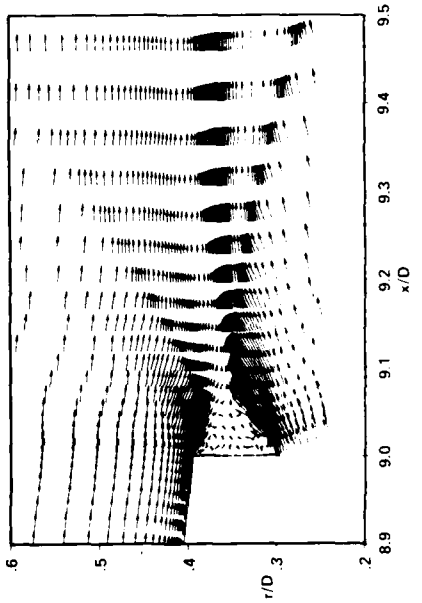

Fig. 2.5.11.1 c, d: Velocity vectors, Test Case 11, solution 17

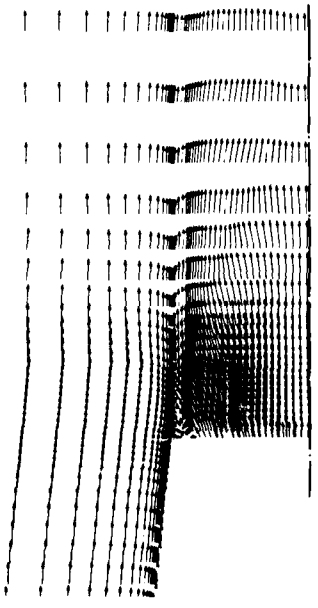

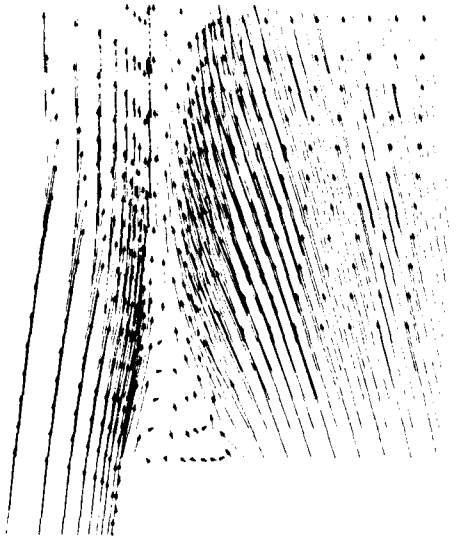

Fig. 2.5.11.1 a, b: Velocity vectors, Test Case 11, solution 16

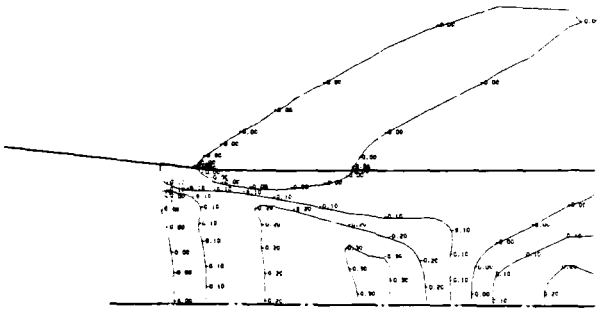

Fig. 2.5.11.2 a: Isobars, Test Case 11, solution 16

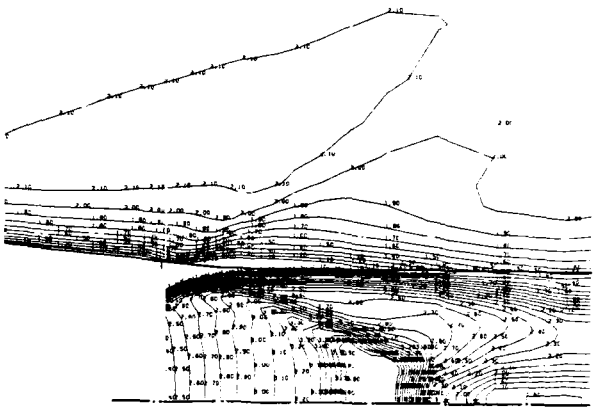

Fig. 2.5.11.3 a: Iso Machlines, Test Case 11, solution 16

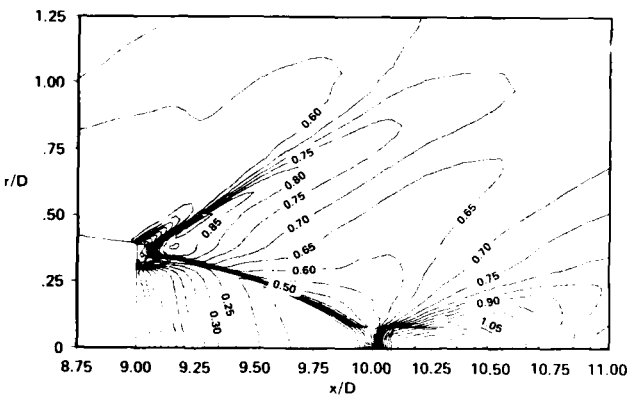

Fig. 2.5.11.2 b: Isobars, Test Case 11, solution 17

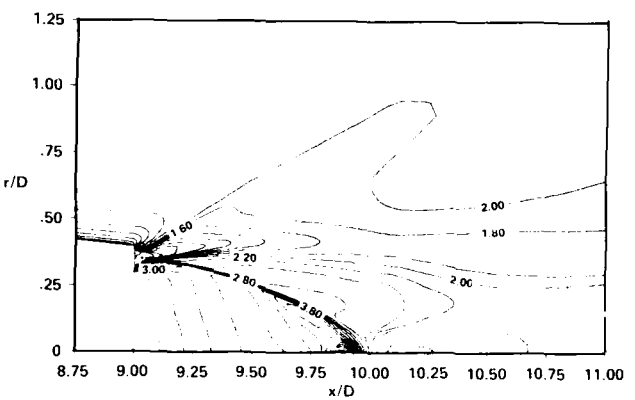

Fig. 2.5.11.3 b: Iso Mach lines, Test Case 11, solution 17

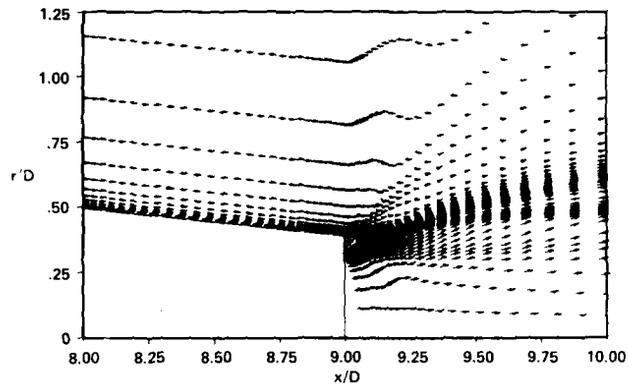

Fig. 2.5.12.1 a, b: Velocity vectors, Test Case 12, solution 17

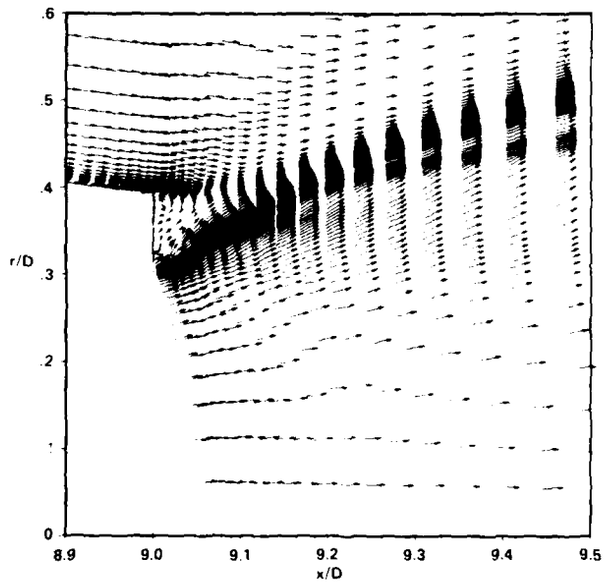

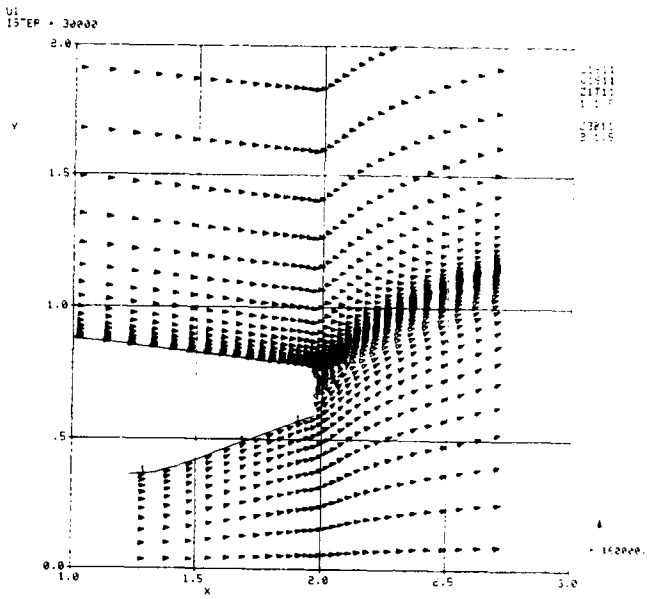

Fig. 2.5.12.1 c, d: Velocity vectors, Test Case 12, solution 18

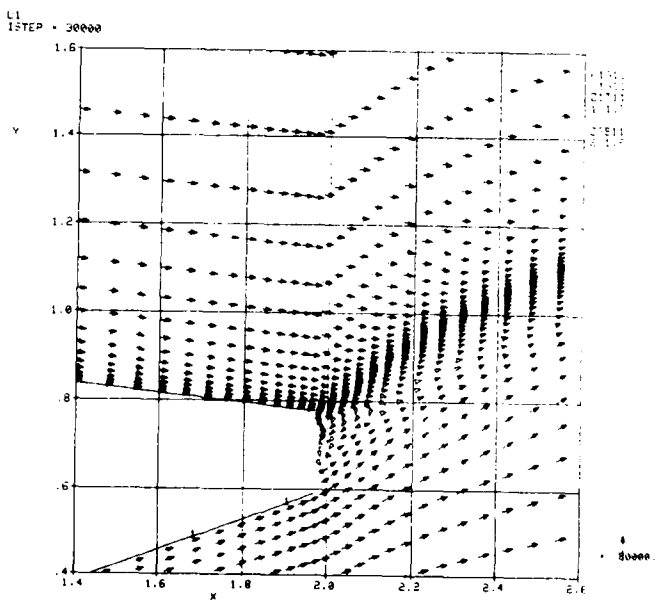

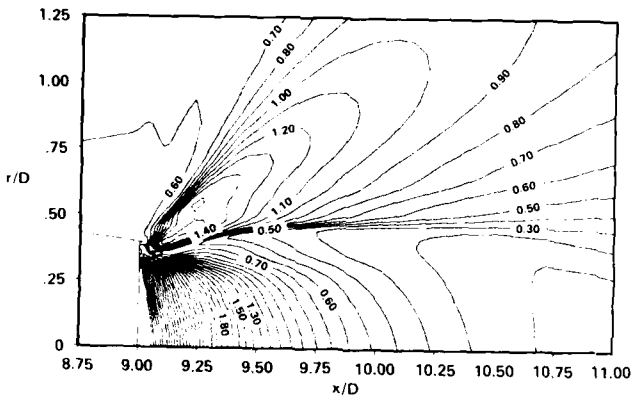

Fig. 2.5.12.2 a: Isobars, Test Case 12, solution 17

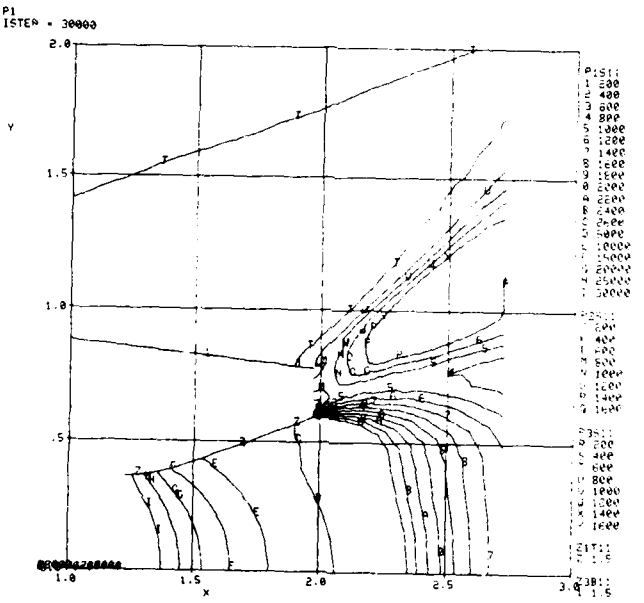

Fig. 2.5.12.2 b: *Isobars, Test Case* 12, solution 18

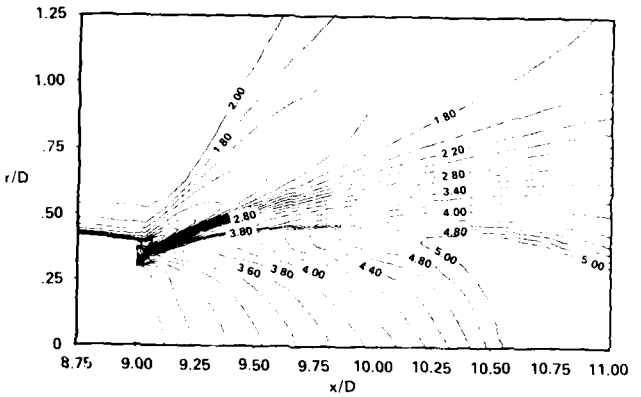

Fig. 2.5.12.3 a: Iso Mach lines, Test Case 12, solution 17

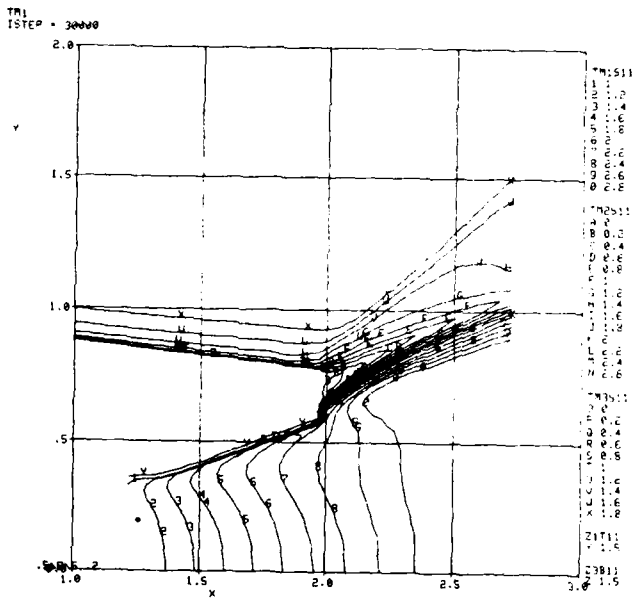

Fig. 2.5.12.3 b: Iso Mach lines, Test Case 12, solution 18

2.6 CONCLUSION AND RECOMMENDATIONS

This theory assessment has attempted to provide an understanding of the state-of-the-art for predicting nozzle afterbody flow interactions. Because the working group agreed to restrict the assessment to axisymmetric nozzle configurations at zero angle-of-attack, the assessment does not provide a complete picture of the state-of-the-art for predicting the interference effects of the engine installation on complete airplane or missile aerodynamics. However, because axisymmetric prediction methods are in a more advanced state of development than three-dimensional methods, the assessment does provide insight into the potential capabilities of analytical methods for predicting nozzle afterbody flows. Because of the rapid changes occurring in computational fluid dynamics, this assessment provides only a "snapshot" of the capabilities of theoretical methods at about the middle of 1984. The rapid growth and improvements of computers and in theoretical methods should, in the future, provide significantly better methods for predicting the effects of engine installation on airplane aerodynamics.

The results of the present theory assessment can be summarized as follows:

- The assessment criteria for theoretical methods should be based on the agreement with measured surface pressure distributions and flow field characteristics and not on boattail pressure drag. The present assessment clearly shows cases where there is very good agreement between predicted and measured drag but where the agreement between measured and predicted surface pressure distributions are very poor.

- Inviscid methods can be used to provide reasonable estimates of wind tunnel wall interference effects. While not investigated in the present assessment, it is also clear that inviscid methods can be used to evaluate support interference effects. In addition, inviscid procedures can be used to provide first order predictions of the occurrence of boundary layer separation when used in conjunction with boundary layer calculation methods.

- At subsonic speeds some of the inviscid/viscous interaction methods provided good prediction of the surface pressure distributions on the sharp-lip nozzle test cases, reasonably good prediction of the location of boundary layer separation, and reasonably good prediction of nozzle pressure drag.

- For the supersonic blunt base test cases, the multiple-component methods provide a reasonable prediction of base pressures, acceptable prediction of separation location on the boattail, and reasonably accurate predictions of the nozzle afterbody pressure drag.

- The Navier-Stokes solutions were in good agreement with the experimental surface pressure distributions up to the location of any boundary layer separation. Because of the poor agreement downstream of separation, the predictions of boattail pressure drag by the Navier-Stokes methods were unreliable. The discrepancies downstream of separation were possibly due to the turbulence models used. For the blunt base test cases, the Navier-Stokes methods provided detailed flow field information and, for some cases, provided good prediction of base pressures. It appears that the Navier-Stokes solutions can provide the experimenter with a valuable diagnostic tool to be used to understand the physics of nozzle afterbody flows.

- Both inviscid and inviscid/viscous interaction methods usually predicted correct trends in pressure distributions and boattail pressure drag as wall blockage was changed and as jet temperature was changed. One Navier-Stokes method was used to predict the effects of jet temperature, and the correct trends were indicated.

- Today's Navier-Stokes calculations generally cost from 5 to 20 times as much as an inviscid/viscous interaction calculation on the same super computer. The cost of multiple-component methods is negligible. The rapid increases in hardware technology and improvements in numerical techniques currently underway may soon make axisymmetric Navier-Stokes codes inexpensive enough for production calculations.

As a result of the assessment of theoretical capabilities made by the working group, the following recommendations are made:

- Computational research should be undertaken to improve two-dimensional modeling of the separation region for inviscid/viscous interaction methods. Navier-Stokes code development should continue with concentration on grid generation, solution algorithms, turbulence modeling, and user friendliness. Detailed studies of the effect of turbulence modeling on practical trailing edge problems should also be undertaken. Emphasis should be given to the development of methods for three-dimensional flows. Zonal approaches as well as complete 3-D Navier-Stokes solutions should be pursued. The 13 AGARD test cases used in the present assessment should be used as a basis for these theoretical developments.

- For present day engineering applications, inviscid/viscous interaction methods and multiple-component methods can be used for design guidance. For 3-D cases, inviscid methods with a 3-D boundary-layer calculation should be used, in particular to give indications of likely separation. Navier-Stokes calculations should be used for diagnostics of the flow about simple configurations.

- Careful "test case" experiments should be undertaken to provide flow field details for the development of turbulence models. Fundamental studies of thick boundary layers merging with thin boundary layers at different energy levels (characteristic of initial regions of shear layer between internal and external flows) should also be undertaken. These experiments should be made at subsonic, transonic, and supersonic speeds. Emphasis should be given to transonic speeds for cases where strong shock interactions occur. Measurements of body pressures, tunnel wall pressures, body and wall boundary layers, flow field velocities, and all Reynolds' stresses in separated flow and mixing regions should be made. In all of these experiments careful measurements of all flow quantities should be made at an inflow boundary normal to the model and well upstream of the nozzle exit. Finally, data similar to that obtained for axisymmetric configurations should be acquired on simple generic 3-D models with well-defined geometry.

3. EXPERIMENTAL ASPECTS

It is generally accepted that one of the best proofs of the validity of a theory is the experiment. On the other hand, theory has helped in many cases to improve the experiment. Examples of this mutual benefit are the detection of systematic errors, the better understanding of available test results, improved concepts for future tests and the monitoring/controlling of the boundary conditions in a wind tunnel test section, to list just a few, but important items.

The following chapters deal with the experimental side only. They are not meant to be a data base for afterbody drag but highlight some topics in experimental afterbody aerodynamics in which progress has been achieved in the past ten years or draw backs have been encountered; in some cases simply the present state of the art is described. Prime emphasis was placed on afterbodies with propulsive jet(s); nevertheless many results presented here will be useful also for afterbodies without jets.

3.1 GENERAL CONSIDERATIONS

Before discussing the very specific subjects of jet simulation (chapter 3.2), testing techniques (chapter 3.3), flow instabilities (chapter 3.4) and errors and correction methods (chapter 3.5), a few general considerations will be presented in the following to illustrate

a) the influence of afterbody drag changes on other parts of the aircraft,

b) the magnitudes of afterbody drag and its sensitivity to pressure integration,

c) the correlation of afterbody drag with some key parameters like effective base area, boattail angle, engine spacing, nozzle interfairings, centre base pressure and afterbody mean slope. These correlations are by no means reliable enough to replace an accurate measurement, but can in many cases be used to predict a trend or drag increment.

3.1.1 Extent of Afterbody Drag Changes

According to the conventional definition*) afterbody drag is the sum of pressure and friction drag of that portion of the fuselage which extends downstream from the maximum cross-section. Normally, these absolute drag values are of minor relevance except if they are used for the verification of computational methods, for the prediction of local aerodynamic loads or for the determination of the best distribution of the instrumentation.

In practical aircraft development, i.e. in optimizing the overall drag and in establishing the drag polars of the complete aircraft, only afterbody drag changes relative to a reference aircraft configuration are used. To date these changes have to be measured since the computed values are not yet accurate enough on complex aircraft configurations at subsonic flight speeds. This is particularly true when boattail separation is present. If in such measurements the afterbody is attached to a balance while the forebody remains non-metric, careful consideration must be given to the forebody drag changes induced by modifications on the afterbody at subsonic speeds. The order of magnitude of this upstream influence for isolated, axisymmetric fuselages (defined in Fig. 3.1.1) is shown in Table 3.1.1 to be $\Delta C_{DP\ FB} \approx 0{,}002$. Whether this value is of relevance depends on the test objective.

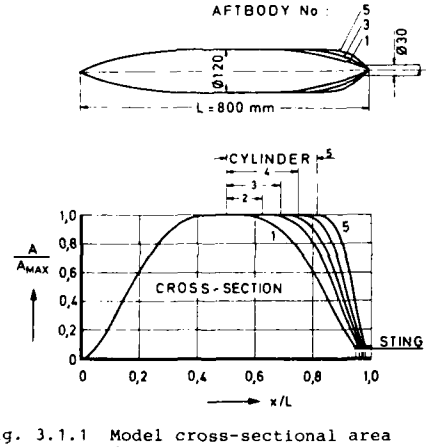

Fig. 3.1.1 Model cross-sectional area distribution, MBB-Afterbodies No. 1 to 5 (Ref. 3.1.)

*) Note: A more sophisticated definition of pressure drag is given in Ref. 3.1.22 (difference between real and potential flow pressures). However, for actual testing of slender 3-D bodies this definition is less practical because of the required effort in computational accuracy.

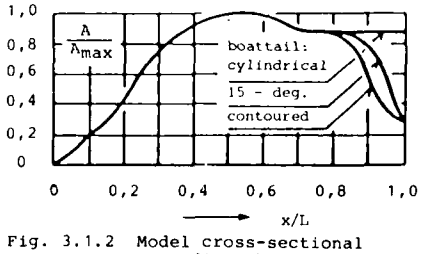

Fig. 3.1.2 Model cross-sectional area distribution (Ref. 3.1.6 and 3.1.3)

Table 3.1.1 Effect of afterbody geometry on forebody drag change, Ref. 3.1.3

"Metric break" at x/L = 0,5				
Ref.	$\Delta C_{D\ FB}$	Obtained from	M_∞	Afterbody change
3.1.2,5 (MBB)	0,0022	Inviscid computation	0,8	No. 1 → No. 3
3.1.2 (MBB)	0,0020	FB balance	0,8	No. 1 → No. 3
3.1.1 (AEDC)	0,0030*	Pressure integration	0,9	No. 1 → No. 5
3.1.6 (AEDC)	0,0018	Pressure integration	0,8	β = 15 deg → cylindrical

*) Afterbody No. 5 had steeper boattailing than No. 3

Table 3.1.2 Comparison of afterbody pressure drag changes, Ref. 3.1.3

1	2	3	4	5	6	7	
Source	Change in afterbody boattailing	Metric break at x/L	$\Delta C_{D\ FB}$	Change of forebody drag relative to: Complete body pressure drag $\frac{\Delta C_{D\ FB}}{C_{D\ CB}}$, %		Change in afterbody pressure drag $\frac{\Delta C_{D\ FB}}{\Delta C_{D\ AB}}$, %	
Ref. 3.1.1 Fig. 13	AB1 → AB5	0,5	0,0030	23	3,6	+4,5	A
Ref. 3.1.6 Fig. 14	15 deg → cylindrical	0,5	0,0018	29	4,7	-5,3	B
	Cylindr. → contoured	0,8	0,0022	35	10	+16	C
	15 deg → contoured	*0,8*	*0,0022*	*10*	5,8	-12	D

Table 3.1.2 relates typical forebody drag changes obtained by AEDC to the pressure drag of the complete body (columns 5 and 6). For example, replacing the cylindrical boattail by the contoured one (defined in Fig. 3.1.2) raises the forebody pressure drag by 35 % or 10 %, depending on whether referred to the pressure drag of the complete body with the low or high drag afterbody (line C). Column 7 relates the pressure drag changes on the forebody to those on the afterbody. The negative sign indicates that the corresponding changes on forebody and afterbody vary in opposite directions. In line D, for example, 12 % of the afterbody improvement is compensated by the associated drag increase on the forebody.

In testing actual aircraft geometries with nonmetric forebodies, the metric break is often placed near the trailing edge of the wing, i.e., downstream of the maximum fuselage cross-section. With variable wing sweep aircraft this station may be as far downstream as x/L = 0,7 up to 0,8. This aggravates the situation, as the upstream influence becomes more pronounced compared with a metric break at x/L = 0,5. Frequently the wing is also nonmetric, i.e., it can be regarded here as part of the forebody. At subsonic speeds any changes in afterbody flowfield will also affect the wing, in particular when the wing is in its swept back position. For a typical afterbody flowfield variation, like afterburning on/off, this induced pressure drag change on the wing is estimated to be of the order of 5 % of the pressure drag of the complete fuselage (Ref. 3.1.2). For a complete tradeoff this value has to be added to column 5 in Table 3.1.2.

Sometimes it has been argued that these induced changes on the forebody are too small to be taken into account, and particularly so when comparing them with the total drag of the complete aircraft model: a typical upstream influence of $\Delta C_{Dp\ FP}$ = 0,002, as shown in Table 3.1.1 for isolated fuselages, becomes roughly 0,0002 when referred to the area of the wing rather than to that of the body cross-section, and two drag counts are normally near the limit of the accuracy attainable in complete model force measurements. However, optimizing the drag of the complete aircraft requires optimization of many, also small, drag sources. In addition, these small pressure drag changes are measurable or can be computed by conventional methods at subsonic speeds. That is, although theory may fail to compute absolute local drag values accurately enough, it is probably well suited to compute the upstream propagation of small pressure increments measured by a few check points near the metric break. In this context, it is suggested to call afterbody drag changes which comprise not only the local changes on the afterbody itself but also those changes induced on all other portions of the aircraft, global afterbody drag changes.

3.1.2 Afterbody Drag Magnitudes and Sensitivity to Pressure Integration

An idealized, axisymmetric fuselage of 15 % relative thickness (afterbody No. 1) showed at $M_\infty = 0,8$ and zero incidence roughly the following positive and negative axial pressure forces acting on the four model portions having solely positive and negative pressure coefficients respectively (see Fig. 3.1.3, data from Fig. 7 in Ref. 3.1.1): At subsonic speeds the positive and negative axial pressure forces on the forebody cancel each other almost completely ($C_{DP\,FB} = -0,001$). On the afterbody this is not quite the case, resulting in a pressure drag coefficient of 0,01. That is, "all" pressure drag of such a complete body stems from the afterbody. In order to assess this value of 0,01 to an accuracy of only 10 % requires the average error in C_p to stay below $\Delta C_p = 0,001$. For measured pressures, this requirement can marginally be fulfilled. However, for the pressures which have been computed even by the most advanced current codes, this accuracy seems to be completely out of reach: typical errors for relatively simple axisymmetric shapes are $\Delta C_{DP} = \pm 0,02$ as has been shown in the preceding part No. 2 on "Computational Methods". Similar accuracies can be obtained (also for three-dimensional shapes) by purely empirical methods, as for example, by the truncated Integral Mean Slope technique described at the end of this chapter (para 3.1.3.3). As a result, improvement is necessary in both, the empirical and theoretical methods. A more comprehensive discussion on measurement errors will be presented in chapter 3.5.

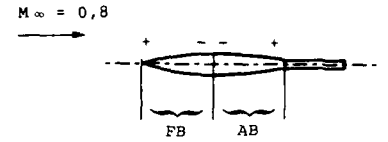

$$\Sigma C_{DP\,PB} \approx \underbrace{+\,0,06 - 0,06}_{FB} + \underbrace{0,055 - 0,045}_{AB} = 0,01 = C_{DP\,CB}$$

Fig. 3.1.3 The problem of obtaining the difference of almost equal magnitudes

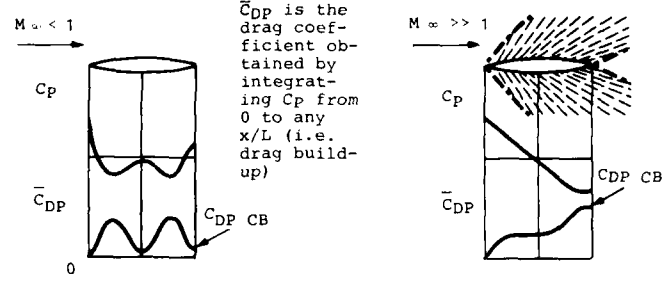

Note:
$\bar{C}_{DP}$ is the drag coefficient obtained by integrating C_p from 0 to any x/L (i.e. drag buildup)

Fig. 3.1.4 Pressure distribution and pressure drag buildup in subsonic and supersonic flow

At supersonic speeds the problem of obtaining the difference between two almost equally large values no longer exists: apart from the pressure rise in the region of the trailing edge shock there is virtually a monotonic increase in pressure drag with the distance from the nose of the body as shown in Fig. 3.1.4. That is why in supersonic flow the pressure drag is considerably easier to evaluate than in subsonic flow (larger tolerable error ΔC_{DP} for the same percentage accuracy). Apart from attaining the maximum flight speed, however, the relative importance of the afterbody drag of turbojet powered aircraft is much smaller in supersonic flow than in subsonic flow, as will be shown in the following.

The variation of forebody, afterbody and complete body pressure drag with Mach number is shown for bodies No. 1 and No. 5 in Fig. 3.1.5, reproduced from Ref. 3.1.1. From the raised level in pressure drag coefficient at supersonic Mach numbers one could be misled into assuming that afterbody drag at supersonic speeds is particularly large and important also for combat aircraft with afterburners.

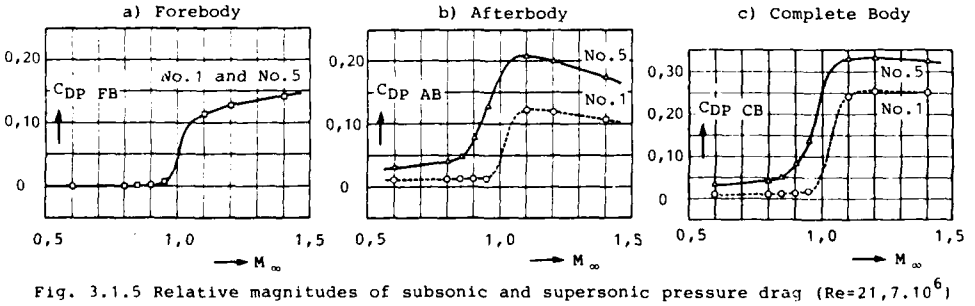

Fig. 3.1.5 Relative magnitudes of subsonic and supersonic pressure drag (Re=21,7.10⁶)

$$\Delta C_F = \left(\frac{F-D}{F_i}\right)_{SINGLE\ REF.} - \left(\frac{F-D}{F_i}\right)_{MODEL} \approx \frac{D_{MODEL} - D_{SINGLE\ REF.}}{F_i} \quad *)$$

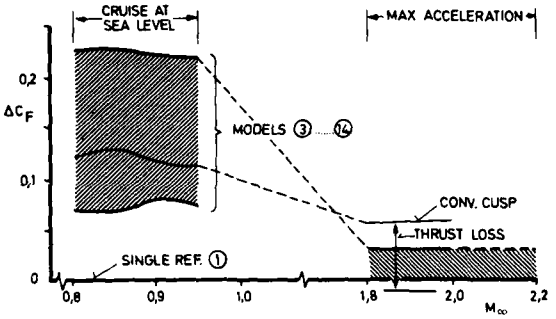

Fig. 3.1.6 Magnitudes of thrust-minus-drag coefficient at subsonic and supersonic flight

*) Note: This approximation does not hold for the "convergent cusp" configuration ($\Delta F/F_i \neq 0$ at supersonic speeds)

Fig. 3.1.6 (Ref. 3.1.7) suggests that rather the opposite is correct: in one test series all 12 twin jet afterbody configurations of a combat aircraft project experienced at subsonic speeds thrust minus drag coefficients C_F which were lower than that of the single jet reference model by up to 0,225. In these tests the thrust of each model was very close to that of the single jet reference model and so ΔC_F is approximately equal to $(D_{Model} - D_{Single\ Ref.})/F_i$ as explained in the same figure. A $\Delta C_F = 0{,}225$, therefore, means that the drag of the worst configuration was higher than that of the reference model by about 22,5 % of the ideal gross thrust. With an assumed ratio of gross thrust to net thrust of two and with net thrust = drag it follows that the aircraft with the worst afterbody had about 45 % more aircraft total drag than an aircraft with the idealized afterbody. The idealized or single jet reference afterbodies are characterized by a boattail of linear distribution of the cross-sectional area, by zero base area and by a single jet the throat area of which is equal to the sum of the throat areas of the twin jet models. The reference model for the subsonic flight regime had a convergent nozzle with a very gradual contraction while the supersonic reference model had an idealized convergent/divergent nozzle matched for $M_\infty = 2$. In order to provide the linear cross-sectional area distribution together with a shallow boattail the subsonic reference model had to be increased slightly in length. The reference models are considered as being the aerodynamic optima. Their main advantage over other reference models with cylindrical boattails is that during an optimization study they indicate how far from the aerodynamic optimum a particular configuration still is and whether further efforts are worthwhile.

Purely from aerodynamic viewpoint, i.e. disregarding nozzle weight and complexity, it will be shown in chapter 3.1.3 that twin jet afterbody configurations can be designed such that they reduce the above 45 % of additional aircraft drag at subsonic flight speeds to about 4 % for a boattail angle $\beta = 15°$ (Fig. 3.1.11) and to about 3 % for $\beta = 10°$ to $12°$ (Fig. 3.1.10). Hence enormous performance improvements seem possible for combat aircraft assigned for long range missions in which nozzle weight is of secondary importance. Fig. 3.1.6 shows further that in the high supersonic regime the drag of the same models/nozzle concepts was only up to 3 % of the ideal gross thrust higher than that of the supersonic reference model ($\Delta C_F = 0{,}03$). This is explained by the fact that the nozzles were here in the maximum reheat position: the ideal gross thrust is considerably higher and the projected areas of boattail and base are reduced due to the larger exit diameter of the matched convergent/divergent nozzles.

The only model having a simple, short flap convergent nozzle with a cusp base ("convergent cusp") experienced a higher ΔC_F. This is explained by the relatively high thrust losses of a convergent nozzle at high jet pressure ratios (≈ 10 at $M_\infty = 1{,}9$). Subtracting those losses from the measured ΔC_F of the "convergent cusp" yields a negative value (caused by the post exit thrust). This means that the afterbody drag of this model was smaller than that of the supersonic reference, the optimum (T-D) configuration. This example illustrates again the close interrelation between drag and thrust. If one of the two components is optimized separately, precise assessment of the interface, particularly in the experiment, is required. This problem will be further expanded in chapter 3.3 on testing techniques. The thrust-minus-drag coefficients in Fig. 3.1.6 were obtained from cold jet model tests. No attempt has been made to correct these data to the true jet temperatures. This will be dealt with in chapter 3.2.1 on "Jet Temperature Effects".

Similar results as in Fig. 3.1.6 are shown in Fig. 3.1.7 for three different types of afterbody/nozzle combinations. These data were derived from wind tunnel tests conducted by SNECMA (Ref. 3.1.8). Two of the afterbodies shown are actually being flown (configurations "C" and "TSS"). The third configuration ("CD") is a more or less ventilated ejector with variable boattail angle. In a similar manner, the shroud of the TSS has variable trailing edge flaps, which move outward to a cylindrical position at $M_\infty > 1{,}2$. At smaller flight Mach numbers the boattail angle of these flaps is a function of M_∞ and varies between 5° and 20°. Tertiary flow then exists. Its drag is included in the external drag of the afterbody. The secondary to primary mass flow ratio W_s/W_j is of the order of 9 % for the TSS and is charged with the free stream momentum. In contrast, the other two nozzle concepts (C and CD) have only small amounts of secondary flow, W_s/W_j being about 0,5 %. Therefore its entry drag (free stream momentum) has been neglected here, particu-

larly as this flow has already been used to cool other aircraft components and has been charged there. It is clear that in an aerodynamic optimization all three flows have to be taken into account.

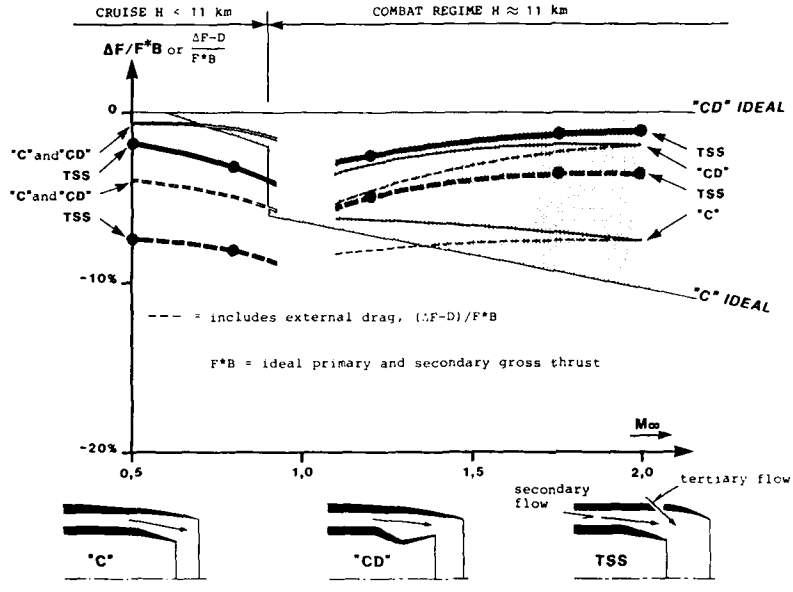

Fig. 3.1.7 Afterbody/nozzle performance, Ref. 3.1.8

The reference value, F*B, is the ideal gross thrust of the primary and secondary flows. The curve "C" IDEAL, therefore, gives the thrust losses of an ideal convergent nozzle resulting from incomplete expansion. The full lines "C", "CD", and "TSS" represent the internal ejector nozzle performance including the pressure force on the base. Performance including the external afterbody drag is shown by the dashed lines.

The losses in gross thrust of a convergent nozzle depend primarily on the jet pressure ratio. In the present example they are as high as 10 % at M_∞ = 2,0 (curve "C" ideal, linear approximation). Due to the overpressure created by the expansion of the jet downstream of the nozzle, these thrust losses are partly compensated by the associated increase in base pressure. The total loss, therefore, is reduced from 10 % to 7,5 % (curves "C"). In spite of this recovery in losses, this configuration is aerodynamically much inferior when compared with the good performance of the CD concept having a total loss of only 2 %.

In summary, for good performance at higher supersonic flight Mach numbers it is important to expand the primary flow in a convergent/divergent nozzle. The external drag, on the other hand, is relatively unimportant. In the present example it is zero at M_∞ = 2,0 and only 2 % of the ideal gross thrust F*B at M_∞ = 1,2. At subsonic cruise, the situation is reversed with the predominant performance penalty being caused by external afterbody drag (difference between full and dotted curves). Note that Figure 3.1.6 shows at M_∞ = 2,0 quite similar results obtained from a different investigation: the configuration "convergent cusp" yields a change in thrust minus drag coefficient ΔC_F = 0,06 which compares well with the (ΔF-D)/F*B = -7,5 % for the "C" afterbody in Figure 3.1.7. The difference in sign and magnitude is due to the different definitions of ΔC_F and (ΔF-D)/F*B. Also, the jet pressure ratio was lower in Figure 3.1.6.

The examples discussed in Fig. 3.1.6 and 3.1.7 show that it is important to consider the losses in internal thrust as well as those attributed to external drag when determining afterbody installed performance across the Mach number range. As will be shown in chapter 3.3, the experimental measurement of these losses can be difficult.

3.1.3 Some Useful Correlations

To date there is no empirical or semi-empirical method which gives predictions of afterbody performance (i.e. thrust-minus-drag) to a similar degree of accuracy as high quality measurements. However, orders of magnitudes and general trends in afterbody drag can be predicted with the aid of published data. In Ref. 3.1.7 for example it was shown how boattail angle, nozzle interfairings, engine spacing and base areas affect the after-

body performance of a typical twin jet, long leaf nozzle configuration at subsonic cruise. An extract of the main results will be briefly repeated in the following together with more recent results on the influence of base area, centre base pressure and afterbody mean slope.

3.1.3.1 Effect of Engine Spacing and Nozzle Interfairing

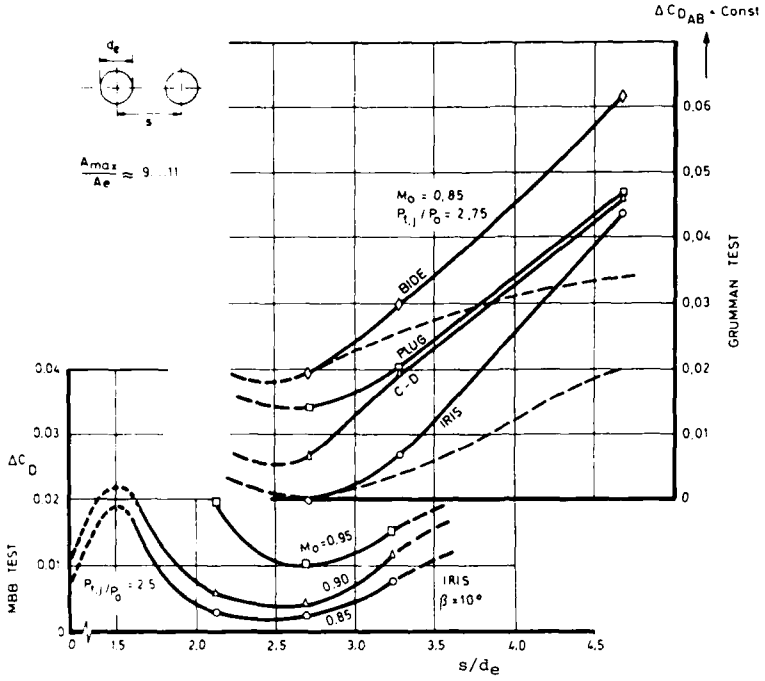

Fig. 3.1.8 Optimization of engine spacing from two different investigations, Ref. 3.1.7

Fig. 3.1.8 shows the variation of incremental afterbody drag with nozzle spacing: There is a clear aerodynamic optimum for spacings s/d_e as close as 2,5 to 2,7. The drag values at zero spacing were obtained from a configuration in which the jet pipes and the two Iris nozzles were squeezed together to form non-circular, double-D shaped exits. Note that the ΔC_D is referred to the single jet reference model having the minimum total (= friction + pressure) drag. This definition of ΔC_D applies to all figures from Ref. 3.1.7. Note also that, throughout the present report, C_D is referred to the maximum fuselage cross-section unless labelled by $()^+$. In such cases the reference area is the wing planform.

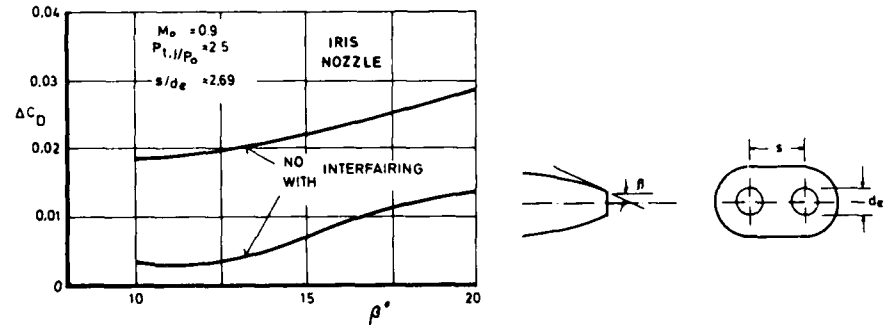

Fig. 3.1.9 Effect of boattail angle and interfairing, Ref. 3.1.7

The beneficial effect of a fairing between the two nozzles is shown in Fig. 3.1.9: The presence of the interfairing reduces the drag by a larger amount than a reduction of the boattail angle from 20° to 10° does, that is $\Delta\Delta C_D \approx 0{,}015$ as compared with $\Delta\Delta C_D \approx 0{,}010$. The combination of both, interfairing and shallow boattail of about 11 degrees, results in the "absolute" minimum realistic total afterbody drag of a twin jet fighter configuration ($\Delta C_D = 0{,}003$). Still lower boattail angles would result in an increase of drag due to greater friction from the increased length to achieve the same zero base area.

3.1.3.2 Effect of Base Areas

As found from wind tunnel tests, the largest changes in subsonic drag occur for variations in base size. Geometric bases located upstream of the nozzle exit plane normally introduce flow separation on adjacent surfaces. The sum of geometric and induced base areas is called effective base area. Fig. 3.1.10 shows this pronounced influence of effective base sizes.

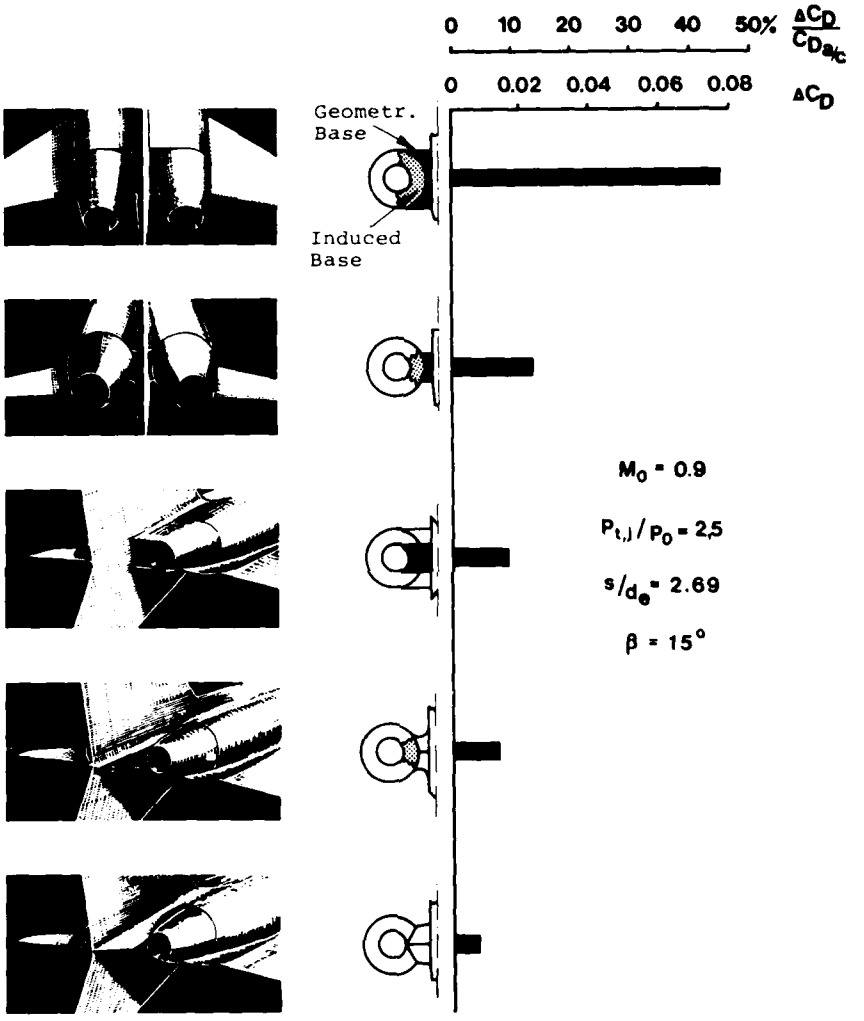

Fig. 3.1.10 Influence of base area between nozzles on drag, Ref. 3.1.7

The worst configuration had an additional drag over that of the single jet reference model of 45 % of the complete aircraft total drag. Note that this reference model had virtually zero pressure drag and a wetted surface which was equal or even smaller than that of all other models in this investigation. Hence the incremental drag $\Delta C_D = 0{,}08$ of this worst configuration represents roughly also the corresponding pressure drag coefficient $C_{Dp\ CB} \approx C_{Dp\ AB} \approx 0{,}08$ (compare also MBB-body No. 5 in Fig. 3.1.5b and c for which the same magnitudes were found at $M_\infty = 0{,}9$).

A similar investigation was conducted by ARA (Ref. 3.1.9) on two classes of twin jet afterbodies: in class 1 the nozzle exit planes were at the same axial position as the rear most point of the fuselage, while in class 2 they were located upstream of the end

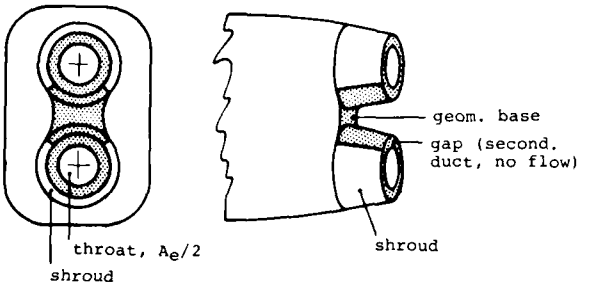

▒ = estimated effective base area $A_{b\ eff}$ includes also annular gap between shroud and throat of convergent nozzle

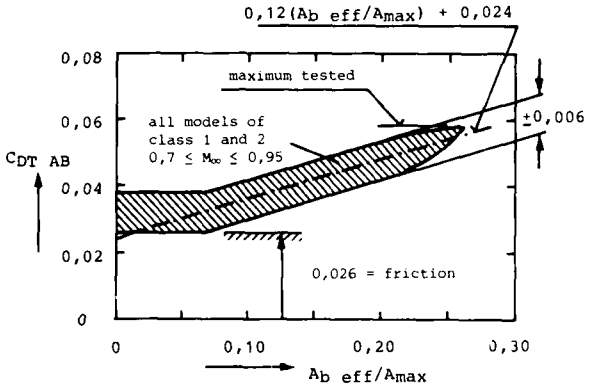

Fig. 3.1.11 Correlation of total afterbody drag (pressure plus friction) with effective base size, Ref. 3.1.9

Table 3.1.3 Values of P_{tj}/P_∞ for Fig. 3.1.11

M_∞ =	0,7	0,8	0,9	0,95
A_c/A_{max} = 0,13	2,1	2,5	3,0	3,4
A_e/A_{max} = 0,07	3,2	3,8	4,5	5,1

of the fuselage (Phantom-type configurations). Fig. 3.1.11 shows the variation of afterbody total drag (i.e. pressure plus friction) with the effective base area. In these tests the geometric base size varied due to the different indentations ("gullies") between the nozzles and due to the different shroud and throat diameters. The trailing edge boattail angle was 10° and 15°, the sum of the two throat areas, A_e, was 7 % and 13 % of the fuselage maximum cross-section A_{max}, while the effective base areas ranged from 0 % to 26,1 % of A_{max}. The jet pressure ratio had different values for each Mach number tested corresponding roughly to those encountered in subsonic cruise (see Table 3.1.3). "The values for the smaller nozzles, which represent a lower bypass ratio engine, have been taken as 1,5 times those of the larger nozzles so that the comparisons are made at approximately the same net engine thrust" (Ref. 3.1.9).

It is remarkable to note that the total drag of all models of class 1 and 2, a total of 21, increases approximately linearly with effective base size for $0,7 < M_\infty < 0,95$:

$$C_{DP\ AB} \approx 0,12\, A_{b\,eff}/A_{max} \pm 0,006$$

For different jet pressure ratios and also for higher Mach numbers (e.g. $M_\infty = 1,3$) this simple relationship is less successful, according to Ref. 3.1.9. A further example of the effect of base area on afterbody pressure drag was published by McDonald and Hughes for an "interceptor type aircraft" as far back as in 1965 (Ref. 3.1.15). Fig. 3.1.12 shows this correlation of increase in aircraft drag versus the square of the base diameter. Note that, in contrast to the other diagrams, the parameter on the abscissa includes the jet area. According to Ref. 3.1.15 this correlation holds for $0,6 < M_\infty < 0,9$, but probably does not hold for conical afterbodies with boattail angles greater than 8° or for curved boattails (circular arc and parabolic) greater than 16°.

Yet another example of the same interrelation is shown in Fig. 3.1.13 by the solid curves (D). They have been reproduced from Ref. 3.1.10 and represent a synthesis of the results in Ref. 3.1.9, 11, 12 and 13. It is assumed that the influence of boattail angle β would largely disappear, had effective bases been used instead of geometric ones. For comparison purposes also the linear relationship of Fig. 3.1.11 is shown as dashed line E. Apart from the lower values curves D and E agree quite well. This may be expected since the data of curve E were also used to establish the curves D of the original diagram.

In Fig. 3.1.14 the correlations of Figs. 3.1.10 (curve C) and 3.1.12 (curves A, B) are compared with each other. For this purpose the curves of Fig. 3.1.12 were converted as follows:

$$C_{DP\ AB} \approx \Delta C_{Do\ a/c} = (C_{DT\ FB} = \text{const} = 0,140)/(C_{Do\ a/c}/\Delta C_{Do} - 1)$$

with $C_{DT\ FB} = C_{Do\ a/c} - C_{DP\ AB}$.

In this conversion it is assumed that the zero lift drag of the aircraft minus the pressure drag of the afterbody stays constant. In addition, the abscissa values of Fig. 3.1.12 were reduced by 0,080 = const to convert $(A_b + A_j)$ into A_b. This implies that A_j is constant in Fig. 3.1.12 and equal to the lowest flight test point, at which A_b must then be zero. Perfect agreement is now shown for the correlation curves B and C. However, because of the

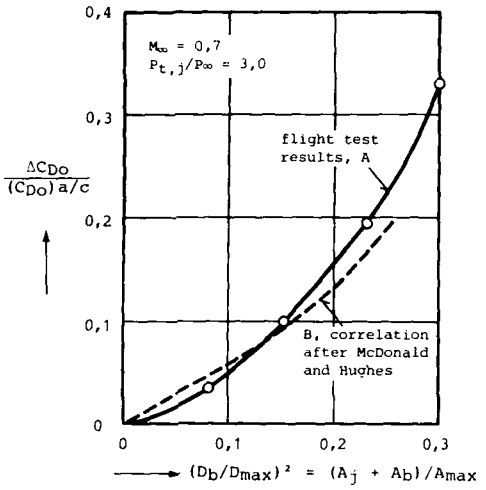

Fig. 3.1.12 Increase in aircraft profile drag due to the sum of jet and base areas, Ref. 3.1.15

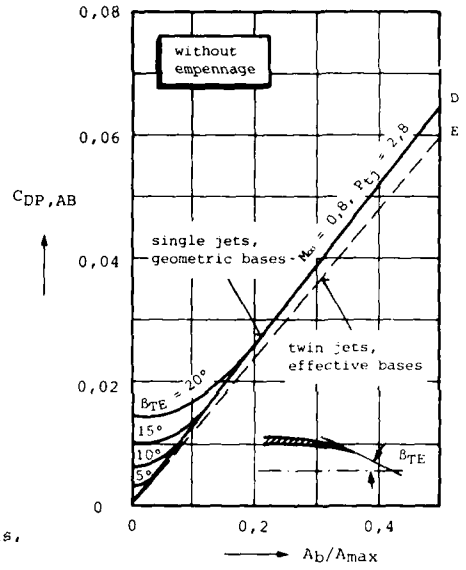

Fig. 3.1.13 Correlation of afterbody pressure drag with base size, without empennage, Ref. 3.1.9 and 10

assumptions made above, this agreement could be fortuitous (for example, had a more representative jet area ratio A_j/A_{max} = 0,10 been used instead of the above 0,080, curves A and B would be slightly shifted to the left in Fig. 3.1.14). Therefore, additional wind tunnel results from the early Tornado development phase were also plotted in the same figure as points No. 1, 2 and 3 (Ref. 3.1.19,20) They confirm curves B and C. This is quite remarkable since very different wind tunnels, testing techniques and aircraft configurations were involved.

Curve C was obtained from a test series in the Boeing 8 ft x 12 ft Transonic Wind Tunnel for the US/FRG AVS (Advanced V/STOL Weapon System) project during 1965 - 1967. Thrust minus drag was measured on a model with metric forebody without wing. This forebody did not duplicate the Tornado but rather the "Iliad" configuration. Point No. 1 represents an early Tornado configuration with a slightly shortened forebody (model 20A) tested in the same wind tunnel with the same test set-up. Points No. 2 and 3 represent also early Tornado configurations, however, tested with model 20B in a different (the ARA 8 ft x 9 ft) Transonic Wind Tunnel. In contrast to model 20A this model had a non-metric forebody and a (non-metric) wing. The one-component balance did not record thrust but afterbody drag only. While the afterbody pressure drag values were readily obtained from incremental force measurements conducted by MBB (Ref. 3.1.19), the effective base areas were taken from an independent assessment made by BAe (Ref. 3.1.20).

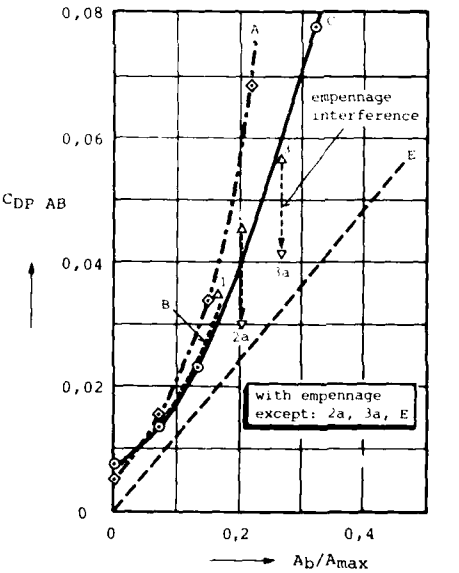

Fig. 3.1.14 Correlation of afterbody pressure drag with base size, with and without empennage, Ref. 3.1.23

There seemed to be a clear discrepancy between the trends shown by the curves ABC and DE. Reanalyzing the ARA data (curve E) in 1984 for the same jet pressure ratio as for curve C i.e. for P_{tj}/P_∞ = 2,5, did not resolve the discrepancy: variations in jet pressure ratio between 2 and 3 had little effect on afterbody drag (Ref. 3.1.18). The most probable reason for this discrepancy finally turned out to be the presence of the empennage. Curves A and C and also the points No. 1, 2 and 3 apply to twin jet configurations with empennages while curves D and E represent configurations without empennages. Curves D apply to single jets and curve E to twin jets. The number of jets, therefore, seems to have little effect on afterbody drag. Points No. 2 and 3 were tested not only with but also without empennage.

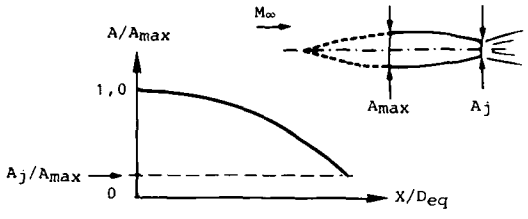

a) Afterbody cross-sectional area distribution

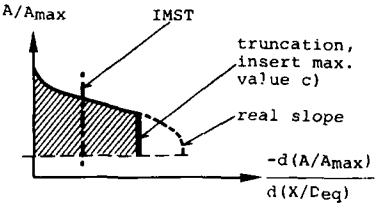

b) Truncated slope distribution

$$D_{eq} = \sqrt{\frac{4}{\pi} A_{max}}$$

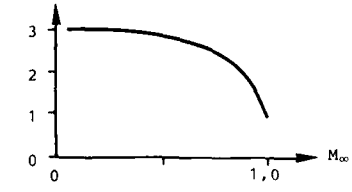

c) Specified maximum slope

Integrate hatched area in b) to obtain integral mean value IMST of truncated slope distribution:

$$IMST = \frac{-1}{1-(A_j/A_{max})} \int_{A_j/A_{max}}^{1,0} \frac{d(A/A_{max})}{d(X/D_{eq})}\, d(A/A_{max})$$

d) Computation of IMST

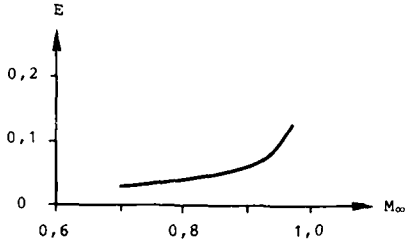

e) Empirical correction factor E, function of M_∞ only

Tail Type	$\Delta C_{D\,Tail}$
	0
	0
	0,006

f) Correction for tail type

g) Predicted afterbody drag

$$C_{DPAB} = E\,(IMST)^{2,77} - \Delta C_{D\,Tail}$$

Fig. 3.1.15 Afterbody drag prediction procedure, Ref. 3.1.17

From the measured difference in afterbody drag the computed profile drag was subtracted to obtain the interference drag. For the horizontal tail an interference drag coefficient of 0,010 was found; the corresponding value for the fin was 0,005. The sum of the two (0,015) is subtracted *from points* No. 2 and 3 in Fig. 3.1.14. These new points, No. 2a and 3a, come closer to curve E but do not quite reach it.

On the whole, fair agreement exists. That is, the trends and the orders of magnitudes seem to be correct. Therefore, for very rough estimates Fig. 3.1.14 could be used to predict afterbody drag and drag changes purely from measured or estimated magnitudes of separated flow areas. Further work should be undertaken to find out whether better agreement between the correlation curves ABCDE can be obtained.

3.1.3.3 Effect of Afterbody Mean Slope

In 1972 Swavely and Soileau (Ref. 3.1.16) presented a method which correlated afterbody pressure drag with the Integral Mean Slope (IMS) of afterbodies. According to Brazier and Ball this method "failed for configurations with base area plots involved regions of steep slopes aft of the point where separation occurs". They suggested, therefore, the Truncated Integral Mean Slope (IMST) approach (Ref. 3.1.17) as a modification of the original method.

In essence, this new method replaces the real [illegible] types of the afterbody cross-sectional area distribution by a specified maximum [illegible] starting from the point at which the real slope distribution exceeds this specified maximum. By integrating this truncated slope distribution over the projected afterbody length $A_{max} - A_j$ the mean value IMST is obtained. The afterbody pressure drag is then [illegible] as explained in Fig. 3.1.15.

The effectiveness of the IMST method is shown in Fig. 3.1.16. The data were obtained for a wide range of variables, that is for single and twin vertical tails, nozzle exit (jet) areas A_j/A_{max} = 0, 0 - 0,40; afterbody lengths X/D_{eq} = 1,42 - 3,60; engine spacings S/D_{eq} = 0,671 - 1,280 and for a matched nozzle exit pressure ratio $P_j = P_\infty$. Bearing in mind that this method does not take into account three-dimensional effects, the agreement between measured and computed afterbody pressure drag appears to be reasonably good (C_{Dp} ± 0,02).

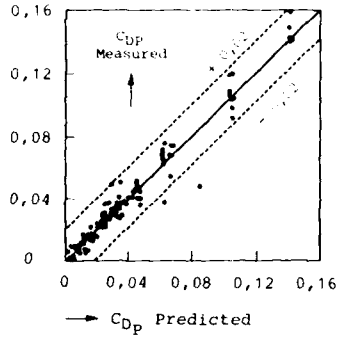

Fig. 3.1.16 Correlation Method Errors, Ref. 3.1.17

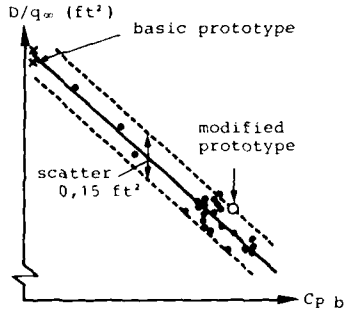

Fig. 3.1.17 Correlation of afterbody pressure drag with centre base pressure, Ref. 3.1.14

3.1.3.4 Correlation of Base Pressure with Afterbody Drag

During Tornado flight development minor geometric changes to the boattail were required to correct an afterbody buffet problem (see also chapter 3.4 on afterbody flow instabilities). Out of the many modifications tested a solution was finally selected which not only eliminated the buffet problem but at the same time reduced the drag of the aircraft by a large amount ($\Delta D/q_\infty$ = 1 ft²), Ref. 3.1.14.

To assess the drag changes of the flying prototype, among other methods, a centre base pressure correlation derived from wind tunnel tests was used, Fig. 3.1.17. This method proved to be powerful and simple: the accuracy is expected to be as good as the standard method with calibrated engines. This correlation will probably not hold for very large geometric changes on the Tornado. For other aircraft types it is expected that a similar correlation can be found.

3.1.4 Concluding Remarks

In the preceding paragraphs a few selected topics in experimental afterbody aerodynamics have been presented, some of which have received increased attention by afterbody specialists over the past years.

Since a data base on afterbody drag was beyond the scope of this report, some correlations of afterbody drag with a few key parameters have been included. These correlations could be useful to predict afterbody drag and to provide design rules during the conceptual phase of an aircraft programme when test results may not yet be available. Later, during prototype flying, drag changes caused by afterbody modifications may be assessed by using the correlations of drag change versus in-flight measured centre base pressure. However, additional work is required to corroborate the correlations presented above. Additional topics in experimental afterbody aerodynamics receiving considerable attention during the past 10 years are discussed in the following chapters.

3.1.5 References

3.1.1 Thompson, E.R. and Smith, C.L., "Afterbody Configuration Effects on Model Forebody and Afterbody Drag", AIAA Paper 81-1443, July 1981; see also Journal of Aircraft, Vol. 19, Sept. 1982, pp. 739-743

3.1.2 Aulehla, F. and Besigk, G., "Fore- and Aftbody Flow Field Interaction with Consideration of Reynolds Number Effects", AGARD-AG-208-II-F, 1975

3.1.3 Aulehla, F. and Besigk, G., "Comment on Afterbody Configuration Effects on Model Forebody and Afterbody Drag", Journal of Aircraft, Vol. 19, Sept. 1982, pp. 798-799

3.1.4 Aulehla, F., "Drag Measurement in Transonic Wind Tunnels", AGARD-CP-242-7, 1978

3.1.5 Aulehla, F. and Besigk, G., "Reynolds Number Effects on Fore- and Aftbody Pressure Drag", AGARD-CP-150-12, 1975

3.1.6 Spratley, A.V., Thompson, E.R., and Kennedy, T.L., "Reynolds Number and Nozzle Afterbody Configuration Effects on Model Forebody and Afterbody Drag", AIAA Paper 77-103, Jan. 1977

3.1.7 Aulehla, F. and Lotter, K., "Nozzle/Airframe Interference and Integration", AGARD-LS-53-4, 1972

3.1.8 Hardy, J.-M., "Etude d'Optimisation d'un Arrier Corps", unpublished contribution to AGARD WG 08B, Jan. 1984

3.1.9 Pozniak, O.M., unpublished ARA reports, 1973 through 1977

3.1.10 Grieb, H., Vedova, R., Enderle, H., and Nagel, H., "Comparison of Different Nozzle Concepts for a Reheated Turbofan", AGARD-CP-301-13, 1981, see also 3.1.21

3.1.11 Henry, B.Z., Cahn, M.S., "Part 1 Preliminary Results of an Investigation at Transonic Speeds to Determine the Effects of a Heated Propulsion Jet on the Drag Characteristics of a Reheated Series of Afterbodies", NACA RN L55 A24a & NACA RM L56 G12, 1955

3.1.12 Reubush, D.E., "Effects of Fineness and Closure Ratios on Boattail Drag of Circular-Arc Afterbody Models with Jet Exhaust at Mach Nos. to 1.3", NASA TN-D-7163, 1973 and "Effect of Fineness Ratio on Boattail Drag of Circular-Arc Afterbodies Having Closure Ratio of 0.50 with Jet Exhausts at Mach Nos. to 1.3", NASA TN-D-7192, 1973

3.1.13 Reid, J., Kurn, A.G., and Crane, J.F.V., "Subsonic Drag of Iris and Translating Shroud Nozzles", unpublished MOD (PE) Data

3.1.14 Leyland, D.C., "Lessons from Tornado Afterbody Development", AGARD-CP-339-8, 1983

3.1.15 McDonald, H. and Hughes, P.F., "A Correlation of High Subsonic Afterbody Drag in the Presence of a Propulsive Jet or Support Sting", J. Aircraft, Vol. 2, No. 3, pp. 202-207 (May - June 1965)

3.1.16 Swavely, C.E. and Soileau, J.F., "Aircraft Aftbody/Propulsion System Integration for Low Drag", AIAA Paper No. 72-1101, Presented at the AIAA/SAE 8th Joint Propulsion Specialist Conference, New Orleans, Louisiana, November 29-December 1, 1972

3.1.17 Brazier, M.E. and Ball, W.H., "Accounting of Aerodynamic Forces on Airframe/Propulsion Systems", AGARD-CP 150-22, 1974

3.1.18 Carter, E.C., unpublished contribution to AGARD WG 08B, 19. April 1984

3.1.19 Unpublished MBB Wind Tunnel Test Reports for Models 20A (1970) and 20B (Phase 1 and 2: 1974, Phase 4: 1975)

3.1.20 Unpublished BAe Assessment of the Tornado Base Separation Areas

3.1.21 Harper, L.R., "The Subsonic Performance of Practical Military Variable Area Convergent Nozzles", AGARD-CP-301-12, 1981

3.1.22 MIDAP, Study Group, "Guide to In-Flight Thrust Measurement of Turbojets and Fan Engines", AGARDograph No. 237, pp 28-29, 1979

3.1.23 Aulehla, F. and Besigk, G., Unpublished Analyses of Ref. 3.1.19, March 1984

3.2 JET SIMULATION

INTRODUCTION

This section deals with the requirements for simulation of the exhaust jet in testing. It is implicit that meaningful tests on afterbody performance must account for or represent the forward interference effects of the presence of the jet. The mechanism whereby the jet plume influences the external flow over the afterbody is discussed in the first subsection 3.2.1 which deals primarily with the effects of the jet temperature. It is common practice to represent the hot flight jet by a cold jet in the wind tunnel. By analysing the mechanism of the influence of a jet plume into a solid body inviscid flow interference effect and a secondary viscous entrainment effect it is possible to define guide lines of the separate interference effects and the means of modifying the cold jet pressure ratio to better improve the total simulation of solid body and entrainment interference.

The methods of providing a model exhaust jet in the presence of intake flow are discussed in subsections 3.2.2 and 3.2.3 for turbine powered simulators and for ejector drive simulators respectively. The bias towards inlet flow provision in these simulators, as distinct from direct blow simulation of the efflux only, is justified by the anticipation that many current airframe flow representations will be of close coupled configurations where inlet and exhaust flow interactions must be assumed to be significant. Direct blow exhaust nozzle simulation is not discussed here as it is considered that, apart from the earth-metric coupling required, the techniques of direct blow are well understood and documented.

Whilst discussing the use of simulators in the 3.2.2 and 3.2.3 subsections full recognition is made of the difficulties of engineering models and their support systems to carry simulators whilst measuring interference-free forces and it is questioned whether the imposed interferences of the experiments are greater than the configuration interferences under investigation. With this theme in mind the final subsection of this section 3.2 is devoted to the concept of the non-interfering support system for the provision of datum drag levels. This technique of annular blown sting support is developed and discussed in subsection 3.2.4 which shows that results obtained this way will essentially be limited to low lift conditions and probably to reheat only afterbody configurations, although this latter limitation may be avoided if afterbody pressure drag via pressure measurement is sufficient.

3.2.1. Jet Temperature Effects

As far back as 1963 Ref. 3.2.1. by Pindzola indicated the need for quantitative relationships between afterbody pressure drag and jet parameters. At that time high temperatures associated with rocket plume effluxes were of more concern. However, more recent data has clearly indicated the significant magnitude of the effect of plume and efflux on the afterbody. In particular, flight data has shown unexplained drag benefits due to reheat which had not been seen in cold jet model tests.

In physical terms the development of the flow and pressures on the afterbody Fig. 3.2.1. may be considered to develop as follows:

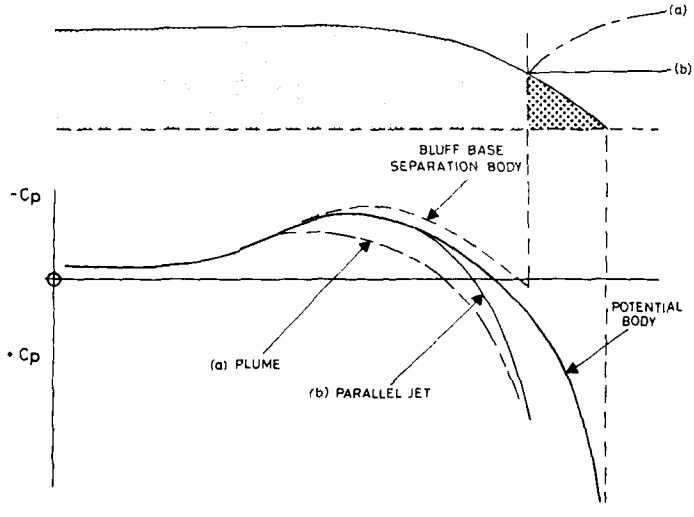

FIG.3.2.1. DEVELOPMENT OF AFTERBODY JET INTERFERENCE

As the separated base of the zero efflux flow condition is gradually filled the base drag is eliminated giving a sharp reduction in drag from the fully separated base condition. (1-2 Fig. 3.2.2)

As efflux pressure is increased the jet flow entrains afterbody flow causing it to accelerate on the boattail giving rise to increased suction drag. (2-3)

As the exhaust pressure ratio increases so the plume diameter increases as the efflux expands to freestream ambient (or near) conditions. The external boattail flow sees the plume as a solid body which increases in size as pressure ratio increases. The forward influence of this plume body causes the boattail flow to recompress giving forward thrusting pressures and reduction of boattail drag. (3-4)

It is this increase of boattail pressure and reduction of drag which is referred to as post-exit thrust which is essentially related to the plume shape and the recovery of the under-expanded exhaust momentum. Hence the form of the post exit drag reduction of the traditional drag v pressure ratio curve.

3.2.1.1. Analysis of the Problem

Modern turbo-jet and turbo-fan effluxes operate in the region 1500°R to 3500°R whilst much afterbody drag testing is conducted with a cold jet near 500°R. Thus the problem is to determine the extent to which jet total temperature (and its associated gas constants) affects the form of the drag - pressure ratio curve. The previous broad description shows how the resultant drag is primarily a function of the jet plume initial expansion angle, final plume diameter, and jet mixing effects which entrain the external afterbody flows, acting somewhat as a jet pump. Thus we have conflicting influences, the drag reduction effect of the solid plume body forward pressure interference and the drag increase due to entrainment giving increased afterbody suctions. These effects are modified by the behaviour of the viscous afterbody flows and by the effect of surface temperature on the boundary layer Fig. 3.2.3.

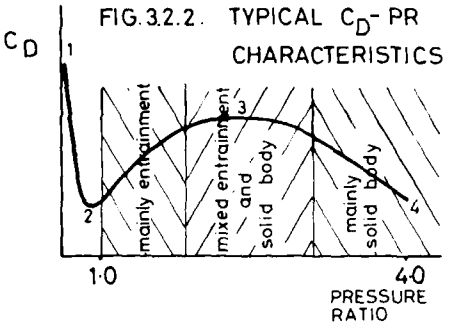

FIG. 3.2.2. TYPICAL C_D- PR CHARACTERISTICS

Experimental work by Compton Ref. 3.2.2. studied the manner in which the exhaust gas physical properties can be related to the jet plume shape and the entrainment and so influence the jet interference on afterbody drag. The jet in Compton's work was obtained with hydrogen peroxide decomposition at values of total temperatures of 646°K and γ = 1.3, 810°K and γ = 1.28 and 1013°K and γ = 1.26. The external afterbody skin temperature was not affected by the temperature of the internal flow. Data of the general form Fig. 3.2.3. was obtained for a range of variables of M_∞, boattail angle, β , and Mj with different jet parameters. This data has been correlated against various plume parameters in an attempt to isolate a critical parameter for prediction purposes.

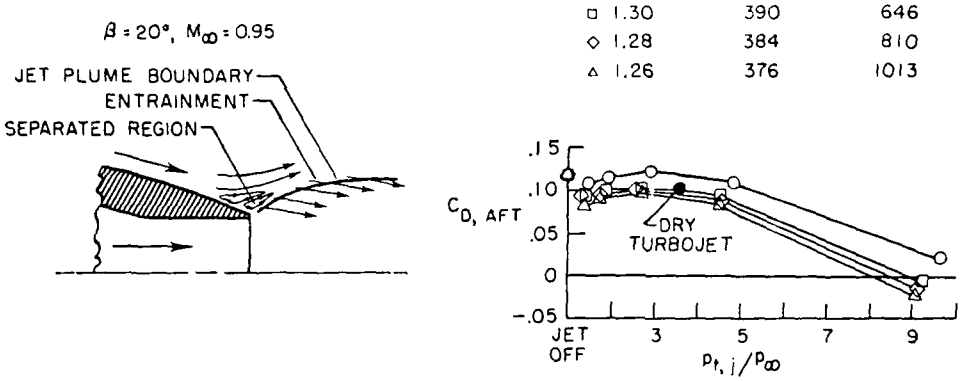

FIG. 3.2.3. EFFECT OF JET EXHAUST GAS PARAMETERS ON JET INTERFERENCE (REF 3.2.2)

Plume blockage has been related to the initial expansion angle of the plume δj which is the Prandtl-Meyer expansion angle of the jet flow when expanding from its internal exhaust static pressure to the external boattail static pressure at the exit plane. Results showed a collapse of the data to a series of parallel curves independent of pressure ratio for values of δj, Fig. 3.2.4.

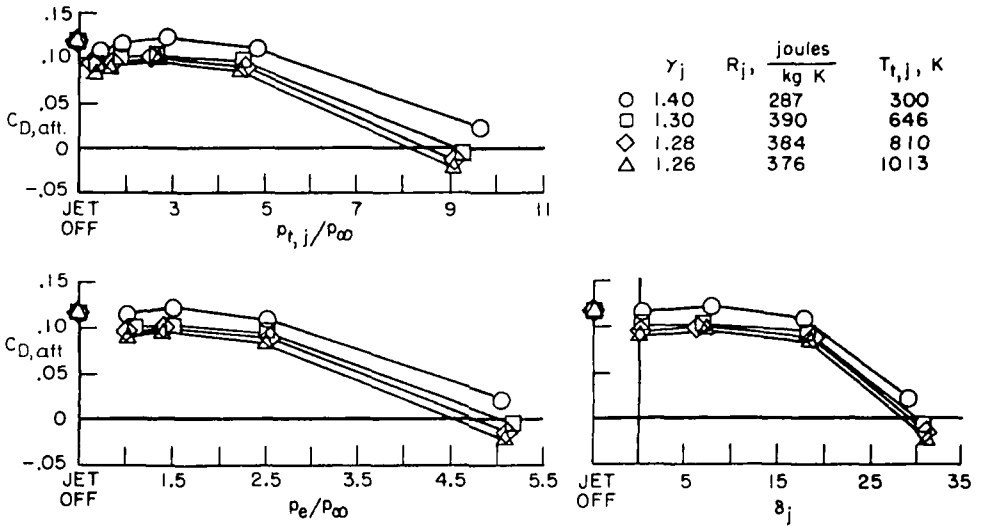

FIG.3.2.4. AFTERBODY DRAG COEFFICIENT AS A FUNCTION OF $p_{t,j}/p_\infty$, AND δ_j. $\beta = 20°$, SONIC EXIT, $M_\infty = 0.95$ (REF. 3.2.2)

It is recommended in Ref. 3.2.2. that for most aircraft configurations and jet pressure ratios the duplication of M_j, nozzle divergence angle θ_j and δ_j will give adequate correlation of plume body interference on the afterbody drag, *including modest supersonic jets (M_j - 2) and jet divergence angle.*

At transonic flow conditions where large base areas or regions of separated flow may exist the plume body forward interference is only part of the story and the jet entrainment through its influence on base drag can be significant. The amount of external body flow entrained by the jet depends upon the momentum of the jet flow in relation to the momentum of the afterbody flow and the edge velocities, energies and characteristics of the two flows. Reference 3.2.3. gives the relationship for entrainment in quiescent flow as

$$\frac{d\ (\text{mass entrained})}{d\ (\text{distance downstream})} \propto (\text{Jet momentum})^{\frac{1}{2}} \quad \rho_\infty^{\frac{1}{2}}$$

Reference 3.2.2. studied the correlation of afterbody drag for constant values of δ_j (i.e. assumed constant plume solid body interference) using various parameters relating momentum, mass flow, kinetic energy, internal energy for the jet and external flows. It was concluded for the particular configurations tested that entrainment effects correlated best with the ratio,

$\frac{R_j T_j}{R_\infty T_\infty}$ i.e. the internal energy/unit mass *without accounting for the difference of specific heat,*

C_v of the two flows.

Compton summarised the temperature effect situation adequately with Figure 3.2.5.

This illustrates how results obtained with a limited jet temperature range may be interpolated and extrapolated to real flight temperature conditions, it does not however give prediction methods to put *corrections into tests which have only been made at cold jet conditions.*

Work reported by Robinson Ref.3.2.6 at the same time as Compton indicated similar trends although the entrainment effects were less pronounced than those on a mean 15° afterbody. In this work, which was conducted in the AEDC 16ft PWT pressure distributions were measured on an isolated axisymmetric model of a military turbojet afterbody with ethylene/air hot jet representation. The results in Fig. 3.2.6 (all for rather high NPR) show that the measured afterbody drag reductions associated with increased jet temperature compare well with the cold jet data corrected for the γ effect on initial plume expansion angle. This correction, for this unseparated boattail, accounts for most of the temperature effect, leaving only a small amount to be accounted for by entrainment at M = 0.9.

In a later reference, further jet temperature effects have been investigated by Robinson (Ref.3.2.4.) using a practical non-axisymmetric nozzle configuration of a General Electric ADEN design as shown in Fig. 3.2.7. The upper surface of this nozzle extends beyond the throat and forms a cowl whereas the lower

surface terminates near the throat. The exhaust plume will therefore be a combination of a forced expansion following the boundary of the inner upper cowl surface and a free expansion from the lower nozzle lip. The jet was represented at 4 temperature levels 500°R, 1200°R, 1500°R and 1900°R by a combustion mixture of ethylene/air. Because of the non-axisymmetric characteristics of the nozzle, water cooling was not applicable and so the external surface was subject to temperature conduction through the model with possible affects on the results.

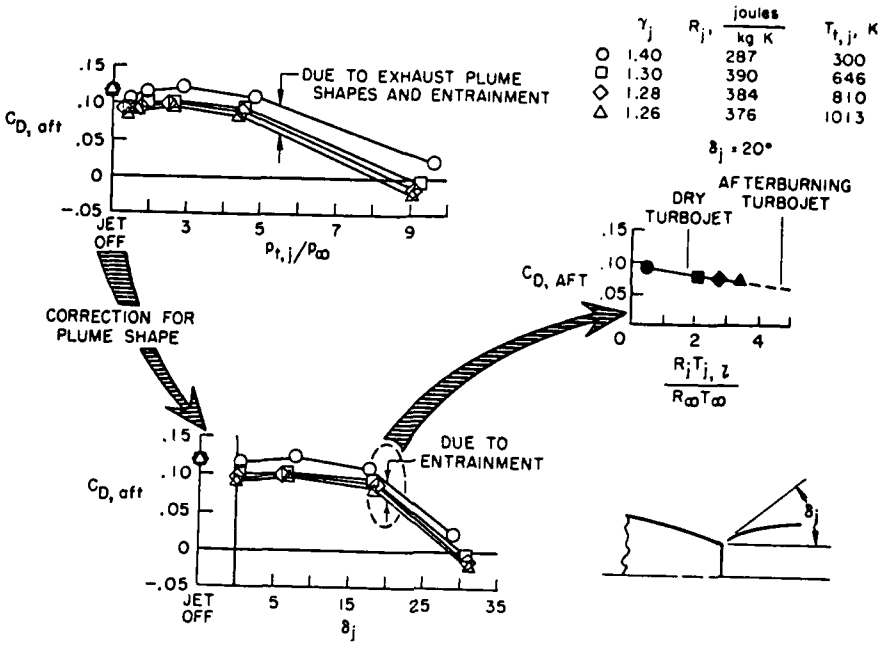

FIG.3.2.5. JET INTERFERENCE COMPARISON PARAMETERS. M_∞=0.95 (REF. 3.2.2)

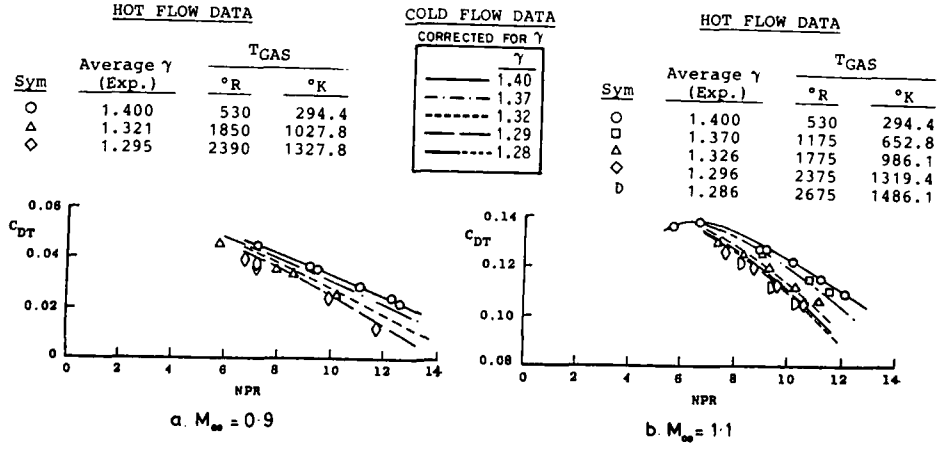

FIG.3.2.6. COMPARISON OF THE COLD FLOW DATA CORRECTED FOR SPECIFIC HEAT RATIOS TO THE EXPERIMENTAL HOT-FLOW DATA AT Re = 2.5 x 10^6/ft. (8.2 x 10^6/m.) (REF. 3.2.6)

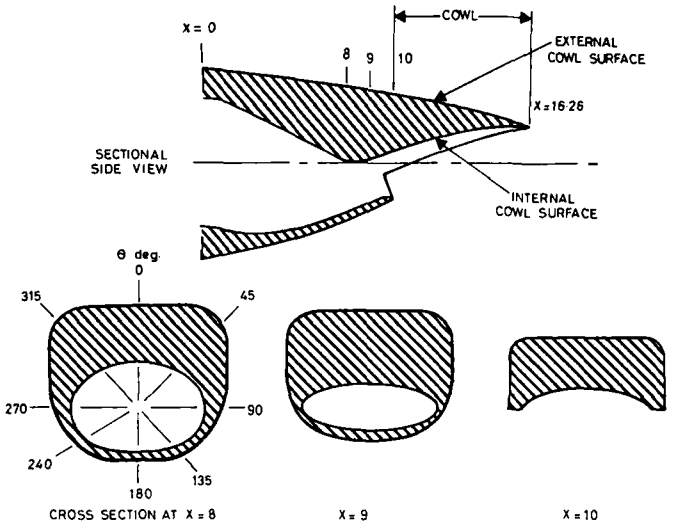

FIG.3.2.7. NOZZLE AFTERBODY GEOMETRY (REF.3.2.4.)

In the experiment, axial pressure distributions were measured along the nozzle surface at 8 radial positions (as shown in Fig. 3.2.7) and integrated for pressure drag. Results were obtained over a range of $0.6 \leq M \leq 1.4$ for NPR from 1.0 to 6.0. The results show that the recompression on the afterbody surface increased with increasing plume temperature both subsonically and to a greater extent supersonically. This gave a corresponding reduction of pressure drag with increasing plume temperature. Examples of this are shown in Fig. 3.2.8. where the nozzle external thrust force is seen to increase with increasing plume

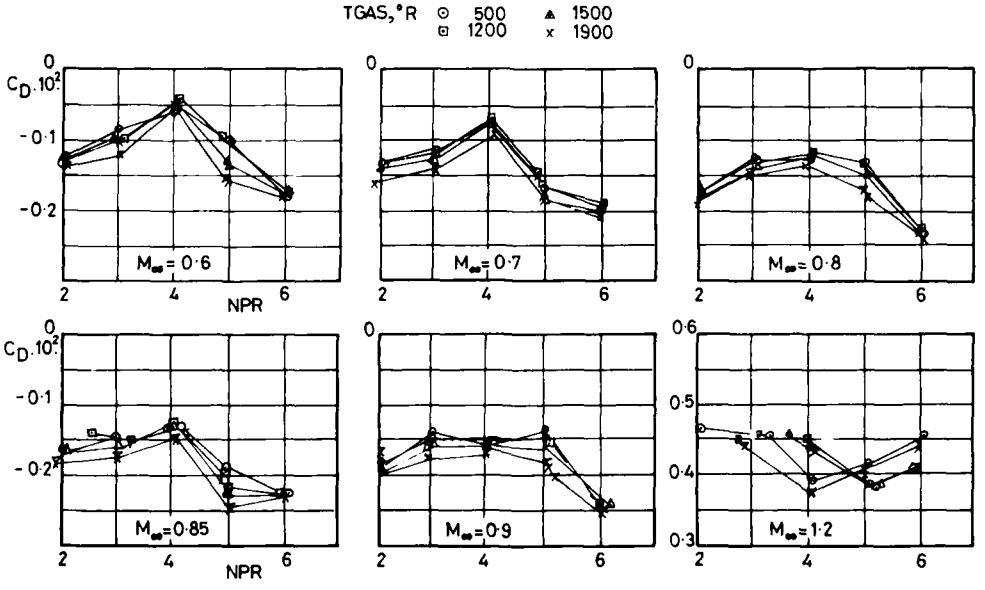

FIG.3.2.8. EFFECT OF MACH NUMBER ON PRESSURE DRAG COEFFICIENT AT FOUR EXHAUST PLUME TEMPERATURES, TOP PRESSURE GENERATOR REF.(3.2.4)

temperature (note that only part of the afterbody is pressure plotted, this giving mainly the thrust recovery region). This figure shows, for the M = 0.6 to 1.4 range and NPR range 1 to 6, the effect of plume total temperature on the top row of pressure taps. Similar results for the bottom row show a much reduced effect of temperature for the subsonic Mach numbers which is somewhat surprising as the lower row and cowl exit is much closer to the plume and its expansion influence. The effect on the lower row for supersonic speeds is, as expected, significantly greater. The level of surface temperatures achieved during the elevated plume temperature runs is not discussed in the report and there must remain a feeling that the skin temperature and its impact on external boundary layer development and the corresponding effect on pressure recovery might be responsible for some of the effects measured. Nevertheless the data is in general conformity with the expected plume temperature effects.

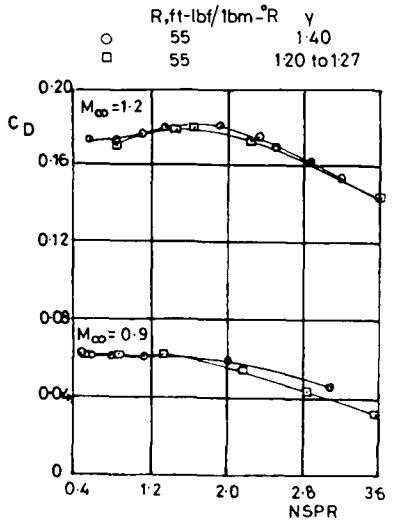

FIG. 3.2.9. 15° BOATTAIL (REF. 3.2.7)

In tests using the same rig at AEDC, Peters and Kennedy (Ref. 3.2.5) studied a range of nozzle variables and included some data on temperature effects. This data which gave afterbody pressure drag derived from pressure integration, and studied in particular the effects of temperature for an attached afterbody θ = 15° and a separated afterbody, θ = 25°, confirmed the significant drag reducing effect of increased jet temperature.

Ref. 3.2.5 results shown in Fig. 3.2.10, demonstrate very well the development of temperature effects on the 25° afterbody for a high subsonic and low supersonic Mach number. The correlations with NPR and A_j show marked differences for the two afterbodies indicating, as did Ref. 3.2.2 the need for some additional parameter to plume size (A_j related) for the high subsonic separated cases. Entrainment correlations on a momentum basis did not produce very good results for the difficult case of M = 0.9.

Kennedy in Ref. 3.2.7 reviews many aspects of testing techniques for afterbodies and considers the constituent parts that go to make up a total temperature effect. Results are presented for tests with hot burned ethylene and with nitrogen gases. This had the effect of separating γ effects at constant temperature and gas constant and showed that whilst there were significant differences in A.B.-drag at the same nozzle expansion pressure ratio (NPR), these differences became negligible when compared at the same nozzle static pressure ratio i.e. same plume shape. These results are illustrated in FIG. 3.2.9 for a 15° boattail for M = 0.9 and 1.2. The value of γ = 1.2 to 1.27 used in the ethylene tests is lower than that for typical turbojet exhausts. Kennedy showed however that for any of the plume shape parameters (diameter, expansion angle or static PR) the drag could be correlated. This indicates a very small residual difference to be attributed to entrainment for the two gases. It is concluded that these negligible γ effects indicates that changes in mass, momentum and kinetic energy of gas (25° in these tests) due to γ changes have no effect on entrainment, but that jet velocity (constant for these tests) may have an effect which could not be demonstrated in these tests.

In further results reported in Ref. 3.2.7 the effect of changes in gas constant R for fixed γ has been studied using mixtures of cold nitrogen and cold hydrogen. These effects (Fig. 3.2.11) are seen to be large in absolute terms but small in relative drag changes due to NPR i.e. the curves of boattail drag v NPR are parallel for the different values of R. Since the drag coefficient increments do not vary with pressure ratio the results indicate that incremental entrainment effects are not a function of the absolute value of parameters that are a function of pressure, such as mass flow, kinetic energy, momentum and velocity at the shear edge of the plume. With gas constants as a variable at a constant pressure ratio and temperature the jet momentum flux is constant but velocity, density and kinetic energy flux vary as $R^{1/2}$, R^{-1} and $R^{1/2}$ respectively. One might expect that the entrainment would increase with increasing R and result in increased drag. The fact that it does not, might be due to the rate of decrease of density (R^{-1}) rather than mass flux ($R^{-1/2}$).

Further work showed results for varying temperature and gas constant. Data was analysed as a function of the product of these two variables and showed that this term collapsed the data reasonably for the same product derived by different R & T. This indicated that R may be used as an alternative variable to T and cold tests may be made to represent hot conditions if a gas of different R is used. This is consistent with the previously referred data which showed large effects of R on drag at a constant NPR, but only small effects on the variation with NPR (i.e. entrainment).

A further useful reference to jet plume effects is given in Zacharias (Ref. 3.2.9). This work was carried out in a jet induction tunnel at DFVLR in Germany was on a series of different afterbody shapes with mean afterbody boattail angles of 7°, 10° and 25°, nozzle pressure ratios (NPR) of 1.0 → 2.4, nozzle temperature ratio (jet total temp ÷ free stream static temp) 1.0 → 2.86 at Mach numbers up to 0.7. The model installation in this instance had a "negative blockage" of about 6% i.e. the tunnel flow area increased from an approximately constant value to a 6% greater value immediately after the nozzle plane. The results obtained cover afterbody pressure distributions, jet total pressure and temperature distributions, jet plume shape, initial jet spread angle.

Zacharias in the analysis of the plume results obtains a useful quantification of the jet entrained mass flow in the form $\frac{m_{jk}}{m_{jo}} = \frac{\text{mass flow entrained}}{\text{initial mass flow of jet}}$ where this parameter is shown to be a near linear

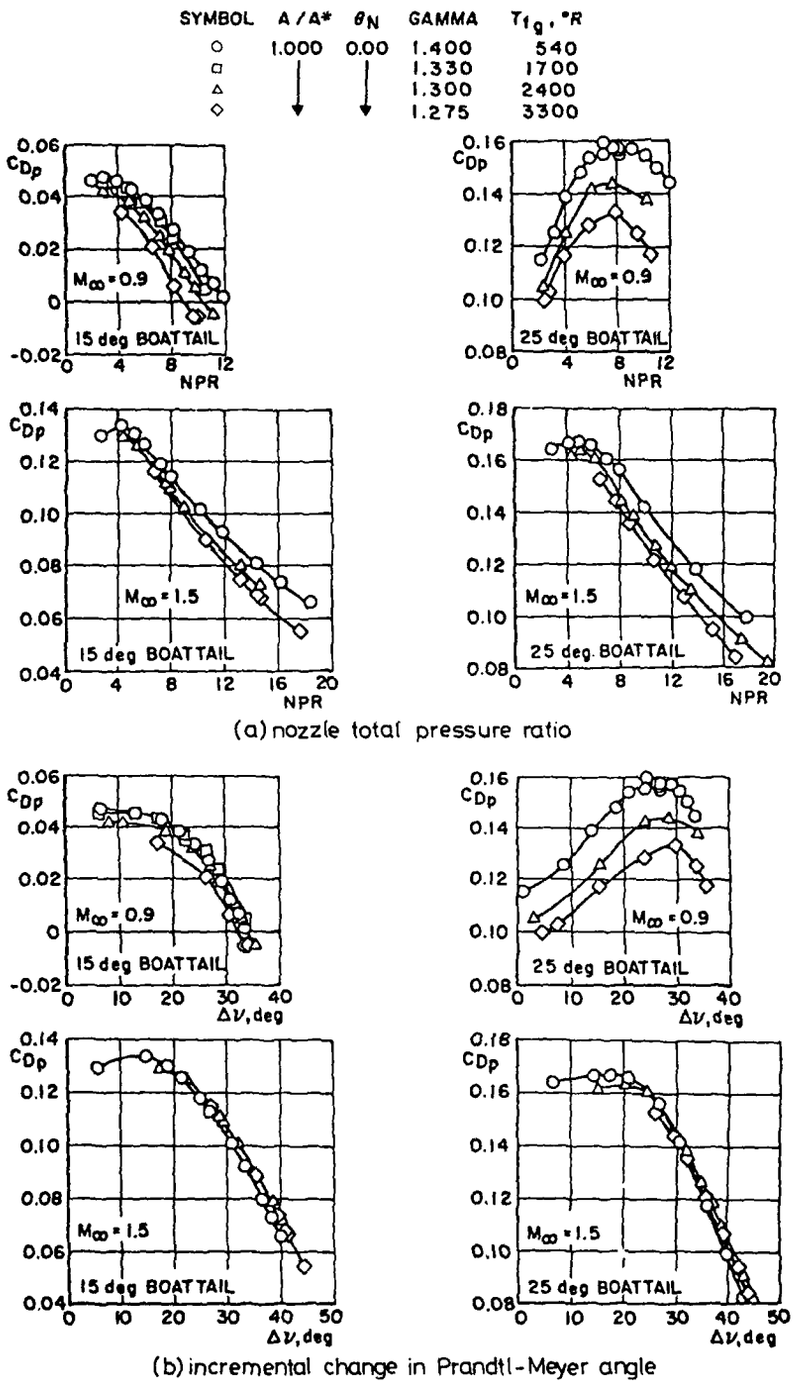

(a) nozzle total pressure ratio

(b) incremental change in Prandtl-Meyer angle

FIG.3.2.10 EXHAUST TEMPERATURE EFFECTS ON AFTERBODY PRESSURE DRAG, $Re_\infty = 2{\cdot}5 \times 10^6$ per foot. (REF 3.2.5)

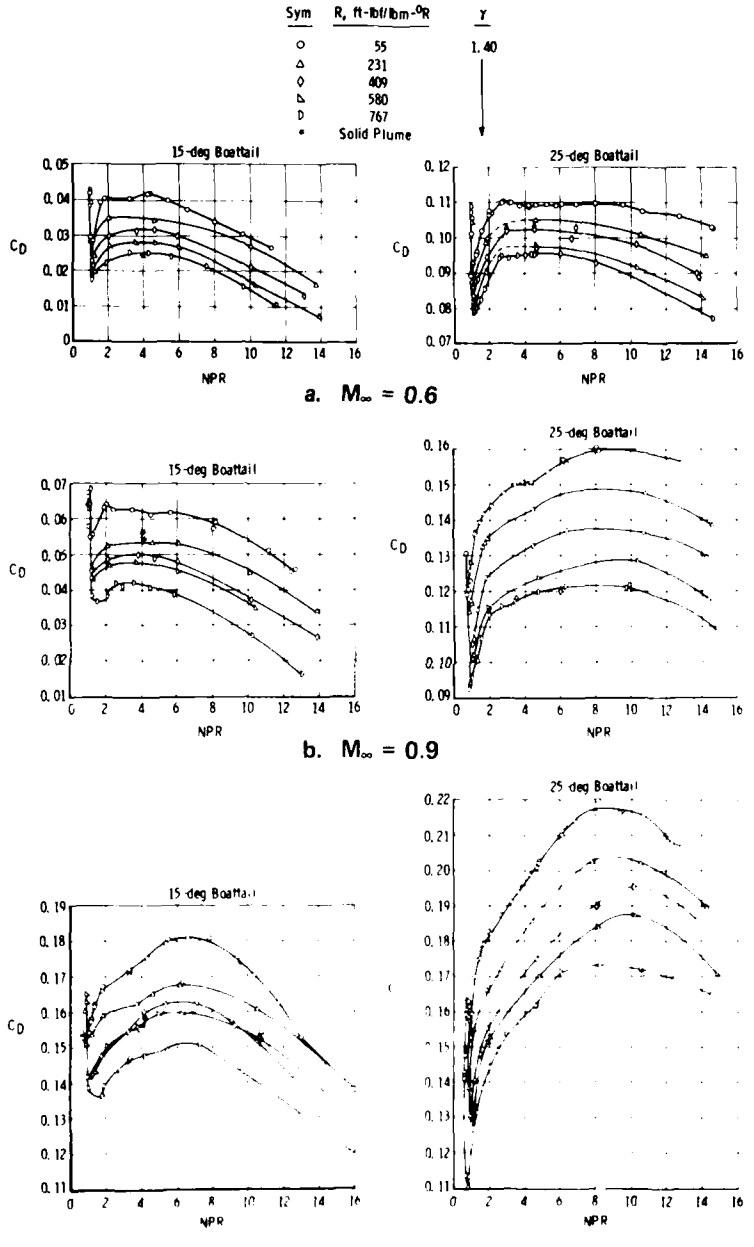

FIG.3.2.11. EFFECT OF EXHAUST GAS CONSTANT VARIATION ON BOATTAIL DRAG COEFFICIENT (REF. 3.2.7)

function of distance downstream of the nozzle plane and jet total temperature ratio. As an example it is shown that the mass flow in the jet profile at a plane 12 nozzle diameters downstream of the nozzle plane for a jet nozzle temperature ratio of 2.86, is twice that which is initially contained in the jet at its exit plane. Treating the increase of mass flow in the jet at any plane as a resultant inflow velocity w_r^* normal to this jet boundary surface the Reference produces the interesting results of the variation of inflow velocity with jet parameters viz:

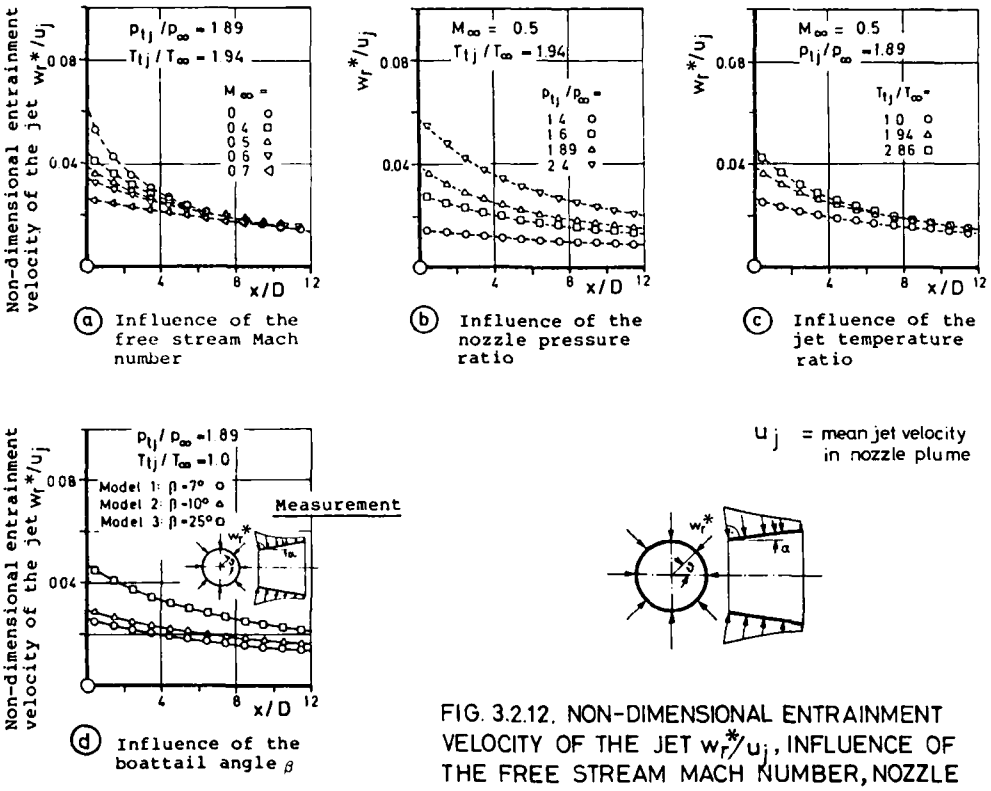

FIG. 3.2.12. NON-DIMENSIONAL ENTRAINMENT VELOCITY OF THE JET w_r^*/u_j, INFLUENCE OF THE FREE STREAM MACH NUMBER, NOZZLE PRESSURE RATIO, JET TEMPERATURE AND AFTERBODY ANGLE.

If for the purposes of analytic analysis of jet flows and entrainment a sink distribution is defined on the boundary of a hypothetical plume then it can be seen that the intensity of the sink reduces with increasing Mach number (i.e. reducing slip velocity), but increases with increasing jet total temperature (i.e. increased slip velocity) and with increasing jet total pressure (i.e. increased jet plume momentum). So the results do follow a logical pattern. Finally it is seen that increase of boattail angle also increases the sink intensity which can perhaps be explained as an increase of impingement momentum of the external stream on the jet stream.

From the empirical analysis of the critical jet spreading angle and the jet sink strength the reference makes a theoretical analysis of the afterbody/jet flow-field using a mathematical model of the potential flow which can be solved by a finite-element method. This is used to determine theoretically the effect of the various test parameters on the afterbody pressure distribution and drag. In particular it is demonstrated a ΔT_{tj} of 500°C gives rise to an afterbody pressure drag reduction of 15% which can be demonstrated by both experimental and theoretical results. It is commented that experimental results with a non-insulated external boattail surface showed a 15% increase in afterbody pressure drag but there is no evidence given of any theoretical analysis to demonstrate this result. This is a good reference but is limited, quite correctly due to the experimental facilities, to Mach numbers up to 0.7. It is likely that the experimental results will not be too greatly influenced by the wall constraint effects of the blockage up to these Mach numbers.

3.2.1.2. A Proposed Correction Technique for High Pressure and Temperature Jets

In a recent paper by Price and Peters (Ref. 3.2.11) a correction technique is proposed to correct afterbody drag for both the effects of jet plume shape (the γ effect) and the effects associated with

jet entrainment (the T effect). It is assumed that an equation of the form:

$$C_{D_{HOT\ JET}} = C_{D_{COLD\ JET}} + \Delta C_{D_\gamma} + \Delta C_{D_T}$$

where ΔC_{D_γ} is associated with the specific heat ratio of the plume and the surrounding air and is used to describe the plume shape effect,

and ΔC_{D_T} is the jet entrainment effect correction term associated with the $R_j\ T_{t_j}$ energy term.

A. The first correction term ΔC_{D_γ} is basically the solid body inviscid interference term and assumes that the solid body interference of a hot jet can be represented by a cold jet at a different nozzle pressure ratio which expands the jet to the same plume diameter.

Ref. 3.2.11 gives the relation:

$$\frac{\text{Plume max. diameter}}{\text{Nozzle exit diameter}} = \frac{D_1}{D_e} = \sqrt{\frac{\left[\frac{\gamma_j + 1}{2}\right]^{-n} \cdot \left[1 + \frac{\gamma_j - 1}{2} \cdot M_1^2\right]^n}{M_1 \cdot (A_e/A^*)}} \qquad \text{where } n = \frac{\gamma_j + 1}{2(\gamma_j - 1)}$$

and $$M_1 = \sqrt{\frac{2}{\gamma_j - 1}\left[NPR^{\frac{\gamma_j - 1}{\gamma_j}} - 1\right]}$$: the isentropically expanded jet Mach number.

and $\frac{A_e}{A^*}$ is the nozzle exit area to throat area ratio.

and NPR is the nozzle expansion pressure ratio of jet total pressure to free-stream ambient pressure.

Hence from this it is a straightforward process to derive a set of matching test pressure ratios with a cold model test gas which will correspond with the range of values for the hot flight engine jet.

B. The second correction term ΔC_{DT} is assumed to be related to the respective internal energy of the jet stream and the entrained external flow i.e. $R_j\ T_j$ ratio. Peters in Ref.3.2.12 shows that the entrainment effect produces a linear variation in afterbody drag as a function of $\log\left(\frac{\rho_e V_e}{\rho_\infty V_\infty}\right)$.

By using a value $\frac{\partial C_D}{\partial \log\left(\frac{\rho_e V_e}{\rho_\infty V_\infty}\right)}$ obtained from the linear part of the C_D v NPR relationship for a cold jet

i.e. the "mainly entrainment" part of Fig. 3.2.2., and the difference between the hot and cold jet value of $\log\left(\frac{\rho_e V_e}{\rho_\infty V_\infty}\right)$ at matched values of $\frac{D_1}{D_e}$ we obtain:

$$\Delta C_{D_T} = \frac{\partial C_D}{\partial \log\left(\frac{\rho_e V_e}{\rho_\infty V_\infty}\right)}_{COLD} \times \left[\log\left(\frac{\rho_e V_e}{\rho_\infty V_\infty}\right)_{HOT} - \log\left(\frac{\rho_e V_e}{\rho_\infty V_\infty}\right)_{COLD}\right]$$

The above analysis is verified by hot and cold tests which give afterbody pressure drag and shows that the value of the slope $\frac{\partial C_D}{\partial \log\left(\frac{\rho_e V_e}{\rho_\infty V_\infty}\right)}$ is approximately the same for the cold jet as that obtained for the hot jet at M = 0.6 and 0.9 at constant values of $\frac{D_1}{D_e}$. An example of this is shown in Fig. 3.2.13.

For M = 1.2 however the slope from the cold jet data does not correlate well with the hot jet data and it is conjectured that this may well be due to the more unrepresentative velocity differences between the jet and the external M = 1.2 stream in the cold model tests. Better data correlation was obtained by using the slope values obtained at the lower Mach number cold tests. The interested reader is recommended Refs. 3.2.11 and 3.2.12 for more detail explanation.

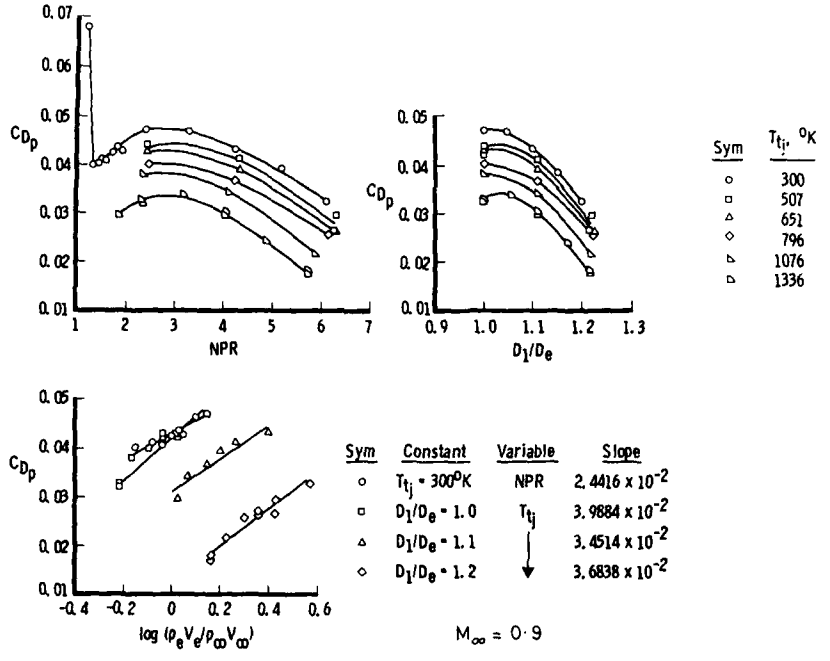

FIG. 3.2.13. JET TEMPERATURE EFFECTS ON AFTERBODY DRAG COEFFICIENT. 15° BOATTAIL A_e/A =1·026 (REF 3.2.12)

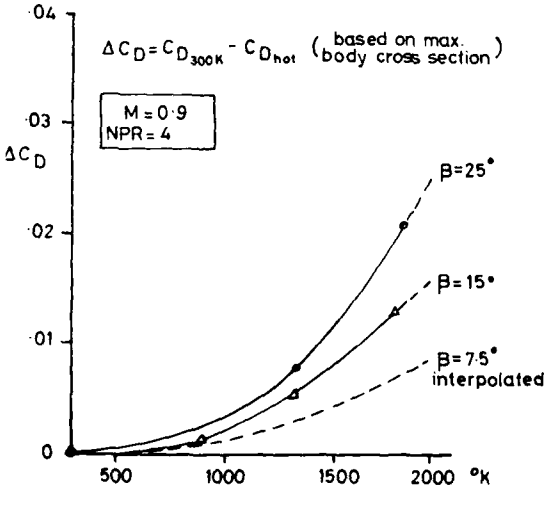

FIG. 3.2.14. (REFS. 3.2.5, 3.2.7)

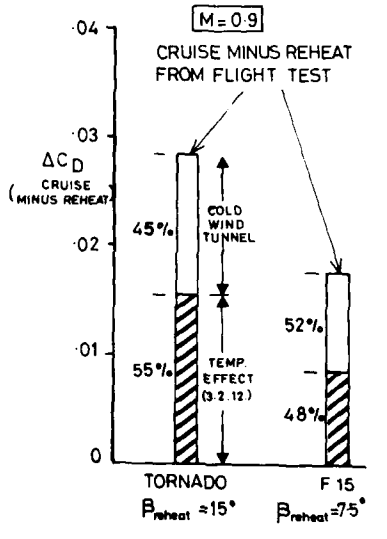

FIG. 3.2.15 (MBB SOURCE)

FLIGHT TUNNEL CORRELATION OF JET TEMPERATURE EFFECTS FOR TWIN JET AFTERBODY

Recent analysis of flight data on Tornado by MBB has shown significant reductions in drag increment due to reheat compared with that measured in cold jet tunnel tests. These measurements, which look only at the reheat increment, showed reasonable correlation with the hot plume effects previously described here and in the references. Data extracted from References 3.2.5 and 3.2.7 are summarised in Fig 3.2.14 showing the typical effect of jet temperature on the 15° and 25° afterbodies. These data have been used to show how this temperature effect brings the flight and cold tunnel tests into line for data interpreted by MBB (Fig. 3.2.15) from References 3.2.8 and 3.2.10 for F 15, and for Tornado.

3.2.1.3. Theoretical Analysis

In Reference 3.2.36 Wilmoth of NASA Langley has developed a viscous-inviscid interaction model to account for jet entrainment effects in the prediction of the subsonic flow over nozzle afterbodies. The representation of the entrainment is by the addition of a displacement thickness surface to the inviscid plume shape. The subsonic flow over the whole afterbody is solved by an iterative method which takes into account the boundary layer and shape of the afterbody, the inviscid plume shape effect, and the effect of the displacement surface on the plume. Calculations have been compared with experimental data to show the effects of entrainment on nozzle boattail drag for a range of free stream and jet flow conditions. The inclusion of jet entrainment effects has been shown to significantly improve the prediction of nozzle boattail drag over that predicted by treating the inviscid plume shape as a solid body.

The predicted variation of boattail drag with jet gas composition and temperature has been shown to be in good qualitative agreement with experimental data. The drag is shown to decrease with either a decrease in the molecular weight or an increase in jet temperature. At high temperatures above 1500 K, however, the predicted afterbody drag reduction with temperature reaches a minimum and from thereon increases. This is at variance with experimental data at these higher plume temperatures and appears to be due to the representation of the entrainment shear layer creating an excessive washing away of the afterbody boundary layer.

3.2.1.4. Conclusions

The effect of jet temperature is likely to be most significant in the transonic flow region where large areas of base or separated afterbody flows occur. The effects are greater for large afterbody angles and can be as large as 35% of the jet-off afterbody drag for high pressure ratios. Temperature effects will thus be configuration sensitive and so prediction methods are difficult to obtain although correction of measured data obtained at limited temperatures may be made by correlation with initial plume divergence angle, plume maximum diameter and the jet/freestream energy ratios.

There is an indication that the use of cold air to simulate a hot low by-pass dry turbojet exhaust can result in a measured value of afterbody drag of the order of 20% above the correct value. Cold jet test data will give pessimistic afterbody predictions.

It is unlikely that elevated jet temperature will become a routine test feature in the near future. Even the more sophisticated CMAPS simulator is deficient in temperature simulation. Expansion of the valuable contributions of References 3.2.2 to 3.2.6 briefly discussed here will be most important on a parametric basis if true extrapolation of model results to full scale is to be achieved. Temperature effects must not be ignored simply because they are difficult to quantify.

3.2.2. Turbine Powered Simulators

Current airframe geometry concepts are leading to compact and closed coupled engine inlet and exhaust configurations. These arise from the need to compact the engine around the centre of gravity to minimise V/STOL out-of-balance vectored thrust forces at low forward speeds. These geometries then give rise to the possible high speed interaction of inlet and exhaust flows. In these conditions it is no longer possible to assume that independent tests of the inlet and the exhaust nozzle may be simply added together. Spillage flows may well influence the afterbody approach flow conditions and afterbody nozzle flows may couple into the inlet flow (although less likely).

To improve the quality of aerodynamic data it becomes a requirement to test inlet and exhaust flows in combination. This requirement has been anticipated for some time in the US and has led to the development of a model engine unit CMAPS (Compact Multimission Aircraft Propulsion Simulator). These units were developed by McDonnell Aircraft Company in conjunction with General Electric and Tech Development Inc. under contract to the U.S. Air Force Aero Propulsion laboratory. This unit is a high performance version of the range of TPS (Turbine Powered Simulators) marketed by Tech Development Inc. for use in civil transport applications of high by-pass fan engines, the major new technology being the development of a 4 stage engine compressor providing an engine pressure ratio range of 1.2 to 4. Much of the calibration and bookkeeping technology of the civil application can be applied to the CMAPS.

It is not the purpose of this document to write a treatise on the subject of the development of the CMAPS and interested readers are referred to References 3.2.13 - 3.2.20. The following sections will describe the CMAPS unit as a piece of operating equipment and its range of simulation.

3.2.2.1 Basic Description of Unit and Equipment

The Figure 3.2.16 shows the

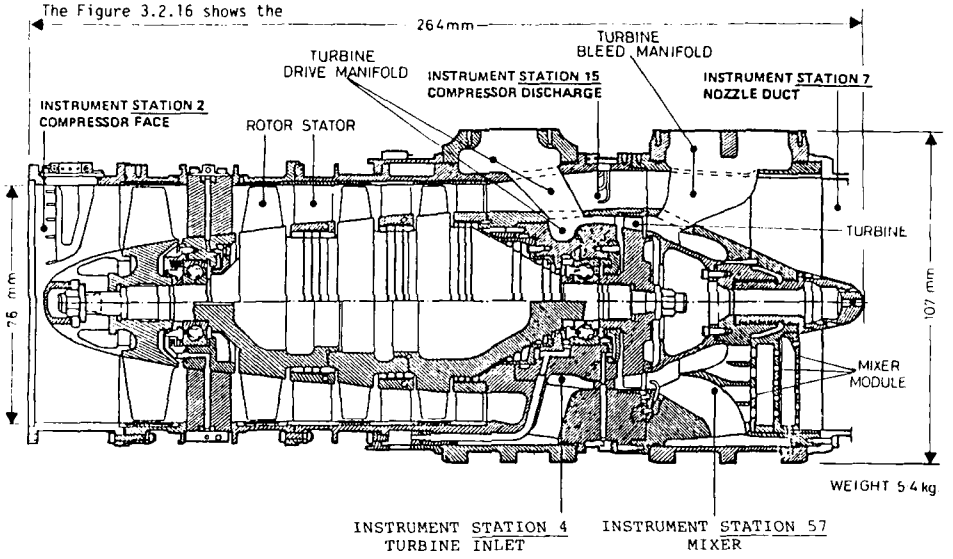

FIG 3.2.16. CROSS SECTIONAL VIEW OF THE CMAPS. (REF. 3.2.20)

compact simulator. This unit has a 4 stage axial compressor which is driven by the power generated by the single stage turbine. The basic performance is defined by

AIRFLOW	MAX FLOW RATE	MAX T	MAX P
Compressor	1.65lbs/sec (Corrected)	150°F	16 psia
Turbine inlet	7 lbs/sec.	200°F	2000 psia
Turbine bleed	7 lbs/sec.	200°F	800 psia

The turbine is driven by the high pressure inlet air which may then be mixed with the compressor air through a mixer/ejector module to provide the exhaust nozzle total pressure air supply. The level of nozzle exhaust total pressure is controlled by the quantity of turbine exhaust air which is bled from the unit via the turbine bleed manifold. Hence, as indicated in the Table, it is possible to exhaust all the turbine drive air external to the exhaust nozzle leaving, as a minimum, the mass flow and total pressure of the compressor. Fig. 3.2.17 illustrates the flexibility of the unit in a simulated dry power configuration. The compressor operating envelope with the CMAPS drive turbine is shown relating

engine pressure ratio and sea-level normalised compressor airflow $W_2 \frac{\sqrt{\theta}}{\delta}$

where $\theta = \frac{\text{inlet total temperature in } ^\circ R}{519}$

and $\delta = \frac{\text{inlet total pressure psia}}{14.7}$

Data is given along lines of constant percentage of the referenced design rotor speed 75,200 rpm. The range of engine pressure ratios obtainable with the unit may be adjusted by replacing the mixer/ejector module with units of different flow area ratio allowing greater engine pressure ratio augmentation. In this way the different requirements of dry power and reheat may be met.

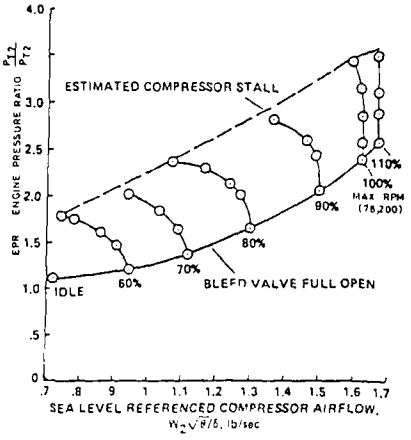

FIG.3.2.17 CMAPS OPERATING ENVELOPE OF ENGINE PRESSURE RATIO AND COMPRESSOR AIRFLOW IN DRY-POWER CONFIGURATION. (REF. 3.2.20)

Instrumentation

The basic CMAPS unit has the following pressure and temperature instrumentation (ref. Fig. 3.2.16).

Station 2 Compressor face 5 rakes of 5 P_T + 5 wall statics.

Station 15 Compressor discharge 2 rakes of 3T_{T_3} and 3 rakes of 3 P_T with 1 wall static each.

Station 7 Nozzle duct 2 rakes of 7T_T, 3 rakes of 7P_T and 5 wall statics.

Station 4 Turbine inlet: 1 P_T + 1 T_T

Station 57 Mixer: 3 statics.

Control System

To integrate this advanced technology unit into the standard test scene it has been necessary to evolve a set of control equipment which is self contained and

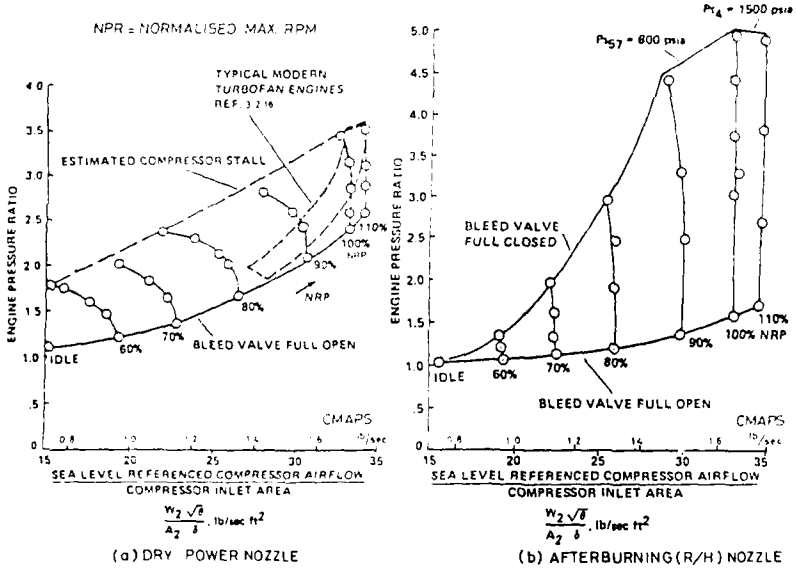

FIG. 3.2.18. SCALED AIRFLOW AND ENGINE PRESSURE RATIO SIMULATION CAPABILITIES OF THE CMAPS. (REF. 3.2.20)

independent of the main tunnel test equipme.' The NASA CMAPS controller is capable of monitoring the health and controlling the airflow and EPR of 2 CMAPS units in a test. The control package provides

(1) Operators console
(2) Data acquisition
(3) Hydraulic power supply
(4) Bearing oil supply and scavenge
(5) Air control and measurement
(6) Transducer environmental control

The operators console monitors a large range of health parameters whilst controlling inlet airflow, and engine pressure ratio automatically. The operator may override the controller at any time to avoid health (of the unit) hazards. RPM control is normally maintained within ±0.5% for E.F. distortions < 15%
and ±1.0% for " " ≥ 25%

In this respect it has been shown that engine face (EF) distortions up to 30% are acceptable to the compressor but in practice it is advisable to work at levels below this.

3.2.2.2. Engine Performance Simulation

Static tests have been conducted to provide the performance data of the simulator. Figs.3.2.18 to 3.2.22 show some results of static tests giving the simulation capabilities of a unit and the corresponding turbine supply and bleed airflow requirements.

Fig. 3.2.18 shows the non-dimensionalised compressor air flow characteristics versus EPR in both the dry and the reheat operating modes. Illustrated on the dry power figure is the operating line of EPR V sea level referenced flow for some modern augmented turbofan engines (Ref. 3.2.15). These two figures demonstrate the effect of two different pancake ejector mixers at the exhaust chamber entry, the reheat case being capable of passing much larger quantities of turbine exhaust air at high pressure into the exhaust chamber where it mixes with and ejector powers the compressor exhaust flow thus increasing the EPR. Included in the figures is the upper limit of EPR associated with the compressor stall for the dry case and the two upper limits of P_T 57 which is the maximum permissible turbine exhaust pressure of 800 psia and P_{T_4}, a turbine inlet pressure limit of 1500 psia. The 1500 psia limit was a structural one in these tests.

Fig. 3.2.19 shows the dimensional compressor airflow characteristic for dry and reheat cases for a range of constant turbine inlet drive pressures P_{T_4}. These correspond with the characteristics of Fig. 3.2.18.

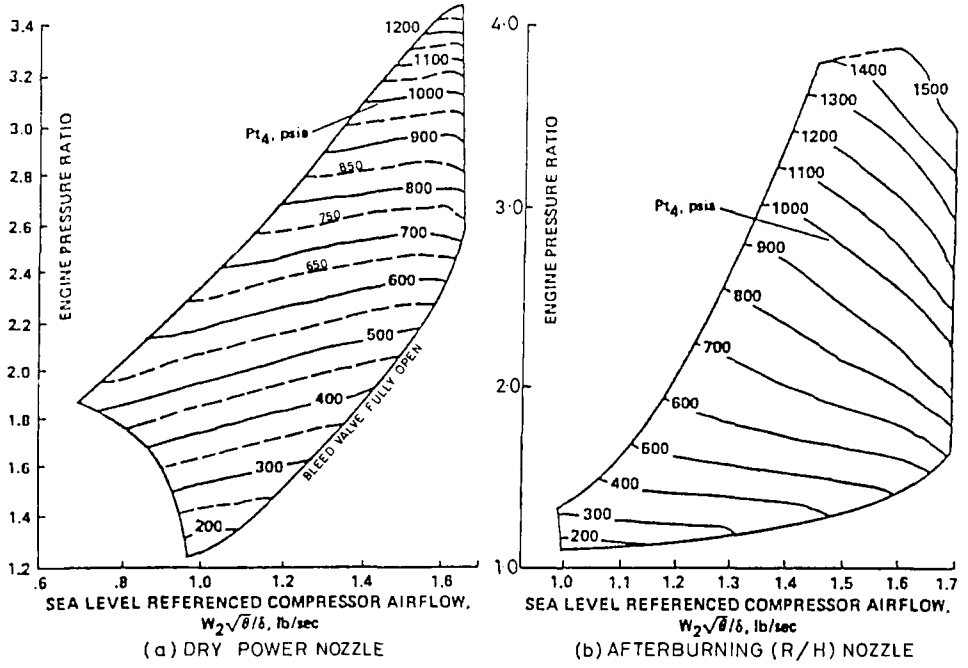

FIG. 3.2.19 CMAPS TURBINE DRIVE PRESSURE REQUIREMENTS AT SEA-LEVEL CONDITIONS; CONTOUR LINES OF CONSTANT TURBINE INLET PRESSURE, P_{t_4}. (REF 3.2.20)

For the dry case it is seen that the engine pressure ratio provided by the turbine is roughly constant with constant turbine inlet pressure and inlet flow is controlled by a combination of turbine exhaust [illegible] with corresponding changes in speed. For the reheat case however turbine drive pressure has a [illegible] with other variables. It should be remembered here that these figures are only typical examples of two different exhaust chamber inlet mixer designs. It is of interest to note Fig. 3.2.20 which gives a linear turbine weight flow versus inlet pressure characteristic that would have been expected indicating a choked inlet flow condition with constant $\frac{w4.\sqrt{\theta}}{\delta}$, corrected turbine airflow.

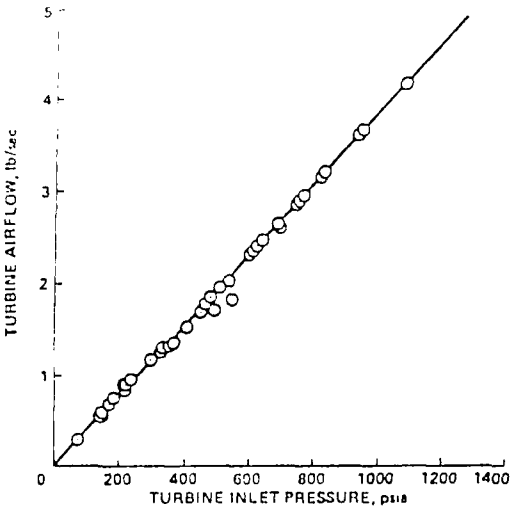

FIG. 3.2.20 TURBINE DRIVE AIRFLOW AS A FUNCTION OF TURBINE INLET PRESSURE, P_{t_4}. (REF. 3.2.20)

Detailed work in Refs. 3.2.15 and 3.2.17 studied the range of variables with different turbine outlet mixers and different exhaust nozzle sizes. For detailed study the reader is referred to Ref. 3.2.17 but broadly the results are summarised as Fig. 3.2.21 from Ref. 3.2.15. This illustrates the flexibility of the unit as a function of exhaust nozzle area. Higher EPR operating lines are associated with the increased quantity of high pressure mixer turbine outlet air needed to fill the larger area nozzles at a given compressor speed. This gives a higher resultant exhaust nozzle total pressure when mixed with the constant outlet pressure of the compressor. Similarly, if all the turbine exhaust air is by-passed through the bleed line (i.e. a solid mixer) a lower EPR operating line results for the larger nozzle areas. These effects combine to provide a large operating envelope for the larger exhaust nozzles. Ref. 3.2.15 also draws attention to the effect of pressure drop in the bleed duct line and how this reduces the total flexibility envelope. In practice, increased bleed line losses (due to pipe sizes) result in higher required turbine drive pressures for a given rotor speed. This gives higher inlet pressure to the mixer with consequent effects on the exhaust nozzle and the compressor back pressure. This has the effect of precluding operation in the lower right hand corner of the flexibility envelope. Other factors like internal Reynolds number and inlet distortion also affect the flexibility map, but to a much lesser extent.

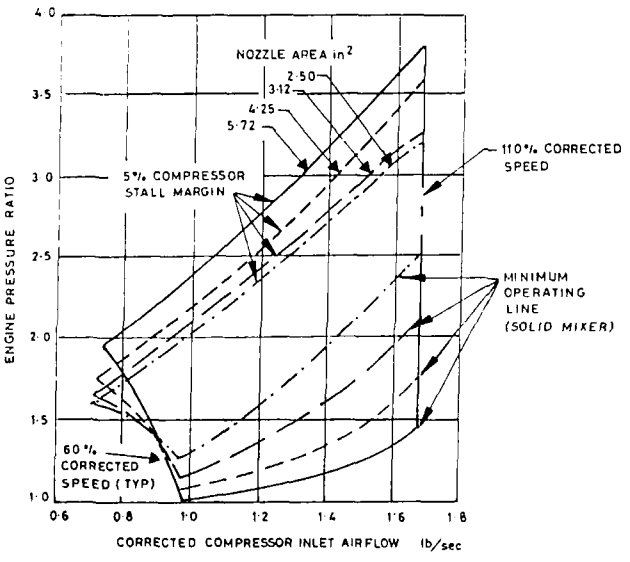

FIG. 3.2.21. PREDICTED MAPS FLEXIBILITY TRENDS (REF. 3.2.15)

Simulation capability relative to advanced engine requirements

Comparison should be made to see whether the CMAPS in its present state is capable of meeting future "paper engine" requirements as well as those of current engines.

Ref. 3.2.16 provides some input to this, showing representative trends of EPR max. versus exhaust nozzle area for maximum dry and maximum reheat power settings.

Fig. 3.2.22 collects these results and relates the required EPR to the scaled exhaust nozzle throat area. Included are both turbojets and fixed/variable cycle turbofans with by-pass ratios

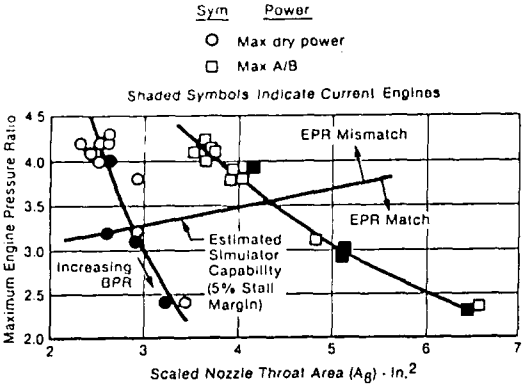

FIG. 3.2.22. TYPICAL MAXIMUM EPR VARIATION FOR ADVANCED ENGINE CYCLES. (REF.3.2.16)

varying from 0.2 to 2. The nozzle size was based on scaling to match the corrected simulator flow with the corresponding engine flow. The three boundary lines in Fig. 3.2.22 give the simulator max. EPR against nozzle area (from Fig. 3.2.21), the dry performance and the reheat performance lines. For the moderate by-pass ratio engines the simulator meets the requirements of EPR max, there is however seen to be a short fall for the turbojet and low by-pass cases. Although most of the points which lie above the simulator boundary are "future engines" there are points corresponding to a current engine which cannot be met.

However, although the maximum point mismatch looks large in Fig. 3.2.22 the error becomes smaller with reduced inlet mass flows. This is illustrated in Fig. 3.2.23 for the case of an engine near the two solid upper points of Fig. 3.2.22.

3.2.2.3 *Calibration Requirements*

The case for the use of a simulator is made for aerodynamic interaction reasons. The value of its use however is entirely dependent upon the evaluation of the simulator forces. If of

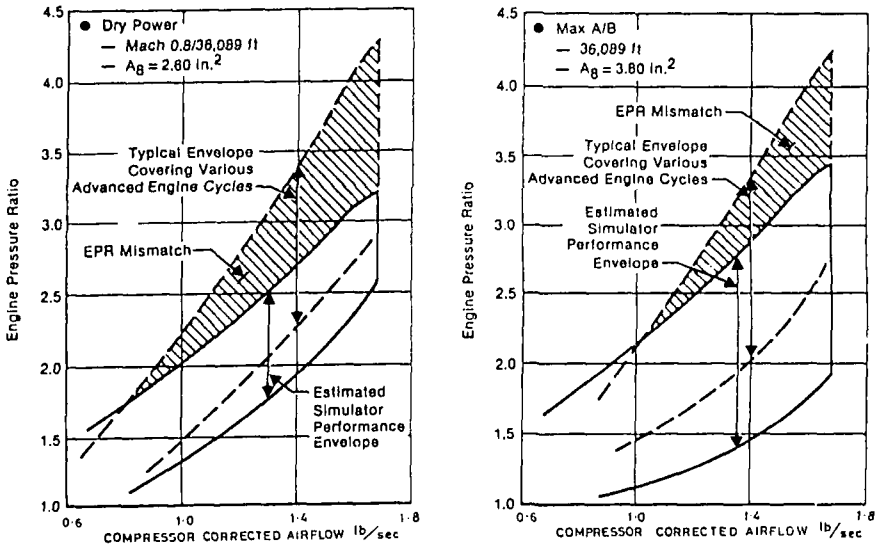

FIG. 3.2.23. COMPARISON OF SIMULATOR ESTIMATED PERFORMANCE WITH ADVANCED ENGINE CYCLES. (REF. 3.2.17)

course a non-metric unit is used then a simple description of mass flow ratio and exhaust pressure ratio is sufficient. However, for the really important interactive cases and complex nozzle geometries where a natural break-line between a non-metric simulation nozzle and a metric airframe shell cannot be created, it is essential to define a simulation thrust accounting system for calibration and isolated, and installed performance.

It is possible to draw upon the significant field of calibration performance which has been devised for civil applications. It is perhaps fortunate that in these applications the accuracy requirements are more stringent than those for military applications.

The basic problem of TPS simulators, and in fact all powered simulators is the size of the component forces e.g. gross inlet momentum and exhaust momentum, relative to the net propulsive force. The interference forces are then, in turn, almost an order of magnitude smaller than the net propulsive force. So, we are trying to discriminate increments which are of the order of 0.25% of the gross

propulsive thrust, when account is taken of the fact that increments are derived from two independent measurements which are each subject to their own errors. It is easy to lose the very terms which we set out to measure in the error scatter of the steps passed through en route.

The use of a CMAPS simulator has of course specific application to VSTOL. For these uses, other components than propulsive forces are important, and calibration of lift and pitching moment is required. This puts further requirements on the general purpose capability of the calibration test rig.

However, the simulator application being specifically discussed here relates to afterbody performance, and in the calibration discussions to follow thrust and drag accounting only are considered, the lift and vectored performance of the simulator being considered part of the stability and control and vector-in-flight aerodynamics.

3.2.2.4 Thrust Calibration Test Systems

The requirements of a calibration system are simple to define:

(1) Correct representation of exhaust nozzle pressure ratio.

(2) Correct inlet total pressure and temperature.

(3) Accurate measurement of primary drive flows.

(4) Accurate measurement of compressor/fan flows.

(5) Accurate measurement of exhaust nozzle flows

but of course in practice, are difficult to achieve. As with all good experimental techniques the success depends upon attention to detail, detail in this instance being the attention to non-uniformity of pressures and temperatures, distortion flow fields, extraneous inlet vorticity etc.

Atmospheric Inlet Calibration Tanks

These tanks, typical of various in use with atmospheric tunnels provide a suck-down capability to simulate the in-tunnel test Mach numbers (hence the term Mach simulation tank). Typically(Ref. 3.2.23 and 3.2.25)is the example shown below:

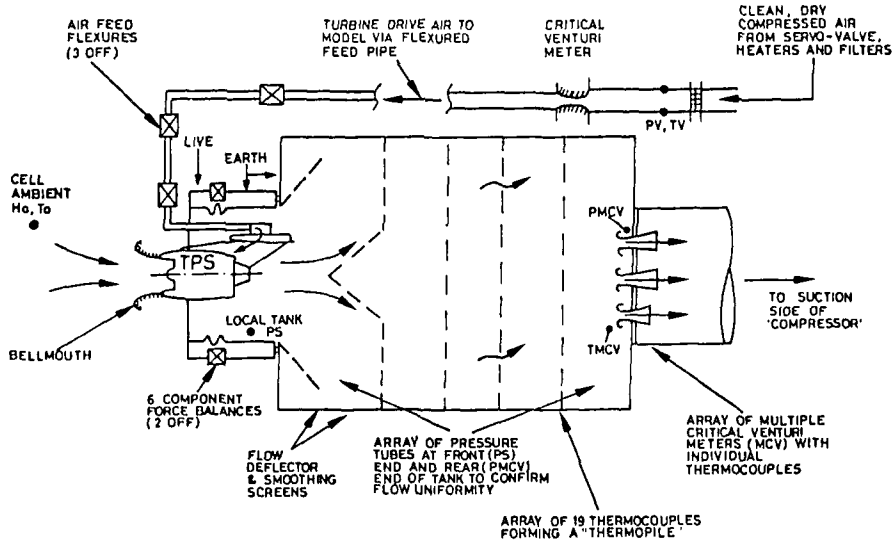

FIG. 3.2.24. BASIC ELEMENTS OF MACH SIMULATION TANK (REF. 3.2.23)

Tests in this type of tank are conducted to determine nozzle coefficients in the presence of quiescent environment and under conditions which match the model internal pressures as they occur in the wind tunnel tests. Test conditions of correct pressure difference across the unit are set up by adjusting the tank depression hence simulating atmospheric total pressure ram inlet air and wind tunnel ambient working section pressure at Mach simulated. Precision flow measurements are made of the inlet drive gas and the total flow passing from the tank (i.e. the sum of the drive gas and the compressor/fan flow). Thrust measurements are made by precision balances on the metric carrier of the tank. A design feature of the tank is the self-compensation of the metric carrier with suction in the tank. This is achieved by a combination of opposed load bellows and with good design it is possible to achieve a metric carrier

whose balances do not respond by more than 1% to the very large suck down forces which occur with tank depression, a system which is a development of Fig. 3.2.24 shown in Fig. 3.2.25. This development, as ARA MST2, has a very accurate thrust capability with virtually zero tank suction interaction. This rig has been specially developed for small civil TPS units requring high precision calibration but the principle may equally be applied to a large CMAPS system.

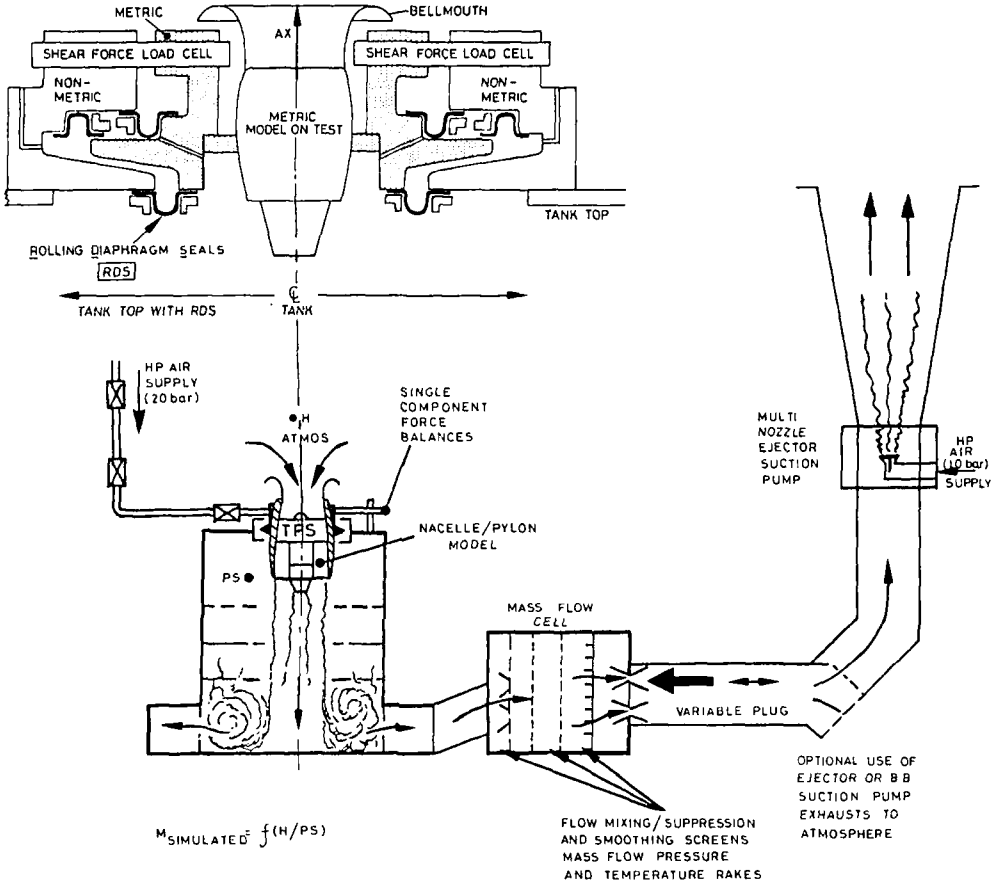

FIG. 3.2.25 HIGH PRECISION VERTICAL SIMULATION TANK

Non-atmospheric Variants

The above principles have been used in various modes at test establishments, Grumman, ONERA and NLR for example to develop their own particular requirement, the variation often being modifications to allow for non-atmospheric inlet flows, to measure more than one component, and to use the in-tunnel balance system for calibration force measurements. An example is given in Ref. 3.2.24 of a TPS calibration bench used in France by ONERA at Modane. In this method which is illustrated in Fig.3.2.26 the two air supplies are taken across the balance, one to feed the fan air through a metric settling chamber and a bellmouth, the other to feed high pressure air to the turbine. Both of these flows are measured accurately by critical venturis. In principle the two air feed streams cross the balance normal to the direction of thrust, any small errors in this are calibrated against the known thrust of an ASME nozzle. The simulated Mach number can be controlled independently of the total mass flow through the unit by regulation of a remote plug nozzle. This provides the great advantage of continuous variation of TPS characteristic (say EPR or Corrected RPM) for constant M simulated. Data analysis will follow a similar pattern to that described.

It has been demonstrated in Refs. 3.2.23, 3.2.24 that high precision data can be obtained in the form of discharge and thrust coefficients for use in the wind-on installed and isolated unit aerodynamic tests. In preparation for general purpose use of the high pressure ratio CMAPS units, calibration facilities are being prepared at NASA Ames Laboratory specific to these requirements. These are described in detail in Ref. 3 2.15 a figure from which is shown (Fig. 3.2.27). The concept shown has incorporated some of the new desirable developments and special requirements of CMAPS with its three-fold air system. Metered air is supplied to the compressor inlet, to the turbine inlet, and from the turbine outlet/exhaust nozzle bleed. This data provides flow information against which the internal CMAPS instrumentation can

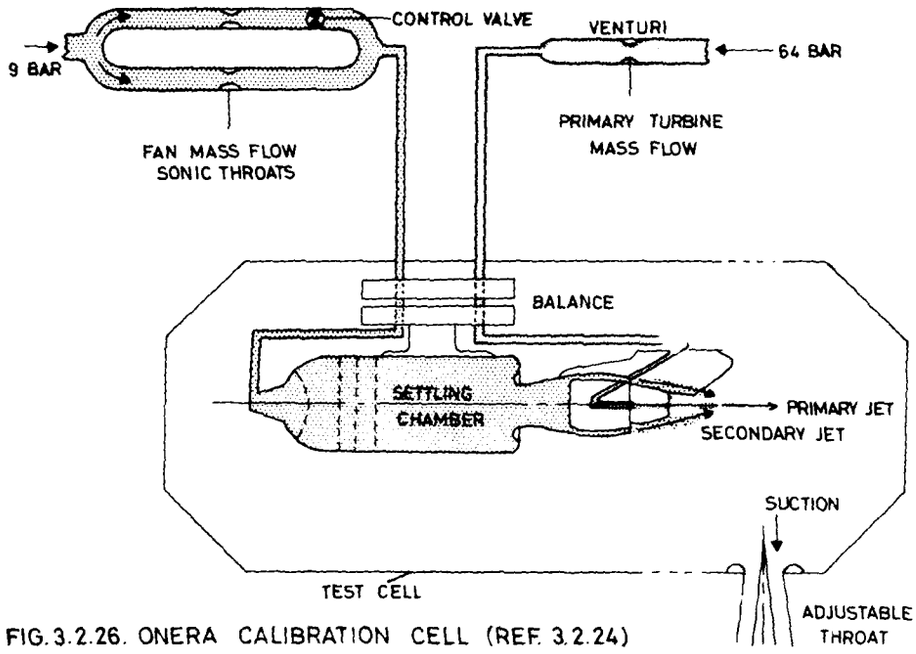

FIG. 3.2.26. ONERA CALIBRATION CELL (REF. 3.2.24)

be calibrated for use in the installed wind tunnel tests. This flow data in conjunction with the axial force balance measurements provides the static thrust calibration.

Simulator Calibration Methods

Each establishment involved in simulator testing will evolve its own data reduction and measurement procedures. In principle the methods are the same but are applied with different attention to detail and emphasis. The accuracy of any system of data reduction is dependent upon the accuracy, stability and

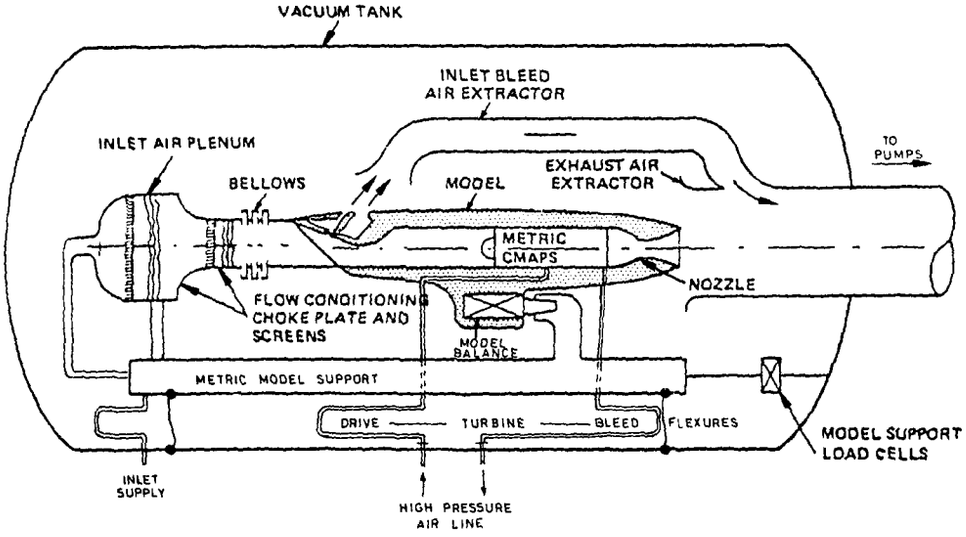

FIG. 3.2.27 PROPULSION SIMULATOR CALIBRATION LABORATORY DESIGN CONCEPT (REF. 3.2.15)

repeatability of the fundamental ingredients of pressure and temperature. It is not essential that a totally comprehensive coverage of basic data is necessary at the reference stations but enough coverage must be provided to guarantee repeatability (i.e. stability) and limited variation with other parameters (such as Corrected RPM). It must be remembered that a calibration of a flow is only a calibration of the instrumentation array in that flow. For that reason, coefficients which should in principle be near unity may well appear at a 90% level, and may vary significantly with other parameters. For this reason it is absolutely essential that no changes in internal flow and instrumentation are introduced between calibration and test. In the event of partial instrumentation failure it is preferable to re-establish new calibration coefficients based on a reduced instrumentation array than to try to repair or replace broken instrumentation. A typical approach to calibration methods for a twin stream TPS for civil application is given in Ref.3.2.23 details are given in Fig. 3.2.28. This shows schematically and the essentials of any calibration system and in-tunnel application bookkeeping process. In the above method particular emphasis is placed on a linked-methodology of flow continuity in the test phase where inlet mass flow and ram drag are linked to the exhaust for gross thrust via an identical mass flow term. The importance of this becomes greater with increased by-pass ratio i.e. as the ratio of gross thrust to net thrust increases.

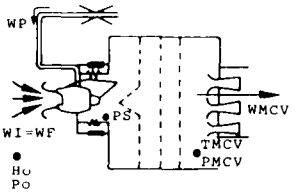

CALIBRATION

MEASURE OR DEFINE		COMPUTE	
PVA, TVA, AVA		WV	HP VENTURI MASS FLOW
PMCV, TMCV, AMCV		WMCV	TOTAL TANK MASS FLOW
WFAN = WMCV - WV		WFAN	FAN NOZZLE MASS FLOW
TI, Ho, PSI, AI	WI = WFAN	CDI	INTAKE DISCHARGE COEFFICIENT
WI, TI, H	$CWI = \frac{WI\sqrt{\theta_I}}{\delta_I}$	CWI	CORRECTED FAN MASS FLOW
RPM, TI	$CRPMI = \frac{RPM}{\sqrt{\theta_I}}$	CRPMI	CORRECTED FAN SPEED
PTP, TP, AP, PS	WP = WV	CDP	PRIMARY NOZZLE DISCHARGE COEFFT
XGP = f(PTP, PS) * WP$\sqrt{TP}$ * [CTP]		XGP	PRIMARY NOZZLE GROSS THRUST
XGF = XBAL - XGP		XGF	FAN NOZZLE GROSS THRUST
PTF, TF, AF, PS, WFAN		CDF	FAN NOZZLE DISCHARGE COEFFT
CTF = XGF/(f((PTF/PS) * WF$\sqrt{TF}$)		CTF	FAN NOZZLE THRUST COEFFT

Calibration Coefficients From MST Boxed Thus [CTF]

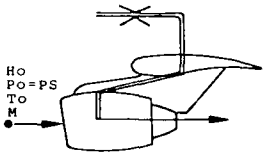

T. W. T.

PVA, TVA, AVA		WV	HP VENTURI MASS FLOW
PTP, TP, PS, AP		CDP	PRIMARY NOZZLE DISCHARGE COEFFT
XGP = f(PTP, PS) * WP$\sqrt{TP}$ * [CTP]		XGP	PRIMARY NOZZLE GROSS THRUST
RPM, TI	$CRPMI = \frac{RPM}{\sqrt{\theta_I}}$	CRPMI	CORRECTED FAN SPEED
[CWI] = f(CRPMI)		CWI	CORRECTED FAN MASS FLOW
WI1 = CWI * $\frac{\delta_I}{\sqrt{\theta_I}}$	COMPARE →	WI1	FAN MASS FLOW
TI, Ho, PSI, AI, [CDI]	COMPARE →	WI2	INTAKE MASS FLOW
PTF, TF, AF, PS, [CDF]	COMPARE →	WFAN	FAN NOZZLE MASS FLOW
XGF = f(PTF/PS) * [CTF] * WF$\sqrt{TF}$		XGF	FAN NOZZLE GROSS THRUST
DRAM = WF * M * $\sqrt{\gamma RT}$		DRAM	RAM DRAG
AF, NF			FORCE BALANCE AF, NF AXIAL AND NORMAL FORCES
DRAG = $\sum_{VECTOR}$ [DRAM, AF, NF, XGF, XGP]			MODEL DRAG
LIFT = $\sum_{VECTOR}$ [AF, NF, XGF, XGP]			MODEL LIFT
$C_D = \frac{DRAG}{0.7PSM^2}$, $C_L = \frac{LIFT}{0.7PSM^2}$		C_D, C_L	MODEL DRAG AND LIFT COEFFICIENT

FIG. 3.2.28 CALIBRATION AND TUNNEL TESTING MASS FLOW AND THRUST & DRAG ACCOUNTING PROCESS (REF 3.2.23)

For the CMAPS calibration, a different approach to the flow accounting needs to be adopted as bleed and scavenge exist in addition to the inlet and drive flows. All airflows entering and leaving the CMAPS are shown in Fig. 3.2.29.

Regulated drive air is supplied to the drive manfold. This passes through the turbine and then enters the fifteen strut bleed module where it is either diverted into the annular bleed manifold or directed through the pancake mixer and thrust trim orifice. The bleed turbine air exits at high pressure (in the region of up to 7000 psia) into the metered bleed air line. The amount of turbine exhaust air that mixes

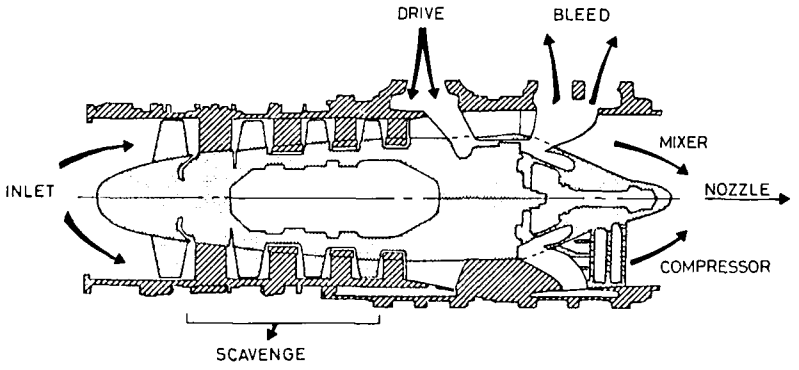

FIG. 3.2.29 CMAPS AIRFLOW DIAGRAM (REF. 3.2.15)

with the compressor air (to form the exhaust nozzle total flow) is controlled by the amount that is bled off to the metered bleed airline. In addition to these flows a small amount of parasitic air escapes from the simulator via the oil scavenge system. Thus the flow continuity requires that:

$$W_{INLET} + W_{DRIVE} = W_{TURBINE\ BLEED} + W_{NOZZLE} + W_{SCAVENGE}$$

all of which, except W_{NOZZLE}, are metered.

Hence the positions of the drive and bleed valves provide a unique combination of inlet and exhaust mass flows and exhaust nozzle pressure ratios. With the extreme range of attitudes of the inlet approach flow conditions the CMAPS calibration will need to be far more comprehensive than that for the civil TPS. In these extremely distorted inlet flows the inlet instrumentation must be sufficient to provide an adequate description of the inlet mass flow. This must be achieved by an array of gauzes and distortion plates in the calibration which can then be related via a distortion flow parameter to the test inlet flow conditions. In practice, of course, it is rarely a requirement to derive accurate drag performance under these conditions of large inlet distortion. It is unlikely that the inlet distortion will reflect in the exhaust nozzle total pressure distribution as only a small part of the nozzle chamber flow is derived from the inlet and that will have been greatly smoothed through the compressor.

3...2.5 Practical Applications of CMAPS

The first consideration to be made in the practical use of the CMAPS will be the applicability of the calibration data and the test performance limitations imposed by the simulator. It cannot be assumed that the simulator will reproduce the performance of the engine over its whole flight envelope. Thus it must be accepted that the expensive and complex "ultimate" model may have limitations which will preclude testing over the full desired range. This will normally be due to inlet distortion and particularly swirl which may well react on the simulator compressor in a different manner from that of the real engine. Whilst this may provide an early warning of "flight problems to come" similar warnings could be obtained from detailed engine face static and dynamic distortion and swirl flow measurements as an inlet test model - probably at a better scale. Simulator calibrations will in general be obtained in a rig of the type described in the previous subsection. These calibrations will initially be made with ideal bellmouth flows into the intake which provide the possibility of achieving calibrations to the accuracy required for T-D performance. If thrust calibration performance is needed at higher flight attitudes then the corresponding inlet and engine face flow field must be provided in the calibration. This can be done with attention to detail for spatial distortion in a similar manner to that for the full scale engine. It is unlikely that the quality of the mass and thrust definition will be good enough for performance T-D analysis but will adequately describe the inlet and exhaust flows for stability and control checks of inlet and nozzle flow effects. If significant swirl is present then it becomes a major task to simulate this in the calibration - particularly if twin swirl arises in the inlet duct due to the airframe environmental conditions.

Aircraft models equipped with CMAPS should be scaled to match the simulator maximum inlet flow capabilities i.e. corrected inlet flow of 1.65 lbs/sec., the maximum CMAPS corrected airflow

$$\text{This gives a model scale} = \sqrt{\frac{1.65}{\text{F.S. Corrected inlet flow (lbs/sec)}}}$$

This typically results in a model scale of about 10% for a twin engine configuration but only about 7% for a single engine geometry. Fig. 3.2.18 illustrates that the simulator will embrace the operating engine pressure ratio range for the typically required dry engine flows. The length of the simulator being 3.5 times the compressor face diameter will present problems when laid out in some advanced airframe VSTOL

configurations. Some typical comparisons are given in the table below

Type	Scale %	Engine L/D	Duct L/D
F4	11	3.1	14
F5	12	-	19
F14	7.5	2.5	11
F15	8.2	2.7	12
F16	8.2	2.7	10.5
F18	10.7	-	11
F20	10.7	-	11.5
F111	7.3	2.5	10.3
B1	7	-	8.5
X29A	10.7	-	12.5
Tornado	10.5	2.8	12.6
AMX	11	3.1	12.3
Mirage 2000	9	2.7	10.7
Mirage 4000	9	2.7	13.4
Viggen	7	2.7	10
Grippin	10.8	-	13.5
Harrier/AV8	6.2	2.3	2.5/5.0

where
Engine L=Bare core
Duct L=Engine face to nozzle
D=Engine Face dia.

(All figures very approximate).

FIG. 3.2.30 APPROXIMATE GEOMETRIC CHARACTERISTICS OF CURRENT AIRFRAMES RELATED TO MODELS SCALED TO CMAPS

It may be assumed that even with a minimum length inlet duct ratio of 3 and similar nozzle length ratio, the overall duct L/D (defined as being from inlet lip to exhaust nozzle plane) for the CMAPS must be of the order of 9. This is seen to be adequate for the representation of all the cases given in the table Fig. 3.2.30 except for the Harrier. But with future plans for VSTOL configurations in flight vertical thrust and close coupled projects it might be questioned that the CMAPS with a minimum L/D (including nozzle) of say 8 is not short enough to represent the close coupled build of the future which is basically its 'raison d'être'. However, the definition of close coupled may be different for different operating modes and so the simulator will find a place in the hover and transitional modes even if the length is too great for the cruise mode.

Cassmeyer in Ref. 3.2.21 makes a paper study of the cost effectiveness of a simulator in comparison with the conventional part-model approach and shows that significant savings in test time may well be achieved. The comparison is made on the basis of a no-cost simulator and control unit, and uses an assumed model for an advanced STOL configuration. A 2-model conventional test technique, consisting of an aero flow-through and a jet-effects model, was compared with a single-model-with-simulator technique. The comparison results are indicated in Fig. 3.2.31.

Models	Data Obtained	Cost Ratio	AEDC Occupancy Hour Ratio
● Conventional Technique Aero F&M Flow-Thru Model 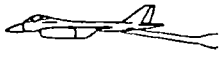 Jet Effects Model 	● Basic Drag Polars ● Inlet Drag Variation ● Nozzle Drag Variation	1.00	1.00
● Simulator Technique Simulator-Equipped Model 	● Basic Drag Polars ● Inlet Drag Variation ● Nozzle Drag Variation	0.96	0.87

Assumptions:
1. Calibrated simulators and user's control console are provided
2. Comparison is for aircraft proposal or system development phases.
3. Models at 10.5% scale based on propulsion simulator size and inlet simulation.

FIG.3.2.31. COST COMPARISON OF TEST TECHNIQUES FOR AERODYNAMIC PERFORMANCE DEFINITION (REF 3.2.21.)

The cost estimates indicate that the building of one propulsion simulator model could provide only 4% saving over the cost of the conventional models indicating that the use of 1 simulator model instead of 2 conventional models is virtually offset by the increased complexity of the former. However, the 13% reduction in wind tunnel occupancy represents a very useful saving. It should also be remembered that the cost of the simulator and all its control equipment has not been included in these calculations.

The application of CMAPS technology into test programmes is still in its infancy and apart from the early programme of operating tests at AEDC the only recorded application of the CMAPS is given in Ref. 3.2.14 by Bailey et al. This describes in detail the model design philosophy applied to the installation of 2 CMAPS into a 9.6% scale V/STOL airframe concept (two slightly different versions were in fact used). The object of the tests was to make a comparison of results obtained with the two simulators with those obtained by the conventional method with a flow through model, and a faired-inlet jet effects model. In order to minimise the effects of errors in the comparison, attempts were made to keep the error sources common (or similar) in the two different

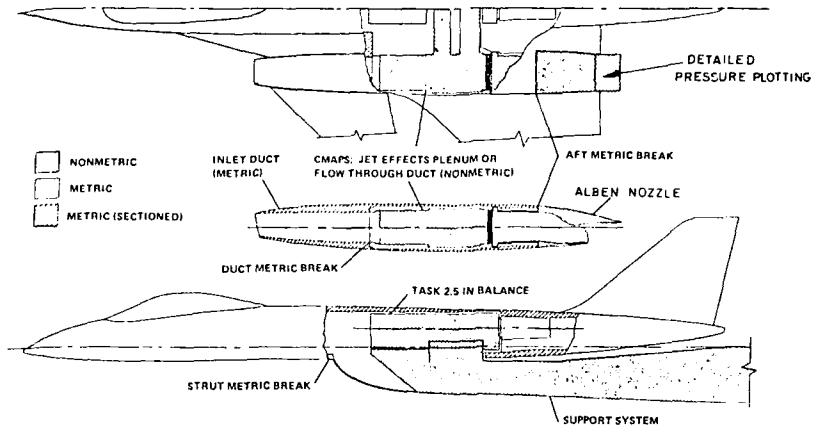

FIG. 3.2.32. METRIC BREAK ARRANGEMENT (REF. 3.2.14.)

model concepts. Thus the tests were planned to have a common support system, common metric/non metric breaks, and common instrumentation. The configuration had two wing mounted nacelles which facilitated the mounting of the non-metric CMAPS from the earthed end of the fuselage balance whilst carrying the majority of the airframe metric on the live end of the balance. This is illustrated in Fig. 3.2.32.

From this Fig. 3.2.32 it is seen that a single support sting is used to duct the drive air into the model and the turbine bleed air from the model. The sting entry is from below the fuselage centre line at the centre of gravity up into a manifold system which distributes the high pressure air ducts out to the two earthed simulators in the wings. The live model shell is mounted on the rear live end of the

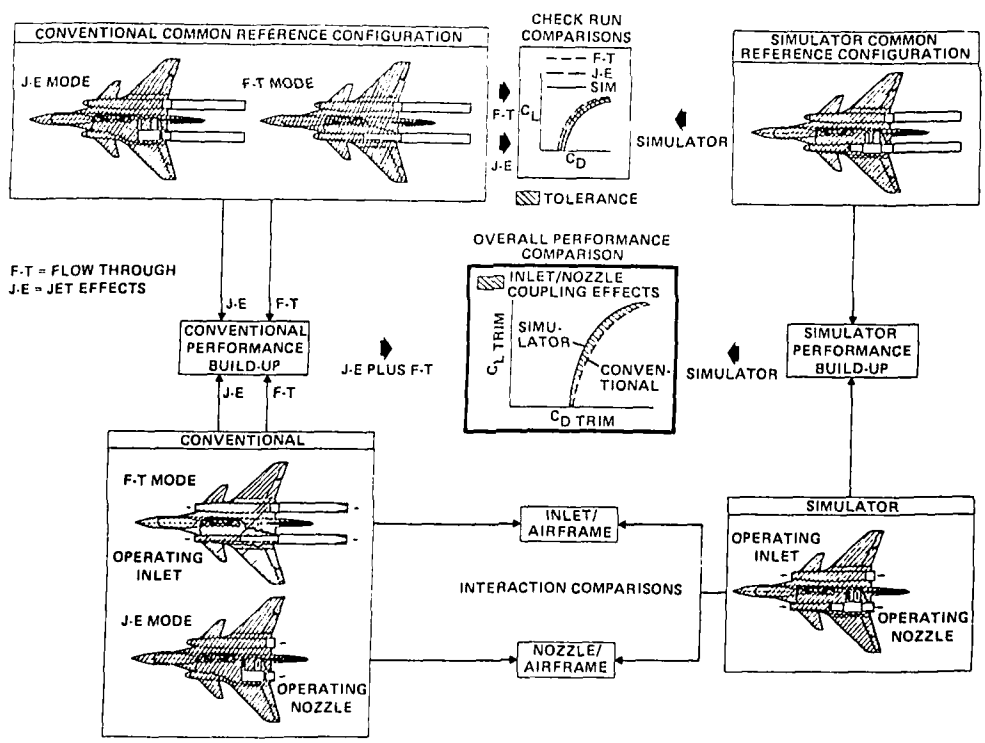

FIG. 3.2.33 TESTING APPROACH SUMMARY (REF. 3.2.14)

balance. This Reference 3.2.14 is particularly recommended to those readers interested in the details of this test programme and concept. Information on seal arrangements and the effects of the hot drive temperature on the balance system is provided in detail. Of particular interest also is a breakdown figure of the testing concept showing commonality to reduce error bias to ensure that a high quality comparison of the simulator versus conventional approach is achieved. This Fig. 3.2.33 is a valuable guide to the build up of an intelligent test programme. This shows how the comparison between the simulator and conventional approach is validated by tests on a common reference configuration which is used on all three model test builds i.e. the flow through (FT), the jet effects (JE) and the simulator. This common reference has a faired inlet and an extended exhaust nozzle with no flow. These builds of the model should give the same results within acceptable tolerance and if this is achieved then it may be assumed that the individual effects of the FT, the JE, and the simulator tests may be validly compared. The results of these tests will be very informative but it must be remembered that it is representative of a nacelle system with an inlet to nozzle separation L/D of 9.5 engine face diameters, which may well prove to be non-close-coupled.

3.2.2.6 Conclusions

The concept of an engine simulator is well founded and has been well executed in the CMAPS work. It has been shown that such a simulator may be operated to provide a full operating map of engine pressure ratio and inlet mass flow for most current and immediate future requirements. Because of the complexity of the operation of CMAPS its use may be limited to aircraft late in the development cycle. In addition the development of minimum interference support systems for metric or non metric installations will be essential if the support interference is to be less than the coupling interference which is the subject of the tests.

The justification for the simulator however is the need for simultaneous representation of inlet and exhaust flow. The critical separation distance between these two flows has not yet been established and that critical dimension will be a function of the operating conditions (i.e. low speed VTOL, in flight vector, or cruise) of the engine duct. In the cruise condition it is likely that the physical dimensions of current engines and inlet and exhaust ducts will keep the overall minimum separation (duct L/D) to a value not less than 7. It may then be questioned whether this is small enough to be critical i.e. give inlet/exhaust mutual interference. It has been found that the mutual interference in civil applications, where duct L/D for the fan nozzle is as low as 2 is only marginal on isolated engine nacelles.

The current simulator design CMAPS has an engine core length of 3.5 inlet diameters which is at least 1 inlet diameter longer than most engines it has to represent. Consequently the representation of a current minimum length VSTOL nacelle cannot be less than a duct L/D of about 8. Hence the present simulator cannot be mounted in a model to represent what is currently a minimum length installation nor what might be achieved in future shorter engines.

There would thus appear to be a strong case for a CCMAPS where the compressor is reduced to 2 stages whilst providing the same engine pressure ratio. In this case the simulator could provide a full simulation of a current minimum length installation.

3.2.3. Ejector Powered Simulators (EPS)

An ejector powered simulator is in essence a ducted jet pump using the high energy pressure input of a set of primary nozzle jets to induce and pressurise a secondary flow. The induced flow forms the inlet duct flow, the inviscid primary and secondary flows form the exhaust nozzle pressurised flow. Thus by definition less flow passes through the inlet than exhausts from the nozzle. This has often been quoted as a negative feature of the EPS relative to the TPS because correct simultaneous simulation of the inlet and exhaust is not possible. The statement is more true in relation to the civil TPS, but if existence of a third flow is allowed (as is the TPS turbine bleed) then the ejector should be allowed an inlet flow bleed which would enhance the inlet flow ratio. Inlet bleed however, being at relatively low total pressure may require a larger flow duct than is practicable - but probably not much greater than that required for the CMAPS turbine bleed.

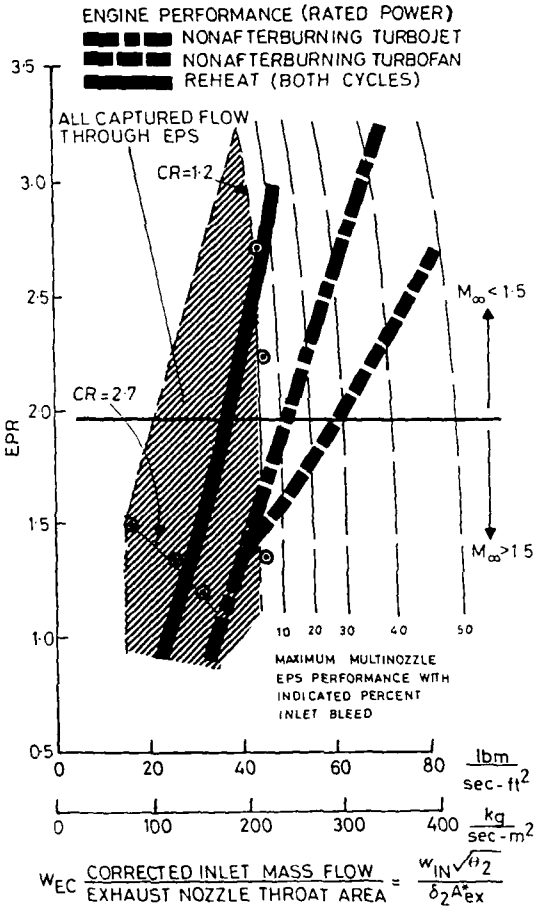

FIG. 3.2.34. PUMPING CHARACTERISTICS OF CURRENT GENERATION ENGINE CYCLES AND EPS. (REF 3.2.26)

Experimental results have shown that a single stage EPS with multiple primary nozzles is capable of producing uniform exhaust flow conditions simulating high performance turbine engines. FIG. 3.2.34 illustrates the pumping characteristics of current generation engine cycles with some projection of in advanced EPS performance from Ref. 3.2.26. The ejector works up one maximum operating line which is the design line for a range of primary pressures. Throttling the exhaust influences the pumping characteristics giving a means of ensuring an operating range to the left of the maximum design line. Expansion to the right of the design line is achieved by inlet flow bleed as illustrated, where percentage bleed is defined in relation to the inlet capture. In principle with independent control of engine pressure ratio via the ejector drive pressure and control of the inlet mass flow via an inlet bleed it should be possible to match the performance range over a major part of the dry mode and the reheat mode, but not with the same ejector. In this respect the EPS model build requiring two ejector installations may be considered more complex than the TPS. Whilst the use of inlet duct bleed as a means of moving the EPS characteristic to the right sounds attractive, the physical size of ducting for 20% bleed at the low pressures of inlet flow may give rise to unacceptable model distortion.

The EPS and TPS have been the subject of many controversial arguments between the protagonists of each. Factors like compactness, unit cost, test cost, repeatability, ease of use, supplementary services, calibration, may be used by each school of thought in turn as a pro-or con- foreach particular simulator . Of these factors the only ones which must be of prime importance are accuracy, repeatability, and degree of simulation. Without good performance of these parameters there is no point in embarking on a test no matter how cheap or simple it might be. Contrary to first impressions, it would appear that the EPS could be more susceptible to errors in operation due to internal deformation or damage to the primary nozzles or screens and pressure dropper plates, than the TPS which might be expected to retain the same basic calibrated performance characteristic as long as it remains operational.

3.2.3.1. Basic Design of Ejector Systems

This section only briefly introduces the basic design objective of the ejector. For more detailed study the reader is referred to Refs. 3.2.26, 3.2.28, 3.2.29, 3.2.30.

Reference 3.2.29 by Wood provided one of the first published detailed analyses of the design and use of "ejector drives for engine simulation in wind tunnel models at high speeds". This work was limited to

simple one dimensional analysis with estimates for system losses. It was in this paper that the first thoughts of inlet flow bleed to concurrently simulate correct inlet and exhaust flows were proposed

Reference 3.2.26 by Smith, Matz and Bauer of AEDC took up the development from this stage and studied the relationship of the experimental ejector to the theoretical one dimensional model defined in this reference by the consideration of mass, momentum, and energy. This work also suggested that it is more suitable to relate the ejector performance to the engine performance via the mass flow and the choked exhaust nozzle exit area A^*_{ex}.

$$\text{i.e. } W_{EC} = \frac{W_{inlet}}{A_{ex}^*}$$

where the mass flow W_{inlet} is the non-dimensional flow parameter $W_{inlet} \cdot \frac{\sqrt{\theta}}{\delta}$, being independent of flight Mach number and altitude. Engine pressure ratio (EPR) with geometrically similar nozzles must also be simulated. Thus Ref. 3.2.26 defined the ejector powered simulator (EPS) performance in terms of W_{EC} v EPR. These parameters for typical engines are shown in FIG. 3.2.34. The reference also introduced the concept of the need to operate at an increased EPR to correctly simulate the hot gas plume effects. Using the results of Ref. 3.2.6 it is suggested that for:

(a) normal 'cold' operating engine conditions of 1800-2200°F, the EPR should be increased by 2-12%

(b) turbofan operating conditions, the EPR should be as for the engine and

(c) reheat operating conditions of 3000-3300°F, the EPR should be increased by 20-50%.

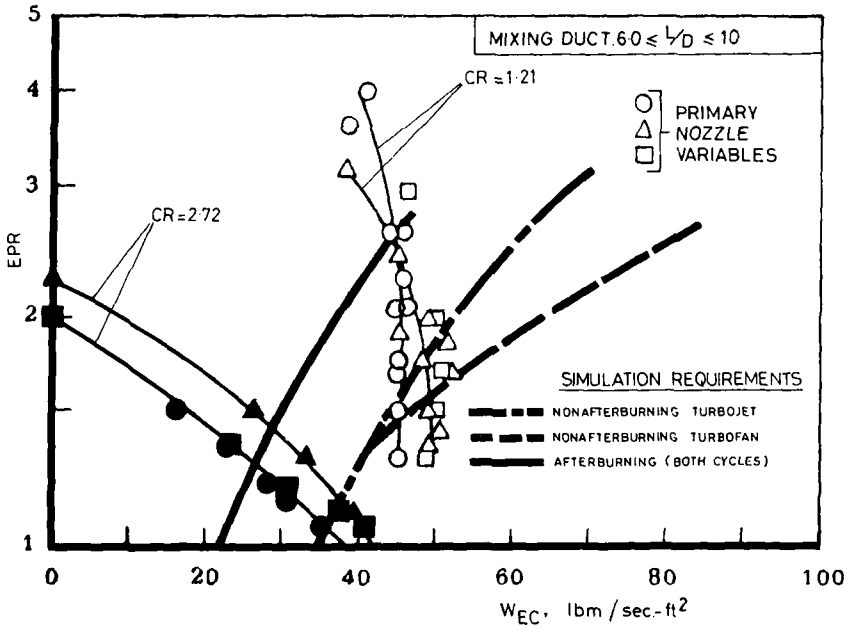

FIG. 3.2.35 EFFECT OF EXHAUST NOZZLE CONTRACTION RATIO CR (REF. 3.2.26)

Ref. 3.2.26 studied the effect of a range of geometric parameters by experiment for both single stage and dual stage ejectors. The important findings were that the ejector mixing duct Mach number should be in excess of 0.6 for maximum performance. This effectively controls the exhaust nozzle contraction ratio to a value less than 1.2. But contraction ratio can be used as a way of degrading an ejector performance to achieve a lower performance requirement e.g. reheat FIG. 3.2.35.

A further factor in ejector performance is the primary nozzle Mach number, the effect of which is shown in FIG. 3.2.36. Theoretical analyses have been used to establish a design criterion to achieve the high performance arm of FIG. 3.2.36. Theoretical study using the momentum and continuity equations for a single stage multi nozzle have established a relationship between the primary nozzle thrust and that of the mixing duct exit which indicates whether or not the high performance mode can be achieved. It was found that an exhaust nozzle contraction ratio less than 1.6 was required with a primary nozzle Mach number of 5. For lower primary Mach numbers the limiting value of contraction ratio reduces significantly as shown in FIG. 3.2.36. Further analysis indicates that a low total temperature of the primary flow is necessary for maximum performance but not too cold to give liquefaction of the primary expanded flow at very high Mach numbers.

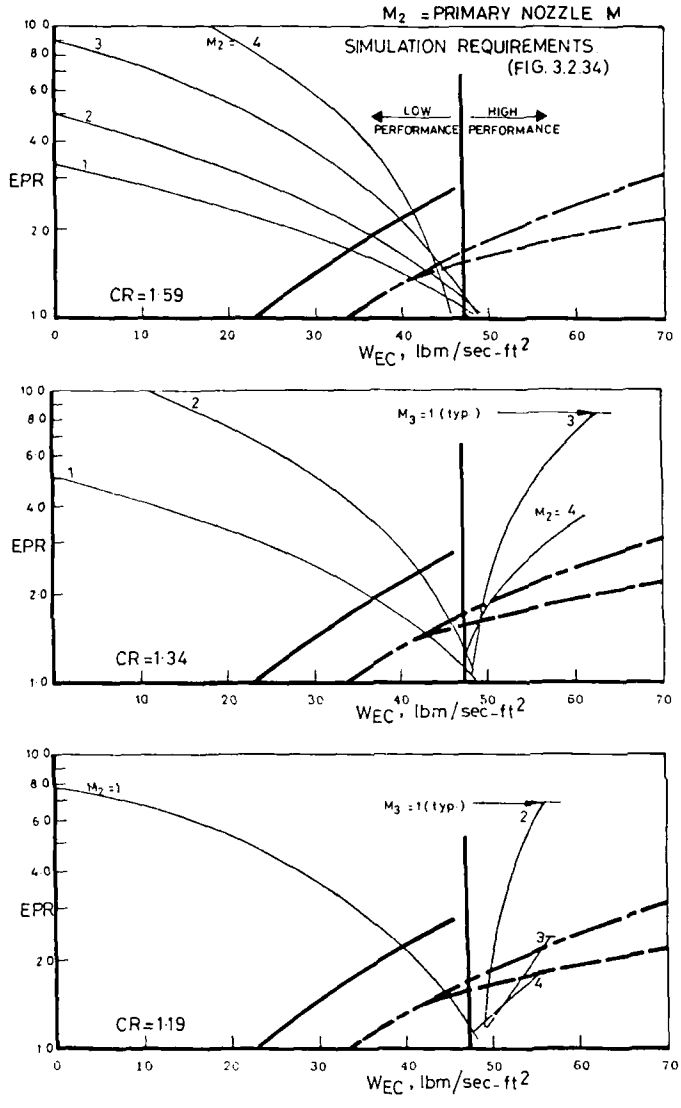

FIG. 3.2.36. THEORETICAL EFFECT OF PRIMARY NOZZLE M_2 FOR VARIOUS LOW VALUES OF CR. (REF. 3.2.26)

Theoretical mixing duct length analysis on the basis of turbulent mixing theory has shown that for acceptable exit pressure profiles a mixing duct length of 6-15 diameters (primary + secondary duct) is required for low by-pass engines and 8-20 diameters for turbojets. In practice this means that the mixing duct must effectively be broken down into smaller elements to achieve a shorter total mixing duct length i.e. a multi nozzle system is required.

Analysis of the performance of a two-stage ejector compared with that of the single stage shows that whilst this provided a higher simulated EPR, the maximum value of W_{EC} was only 70-90% of that of the single stage ejector. The advantage of the 2 stage system is the flexibility of operating range which can be achieved with variation of primary drive pressure. With a judicious choice of geometry of the two stages it may be possible to operate an EPS over the shaded band of FIG. 3.2.37.

Whilst the demonstrated flexibility could be an advantage the two-stage ejector is not recommended for reasons of its greater length and lower W_{EC}.

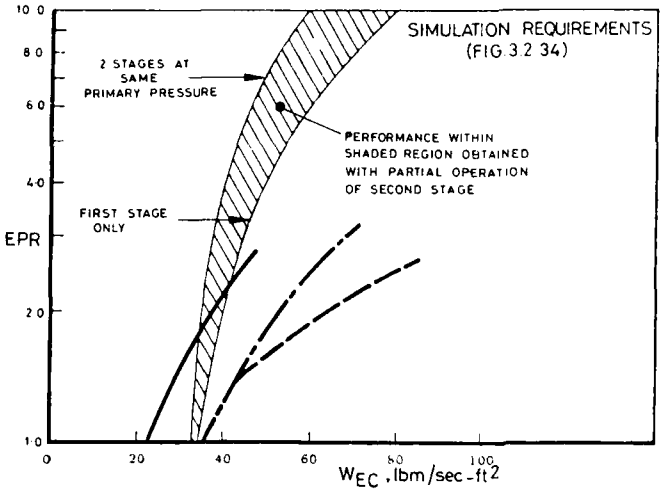

FIG. 3.2.37 THEORETICAL PERFORMANCE OF A TWO STAGE EPS. (REF. 3.2.26)

Ref. 3.2.28 utilises an empirical factor plus one dimensional theory approach which has the advantage of simplicity in comparison with three-dimensional methods, and versatility in comparison with a purely empirical approach. The manual data of this Ref. is limited to air-to-air ejectors having a primary to secondary temperature ratio of unity. It is also a requirement that the primary nozzle is fully expanded such that the primary exit static pressure P_1 equals the secondary static pressure P_3, thus giving no internal primary nozzle separation.

The design of an ejector system must be a series of compromises where priorities are applied and the degree of match of the required final parameters must be accepted or re-iterated. For a specific engine simulation a decision is required at the initial stage as to whether the exhaust or the inlet flow must be correctly simulated, and in either case

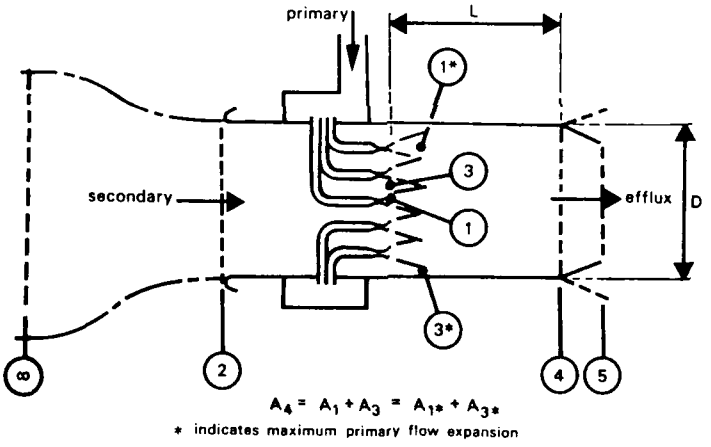

FIG. 3.2.38 BASIC EJECTOR DEFINITIONS (REF 3.2.28)

the degree to which one parameter should be optimised and whether inlet bleed is permitted for inlet flow simulation. The required ejector mass flow ratio may be calculated directly as a function of the full and model scale temperatures:

$$\text{Ejector mass flow ratio} = \frac{\dot{m}_2}{\dot{m}_1} = \frac{\sqrt{(TR)_\infty}}{\sqrt{(TR)_j \cdot (YR)_j} - \sqrt{(TR)_\infty}}$$

where (TR) = Full scale to model static temperature ratio at ∞ or jet pipe j conditions.

and (YR) = Full scale to model γ Ratio at jet pipe conditions

alternatively if other parameters are known use:

$$\frac{\dot{m}_2}{\dot{m}_5} = \frac{\dot{m}_2}{\dot{m}_1 + \dot{m}_2} = \frac{\text{Mass flow ratio}}{\text{Mass flow ratio} + 1}$$

where $\dot{m}_2 = Q_\infty \cdot Ae \cdot P_{O_\infty}\left[\frac{A_\infty}{A_e}\right]$ where $\left[\frac{A_\infty}{A_e}\right]$ is the known capture area ratio.

and $\dot{m}_5 = Q_5 \cdot A_5 \cdot (NPR.P_\infty)$

Then $$\frac{\text{Mass flow ratio (MFR)}}{MFR + 1} = \left[\frac{P_{C_\infty}}{P_\infty}\right]\left[\frac{1}{NPR}\right]\left[\frac{A_\infty}{A_e}\right]\frac{A_e}{A_5}\cdot\frac{Q_\infty}{Q_5}$$

where $\frac{P_{O_\infty}}{P_\infty}$ is the total to static pressure ratio of the free stream = $f(M_\infty)$

NPR is the exhaust nozzle pressure ratio

and Q is the total pressure non-dimensional mass flow function $\frac{\dot{m}\sqrt{T}}{A.P_O} = f(M)$

Reference 3.2.28 proposes certain design constraints as determined from experience or good practice:

(a) A choked efflux at station 5 has been shown to give improved back pressure at station 4. It is suggested that an exhaust nozzle contraction ratio of the order of 1.11 be used thus limiting M_4 to less than 0.68. Smaller values are recommended if there is a likelihood of M_4 going supersonic.

(b) The duct feeding the primary nozzle must in practice be of limited cross sectional area and the Mach number in this duct should not be greater than about 0.3. This then defines the size of the choked throat of the primary nozzles which in turn defines A_4 depending upon the Mach number at the exit of the expanded primary nozzle.

(c) M_3 should be as low as possible to reduce losses in the secondary flow past the primary nozzle assembly.

Loss factors

These are empirical allowances for the various losses that occur in the regions of the ejector duct flow:

(a) mixing duct between stations 1/3 and 4 by the momentum equation:

$$P.P.\frac{(1 + 1.4\,M_1^2)}{(1 + 0.2\,M_1^2)^{3.5}} + SP.\frac{(1 + 1.4\,M_3^2)}{(1 + 0.2\,M_3^2)^{3.5}} = 1 + CM_4^2$$

where $P.P. = \frac{C_D\,P_{O1}}{P_1\,A_R}$

and $SP = \left[\frac{P_{O2}}{P_1}\right]\left[\frac{A_R - 1}{A_R}\right]$

for $A_R = \frac{A_4}{A_1}$ and C_D = Primary nozzle discharge coefficient

This loss coefficient C includes the loss in momentum due to

(a) Secondary total pressure losses

(b) Secondary/primary mixing transfer losses

(c) Mixing duct wall friction losses

(d) non-isentropic mixing processes

In Ref. 3.2.28 it was shown that within limits

$$C = 1.51 + 0.019\,.\,\bar{n}$$

where n is the number of primary nozzles for a mixing duct length

$$1 \le \frac{\sqrt{n}}{D} \le 10$$

where D = mixing duct diameter

or $D = \sqrt{d_o^2 - d_i^2}$ for an ejector in an annulus of d_o outer diameter and d_i inner diameter.

This loss factor applies to non choked exhaust nozzle flows at station 5. As previously mentioned, choking at station 5 improves the upstream flow quality and uniformity and the C factor is found to be reduced by about 0.06. The above values of C assume a well-designed ejector duct system with no separation of the primary nozzle flows, non choked secondary flow in the primary plane and a mixing duct length equal to or in excess of L. For the primary nozzle discharge coefficient C_D, primary total pressure loss coefficient may be incorporated for losses which occur in small primary feed pipes less than 12mm diameter. For primary nozzle throat diameters greater than this value the effective C_D is near 0.99. The value of C_D may be taken to vary linearly between 0.99 at 12mm diameter to 0.90 at 1mm diameter. This data is applicable to primary convergence angles of 15° for convergent sonic nozzles and 24°/14° for con-di nozzles.

Mechanical design features

Ejectors for engine simulation are generally specialised and it is difficult to generalise a 'best design', nevertheless 'good design' features should be incorporated to optimise a given requirement. Some such features are:

(a) low secondary Mach number approach to the contraction area created by the presence of the primary ducts. The secondary duct Mach number should be at its greatest at the plane of the primary nozzle exhaust.

(b) efficient primary nozzle design. This may be achieved by the use of sharp lipped primary nozzles (to avoid inefficient regions of base flow) and the use of individual tubes feeding each primary nozzle FIG. 3.2.39(a) in preference to a communal rake arm FIG. 3.2.39(b) feeding a series of nozzles in the trailing edge.

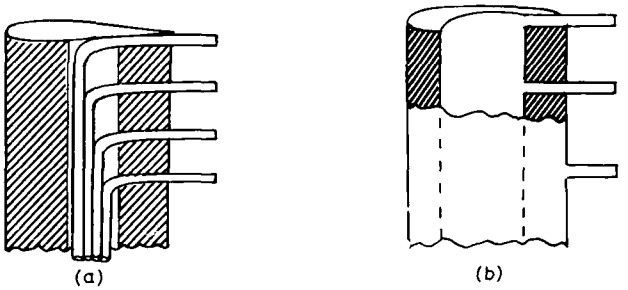

FIG. 3.2.39 PRIMARY EJECTOR NOZZLE RAKES

(c) Use of multiple primary nozzles reduces the optimum length of mixing duct for efficient energy mixing. This also has the benefit of greatly reduced ejector noise.

Optimum performance requires that the duct be adequately covered by primary nozzles and for thin annulus arrangements as in low by-pass geometries it may be difficult to ensure adequate overlap with the optimum number of nozzles. Thus before settling on a final arrangement, a geometric 'end view' should be studied to ensure that there are no blank areas which will reflect as holes in the efflux total pressure. Area spacing should be carried out by positioning nozzles such that equal diameter circles drawn about each nozzle centre cover the induced duct area to the maximum possible effect. Increased numbers of primary nozzles may be seen to be necessary. The positioning of the nozzles will also be governed by the blockage imposed by the primary nozzle assembly. Where only a small number of nozzles is required for optimum performance (as given by momentum and loss calculations) the value of n may need to be increased if peaks in the total pressure profiles are to be avoided. As a guide it has been found that to suppress nozzle pressure profile peaks values of the relation

$$n \cdot \frac{L}{D} \geq 28 \; M_4$$ should be achieved for a non-choked station 5. For a choked nozzle the basic minimum design value may be used.

3.2.3.2. Some Typical Applications of EPS Units

To illustrate some typical features of ejector designs for an in-fuselage configuration data is drawn from Ref. 3.2.31.

A single engine fuselage configuration with earthed ejector simulator is illustrated in FIG.3.2.40. The model was supported on a 6 component balance via a block support strut. The design was typically highly congested in the centre of gravity area where it is desirable to keep the balance CG closely positioned whilst not forcing the ejector plane too far aft. The solution was the design of a special annular balance which permitted an internal axial duct from the inlet to the ejector plane. The non-reheat ejector comprised 14 nozzles whilst the reheat case had 24. The general philosophy of the model was an earthed ejector and nozzle with live airframe shell carried on the annular balance. A live/earth seal was fitted between the front end of the earthed ejector duct and the live internal inlet duct. With such an arrangement of course the quality of the nozzle flow (being non-metric)

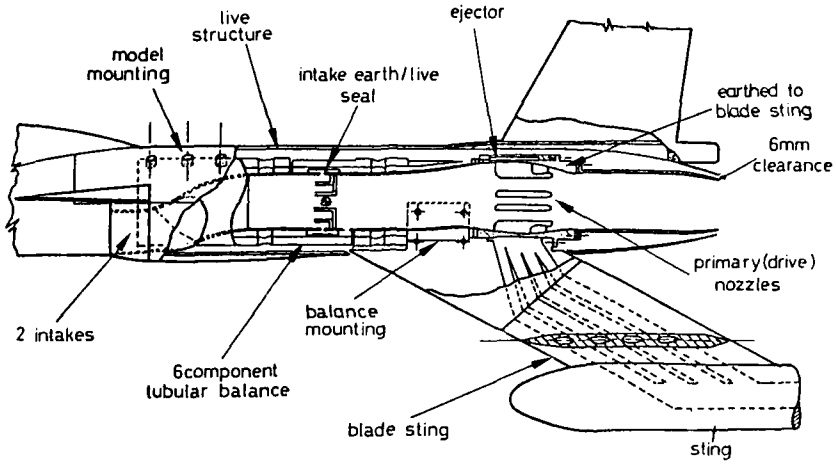

FIG. 3.2.40. SINGLE ENGINE SCHEMATIC DESIGN WITH NON-METRIC EJECTOR. (REF. 3.2.31)

was not so important and it was not essential to optimise the mixing. The metric/non metric duct break requires careful attention to the balance of measured force, the loads on the balance being a combination of:

$$F_{BAL} = F_{AERO} - F_{RAM} + F_{DUCT\ SPLIT} + F_{\substack{SEAL \\ TARE}} + F_{\substack{BODY \\ PRESS}} + F_{BLADE} \quad \text{- - - - - - - FIG. 3.2.41.}$$

The pressure tare items of split, seal, and body cavity are all items applied to experimentally determined areas.

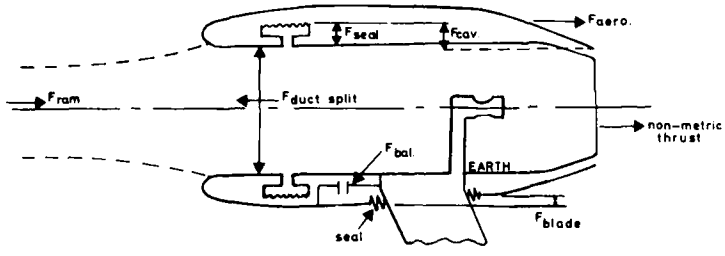

FIG. 3.2.41. FORCES ON EARTHED EJECTOR AND DUCT SYSTEM

The effect of deflection on the seal calibration must also be determined experimentally. Duct split momentum force is a function of the duct flow distribution and is likely to vary with test conditions. The position of the duct split force vector is also important due to its possible pitching moment interaction. The F_{RAM} term for inlet momentum is coupled through mass continuity to the $F_{DUCT\ SPLIT}$ term which minimises the mass accuracy requirements. Accurate calibration of some of these momentum and tare terms requires the use of a simulator test tank similar to that discussed in section 3.2.2.

A similar build could be designed with a live ejector simulator. In this case the problems of seal interference and split line momentum and mass flow calibrations are exchanged for the need to transfer high pressure air feed lines across the metric break between the blade support and the live ejector. The use of a live gross nozzle thrust requires its calibration against internal instrumentation to an accuracy appropriate to the required airframe drag accuracy. In principle the live EPS FIG. 3.2.42. is more simple to bookkeep than the earthed EPS requiring

$$F_{BAL} = F_{AERO} - F_{RAM} + F_{\substack{GROSS \\ THRUST}} + F_{\substack{BLADE \\ TARE}}$$

In general the percentage accuracy of gross thrust determination of any system must be of the order of the net thrust i.e. gross thrust - ram drag. For a fighter application, where the by-pass ratio is usually low the net thrust is of the order of half the gross thrust, so for drag determination to 1 drag count (0.0001) we have a requirement of about 0.3% in net thrust (equal to drag) and a corresponding gross thrust requirement of 0.15%. This of course is very extreme and sights normally have to be set lower at say 4 drag counts, as a significant number. The question that remains is, will it be possible to calibrate ejector simulator exhaust flows to this order of accuracy?

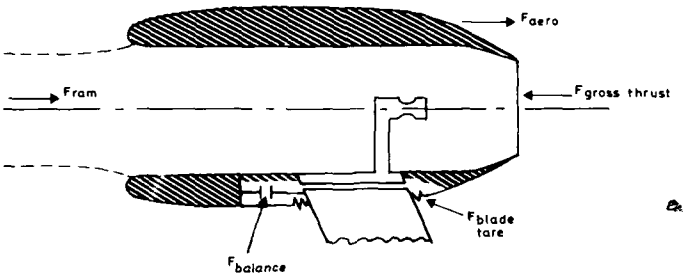

FIG. 3.2.42. FORCES ON LIVE EJECTOR

It is obvious that the main problem of this system, even if the gross thrust calibration can be shown to be satisfactory, is the design and operation of a successful high pressure air transfer system with calibrated pressure and deflection tares.

The one system which may be attractive to the model design might be an earthed ejector protruding into the flow of a fully metric duct. This is attractive in the avoidance of a high pressure air transfer requirement of the live ejector system and the avoidance of the duct live/earth split of the earthed ejector system, the only design requirement being that of a seal between live duct and earthed ejector tube. Such a scheme is shown diagrammatically in FIG. 3.2.43.

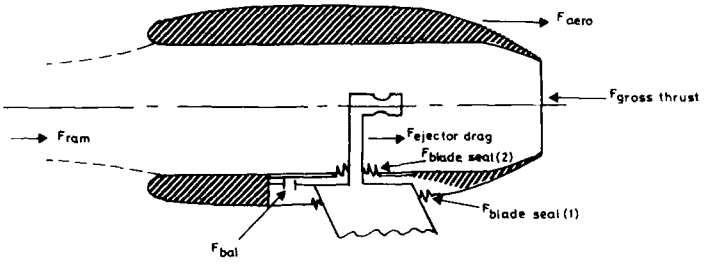

FIG. 3.2.43 FORCES ON LIVE DUCT WITH EARTHED EJECTOR

It will be seen that this system introduces a new term $F_{\text{EJECTOR DRAG}}$ because the exit momentum is modified due to the earthed force on the ejector body. The accounting and calibrating of this arrangement is difficult but the mechanical advantages are such as to make a solution worth pursuing. There is no recorded evidence of such a scheme being used.

Of particular interest is the potential of the EPS for simulation of vectored jets. The extreme simulator requirement must be that of a Harrier or AV8B type installation. Physically it should be possible to provide a dual ejector system to represent both front and rear nozzle pairs whilst giving reasonable air inlet flows. The integrated geometry however almost precludes the use of a live ejector with the attendant problems of live/earth airfeed systems across the balance at the aircraft CG between the nozzles. The whole concept of a 4 nozzle split with different NPR for front and rear pairs makes the problem formidable. Any solution will probably only be suitable for stability and control work, the thrust analysis being very complex.

It is perhaps symptomatic of the whole problem of engine simulation that: the airframe configuration that most needs complete representation is the most difficult to achieve.

3.2.3.3. EPS Units Designed Using the Criteria of Reference 3.2.26 by Smith, Matz and Bauer

Ejector design features developed in the above reference are summarised earlier in this chapter and also discussed in Ref. 3.2.32. Using this data two pairs of ejector nacelles were designed for a 6% scale model of the North American Rockwell B1. The two sets of nacelles represented

A. A subsonic cruise dry power operating condition with W_{EC} = 57.7 lb/sec.ft^2 at an EPR of 1.66. Because of the short length of this nacelle unit it was necessary to go to a 19 unit multi nozzle primary with an exhaust nozzle contraction ratio near the optimum at 1.19. The previous work in the Ref. indicated that the maximum performance might be expected to give a W_{EC} of about 50 lb/sec.ft^2. Thus it was expected that some inlet bleed would be required for full matching at this operating point.

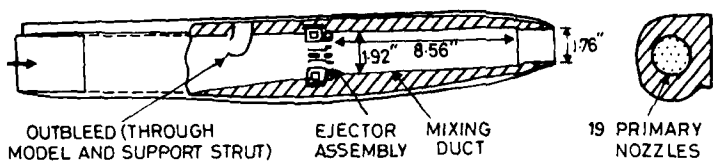

FIG. 3.2.44. EPS CONFIG. OF 6% B1 MODEL IN SUBSONIC MODEL BUILD (REF. 3.2.32)

Calibration of two of these units gave surprisingly similar results. The inlet mass flow for the basic no-bleed unit was about 5% lower than the predicted 50 lb/sec.ft^2. Using an inlet flow scoop as shown in the FIG. 3.2.44 perating at its max. flow, some 20% increase in inlet mass flow could be obtained. The calibration results for the two subsonic units are given in FIG. 3.2.45.

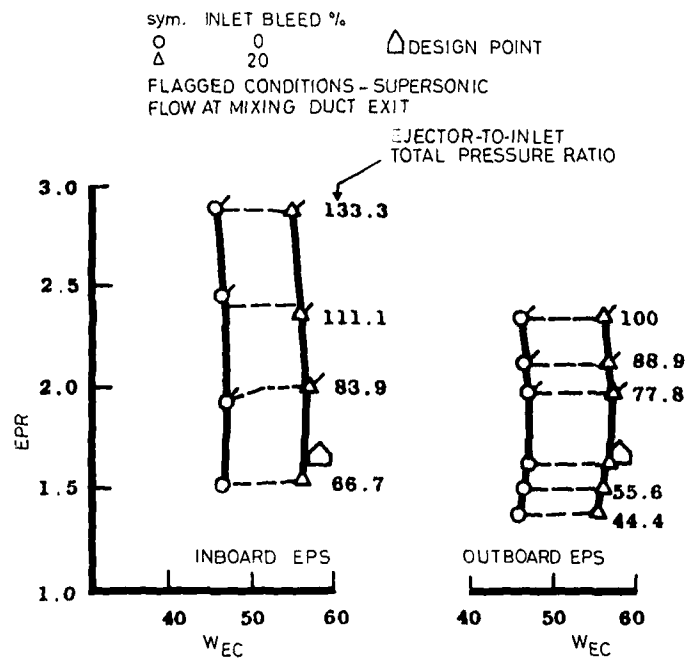

FIG. 3.2.45. CALIBRATION RESULTS OF TWO SUBSONIC EPS UNITS (REF. 3.2.27)

These show the similarity of the performance and the effectiveness of the inlet bleed in giving an operating point very close to the required design point. It will be noted how the mixing duct flow became supersonic for values of EPR more than 1.8. For higher values of EPR there is an abrupt change from subsonic to supersonic mixing duct flow and the exhaust total pressure distribution becomes very non-uniform.

B. A supersonic dash point with W_{EC} = 32.3 lb/sec.ft^2. This unit was developed from a 19 to a 22 primary nozzle build and because of the constraints of the B1 nacelle shape the maximum obtainable exhaust nozzle contraction ratio was 1.1 giving a mixing duct Mach number at the rather high value of 0.7 rather than the optimum 0.6. To improve the anticipated poor mixing duct flow, screens were added one diameter upstream of the exhaust plane. As the required value of W_{EC} was well within the design capability of the ejector, there was no requirement to boost W_{EC} with inlet bleed. The layout of this build is shown in FIG. 3.2.46.

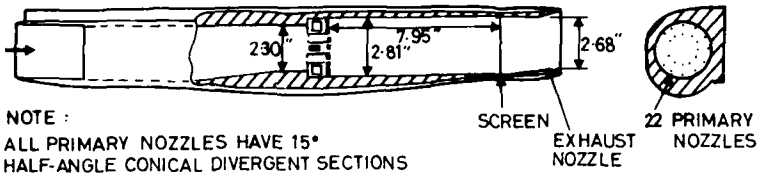

FIG.3.2.46. EPS CONFIG. OF 6% B1 MODEL IN SUPERSONIC DASH BUILD (REF. 3.2.32)

The initial calibration of this build gave values of inlet mass flow some 25% below the design value with significant exhaust nozzle flow distortion. The large exhaust nozzle associated with this operating point and correspondingly high mixing duct Mach number was the cause of supersonic mixing duct flows as found in the higher pressure ratio operating conditions of the subsonic build. The inlet induced flow was found to be limited by choking in the plane of the ejector nozzle support struts. To alleviate the problems, the inlet air mass flow was boosted by the use of the inlet bleed duct of the subsonic build and the choking in the ejector was alleviated by removing some of the primary support struts and nozzles and replacing them with other nozzles nearer the periphery. The distribution was finally improved by the addition of a large open area ratio screen (7% blockage) which did not completely eliminate the supersonic core but also did not reduce the W_{EC} as did a higher blockage screen. The results of the calibration of the two supersonic dash units are given:

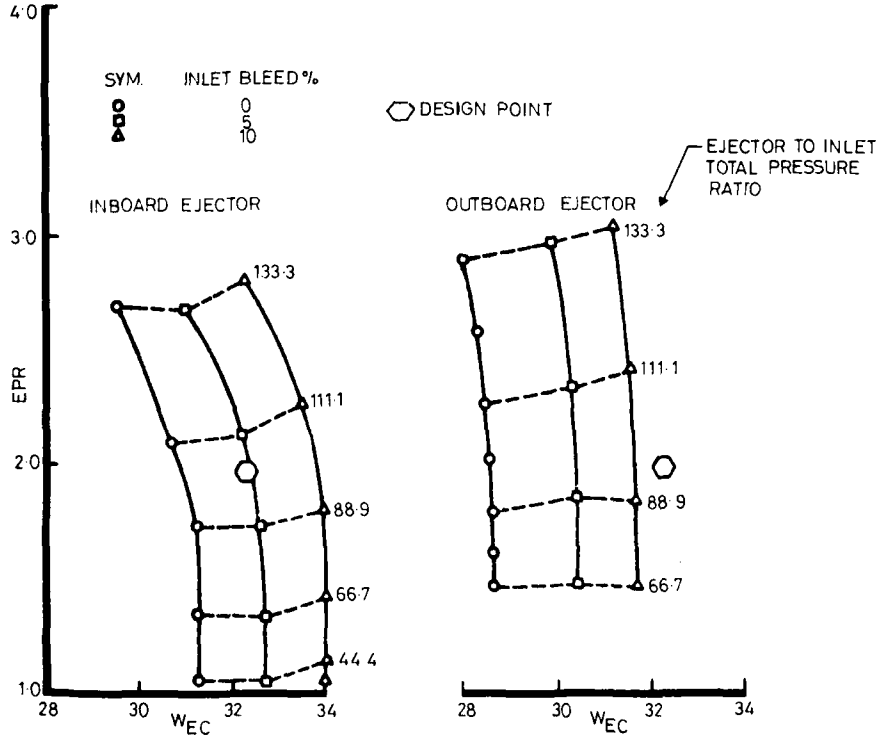

FIG. 3.2.47 CALIBRATION RESULTS OF TWO SUPERSONIC DASH EPS UNITS. (REF. 3.2.27)

These results show that the units matched the design requirements well after the above modifications and of course by the addition of 5-10% inlet flow bleed.

The above results are only a small selection of the detail design features described in Ref. 3.2.27. The effect of various parameters on the design performance are given in detail in that Reference which is recommended.

3.2.3.4. Calibration Requirements

These are very similar to those described in 3.2.2 on TPS calibration. Again it is worth restating that a calibration of a simulator is only as good as its instrumentation and is a calibration of that instrumentation. Very little information is available on the calibration and repeatability of EPS units. In the previous section it was questioned whether it would be possible to calibrate a unit to meet the required gross thrust accuracy needed for metric EPS installations measuring drag. The possibility must be a function of the adequacy of the ejector tube mixing with its attendent instrumentation plane uniformity. There is no data on combined temporal and spacial uniformity and very little information on the effect of inlet flow distortion. Basically the EPS is not as well documented as the TPS or CMAPS and must start at a disadvantage in this respect.

Whilst it is frequently quoted that robustness is an important advantage of the EPS, presumably because damage is not so catastrophic, it is nevertheless liable to changes in calibration due to small movement of the primary nozzle array. For the TPS unit it has been well demonstrated that calibrations are very repeatable, the outlet from the compressor or fan being well and truly mixed by their high speed rotation. For the ejector however, if the length is kept to that of a useable simulator, the exhaust flow contour is likely to reflect the total pressure tubes of the primary nozzles. If this is the case then it is imperative that the flow contour is absolutely constant in time and space. If a total pressure tube is critically positioned in an area of steep pressure gradient, then its contribution to the nozzle coefficients can be changed by minute movements of the flow field.

As with most problems, the calibration of the EPS can undoubtedly be solved by great attention to detail, but in principle it is likely that the EPS will need more check calibration than the TPS. It is also likely that the EPS will be more susceptible to variations in the contours of total temperature arising from the expanded primary nozzle flows than the total temperature variations at the exhaust of a TPS. This is almost certainly true for the conventional civil TPS with its separate fan and core flows but the CMAPS configuration with its mixing nozzle is becoming very similar to a multi nozzle ejector - with similar flow and temperature non-uniformity problems.

3.2.3.5. Conclusions

The ejector powered simulator has been shown to be capable of providing an adequate simulation of the flow requirements of current engines through the full dry and reheat cycles. For the maximum dry conditions of large engine pressure ratio with large non-dimensional mass flows it is necessary to bleed off significant quantities of the inlet captured flow before the ejector mixing plane. The high performance ejector needs refined design to meet the maximum operating points, using multi primary nozzles with high supersonic exhaust and high total pressure. Care has to be exercised to keep the mixing duct Mach number reasonably high without allowing it to go supersonic. Equal care is necessary to ensure adequate mixing for ejector efficiency whilst providing uniform flow at the nozzle plane.

It is likely that the EPS will suffer the same objections as the CMAPS for the particular application of close coupled simulation. It is probable in fact that the L/D of a high performance EPS will be greater than that of CMAPS.

There is no doubt that the ejector has its place in the non-metric application where the precise performance of the unit is less important than its basic simulation of the inlet and exhaust flows. This does not mean however that it is less likely to be able to meet the stringent calibration requirements of a live simulator unit, but there is currently less evidence of the uniformity of an ejector exhaust flow both in time and space, and in relation to pressure and temperature distribution.

The economies of the ejectors should not be taken for granted. The requirement of different units to match dry and reheat performance, and the need for more frequent calibration contribute to the expense of the EPS. But of course the advantage of maintaining the design and manufacture in-house and the flexibility of size of custom -build units is an attraction over the TPS.

3.2.4 ANNULAR JET

The concept of plume interference on afterbody pressures has been illustrated previously in Fig. 3.2.1., and discussion in sub chapter 3.2.1. considers how the plume may be thought to act as a solid body flow interference mechanism which gives buoyancy forces and viscous interactions on the afterbody. The entrainment flows in the mixing layer between plume and external flow induce afterbody flow velocity changes which in turn affect the afterbody pressure distribution and drag.

For exhaust blowing tests using a special model the existence of an interfering support strut system has to be accepted, and it is assumed that incremental effects of blowing and geometry are measured accurately in spite of the presence of the interference. As an alternative to special blowing tests a solid body mounted aft of the model might be used to give the equivalent 'jet solid body' forward interference. This will only be representative of one NPR condition for one external Mach number and will not of course provide the entrainment. As an alternative to this an annular jet may be introduced into the rear of a model supported on a high pressure blowing sting. This has the advantage of minimum support interference and provides a means of linking with the conventional aerodynamic forces model. This annular jet data can then be used as the absolute drag data link between the aerodynamic model and the special blow test model which only provides the incremental blow effect. These concepts are illustrated in Fig. 3.2.48.

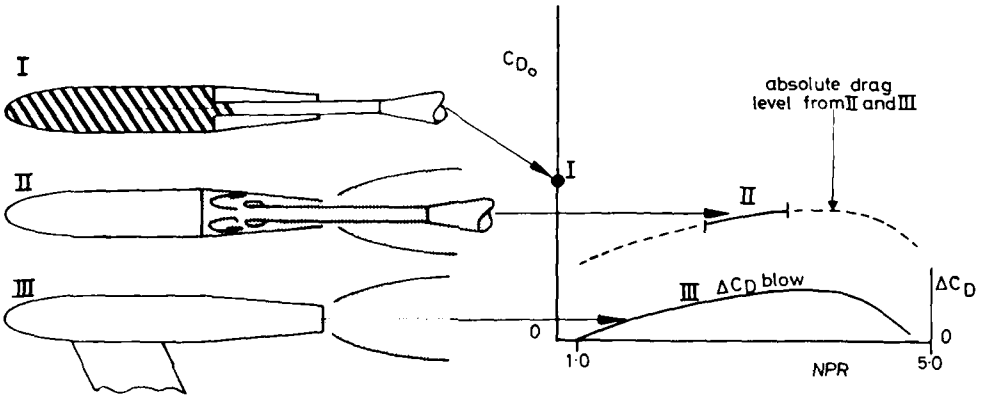

FIG.3.2.48. TEST BUILDS FOR ABSOLUTE DRAG.

The test conditions of this annular jet model will be limited by clearance dimensions but will provide a datum to which C_L and β effects may be added as determined by the aerodynamic test model. This latter does of course assume the exhaust effects to be small in comparison with the attitude effects.

3.2.4.1. Development of the Annular Jet System

Early reference to the concept of annular support/jet support systems is made by Bowers Ref. 3.2.33 In this work comparison of afterbody pressure results was made for a typical single engine fighter afterbody in the cruise and reheat nozzle configurations. It was concluded from this work that the case of the cruise nozzle where the ratio of sting to nozzle diameter was 0.93 gave poor simulation results due to the non representative plume diameter and length. For the reheat nozzle with sting to nozzle diameter ratio of 0.67 the representation was very much better and the plume diameter and jet wave length was much closer to that of the full nozzle flow. The indication from this work was that reasonable representation of a free jet plume may be obtained with an annular jet if the initial cell construction of the annular plume can be made to approach that of the free jet. The concept of correct initial expansion of the jet from the nozzle boundary is an obvious requirement but the post exit blockage effect associated with the plume maximum diameter is also necessary. Bowers also refers to the practical aspects of the applicability of the annular nozzle concept to single nozzle configurations compared with the twin nozzle and rectangular and plug nozzle. Some data is available on the use of annular jets and solid sting jet simulators in Ref. 3.2.34. This work showed that for a F4 type configuration with a fully expanded cylindrical exhaust the simulation by a solid cylindrical sting was good. For a rear twin nozzle 'Fill type' configuration however, significant differences were noted particularly for the large afterburning type nozzles.

Results of tests on a twin nozzle configuration with annular jet representation showed good correlation of drag for NPR < 5 if the NPR of the annular jet was adjusted to give the plume maximum diameter Fig. 3.2.49.

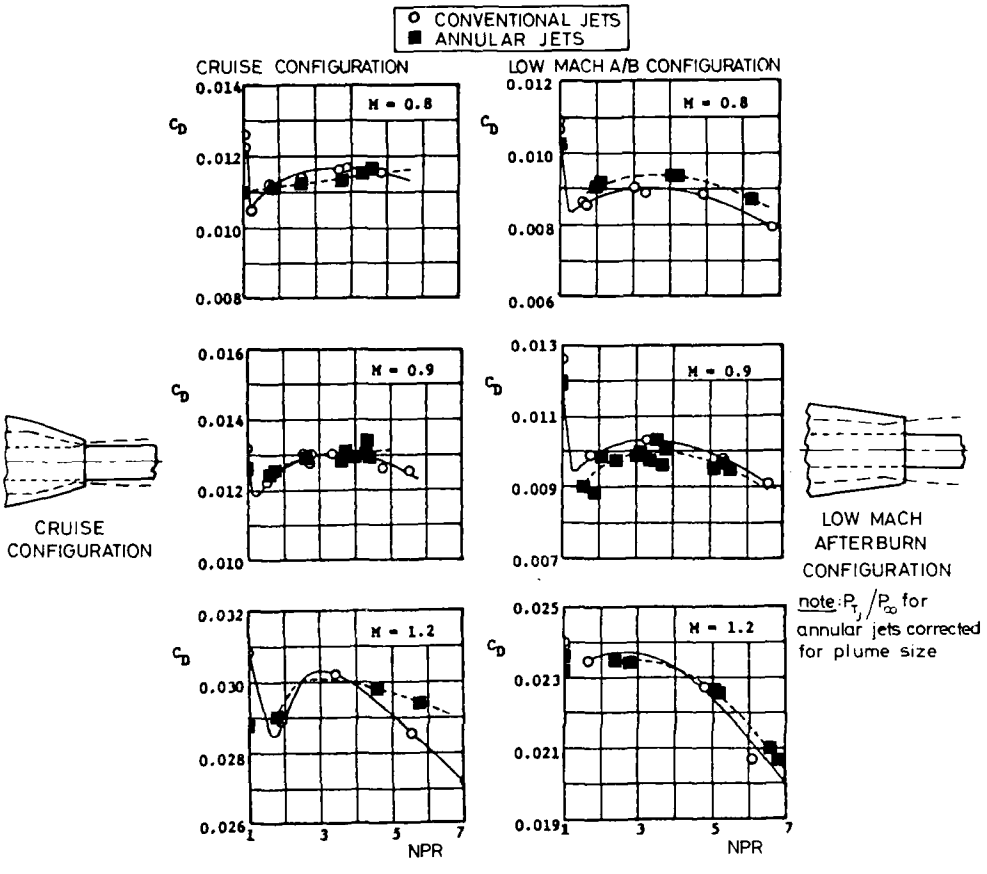

FIG. 3.2.49. COMPARISON OF AFTERBODY DRAG WITH CONVENTIONAL AND ANNULAR JETS FOR A TWIN-ENGINE FIGHTER MODEL WITH PLUME CORRELATION AND CORRECTION FOR STING EFFECTS. (REF. 3.2.34)

Reference to the design and concepts of the annular jet are given in Ref. 3.2.35 by Price where a parametric study was made of exhaust nozzle area ratio and sting-nozzle exit diameter ratio. The tests were made in the AEDC 16T at M = 0.6, 0.9 and 1.2 with a range of nozzle area expansion ratios from 1 to 1.5 and sting to nozzle diameter ratios of 0 to 0.95. It is of interest to note these experiments were made in the presence of a model support strut and of necessity it was assumed that this had no effect on the incremental findings of the study. Also, not unreasonably, the tests were *made with ambient temperature exhaust air.*

A typical example from the above work illustrates the effect of increasing sting diameter on the afterbody external pressure drag (Fig. 3.2.50). This effect is most strongly marked at fairly high levels of NPR at conditions where the nozzle is severely under - expanded. The effect is to significantly reduce the pressure recovery on the boattail giving an increase in pressure drag. Data *is also presented illustrating the effect of nozzle expansion ratio on afterbody drag for constant* sting ratios. This indicates how for large sting sizes the afterbody interference is predominantly due to the sting irrespective of the expansion ratio (Figs. 3.2.51a-d). In general it may be observed that the true (no sting) NPR effects are well-simulated, qualitatively, for sting diameters less than 0.7 x jet diameter.

It was noted that there were no significant effects of incidence in the range up to 6° on the plume simulation behaviour of the annular jet.

Analysis in Ref. 3.2.35 of schlieren photographs and pressure distributions along the sting within the plume has allowed correlation between the full diameter nozzle jet results and those obtained with an annular nozzle. Plume shapes calculated by the method of characteristics are illustrated in *Fig. 3.2.52 and indicate that for under-expanded jets of the same nozzle area ratio and NPR the*

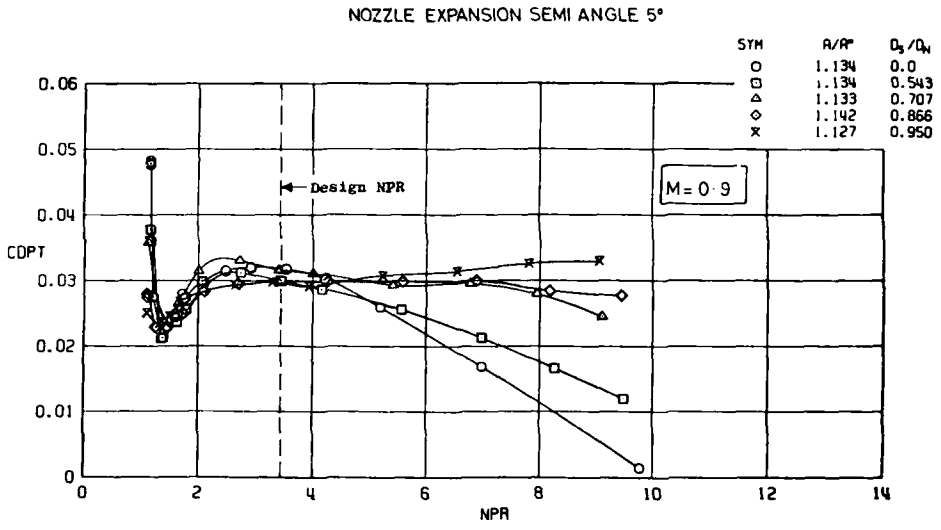

FIG.3.2.50. EFFECT OF ANNULUS SIZE ON THE AFTERBODY PRESSURE DRAG (REF. 3.2.35)

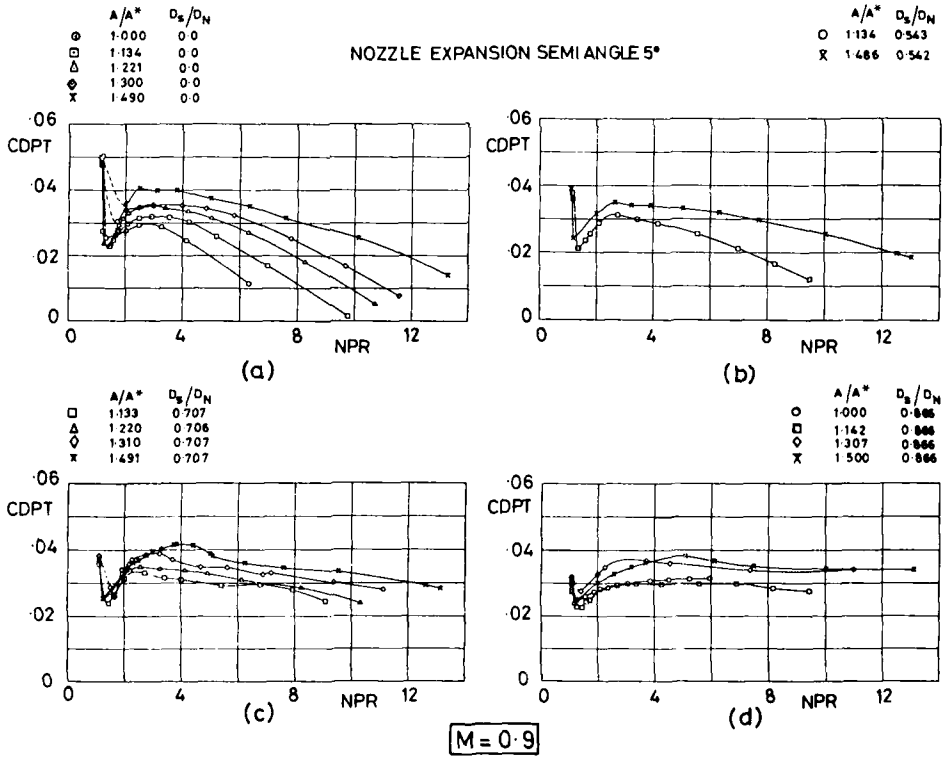

FIG.3.2.51. EFFECT OF STING SIZE ON AFTERBODY PRESSURE DRAG FOR A VARYING NOZZLE EXPANSION RATIO (REF. 3.2.35)

annular nozzles produce plumes of smaller maximum diameter and shorter cell wave length than do full nozzles. This is an expected feature as the compression and expansion waves of the jet propagate along characteristic lines until they reflect from a solid or a free boundary. Thus a movement of the solid sting boundary towards the free boundary (as the sting diameter ratio increases) will shorten the characteristic path lengths. Compression waves reduce the free boundary diameter whilst expansion waves increase it. For the annular jet the sting surface being close to the free boundary will cause wave -plume boundary interactions to occur over shorter axial distances giving a reduction of both initial plume length and diameter. The effect of sting diameter is illustrated in Fig. 3.2.53 and results indicate quantitative effects as in Fig. 3.2.54.

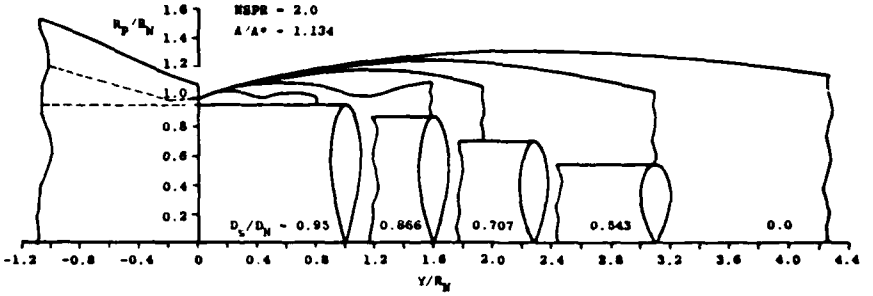

FIG. 3.2.52 VARIATION OF PLUME SHAPE WITH ANNULAR JET STING SIZE AS DETERMINED BY METHOD OF CHARACTERISTICS (REF. 3.2.35)

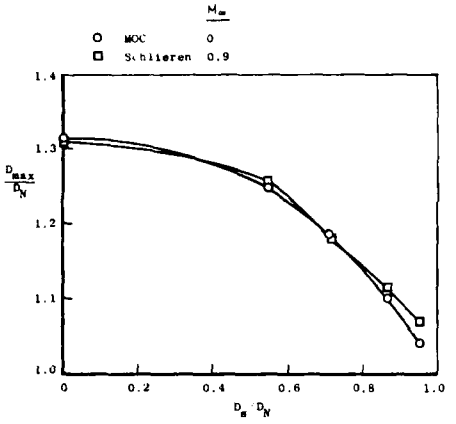

FIG. 3.2.53 VARIATION OF PLUME MAXIMUM DIAMETER WITH STING DIAMETER, NSPR≈2·0, A/A* 1·13. (REF. 3.2.35)

The results have been correlated to obtain 'simulation' pressure ratios for the annular jet which will give the same plume maximum diameter as that obtained without a sting. Calculated plume maximum diameters have been obtained by the method of characteristics and by a one-dimensional continuity relationship of the jet mass flow. NPR levels to give the same simulation maximum jet plume size tend to be the same irrespective of which calculation method is used for the predicted maximum plume diameter hence the one dimensional method (being simpler) is recommended. A typical derived curve from these results is shown in Fig. 3.2.54 which relates NPR for different sting diameter ratios for a given nozzle expansion ratio and Mach number. A corresponding correlating relationship is also illustrated in Fig. 3.2.55 for different nozzle expansion ratios at a fixed sting ratio and M. Thus from these correlating plots it may seem that plume diameter may be changed by either changing NPR for a given nozzle area ratio or by changing area ratio for a given NPR. Thus area ratio itself need not be matched (although the corresponding correct exhaust angle should be) as long as the combination of area ratio and NPR is such that the maximum plume diameter is matched.

These features of interchangeability of nozzle area ratio, sting diameter ratio and NPR, through the correct simulation of plume diameter, provide scope for economic test programmes where either it is more suitable to limit the hardware or the blowing pressure level. It should be noted however that sting/nozzle diameter ratios in excess of 0.7 can give rise to poor plume representation at transonic Mach numbers.

The results of this Reference 3.2.35 may be used to provide reasonable simulation conditions for annular jets for nozzle expansion ratios and Mach numbers where drag follows the normal trends of decreasing drag with increasing nozzle pressure ratio and plume diameter.

3.2.4.2. Practical Application of the Annular Jet

The design of a rear sting support system has various conflicting requirements:

(a) Model - sting clearance.
(b) Sting strength
(c) Sting mass flow

Item (a) can be controlled by careful layout of the sting and balance flexibilities in relation to the centre of pressure of load and its movement with test parameter (M, α etc). The deflection is also a function of

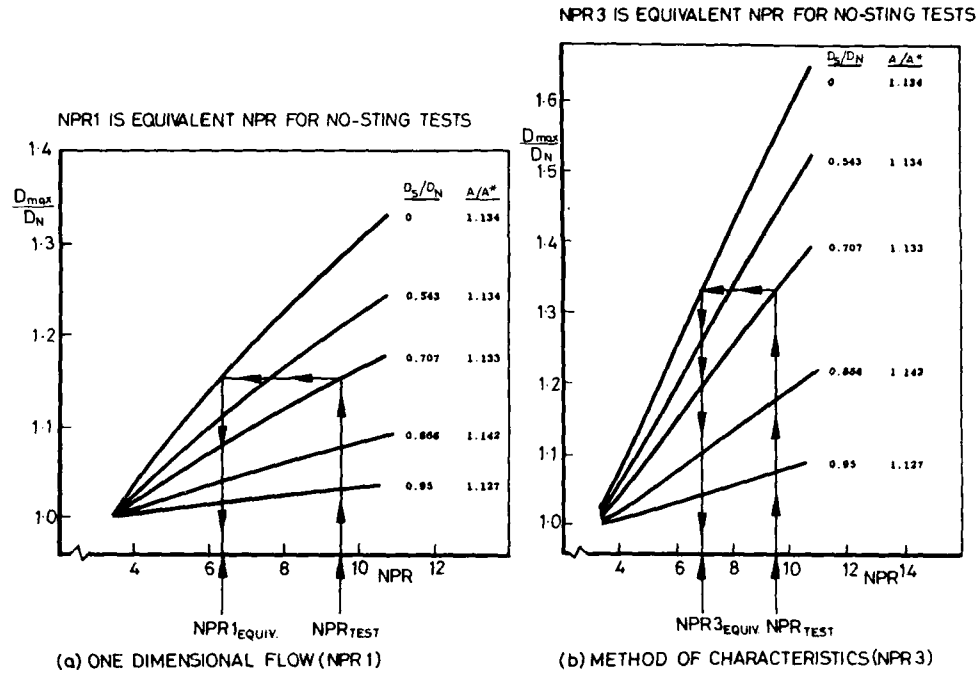

FIG. 3.2.54. ILLUSTRATION OF PROCEDURE FOR DETERMINING THE CORRELATION PRESSURE RATIOS (REF. 3.2.35)

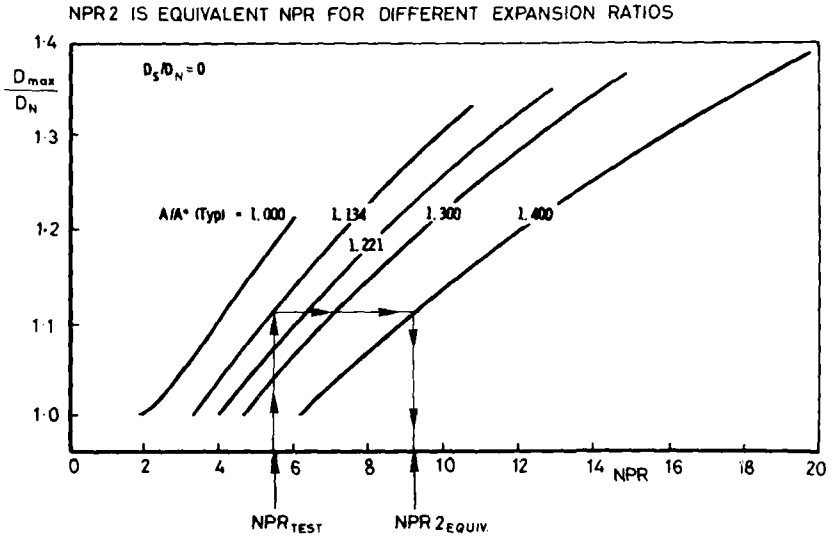

FIG. 3.2.55 ILLUSTRATION OF PROCEDURE FOR DETERMINING THE CORRELATION PRESSURE RATIO NPR 2 (REF. 3.2.35)

the magnitude of the loads which may be controlled in the same way as the sting stress is controlled. Item (b) is a function of the required clearance (a) and the hole size for mass flow (c) and of course the loads dictated by the model shape and areas etc.

The foregoing discussion has mainly pre-supposed that the annular jet occurs in the annulus between the sting and the model nozzle exit which is true for a pressure plotted afterbody model FIG. 3.2.56(a) For a force model however, where a sting support will provide the minimum datum interference condition, pressure forces in the internal nozzle of the model may not be permitted. A model/sting design of the type shown in Fig. 3.2.56(b) will be required where the sting to nozzle diameter is of necessity less than 0,7 to permit even a minimum range of model incidence within the clearance.

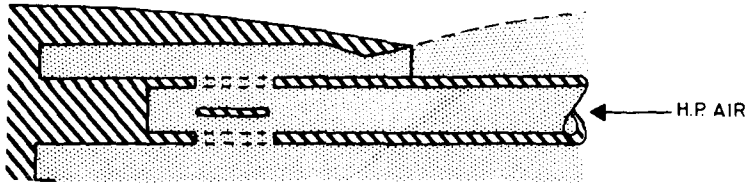

(a) AFTERBODY PRESSURE MEASUREMENTS

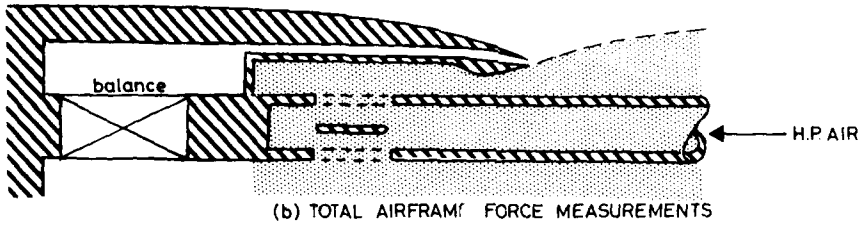

(b) TOTAL AIRFRAME FORCE MEASUREMENTS

FIG. 3.2.56. ARRANGEMENTS OF ANNULAR JET STING SUPPORT SYSTEM FOR COMPLETE OR PART MODELS.

3.2.4.3. Conclusions

The concept of the annular exhaust jet representation is a valuable one. It is shown that good representation of the solid body interference due to a jet can be provided by annulus ratios of d sting/d nozzle less than 0.7. Improved simulation is obtained by operating the annular jet at different NPR values from the no-sting NPR in order more closely to provide the correct initial plume cell diameter and length.

The annular jet may be used to provide the means of measuring a minimum support interference datum condition for use with more specialised or representative jet-effects models. Such reference datum tests will of necessity be limited to very restricted model attitudes. The use of the annular jet is of course restricted to simple nozzle shapes but can have application to twin nozzle geometries.

3.2.5 REFERENCES

3.2.1.	Pindzola, M	Jet simulation in ground test facilities AGARDOGRAPH 79. Nov. 1963.
3.2.2.	Compton, W.B.	An experimental study of jet exhaust simulation AGARD CP 150-16
3.2.3.	Hill, B.J.	Measurement of local entrainment rate in the initial regions of axisymmetric turbulent air jets. J.Fl. Mech. 1972. Vol.51 Part 4. 773-779.
3.2.4.	Robinson, C.E.	Exhaust plume thermodynamic effects on non-axisymmetric nozzle afterbody performance in transonic flow. AEDC TR-78-24
3.2.5.	Peters, W.L. and Kennedy, T.L	An evaluation of jet simulation parameters for nozzle/afterbody testing at transonic Mach numbers. AIAA. 77-106
3.2.6.	Robinson, C E., High and Thomson	Exhaust plume temperature effects on nozzle afterbody performance over the transonic Mach number range. AGARD CP 150-19.
3.2.7.	Kennedy, T.L.	An evaluation of wind tunnel test technique for aircraft nozzle afterbody testing at transonic M. AEDC TR 80-8
3.2.8.	Martens, R.F.	F15 Nozzle/Afterbody Integration J. Aircraft Vol. 13 No.5. May 1976
3.2.9.	Zacharias, A.	An experimental and theoretical investigation of the interaction between the engine jet and the surrounding flow field with regard to the pressure drag on afterbodies. AGARD CP 308-8
3.2.10.	Plant, T.J., et al.	Flight measured effects of boattail angle and Mach number on the nozzle afterbody flow of a twin-jet fighter. AIAA 18th Aerospace Sci. Meeting. Jan. 1980.
3.2.11.	Price, E.A. and Peters, W.L.	Test techniques for jet effects on fighter aircraft. AGARD CP-348-24
3.2.12.	Peters, W.L.	Experimental method for correcting nozzle afterbody drag for the effects of jet temperature. AEDC-TR-80-38.
3.2.13.	Bailey, R.O. Harper, M. and Jannetta,T.	Evaluation of turbo-propulsion simulators as a testing technique for fighter aircraft. AIAA Paper 79-1149.
3.2.14.	Bailey, R.O. Mraz, M. & Hiley, P.	The design of a wind tunnel VSTOL fighter model incorporating turbine powered engine simulators. AIAA 81-2635.
3.2.15.	Harper, M.	The propulsion simulator calibration laboratory at Ames Research Center. AIAA Paper 82-0574.
3.2.16.	Wagenknecht, C.D. Hoff, G.E., and Norbut, T.J.	Performance calibration results for a compact multimission aircraft propulsion simulator. AIAA-82-0254.
3.2.17.	Eigenmann, M.F., Devereaux, P.A. and Wagenknecht, C.D.	An improved propulsion system simulation technique for scaled wind tunnel model testing of advanced fighters. ICAS-82-4.8.3.
3.2.18.	Wagenknecht, C.D., Dusa, D.J. and Norbut, T.J.	Performance capability for a compact multimission aircraft propulsion simulator. AIAA-83-1358
3.2.19.	Bailey, R.O., Smith, S.C. and Gustie, J.B.	Propulsion simulation test technique for V/STOL configurations. SAE Technical Paper Series. 83-1427
3.2.20.	Smith, S.C.	Determining compressor inlet airflow in the compact multimission aircraft propulsion simulators in wind tunnel applications. AIAA-83-1231
3.2.21.	Cassmeyer, C.C.	Propulsion system simulation technique for scaled wind tunnel model testing. AIAA 83-7049
3.2.22.	Dusa, D.J., Wagenknecht, C D. and Norbut, T.J.	Development of a turbojet engine simulator for scale model wind tunnel testing of multi-mission aircraft. ISAE PARIS 83 399-407
3.2.23.	Harris, A.E. and Carter, E.C.	Wind tunnel test and analysis techniques using powered simulators for civil nacelle installation drag assessment. AGARD CP No.301-24.
3.2.24.	Becle, J.P. et Perin, R.	Essais en Soufflerie De Maquette Motorisees - Comparaison De Deux Methodes De Simulation Des Jets Des Reacteurs. AGARD CP No.301-23.

3.2 25.	Fromm, E.H.	The Boeing flight simulation chamber for static calibrations of engine simulations. Subsonic aerodynamic testing association May 1976.
3.2.26.	Smith, G.D et al	Analytical and experimental investigation of ejector powered simulators for wind tunnel models. AEDC-TR-76-128. Jan. 1977.
3.2.27.	Robinson, C.E. et al.	Evaluation of an ejector powered engine simulator at transonic Mach numbers. AEDC-TR-78-69. July 1979.
3.2.28.	Whitaker, R	Ejector design manual BAe. Report AXR 45.
3.2.29.	Wood, M.N.	The use of injector units for engine simulation on wind tunnel models at high speed. RAE TR 71215
3.2.30.	Wood, M.N. and Howard, J.B.W.	The development of injector units for jet-lift engine simulation on low speed tunnel models. RAE TR 65020.
3.2 31.	Whitaker, R.	Initial development of techniques for the use of ejector powered simulators in high speed combat aircraft models. B.Ae. Report AXR 98 and other unpublished data.
3.2.32.	Matz, R. and Smith, G.	Ejector powered engine simulators for small scale wind tunnel models of high performance aircraft. AEDC TR 78-826.
3 2.33.	Bowers, D.L.	Investigation of the annular sting support concept for afterbody nozzle testing. AIAA 77-961.
3.2.34.	Glidewell, R.J. and Fanning, A I.	Twin jet exhaust system test techniques. AGARD CP-150-15
3.2.35.	Price, E.A.	A parametric investigation of the annular jet concept. AEDC TR 77-104.
3.2.36.	Wilmoth, R G	Viscous-inviscid calculations of jet entrainment effects on the subsonic flow over nozzle afterbodies. NASA Tech Paper 1626.

AD-A172 341 REPORT OF THE WORKING GROUP ON AERODYNAMICS OF AIRCRAFT AFTERBODY(U) ADVISORY GROUP FOR AEROSPACE RESEARCH AND DEVELOPMENT NEUILLY-SUR-SEINE (FRANCE) JUN 86 4/4

UNCLASSIFIED AGARD-AR-226 F/G 20/4 NL

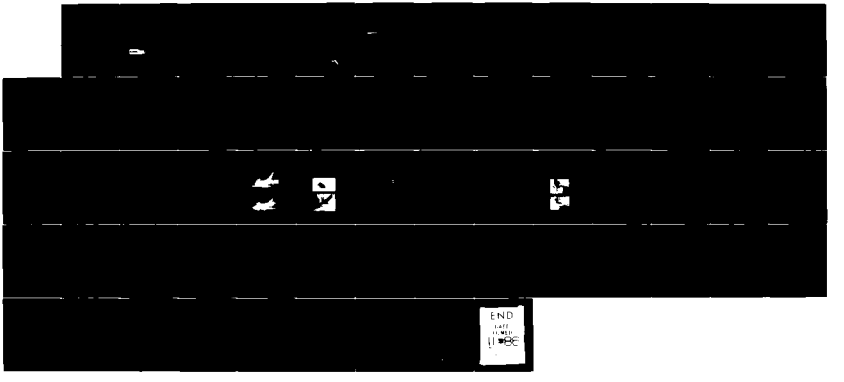

END
DATE FILMED
11-86
DTIC

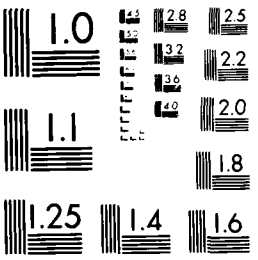

3.3 STATE-OF-THE-ART ASSESSMENT OF TESTING TECHNIQUES FOR AIRCRAFT AFTERBODIES

3.3.1 Introduction

Wind tunnel testing for aircraft afterbodies is at best a series of compromises. For either aircraft development or general technology tests, perfect models and test facilities are never available. Often, existing hardware such as force balances or model support systems are used as an economy measure. This factor alone often leads to compromises in testing techniques. In addition to the usual restrictions of limited funds and time, other major considerations can include: size of tunnel available, model size, model detail, model support type, if and how to determine model lift, drag, thrust and pitching moment, accuracy required, and simulation of exhaust flow and inlet flow. The test objectives, however, should be the overriding factor. What is to be measured should come before what can be measured.

Offered as an example of the difficulties of the issue of what can be and what should be measured are highly integrated nozzles as shown in Fig. 3.3.1. For some afterbody force measurements, test rigs can determine the afterbody drag separately from the thrust of the nozzle. This technique avoids the difficulty of determining the thrust to a similar degree of accuracy as drag. However, with more complicated nozzles, like the isentropic ramp and the blow-in-door ejector, the separation of thrust and drag becomes more and more impractical. For the isentropic ramp nozzle this separation becomes almost impossible because of the interaction of the flows over the thrust and drag producing surfaces. As indicated in Fig. 3.3.2, the external flow over the boattail interacts with the primary jet and secondary (cooling) flow. The primary nozzle with a fixed (small) divergence section will run off-design with related high thrust losses depending on the base pressure P_c. As shown, this pressure and the resulting nozzle thrust are functions of nozzle pressure ratio and secondary flow rate. Therefore, in addition to difficult force measurement, it is necessary to duplicate the three merging flows precisely in order to obtain wind tunnel results which are representative of the full scale flight case.

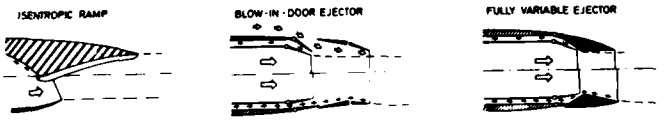

FIG. 3.3.1 HIGHLY INTEGRATED NOZZLES (REF. 3.3.41)

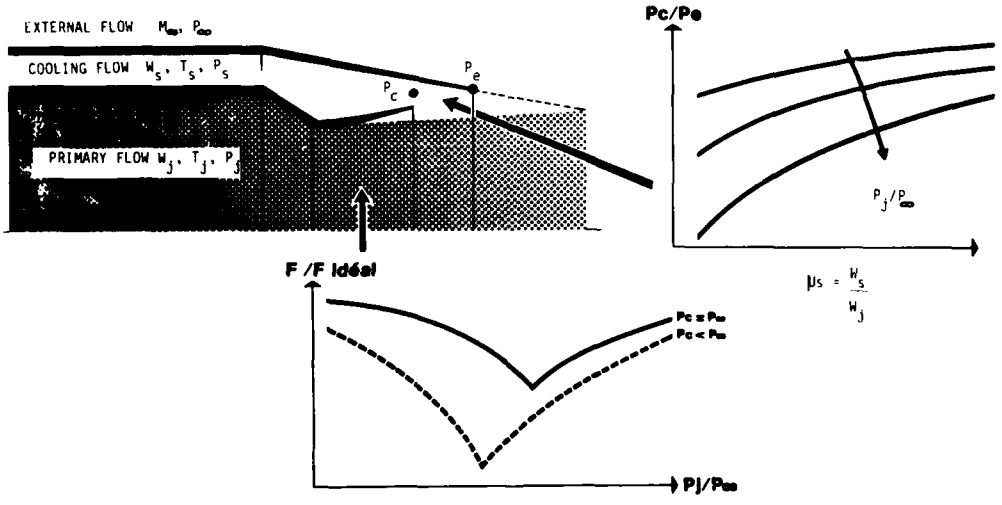

FIG. 3.3.2 INTERACTION OF PRIMARY, SECONDARY AND EXTERNAL FLOWS

The complexity and diversity of state-of-the-art afterbody testing techniques are illustrated in Fig. 1.4.5 and 3.3.3. Given the task of determining the surface pressures on a series of axisymmetric nozzle boattails, each participant in an AGARD study (Ref. 3.3.1) evaluated the available facility and test apparatus with respect to the test objectives and developed the diverse facility/model arrangements shown in the first figure. Struts, strut/stings, forward/aft sting supports, and perforated and slotted wall test sections with minimal to high blockage were used to obtain the test data. For full aircraft afterbody models, the support system consideration alone entails choices ranging from a nose mount to a half plane reflection, as shown in Fig. 3.3.3. These figures illustrate most but not all common aircraft afterbody test arrangements.

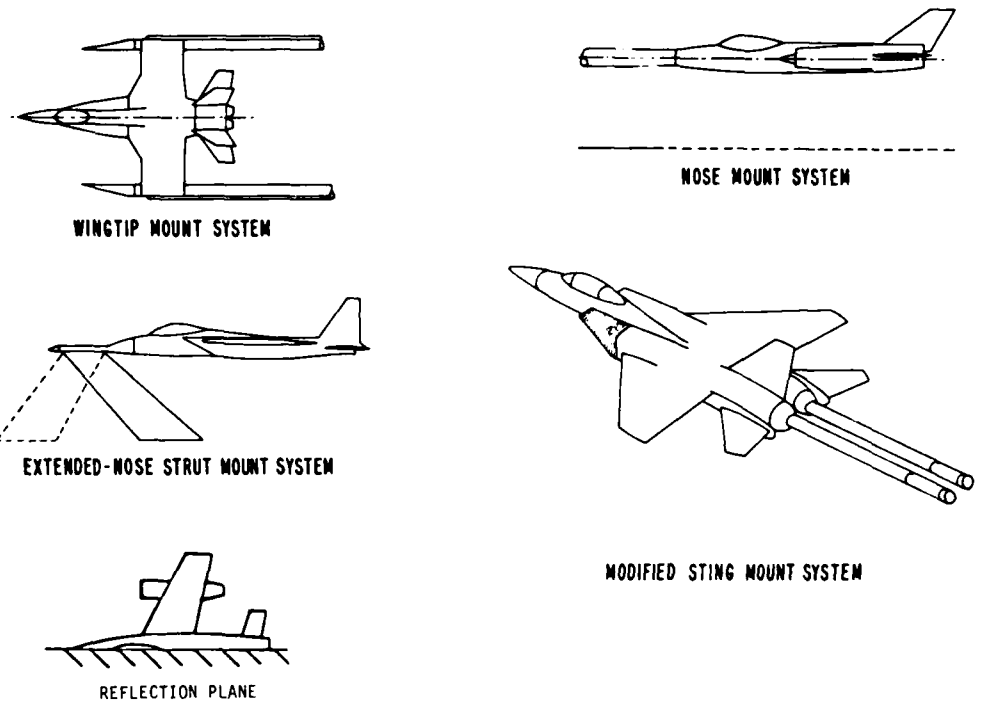

FIG. 3.3.3 JET EFFECTS MODEL SUPPORT SYSTEMS (REFS. 3.3.3,3.3.4)

This section will address and assess the state-of-the-art of testing techniques for aircraft afterbodies. Included will be force balance arrangements, the use of pressures to determine the afterbody pressure forces, model support considerations, a discussion of areas of uncertainty, information on testing techniques for advanced aircraft and a final summary and recommendations.

3.3.2 Force Balances

3.3.2.1 State-of-the-Art Metric Arrangements

The force balance techniques used for afterbody testing are as varied as the individual tests themselves. Fig. 3.3.4 shows six different model support configuratio·s which measure the afterbody forces with one or more force balances. The total metric model thrust-minus-drag arrangement (A) is considerably different from the three afterbody only thrust-minus drag configurations (B, C, D) and the afterbody drag balance models (E, F). Even if the installed afterbody/nozzle is the only emphasis of the model design, as in Fig. 3.3.5, the balance arrangement can vary from total thrust-minus-drag, to separate balances for thrust and drag, to a thrust-minus-drag balance with a separate shell drag balance, to a thrust-minus-drag balance with a calculated thrust value. There is no convention or standard for afterbody/nozzle force balance arrangements.

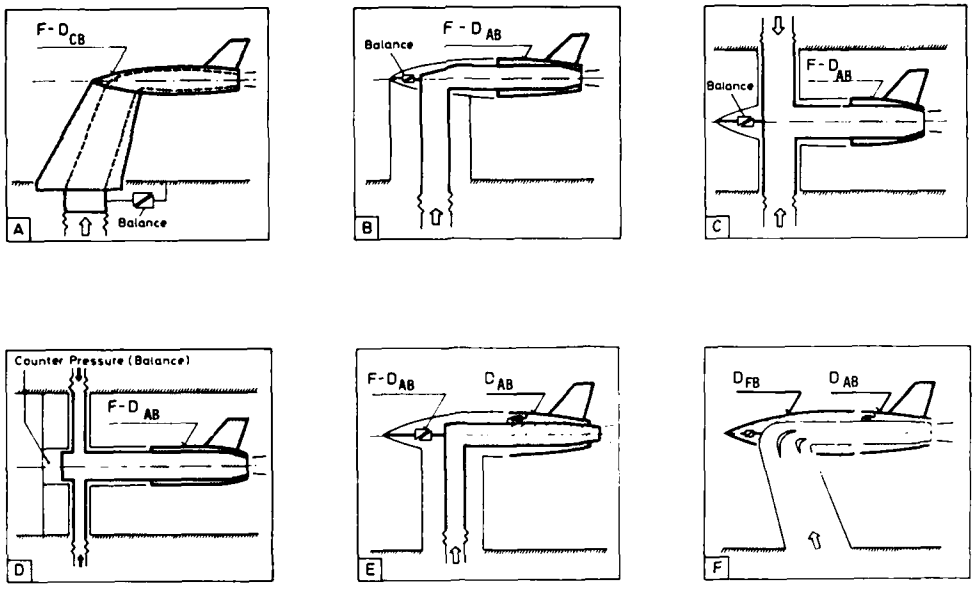

FIG. 3.3.4 AFTBODY DRAG TEST RIGS (REF. 3.3.5)

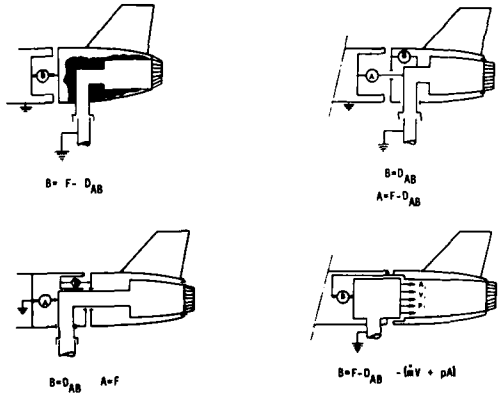

FIG. 3.3.5 WIND TUNNEL TESTING SCHEMES FOR INSTALLED AFTERBODY/NOZZLE PERFORMANCE (REF. 3.3.6)

Force balances should be carefully sized to provide the parametric visibility required to satisfy the test objectives. If the force balance, for example, is sized for full thrust loads, then it is probably oversized to get accurate aerodynamic loads. For the B-1 podded engine nacelle (shown in Fig. 3.3.11), if the aircraft had also been metric with the nacelle, then the desired afterbody increments would have been hidden in the data scatter.

Multiple force balances are often used to separately determine forces on different model sections. A typical force balance system which measures the external and internal aerodynamic forces consists of two balances: a main balance to determine lift and thrust-minus-drag of the afterbody and a thrust balance to measure nozzle normal and axial forces. While this arrangement allows determination of component forces, afterbody drag is now determined as a small difference of two large numbers. A generic pod with this balance arrangement is shown in Fig. 3.3.6 and a full aircraft model similarly fashioned is presented in Fig. 3.3.7. This aircraft model has an afterbody balance, a nozzle thrust-minus-drag balance and provisions for a forebody balance.

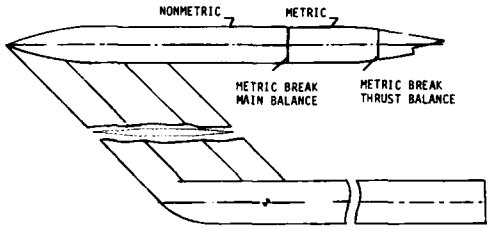

FIG. 3.3.6 GENERAL ARRANGEMENT OF TWIN BALANCE MODEL (REF. 3.3.7)

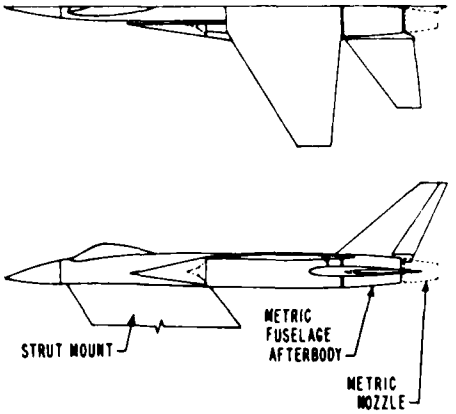

FIG. 3.3.7 LARGE SCALE AFTBODY/NOZZLE MODEL (REF. 3.3.4)

A recent trend which will receive much attention in the future due to the interactive nature of the propulsion system and the vehicle aerodynamics is fully metric models. These models can incorporate a nonmetric vertical tail as a portion of the support system (Fig. 3.3.8) or be fully metric with a horizontal metric break at the support strut. Further discussion of fully metric models will follow in Section 3.3.6, Testing Techniques for Advanced Aircraft with Highly Interactive Flow Fields.

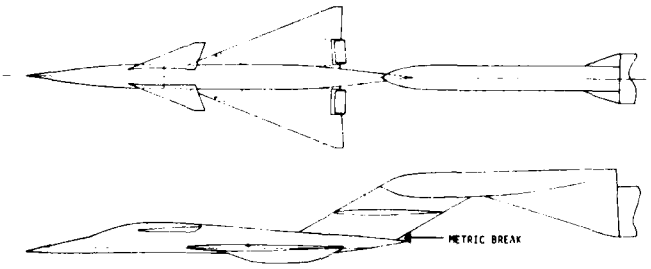

FIG. 3.3.8 GENERAL ARRANGEMENT OF MODEL AND SUPPORT SYSTEM (REF. 3.3.9)

Hybrid arrangements use force balances in combination with integration of surface pressures to avoid taking a difference of two large force balance values to get a relatively small drag number. A model of a supersonic point design aircraft, Fig. 3.3.9, was configured with an aircraft balance and a nozzle thrust-minus-drag balance. The metric external nozzle surfaces were instrumented with surface pressures to determine afterbody lift, drag, and pitching moment. An alternative to this arrangement, also shown in Fig. 3.3.9, is to make the nozzle thrust and boattail surfaces nonmetric and determine the nozzle external aerodynamic forces by a pressure area integration. This is another variation of the fully metric approach discussed in the previous paragraph.

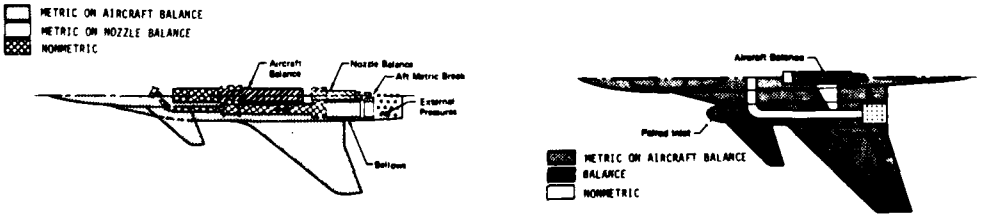

FIG. 3.3.9 HYBRID FORCE SYSTEM MODELS (REFS. 3.3.11, 3.3.12)

3.3.2.2 Inherent Problems

The force balances used in afterbody force measurement provide useful information for the areas they are metering. Force balances, however, are often complicated and their output requires corrections to provide data with acceptable levels of repeatibility and accuracy. These terms are a function of at least the bare balance calibration, pressure area tare forces, including cavity, metric seal, and base pressures; flow momentum tares; and combined loading interactions. For example, the force balance in Fig. 3.3.10 has a bellows system that must be calibrated as a function of pressure to determine the change in measured load with nozzle pressure ratio. Balance corrections should also account for nonrepresentative forces due to internal cavities and metric break gaps. The cavity tares are calculated using the difference in pressures inside the cavity and the freestream static pressure over the internal projected area. The metric break tares are from seal tension and from pressures on metric break surfaces. For the B-1 nacelle test arrangement in Fig. 3.3.11, with metric afterbody and nozzle, the supersonic corrections for cavity pressures, metric seal and minor corrections for labyrinth seal and base pressure resulted in a corrected axial force more than twice the balance measured load, Fig. 3.3.12. Subsonically, Fig. 3.3.13, with the cavity pressure correction and metric seal correction in opposite directions, the corrected axial force was just less than double the measured load.

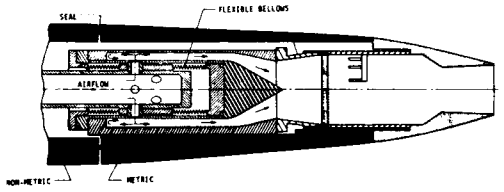

FIG. 3.3.10 INTERNAL FLOW THROUGH BALANCE ASSEMBLY (REF. 3.3.42)

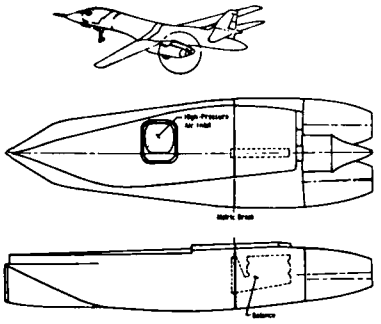

FIG. 3.3.11 FORCE BALANCE NACELLE CONFIGURATION (REF. 3.3.14)

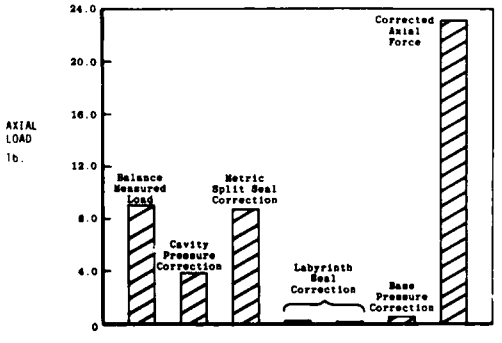

FIG. 3.3.12 BALANCE FORCES AND CORRECTIONS AT SUPERSONIC SPEEDS (REF. 3.3.14)

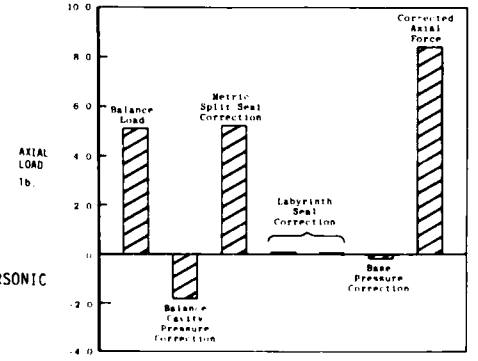

FIG. 3.3.13 BALANCE FORCES AND CORRECTIONS AT SUBSONIC SPEEDS (REF. 3.3.14)

Another concern with force balances is the aerodynamic effect of the small yet definite gap at the metric break. Since the model may flex under load, a forward or aft facing step may appear affecting the data. A change in pressure coefficient between a locked and taped metric gap and an open unlocked metric gap is shown in Fig. 3.3.14. Pressure coefficient changes as large as ±0.06 are evident in the data.

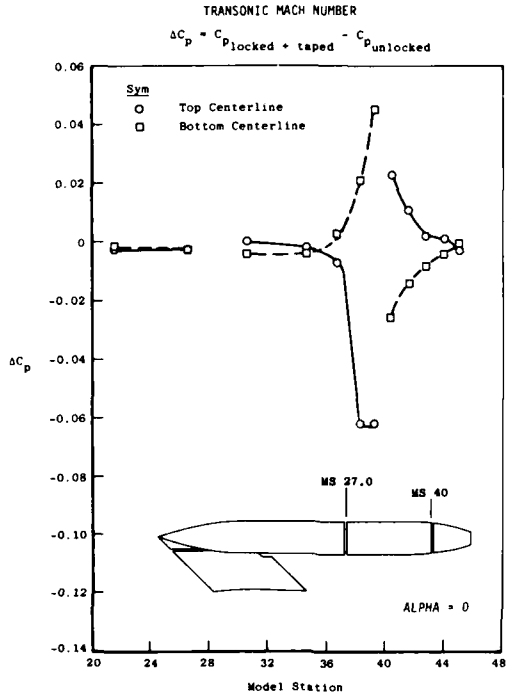

FIG. 3.3.14 EFFECT OF METRIC BREAK ON MODEL PRESSURE DISTRIBUTION (REF 3.3.14)

The model previously illustrated in Fig. 3.3.7, demonstrated the use of two force balances with two metric breaks. Such multiple balance arrangements can introduce complex model interactions and increased data uncertainty. For all model hardware, a complete error analysis prior to detailed model design or prior to utilization of existing hardware should be conducted to evaluate the predicted data uncertainty against the test objectives. A sensitivity analysis or partial error analysis of critical parameters may be acceptable in some instances.

3.3.2.3 Summary Comments - Force Balances

Force balances are powerful testing tools for determining afterbody nozzle forces and moments. Great care must be given to accounting for all tares and corrections, and to the measured levels of accuracy and repeatability versus the levels required to meet the test objectives.

Past experience should serve as a guide for new model balance arrangements and can point out potential error sources for existing model force balance hardware.

New hardware should be designed and built considering the test objectives, the test facility and the configuration itself.

3.3.3 Surface Pressures (Pressure Area Integration)

If surface static pressures are available, a pressure area integration can be an attractive alternative to the use of force balances to determine afterbody/nozzle forces. In addition, when comparing wind tunnel model and flight vehicle characteristics, the use of pressure coefficients and pressure integrated forces is considered a reliable technique. On an YF-17 model (Ref. 3.3.16), for example, one side of the wind tunnel model was instrumented with 60 static pressure orifices on the nozzle boattail, 128 on the nacelle, and 19 on the forebody. The flight vehicle had 39 fuselage pressure orifices and 32 nozzle orifices located as close to the wind tunnel positions as possible. This distribution of pressures allowed good wind tunnel-to-flight comparisons of the local flow phenomena and forces.

On the B-1 nacelle aftend, over 200 pressures on both the wind tunnel model and flight vehicle (Fig. 3.3.15), were utilized for not only a wind tunnel to flight comparison but also a force balance to pressure area integration comparison on the wind tunnel model. As shown in Fig. 3.3.16, the pressure area integrated subsonic drag plus estimated skin friction drag compares well with the force balance value and at supersonic speeds follows the same trend. The difference in supersonic drag values was attributed to an inaccurate metric seal correction due to widely varying seal pressures around the nacelle. Note that while both wing sweep and nozzle setting are varying across the Mach number range, comparisons of forces from balances and pressure area integration are conducted on equivalent configurations.

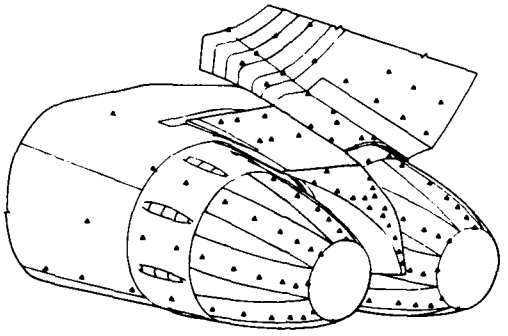

FIG. 3.3.15 B-1 AFT NACELLE SURFACE PRESSURE INSTRUMENTATION (REF. 3.3.30)

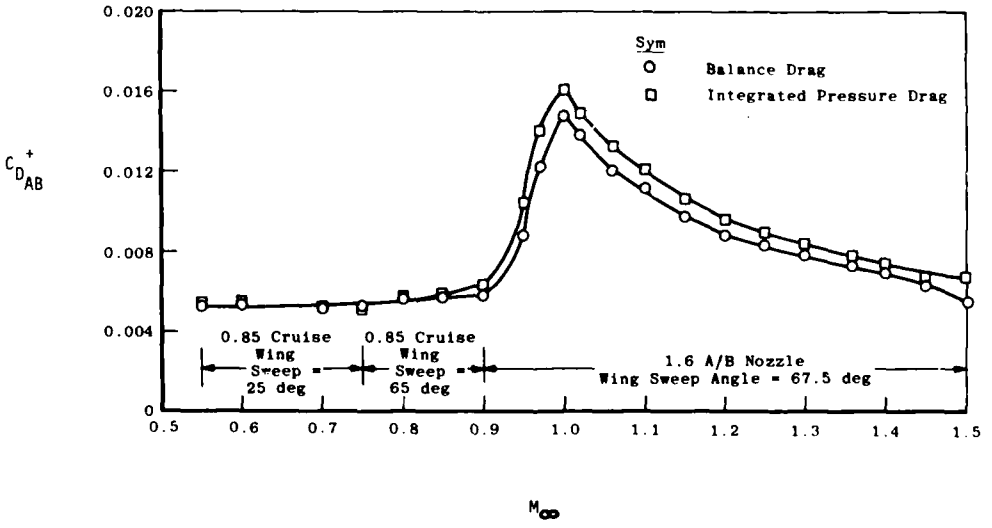

FIG. 3.3.16 COMPARISON OF DRAG COEFFICIENT MEASUREMENT TECHNIQUES (REF. 3.3.14)

3.3.3.1 Inherent Problems

Kennedy (Ref. 3.3.14) points out that the largest potential problem with determining forces with a pressure area integration is not having adequate coverage in critical areas. Complex configurations or truly three-dimensional shapes which have severe pressure gradients are difficult to measure with this technique. For the reasonably clean YF-17 afterbody, Lucas (Ref. 3.3.16) compared a 70 orifice pressure area integration with a 200 orifice pressure area integration. For this comparison the axial force differences were within the data repeatability of 3 axial force counts (±0.0003), Fig. 3.3.17. Analytical techniques should be used to determine orifice placement.

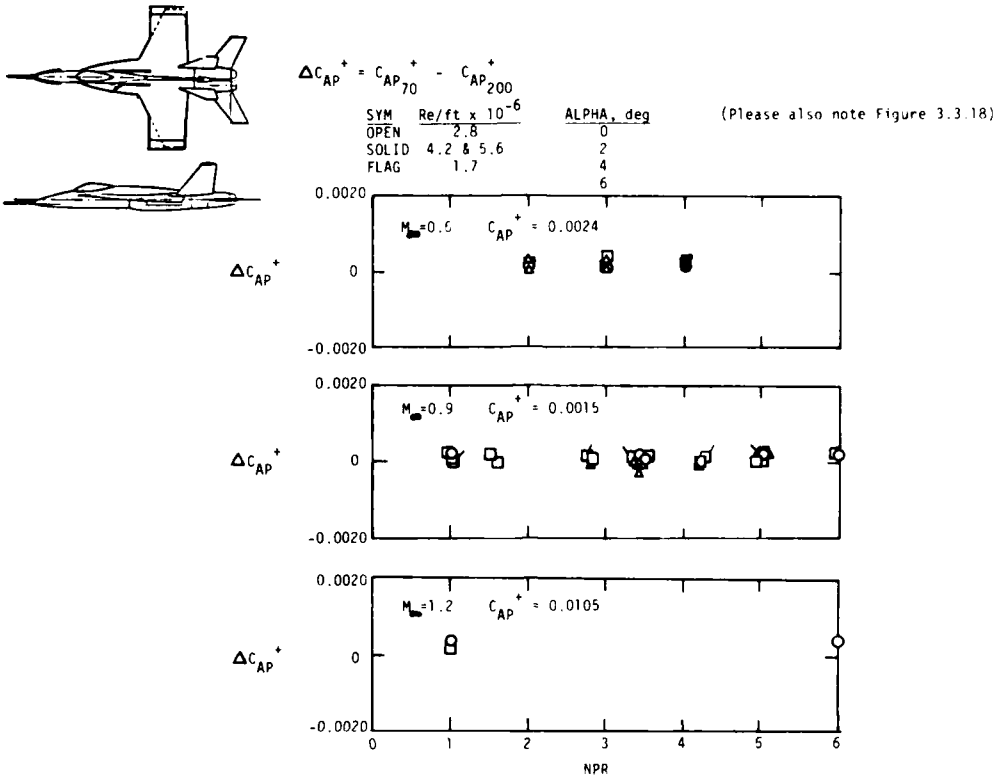

FIG. 3.3.17 EFFECT OF LIMITED ORIFICE INTEGRATION ON CRUISE NOZZLE (REF. 3.3.16)

If a pressure area integration is to replace a force balance arrangement for a complex afterbody configuration or full vehicle, a large number of pressure orifices are required. As many as 700 pressures have been specified in past efforts. This requirement can result in mechanical as well as financial problems. Pressure tube routing for multiple tubes will complicate model volume design and model configuration changes. This and the additional high cost can be prohibitive factors when using this technique in many research efforts.

While a force balance measures all forces on the metric portion of the model, a pressure area integration can only determine the pressure effect and a calculated skin friction drag term must be added. This term can be a large contributor to the subsonic afterbody drag (Ref. 3.3.3). The state-of-the-art calculated skin friction drag is generally believed accurate if there are no separated areas or if the separation location is well defined (Ref. 3.3.17).

Two final considerations for the pressure area integration technique are orifice size and imperfections. For most conventional facilities, orifice size is determined by lag times for pressures to stabilize relative to the cost of wind tunnel operation. Larger orifices and tubes reduce lag times and thereby reduce testing time. In high Reynolds number facilities, however, the model boundary layer is small relative to nominal orifice diameters or local imperfections due to the pressure orifice installation. As discussed by Kilgore in Ref. 3.3.18, when the boundary layer thickness is very small compared with the orifice diameter, the streamline curvature can change near the orifice with eddies set up in the orifice resulting in a measured static pressure significantly higher than the actual value. Experimental data also indicates that orifice imperfections such as burrs can produce flow separation leading to incorrect measured pressure values. Additional imperfections include out-of-round orifices, particles in the orifice, and orifices not flush to the model surface. This type of bias error needs to be considered if testing is at high Reynolds number and accuracy is desired to within two (C_D = ± 0.0002) drag counts.

3.3.3.2 Summary Comments - Pressure Area Integration

Pressure area integration is a viable alternative to the use of a force balance to determine total afterbody forces if the pressures are adequately distributed over critical areas and skin friction drag is accurately calculated.

Difficulties may arise for several reasons: complex configurations with sharp local cross-sectional area changes and the resulting large pressure gradients may be difficult to adequately cover with pressure orifices, the model fabrication cost may be excessive if large numbers of orifices are required, and orifice size limits or imperfections may limit data accuracy if testing is done in a high Reynolds number wind tunnel facility.

3.3.3.3 Force Balance versus Pressure Area Integration

The forces on most aircraft/afterbody configurations can be determined using either a force balance or a pressure area integration. As shown in Fig. 3.3.16 and 3.3.18, the subsonic B-1 nacelle axial force can be accurately predicted with either method after the balance corrections and estimated skin friction are accounted for.

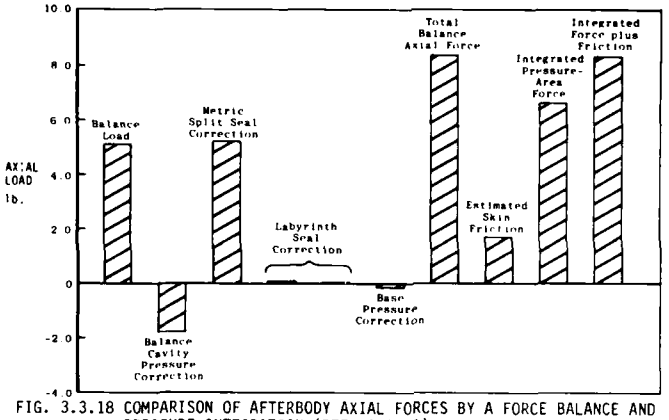

FIG. 3.3.18 COMPARISON OF AFTERBODY AXIAL FORCES BY A FORCE BALANCE AND PRESSURE INTEGRATION (REF. 3.3.31)

Similar results were seen in an Aeritalia study (Ref. 3.3.29) for a single engine fighter aircraft model. Forces from limited pressure orifices and a six component balance showed the same trends. The conclusions of that study were that the number and distribution of pressure orifices have to be carefully addressed and that a good comparison of force balance and integrated values was possible due to limited test conditions and a simple geometry.

The choice of pressure area integration versus force balance depends on many factors. Besides satisfying test objectives, factors such as cost, complexity, time for model changes versus available test time, model scale, and model support must be considered. The configuration and forces to be determined may eliminate pressure area integration if internal nozzle forces must be included or a strong internal/external flow interaction is present. In some cases, the proper pressure instrumentation may give more accurate information on the change in drag or the source of afterbody/nozzle forces. The choice of pressure area integration or force balance must be made early in the planning process, based on engineering consideration of the many factors involved.

3.3.4 Wind Tunnel Model Support

Support structure in some form must be used for afterbody nozzle testing due to high pressure air supply requirement. Support hardware varies from facility to facility and model to model. Previous figures (3.3.3-8) have shown the diversity of support techniques. Even for the same afterbody in the same facility, the support system can vary from a wing tip support to a strut to a blown sting, Fig. 3.3.19. The support is required to have strength and rigidity to withstand the aerodynamic loads plus a margin of safety, provide space for instrumentation and high pressure air lines, and yet be small enough to produce acceptable flow interference (one of the most cited reasons that wind tunnel and flight data do not agree). These three support systems mentioned are the most prevalent types in use and the discussion of the state-of-the-art will center on these alternatives.

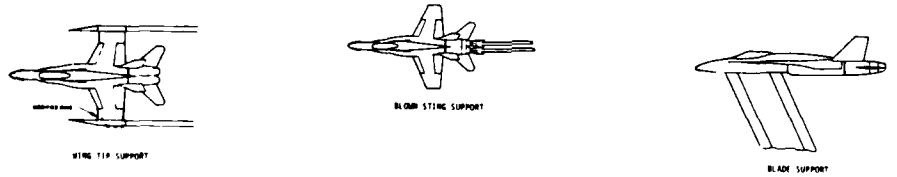

FIG. 3.3.19 YF-17 WIND TUNNEL MODEL SUPPORT SYSTEMS (REF. 3.3.3)

3.3.4.1 Sting Support - Unblown/Blown

The sting support system has long been used for afterbody testing, promising minimal aerodynamic interference compared to other systems. The support is sized by the strength requirements based on model weight, dynamics, expected aerodynamic loads, and test conditions. The sting support offers the advantage that all blockage contributions are downstream of the model and the support minimizes the aerodynamic interference on the model. It may however, have limited capability in a highly dynamic force environment and at angle-of-attack, and may not be applicable for advanced nozzles which are not axisymmetric. The promise of minimum interference has kept this technique in development.

If the sting support satisfies structural requirements, then the remaining consideration is how well the free exhaust plume is simulated. This was discussed in some detail in Section 3.2, Progress in Jet Simulation. A free jet affects the nozzle afterbody forces through entrainment and blockage. If the sting is solid with no flowing jet, only the blockage is simulated. Previous efforts have contoured the support sting near the nozzle to approximate the local plume contours. These are acceptable generally at only one nozzle pressure ratio. An effort by Porrato, Ref. 3.3.24, investigated the impact on nozzle boattail pressures of a solid sting support through the nozzle relative to jet-off and jet-on test conditions. A transonic test was conducted with a single engine fighter aircraft instrumented with a six component balance and sixty one pressure orifices. The boattail pressures with the dummy sting versus a free jet-off condition showed much more pressure recovery, and therefore, lower drag on the boattail. The lift and pitching moment did not change. The jet-on comparison was similar except that the effect was not as pronounced. The dummy sting boattail drag was approximately twenty percent lower than the jet-on afterbody drag value. Some jet simulation is required with a sting support to reproduce flowing jet aerodynamics.

The annular or blown sting support system maintains the interference free features of the sting support and produces a conduit for high pressure air to the model for the flowing jet. This technique has been developed primarily at Arnold Engineering Development Center for large scale aircraft models. Price, Ref. 3.3.25, discusses development of the annular sting for an F-16 configuration. The model arrangement for determining sting interference is shown in Fig. 3.3.20. The difference in axial force between a full jet plume and an annular jet plume was five axial force counts with an average of 2-3 counts across the Mach number range.

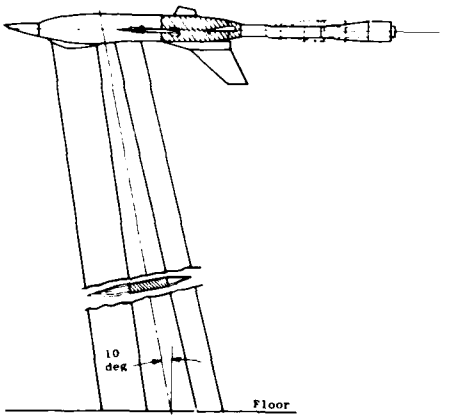

FIG. 3.3.20 STING SUPPORT PARAMETRICS MODEL (REF. 3.3.25)

Price and other researchers have completed sufficient parametric support studies to establish guidelines for the design of the geometric features of these systems. For example, in a complementary research effort to establish the impact of sting taper on boattail pressures (Fig. 3.3.21), the results indicated that the sting flare should be at least 3 body diameters downstream of the nozzle base with a 10 degree boattail and 5 body diameters downstream of a cylindrical boattail to minimize base pressure interference, Ref. 3.3.28.

3.3.4.2 Summary Comments

Empirical data exists and should be used during model design to determine the effectiveness of a blown sting to simulate the flowing jet (Section 3.2) and to provide minimum support interference.

This testing technique should be given strong consideration wherever test objectives, test facility or test hardware allows its use.

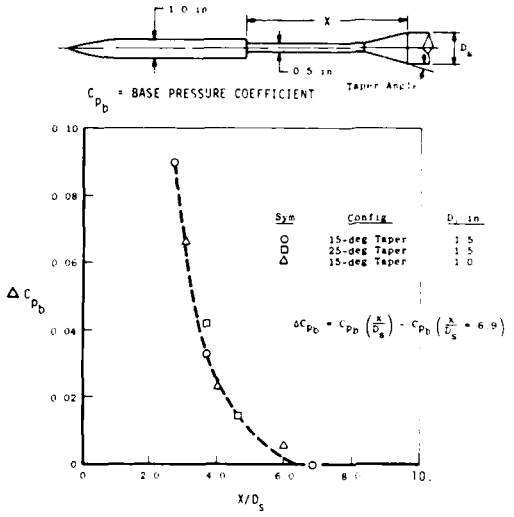

FIG. 3.3.21 EFFECT OF STING LOCATION ON MODEL BASE PRESSURES, M= 0.9 (REF. 3.3.14)

3.3.4.3 Wingtip Support

While first introduced in the early 1950's, the wingtip support has recently been used as an afterbody testing technique in the European technical community, NASA Langley, and Arnold Engineering Development Center. The YF-17 and F-16 plus other aircraft have been tested with this support system (Refs. 3.3.14, 25, 27, 28, and 29). A typical installation is shown in Fig. 3.3.22. Note that the wing must be modified outboard for structural strength. Questions remain relative to the impact of wing planform changes on normal force at high angles-of-attack and on wing downwash at transonic Mach numbers.

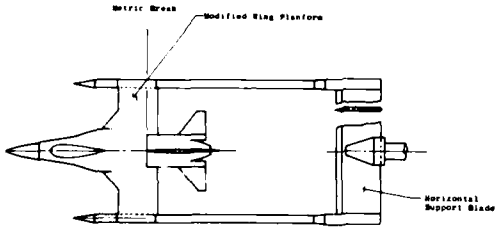

FIG. 3.3.22 WINGTIP SUPPORT INSTALLATION (REF. 3.3.25)

Interference for this system is determined by comparing axial forces with an "interference free" sting support and dummy wingtip support hardware to data with the model supported by a sting only. Representative interference numbers for axial and normal force relative to the sting supported model are shown in Fig. 3.3.23. Significant problems are evident between 0.8 and 1.1 Mach number, both in axial and normal force. It should be noted that unpublished data does indicate successful use of this technique up to 0.92 Mach number with specially designed transonic wingtip bodies. Aulehla in Ref. 3.3.41 presents a computational approach to determining wingtip support interference. Based on a simplified panel computation, the distance from the yoke to the model trailing edge was increased resulting in the selected support configuration for a supersonic Tornado aftbody test. In isolating the interference, parametric hardware has been tested with variations of the boom tips, and span, shape, chord, and location of the downstream blade. Some of these variations are shown in Fig. 3.3.24. Price (Ref. 3.3.28) presents design parameters to guide use of this technique. For example, boom tips should be shaped such that supersonically, neither the shock nor expansion from the tips intersects the portion of the model of interest. Other design guidelines are available in this reference for the effect of altering the wing tip support spacing as well as the geometry and location of the aft support blade.

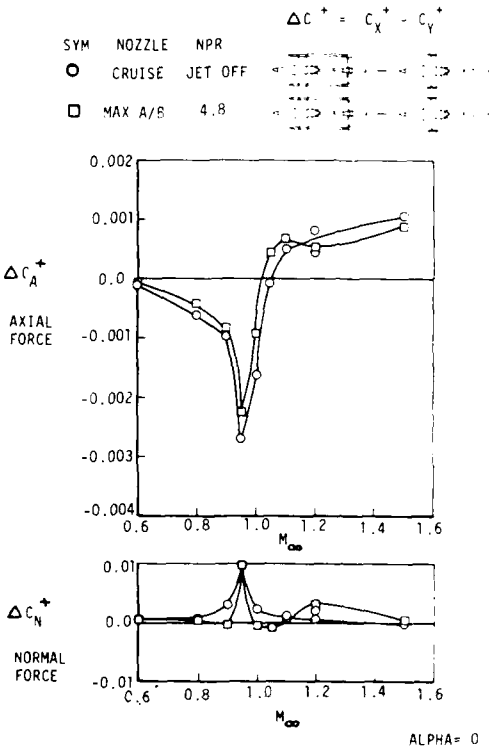

FIG. 3.3.23 EFFECT OF WINGTIP SUPPORT SYSTEM ON AFTERBODY FORCE COEFFICIENTS, F-16 (REF. 3.3.14)

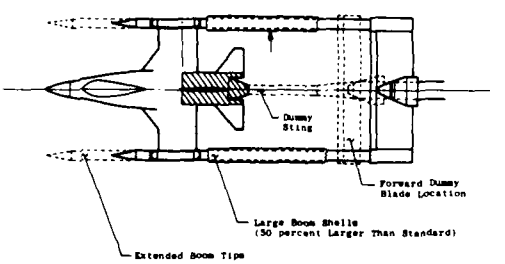

FIG. 3.3.24 WINGTIP SUPPORT PARAMETRICS (REF. 3.3.25)

3.3.4.4 Summary Comments

The wingtip support is a viable alternative especially for incremental afterbody/nozzle testing, avoiding the 0.8 to 1.1 Mach number range. This technique permits only the afterbody to be metric and the wing planform geometry is distorted.

Confidence in this technique is enhanced by the design guidelines for geometric parametrics which enable design and fabrication of a minimum interference support system.

3.3.4.5 Strut Support

While much maligned in some quarters as a high interference system, the strut support continues to be used for many tests. The diversity of application was shown in Fig. 3.3.3 and in other illustrations with this text. This technique can meet most of the criteria for a support arrangement, that is, strength and rigidity and duct space for instrumentation and high pressure air, but often can contribute to unacceptable tunnel blockage and model flowfield interference, presents some difficulties at high angles-of-attack and should not be used for yaw testing. Kennedy (Ref. 3.3.14) states that in many cases the strut blockage is the same or larger than the model blockage and that the flow interference can be large, especially near the model. The extent of this strut interference has been determined for full aircraft models. For an F-16 model (Ref. 3.3.25), the interference in axial force is large between 0.95 and 1.2 Mach number (Fig. 3.3.25) and generally less than 0.01 in normal force coefficient across the Mach number range (Fig. 3.3.26). Glidewell (Ref. 3.3.22) indicates that for a twin engine fighter configuration, a strut could be properly designed to produce small interference subsonically and supersonically. Transonically, however, the strut interference could be 20 axial force counts (0.0020) or 40 percent of the subsonic afterbody drag value. Wind tunnel tests with the B-1 aircraft (Refs. 3.3.15 and 3.3.30) determined the strut effect in the afterbody nacelle region to be 2.8 drag counts at 0.85 Mach number and 6 drag counts at 1.2 Mach number. The model was tested inverted, that is, strut on the top of the model, to reduce this interference.

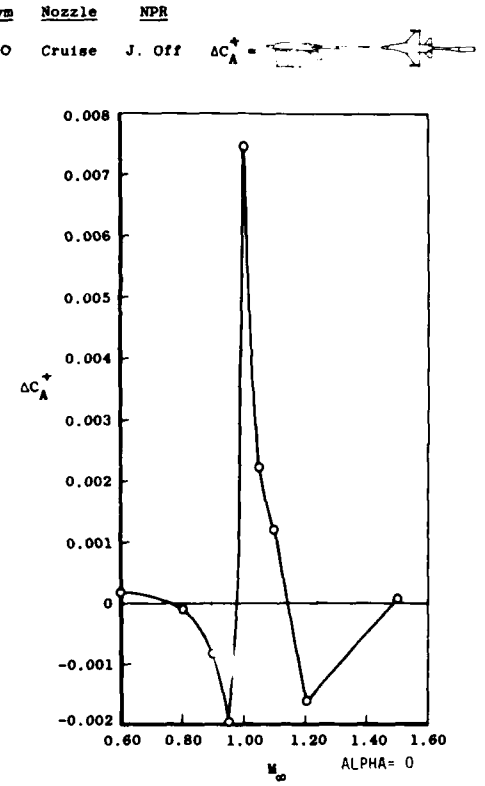

FIG. 3.3.25 EFFECT OF STRUT INTERFERENCE ON AFTERBODY AXIAL FORCE COEFFICIENTS (REF. 3.3.14)

Parametric studies to reduce or isolate strut interference have been conducted by German (Ref. 3.3.26). Typical variables investigated are shown in Fig. 3.3.27. From this data, emphasizing afterbody/nozzle test arrangements, German concluded that the interference above 0.99 Mach number is from disturbances originating at the strut leading edge which are reflected from the tunnel wall to the afterbody. The interference can be minimized by a swept strut at an optimum location and sweep angle. Of more importance, this reference is a source of design guidelines which can be used to minimize interference of new strut hardware or to predict the interference of existing hardware.

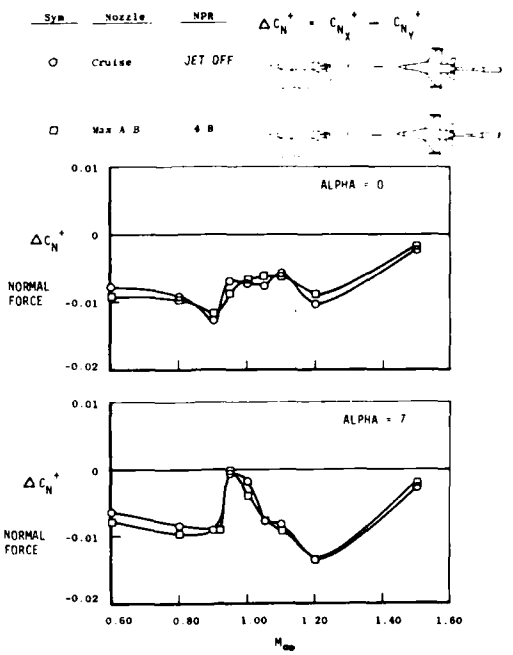

FIG. 3.3.26 STRUT INTERFERENCE ON NOZZLE/ AFTERBODY NORMAL FORCE (REF. 3.3.25)

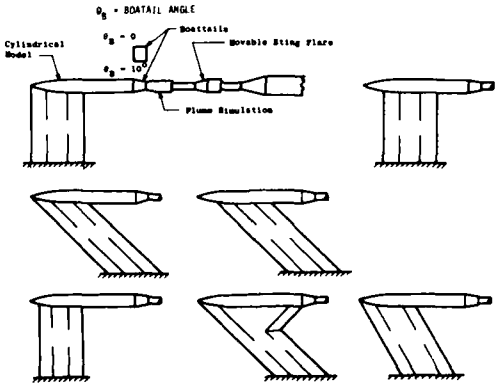

FIG. 3.3.27 STRUT SUPPORT PARAMETRICS (REF. 3.3.26)

3.3.4.6 Summary Comments

Despite all of the problems identified with a strut support, this arrangement may be the "best" to satisfy particular test objectives and will continue to be used. For example, test programs seeking total aircraft forces may require this technique.

Great care is required from at least 0.95 to 1.2 Mach number to minimize strut interference. Maximum utilization of empirical design guidelines, past experience, and computational tools should be considered when use of new or existing strut arrangements are proposed.

3.3.4.7 Summary Comments - Wind Tunnel Model Support

The predominant wind tunnel model support systems are the annular sting, wingtip support, and strut support. Each has advantages and disadvantages relative to particular test objectives. After the strength, rigidity and ducting requirements have been satisfied, the interference must be evaluated. Support interference for these three systems on the F-16 is summarized in Fig. 3.3.28. Note that for this configuration, the annular sting shows the smallest change in axial force due to the presence of the support, followed by the strut, which has particularly high interference between 0.95 and 1.2 Mach number and then the wingtip support. It should be emphasized that the support system is determined as a minimum by the test objectives, available test hardware, and test facility. Empirical guidelines and computational methods are available to indicate the problem areas associated with a particular support system.

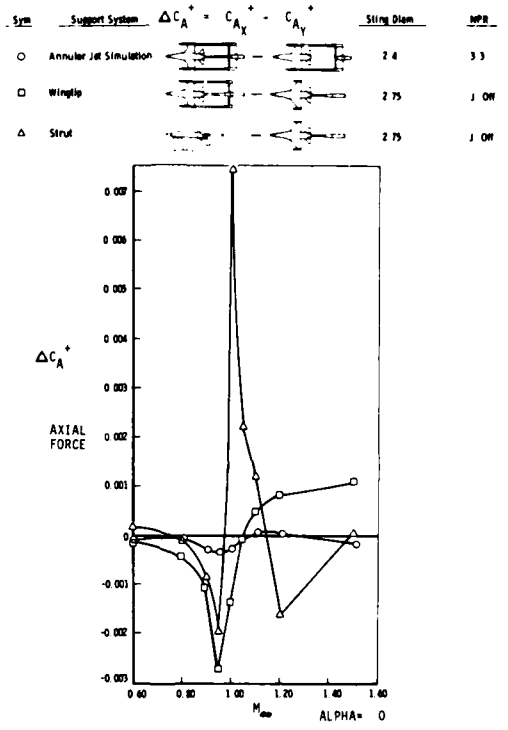

FIG. 3.3.28 COMPARISON OF INTERFERENCE ON NOZZLE/AFTERBODY AXIAL FORCE FROM STING, WINGTIP, AND STRUT SUPPORT SYSTEMS, CRUISE NOZZLES (REF. 3.3.25)

3.3.5 Areas of Uncertainty

As in any area where engineering judgement is involved, the choice of a particular test arrangement is often more art than science, with all options compromised in some fashion. Topics which are currently uncertain in this discipline include the choice of full versus partial model simulation, full versus partial metric models, and the extent of model fidelity required for proper determination of forces. This section will discuss the issues surrounding these topics and offer general guidelines.

3.3.5.1 Full versus Part Model (Simulation and Metric Arrangement)

The question of how much of the test configuration should be simulated or metric is unresolved. Jaarsma, Ref. 3.3.6, presents a good review of the advantages and disadvantages of testing partial and complete models. The advantages of partial models are: larger scale, perhaps a scaled boundary layer, better accuracy due to a smaller area on the force balance, more instrumentation, more detailing, better data for basic investigations, parametric test possible at less cost, and the data can be used to develop and verify theory. The primary disadvantage is that the cylindrical forebody typically used is to some degree an unrealistic simulation and the airframe installation effects are missed. For a complete aircraft representation, the advantages are: better external flow simulation and duplication of nozzle environment, better accounting of mutual interferences and the forebody influence, more accurate simulation of aircraft aerodynamics and plume interference. Disadvantages

are: smaller model for a given facility, limited instrumentation allowed in smaller volume and difficult simulation of secondary and tertiary air. While some basic testing still utilizes a generic pod type body, most large scale tests have full model representations.

Usually the forebody and afterbody are treated as separate areas, with the afterbody changes assumed to be affecting that region only. Data with the same forebody and changing afterbodies shown in Fig. 3.3.29. The change in forebody drag from afterbodies 2-5 to afterbody 1 is probably only significant for afterbody 5 with the steepest boattail. Note that the body is somewhat short coupled and a higher fineness body may not show an interaction. Additional data is presented for the model shown in Fig. 3.3.30 which was tested with three boattail configurations across the Mach number range. The resulting afterbody drag difference for the three boattail configurations is significant (Fig 3.3.31), but the forebody drag difference (Fig. 3.3.32) is not (on the order of 0.002).

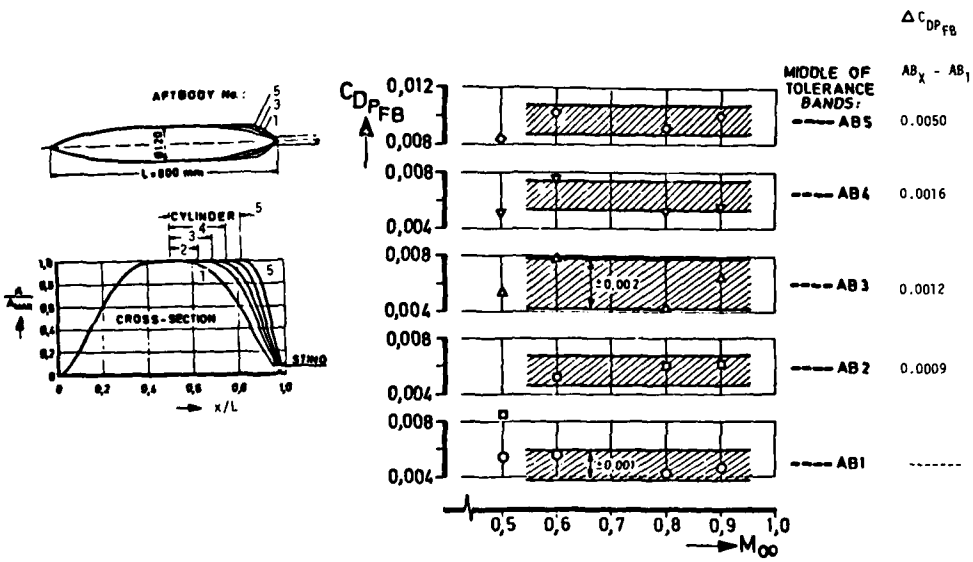

FIG. 3.3.29 FOREBODY PRESSURE DRAG CHANGE WITH AFTERBODY CONTOUR (REFS. 3.3.33,3.3.41)

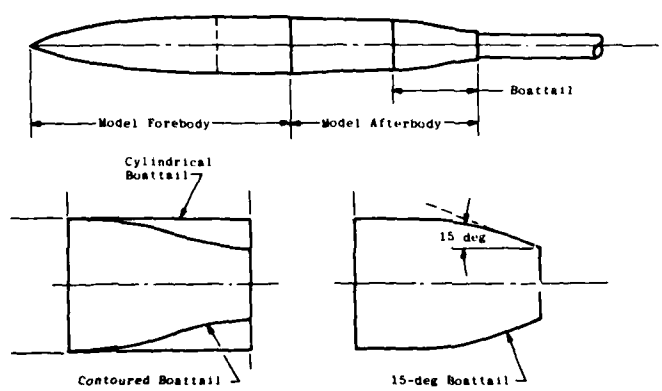

FIG. 3.3.30 MODEL TO STUDY EFFECT OF AFTERBODY CONFIGURATION ON FOREBODY DRAG COEFFICIENT (REF. 3.3.14)

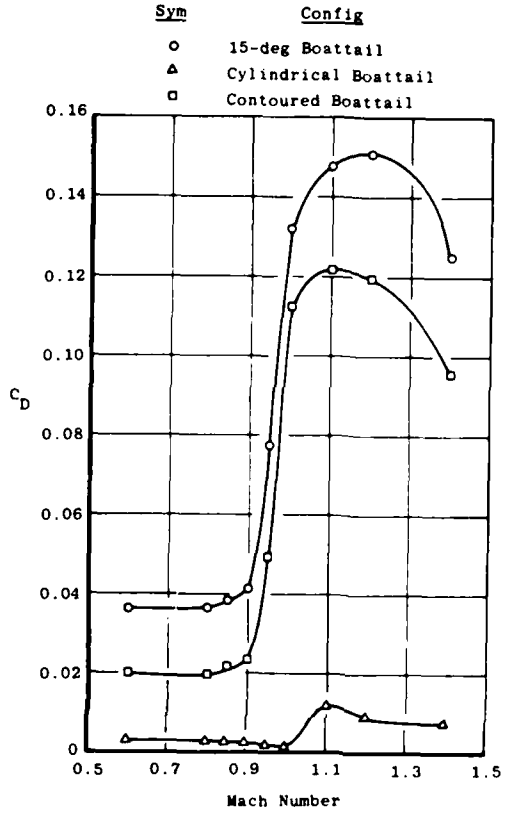

FIG. 3.3.31 AFTERBODY DRAG COEFFICIENT FOR VARIOUS CONFIGURATIONS (REF. 3.3.14)

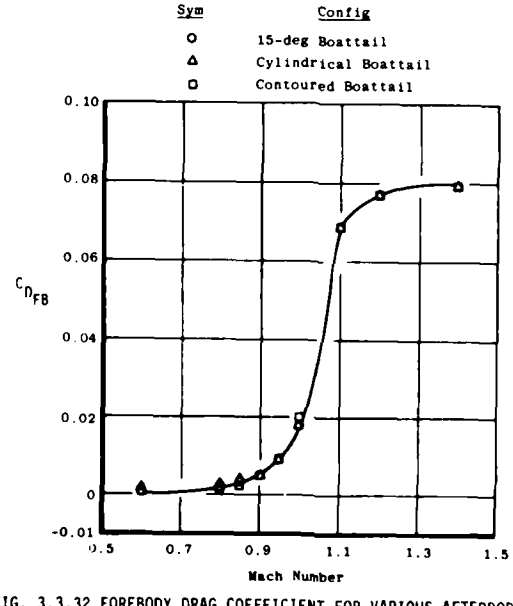

FIG. 3.3.32 FOREBODY DRAG COEFFICIENT FOR VARIOUS AFTERBODY CONFIGURATIONS (REF. 3.3.14)

Another side of the full versus part model simulation question is how much of the model should be metric. In comments offered by representatives from testing and aircraft organizations, the metric extent of the model depends heavily on the test objectives, for example, how much visibility is required for configuration parametrics. The critical metric break placement is determined by the fineness ratio of the configuration and the extent of the influence of the model parametrics. For the entire aircraft model shown in Fig. 3.3.33, changing the nozzle power setting from maximum reheat to dry produced a pressure coefficient change of 0.017 at a location where the area distribution was 80 percent of maximum cross sectional area. Obviously, for this configuration, the metric break is not positioned far enough upstream to account for the entire effect of afterbody changes. Is there enough influence of afterbody configuration changes on the forebody to warrant a fully metric forebody simulation? The question may not need an answer. The current trend is toward use of advanced computational tools to calculate interference and fully metric wind tunnel models for near term and advanced aircraft configurations which exhibit a tendency of strong inlet and nozzle flow interactions.

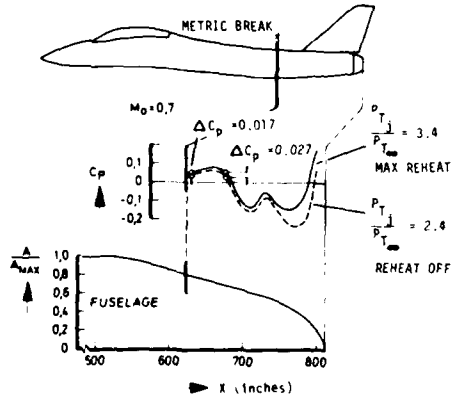

FIG. 3.3.33 EFFECT OF NOZZLE POSITION ON PRESSURE DISTRIBUTION (REF. 3.3.33)

3.3.5.2 Extent of Model Fidelity

Other factors related to afterbody testing are the effect of inlet fairing on afterbody flow, effect of deflection of local empennage surfaces, the impact of secondary and tertiary auxiliary flows, and the need for model detail. An additional paragraph on other qualitative/ quantitative assessments of afterbody flows is also included. These items will each be discussed briefly as they relate to afterbody testing techniques.

3.3.5.3 Inlet Fairing

A common procedure for jet effects testing is to fair over the inlet with an aerodynamic contour. The effect of fairing the inlet or varying inlet mass flow is evident in Figs. 3.3.34 and 3.3.35. For the B-1 with a close coupled nacelle (Ref. 3.3.31), changes in inlet mass flow ratio were evident in the drag of the reference nozzles over an angle of attack range at 0.80 Mach number. For a sting mounted F-16 tested at AEDC, Fig. 3.3.35, a range of inlet fairings from full flow-through, 50 percent flow-through, aerodynamic fairing and blunt fairing produced changes in both afterbody axial and normal force across the Mach number range. The effect was larger above 0 degrees angle-of-attack and above 0.9 Mach number. Obviously this effect is dependent on the configuration being tested and is part of the discussion of utilization of turbine powered simulators.

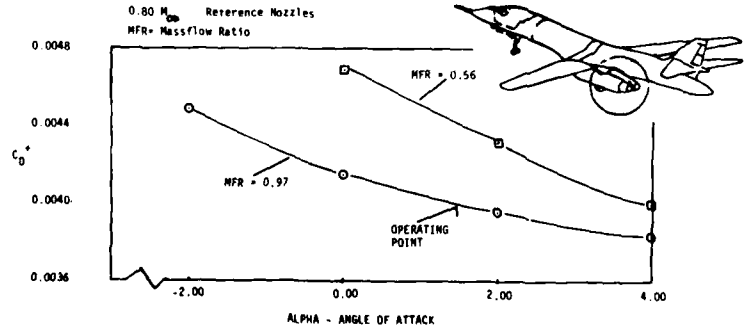

FIG. 3.3.34 INLET MASSFLOW EFFECT ON AFTERBODY DRAG COEFFICIENT (REF. 3.3.31)

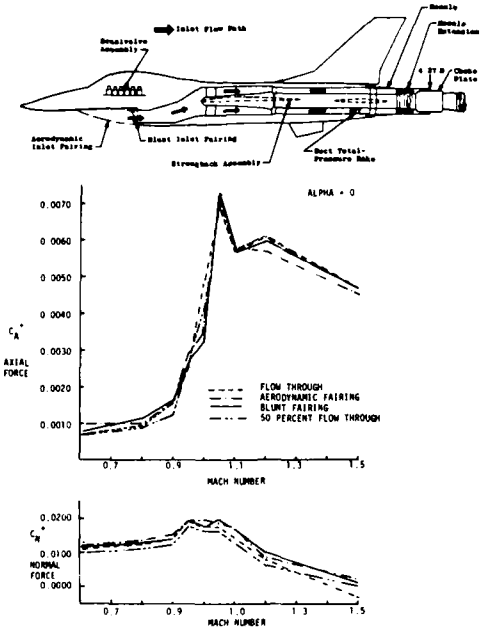

FIG. 3.3.35 EFFECT OF INLET FAIRING CONFIGURATIONS ON AFTERBODY FORCE COEFFICIENTS (REF. 3.3.14)

3.3.5.4 Impact of Empennage Surfaces

If the installed afterbody configuration is in the vicinity of deflected empennage surfaces, then the tail/afterbody interaction should be investigated. Leavitt (Ref. 3.3.35, representative of many documents in this area) states that this interaction is present throughout the Mach number range and is a significant part of the total afterbody drag. Especially at higher Mach numbers, if empennage surfaces are present, then empennage deflection should be included in afterbody testing.

3.3.5.5 Impact of Secondary and Tertiary Auxiliary Flows

All air taken onboard an aircraft for auxiliary system use is eventually dumped overboard. In model testing, the effect of the primary nozzle flow is accounted for but the secondary flows, such as environmental control system (ECS) and engine bay purge, are often not simulated. In a B-1 wind tunnel-to-flight afterbody pressure distribution correlation, the inadequate simulation of the ECS was partially responsible for a mismatch between wind tunnel and flight pressures in the inner nozzle region. Inlet bleed and bypass flows also showed an influence on the B-1 afterbody pressures. For the F-16 (Ref. 3.3.36), a simulation of the engine bay purge flow changed the axial force coefficient across the Mach number range, Fig. 3.3.36. For aircraft with secondary air exhausts in the afterbody region, a simulation of that flow in the wind tunnel model should be considered.

3.3.5.6 Need for Model Detail

How much model detail is necessary for subscale testing? Rooney (Ref. 3.3.37) suggests inclusion of protuberances, excrescences and flaps. Fig. 3.3.37 shows an F-14 afterbody model which simulates gun pods, inlet bleed, wing fences, and the glove vane. Leyland (Ref. 3.3.21) indicated that for the Tornado aircraft, the model must have adequate aircraft detail and if the aircraft is changed, a retest is advised. As the introduction to this section suggests, larger models can have more aircraft detail. The extent required is undetermined.

3.3.5.7 Other Qualitative and Quantitative Afterbody Testing Techniques

The key to utilization of both computations and experiments is understanding the flow physics involved in the afterbody area. If a "fix" is required for a production, development or a "paper" aircraft, the local flow phenomenon creating the problem and the changes in the local flow as a result of the "fix" must be known to adequately assess progress towards a solution. Techniques available to develop this physical understanding are flow visualization, hot film measurements for wall skin friction, local flow measurement (including upstream, downstream, and sidewall) of angularity, total pressure, velocity, and total temperature, and nonobtrusive techniques such as laser doppler velocimeter (LDV) for flowfield velocity determination. In the wind tunnel and inflight, oil and tufts

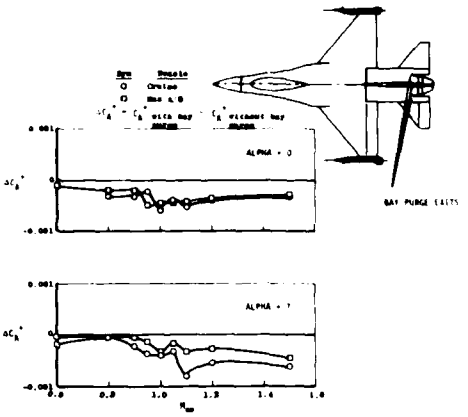

FIG. 3.3.36 EFFECT OF BAY PURGE FLOW ON NOZZLE/AFTERBODY AXIAL FORCE COEFFICIENT (REF. 3.3.36)

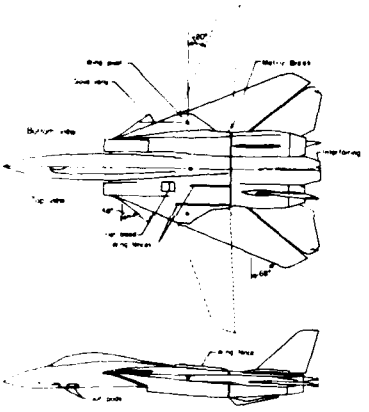

FIG. 3.3.37 MODEL GEOMETRIC DETAILS (REF. 3.3.23)

can be used to indicate regions of separation or high turbulence. Oil has been used in the B-1 wind tunnel test program and has also been used successfully in the inflight Tornado development program. Tufts, both in B-1 wind tunnel and flight tests, have been used for a qualitative flow assessment. Additional qualitative testing can be accomplished in water tunnels especially when thrust reverser impingement and reingestion is to be studied. This test technique will increase in importance as advanced aircraft rely on thrust reverser technology for short field landing capability. Flow visualization techniques for afterbody flow fields, while more art than science, play an important role in the study of afterbody aerodynamics.

Laser doppler velocimeters can provide good quantitative flow field characteristics in near wake, and reversed and separated flow fields which can not be accurately measured by probes or hot wire anemometers. Heltsley, Ref. 3.3.40, used an LDV to produce the velocity profiles for the axisymmetric nozzle shown in Fig. 3.3.38. This technique can be used to produce detailed data to assist computational method development and verification.

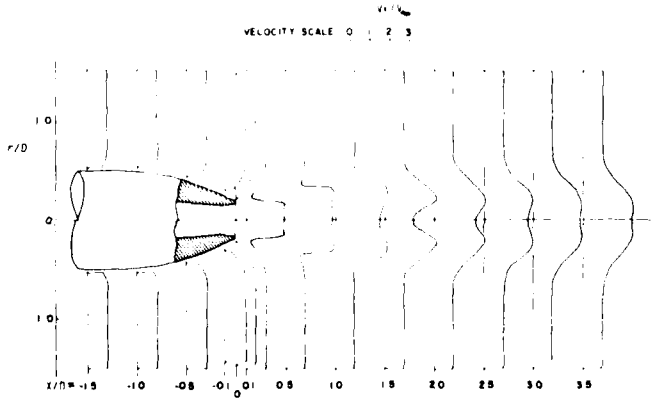

FIG. 3.3.38 AFTERBODY/NOZZLE VELOCITY PROFILES (REF. 3.3.40)

3.3.6 Testing Techniques for Advanced Aircraft with Highly Interactive Flow Fields

Thrust vectoring, thrust reversing and propulsive lift for takeoff and landing and inflight are technologies associated with near term and advanced aircraft. A propulsive lift configuration shown in Fig. 3.3.39, not unlike the current Harrier, is utilizing ejectors and forward lift jets or engines for short take-off and landing capability. Current practice is to use completely metric models with tandem thrust-minus-drag nozzle balances or nonmetric boattails with surface pressures for nozzle drag. Test objectives should determine the metric arrangement. Lowspeed tests for advanced aircraft with thrust reversers, often with the reversed thrust nonmetric, are conducted to determine the stability and control aspects of these installations. If a turbine powered simulator is required to be metric for closely coupled aircraft, a whole new area of force balance arrangements must be investigated. The testing techniques required to capture all of the direct and induced forces for these highly integrated aircraft should be the emphasis of ongoing and future testing technique development.

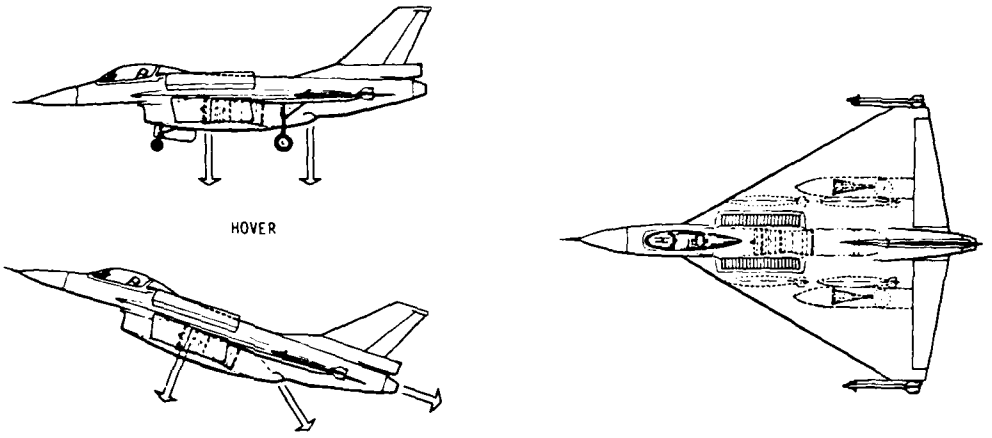

HOVER

SHORT TAKEOFF AND TRANSITION

FIG. 3.3.39 ADVANCED PROPULSIVE LIFT AIRCRAFT (REF. 3.3.39)

3.3.7 Final Summary and Recommendations

The choice of wind tunnel testing techniques for aircraft afterbodies must include consideration of many factors with the test objectives, available facilities and model hardware the most important. Sometimes there is no "best" testing technique to meet the test objectives. A general assessment of the state-of-the-art of afterbody testing techniques concludes the following:

Force balances, while powerful testing tools, must be used with great care to minimize and account for all tares and corrections, and an assessment should be made of the predicted levels of accuracy and repeatability versus the levels required to meet the test objectives. A complete error analysis, or if appropriate a sensitivity analysis or partial error analysis of critical parameters, should be conducted.

Pressure area integration can be a viable alternative for afterbody force measurement if the configuration is not overly complex and coverage in critical high pressure gradients is adequate. Analytical methods should be utilized to properly place pressure orifices.

The wind tunnel model support must be chosen with great care, considering at least the test objective, available test hardware and test facility. The most prevalent systems are the sting, wingtip, and strut support. The sting support, especially the annular sting with a flowing jet simulation, offers minimum interference but is limited when forces are highly dynamic and when higher angle-of-attack data is desired. The wingtip support is especially appropriate for determining incremental afterbody/nozzle forces if testing between 0.8 to 1.1 Mach number is avoided. Use of this technique is applicable only to a metric afterbody and requires a distorted wing planform. Use of the strut support between 0.95 to 1.2 Mach number requires great care to minimize strut interference. If full aircraft forces at higher angles-of-attack are required, this system may be preferred. If resources allow, support system interference corrections should be defined and applied. Design guidelines referenced in this document should be utilized to determine the optimum support technique.

While the current trend is toward fully metric wind tunnel models, the extent of model simulation and model surfaces to be metric should be determined by the fineness ratio of the configuration and the predicted extent of the influence of the model parametrics.

Other factors which should be considered include the inlet fairing, location of deflectable empennage surfaces, secondary and tertiary auxiliary flows in the afterbody region and the extent of the model detail required.

The key to utilization of both computations and experiments is understanding the flow phys involved in the aftbody area. Techniques available to develop this physical understanding are flow visualization, hot film measurements for wall skin friction, local flow measurement of angularity, total pressure, velocity, and total temperature, and nonobtrusive techniques such as laser doppler velocimeter (LDV) for flowfield velocity determination. These techniques should be considered and incorporated whenever possible to add to the understanding of this flow phenomenon.

Near term and advanced aircraft configurations are featuring thrust vectoring, thrust reversing, and propulsive lift capability. Special advanced and more complex testing techniques are required to determine all of the direct and induced forces. These techniques should be emphasized for future testing technique development.

Finally, development and evaluation of testing techniques for afterbody exhaust nozzle testing will continue to demand high levels of resources, both manpower and financial, as exhaust nozzle integration plays an ever increasing role in future aircraft evolution.

3.3.8 REFERENCES

3.3.1.		Improved Nozzle Testing Techniques in Transonic Flow AGARDograph 208. September 1975.
3.3.2.	Laughrey, J. A.	Comparison of Testing Techniques for Isolated Axisymmetric Exhaust Nozzles in Transonic Flow. AIAA Paper No. 75-1292. October 1975.
3.3.3.	Hunt, B. L. and Gowadia, N. S.	Determination of Throttle-Dependent Drag for Fighter Aircraft. AIAA Paper No. 81-1692. August 1981.
3.3.4.	Antonatos, P. P. et al.	Assessment of the Influence of Inlet and Aftbody/Nozzle Performance on Total Aircraft Drag. AGARD CP-124. April 1973.
3.3.5.	Aulehla, F. and Besigk, G.	Reynolds Number Effects on Fore- and Aftbody Pressure Drag. AGARD CP-150. September 1974.
3.3.6.	Jaarsma, F.	Experimental Determination of Nozzle Characteristics and Nozzle Airframe Interference. AGARD LS-53. May 1972.
3.3.7.	Capone, F. J.	Aeropropulsive Characteristics of Twin Nonaxisymmetric Vectoring Nozzles Installed with Forward-Swept and Aft-Swept Wings. NASA TP-1778. March 1981.
3.3.8.	Schnell, W. C. and Grossman, R. L.	Vectoring Non-Axisymmetric Nozzle Jet Induced Effects on a V/STOL Model. AIAA Paper No. 78-1080. 1978.
3.3.9.	Capone, F. J. and Reubush, D. E.	Effect of Thrust Vectoring and Wing Maneuver Devices on Transonic Aeropropulsive Characteristics of a Supersonic Fighter Aircraft. NASA TP 2119. February 1983.
3.3.10.	Pendergraft, O. C. and Bare, E. A.	Effect of Nozzle and Vertical Tail Variables on the Performance of a Three-Surface F-15 Model at Transonic Mach Numbers. NASA TP-2043. August 1982.
3.3.11.	Hiley, P. E. and Bowers, D. L.	Advanced Nozzle Integration for Supersonic Strike Fighter Application. AIAA Paper 81-1441. July 1981.
3.3.12.	Wallace, H. W. and Bowers, D. L.	Advanced Nozzle Integration for Air Combat Fighter Application. AIAA Paper No. 82-1135. June 1982.
3.3.13.	Smith, G. D. et al.	Analytical and Experimental Investigation of Ejector-Powered Engine Simulators for Wind Tunnel Models. AEDC-TR-76-128. January 1977.
3.3.14.	Kennedy, T. L.	An Evaluation of Wind Tunnel Test Techniques for Aircraft Nozzle Afterbody Testing at Transonic Mach Number. AEDC-TR-80-8. November 1980.

3.3.15.	Richey, G. K. et al.	Wind Tunnel/Flight Test Correlation Program on the B-1 Nacelle Afterbody/Nozzle at Transonic Conditions. AIAA Paper No. 78-989. July 1978.
3.3.16.	Lucas, E. J.	Evaluation of Wind Tunnel Nozzle Afterbody Test Techniques Utilizing a Modern Twin Engine Fighter Geometry at Mach Numbers from 0.6 to 1.2. AEDC-TR-79-63. October 1980.
3.3.17.	Pozniak, O. M.	A Review of the Effect of Reynolds Number on Afterbody Drag. AGARD CP-301. May 1981.
3.3.18.	Kilgore, R. A.	Model Design and Instrumentation Experiences With Continuous Flow Cryogenic Tunnels. AGARD-LS-111 (9). 1980.
3.3.19.	Kilgore, R. A.	Selection and Application of Instrumentation for Calibration and Control for a Continuous-Flow Cryogenic Tunnel. AGARD-LS-111 (11). 1980.
3.3.20.	Doonan, J. G. et al.	A High Speed Wind Tunnel Test Evaluation of STOL Dedicated Advanced Exhaust Nozzle Concepts. AIAA Paper No. 83-1225. June 1983.
3.3.21.	Leyland, D. C.	Lessons from Tornado Afterbody Development. British Aerospace.
3.3.22.	Glidewell, R. J. and Fanning, A. E.	Twin Jet Exhaust System Test Techniques. AGARD CP-150. September 1974.
3.3.23.	Reubush, D. E. and Carlson, J. R.	Effects of Installation of F101 DFE Exhaust Nozzles on the Afterbody-Nozzle Characteristics of the F-14 Airplane. NASA TM 83250. March 1982.
3.3.24.	Porrato, F.	Some Results about the Influence of a Rear Sting on the Aerodynamics of an Aircraft Afterbody Model. AERITALIA Doc. 65/TR/T306/83012. May 1983.
3.3.25.	Price, E. A.	Investigation of F-16 Nozzle-Afterbody Forces at Transonic Mach Numbers with Emphasis on Support System Interference. AEDC-TR-79-56. December 1979.
3.3.26.	German, R. C.	Strut Support Interference on a Cylindrical Model with Boattail at Mach Numbers from 0.6 to 1.4. AEDC-TR-76-40. May 1976.
3.3.27.	Lucas, E. J. et al.	Comparison of Nozzle and Afterbody Surface Pressures From Wind Tunnel and Flight Test of the YF-17 Aircraft. AIAA Paper No. 78-992. June 1978.
3.3.28.	Price, E. A.	Interference on a Model Afterbody from Downstream Support Hardware at Transonic Mach Numbers. AEDC-TR-80-27. January 1981.
3.3.29.	Porrato, F.	Comparison Between Main Balance Measurements and Surface Pressure Integration on an Afterbody Model. AERITALIA Doc. 65/RT/T306/83013. May 1983.
3.3.30.	Schoelen, F. J.	B-1 Inlet and Nozzle Flight Performance Determination Program. AIAA Paper No. 81-1852. August 1981.
3.3.31.	Richey, G. K. et al.	Wind Tunnel/Flight Test Correlation on the B-1 Nacelle Afterbody/Nozzle. AIAA Paper No. 76-673. July 1976.
3.3.32.	Brazier, M. E. and Ball, W. H.	Accounting of Aerodynamic Forces on Airframe/Propulsion Systems. AGARD CP-150. September 1974.
3.3.33.	Aulehla, F. and Besigk, G.	Fore and Afterbody Flow Field Interaction With Consideration of Reynolds Number Effects. AGARD AG-208. September 1975.
3.3.34.	Robinson, C. E. et al.	Exhaust Plume Temperature Effects on Nozzle Afterbody Performance over the Transonic Mach Number Range. AGARD CP-150. September 1974.
3.3.35.	Leavitt, L. D.	Effects of Various Empennage Parameters on the Aerodynamic Characteristics of a Twin-Engine Afterbody Model. AIAA Paper No. 83-0085. January 1983.
3.3.36.	Price, E. A.	An Investigation of F-16 Nozzle-Afterbody Forces at Transonic Mach Numbers with Emphasis on Model Scale Effects. AEDC-TR-80-57. September 1981.

3.3.37.	Rooney, E. C. and Craig, R. E.	Development of Techniques and Correlation of Results to Accurately Establish the Lift/Drag Characteristics of an Air Breathing Missile from Analytical Predictions, Sub-Scale and Full-Scale Wind Tunnel Tests and Flight Tests. AGARD Specialists Meeting Aircraft Performance Prediction Methods. October 1977.
3.3.38.	Smith, R. H.	Problems in Correlation Caused by Propulsion Systems. NASA Wind-Tunnel/Flight Correlation 1981. November 1981.
3.3.39.	Foley, W. H.	An Integrated Aerodynamic/Propulsive Design for STOVL Fighter/Attack Aircraft. ICASE-82-1.6.2. August 1982.
3.3.40.	Heltsley, F. L. and Crossway, F. L.	Twin-Component Simultaneous LDV Turbulence Measurements in an Axisymmetric Nozzle Afterbody Subsonic Flow With a Cold, Underexpanded Supersonic Jet. AEDC-TR-82-27. June 1983.
3.3.41.	Aulehla, F.	Drag Measurement in Transonic Wind Tunnels. AGARD CP-242. October 1977.
3.3.42.	Capone, F. J.	Aeropropulsive Characteristics at Mach Numbers up to 2.2 of Axisymmetric and Nonaxisymmetric Nozzles Installed on an F-18 Model. NASA TP-2044. August 1982.

3.4 AFTERBODY FLOW INSTABILITIES (BUFFETING)

The presence of separated flow regions either on an aircraft's wing or fuselage or in cavities and bomb bays provides a sufficiently large energy source to disturb the airframe. As a result, the performance of the aircraft may be limited by the disturbance-induced rigid and elastic vibrations, which may furthermore cause degradations of the handling characteristics.

The highly undesirable rigid motions of the aircraft at angles of attack beyond the onset of separation are referred to in the longitudinal axis as "bouncing" and "pitch-up", and in the lateral/directional axis as "wing rocking", "wing dropping" and "nose slicing". These phenomena belong to the flight mechanics problem area and have a direct effect on aircraft controllability and the pilot's ability to hold an accurate flight path (Ref. 3.4.1). Elastic mode vibrations may also exist, due to flow separation induced excitation forces and changes in aerodynamic damping of the elastic modes. Both rigid and elastic motions of the aircraft may degrade the combat capability, either by influencing the pilot or disturbing the sensor platform signals and thus affecting controlled aircraft handling qualities. This may not necessarily be considered as a flight limit, but it gives an indication of adverse effects like degradation of longitudinal and lateral stability.

Afterbody or tailplane buffeting can be provoked by flow separations on the rear fuselage, but often it can also be caused by flow separations outside this region, for instance by the wing wake or by wing vortex breakdown. Sometimes afterbody buffet even occurs at steady and level flight, leading to inconvenient or even unacceptable ride qualities and tracking characteristics. Both rigid and elastic mode vibrations at the pilot's seat caused by such afterbody flow separation phenomena may lead to pilot ratings from smooth to distressing, see fig. 3.4.1. Even structural damages may occur.

BUFFET/VIBRATION/TURBULENCE LEVELS

Suggested Pilot Rating Scheme

Pilot Rating	Category	Description
1	Nil	Completely smooth
2	Very light	Just perceptible
3	Light	Noticeable without concentration
4	Light-moderate	Mildly annoying
5	Moderate	Annoying
6	Moderate-heavy	Distracting
7	Heavy	Uncomfortable
8	Severe	Distressing
9	Disastrous	Structural damage/loss of control

Fig. 3.4.1 Pilot rating scheme for buffet evaluation

Examples of tail buffeting induced by the wing wake are less serious now because of the care with which tailplane positions are selected. The tailplane position selected is inevitably a compromise between many mutually conflicting requirements (e.g. longitudinal stability at high speeds and low lift coefficients and at low speeds and high lift coefficients, or even by noise alleviation constraints) and hence tail buffeting can normally be anticipated somewhere within the flight envelope. Tail buffeting needs not necessarily be harmful, as for instance on some aircraft buffeting provided a natural warning of the wing stall. Tail buffeting excited by wing flow separations will be sensitive to any devices which alter these separations, such as vortex generators, flaps or engine nacelles. A possible hazard which has occurred on a combat aircraft is tail buffeting excited by the carriage of pylon-mounted external stores under the wing and fuselage. Preventing the flow separations by increasing the gap between the store and the wing or by reducing the thickness/chord ratio of the pylons removed this type of tailplane buffeting.

The actions to be taken in order to eliminate afterbody buffet should consist first of identifying and possibly removing the buffet source outside the afterbody. If the problem is due to the wing wake, changes can be made on the wing by providing vortex generators, fences, etc. or on the tail by changing the vertical position, anhedral, etc. If the separation is provoked by the fuselage shape, local fuselage contour changes can be made, or modifications can be applied on the tail, by providing root strakes, vortex generators, profile variation etc. Ref. 3.4.2 presents a different method to reduce the vibration level at the pilot's seat or at the sensor platform by means of an active control system with feedback of the fuselage accelerations to the tailplane servo in correct phase relationship. It is to be noted, however, that despite a great alleviation of the elastic vibrations the actual buffet source (flow separation) is still present together with possibly adverse effects on other parameters, as for instance drag or directional stability. The method was once proposed for Tornado but not pursued, after a modification of the afterbody geometry could be found which suppressed the separation on the afterbody, i.e. after the buffet source itself could successfully be removed. The corresponding development is described, together with the similar example of FIAT G91Y, in the next sections.

3.4.1 Afterbody Buffeting Evaluation and Possible Improvements

Although some progress has been made in theoretical methods for predicting buffet onset conditions, particularly at subsonic speeds, no adequate theoretical method exists for calculating the unsteady aerodynamic excitation forces in fully developed separated flow at transonic speeds. The determination of these excitation forces from wind tunnel model tests for subsequent use in structural response calculations requires many assumptions that need to be validated. A fundamental question that needs to be resolved is whether the unsteady aerodynamic excitation forces derived from pressure measurements on a rigid model may be extrapolated to an identical but elastic (responding) aircraft. In addition the practical significance of Reynolds number effects on separated flow in terms of the effects on elastic and rigid body response needs to be determined, as well as the effect of angle of attack on buffeting severity. The semi-empirical prediction of afterbody buffeting may follow for example the procedure as described in Ref. 3.4.3.

In spite of these uncertainties several prediction techniques have shown to give results that compare favourably with flight data for certain categories of buffeting, most notably wing buffet onset and, to some extent, buffeting intensity. However, experience has shown that the critical consideration is not always the wing buffet loads but sometimes the excessive fatigue loads on tail surfaces, which could lead to degradation of performance through increased drag and decreased lateral stability which detracts from tracking capability.

Another remarkable feature showing the difficulties of trying to predict afterbody buffeting from model tests is depicted in Fig. 3.4.2 for an early Tornado configuration investigated during afterbody development flying. It shows a significant reduction of inflight accelerometer measured buffet levels for idle power compared to max dry (military) power engine setting, which was normally corroborated by the pilot's ratings.

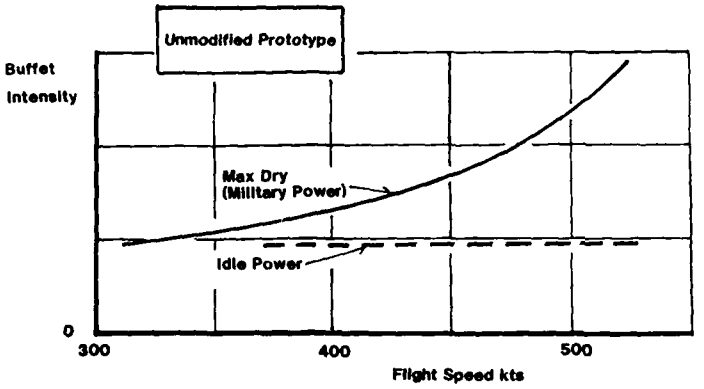

Fig. 3.4.2 Buffet intensity dependence on engine power setting

This behaviour indicates that afterbody buffet could neither have been discovered on the six-component flow-through model with its low nozzle pressure ratios, corresponding to about idle power, nor on an afterbody model duplicating the actual flight nozzle pressure ratios but being equipped with a one-component (axial force) balance only.

A further example where very unsteady flow separations on the nozzle external surface seem to have been detected in flight test only, is reported in Ref. 3.4.4 for the F-15 where nozzle external flaps experienced structural failure, leading to removal of the flaps. For such reasons it is quite difficult in most cases to detect possible afterbody buffeting phenomena already during model testing. In particular this is not only a matter of model instrumentation, but also a feature of the models themselves, which are usually not able to represent the structural characteristics of the full scale aircraft correctly. Flutter/buffeting models, on the other hand, are not equipped with adequate jet simulation devices and are, therefore, also not able to reveal jet induced forces on the afterbody. In this context it is worth remarking, as a further complication, that on occasion low pilot buffet ratings at idle power did not necessarily correlate with correspondingly low accelerometer measured vibration signals. There are indications that this may be due to different buffet frequency contents at normal and idle power, respectively, i.e., while the overall accelerometer signal is unchanged, some of the pilot distracting low frequency content is reduced at idle power.

In Ref. 3.4.5 for the Tornado and later in the present contribution for the FIAT G91Y it is shown that it may be possible to cure the afterbody buffet problem by sometimes relatively small afterbody configuration changes, e.g. gully modification, filler pieces, vortex generators (Fig. 3.4.3 - Fig. 3.4.4).

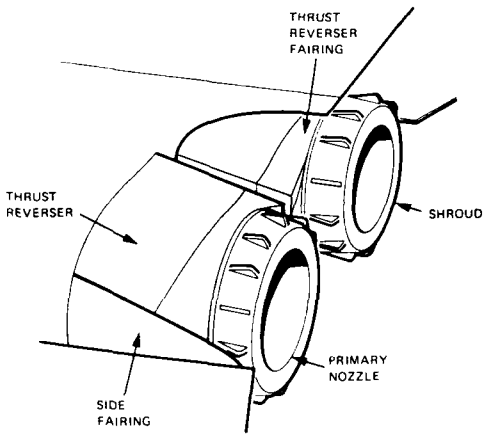

a) PROTOTYPE AFTERBODY (UNMODIFIED)

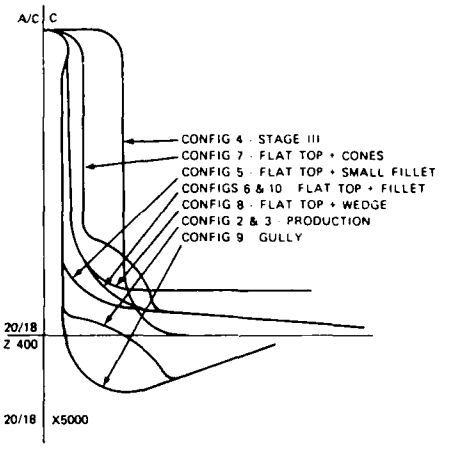

b) AFTERBODY UPPER SURFACE PROFILE : REAR VIEW SHOWING CONFIGURATIONS TESTED

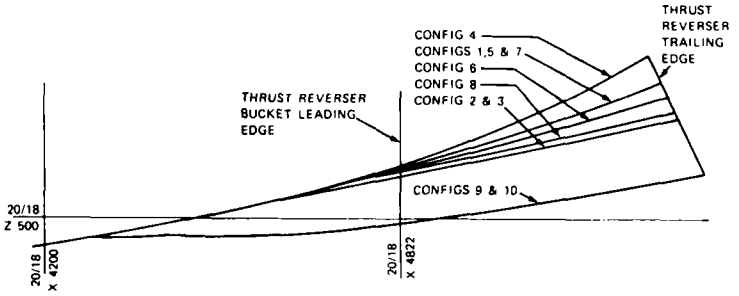

c) AFTERBODY LOWER SURFACE PROFILE ON AIRCRAFT CENTER LINE SHOWING CONFIGURATIONS TESTED

Fig. 3.4.3 Afterbody modifications tested during research programme (Ref. 3.4.5)

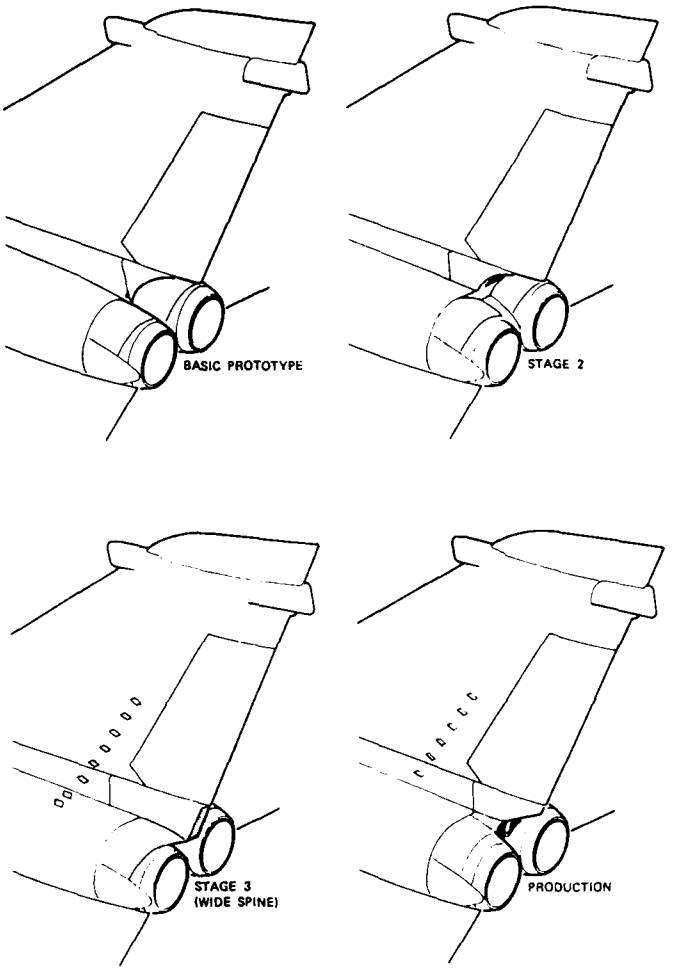

Fig. 3.4.4 Most important flight tested afterbody configurations (Ref. 3.4.5)

It should be pointed out that the remedial measures have to be selected carefully since often other items, e.g. directional stability or afterbody drag, may also be affected. Therefore, a proper compromise is required between all the aerodynamic and structural aspects, as is shown in Ref. 3.4.5 in the course of the evaluation of the Tornado production afterbody configuration. Figs. 3.4.5, 3.4.6 and 3.4.7 depict, that the finally chosen "production" afterbody configuration almost completely restored the desired stability and afterbody drag goals, together with virtually complete removal of the afterbody buffet.

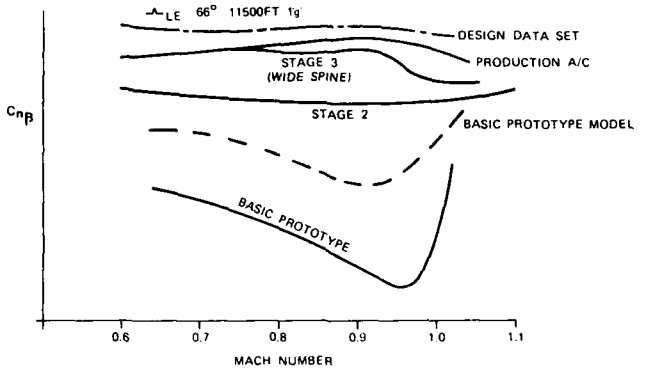

Fig. 3.4.5 Tornado - directional stability (Ref. 3.4.5)

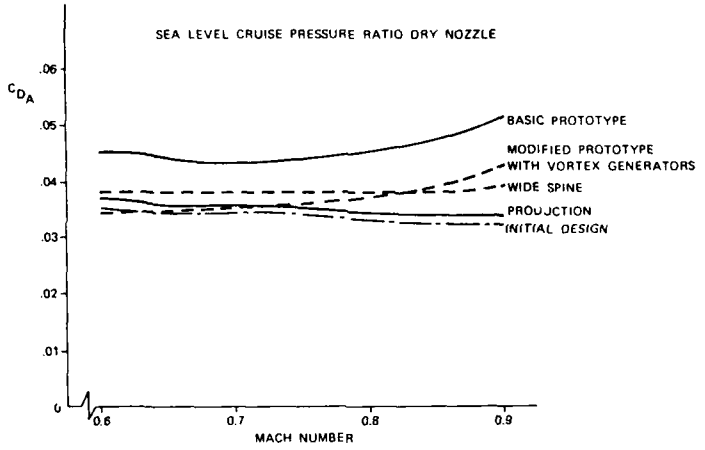

Fig. 3.4.6 Tornado - afterbody drag in flight test development (Ref. 3.4.5)

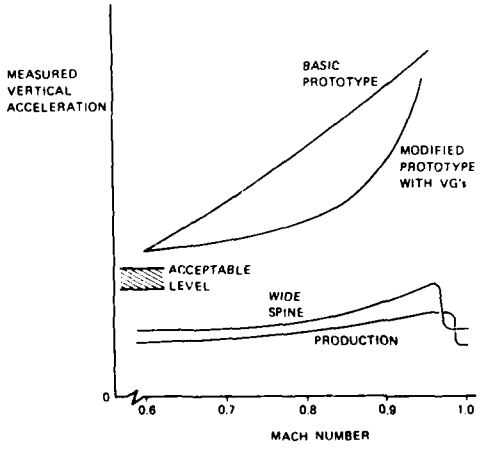

Fig. 3.4.7 Tornado - effects of rear fuselage modifications on cockpit vibration (Ref. 3.4.5)

Buffet flight testing can thus be viewed as the final field trials which yield the qualitative and quantitative performance data and which indicate the degree of success attained by the designer. From an operational standpoint such testing is essential since it relates the pilot's opinion of the aircraft's maneuvering qualities to the engineering data. Finally, buffet flight testing is an invaluable source of data (fluid dynamics, structures, stability and control etc.) which design engineers can use to correlate theoretical and wind tunnel results.

In the past, buffet testing consisted primarily of obtaining pilot opinion data on buffet onset and the relative buffet intensity, and measurements of the normal load factor at the center of gravity. Consequently such tests related buffet onset to the pilot's tolerance of load factor vibrations, and other aircraft structural characteristics and only weakly to the air flow separation phenomena. Current buffet flight testing has progressed to an advanced state such that highly accurate engineering data are obtained and more thorough understanding of the flow fields, shock interactions, air loads, structural responses etc. is gained.

In general, flight instrumentation for buffet tests should include static pressure taps, total pressure and boundary layer rakes, accelerometers, strain gauges, aircraft attitude sensors, high speed camera, wing/afterbody/tailplane tufts and a cockpit event marker. Furthermore it is highly desirable also to perform instantaneous pressure recordings in flow regions, which are known (e.g. blunt base areas, or from inflight tuft/oil flow pictures) or are expected, to be separated. In the case of buffet flight testing of an operational aircraft, allowable instrumentation modifications may be limited (due to outside constraints), and close coordination must be maintained between the test engineer and the modification facility to assure optimum installation locations.

3.4.2 A Typical Example: FIAT G91Y

A typical example of afterbody (mainly horizontal tail) buffeting and of the successful solution of the problem is the case of the FIAT G91Y fighter. In this case the buffet, associated with a deterioration of the lateral-directional characteristics, was occurring in the high transonic range and was ascertained to be caused by fuselage flow separation below and aft of the tailplane root. Proper transonic wind tunnel and flight tests provided an understanding of the phenomenon and allowed the necessary configurational changes to be made.

3.4.2.1 Analysis of the Problem

In the course of early flight tests conducted on the first prototype (NC1) of the twin jet FIAT G91Y fighter, some unexpected aerodynamic instability in the afterbody zone was evident. Two were the main effects, provoked by the flow separations on the rear fuselage:

- an increased bending vibration level of the horizontal tailplane on the FIAT G91Y. compared with the FIAT G91T which is the trainer version of the former with a single jet afterbody
- a decreased directional stability margin (Cn_β) which at particular side-slip angles degenerated into instability.

After each flight, the vibration envelope, expressed as the mean value of the highest oscillation amplitudes recorded in a time interval of about 3 seconds was calculated and plotted versus Mach number. A typical sample is shown in figure 3.4.8 where similar data relevant to G91T are reported for comparison.

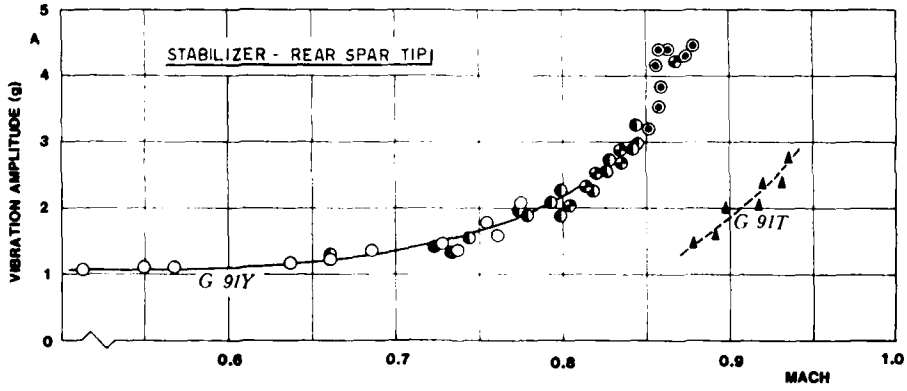

Fig. 3.4.8 FIAT G91Y and G91T - vibration amplitude of stabilizer rear spar tip versus Mach number (different symbols identify different flight tests)

Note in this figure that, despite the obvious configurational variants in the rear fuselage between the two aircraft (G91T is a single engine, Fig. 3.4.9, G91Y is a twin engine, Fig. 3.4.10), the horizontal tailplane vibration envelopes are comparable up to M_∞ = 0.78 (with a maximum vibration level of about 2 "g"), then the curve relevant to G91Y shows a clean divergence which brings the vibrations level to 5 "g" at Mach number equal to 0.9. This means, among other things, that the vibrations level considered acceptable by pilots (about 2 "g" to 3 "g") shifts from M_∞ = 0.9 for G91T down to M_∞ = 0.82 for G91Y.

Fig. 3.4.9 FIAT G91T - single engine

Fig. 3.4.10 FIAT G91Y - twin engine

If the phenomenon is analysed in terms of power spectrum, e.g. resolving the vibration in its components at different frequencies (in a range between 0 and 200 Hz), it is possible to discriminate what is forced oscillation from the eigenmodes of the stabilizer structure. Performing this exercise it is interesting to note (for speed beyond M_∞ = 0.75) the presence of a vibration band between 20 and 35 Hz in a range where ground tests exclude the presence of structural modes. This vibration level is therefore to be attributed to a forced excitation (buffet) acting in a vertical direction in a frequency range around 25 Hz. Finally it is noted that the buffeting level, recorded normally for straight and level flight conditions, increases obviously with load factor (n_z), becoming for n_z = 4.8 three times the value corresponding to straight and level flight.

3.4.2.2 Solution of the Problem

Aiming to restore the G91Y fighter to about the same buffeting levels appropriate to the G91T, an extensive campaign of tests, both in the wind tunnel (low/transonic speed) and in flight, was carried out.

The first series of low speed wind tunnel tests, conducted on a 1/10 scale model, Figs. 3.4.11 and 3.4.12, was devoted to measuring the pressure distribution on the afterbody, with the aim to find out the causes of the increased tailplane vibration recorded in flight and to identify possible geometry reshaping suitable to solve the problem.

Fig. 3.4.11 FIAT G91Y - 1:10 scale wind tunnel model

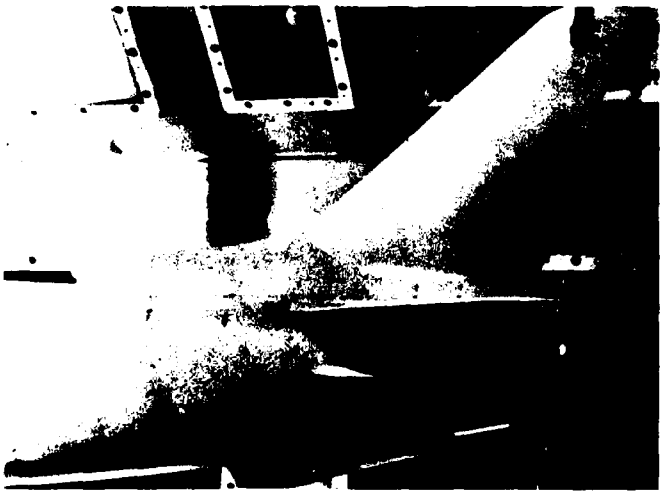

Fig. 3.4.12 FIAT G91Y - 1:10 scale wind tunnel model

Test results showed a regular path of the streamlines along the fuselage with the exception of a remarkable negative pressure peak below the horizontal tailplane leading to shock waves and subsequent flow separation. Among the tested changes of the afterbody shape, aiming to reduce the negative peak, the most effective ones were to increase the length and width of the fuselage aft of the horizontal tailplane (modifications "A" and "E" in Fig. 3.4.13).

Aiming to check the effectiveness of the proposed solution, and to study more deeply other possible variants, a second series of low speed wind tunnel tests was performed on a 1/5 scale complete model. Test results, which basically confirmed the indications derived from the first wind tunnel series, further indicated that it was necessary to couple to the previous shape modifications a "thinning" of the afterbody below the stabilizer, thus giving the rear fuselage a "wasp-waist" contour and finally shifting the horizontal tailplane 25 mm (full scale) upward (Fig. 3.4.14). Transonic wind tunnel tests, conducted both on the original and on the modified configurations, confirmed the validity of the proposed afterbody reshaping.

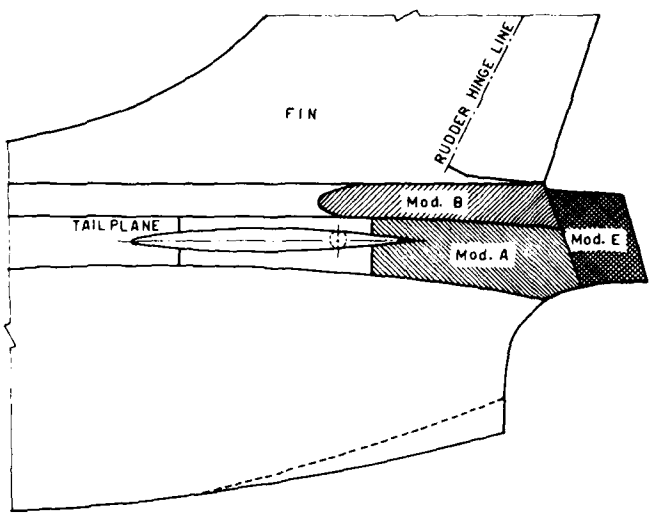

Fig. 3.4.13 FIAT G91Y - afterbody reshaping after 1st series of wind tunnel tests

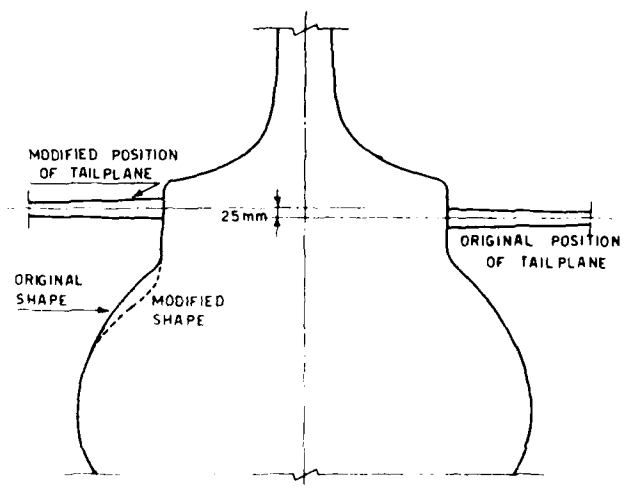

Fig. 3.4.14 FIAT G91Y - afterbody reshaping after 2nd series of wind tunnel tests

With respect to the original fuselage configuration, significant improvements of tailplane vibration level, of drag and of directional stability have been obtained:

- the aerodynamic drag reduction (Fig. 3.4.15), due also to the better base pressures recovery (Fig. 3.4.16) is equivalent to the drag of two wing pylons

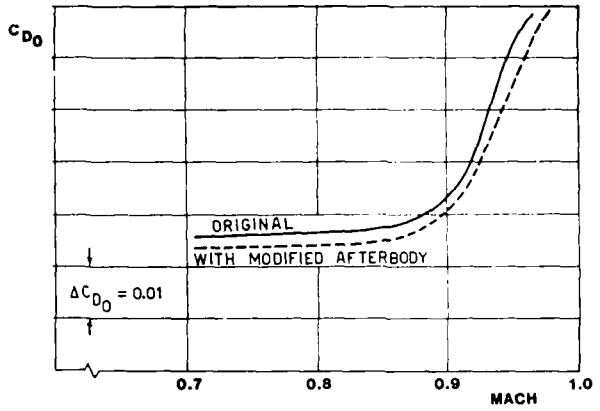

Fig. 3.4.15 FIAT G91Y - zero lift drag versus mach number with/without modified afterbody

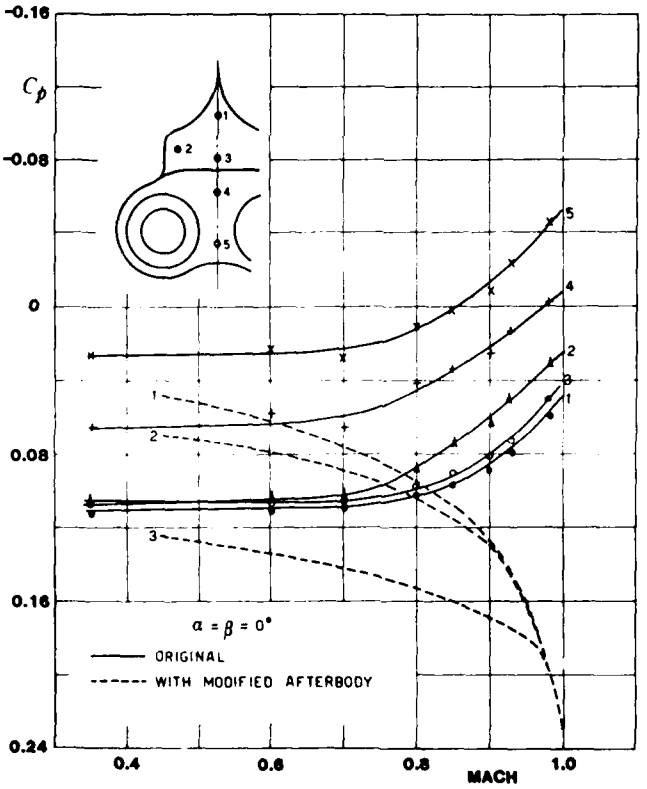

Fig. 3.4.16 FIAT G91Y - effect of afterbody modifications on base pressure recovery

- the improvement in directional stability (Fig. 3.4.17) is remarkable and the stability appears completely restored throughout the whole speed range. This improvement, particularly significant at moderate sideslip angles (0° to 4°), is clearly due to the less adverse pressure gradient provided by the modified afterbody (Fig. 3.4.18), which implies a rearward shifting of the lateral centre of pressure

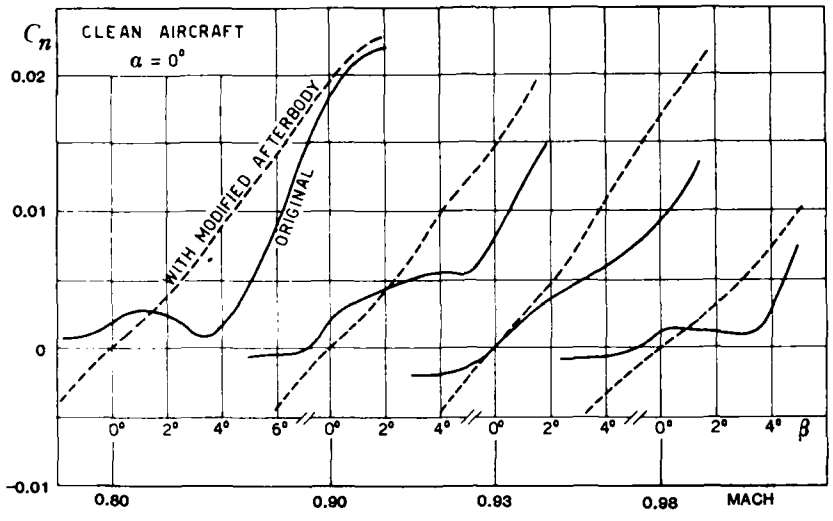

Fig. 3.4.17 FIAT G91Y - effect of afterbody modifications on directional stability

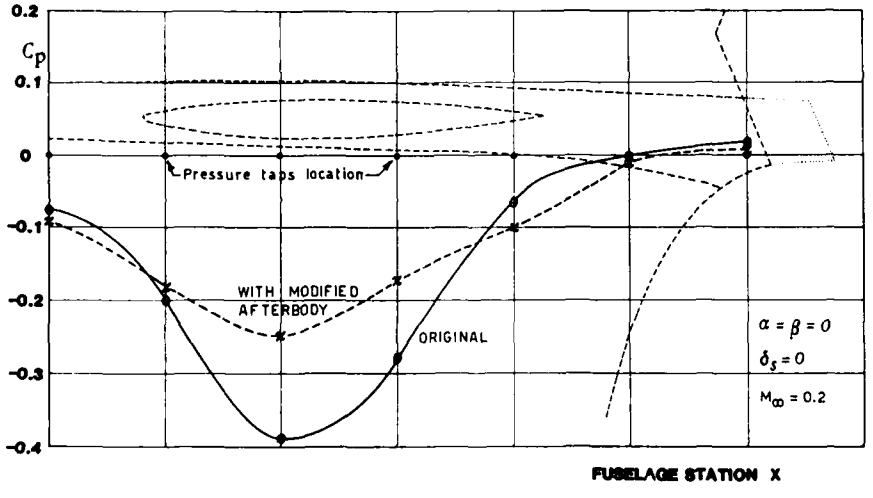

Fig. 3.4.18 Effect of afterbody reshaping on pressure distribution along the fuselage (G91Y)

- the vibrations level of the horizontal tailplane, expressed in terms of the maximum deviation from the mean value of the bending moment, is reduced by at least 50% with the complete removal of the peak at $M_\infty = 0.95$ (Fig. 3.4.19)

- finally oil flow visualizations (Figs. 3.4.20 and 3.4.21) show that flow separation areas present on the afterbody of the original configuration have vanished on the modified configuration.

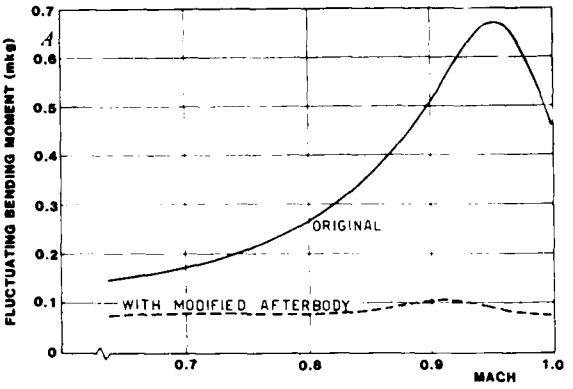

Fig. 3.4.19 FIAT G91Y - effect of afterbody modification on tail buffeting

Fig. 3.4.20 FIAT G91Y - oil flow visualization on the original afterbody (transonic speed)

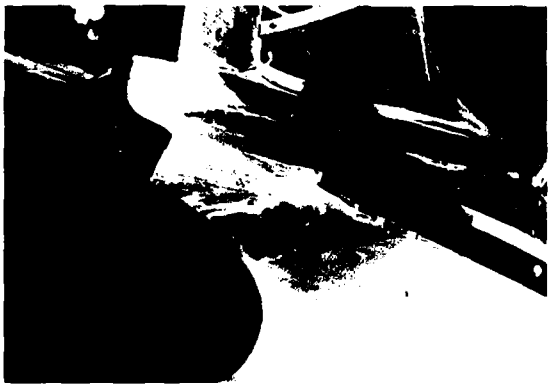

Fig. 3.4.21 FIAT G91Y - oil flow visualization on the modified afterbody (transonic speed)

The final confirmation of the effectiveness of the afterbody reshaping tested in transonic wind tunnel came at higher Reynolds number during flight tests. Flight results showed a remarkable improvement of the afterbody buffeting level (Fig. 3.4.22), as is evident looking at the curve displaying the vibration amplitude of the horizontal tailplane tip, which is no longer monotonically increasing (for the speed range tested) as in the original configuration, but presents a break at about $M_\infty = 0.89$ and then a decrease beyond this Mach number. As far as the directional stability is concerned, while in-flight measurements were not performed, pilot's statements confirmed the improvement also for this item.

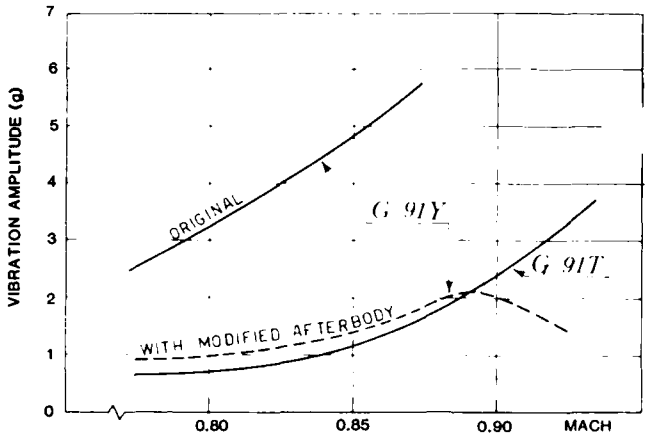

Fig. 3.4.22 FIAT G91Y - effect of afterbody modification on tail buffeting (flight test)

3.4.3 Conclusions and Recommendations

The examples presented show that the task to predict, detect and cure afterbody buffeting is a very delicate one, requiring proper model/aircraft instrumentation together with careful analysis of the test results to allow a definition and selection of remedial measures, if necessary. It is worth remarking that twin jet configurations, especially with close-spaced engines, seem to be more sensitive to unsteady local flow separations in the afterbody/nozzle region due to the much more complex flow field compared with single jet configurations.

In summary afterbody buffet cannot be considered a trivial problem and checks leading to corrective measures are an essential feature of afterbody testing. Following the foregoing discussions, some recommendations are given for simulation requirements and instrumentation:

a) model testing

- correct afterbody geometry
- duplication of actual nozzle pressure ratios
- flow visualization (usually by oil flow pictures)
- recording of instantaneous pressures (kulites) at least in regions where the afterbody flow is supposed or known (e.g. by flow visualization) to be separated or "critical" (gully between engines, fuselage/fin/tailplane intersection)
- tail root strain gauges and/or tail tip accelerometers

b) prototype flight testing

- pressure and acceleration instrumentation corresponding to model tests
- additional accelerometers, preferably at the cockpit station (the commonly used c.g. station accelerometers do not necessarily record the pilot perceived vibrations due to fuselage bending)
- pilot buffet rating evaluation
- flow visualization (oil flow pictures, tufts)

3.4.4 References

3.4.1 AGARD Advisory Report No. 82
"The Effects of Buffeting and other Transonic Phenomena on Maneuvering Combat Aircraft", AGARD-AR-82, July 1975

3.4.2 O. Sensburg, J. Becker and H. Hönlinger
"Active Control of Flutter and Vibration of an Aircraft", Proceedings of the IUTAM Symposium on Structural Control 1979

3.4.3 J. Becker
"Bewegungsinduzierte Luftkräfte bei abgelöster Strömung und ihre Übertragung auf die Ermittlung der Strukturresponse", Dissertation, 1983

3.4.4 G.K. Richey, L.E. Surber, B.L. Berrier
"Airframe Propulsion Integration for Fighter Aircraft", AIAA-83-0084
AIAA 21st Aerospace Sciences Meeting, Reno, January 1983

3.4.5 D.C. Leyland
"Lessons from Tornado Afterbody Development", AGARD-CP-339, FMP Symposium on Ground/Flight Test Techniques and Correlation, Cesme, October 1982

3.5 ERROR ANALYSIS AND CORRECTION METHODS FOR AFTERBODY TESTS

As discussed in Chapter 3.3, many compromises are made when planning and conducting afterbody wind tunnel tests. Contributors to these compromises include consideration of time, funds, tunnel availability plus the choices of models, support and data measurement systems that may be used. Because of so many conflicting requirements, the test objectives, including required data accuracy, need to be well defined prior to finalizing the above choices. Test objectives can include a comparison of afterbodies (Ref. 3.5.1 and 3.5.2); afterbody force increments for total aircraft performance (drag) prediction (Ref. 3.5.3 and 3.5.4); general improvement of testing techniques (Ref. 3.5.5); and validation or improvement of computational methods such as those discussed in Section 2.0 of this report.

In defining the test objectives careful consideration must be given to the desired accuracy of the results. In other words; how accurate must be data be to give acceptable answers. Ref. 3.5.6 suggests a $\pm C_D^+ = 0.0001$ (1 aircraft drag count) as a desired accuracy requirement for total drag. Of course, experimental determination of the total drag for a fighter aircraft normally involves an assessment of incremental drags caused by afterbody/nozzle geometry and engine power changes. These incremental drag coefficients can be a significant part of the total drag and need to be determined as accurately as possible with Ref. 3.5.6 again recommending accuracy to within $\pm$ 0.0001 on ΔC_D^+. As will be discussed, these desired requirements are very seldom achieved. Along with errors caused by support systems, force balances, model surface pressure measurements, metric breaks, etc., significant contribution to the overall error can, in many cases, be attributed to inaccurate determination of free stream or tunnel flow parameters such as static and total pressures (P_∞ and P_{t_∞}), angle of attack (α) and Mach number (M_∞).

This chapter is an assessment of the influence of errors in measured (e.g. P_∞, P_{t_∞}, q_∞) variables on the uncertainty of calculated performance parameters (e.g. C_D^+, C_L^+) applicable to afterbody aerodynamics. Discussed initially is the relevance of accuracy, error, uncertainty, etc. along with some definition of the terms as they are being used in the literature. Following this is a section assessing the importance of accurate measurement or determination of tunnel flow parameters such as P_∞, α and M_∞. The influence on these variables of pressure gradients, blockage, wall angle, porosity, etc. is then discussed. Prior to the conclusions and recommendations, some of the uncertainties existing in determining in-flight drag are presented.

Of course there are many methods, analytical and otherwise, of correcting lift and drag values of two-dimensional and three-dimensional bodies for errors due to wall interference, blockage etc. It is not meant to slight these methods,but only to keep the discussions here to those more applicable to afterbody tests.

3.5.1 Error Analysis, Uncertainty and Test Data Repeatability

A complete discussion of an error or uncertainty analysis of experimental test results is beyond the scope of this chapter, however, there is a need for clarification of some of the terms used and an understanding of why such an analysis should be undertaken. Various terms are used in the literature to describe the accuracy of measured data and the quantities determined from the data. It is recommended that references 3.5.6, 3.5.7, 3.5.8 and 3.5.9 be consulted for in depth examples of procedures currently used to conduct an uncertainty analysis and for further clarification of the many terms used.

Uncertainty is one of the more prevalent terms used and, in general, consists of systematic and random errors with systematic errors sometimes referred to as bias or fixed errors. The methods of combining random and systematic errors differ according to the preference of a particular author or experimental test group, however, the magnitude of the uncertainties so determined do not differ greatly. Some estimates are more conservative than others. The difference can be mainly attributed to the various methods used to estimate the systematic errors as similar statistical methods are used to estimate random errors. A comprehensive pretest uncertainty analysis is recommended by many authors (e.g. Ref. 3.5.10) but in many situations, because of the complexity of the test, lack of time, lack of appropriate data from previous tests, etc., this is often difficult to accomplish.

If an in depth uncertainty analysis is not or cannot be accomplished, then there is still a need to know the sensitivity of the computed parameters (e.g. C_D) to possible errors in the measured parameters (e.g. P_∞) if the correct test equipment and procedures are to be chosen in order to minimize the uncertainty of the results. A post-test analysis should always be done to assess data scatter, determine repeatability and, if possible to improve the pre-test uncertainty analysis of future tests.

3.5.1.1 Definition of Terms

The following definition of terms used in uncertainty analyses were obtained from the various noted references and are offered here as an attempt to clarify this discussion of errors, their causes and methods that might be used to estimate and correct them. The list is by no means exhaustive and some definitions may differ with other sources.

Error (Ref. 3.5.9) - The difference between a measured value and the "true" one. Normally the "true" value is unknown and the magnitude of the error is hypothetical. In some cases (Ref. 3.5.7) the "true" value is assumed to be that given by the reference value by the National Bureau of Standards (NBS).

Systematic (bias) error (Ref. 3.5.9) - When the values determined by repeated measurements are in error by the same amount or (Ref. 3.5.7) the difference between the average of all possible measured values and the "true" value.

Random error (Ref. 3.5.9) - When the values determined by repeated measurements do not agree exactly.

Uncertainty (Ref. 3.5.7) - The maximum error reasonably expected for the defined measurement process. Normally consists of systematic and random errors.

Error Limit (Ref. 3.5.8) - Similar to uncertainty but differs in method of estimating systematic errors. In general total Error Limit will be less than total uncertainty as defined above.

From a review of the literature it appears that the term "accuracy" is generally used to mean the closeness or agreement between a measured value and a standard or "true" value (e.g. Ref. 3.5.7), however, a more restrictive definition is given in Ref. 3.5.9 by the explanation that if an experiment has small systematic errors, it is said to have high "accuracy". Also in Ref. 3.5.9 there is a similar definition for precision in that if an experiment has small random errors, it is said to have high "precision". This latter definition is similar to that given for precision error in Ref. 3.5.7. Namely precision error is the random error observed in a set of repeated measurements.

The above terms and discussion apply specifically to the errors and uncertainties of measured values of test data. When performance parameters, such as drag and lift coefficients (C_D*,C_L*) are calculated from measured test values then there needs to be consideration of how the errors or uncertainty in these measured values influence the uncertainty of the calculated parameters. Or in other words, how do the errors in the measurement propagate through the data reduction equations. For an in depth discussion of error propagation one is referred to reference 3.5.7 and 3.5.8. A common procedure to estimate the uncertainty of a calculated parameter is to use what is referred to as the Taylor series method which leads to the determination of influence coefficients (the partial derivatives in the Taylor series expansion).

Many times it is difficult to analytically determine the influence coefficients and dimensionless influence coefficients are used to estimate what the percentage change in a calculated value would be for a given percent change in a measured value. This estimation of the influence coefficients is sometimes referred to as a sensitivity analysis and in some situations may be the extent of a pre-test or post- test uncertainty analysis. Such an analysis does give an indication of what the error in the calculated parameter might be for a given error in a measured value.

In general a sensitivity analysis assumes that errors in other measured values are minimal or insignificant. A detailed uncertainty analysis takes into consideration all possible errors of the measured values and their influence on the uncertainty of the final calculated parameters.

3.5.1.2 Pre-Test Uncertainty Analysis

As recommended by many authors (e.g. References 3.5.6, 3.5.7, 3.5.8, 3.5.10 and 3.5.11) one should perform an uncertainty analysis prior to a test to estimate the maximum error that can be reasonably expected. The three main reasons being; selection of the "best" test method, selection of the "best" instrumentation and to give the range of test conditions required to achieve the test objectives. The depth of pre-test analyses varies from an estimate of the sensitivity of a drag coefficient to an error in free stream static pressure to a detailed examination of the combined effects on the drag coefficient (and other calculated parameters) of errors in pressure measurements, force balance measurements, angle of attack etc. An example of an in depth pre-test uncertainty analysis is given in Ref. 3.5.6 for a planned test on a transport aircraft. The main contributors to the uncertainty in the drag coefficient were considered to be errors in Mach number, balance forces, angle of attack, Reynolds number, static and total pressure, temperature, internal drag plus model base and cavity pressures and the influence of pressure (Mach) gradients, stream curvature, stream upwash and tunnel humidity. In the example it was assumed that the systematic (or bias) errors of the individual contributors were of the same magnitude as the random errors. The procedure followed was to calculate the contribution of each of the error sources using the

root-sum square method to come up with a total uncertainty, at M_∞ = 0.8, of ± 0.0008 (8 aircraft drag counts) in C_D+. A more detailed explanation is much beyond the scope of this chapter, however, it is important to note that the assumption each contributor to the total uncertainty had a systematic error equal to its random error is at best a rough estimate and points out one of the main difficulties in conducting a reliable pre-test uncertainty analysis. Namely, what are the systematic errors and how do they influence the resultant total uncertainty? The reasoning followed in Ref. 3.5.6 for assuming bias errors to be of the same magnitude as random errors was that for state of the art pressure transducers, strain gage balances and temperature sensors their systematic errors are roughly equivalent to their random errors, therefore, it was assumed that other error sources just might have the same level of systematic errors as their random errors. Another not as complicated example of a pre-test uncertainty analysis which uses the procedures of Ref. 3.5.2, is given in Ref. 3.5.11.

Results of pre-test uncertainty analysis directly applicable to afterbody testing are given in Ref's 3.5.12 through 3.5.16. A typical example of uncertainties in pressure coefficients plus afterbody axial and normal force coefficients for a single engine fighter aircraft is given in Table 3.5.1. The uncertainties in the pressure coefficients were determined by combining the instrumentation uncertainties using the Taylor series method or error propagation as suggested in Ref. 3.5.7. The uncertainty in the pressure coefficient was then integrated over the projected areas to obtain the uncertainties in the axial and normal force coefficients.

Table 3.5.1 Pre-Test Uncertainties (Ref. 3.5.12)

M_∞	Parameter		
	U_{Cp}	U_{CA}+	U_{CN}+
0.6	± 0.0127	± 0.0008	± 0.0070
0.9	± 0.0091	± 0.0006	± 0.0050
1.2	± 0.0066	± 0.0004	± 0.0040
1.5	± 0.0060	± 0.0004	± 0.0030

Pre-test uncertainties for a twin-jet fighter afterbody, similarly determined as above, are shown in Table 3.5.2. To be noted is the improvement in the uncertainties as the Reynolds number increased.

Table 3.5.2 Pre-Test Uncertainties (Ref. 3.5.13)

M_∞	Re X10^{-6}	Parameter	
		U_{Cp}	U_{CA}+
0.6	14.9	± 0.02493	± 0.00027
	59.6	± 0.00985	± 0.00018
0.8	14.8	± 0.01809	± 0.00018
	42.0	± 0.00817	± 0.00011
0.9	14.8	± 0.01644	± 0.00016
	58.8	± 0.00579	± 0.00009
1.2	14.9	± 0.01378	± 0.00013
	48.0	± 0.00533	± 0.00007

The uncertainties reported in Ref. 3.5.14 and shown in Table 3.5.3 are for an axisymmetric model that was tested at zero angle of attack.

Table 3.5.3 Pre-Test Uncertainties (Ref. 3.5.15)

M_∞	Parameter	
	U_{Cp}	U_{CDPAB}
0.6	± 0.0116	± 0.0061
0.9	± 0.0070	± 0.0036
1.2	± 0.0056	± 0.0029

These examples of afterbody pre-test uncertainties will be further discussed in the next section when data repeatability for the referenced tests are presented.

In Ref. 3.5.16 is a comparison of wind tunnel and flight test presssure coefficients of a twin-jet fighter. The pre-test uncertainties of the pressure coefficients were reported in Ref. 3.5.13 and are partially repeated in Table 3.5.2. The flight test uncertainties and observed scatter from Ref. 3.5.16 are shown in Table 3.5.4.

Table 3.5.4 Flight Test Pressure Coefficient Uncertainties and Scatter (Ref. 3.5.16)

M_∞	Altitude (meters X10^{-3})	Parameter	
		U_{C_p} (Estimated Uncertainty)	C_p (Observed Scatter)
0.6	7.8	$\pm$ 0.024	$\pm$ 0.005
0.6	12.2	$\pm$ 0.048	$\pm$ 0.009
0.9	8.4	$\pm$ 0.014	$\pm$ 0.008
0.9	15.2	$\pm$ 0.035	$\pm$ 0.011
1.2	7.6	$\pm$ 0.006	$\pm$ 0.002

3.5.1.3 Post Test Analysis

A detailed description of what a post-test analysis should be is given in Ref. 3.5.8. The main point being that with test data available statistical calculations can be made that apply to random errors but estimation of systematic errors can only be made from the pre-test uncertainty analysis or possibly by using different methods to determine the same performance parameter.

In afterbody testing the most common post-test parameters reported are repeatabilities and scatter of force and pressure coefficients. Repeatability and scatter are two terms that are sometimes used in the literature to mean the same thing. In the discussion here an attempt will be made to use scatter as the variability of data during a single test with repeatability being the variability of data in a series of repeated tests. Examples of repeatability reported in the literature are shown in tables 3.5.5 and 3.5.6. The axial normal and drag coefficients were determined using pressure area integration techniques.

Table 3.5.5 Axial and Normal Force Repeatability from Tests (Ref. 3.5.12)

M_∞	Parameter				
	Avg ΔC_A^+	Max ΔC_A^+	Avg ΔC_N^+	Max ΔC_N^+	Number of Repeats
0.6	0.00016	0.00045	0.00137	0.00385	12
0.9	0.00009	0.00017	0.00097	0.00247	18
1.2	0.00012	0.00038	0.00074	0.00210	18
1.5	0.00002	0.00006	0.00027	0.00115	12

Table 3.5.6 Drag Coefficient Repeatability (Ref. 3.5.15)

M_∞	Parameter
	ΔC_{DPAB}
0.6	0.0015
0.9	0.0014
1.2	0.0028

Corresponding pre-test uncertainties are given in tables 3.5.1 and 3.5.3 respectively. A comparison of the repeatability values to the pre-test uncertainty values shows a significant difference with the repeatability values being on the order of four to five times less at subsonic Mach numbers. A similar order of magnitude is evident between the observed scatter and pre-test pressure coefficient uncertainties reported in Ref. 3.5.16 and shown in Table 3.5.4., the scatter being obtained from averaging several Scanivalve cycles. Comparing repeatability and scatter with pre-test uncertainties to determine if one is "better" than the other is not a valid comparison as repeatability or scatter are most likely random errors and pre-test uncertainties include random plus systematic errors. A post-test uncertainty would include not only the random error estimated from repeated tests, but a systematic error estimated from the pre-test uncertainty analysis or if the proper test methods were accomplished, a new estimated value.

Normally, as reported in the literature, repeatability is calculated by averaging values from repeated tests rather than using statistical methods to determine an estimate of their standard deviation and to check if the values from each test are statistically relevant. It is stated in many of the references that repeatability is a

good measure of the quality of the test arrangement if the tests being conducted are to obtain incremental drag data, i.e., to assess the change in afterbody drag for changing nozzle geometry and engine power setting.

There is validity to this assumption, however, as will be discussed in section 3.5.2.1, a systematic error in tunnel or free stream static pressure can cause an error in the drags, particularly if the projected area of the afterbody changes with the configurational changes.

In a series of tests with the Tornado afterbody model a reference or datum model was retested during each phase of the series. The phase to phase repeatability of afterbody pressure drag, reported in Ref. 3.5.18 as D/q (ft^2) versus nozzle pressure ratio is shown in Fig. 3.5.1 with the "scatter", at sea level cruise, being given as $\Delta D/q = 0.08\ ft^2$ which is equivalent to a ΔC_D^+ of 0.00028 or 2.8 aircraft drag counts. No pre-test uncertainty values were given in the reference, however, it was stated that the repeatability is probably a better measure of the quality of the rig than estimated uncertainty.

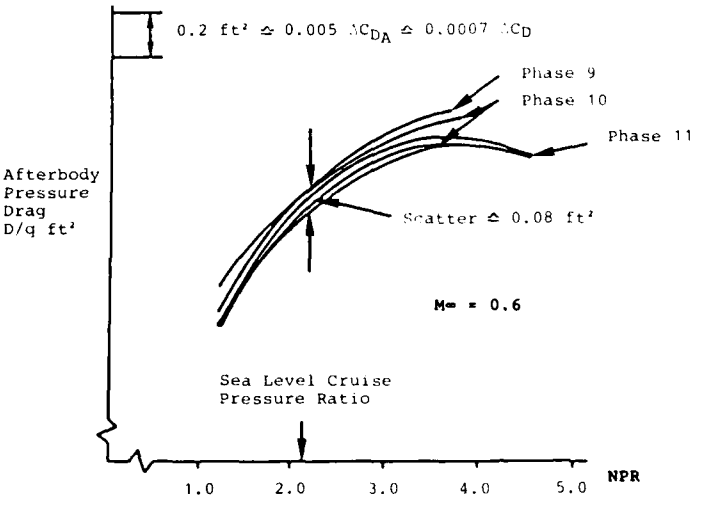

Fig. 3.5.1 Tornado Afterbody, Phase to Phase Repeatability (Ref. 3.5.18)

3.5.1.4 Summary; Error Analysis, Uncertainty and Test Data Repeatability

From a review of the literature it appears that, for afterbody testing, determining a post-test uncertainty value from the test results is very seldom if ever done. Limited pre-test uncertainty or sensitivity analysis are done which can help determine the correct instrumentation and test procedures. The test data repeatability values shown above can possibly be used as indications of the validity of incremental drag coefficients, but a more in depth analysis of the results needs to be accomplished if the accuracy of absolute drag coefficients is required. It is not surprising that the repeatability values are lower than pre-test uncertainty values as the uncertainty normally includes both random and systematic errors and is defined as the maximum error reasonably expected for a particular test arrangement. However, whenever pre-test uncertainty greatly exceeds the repeatability values than this should warrant further analysis of the results.

3.5.2 Errors in Pressure, Mach Number, Angle of Attack, etc.

In the preceding section several sources of errors (e.g. static and total pressures, Mach number,angle of attack, balance forces etc.) were mentioned as influencing the pre-test uncertainties and the test data scatter and repeatability. As mentioned previously this chapter is concentrating on errors in those variables directly associated with tunnel or free stream flow conditions. Not all flow conditions are covered in this chapter, however, after a review of reports published over the past ten to fifteen years, it is believed that the variables presented here are the more critical ones in regard to afterbody testing.

3.5.2.1 Errors in Static Pressure and Mach Number

One of the more critical measurements of tunnel flow conditions is the static pressure. What may appear as a relatively small error in static pressure can be the origin of a rather large inaccuracy in aircraft drag determined from either force balance measurements or pressure area integration. This is particularly true in the determination of the absolute drag of a part body such as an afterbody where the error in P_∞ is proportional to the projected area. However, an incremental drag coefficient

should not be in error due to a constant error in P_∞ if the projected area between the two configuration remains the same.

In Fig. 3.5.2 isentropic relations were used to show how much a small error in free stream static pressure will change free stream Mach number and the ratio $\Delta P_\infty / q_\infty$. Assuming there are no other errors (e.g. in the total pressure), it can be shown that the error in P_∞ / q_∞ is related to the error, ΔC_p, in pressure coefficient and to the cavity pressure of a force balance. It can further be shown (Ref. 3.5.10) that for an error in P_∞/q_∞ of 0.01, the related error in afterbody pressure drag coefficient is approximately $\Delta C_{DP}{}^{+} = 0.0010$ (10 aircraft drag counts) for the typical fighter aircraft. As can be seen from Fig. 3.5.2 for a pressure drag coefficient to have an error no larger than $\Delta C_{DP} = 0.0001$ (1 aircraft drag count)the error in the measured static pressure must be no greater than approximately 0.04 % and that the error in calculated Mach number would be within 0.0004 which is a value significantly smaller than normally quoted by most tunnel operators. A typical value being 0.003. However, it has been shown that using the accuracy in static pressure corresponding to this typical accuracy in Mach number has generated some incorrect afterbody pressure data from wind tunnels with perforated walls. Fig. 3.5.3 showing an increase in afterbody drag with increasing Reynold number is typical of this incorrect data. Of particular interest are cases 1, 2, 3 and 6 because of a re-evaluation of the test section static pressures since the results were published.

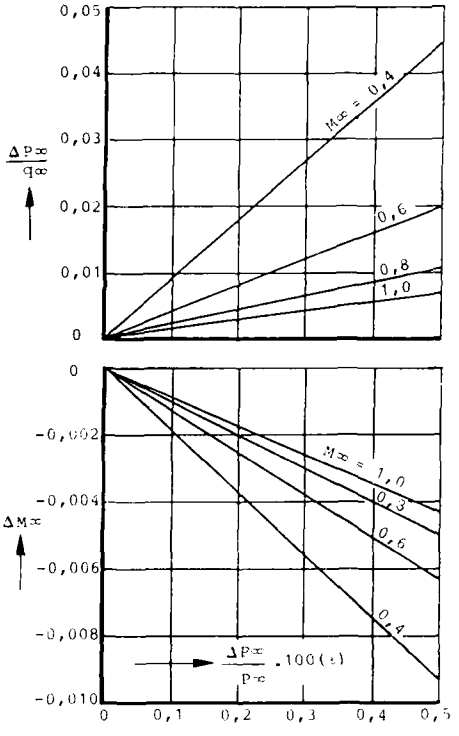

Fig. 3.5.2 Influence of Error in P_∞ on $\Delta P_\infty/q_\infty$ and M_∞

A detailed analysis of the static pressures for cases 1 and 3 is given in Ref's 3.5.5, 3.5.17 and 3.5.19. Pressure changes on the model as Reynolds number was changed are indicated in Fig. 3.5.4. Further evaluation of the variation of the mean values of the pressure coefficient on the model and on the wall (Fig. 3.5.5) showed a similar trend with Reynolds number. From this information it was suggested in Ref. 3.5.17 that a systematic error in static pressure could be the reason for the observed variation in Fig. 3.5.3 of afterbody drag with Reynolds number

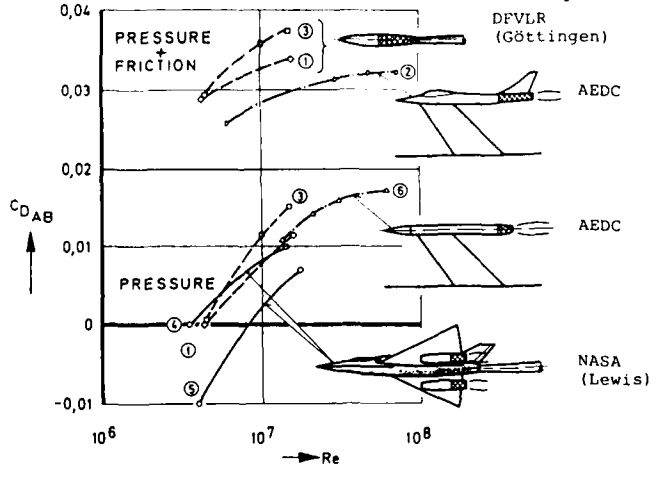

Fig. 3.5.3 Reynolds Number Effect on Aftbody Drag (Ref. 3.5.17)

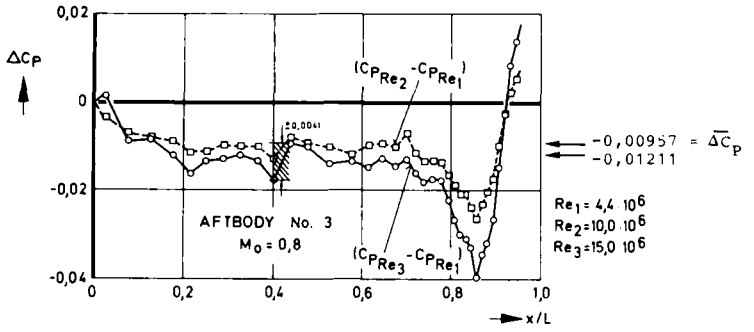

Fig. 3.5.4 Change in Body Pressure Distribution Due to Reynolds Number (Ref. 3.5.17)

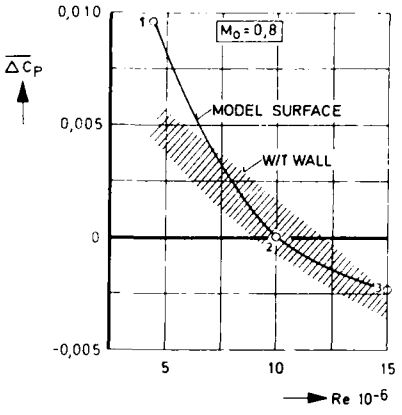

Fig. 3.5.5 Comparison of Averaged Changes in Pressure Coefficients on Model and Tunnel Wall (Ref. 3.5.17)

and it was shown that an average or mean of the tunnel wall pressures was a much better indication of the free stream static pressure change. As reported in Ref. 3.5.5, the scatter in forebody pressure drag was reduced from $\Delta C_{DPFB} = \pm 0.003$ to ± 0.001 for most test cases using the average wall pressures as the free stream static wall pressures.

The tests for cases 1 and 6 were conducted in the AEDC 16 foot transonic tunnel which was calibrated over a range of Reynolds numbers after publication of the results in Fig. 3.5.3. Some results of the recalibration are shown in Fig. 3.5.6 which indicates by the slope of the line showing the difference in Mach numbers determined by the centerline static pressure and plenum chamber static pressure that there is a systematic variation in plenum chamber static pressure above a Reynolds number of approximately 1.5 x 10^6/ft.

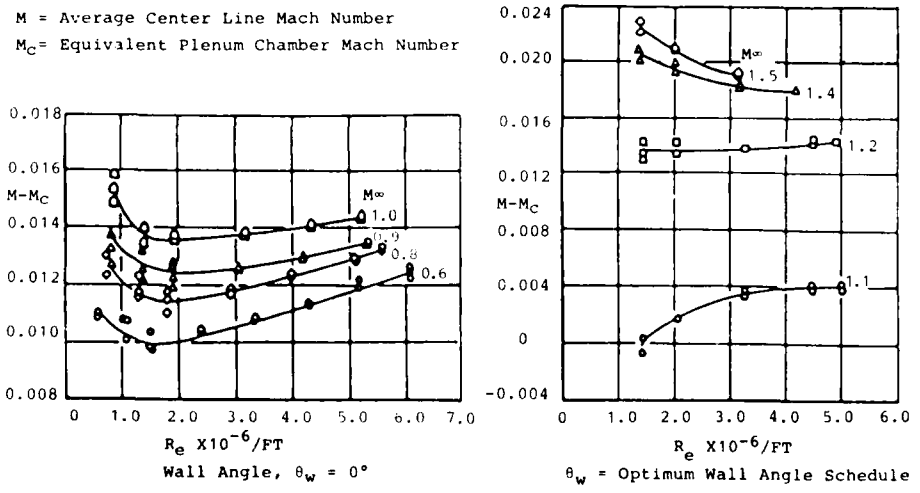

Fig. 3.5.6 AEDC 16 T Mach Number Calibration for Various Reynolds Numbers (Ref. 3.5.20)

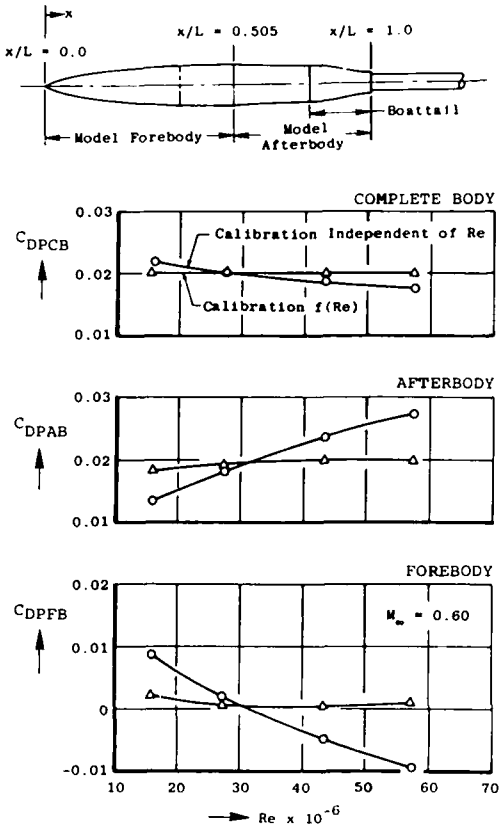

Fig. 3.5.7 Effect of Tunnel Calibration on Pressure Drag for Contoured Boattail Configuration M_∞ = 0.60; AEDC 16 T (Ref. 3.5.21)

For example at M_∞ = 0.6 the increase in M_C between Reynolds numbers 3 x 10^6/ft and 6 x 10^6/ft is approximately 0.002. Assuming a ΔM_∞ of 0.002 at M_∞ = 0.6 in Fig. 3.5.2 gives a 0.16 % change in P_∞ and a value of 0.007 for the change in P_∞/q_∞ which for the typical afterbody is equivalent to a change in pressure drag of $\Delta C_{DPAB}{}^+$ = 0.0007 (7 aircraft drag counts). Another example of the error in part body pressure drag when using results of a single Reynolds number calibration is given in Ref. 3.5.21 from which Fig. 3.5.7 was obtained

The results for M_∞ = 0.6 show that, using data with the tunnel calibrated for Reynolds number, practically all variation of pressure drag with Reynolds number is eliminated on both the fore and afterbody. It is interesting to note that the change in afterbody pressure drag between Reynolds number of 30 x 10^6 and 60 x 10^6 (model length is 10.8 ft) was approximately ΔC_{DPAB} = 0.008 or a $\Delta C_{DPAB}{}^+$ = 0.0008 for the typical fighter. The model tested had the area distribution of the typical fighter. As can be seen by the decreasing slope of the curves (Fig. 3.5.6) this systematic variation in static pressure becomes less significant as Mach number is increased from 0.6 to 1.0. It should be pointed out that the trends shown in Fig. 3.5.6 are within the estimated uncertainty of Mach number for the 16T tunnel. Other variations of afterbody drag with Reynolds number have been attributed to causes other than an error in free stream static pressure. For a good summary and discussion of these causes, Ref. 3.5.22 should be reviewed.

A reason for the incorrect plenum chamber pressures as Reynolds number is varied in transonic tunnels with perforated walls is discussed in Ref. 3.5.5. It is postulated that the holes act like flush boundary layer inlets and when the Reynolds number is increased and the boundary layer becomes thinner this results in an increased pressure recovery through the "inlets" or holes. Similar data showing increased pressure recovery has been observed also for pressure measuring orifices as the boundary layer thickness is decreased.

3.5.2.2 Errors in Angle of Attack

In Ref. 3.5.6 it is concluded that an error in angle of attack is one of the largest contributors to the pre-test uncertainty in the total drag of a transport aircraft. It was stated in Ref. 3.5.6 that to maintain an accuracy in $C_D{}^+$ to a $\Delta C_D{}^+$ = 0.0001 that the error in angle of attack needs to be no greater than $\Delta\alpha$ = 0.01°. What the allowable error in angle of attack should be for afterbody tests is shown in the following examples where it is assumed that determination of complete or part body drag is to be within $\Delta C_D{}^+$ = 0.0001 or ΔC_D = 0.001 depending on which reference area is being used, i.e. wing or maximum cross section.

The first example involves an axisymmetric model that was used to investigate several different afterbodies (Ref. 3.5.5, 3.5.17 and 3.5.19). Axisymmetric and equivalent bodies of revolution (EBOR) models have been and still are extensively used, particularly when investigating new afterbody geometries or when general knowledge of afterbody test techniques is desired. In most of these tests, particularly where afterbody drag (and perhaps forebody drag) is being evaluated it is critical that the angle of attack be as close to zero as possible. How critical this might be was evaluated in Ref. 3.5.5. The sting mounted model used in this case had only one complete row of pressure orifices along its top meridian that were used to measure the pressures from which the pressure drags were calculated. A few orifices were on the bottom of the model to obtain check pressures. This is not an uncommon procedure and is done by many

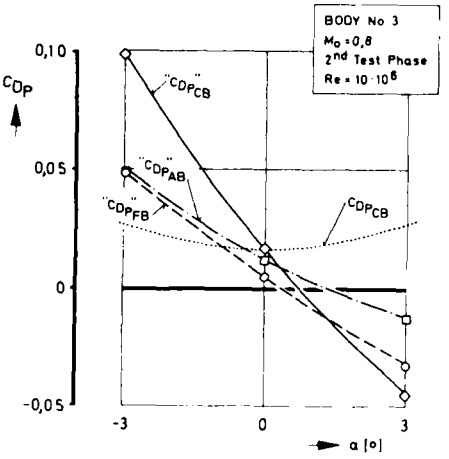

Required α-Accuracy	"CB"	"FB"	"AB"
$\frac{\Delta\alpha}{\Delta C_{DP}=0,001}$ =	0,0417°	0,0714°	0,100°

Fig. 3.5.8 Pressure Drag from Integrated Upper Pressure Row (Ref. 3.5.5)

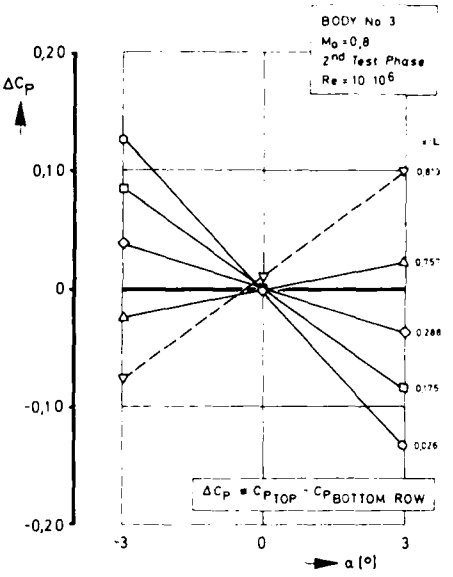

$\frac{x}{L}$ =	0,026	0,175	0,288	0,757	0,819
$\frac{\Delta C_P}{\Delta\alpha}$ =	-0,0475	-0,028	-0,013	+0,008	+0,030

Fig. 3.5.9 Check Pressure Difference versus Indidence (Ref. 3.5.5)

investigators. In Fig. 3.5.8 values of the complete and part body drag coefficients (i.e. "C_{DPCB}", "C_{DPFB}" and "C_{DPAB}) were determined, using the top row pressures as the model angle of attack was varied. The dotted curve identified by C_{DPCB} is what the "true" complete body pressure drag would be if computed with adequate pressures or by subtracting the correct friction drag from an accurate balance force.

Also shown in Fig. 3.5.8 is a table indicating the required accuracy in angle of attack (or how close must the model be to $\alpha = 0°$) in order that the errors in the respective drag coefficients do not exceed $\Delta C_{DP} = 0.001$. As can be seen the tolerance on α is greater for the forebody and afterbody pressure drags than it is for the complete body, i.e. 0.0714° and 0.100° respectively versus 0.0417°. These tolerances should not be a difficult measurement for state-of-the art angle of attack instrumentation, however, tunnel flow angularity may sometimes be difficult to assess.

Results of using pressures measured on the bottom of the axisymmetric model are given in Fig. 3.5.9. The differences in pressure coefficients at five different locations were measured as the model was varied from $\alpha = -3°$ to $\alpha = +3°$ from which was calculated the sensitivity of the pressure changes to the angle of attack. Information from the table in Fig. 3.5.9 can be used with the table in Fig. 3.5.8 to determine a critical ΔC_p that should not be exceeded to maintain $\Delta C_{DP} \leq 0.001$ (as far as an error due to angle of attack). For example; from Fig. 3.5.9 at X/L = 0.026, $\Delta C_p/\Delta\alpha$ = 0.0435/degr. and from Fig. 3.5.8 $\Delta\alpha/(\ ^{"}C_{DPCB}\ = 0.001) = 0.0417°$ and multiplying the two sensitivities indicates that the pressure coefficient differences at X/L = 0.026 should not exceed $\Delta C_p = 0.00181$ if α is not to be in error more than 0.0417° and that the error in C_{DPCB} is not to exceed $\Delta C_{DPCB} = 0.001$. As is apparent the use of the such check pressures can be helpful, but, as discussed in Ref. 3.5.5 the location of the check orifices can be critical.

Angle of attack effects on a typical aircraft afterbody are shown in Fig. 3.5.10 with results for three different afterbody/nozzle configurations which are normally tested when afterbody closure and throttle dependent drags are to be determined. There are two points to be made here. One being that an error in angle of attack is more critical as the angle increases and the other is the importance of determining incremented drags at the correct angle of attack. It can be seen by the slopes of the curves for the cruise or reheat nozzles that an error in angle of attack is not as critical near $\alpha = 0°$. For example the sensitivity of the cruise nozzle between $\alpha = 2°$ and $\alpha = 6°$ would be $\Delta C_{DAB}{}^{+}/\Delta\alpha = 0.0010$/degr. and for $C_{DAB}{}^{+}$ not to be in error greater than $\Delta C_{DAB}{}^{+} = 0.0001$ (due to an error in α) then the error in angle of attack should not be greater than $\Delta\alpha = 0.1°$ which is the same value as determined for $\Delta C_{DPAB} = 0.001$ (Fig. 3.5.8) in the above for the axisymmetric nozzle and again is a value that is not

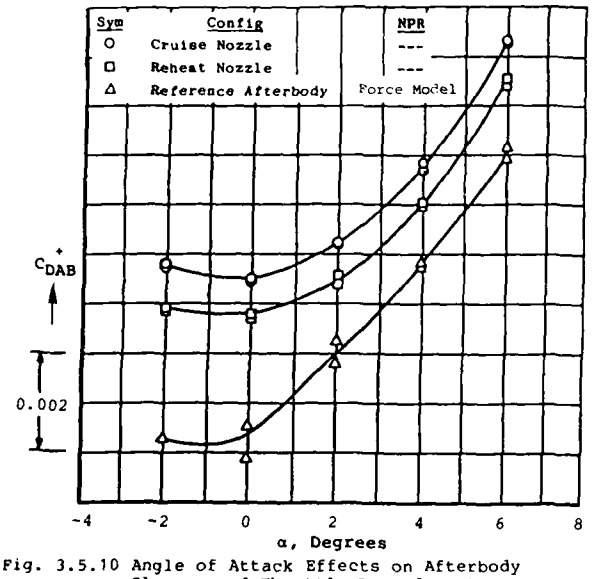

Fig. 3.5.10 Angle of Attack Effects on Afterbody Closure and Throttle Dependent Drags (Ref. 2.5.10)

difficult to measure. As for the second point, it is not infrequent that incremental drags determined at zero angle of attack are used indiscriminately at other angles of attack. An example of why this may not be a good procedure is to look at the differences in drag increments between the reference model and reheat model (Fig. 3.5.10) at $\alpha = 0°$ and $\alpha = 3°$. The increment at $\alpha = 0°$ is $\Delta C_{DAB}^{+} = 0.0024$ and at $\alpha = 3°$ is $\Delta C_{DAB}^{+} = 0.0014$, a difference of 0.0010 or 10 aircraft drag counts which could be of the order of 5 % of the zero lift drag at subsonic cruise. However, a check of the drag increments at the same angles of attack between the reheat and cruise nozzles shows that the increment remains the same, i.e. $\Delta C_{DAB}^{+} = 0.0007$ at $\alpha = 0°$ and $\alpha = 3°$. So these types of incremental drag changes are definitely configuration dependent and need to be allowed for when planning a test.

3.5.2.3 Errors in Total Pressure and Temperature

An error in total pressure along with an error in static pressure, both measured tunnel variables, will cause an error in the Reference Mach number which is a calculated variable. In Ref's 3.5.6 and 3.5.11 it is shown that Mach Number is quite sensitive to errors in both pressures, particularly at low subsonic Mach numbers. With proper instrumentation the error in total pressure should not be as great as the error in static pressure as previously discussed, however, when determining the uncertainty in Mach number both the uncertainty in total and static pressure need to be taken into account (see Ref. 3.5.6).

Similar consideration is needed when calculating Reynolds number from the measured variables of total static pressures plus total temperatures. The uncertainty requirements for these measured variables to minimize the uncertainty in the calculated Reynolds number are again discussed in Ref. 3.5.6.

3.5.2.4 Summary; Errors in Pressure, Mach Number, Angle of Attack etc.

The tunnel or free stream static pressure is perhaps the most critical measurable tunnel variable to be determined in afterbody testing, particularly when part body forces are being calculated. A test requirement of determining the drag, either total or part body, to within 1 aircraft drag count ($\Delta C_D = 0.0001$) is difficult to achieve when considering only errors in static pressure and angle of attack, let alone the many other small errors that may enter into the determination. Variation of afterbody drag with Reynolds number has been shown to be attributed to incorrect values of free stream static pressures (systematic error) which, in turn, were improved by a more precise calibration of the tunnel (AEDC 16 T) or by using averaged wall pressures as the "correct" static pressure (Göttingen 1 meter Tunnel). Angle of attack errors can affect integrated pressure drags, particularly if obtained from a single row of pressures. However, with proper check instrumentation and data it is possible to correct and maintain α within the required uncertainty. Tunnel total pressure and temperature are critical measurements to calculate Mach and Reynolds number but should not normally be a problem in afterbody testing.

3.5.3 Influence of Pressure Gradient, Blockage, Wall Angle etc.

Calibration techniques for the majority of transonic wind tunnels normally do not include corrections for changes to the calibration due to installation of a model or change in attitude of a model. Also during the empty tunnel calibration a test section pressure or Mach gradient may be determined, but, whether or not this gradient changes with model installation is normally not taken into account. The empty tunnel gradient is sometimes used to calculate a "buoyancy" effect which may be used to change the final drag value. In general, the change in test section flow conditions due to model

installation is attributed to blockage with a change in blockage affecting the pressure distribution in the test section and along the walls. Some small axisymmetric tunnels have the model supported through the throat which contributes to a different type of "blockage" than a model supported by a sting or strut.

During the following discussion both the influence of blockage and a change in pressure gradient may be discussed at the same time (i.e. a change in blockage causes a change in the pressure distribution). Of course there can be a change in pressure distribution with no change in blockage (e.g. with a change in afterbody geometry). The principal measurable variable influenced by a change in the pressure gradient and blockage is the tunnel static pressure. Whether or not there needs to be a correction for this change is discussed in the following examples.

Other factors that might change the tunnel calibration and cause an error in the test data include wall angle, porosity and humidity. They can also become important in afterbody testing and should, therefore, be carefully watched and kept well within the usual limits (e.g. avoidance of condensation). These parameters will be briefly discussed in para 3.5.3.2.

3.5.3.1 Influence of Pressure Gradient and Blockage

As pointed out in Ref. 3.5.5 and partially described in Fig. 3.5.11, conventional transonic tunnels cannot completely simulate free flight flow past model. It is therefore not surprising that the test section will have some longitudinal pressure gradients not representative of free flight and that these gradients will vary dependent on the size and attitude of a model (blockage), area distribution of a model and change in wall boundary layer growth when the tunnel total pressure is varied. The effect of three of these factors (presence of model, model geometry change and total pressure change) is shown in Fig. 3.5.12 for results using the axisymmetric models previously discussed (section 3.5.2.1). The pressure gradient was approximated by averaging all wall pressures between X/L = 0.0 to x/L = 0.5 and then between x/L = 0.5 to x/L = 1.0, taking the difference between these two averages and dividing by x/L = 0.5 (see Fig. 3.5.12).

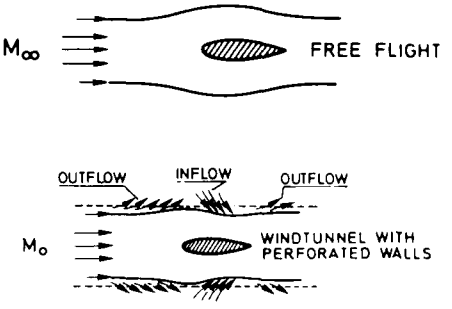

Fig. 3.5.11 Flow Field in Conventional/ Transonic Wind Tunnel and in Free Flight

As can be seen introduction of the model (Body No. 1) made the gradient less positive as did a change in body geometry to a more severe boattail (Body No. 3). In fact the gradient became negative with the presence of Body No. 3, except at the highest Reynolds number. Interference free wall pressure gradients are identified on the figure as computed target values (free flight) for bodies 1 and 3. These are computed pressure gradients along an imaginary wall in unconfined flow at the corresponding position of the real tunnel wall.

Only for body number 1 at the highest Reynolds number was "interference free" flow attained in this linearized approximation. Further analysis of the pressure gradients produced by bodies number 1 and 3 is presented in Ref. 3.5.5 with the conclusion that measured wall pressures are very sensitive to small changes in model geometry and can be used as inputs for tunnels with adjustable walls and to adjust or correct calibrations of conventional tunnels.

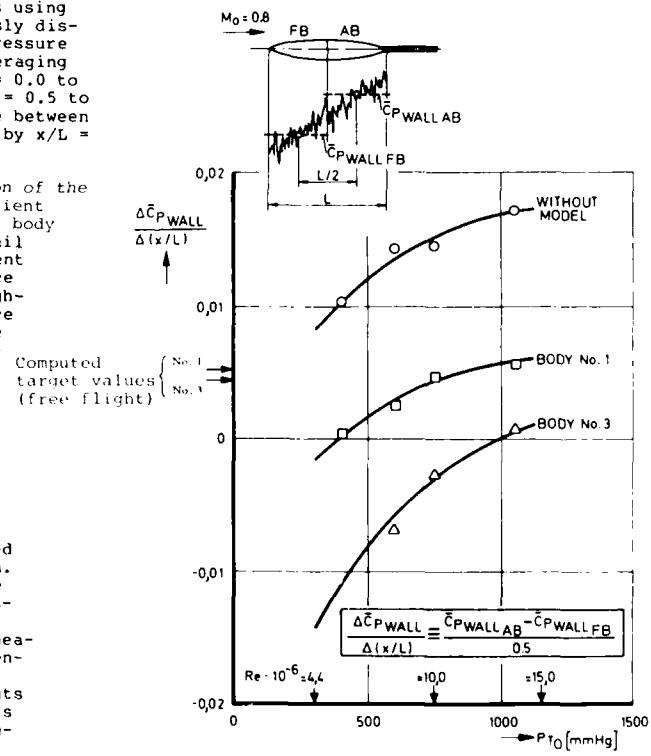

Fig. 3.5.12 Change of Tunnel Pressure Gradient; Göttingen 1 Meter Tunnel (Ref. 3.5.5)

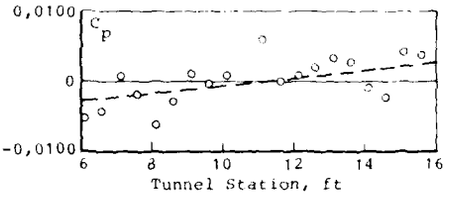

Fig. 3.5.13 Empty Tunnel Centerline Pressure Distribution and Gradient at M_∞ = 0.8; AEDC 16T (Ref. 3.5.10)

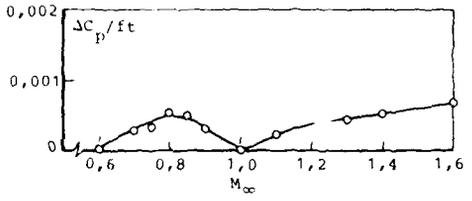

Fig. 3.5.14 Empty Tunnel Pressure Gradient; AEDC 16T (Ref. 3.5.10)

In Ref. 3.5.10 the results of the empty test section (AEDC 16T) pressure gradient (Fig. 3.5.13) were used to determine the "buoyancy" correction for a 10 foot long fighter aircraft model. The correction determined ($\Delta C_D^+ = 0.00022$) was stated to be well within the uncertainty of the usual model data and therefore a buoyancy correction was not required. As can be seen from Fig. 3.5.14 the gradient at $M_\infty = 0.8$ is the most severe subsonic gradient in the AEDC 16T. All gradients shown are stated to be within the uncertainty of the tunnel calibration data.

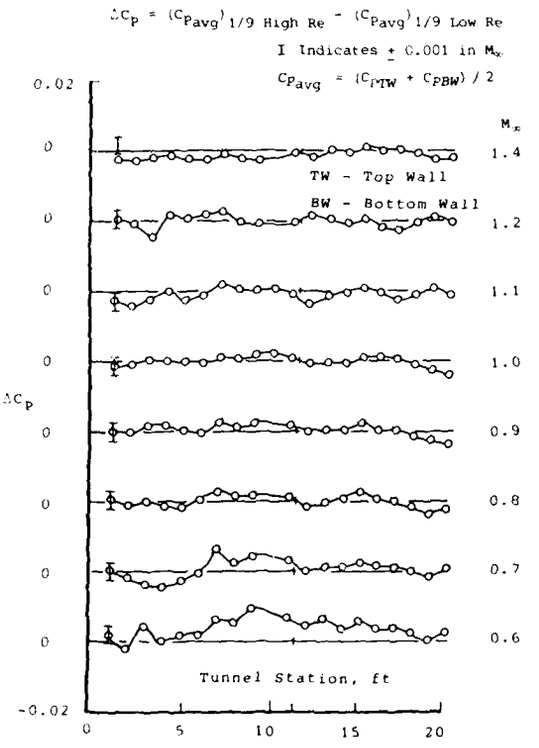

Fig. 3.5.15 Effect of Reynolds Number on Test Section Wall Static Pressures, 1/9 Scale Model; AEDC 16T (Ref. 3.5.23)

An indication of the change in pressure gradients in the AEDC 16 foot transonic tunnel with a change in Reynolds number (or total pressure) is discussed in Ref. 3.5.23 with results presented here in Fig. 3.5.15. The information shown is derived from a test of a 1/9 scale fighter model where the change in pressures at the high and low Reynolds number were used at each Mach number. Tunnel calibration data used was that reported in Ref. 3.5.20 and also discussed in section 3.5.2.1 of this chapter.

It was concluded in Ref. 3.5.23 that the changes in wall pressures with the change in Reynolds numbers are not significant for most Reynolds numbers except at Mach number 0.6 where the change in pressure gradient is not corrected by the current tunnel calibration. It was assumed that the uncertainty in the measurements correspond approximately to a deviation of ± 0.001 in Mach number.

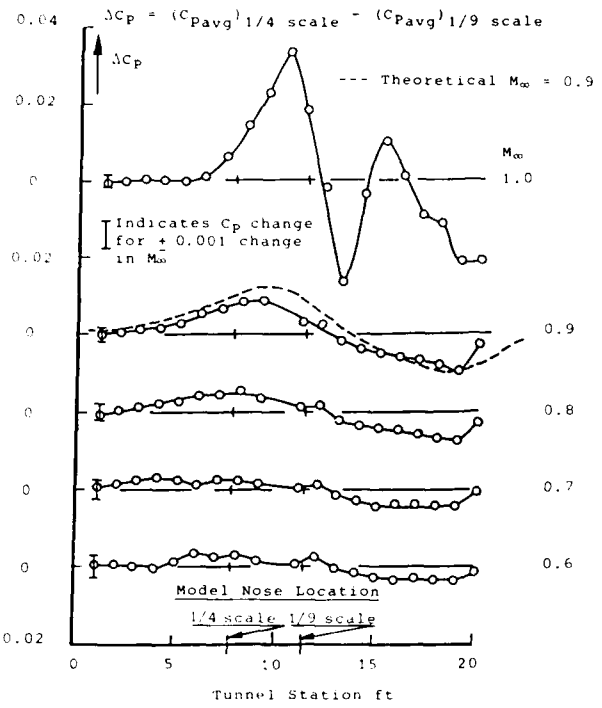

Fig. 3.5.16 Effect Model Size on Test Section Wall Static Pressures; AEDC 16T (Ref. 3.5.23)

The effect of a model size change (blockage) was presented and discussed in Ref. 3.5.23 for 1/4 and 1/9 scale fighter models in the AEDC 16 foot transonic tunnel. Some results are shown in Fig. 3.5.16 in which the differences in the average of the top and bottom test section wall pressures for longitudinal locations along the test section are given. As is noted in Ref. 3.5.23 even if there is at subsonic speeds a measurable effect of model size on test section wall pressures, the effect does not extend upstream of the test section and the model size influence on the averaged wall pressure is negligible. A calculated pressure distribution, at Mach number 0.9, shows good agreement with the measured distribution, with the theoretical distribution being determined by modeling the configurations as equivalent bodies of revolution and assuming a linear wall characteristic boundary condition. Also discussed in Ref. 3.5.23 was the effect of change in attitude (α = 0° to α = 6°) for the two different scaled models with the larger model showing the much greater effect on the wall pressures. However, when the pressures were averaged at each test section station the result was a $C_{Pavg} \approx 0$ for all stations.

For afterbody tests which are conducted in circular tunnels, in which the axisymmetric model is supported through the bellmouth of the tunnel, the static reference pressure may be located on either the tunnel wall or on the model ahead of the afterbody. It has been observed (Ref. 3.5.24) that the static reference pressure in such a test arrangement, can definitely be influenced by a change in afterbody geometry or by a change in model size (change in "blockage") making it difficult to establish the correct P_∞ and M_∞ for the flow over the afterbody.

3.5.3.2 Influence of Wall Angle, Porosity and Humidity

Besides the influence of pressure gradients and blockage, which are the most discussed and analyzed in the literature, other factors that can influence transonic test section flow parameters include wall angle, test section porosity and humidity. In Ref. 3.5.5 (section 2.3) it was proposed that changing the wall angle, at subsonic conditions, could be a way of changing the pressure gradient to the correct "free stream" pressure distribution at the wall.

Variable wall tunnels essentially use this same principle, but very little has been done in regard to afterbody testing in conventional tunnels. Another example of the use of a variable wall angle was presented in Ref. 3.3.23 where a zero angle was maintained subsonically and a predetermined schedule supersonically in the AEDC 16T. Accordingly the pressure distributions and gradients obtained were within the measurement uncertainties of the tunnel instrumentation.

In general transonic tunnel porosity is used to maintain uniform transonic flow and to minimize shock reflections. Discussed in Ref. 3.5.24 are test results showing a significant influence of porosity on afterbody pressure distributions at 0.9 and 0.95 Mach number as the porosity was changed from 2 % to 6%, however, there was negligible effect below 0.9 Mach number. In Ref. 3.5.23 are presented the results of tests investigating the effects of humidity in both subsonic and supersonic regimes with the conclusions that, in the AEDC 16T, the tunnel should be operated at free stream temperatures above the dew point, however, it is shown that this is not always possible at supersonic Mach numbers.

3.5.3.3 Summary; Influence of Pressure Gradient, Blockage, Wall Angle etc.

In general, a change in blockage changes the wall pressure distribution which leads to a change in the wall pressure gradient and the effective tunnel static pressure. Results discussed here show that for the Göttingen 1 metre tunnel there is a significant change from the empty tunnel wall pressure gradient when a model is installed, when the afterbody shape is changed and when the tunnel total pressure (Reynolds number) is changed. However, it has been shown previously that it is possible to average the wall pressures in the tunnel to obtain a corrected tunnel static pressure. For the larger AEDC 16 foot tunnel the empty tunnel pressure gradient indicated some changes with a change in model size, model attitude and tunnel total pressure (Reynolds number), but the changes were mostly within the uncertainties of the measurement instrumentation and the accuracy of the current tunnel calibration. A change in wall angle and porosity can significantly affect the test section flow condition and, therefore, requires appropriate tunnel calibrations and setting of wall schedules.

3.5.4 Comparison of Wind Tunnel and Flight Test Results

As pointed out in Chapter 3.3 (section 3.3.3) measuring surface pressures for determination of afterbody pressure drag is probably the best source of data when comparing afterbody/nozzle forces between wind tunnel and flight tests. Two test programs cited were the YF-17 (Ref. 3.5.13 and 3.5.16) and B-1 (Chapter 3.3 Reference 30) programs where extensive pressure instrumentation was used on both the models and the flight vehicles. Some of the results pertaining to the YF-17 program on pre-test uncertainties and post-test repeatabilities and scatter of pressure coefficients have already been discussed in sections 3.5.1.2 and 3.5.1.3.

Ref. 3.5.8 should be referred to for a detailed description of how to determine the in-flight thrust uncertainty which can in turn be used to estimate the in-flight total aircraft drag uncertainty.

3.5.5 Conclusions and Recommendations

A more complete discussion of error or uncertainty analysis would of course include errors due to force balances, local static pressures, model support systems etc. This chapter stressed the errors in the tunnel variables of static and total pressure, angle of attack, Mach number, temperature etc. and the influence on these errors of test section pressure gradient, blockage, wall angle, porosity and humidity. The uncertainty of these errors includes random and systematic errors and is the maximum error that can be reasonably expected. A systematic error is usually the more difficult to determine. A pre-test uncertainty analysis of these errors should be done to help determine the best instrumentation, test equipment, test methods and range of test conditions that will accomplish the test objectives.

For the majority of current afterbody tests, post-test analyses consist of determining repeatibility (or scatter) values without any attempt to estimate the post-test uncertainty. Repeatability is a good indication of the quality of the data when incremental values of drag are desired. However, a repeatability value is normally a measure of the random error of the test result and does not give a direct indication of any systematic errors that might be involved, although repeatability for several tests of the same configuration might include an unknown systematic error.

Post-test systematic errors can sometimes be estimated or at least identified by using widely different test or computational methods. Such a systematic error in the tunnel static pressure was shown to be the reason for a false variation in afterbody pressure drag with a change in tunnel total pressure or Reynolds number. A corrected static pressure was determined by a tunnel recalibration to determine the sensitivity of static presssure to Reynolds number or, as in another case, by determining a tunnel static pressure from an average of wall pressures.

It is concluded that computational methods need to be used not only for improving the understanding of the flow around the model, but also for understanding the interaction of the flows between the model and tunnel walls to compute adjustment factors to correct (or reduce) errors in the derived parameters (e.g. C_D^+, C_L^+). Such corrections could be incorporated into pre-test and post-test uncertainty analysis.

Drag coefficients to within $\Delta C_D^+ = \pm 0.0001$ are not usually attained even in the best tunnels where it is shown that errors due to variations in static pressure, pressure gradient, blockage, model size etc. are small and within the uncertainty of the measurement instrumentation. If such accuracy as $\Delta C_D^+ = \pm 0.0001$ is required or desired more attention will have to be paid towards pre-test and post-test uncertainty analyses. It is acknowledged that wind tunnel test facilities do strive to give useful data to the user, be it absolute or incremental data, however, it is believed that a review and use of knowledge gained over the past 10 years in the area of pre-test and post-test error analysis would improve the accuracy of the results of current afterbody tests.

3.5.6 REFERENCES

3.5.1	Richey, G.K., Surber, L.E. and Laughrey, J.A.	Airframe/Propulsion System Flow Field Interference and the Effect on Air Intake and Exhaust Nozzle Performance, AGARD-CP-150-(23), March 1975
3.5.2	Aulehla, F. and Lotter, K.	Nozzle/Airframe Interference and Integration, AGARD-LS-53(4), May 1972
3.5.3	Brazier, M.E. and Ball, W.H.	Accounting of Aerodynamic Forces on Airframe/Propulsion, Systems, AGARD-CP-150 (22), March 1975
3.5.4	Grellman, H.W.	YF-17 Full Scale Minimum Drag Prediction, AGARD-CP-242 (18), May 1978
3.5.5	Aulehla, F.	Drag Measurement in Transonic Wind Tunnels, AGARD-CP-242 (7), May 1978
3.5.6	Stanewsky, E. and Steinle, F.	Report of the AGARD FDP TES Conveners Group "Wind Tunnel Flow Quality and Data Accuracy Requirements", AGARD-AR-184, November 1982
3.5.7	Abernethy, R.B., et al	Handbook, Uncertainty in Gas Turbine Measurements, AEDC-TR-73-5, February 1973
3.5.8	MIDAP Study Group	Guide to In-Flight Thrust Measurement of Turbojets and Fan Engines, AGARD-AG-237, January 1979
3.5.9	Beers, Y.	Introduction to the Theory of Error, Addison-Wesley Publishing Co, Inc. 1958
3.5.10	Kennedy, T.L.	An Evaluation of Wind Tunnel Test Techniques for Aircraft Nozzle Afterbody Testing at Transonic Mach Numbers, AEDC-TR-80-8, November 1980
3.5.11	Stiles, R.J. and Boedicker, C.A.	An Example of Uncertainty Analysis in Compressor Testing, USAFA-TR-83-2, Air Force Academy Aeronautics Digest, Spring/Summer, 1982
3.5.12	Price, E.A. Jr.	An Investigation of F-16 Nozzle Afterbody Forces at Transonic Mach Numbers with Emphasis on Support System Interference, AEDC-TR-79-56, AFAPL-TR-79-2099, December 1979
3.5.13	Lucas, E.J.	Evaluation of Wind Tunnel Nozzle Afterbody Test Techniques Utilizing a Modern Twin Engine Fighter Geometry at Mach Numbers from 0.6 to 1.2, AEDC-TR-79-63, October 1980
3.5.14	Price, E.A., Jr.	An Investigation of F-16 Nozzle Afterbody Forces at Transonic Mach Numbers with Emphasis on Model Scale Effects, AEDC-TR-80-57, AFWAL-TR-81 2110, September 1981
3.5.15	Price, E.A., Jr.	Interference on a Model Afterbody from Downstream Support Hardware at Transonic Mach Numbers, AEDC-TR-80-27, January 1981
3.5.16	Lucas, E.J., Fanning, A.E. and Steers, L.	Comparison of Nozzle and Afterbody Surface Pressures from Wind Tunnel and Flight Test on the YF-17 Aircraft, AIAA Paper 78-992, July 1978
3.5.17	Aulehla, F. and Besigk, G.	Fore and Aftbody Flow Field Interaction with Consideration of Reynolds Number Effects, AGARD-AG-208 (IIF), October 1975
3.5.18	Leyland, D.C.	Lessons from Tornado Afterbody Development, AGARD-CP-339 (8), October 1982
3.5.19	Aulehla, F. and Besigk, G.	Reynolds Number Effects on Fore and Aftbody Pressure Drag AGARD-CP-150 (12), March 1975
3.5.20	Jackson, F.M.	Calibration of the AEDC-PWT 16-Foot Tunnel with the Propulsion Test Section at Various Reynolds Numbers, AEDC-TR-77-121, August 1978
3.5.21	Spratley, A.V. Thompson, E.R. and Kennedy, T.L.	Reynolds Number and Nozzle Afterbody Configuration Effects on Model Forebody and Afterbody Drag, AIAA 77-103, January 1977

3.5.22	Pozniak, O.M.	A Review of the Effect of Reynolds Number on Afterbody Drag, AGARD-CP-301 (16), May 1981
3.5.23	Lucas, E.J.	Model Size and Humidity Effects on Selected Calibration Parameters for the 16 ft Transonic Wind Tunnel at AEDC, AEDC-TR-81-17, November 1981
3.5.24	Laughrey, J.A. Richey, G.K. and Ferri, A.	Data Variance Due to Different Testing Techniques, AGARD-AG-208 (IIE), October 1975

3.6 CONCLUSIONS AND RECOMMENDATIONS (EXPERIMENTAL PART)

In the foregoing, detailed conclusions and recommendations were presented after the discussion of each topic. In the following, only the major issues are repeated together with additional thoughts which emerged from discussions among working group members during and after their last meeting in June 1984.

3.6.1 General Considerations

3.6.1.1 Extent of Afterbody Drag Changes

Subsonically, all geometric changes on the boattail will also affect the drag of the remaining aircraft portions. Typically, these changes in fuselage forebody drag are below $\Delta C_{DFB} = 0{,}005$ - in most cases even below 0,002 - and are, therefore, neglected in most cases (reference area is the fuselage maximum cross-section). Alternatively, a correction term may be computed for tests with a non-metric forebody from a few check pressures near the metric break. To do so, it is recommended that these upstream and lateral pressure changes be computed for subsequent integration of these pressure increments. This assumes that only small drag increments will be obtained and that the computation serves essentially as a tool to help extrapolate the pressure changes measured at a few check points over the non-metric portions of the model.

3.6.1.2 Drag Correlations

Present theoretical, empirical, and semi-empirical methods neither reach the accuracy of high quality measurements nor do they meet the requirements of project performance assessments. However, orders of drag magnitude can be predicted with the aid of published data and correlations as given for example by McDonald and Hughes (Ref. 3.1.15), by Pozniak (Ref. 3.1.9), by the Truncated Integral Mean Slope technique of Brazier and Ball (Ref. 3.1.16) and by the data of Aulehla and Lotter (Ref. 3.1.7). It is recommended that these four correlations be used and that further validation of these methods be undertaken.

3.6.2 Jet Simulation

3.6.2.1 Jet Temperature Effects

Omission of simulating the hot jet in a wind tunnel test results in pessimistic drag values for the aircraft, that is, up to 35 % of the jet-off afterbody drag. Since simulation of the full afterburning jet temperature in wind tunnel force models is difficult, it is recommended that such tests be conducted with cold jets and that the corrections of the type presented in chapter 3.2.1 be applied afterwards. As these corrections were developed for single jets, it is further recommended that such correlations be also developed for twin jet configurations.

3.6.2.2 Turbine Powered Simulators

The justification for Compact Multimission Aircraft Propulsion Simulators (CMAPS) is the need for simultaneous representation of the inlet and exhaust flows. For long coupled configurations with core engine length to engine face diameter L/D = 8,5 (B-1) .....11 (F-18) in the cruise mode, the inlet/exit interference is expected to be small, since on civil applications with isolated nacelles (L/D = 2) these effects are only marginal. Perhaps one should wait for the test results of ref. 3.2.13 for a L/D = 9,5. For long coupled configurations in the V/STOL and thrust vectoring mode, CMAPS will probably have an application; for short coupled configurations in the cruise mode there is a case for the development of a still shorter simulator, a C-CMAPS. The operation of CMAPS behind highly distorted inlet flows typical of many combat aircraft is not yet fully resolved. The calibration of CMAPS for such flows with strong swirls requires additional development work.

3.6.2.3 Ejector Powered Simulators

The Ejector Powered Simulator (EPS) has been shown to be capable of providing an adequate simulation of the inlet and exit flows for dry and reheat operation. It may, however, be necessary to bleed significant quantities of inlet flow. Also, different units to simulate dry and reheat conditions are necessary. The flexibility of size is probably the main advantage over the TPS and CMAPS. Further development of the EPS for short coupled configurations is recommended.

3.6.2.4 Annular Jet Sting

The concept of a single (or multiple) rear sting with annular jet(s) was shown to provide good representation of the interference for sting to nozzle diameters less than 0,7. The annular jet may be used to provide 6-component aeroforce measurements with a minimum support interference datum condition in combination with a special jet effects model. The

inlet flow is, of course, not simulated by this method. It is recommended that the problem of the clearance between sting and force model be further investigated (implications of metric thrust, controlled sting off-set etc.).

3.6.3 State-of-the-Art Assessment of Testing Techniques for Aircraft Afterbodies

3.6.3.1 Separation of Thrust and Drag

In chapter 3.3.2 it was shown that almost all possible arrangements of drag and thrust-minus-drag test rigs have been used in the past. There is no unique or "best" testing technique. As is obvious with force balances, great care must be given to the correct positioning of the metric break and to the accurate assessment of all tare and calibration forces. However, with highly integrated nozzles like the blow-in-door eject r or the isentropic ramp, the correct simulation of the (geometric) interfaces between the internal and external flows is very difficult to achieve if thrust and drag are measured by separate (flexible) balances. This is because of the movement of the two systems relative to each other. It is thus recommended that for these cases thrust-minus-drag be measured.

3.6.3.2 Drag Assessment by Force Measurement and by Pressure Integration

The basic question whether to use balance force measurements or surface pressure integration on complex (3-D) aircraft configurations is essentially answered by the phase of a project: during the early development stage, in which a large number of different afterbody configurations are tested, drag assessment from measured surface pressures is impractical and too expensive. This is due to the incorporation of modifications like the addition of filler pieces and fairings, and the removal of material by "filing-off" etc. However, during the later stage of a program when the configuration is close to being frozen, confirmatory tests with pure pressure plotting may be preferable in that this provides more detailed (local) information, e.g. the assessment of aerodynamic loads, the correct positioning of secondary inlets and exits etc. Also, comparative full-scale flight tests are usually done by pressure plotting purely from structural reasons (metric break). No further activities in this respect are recommended.

3.6.3.3 Wind Tunnel Model Support

Out of the predominant wind tunnel support systems, i.e., strut, wing tip, and annular jet sting, probably only the last one should receive further work for refinement (see also paragraph 3.6.2.4). Advanced computational methods should be utilized to calculate as far as possible the interference of the wind tunnel support.

3.6.3.4 Areas of Uncertainty

In choosing the optimum test arrangement for a particular test objective many additional aspects need to be considered; some of the most important ones were discussed in section 3.3.5, as for example: Complete versus part model duplication, upstream influence of geometric afterbody changes, location of the metric break, the effects of inlet fairing, of tail plane deflections, the effects of bleed and purge flows, and the need for duplication of model details as well as qualitative and quantitative flow measurement techniques to better understand the physics of the afterbody flow field. In the past, some of these items e.g., the location of the metric break and the amount of the upstream influence were the focus of controversy among specialists. However, with the present experimental knowledge and the power of current computational codes, most of these controversies have been settled because appropriate correction terms can be computed as explained in paragraph 3.6.1.1.

3.6.4 Afterbody Flow Instabilities

Unsteady flow separation may cause afterbody buffeting, which - in severe cases - can render the ride qualities of an aircraft and its function as a weapon platform completely unacceptable. To detect this phenomenon early in the development stage of an aircraft it is necessary that in wind tunnel afterbody testing at least the following two items are provided:

a) the oscillating afterbody flow field (excitation) and

b) suitable sensors of this excitation

The correct response of the elastic aircraft structure, of course, cannot be obtained from a "rigid" wind tunnel model but may be computed from the measured excitation distribution and the known aircraft structural characteristics. Item a, the excitation, normally is provided if both the afterbody geometry and the jet pressure ratio, are correctly duplicated. Dynamic pressure transducers, item b, will respond to these excitation pressures on a standard ("rigid") afterbody model; if provided in sufficient number, they will also give the distribution of the excitation. The dynamic signals of a strain gauge force balance cannot show afterbody buffeting directly. This is because the model differs from the aircraft in mass, stiffness and damping. However, the onset of buffet can be detected provided the resonance frequencies of the model have been determined in a separate test and are filtered from

the balance output. Naturally, the power spectral density is then also not representative. Therefore, in such afterbody buffet tests at least a limited number of dynamic pressure pick-ups should be provided. To cure afterbody buffeting corrective actions like reshaping of the afterbody and the installation of vortex generators may then be taken at an early stage of an aircraft development programme.

3.6.5 Error Analyses and Correction Methods

Although the principles of finding and correcting errors have been well known for a very long time, draw-backs continue to occur in the development of aircraft due to the fact that often relevant systematic errors are detected too late in the programme or sometimes not at all. Typical examples for this are the spurious Reynolds number trends of transonic wing shock locations and afterbody pressure drag values obtained from variable density wind tunnels. A further example is the afterbody drag measured by hot jet models with insufficient insulation of the outer model surface.

As recommended by many authors a careful pre-test analysis should always be made. This will not only help in making the optimum choice of instrumentation, test set-up and testing facility, but will also contribute to reduce systematic and random errors. However, because of lack of time and funds and, above all, because of the complexity of a comprehensive error analysis, the latter is normally not accomplished. In such cases at least a simple study should be conducted in which the sensitivity of computed quantities (e.g. C_D) to possible errors in the measured values (e.g. P_∞) for a varying parameter like the location of the metric break is assessed. A post-test analysis of random and systematic errors should also always be made in order to decide whether or not the test needs repeating with improved equipment.

Usually, systematic errors are only detected by switching to very different methods, for example, by using a different test rig or wind tunnel type, a different test fluid or by changing from wind tunnel to flight test or from experiment to theory. Sometimes, however, it may suffice to widen the field of observation, i.e. not restrict oneself to the changes on the test article, for example the afterbody, but to record also the pressure changes on the non-metric forebody and on the wind tunnel walls. A systematic error like an unintended small shift in tunnel pressure level may then be detected. This, however, normally requires that the scatter in the wall pressure distribution be first reduced by averaging/filtering. That is, a reduction of random errors is here a prerequisite for the detection of a systematic error. Monitoring of the wall pressures as a routine is, therefore, recommended for all wind tunnel tests. Finally, computational methods should be used wherever possible to better understand experimental results and to better plan new test concepts.

CONCLUDING REMARKS

Since detailed conclusions and recommendations were given in the previous chapters, only general concluding remarks will be made here.

In the ten years since publication of AGARDograph 208, much progress has been made both on experimental and numerical methods. Especially, the computational fluid dynamics (CFD) research and development has now reached the level of applicability for simple (single jet) geometry using viscous/inviscid interaction methods or solutions of the Navier-Stokes equations. Because of the tremendous progress which can be expected from the use of Vector-Computers within the next years, this part of the report may be considered to be only a "snapshot" from "Status 1984". At least this part of the present WG08 report should be revised in time, considering especially the progress of computational methods for three-dimensional viscous flow.
Experimental techniques have reached a very high level of reliability if proper correction procedures are applied and error analysis is performed as recommended.

It can be definitely stated that numerical analysis will not replace the wind tunnel test, but as an outcome of the Working Group, it may be stated that numerical analysis will play a more and more important role as a supplement to the experiment in the future.

AD-A172342

REPORT DOCUMENTATION PAGE

1. Recipient's Reference	2. Originator's Reference	3. Further Reference	4. Security Classification of Document
	AGARD-AR-226	ISBN 92-835-1533-1	UNCLASSIFIED

5. Originator Advisory Group for Aerospace Research and Development
North Atlantic Treaty Organization
7 rue Ancelle, 92200 Neuilly sur Seine, France

6. Title AERODYNAMICS OF AIRCRAFT AFTERBODY

7. Presented at

8. Author(s)/Editor(s)	9. Date
Various	June 1986
10. Author's/Editor's Address	**11. Pages**
Various	348

12. Distribution Statement This document is distributed in accordance with AGARD policies and regulations, which are outlined on the Outside Back Covers of all AGARD publications.

13. Keywords/Descriptors

Aerodynamic configurations
Aerodynamic characteristics
Afterbodies
Drag
Fighter aircraft

14. Abstract

Aircraft afterbody design is still one of the most critical problems for industry, especially in fighter aircraft development. The flow around the rear part of the fuselage is characterized by the simultaneous occurrence of interfering physical phenomena such as thick turbulent boundary layers, viscous flow separation, hot jet interference at the base and the boat tail, and jet plume expansion in three-dimensional transonic and supersonic flow. Even experimental techniques hardly fulfill requirements for correct wind tunnel simulation of all effects.

Drag prediction and drag minimization procedures for complex configurations are strongly dependent on the reliability of numerical and experimental flowfield simulation.

This publication reports on the progress which has been made by the AGARD ~~PDP~~ Working Group WG08, established to evaluate the state-of-the-art in experimental and computational techniques for aircraft afterbodies.

AGARD Advisory Report No.226 Advisory Group for Aerospace Research and Development, NATO AERODYNAMICS OF AIRCRAFT AFTERBODY (Report of Working Group-08) Published June 1986 348 pages Aircraft afterbody design is still one of the most critical problems for industry, especially in fighter aircraft development. The flow around the rear part of the fuselage is characterised by the simultaneous occurrence of intertering physical phenomena such as thick turbulent boundary layers, viscous flow separation, hot jet interference at the base and the boat tail, and jet plume expansion in three-dimensional transonic and supersonic P.T.O.	AGARD-AR-226 Aerodynamics configurations Aerodynamic characteristics Afterbodies Drag Fighter aircraft	AGARD Advisory Report No.226 Advisory Group for Aerospace Research and Development, NATO AERODYNAMICS OF AIRCRAFT AFTERBODY (Report of Working Group-08) Published June 1986 348 pages Aircraft afterbody design is still one of the most critical problems for industry, especially in fighter aircraft development. The flow around the rear part of the fuselage is characterised by the simultaneous occurrence of interfering physical phenomena such as thick turbulent boundary layers, viscous flow separation, hot jet interference at the base and the boat tail, and jet plume expansion in three-dimensional transonic and supersonic P.T.O.	AGARD-AR-226 Aerodynamics configurations Aerodynamic characteristics Afterbodies Drag Fighter aircraft
AGARD Advisory Report No.226 Advisory Group for Aerospace Research and Development, NATO AERODYNAMICS OF AIRCRAFT AFTERBODY (Report of Working Group-08) Published June 1986 348 pages Aircraft afterbody design is still one of the most critical problems for industry, especially in fighter aircraft development. The flow around the rear part of the fuselage is characterised by the simultaneous occurrence of interfering physical phenomena such as thick turbulent boundary layers, viscous flow separation, hot jet interference at the base and the boat tail, and jet plume expansion in three-dimensional transonic and supersonic P.T.O.	AGARD-AR-226 Aerodynamics configurations Aerodynamic characteristics Afterbodies Drag Fighter aircraft	AGARD Advisory Report No.226 Advisory Group for Aerospace Research and Development, NATO AERODYNAMICS OF AIRCRAFT AFTERBODY (Report of Working Group-08) Published June 1986 348 pages Aircraft afterbody design is still one of the most critical problems for industry, especially in fighter aircraft development. The flow around the rear part of the fuselage is characterised by the simultaneous occurrence of interfering physical phenomena such as thick turbulent boundary layers, viscous flow separation, hot jet interference at the base and the boat tail, and jet plume expansion in three-dimensional transonic and supersonic P.T.O.	AGARD-AR-226 Aerodynamics configurations Aerodynamic characteristics Afterbodies Drag Fighter aircraft

flow. Even experimental techniques hardly fulfill requirements for correct wind tunnel simulation of all effects.

Drag prediction and drag minimization procedures for complex configurations are strongly dependent on the reliability of numerical and experimental flowfield simulation

This publication reports on the progress which has been made by the AGARD-FDP Working Group WG08, established to evaluate the state-of-the-art in experimental and computational techniques for aircraft afterbodies.

ISBN 92-835-1533-1

flow. Even experimental techniques hardly fulfill requirements for correct wind tunnel simulation of all effects.

Drag prediction and drag minimization procedures for complex configurations are strongly dependent on the reliability of numerical and experimental flowfield simulation

This publication reports on the progress which has been made by the AGARD-FDP Working Group WG08, established to evaluate the state-of-the-art in experimental and computational techniques for aircraft afterbodies.

ISBN 92-835-1533-1

flow. Even experimental techniques hardly fulfill requirements for correct wind tunnel simulation of all effects.

Drag prediction and drag minimization procedures for complex configurations are strongly dependent on the reliability of numerical and experimental flowfield simulation

This publication reports on the progress which has been made by the AGARD-FDP Working Group WG08, established to evaluate the state-of-the-art in experimental and computational techniques for aircraft afterbodies.

ISBN 92-835-1533-1

flow. Even experimental techniques hardly fulfill requirements for correct wind tunnel simulation of all effects.

Drag prediction and drag minimization procedures for complex configurations are strongly dependent on the reliability of numerical and experimental flowfield simulation

This publication reports on the progress which has been made by the AGARD-FDP Working Group WG08, established to evaluate the state-of-the-art in experimental and computational techniques for aircraft afterbodies.

ISBN 92-835-1533-1

AGARD

NATO OTAN

7 RUE ANCELLE · 92200 NEUILLY-SUR-SEINE

FRANCE

Telephone (1) 47.45.08.10 · Telex 610176

DISTRIBUTION OF UNCLASSIFIED AGARD PUBLICATIONS

AGARD does NOT hold stocks of AGARD publications at the above address for general distribution. Initial distribution of AGARD publications is made to AGARD Member Nations through the following National Distribution Centres.Further copies are sometimes available from these Centres, but if not may be purchased in Microfiche or Photocopy form from the Purchase Agencies listed below.

NATIONAL DISTRIBUTION CENTRES

BELGIUM
Coordonnateur AGARD – VSL
Etat-Major de la Force Aérienne
Quartier Reine Elisabeth
Rue d'Evere, 1140 Bruxelles

CANADA
Defence Scientific Information Services
Dept of National Defence
Ottawa, Ontario K1A 0K2

DENMARK
Danish Defence Research Board
Ved Idraetsparken 4
2100 Copenhagen Ø

FRANCE
O.N.E.R.A. (Direction)
29 Avenue de la Division Leclerc
92320 Châtillon

GERMANY
Fachinformationszentrum Energie,
Physik, Mathematik GmbH
Kernforschungszentrum
D-7514 Eggenstein-Leopoldshafen

GREECE
Hellenic Air Force General Staff
Research and Development Directorate
Holargos, Athens

ICELAND
Director of Aviation
c/o Flugrad
Reyjavik

ITALY
Aeronautica Militare
Ufficio del Delegato Nazionale all'AGARD
3 Piazzale Adenauer
00144 Roma/EUR

LUXEMBOURG
See Belgium

NETHERLANDS
Netherlands Delegation to AGARD
National Aerospace Laboratory, NLR
P.O. Box 126
2600 AC Delft

NORWAY
Norwegian Defence Research Establishment
Attn: Biblioteket
P.O. Box 25
N-2007 Kjeller

PORTUGAL
Portuguese National Coordinator to AGARD
Gabinete de Estudos e Programas
CLAFA
Base de Alfragide
Alfragide
2700 Amadora

TURKEY
Department of Research and Development (ARGE)
Ministry of National Defence, Ankara

UNITED KINGDOM
Defence Research Information Centre
Kentigern House
65 Brown Street
Glasgow G2 8EX

UNITED STATES
National Aeronautics and Space Administration (NASA)
Langley Research Center
M/S 180
Hampton, Virginia 23665

THE UNITED STATES NATIONAL DISTRIBUTION CENTRE (NASA) DOES NOT HOLD STOCKS OF AGARD PUBLICATIONS, AND APPLICATIONS FOR COPIES SHOULD BE MADE DIRECT TO THE NATIONAL TECHNICAL INFORMATION SERVICE (NTIS) AT THE ADDRESS BELOW.

PURCHASE AGENCIES

Microfiche or Photocopy
National Technical
Information Service (NTIS)
5285 Port Royal Road
Springfield
Virginia 22161, USA

Microfiche
ESA/Information Retrieval Service
European Space Agency
10, rue Mario Nikis
75015 Paris, France

Microfiche or Photocopy
British Library Lending
Division
Boston Spa, Wetherby
West Yorkshire LS23 7BQ
England

Requests for microfiche or photocopies of AGARD documents should include the AGARD serial number, title, author or editor, and publication date. Requests to NTIS should include the NASA accession report number. Full bibliographical references and abstracts of AGARD publications are given in the following journals:

Scientific and Technical Aerospace Reports (STAR)
published by NASA Scientific and Technical
Information Branch
NASA Headquarters (NIT-40)
Washington D.C. 20546, USA

Government Reports Announcements (GRA)
published by the National Technical
Information Services, Springfield
Virginia 22161, USA

Printed by Specialised Printing Services Limited
40 Chigwell Lane, Loughton, Essex IG10 3TZ

ISBN 92-835-1533-1

END

DATE
FILMED

11-86

DTIC